EUROPEAN ORGANIZATION FOR NUCLEAR RESEARCH
CERN - PS DIVISION

CERN/PS 2000-007 (DR)

PROTON-ION MEDICAL MACHINE STUDY (PIMMS) PART II

Accelerator Complex Study Group*
supported by the Med-AUSTRON, Onkologie-2000 and the TERA Foundation
and hosted by CERN

ABSTRACT

The Proton-Ion Medical Machine Study (PIMMS) group was formed following an agreement between the Med-AUSTRON (Austria) and the TERA Foundation (Italy) to combine their efforts in the design of a cancer therapy synchrotron capable of accelerating either light ions or protons. CERN agreed to support and host this study in its PS Division. A close collaboration was also set up with GSI (Germany). The study group was later joined by Onkologie-2000 (Czech Republic). Effort was first focused on the theoretical understanding of slow extraction and the techniques required to produce a smooth beam spill for the conformal treatment of complex-shaped tumours with a sub-millimetre accuracy by active scanning with proton and carbon ion beams. Considerations for passive beam spreading were also included for protons. The study has been written in two parts. The more general and theoretical aspects are recorded in Part I and the specific technical design considerations are presented in the present volume, Part II. An accompanying CD-ROM contains supporting publications made by the team and data files for calculations. The PIMMS team started its work in January 1996 in the PS Division and continued for a period of four years.

*Full-time members: L. Badano[1)], M. Benedikt[2)], P.J. Bryant[2)] (Study Leader), M. Crescenti[1)], P. Holy[3)], A. Maier[2)+4)], M. Pullia[1)], S. Reimoser[2)+4)], S. Rossi[1)],
Part-time members: G. Borri[1)], P. Knaus[1)+2)]
Contributors: F. Gramatica[1)], M. Pavlovic[4)], L. Weisser[5)]
1) TERA Foundation, via Puccini. 11, I-28100 Novara.
2) CERN, CH 1211 Geneva-23.
3) Oncology-2000 Foundation, Na Morani 4, CZ-12808 Prague 2.
4) Med-AUSTRON, c/o RIZ, Prof. Dr. Stephan Korenstr.10, A-2700 Wr. Neustadt.
5) Sommer & Partner Architects Berlin (SPB), Hardenbergplatz 2, D-10623 Berlin.

Geneva, Switzerland
May 2000

PREAMBLE

A few years ago, when it became apparent that light-ion beams might be a better tool than protons for oncologists to treat certain deep-seated tumours, a collaboration between CERN, Med-Austron, GSI, Onkology-2000 and TERA started an investigation of possible approaches and design specifications. After clarification of these issues, the collaboration partners set up the PIMMS Study Group hosted by CERN in order to produce a reference design for a facility which could produce light-ion and proton beams. After a while GSI decided to pursue its own approach based on experience gained with its SIS synchrotron and associated test facility.

The aim of the reference design was to combine the expertise of the collaboration partners with the experience of CERN and to produce an optimized, state-of-the-art design which considers the synchrotron, the extraction process, the transfer lines and the gantries as a whole. Keeping in mind that this facility will be operated in a hospital environment, the approach favours simplicity, reliability and inherent stability by design, requiring minimum tuning and avoiding an elaborate control system.

This second part of the PIMMS report gives a complete and consistent set of parameters and a rather detailed description of the components of the reference design, providing a solid basis for the engineering of a leading-edge facility and a reference for comparison with possible future alternative solutions.

Kurt Hübner
Director of Accelerators

PREFACE

The underlying theory for the medical synchrotron design can be found in Part I published in CERN-PS/99-010 (DI). The present report, Part II, presents the mechanical and magnetic details of the design with explanations for the choices. The level of explanation and detail sometimes makes it difficult to get an overview of the design and make quick reference to its parameters. To solve this problem, the reader is recommended to consult the PIMMS Parameter List. Normally, this would be a separate document, but for convenience, it is included here as Appendix DD. There is also an accompanying CD-ROM that not only has all the reports produced by the study team, but also the lattice files and program that was used for the optical design, the input files for the magnetic field calculations and the drawings of the elements and layouts.

The success of ion therapy for cancer treatment will depend on a number of specific issues:

- An efficient solution being found for ion gantries.
- Demonstration that an ion synchrotron with gantries can be reliable and easy to operate in a hospital environment.
- A smooth beam spill to shorten the treatment times.
- Efficient exploitation of the high precision that ions offer.

With these points in mind, the PIMMS team has put considerable effort into:

- The design and error evaluation of the novel 'Riesenrad' (or 'independent-cabin') gantry.
- The design of operational functions that are orthogonal, for example, beam size adjustments at the patient do not affect the optical settings in the gantries, which makes the sensitivity to mechanical errors during rotation constant at all energies and all beam sizes.
- The design of a slow extraction scheme that is driven by a betatron core, leaves all optical functions constant during extraction, has a property called 'intrinsic smoothing' and allows additional smoothing by 'empty-bucket channelling'.
- The design of high-precision optics by the use of 'rotators' and concepts such as the 'bar' of charge.

These innovations have made the overall size of the complex a little larger than might be expected, but the separation of functions improves performance, simplifies machine operation and makes diagnostics more modular.

The PIMMS Team

CONTENTS PART II

* * *

CO-ORDINATE SYSTEM

Right-handed, curvilinear co-ordinate system (x, s, z) for the beam:
x is directed radially outwards in an anticlockwise ring

s is the direction along the beam
z is the vertical co-ordinate
ρ is the local radius of curvature

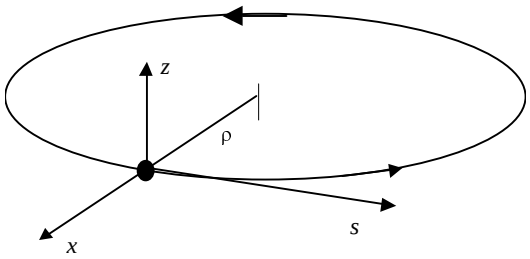

y is used as a general transverse co-ordinate that can replace either x or z.

FREQUENTLY-USED SYMBOLS AND ABBREVIATIONS

Subscript $_0$	denotes a reference value evaluated, e.g. at the origin, on central orbit, or at rest.
$< >$	Average over a distribution.
$\dot{}$, $'$	differentiation wrt time, differentiation wrt to s or $\Delta p/p$.
Superscript ^{T}	denotes transpose of a matrix.
Δ, δ, d	macroscopic, microscopic and infinitesimal steps.
FWHH	full width at half height.
RMS	root mean square.
F, D	focusing and defocusing lenses.
ES, MS	electrostatic and magnetic septa.
i	imaginary number.
rf	radio frequency.
wrt	with respect to.
dc	direct current.

NOMENCLATURE

A	atomic mass in atomic mass units.
$A = \sqrt{X^2 + X'^2}$	normalised betatron amplitude.
A_0, A_r	dc and ripple amplitudes of the particle spill intensity [particle/s].
A_m, B_m	harmonic coefficients in a 2-dimensional magnetic field.
A_b, A_{sb}	rf bucket area, stationary rf bucket area [eV rad].
$\boldsymbol{B}$, B_x, B_s, B_z	magnetic induction vector and components [T].
C	machine circumference.
C_x, C_x', S_x, S_x''	etc. principal trajectories (cosine and sine-like).
$\boldsymbol{D}$, D_x, D_z	dispersion vector and components [m].
$\boldsymbol{D}_n$, $D_{n,x}$, $D_{n,z}$	normalised dispersion vector and components.
D	diffusion constant.
e	elementary charge.
E_x, E_z	emittance (area phase space area) quoted with π apparent e.g. 10π mm mrad. Unless otherwise stated the emittance of a distribution will be the RMS value.

$\boldsymbol{E}$, E_x, E_s, E_z	electric field vector and components [V/m].
E, E_0	total energy, rest energy of a particle [eV].
F	duty factor for spill quality.
f	frequency [s^{-1}].
G	space-charge form factor.
h	perpendicular distance (normalised) from the separatrix to the origin.
h	rf harmonic number.
H_b, H_{sb}	rf bucket height, stationary bucket height [eV].
$\boldsymbol{H}$	Hamiltonian.
$\boldsymbol{I}$	identity matrix.
I	current [A].
j	current density [A/m^2].
K	improvement factor for speed of crossing into the resonance.
$K(s)$	general focusing constant (equivalent to spring constant for simple harmonic motion) [m^{-2}].
$k = (1/B\rho)(dB_z/dx)_0$	normalised (by momentum) quadrupole gradient [m^{-2}].
$k' = (1/B\rho)(d^2B_z/dx^2)_0$	normalised (by momentum) sextupole gradient [m^{-3}].
L	thickness of a scatterer [units consistent with L_r].
L_r	radiation length [units consistent with L].
ℓ_s	effective magnetic length of a sextupole [m].
m, m_0	particle mass and rest mass[eV] also used as an integer.
m_e	mass of electron [MeV].
$\boldsymbol{M}$, m_{11}, m_{12}, etc.	transfer matrix and elements of transfer matrix.
N	number of particles.
N_A	Avogadro's constant.
n	integer.
p	momentum [eV/c].
p, q	co-ordinates in a rotating system (rotator).
Q	spill quality.
$Q_{x,z}$	betatron tunes.
$q = ze$	charge [C].
r_e	classical radius of the electron [m].
$\boldsymbol{R}$	rotation matrix.
R	average radius of machine [m].
R	range of a particle in an absorber [m].
$S = (1/2)\beta_x^{3/2}\ell_s k'$	normalised (by β) sextupole strength [$m^{-1/2}$].
T, t_D	time [s] and dwell time on a mini-voxel [s].
T,	kinetic energy [eV].
T, T_{spill}	transit time [s], spill length [s].
u, u', v, v'	co-ordinates in a rotating frame (gantry).
V	voltage [V].
V	volume [m^3].
v_{scan}	scanning velocity of beam spot [ms^{-1}].
W	FWHH of beam spot distribution equal to size of a voxel [m].
$\boldsymbol{W} = \boldsymbol{y}^T\boldsymbol{\sigma}^{-1}\boldsymbol{y}$	motion invariant.
x, s, z	local curvilinear co-ordinate system for the beam [m].
X, X', Z, Z'	normalised co-ordinates.
Y	used to replace X'.

z, z_{inc}	net number of electronic charges on a particle, net number of charges on a particle incident on a scatterer.
Z	atomic number.
Z	impedance [Ω].
α	adiabaticity factor.
$\beta = v/c$	relativistic β.
$\gamma = m/m_0$	relativistic γ.
γ_t	γ at transition.
$\alpha_{x,z}$, ,$\beta_{x,z}$, $\gamma_{x,z} = (1+\alpha_{x,z}^2)/\beta_{x,z}$	Courant and Snyder functions(β [m], γ[m^{-1}].
$\varepsilon = 6\pi.\delta Q$	modified tune distance.
$\phi = dN/dt$	particle flux [s^{-1}].
ϕ, ϕ_s	rf phase, synchronous rf phase [rad].
Φ	magnetic flux.
$\Gamma = \sin\phi_s$	
$\eta = \gamma^{-2}-\gamma_t^{-2}$	phase slip factor.
$\kappa(s_0) = \frac{1}{24\sqrt{\pi C}} \int_{s_0}^{s_0+C} \beta_x^{3/2} \left[\frac{-1}{\lvert B_0\rho \rvert} \left(\frac{d^2 B_z}{dx^2} \right)_0 \right] \exp(3i\mu_x) ds$	resonance driving term.
λ, Λ	normalised trajectory co-ordinates measured in units of h.
$\lambda = dN/ds$	linear particle density in a spill, or entering a resonance.
$\mu_{x,z}$	betatron phase advance [rad].
θ_0	projected RMS (or characteristic) scattering angle [rad].
θ_s	scattering angle [rad].
ρ	radius of curvature [m].
ρ	linear particle density along the side of an unstable triangle and in distributions.
σ	root mean square value of a distribution with respect to the average.
$\boldsymbol{\sigma}$	sigma matrix.
τ	time constant [s].
Ω_s	synchrotron frequency [s^{-1}].
ω	angular frequency [s^{-1}].
$\Psi = dN/d(\Delta p/p)$	particle density in momentum space.

* * *

II-1 INTRODUCTION

The primary aim of this report is to present a design of a facility that would allow the direct clinical comparison of protons and carbon ions for cancer therapy using high-precision active scanning. As a secondary aim, the facility should also be capable of delivering proton beams by passive spreading. For these tasks a synchrotron using a third-integer slow extraction is preferred, since it offers the flexibility needed for dual-species operation and the variable energy needed for active scanning. The principal design requirement is that of a smooth spill, but as much emphasis as possible will be given to reliability and simplicity of operation. The underlying theory is given in Part I, the companion volume of this report [1]. A review of the overall design constraints, the key design decisions and some main parameters will be made in this chapter.

1.1 GENERAL SPECIFICATIONS AND DESIGN PHILOSOPHY

The general specifications for the machine are based on the following premises for the clinical requirements [2],

- A treatment will be on average 30 fractions with 2 Gray per fraction.
- An acceptable treatment time is 2 to 3 minutes per fraction.
- The maximum size of the treatment volume is assumed to be 2 litre when using active scanning and 7.5 litre when using passive scanning.
- An acceptable maximum depth is assumed to be ~27 cm.
- An acceptable minimum depth is assumed to be ~3.5 cm.
- In order to fully exploit all treatment rooms, the machine should be capable of switching species within a few machine cycles.
- The range in intensity extracted (particle/s) should be 1 to 650.

The above guidelines lead to the general performance specification that is given in Table 1.1. The extraction energies are adjusted such that the penetrations are approximately equal (~3.5 cm) at the lowest extraction energies of 60 MeV for protons and 120 MeV/u for ions. The maximum carbon ion energy of 400 MeV/u corresponds to a penetration of ~27 cm and was agreed by common consensus as being sufficient for irradiation therapy. The top proton extraction energy is essentially unlimited, since the machine has the potential to produce protons up to ~1200 MeV[*] , but a nominal maximum of 250 MeV is quoted for the passive spreading and 220 MeV (~30.5 cm penetration) for the active scanning. The latter has been chosen by making the ratio of the magnetic rigidities between the lowest and highest extraction energies approximately the same for the two species. This has been done in order that the phase-shifter-'stepper' module in the extraction line has the same ranges for betatron phase and amplitude variation for both types of particle. This point is important for apertures and optical solutions. The nominal intensity variation will be obtained by changing the current delivered by the source (1:65) and by changing the speed with which the betatron core moves the 'waiting' beam into the resonance (1:10 minimum).

[*] The production of such high energy protons constitutes a radiation hazard and, for this reason, the rf frequency is hardware-limited to ~2.85 MHz ,which allows the ions to reach their highest extraction energy, but limits the protons to ~400 MeV.

In addition, the scanning system will also be able to vary the level of the delivered dose over a more limited range. These figures are nominal values and, in many cases, it will be possible to extend the range considerably. For example, the variation of 1:10 quoted for the betatron core is a limit set by the low-energy proton operation due to the 'granularity' of the DAC. At the higher energy levels required for carbon ions, it will be possible slow the betatron core further to give at a range of say 1 to 50.

PIMMS performance parameters

	Active scanning (pencil beam)	**Passive scanning (large cross-section beam)**
Extraction energies for carbon ions	120-400 MeV/u	-
Extraction energies for protons*	60-220 MeV	60-250 MeV
Beam distributions	Gaussian in direction perpendicular to scan. Near-rectangular in scan direction	Flat to ±2.5% over circular 'good-field' region with near-gaussian tails
Nominal treatment times with carbon ions	60 spills in 2.4 min	-
Nominal treatment times with protons	60 spills in 2.25 min	120 spills in 3 min
Nominal doses delivered	2 Gray in 2 litre	2 Gray in 7.5 litre
Number of carbon ions in one spill at patient	4×10^8	-
Number of protons in one spill at patient	10^{10}	2×10^{10}
Start of spill can be triggered for synchronisation of breathing	Yes	Yes
Spot size variation at all energies (FWHH, full-width half-height).	4-10 mm	-
Intensity levels	The spill rate within a spill can be adjusted by the rate of change of the betatron core. A minimum variation of 1:10 is expected for the lowest energy protons and a maximum of 1:50 for the highest energy ions. Wider variations from spill to spill can be obtained by changing the beam intensity at injection 1:65. The number of intermediate levels is more a function of the control system than a fundamental limit	
Energy levels	The number of energy steps is limited only by the control system	
Scanning system under study.	20 cm × 18 cm	'Good-field' region 11 cm dia.

* The top extraction energy for protons is purely nominal. The accelerator can deliver protons up to 1.2 GeV.

Table 1.1 PIMMS performance parameters

In order to translate these performance figures into a machine design for high-precision scanning, several accelerator design choices have to be made. These are listed and briefly explained below:

- **The application of emittance dilution at injection**. This is necessary to equalise the transverse emittances of the two particle species over the extraction energy range and to reduce the space-charge tune shift at injection of the protons in the passive beam spreading mode. It is also convenient for the beam delivery optics that the emittances are larger than those typically obtained from linear accelerators.
- **Use of a uniform, wide momentum, medium transverse emittance beam for extraction**. This implies a preference for single-turn injection or multi-turn into precise emittances. The preference for a uniform beam in momentum also implies that stochastic

beam shaping would be an advantage [Part. I Section 6.2]. The wide momentum spread is obtained before extraction by placing the beam on the unstable fixed point of the rf. The insistence on precise emittances is for two reasons. Firstly, with the type of extraction chosen, the horizontal emittance determines the momentum spread in the extracted beam and, secondly, the vertical emittance affects directly the spot size at the patient.

- **Use of the acceleration-driven, amplitude-momentum extraction technique [Part. I Section 3.4] with the Hardt Condition [Part. I Section 3.6 and Ref. 3]**. This technique mixes the emittances of the particles being extracted so that there is a spread in the transit times in the resonance [Part. I Sections 4.1 to 4.3 and Ref. 4]. This affords some intrinsic smoothing of the spill [Part. I Sections 4.4 and 4.5 and Ref. 5]. The Hardt Condition imposes one particular relationship between the momentum and the emittance which gives minimum losses on the extraction septum by extracting all particles along the same separatrix.
- **Use of a betatron core for accelerating the beam into the resonance [Part. I Section 6.1 and Ref. 6]**. A betatron core is simple, reliable and smooth in its action. All lattice parameters can be kept constant during extraction.
- **Use of an rf empty bucket to channel the beam into the resonance [Part. I Section 6.5 and Ref. 7 and 8]**. This technique provides the front-end acceleration needed to desensitise the machine to ripple. Although other techniques exist, the rf bucket is effective and extremely cheap to apply since it uses the main rf cavity for acceleration. Front-end acceleration is only possible with an acceleration-driven extraction.
- **Use of the bar-like shape of the extracted beam in phase space [Part. I Chapter 9]**. The narrow shape of the beam in phase space can be exploited to control the horizontal beam size by including a phase shifter at the entry to the extraction line. This module will control the horizontal beam size in all gantries and fixed beam lines in the complex.
- **Use of a 'stepper' [Part. I Chapter 9].** Like the phase shifter mentioned above, this module is placed at the entry to the extraction line and controls the vertical beam size in all gantries and fixed beam lines. The 'stepper' can be separate or integrated with the phase shifter module mentioned above.
- **Use of 'rotators' [Part. I Sections 8.5 to 8.8 and Ref. 9].** A rotator makes the beam optics of a gantry-based delivery system completely independent of the gantry rotation. This includes the dispersion vector as well as the betatron phase spaces. The inclusion of the dispersion in the rotation matching is the essential feature that makes the alternative gantry mentioned below a viable proposition.
- **Investigation of an alternative gantry design [Part. I Section 9.3].** The high magnetic rigidity of the carbon ions stimulated an investigation of an alternative gantry design that became baptised the 'Riesenrad'. This design relies on the use of a rotator to match the dispersion function. The main advantages, are that it has much lower power consumption and weight than a conventional iso-centric gantry and the heavy magnetic equipment is kept near the axis.

1.2 DILUTED RING EMITTANCES

The next stage is to determine the transverse beam emittances in the ring that will decide the machine aperture. The main points concerning these key parameters are summarised below:

- **Normalised vertical emittances for the protons and ions:** These are chosen so that the two species will have approximately equal geometrical emittances over the range from the lowest to the highest extraction energy for each particle (as mentioned above the extraction energies have approximately the same ratio of magnetic rigidity for the two particles). The match cannot be perfect, but the idea is to have similar extraction conditions for the two particles. The numerical values for the emittances are chosen to achieve the wanted beam spot sizes at the patient of 4 to 10 mm for FWHH, which requires the betatron amplitude to be variable over the ratio of 1:13.4. Finally, this has to

be possible over the range of 2 in magnetic rigidity. This has proven to be technically feasible, whereas unequal emittances for the two species could increase the requirements to a point where the equivalent of two 'steppers' might be needed.

- **Normalised horizontal emittances for the protons and ions:** These are chosen so that the extracted beam momentum spread is of the order of one per mil, which restricts the range of the spiral step within the momentum bite and makes it possible to achieve a large enough step without excessively strong sextupole fields. It is also necessary to have an emittance for the protons that is large enough to reduce the space-charge tune shift at injection.
- **Emittance dilution for the protons and ions:** Fortunately, linac emittances are typically small (~1π mm mrad total normalised) and they can be diluted in a flexible and controllable way to meet the above requirements.

Table 1.2 summarises the final emittance values that have been chosen.

PIMMS diluted beam emittances in the ring

	Lowest extraction energy	**Top extraction energy**
Protons		-
RMS norm. horiz. emittance* [mm mrad]	0.519π	0.519π
RMS geom. horiz. emittance [mm mrad]	1.4286π	0.6679π
Total geom. horiz. emittance [mm mrad]	7.1429π	3.3393π
RMS norm. vert. emittance* [mm mrad]	**0.519π ***	**0.519π ***
RMS geom. vert. emittance [mm mrad]	1.4286π	0.6679π
Total geom. vert. emittance [mm mrad]	7.1429π	3.3393π
Carbon ions		
RMS norm. horiz. emittance* [mm mrad]	0.7482π	0.7482π
RMS geom. horiz. emittance [mm mrad]	1.4286π	0.7324π
Total geom. horiz. emittance [mm mrad]	7.1429π	3.6622π
RMS norm. vert. emittance* [mm mrad]	0.7482π	0.7482π
RMS geom. vert. emittance [mm mrad]	1.4286π	0.7324π
Total geom. vert. emittance [mm mrad]	7.1429π	3.6622π

* The RMS, normalised, vertical, proton emittance is the key value from which all others are derived.

Table 1.2 PIMMS diluted beam emittances in the ring

The fundamental choice in Table 1.2, from which the other parameters are derived, is the RMS, normalised, vertical emittance of the diluted proton beam, which is chosen to suit the spot sizes at the patient. The normalised ion emittance is then determined by equating the geometrical emittances for the two types of particle at the lower injection energy, as explained above. Finally, the normalised horizontal emittances have been made equal to the normalised vertical emittances for each particle. While creating a simple symmetric situation, this also provides an acceptable momentum spread in the extracted beams (see above) and later, this will be seen to satisfy the space-charge requirements for the protons.

1.3 CONSTRAINTS ON THE EXTRACTION LINES

Table 1.3 continues the discussion of vertical beam sizes by relating the emittances of Table 1.2 to the vertical spot sizes at the patient and, in so doing, determines the vertical betatron amplitude values at the patient and the ranges needed from the 'stepper' for the two species at their lowest and highest extraction energies. The 'stepper' will be mounted in the extraction line close to the main ring so that it can serve all beam delivery systems, but it can equally well be integrated into the design of each gantry.

The horizontal spot size at the patient does not depend on the ring emittances, but on the spiral step from the resonance. First, the spiral step* is made equal to the maximum spot size of 10 mm and then variations in the spot size are obtained by means of the phase shifter. In theory, the special geometry of the so-called 'bar' of charge will produce horizontal spot sizes from 10 mm down to 2 mm, well below the specified 4 mm. The phase shifter is installed in the extraction line close to the main ring so that, like the 'stepper', it can serve all beam delivery systems. It is an academic point whether the phase shifter and 'stepper' are designed as separate units or as a combined unit. Concerning the lattice configuration for the resonant extraction, the position of the electrostatic septum and the ring chromaticities are chosen according to the Hardt Condition, which leaves only the radial position of the electrostatic septum to be decided. This last parameter is a compromise between requiring either a too wide aperture, or a too strong sextupole. The consequences of reducing or increasing the spiral step and the radial position of the electrostatic septum are discussed in Sections 3.2.6 and 3.2.7. Table 1.4 summarise these points and with Table 1.3 defines the boundary conditions for the design of the extraction lines.

'Stepper' range for controlling vertical beam size

1. Assuming a gaussian distribution, then FWHH = 2.355 σ
2. For a 4 mm spot, σ = 4/2.355:= 1.699 mm
3. For a 10 mm spot, σ = 10/2.355 = 4.247 mm
4. Noting that the vertical beta function, $\beta_z = \sigma^{2}*\pi/E_{z,RMS}$ where E_z is the RMS, geometric emittance.

For protons	**60 MeV**	**250 MeV**
RMS emittance, E_z [mm mrad]	**1.4286π**	0.6679π
Range for β_z [m]:		
4 mm spot	2.02	4.32
10 mm spot	12.62	27.00
For ions	**120 MeV/u**	**400 MeV/u**
RMS emittance, E_z [mm mrad]	**1.4286π**	0.7324π
Range for β_z [m]:		
4 mm spot	2.02	3.94
10 mm spot	12.62	24.62

Table 1.3 'Stepper' range for controlling vertical beam size

* In fact, there is a range in the size of the spiral step that affects the FWHH of the final beam spot. This effect is compensated in a final correction applied in the gantry, see Section 5.1.2.

Resonance configuration and phase shifter range	
Hardt Condition	YES
Radial position of electrostic septum [mm]	35
Nominal spiral step [mm]	10
Minimum range of phase shifter [degree]	90°

Table 1.4 Resonance configuration and phase shifter range

1.4 INJECTION ENERGY AND THE INJECTION CHAIN

The emittance dilution required in the ring partially de-couples the injection chain making emittances and matching parameters flexible. The firm constraints are injection energy, beam current and duty cycle. While the beam current and duty cycle are determined by the clinical dose requirements and are subject to purely technological limits, the injection energies for the two species will be compromises since there are no absolute 'best' solutions.

The main points to be considered are:

- The operation becomes easier the higher the magnetic rigidity and more difficult the lower the rigidity due mainly to closed-orbit and focusing perturbations.
- The stripping efficiency for the carbon ions improves with energy and becomes close to 100% above 7 MeV/u. However, at the same time the revolution time diminishes leaving less time to fill the ring with a single-turn injection. This leaves a window between 5 and 7 MeV/u for single-turn injection. Multi-turn injection is similarly affected, but has a larger window.
- It should be noted that the protons have the additional problem of space charge at injection that pushes the 'unloaded' working point up towards the integer resonance. This increases the sensitivity of the machine to closed-orbit errors principally via the $\sin(Q\pi)$ term.

Figure 1.1 summarises the main conditions concerning the injection energy. A good choice would be to choose both injection energies to correspond to 0.7 Tm magnetic rigidity. However, the study was eventually based on a higher value of 0.76 Tm for the carbon ions (7 MeV/u) and a lower value of 0.65 Tm for the protons (20 MeV). The former was chosen in order that the linac might later be upgraded for use with alpha particles to create an astatine isotope and the latter was chosen to limit cost. However, the question of injection energy is discussed further at the end of the report where alternative scenarios are presented.

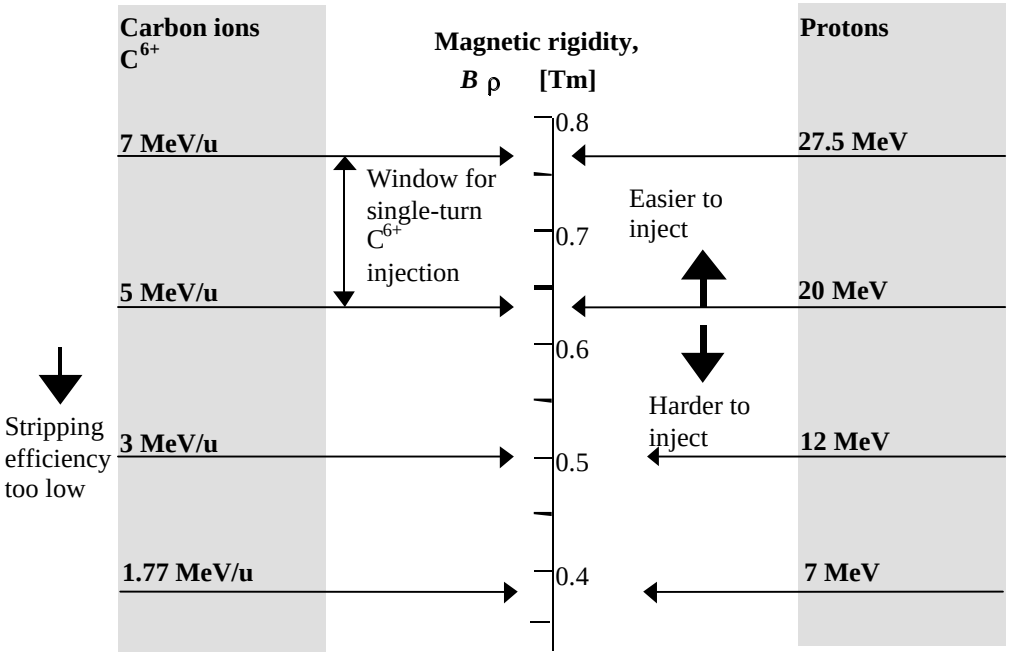

Figure 1.1 Comparison of injection energies for C^{6+} and protons

1.5 BEAM INTENSITIES

The clinical requirements detailed in Section 1.1 and Table 1.1 are converted into maximum particle numbers to be delivered to the patient during a single spill in Tables 1.5, 1.6 and 1.7. In these tables, the particle numbers are traced backwards through the accelerator chain to determine specifications for the particle sources assuming the more demanding, single-turn injection. The losses used in these tables are estimated values. Tables 1.5 to 1.7 are based on single-turn injection that is more demanding for the ion source than multi-turn injection which is described Chapter 7.

Proton active scanning (based on voxel scanning, raster has less loss)
2 Gray in 2 litre with 60 spills in 2.25 min (0.72 s ramp+1 s spill+0.52 s ramp)*

Point in acceleration chain	Efficiency	1/Efficiency	# of particles
At patient (for single spill)			**1.00×10^{10}**
Scanning (5 ms/voxel+1.5 ms loss switching)	77%	1.30	1.30×10^{10}
Transfer line	100%	1.00	1.30×10^{10}
Extraction (ES 95%, MS 95%)	90%	1.11	1.44×10^{10}
Stabilising start of spill	90%	1.11	1.60×10^{10}
Acceleration	100%	1.00	1.60×10^{10}
Trapping	90%	1.11	1.78×10^{10}
Injection (single turn)	95%	1.05	1.87×10^{10}
Linac	85%	1.18	2.20×10^{10}
RFQ	85%	1.18	2.59×10^{10}
LEBT	90%	1.11	2.88×10^{10}
Contingency	90%	1.11	3.20×10^{10}
No. of particles from source per fill			**3.20×10^{10}**

* Maximum cycle times taken form Table 3.5 from Section 3.3

Table 1.5 Particle inventory for proton active scanning

Proton passive spreading (spill with high loss scatterer)
2 Gray in 7.5 litre with 120 spills in 3 min (0.72 s ramp+0.25 s spill+0.52 s ramp)*

Point in acceleration chain	Efficiency	1/Efficiency	# of particles
At patient (for single spill)			**2.00×10^{10}**
Scanning (passive spreading)	40%	2.50	5.00×10^{10}
Transfer line	100%	1.00	5.00×10^{10}
Extraction (ES 95%, MS 95%)	90%	1.11	5.54×10^{10}
Stabilising start of spill	90%	1.11	6.16×10^{10}
Acceleration	100%	1.00	6.16×10^{10}
Trapping	90%	1.11	6.84×10^{10}
Injection (single turn)	95%	1.05	7.20×10^{10}
Linac	85%	1.18	8.47×10^{10}
RFQ	85%	1.18	9.96×10^{10}
LEBT	90%	1.11	1.11×10^{11}
Contingency	90%	1.11	1.23×10^{11}
No. of particles from source per fill			**1.23×10^{11}**

* Maximum cycle times taken form Table 3.5 from Section 3.3

Table 1.6 Particle inventory for proton passive spreading

Carbon ion active scanning (based on voxel scanning, raster has less loss)
2 Gray in 2 litre, with 60 spills in 2.4 min (0.87 s ramp+1 s spill+0.52 s ramp)*

Point in acceleration chain	Efficiency	1/Efficiency	# of particles
At patient			**4.00×10^{8}**
Scanning (voxel 5 ms, switching 1.5 ms)	77%	1.30	5.19×10^{8}
Transfer line	100%	1.00	5.19×10^{8}
Extraction (ES 95%, MS 95%)	90%	1.11	5.76×10^{8}
Stabilising start of spill	90%	1.11	6.40×10^{8}
Rebunching to change harmonic	90%	1.11	7.11×10^{8}
Acceleration	100%	1.00	7.11×10^{8}
Trapping	90%	1.11	7.90×10^{8}
Injection (single turn)	95%	1.05	8.31×10^{8}
Stripping	95%	1.05	8.75×10^{8}
Linac	85%	1.18	1.03×10^{9}
RFQ	85%	1.18	1.21×10^{9}
LEBT	90%	1.11	1.35×10^{9}
Contingency	90%	1.11	1.49×10^{9}
No. of particles from source per fill			**1.49×10^{9}**

* Maximum cycle times taken form Table 3.7 from Section 3.3

Table 1.7 Particle inventory for carbon ion active scanning

1.6 PARTICLE FLUXES, COUNTING RATES AND BEAM POSITION

1.6.1 Active scanning

The number of particles stored in the machine for active scanning has been based (with many approximations) on the nominal doses given in Table 1.1. The maximum scanning area depends on the design of the beam delivery equipment and

has also been specified in Table 1.1. The specifications for the particle counters in the 'nozzle', however, require additional explanation.

The beam spot sizes range from 10×10 mm^2 to 4×4 mm^2 FWHH. To avoid unnecessary complications with asymmetric distributions, it will be assumed that the beam spots are uniformly populated and have hard edges at the FWHH values. Using the maximum spot size (10×10 mm^2), the nominal spill time (1 s) and the maximum particle number in the machine (10^{10} protons or 4×10^8 carbon ions), a *nominal maximum flux*, Φ, can be defined as,

$$\Phi = \frac{\mathrm{d}^2 N}{\mathrm{d}S\ \mathrm{d}t} = 10^8\,\mathrm{mm}^{-2}\mathrm{s}^{-1} \text{ for protons;} \quad \Phi = \frac{\mathrm{d}^2 N}{\mathrm{d}S\ \mathrm{d}t} = 4\times 10^6\,\mathrm{mm}^{-2}\mathrm{s}^{-1} \text{ for carbon ions,}$$

where N is the number of particles, S the area and t is the time. This can be considered as a maximum condition for the particle counters in the 'nozzle'. Note that the machine can, in fact, deliver more particles per second (for the passive spreading mode) and more particles per unit area with smaller spot sizes, but these cases will not be considered for the nominal maximum flux for active scanning.

The on-line dosimetry has been based on a certain number of measurement bins in a nominal 'dwell' time over any given point in the tumour. Two examples have been investigated:

- Voxel scanning with a clock rate of 20 kHz and nominally 100 bins per voxel giving 5 ms irradiation time per voxel (Part I Section 5.12).
- Raster and mini-voxel scanning with a clock rate of 10 kHz and nominally 50 bins giving 5 ms irradiation time to any given point (Part I Chapter 11).

Thus, the particle counters need to deliver their particle counts with a clock frequency of at least 10 kHz and negligible electronic delay compared to the clock period for the readout.

The principle of the on-line dosimetry is to maintain a ±2.5% uniformity in the delivered dose by maintaining the same time structure (i.e. the number of measurement bins per position), but changing the average spill rate (dN/dt) so that dose is always nominally achieved in 5 ms (this assumes the degree of modulation of the spill is the same at all levels). The range required for the spill rate then comes from two sources:

- Dose levels vary between the distal and proximal slices in the tumour by a maximum factor of 100.
- For a given dose level, 6.25 times fewer particles are needed for a 4×4 mm^2 spot compared to a 10×10 mm^2 spot.

The situation is a little more complicated than indicated above because the dose requirements fall off very rapidly as one moves away from the distal slice. This is because the accumulated entry doses of the more distant slices are far from being insignificant. The present PIMMS particle numbers are such that the distal slice would require to be painted nearly five times (if calculated in Gray, but closer to 2.5 times if the RBE is included). The intention therefore is to paint the most distal 2 or 3 slices more than once and then to reduce the beam intensity so as to keep the' dwell'

or painting time at 5 ms. Thus, on a strict accounting basis, a dynamic range of 1:40 (instead of 1:100) is needed for the flux and 1:250 (instead of 1:625) is required for the spill rate dN/dt. However, since the machine will be able to fulfil the wider dynamic range and there may be future upgrades in intensity, the proposed specification in Table 1.8 for the counters in the 'nozzle' does not include the reduction that comes from the multi-painting.

There are two possible techniques for controlling the spill rate:

- The ramp rate of the betatron core
- The beam intensity stored in the ring at injection

The betatron core is very sensitive to the frequencies introduced by the DAC steps. This limits the dynamic range of the betatron core (for extraction purposes) to 1:10 at the lowest proton energy, to 1:50 at the highest ion energy. It appears possible that the injected current in the ring could be varied over a range of 1:65. This depends on the loss of sensitivity in the position monitors etc. being acceptable. The result is that in almost all cases the ring will be able to vary its spill rate over a much wider range than is strictly needed.

Specification of particle counters in the 'nozzle' for active scanning		
Protons:	**Maximum**	**Minimum**
Count rate, dN/dt [s^{-1}]	10^{10}	1.6×10^7
Flux density, $d^2N/(dS\ dt)$ [$mm^{-2}\ s^{-1}$]	10^8	10^6
Carbon ions		
Count rate, dN/dt [s^{-1}]	4×10^8	6.4×10^5
Flux density, $d^2N/(dS\ dt)$ [$mm^{-2}\ s^{-1}$]	4×10^6	4×10^4
Measurement bin [μs]	50 or 100	
Clock frequency [kHz]	10 or 20	

Table 1.8 Specification of particle counters in the 'nozzle' for active scanning

1.6.2 Passive spreading

For passive spreading the situation is simpler with only protons to be considered. The particle number is higher (2×10^{10}), but the dose is spread over a larger area (20×20 cm^2) and delivered over a longer time bin (250 ms). In this case, the counters must be able to accumulate the total number of particles and to indicate that a pre-determined threshold has been reached with an accuracy of ±2.5%. The principle is to keep a reasonable irradiation time (200 ms), to divide this into 200 or more measurement bins and to adjust the intensity in the machine or the ramp rate of the betatron core to deliver approximately the correct number of particles in that time. As before, the distal to proximal doses will have a maximum ratio of 1:100, but the distal slice may be painted several times. The specification is written in Table 1.9 in an analogous way to Table 1.8.

Specification of particle counters in the 'nozzle' for passive spreading		
Protons:	**Maximum**	**Minimum**
Count rate, dN/dt [s^{-1}]	8×10^{10}	8×10^{8}
Flux density, $d^2N/(dS\ dt)$ [$mm^{-2}\ s^{-1}$]	2×10^{6}	2×10^{4}
Measurement bin [ms]	≤10	
Clock frequency [kHz]	≥1 kHz	

Table 1.9 Specification of particle counters in the 'nozzle' for passive spreading

1.6.3 Beam position measurement

The beam position is only needed for active scanning and at a lower sampling rate than the particle flux. Sampling the position at a few kHz with a precision of ±0.1 FWHH of the spot is sufficient. The slower sampling rate relies on the fact that the response of the magnet system is limited to 10 m/s at the maximum extraction energy. In 1 ms, this corresponds to a movement of 1 mm (i.e. 10% of the largest spot). To maintain this precision over the full range of rigidity and spot size, the position needs to be sampled at a few kHz.

1.7 SUMMARY

The design study will be based on the principal parameters and design choices reviewed above. The ring is designed for a high stability of the extracted beam. The extraction line and gantry designs are intimately related to the ring design and the extraction parameters. Thus the ring, extraction lines and gantry form an integral design. In contrast, the injection lines and linacs are somewhat decoupled from the rest of the complex by the emittance dilution at injection into the ring. It is therefore somewhat easier to modify the injection chain than the extraction chain. The basic design with some alternative scenarios will be presented in the sequence,

- The main ring
- The extraction lines and gantry.
- The injection chain.
- Alternative scenarios, such as a lower injection energy for the protons.

For quick reference, the parameters, tolerances and layout drawings are collected together and presented separately in a parameter list [10].

References

[1] PIMMS Group, *Proton-Ion Medical Machine Study (PIMMS), Part I*, CERN-PS/99-010 (DI).

[2] U. Amaldi, M. Silari (editors), *The TERA project and the centre for oncological hadrontherapy*, The TERA Foundation, (INFN, Frascati, 1995, II Ed.).

[3] W. Hardt, *Ultraslow extraction out of LEAR (transverse aspects)*, CERN Internal Note PS/DL/LEAR Note 81-6, (1981).

[4] M. Pullia, *Transit time for third order resonance extraction*, CERN/PS 96-36 (DI).

[5] M. Pullia, *Time profile of the slowly extracted beam*, CERN/PS 97-50 (DI).

[6] L. Badano, S. Rossi, *Characteristics of a betatron core for extraction in a proton-ion medical synchrotron*, CERN/PS 97-19 (DI).

[7] R. Cappi, C. Steinbach, *Low frequency duty factor improvement for the CERN PS slow extraction using rf phase displacement techniques*, Accel. Conf., Washington, IEEE Trans. Nucl. Sci., Vol. **NS-28**, No. 3, (1981).

[8] M. Crescenti, *RF empty bucket channelling with a betatron core to improve slow extraction in medical synchrotrons*, CERN/PS 97-68 (DI), (Jan. 1998).

[9] L.C. Teng, Private communication, Laboratory notebook (Jan. 1970) and Internal Report LL-134 (Oct.1986).

[10] PIMMS *Parameter List.* Normally, this would be published as a separate document, but for convenience, it has been included here as Appendix DD.

* * *

II-2 THERAPY COMPLEX

Before entering the mechanical details of the accelerator complex, it is useful to step back and take a more holistic view of the therapy centre in which the different activities are integrated. Once this has been done, the chapter sets out the basic nomenclature that will be used to define the accelerator elements and makes some general statements concerning the design techniques.

2.1 THE FACILITY

2.1.1 General layout

The facility is planned on a green-field site with access from two sides (see Figure 2.1). The layout considers a strict separation between public access (patients) and non-public access (scientists). The layout is split into four main areas:

- The **S*cience Area***, where the doctors, treatment planners, biologists and accelerator physicists etc. will work and find their offices, laboratories, computer centre and workshops. There will be a common lobby, administration area, auditorium and library.
- The ***Accelerator and Transfer Line Area*** containing the main synchrotron ring, the linacs and the main extraction transfer line from which the beam is diverted into the various treatment rooms.
- The ***Medical Area*** (ambulatory), which includes patient reception, examination, preparation etc.
- The ***Treatment Area***, which includes preparation rooms and the five treatment rooms; three with gantries and two with fixed beam lines.

The clear separation between areas allows for the further development of each part as the design intensifies and the whole project evolves. Thus, the further development of any part of the project will not disturb the functionality of the other parts. Access to the treatment spaces is granted directly from the outside to allow for the installation of the heavy equipment. The patient accesses a facility that shows a conventional hospital-like environment. The patient does not face the more industrial like complex of the accelerator side.

2.1.2 The '*Science area*'

This part of the building houses all the necessary functions for the science area of the facility. Workshops, laboratories, computer centre and offices are combined to offer ideal research possibilities, make the computationally-intensive treatment plans, produce patient-specific equipment and to operate the accelerator and beam lines. Nevertheless, flexibility to accommodate other functions is maintained. This part can "grow" individually. Attached to this area is an auditorium, the library, the cafeteria and space for administration functions. Short distances connect the accelerator to the medical complex.

2.1.3 The '*Accelerator and transfer line area*'

A large hall houses the two linacs and the synchrotron including the (local) shielding and the cooling equipment. Trucks carrying the heavy magnets can drive directly into the hall. The main extraction transfer line runs parallel to the linacs, but in the opposite direction, hence creating a tighter overall layout. Adequate space for shielding is provided. This area is a radiation zone with no access during operation and restricted access during shutdown periods.

2.1.4 The '*Medical Area*'

The medical spaces for reception, registration, diagnosis and preparation of the patients are housed in a two-storey structure with a basement. A centrally located lobby splits the building. The building can expand along its longitudinal axis and be shifted "up and down" depending on future space requirements and the final layout of the treatment spaces. Short distances to the latter are foreseen.

Possible patient care rooms can be located on the second half of the second floor. A dear distinction between public and closed areas allows for easy orientation. Natural daylight illumination and the small-scale design will help not to intimidate the patient but to make him feel comfortable in a friendly and reassuring atmosphere.

2.1.5 The '*Treatment area*'

The 'focal' points are the centrally located treatment rooms. They represent the interface, between the three main activities or services that prepare the patient, calculate the treatment plan and operate the accelerator. The patient preparation areas are situated directly outside the labyrinths with the waiting areas adjacent. Five treatment rooms are planned and a biology space is foreseen for possible future development. Shielding is according to specification.

The treatment space area can "grow" along the direction of both the transfer line ("left and right") and - to a certain degree - along the direction of the beam lines inside the five treatment rooms ("up and down") without changing the general layout. Outside access from "top and bottom" is foreseen. A basement houses necessary HVAC equipment.

Once the patient has been prepared and aligned in his body mould, the entire accelerator complex is put under computer control to execute the treatment plan. Normally, there will be no human intervention during treatment and the computer will also manage unforeseen situations and emergencies. The supervising doctor and machine operators will monitor the treatment, but will only be able to make an emergency termination of the treatment.

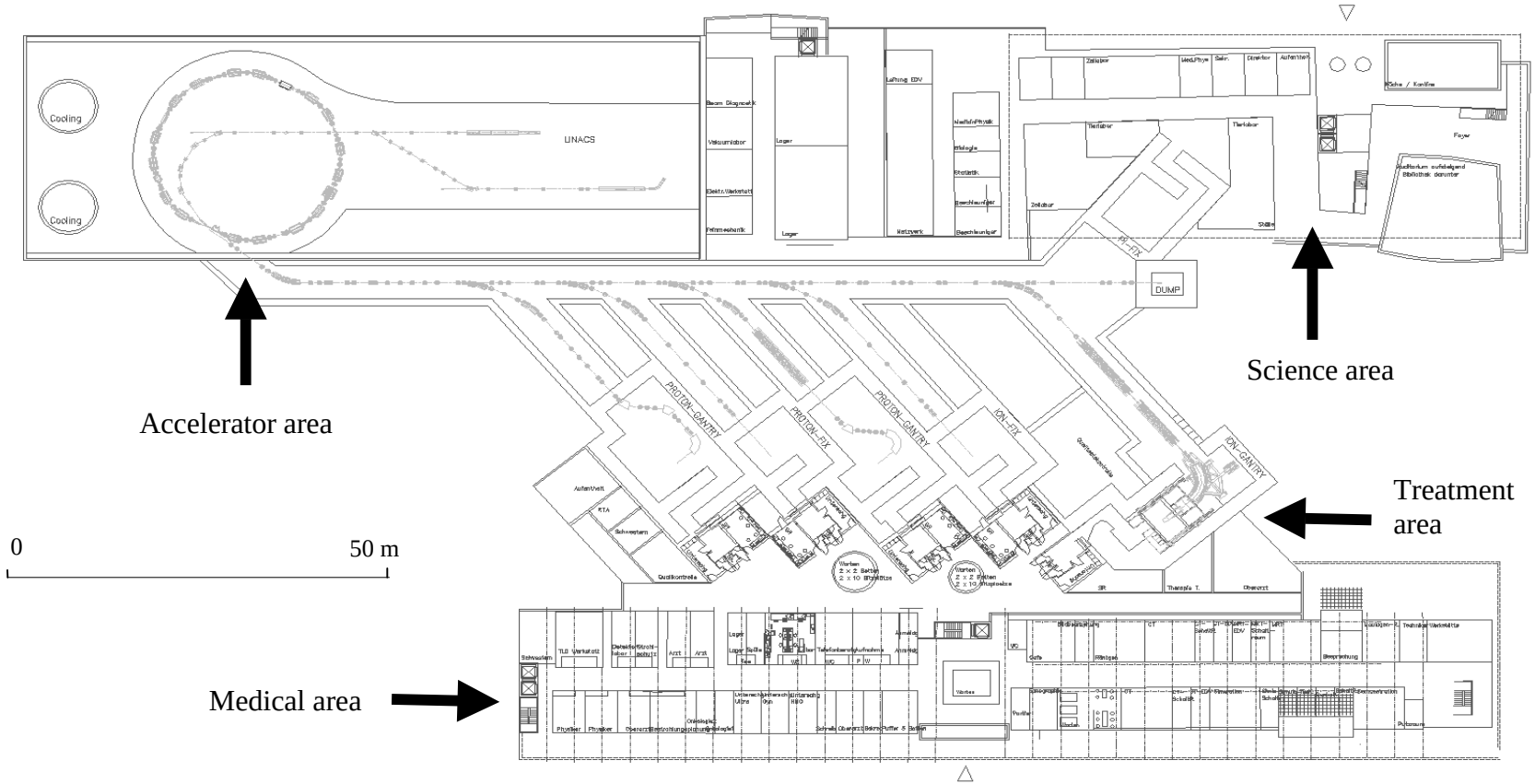

Figure 2.1 Layout of the PIMMS cancer therapy centre

2.2 NOMENCLATURE FOR THE ACCELERATOR COMPLEX

The accelerator complex comprises two injection chains (protons and carbon ions), a synchrotron and an extraction line that can be extended in a modular fashion to serve several short beam channels to treatment rooms with fixed beam lines or gantries. The different sections are given two-letter mnemonics to aid recognition (see Table 2.1). The carbon ion injection channel is a short section of line that connects to the proton line and the last section of the proton line is used by both types of particle.

Mnemonics for sectors in the accelerator complex

Proton linac	PL	Main ring	MR
Carbon linac	CL	Main extraction line to dump	EX
Injection line from proton linac to main ring	IP	Secondary extraction lines from the main extraction line to treatment rooms	T1, T2, T3 etc,
Injection line from carbon linac to proton injection line	IC		

Table 2.1 Mnemonics for the accelerator complex

Similarly, the elements in these sections are also given a two-letter mnemonic (see Table 2.2).

Mnemonics for accelerator elements

BC	Betatron core	MB	Main dipole in synchrotron	SA	Scatterer
BU	Bumper dipole	MS	Magnetic septum	SC	Beam scraper
CA	RF cavity	PM	Profile monitor	SH	Schottky monitor
CO	Collimator	PX	Horiz. beam position monitor	SS	Straight section (drift space)
CT	Fast current transformer	PY	Vert. beam position monitor	ST	Beam stopper
DC	Slow current transformer	QA	Air-cored, correction quad.	SV	Sector valve
DK	Dump bumper	QF	Focusing quadrupole	SW	Switching dipole in lines
DP	Beam dump	QD	Defocusing quadrupole	VC	Vert. corrector dipole
ES	Electrostatic septum	QK	Tune kicker	VG	Vacuum gauge
FO	Stripping foil	QR	Rotating quadrupole	VP	Vacuum ion pump
HB	Horiz. bending dipole in lines	QS	Skew quadrupole	WB	Wide-band pickup
HC	Horiz. corrector dipole	RA	Raster scanning dipole	XC	Chromaticity sextupole
IC	Ionisation chamber	RF	Ridge filter	XR	Resonance sextupole
LS	Scintillation screen				

Table 2.2 Mnemonics for the accelerator elements

The uniqueness of the element names is based on the sequential numbering of the drift spaces between the linear lattice elements (i.e. the main dipoles and quadrupoles) following the rules given below:

- Element numbering is in the beam direction.
- The principal drift spaces between the linear lattice elements (i.e. the main dipoles and quadrupoles) are numbered sequentially.

- In the main ring, numbering starts with the drift section in which the injection and extraction are situated.
- The linear lattice elements take their number from the upstream space, for example, the sequence SS MR 01; QF MR 01; SS MR 02; MB MR 02; etc. refers to the main ring straight section 01, followed by quadrupole 01, followed by straight section 02, followed by main dipole 02 and so on.
- Sub-division of the principal drift spaces is done by adding a decimal number (e.g. SS IP 03-01 is the first sub-section of the drift space number 03 in the proton injection line).

Format for drift spaces:	SS	MR	05	-	02
	Element mnemonic	Sector mnemonic	Drift space		Sub-space

- The auxiliary elements, for which principal drift spaces have to be sub-divided, take their numbers from the upstream sub-space (e.g. BS MR 03-01 is the beam scraper after space SS MR 03-01).

Format for element names:	BS	MR	03	-	01
	Element mnemonic	Sector mnemonic	Drift space		Sub-space

2.3 THE ACCELERATOR COMPLEX

Figure 2.2 shows the layout of the injection chain with separate linacs for the protons and carbon ions, the synchrotron, transfer lines, gantries and fixed beam delivery stations of the PIMMS complex. The design is not site related and is meant to be a demonstration, or generic, layout.

It has not been possible to design the linacs within the framework of the study and the emittances and lattice parameters used are somewhat arbitrary. Since there will be a controlled emittance blow-up between the injection lines and the ring (see Sections 1.1 and 1.2), these parameters are de-coupled, to a large extent, from the rest of the complex and this lack of detail is less important. Although individual linacs are shown, it may be possible to combine the acceleration of the protons and carbon ions into a single RFQ and linac [1], albeit with a probable reduction of the proton energy. The implications of a lower proton injection energy are discussed in Section 9.2

The ring is designed specifically to feed particles smoothly into the resonance and to suppress ripple in the extracted beam spill. The optical design from the ring to the beam delivery stations follows an integrated scheme and care should be taken to understand the principles if any changes are required.

The beam delivery stations:

- A proton gantry for active scanning (line T1),
- A proton fixed beam line with active scanning (line T2),
- A proton gantry for passive spreading (line T3),
- A carbon-ion fixed beam line with active scanning (line T4),
- A carbon gantry for active scanning (line T5),

have been chosen simply as examples of the different possibilities and do not represent any definite proposal.

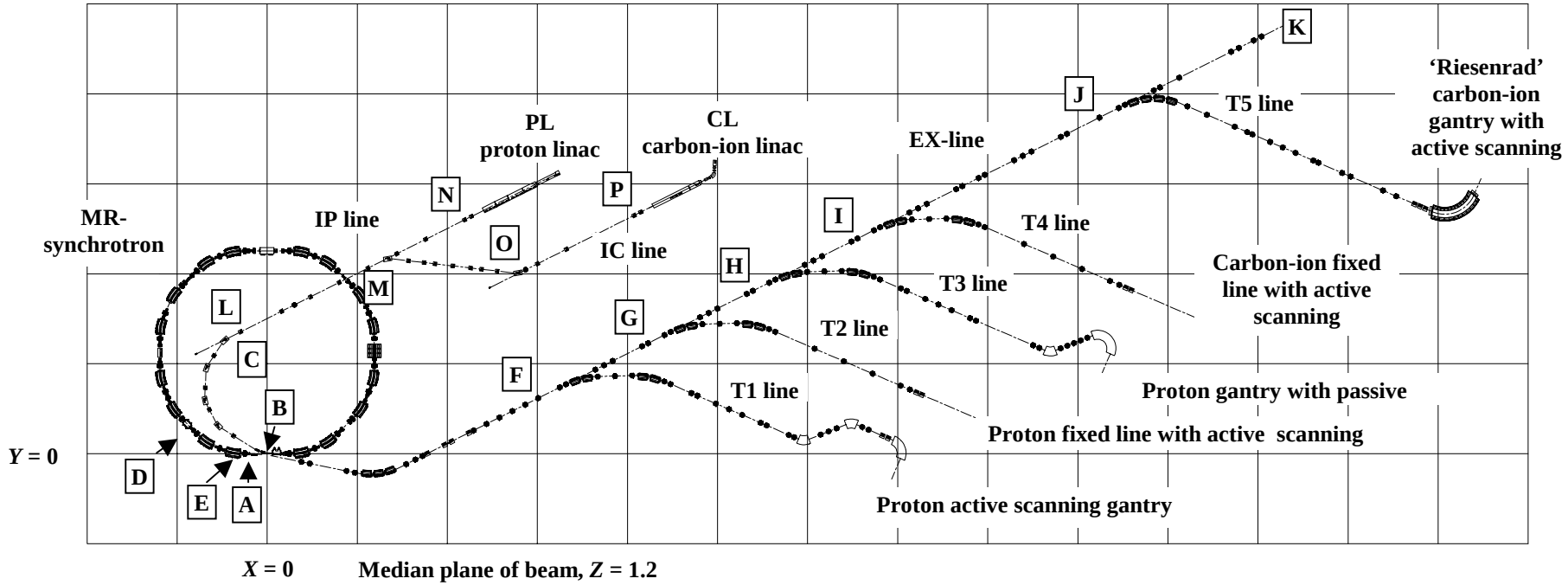

Figure 2.2 PIMMS accelerator complex

2.4 GENERAL DESIGN AND CONSTRUCTION

The magnets in the ring have 1.5 mm laminations and the yokes are assembled without solid end plates. The laminations are not the thinnest possible since some eddy current smoothing has been preserved to help filter out ripple at kHz frequencies that could affect the spill. The quasi-dc magnets in the transfer lines are also laminated with 1.5 mm laminations for ease and precision of setting, but have end plates for convenience of construction. All magnets are assumed to be constructed with the 'Cockerill' steel used for the CERN SPS dipoles (see permeability curve in Figure 2.3, curve A) and have either air-cooled or water-cooled copper coils. Ferrite kickers are assumed to be built with the ferrite Philips BC11 (see Figure 2.3, curve B). The rf cavity departs from a conventional design inasmuch as it is loaded with VitroVac™, an amorphous iron tape wound on spools, rather than the classic ferrite rings. If a conventional ferrite-loaded cavity were to be used, a more powerful bias supply would be needed for tuning and the cavity itself would require approximately 20 cm of additional longitudinal space in the ring.

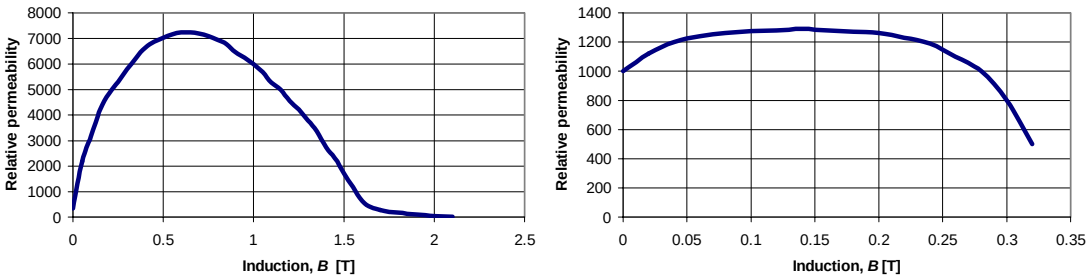

(a) 'Cockerill' steel (b) Philips 8C11 ferrite

Figure 2.3 Permeability curves used for magnet calculations

Two-dimensional and three-dimensional magnetic field calculations have been made with either OPERA [2] or MERMAID [3] and, in some cases, with both programs. For the main ring dipoles and the 'Riesenrad' 90° dipole, the philosophy is to make a 2-D design* and then to add end shims at the time of the magnetic measurements. This procedure has been chosen because these magnets have lengths comparable (or longer) than the local betatron amplitude functions and it is better therefore to correct their errors locally. In contrast, the shorter main ring quadrupole has been designed in 3-D and the profile contains the distributed corrections for the transverse and longitudinal truncations of the pole. The other magnets have been designed in 2-D and a 3-D check has been made on the integrated field quality. For correction magnets, septa etc., this is sufficient, but for certain magnets, such as the transfer line quadrupoles, further work in three dimensions would be advisable.

In general, yokes are built in at least two sections, so that the magnets can be opened for repair and maintenance on the vacuum system. There is a preference for bolting the yoke sub-sections together. However, the main dipole, quadrupole and

* The 2-D calculations of the 'Riesenrad' dipole have been made in a cylindrical co-ordinate system (r, θ, z) where the azimuthal angle is assumed constant. In this way, the strong curvature of the 90 degree magnet is taken into account exactly.

sextupole units can also be found in the references as fully welded designs. The 'Riesenrad' dipole also has a welded construction because of lack of space in the gantry structure. However, this point should be considered critically before making the execution design. The sub-sections of large magnet yokes are generally constructed with externally welded tie bars, but small magnets are preferentially glued and bolted. Laminations are glued to prevent 'ringing' and in the main dipole to create a laminated but solid end plate. In large dipoles and quadrupoles, where the field is determined by the iron shape, the coils are seated on polyurethane pads and held in position with a pre-stress. In septa and steering dipoles, where the coil position relative to the yoke (and especially the gap between the coil end and the yoke) are important, the coils are made exactly to size and are held by the yoke with an intermediate sheet of 60 micron Kapton™.

Lattice calculations have been carried out with WinAGILE [4] and MAD [5] and, in the case of the slow extraction, the program FERMEX [6] has also been used. RF calculations have been carried out with an analytical code RFAC [7], ESME [8] and TSC1D [9] for 1-D space-charge problems.

References

[1] K.D. Gross, M. Pavlovic (editors), *Proposal for a dedicated ion beam facility for cancer therapy*, (Sept. 1998) available from GSI, Darmstadt. Dual species linac is based on: U. Ratzinger, B. Schlitt, *Design of a carbon injector for a medical acccelerator complex*, Proc. 6th EPAC, Stockholm (1998).

[2] Vector Fields Ltd., *OPERA 2D* and *OPERA 3D*, (24 Kidlington, Oxon, OX5 LJE, UK).

[3] SIM Ltd., *Mermaid, Magnet design in two and three dimensions*, Novosibirsk, (1994).

[4] P.J. Bryant, *AGILE program for synchrotron lattice design*, http://nicewww.cern.ch/~bryant.

[5] H. Grote, F. Iselin, *The MAD program, Users' reference manual*, CERN/SL/90-13 (AP), (1990).

[6] C. Steinbach, Private communication, *FERMEX program for slow extraction optimisation*.

[7] M. Crescenti, S. Rossi, Private communication, *Analytical code RFAC for acceleration programmes*, (1999).

[8] J. MacLachlan, *User's Guide to ESME v. 8.2*, (1996).

[9] P. Knaus, *Simulation of Space Charge Dominated Beams and Experimental Tests*, Ph.D. thesis, Inst. f. Exp. Kernphysik, Univ. Karlsruhe (TH), to be published.

* * *

II-3 DESIGN OF THE MAIN RING

3.1 LATTICE

The lattice is based on two symmetric, achromatic arcs (μ_x and $\mu_z = 360°$ with bending = 180°) that have been de-tuned and joined by two dispersion-free straight sections. The evolution from simple FODO arcs to the final lattice is traced below.

The starting point for the design was a symmetric, 1:1 transfer (i.e. μ_x and $\mu_z = 360°$), achromatic (i.e. closed dispersion bump) arc with 180° of bending based on a FODO cell* (see Figure 1(a)). The F-quadrupole was then split to form a FODOF lattice with longer drift spaces after each pair of dipoles (see Figure 1(b)), while maintaining all the other optical properties. The advantage of splitting the F-quadrupole and introducing long drift spaces is that the β_x and β_z lattice functions are relatively constant across the drifts and the basic optics is very tolerant towards changes in these drifts. Arcs with the 1:1 transfer property are also extremely useful at the start of matching, since they return at the exit all lattice parameters presented at the entry and always with the same phase advance. A symmetric structure has the further advantage of requiring fewer quadrupole families. The FODOF arc can be described alternatively as a series of triplets, in which the β_x is kept small and the vertical focusing of the rectangular dipoles is used to limit the peaks in β_z.

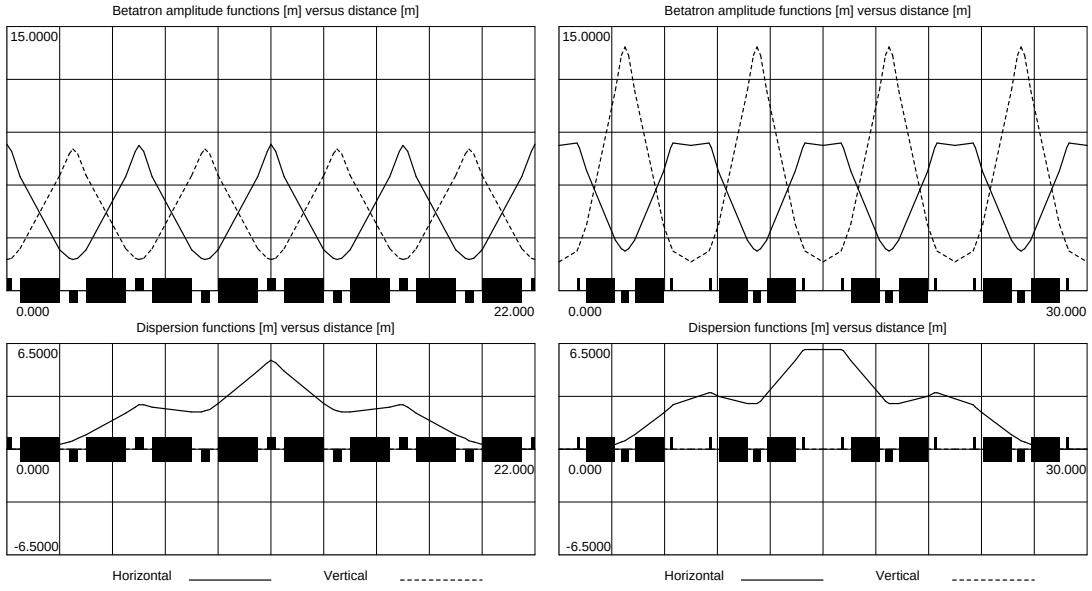

(a) FODO arc
Bend = 180°
$\mu_x = \mu_z = 360°$
$\beta_{x,in} = \beta_{x,out} = 8.29$ m
$\beta_{z,in} = \beta_{z,out} = 1.74$ m
2 quadrupole families

(b) FODOF arc
Bend = 180°
$\mu_x = \mu_z = 360°$
$\beta_{x,in} = \beta_{x,out} = 8.28$ m
$\beta_{z,in} = \beta_{z,out} = 1.66$ m
2 quadrupole families

Figure 3.1 Lattice functions of FODO (a) and FODOF (b) achromatic arcs

* In this nomenclature, F = focusing quadrupole, D = defocusing quadrupole and O = dipole.

A ring was then formed by joining two FODOF arcs by long drift spaces and reducing the tunes to about 1.7 in both planes to ensure stability. This provided the lattice functions shown in Figure 3.2(a). Note that the closed dispersion bumps have been temporarily lost in this procedure. The final stage was to mould this basic form into the PIMMS lattice as shown in Figure 3.2(b). The dispersion-free regions were re-established for the rf cavity and resonance-driving sextupole and all the drift spaces were customised to suit the equipment, which resulted in a modest increase in total length. The lattice functions in the septa were reduced for aperture reasons and phase advances were optimised for extraction. To meet all the requirements, it was found necessary to divide the F-quadrupoles into two families (QF1 and QF2) to ensure enough flexibility in the matching. The final ring has relatively smooth focusing with betatron amplitude functions that vary between 4 and 16 m and the lattice is tolerant of being tuned over a wide range due to its underlying structure of two 1:1 transfer arcs. Since there are three quadrupole families, the dispersion can be maintained at zero in the long straight sections when tuning the lattice.

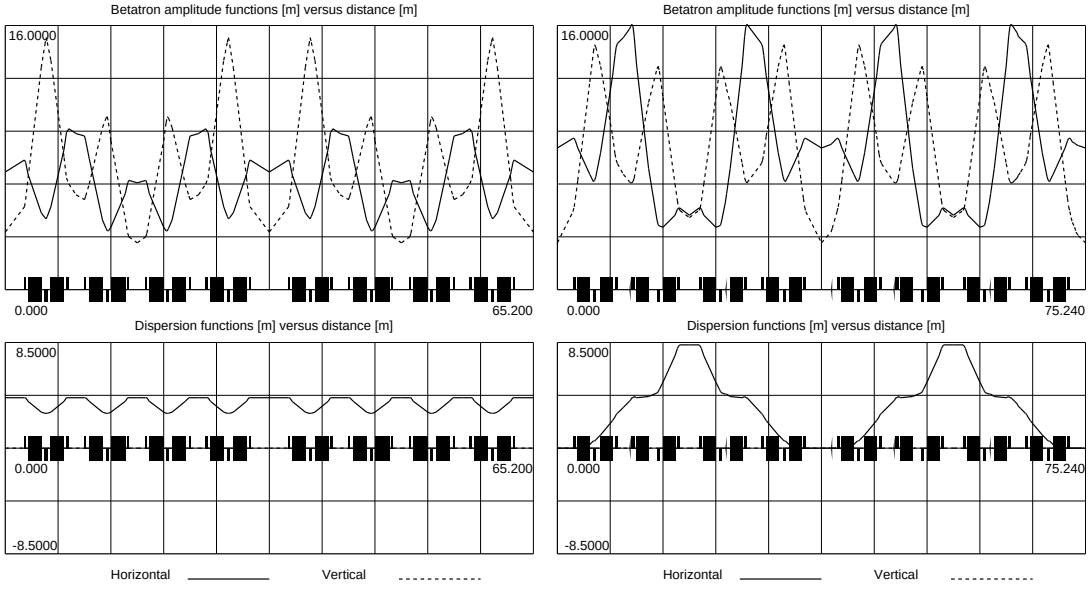

(a) Base ring
Bend = 180°
$Q_x = Q_z = 1.7$
2 quadrupole families

(b) PIMMS
Bend = 180°
1 dipole family (MB)
$Q_x = 1.6666^0$
$Q_z = 1.7200^0$
3 quadrupole families (QF1, QF2, QD)

Figure 3.2 Lattice functions of the prototype ring and the final PIMMS ring

For extra clarity Figure 3.3 repeats the lattice functions of the ring and relates these functions to the geometry. The positions of the quadrupole chains QF1, QF2, and QD, the sextupole chains F- and D-types and some other key elements are also indicated. Note that the electrostatic septum is situated in the second half of the closed dispersion bump of the second arc and the magnetic septum is placed directly after the closure of the dispersion bump according to the basic principles discussed in Part I, Chapter 3. The injection and extraction are combined in one long, dispersion-free, straight section and the rf cavity occupies the other.

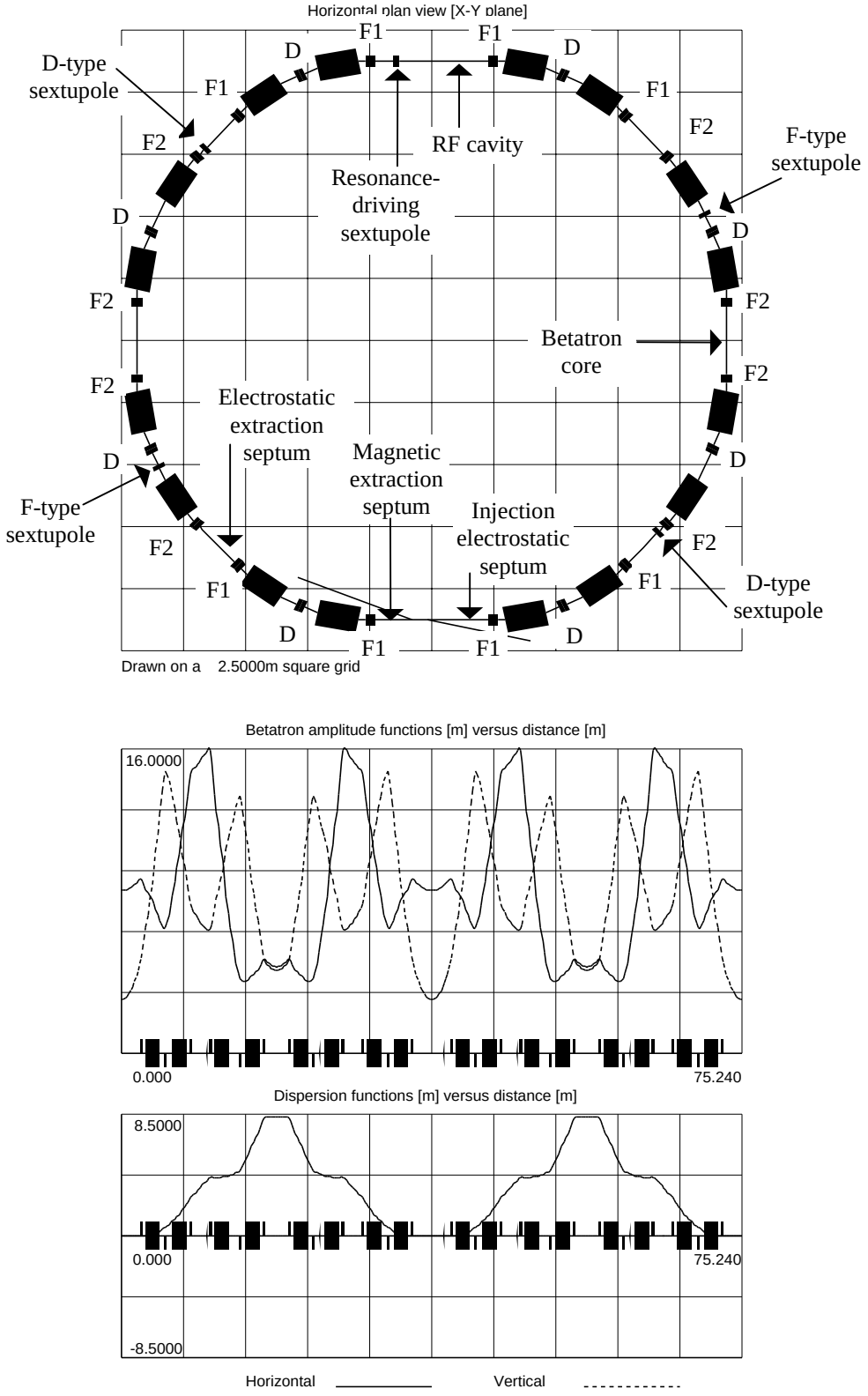

Figure 3.3 Synchrotron geometry and lattice functions

[The origin of the lattice functions is at the centre of the bottom drift space that is used for injection and extraction and the functions from left to right correspond to an anticlockwise movement around the ring returning to the same point.]

3.2 EXTRACTION

3.2.1 Layout of extraction elements

Figure 3.4 indicates the layout of the elements in the ring for exciting the $Q_x = 5/3$ resonance, accelerating the beam into the resonance and extracting the separatrix. The position of the betatron core is not critical and it has been placed in a vacant straight section on the right-hand side. The remaining elements have a definite configuration that fits in with a closed dispersion bump in the left-hand arc. Figure 3.4 shows this configuration, with the orientation of the stable triangle, the extraction separatrix and the principal lattice parameters. The resonance sextupole is the first element and is placed in a dispersion-free region before the arc. The phase advance to the electrostatic septum is well above the permissible minimum of 210° and close to the ideal of 225° (see Part. I, Section 3.4). The phase advance to the magnetic septum is a comfortable 51°, which gives 78% of the kick that would be available if the phase advance were 90°. The dispersion functions are correctly configured with $D_x > 0$ and $D_x' < 0$ at the electrostatic septum for the Hardt condition. At the resonance sextupole, $\beta_z < \beta_x$ to reduce coupling. At the electrostatic septum, β_x is close to the absolute maximum to enhance the kick and, at the magnetic septum, β_z is close to the absolute minimum to reduce the aperture requirements in the septum magnet.

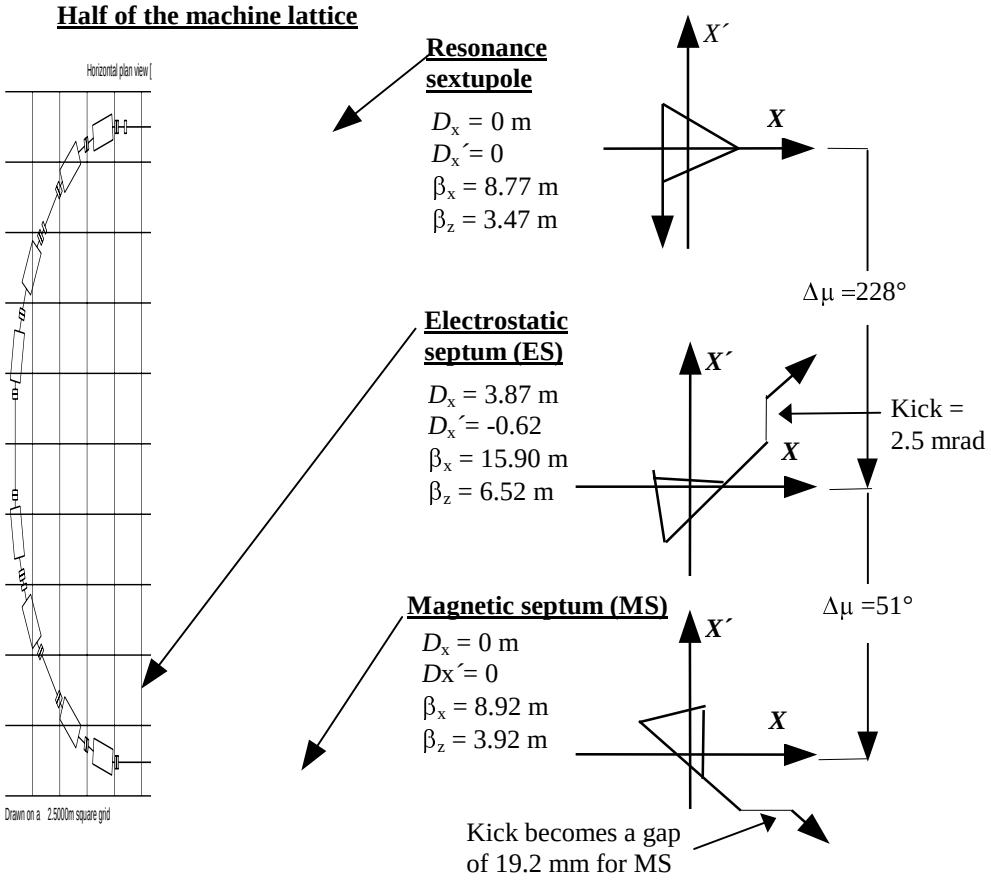

Figure 3.4 The extraction configuration

3.2.2 Optimisation of the resonant extraction in phase space

Figure 3.5 shows the phase-space at the electrostatic septum using the program AGILE [1]. The spiral step has been optimised to 10 mm and the Hardt condition has been applied (i.e. the on- and off-momentum separatrices reach the septum with the same angle). The spiral step is adjusted by changing the resonance sextupole strength and the Hardt condition is optimised by changing the horizontal chromaticity.

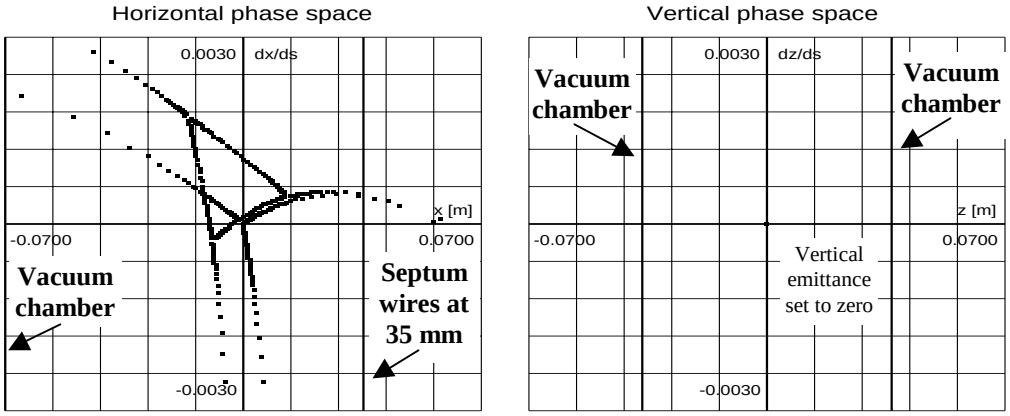

Figure 3.5 Phase-space picture of extraction at entry to electrostatic septum
[Protons at 60 MeV, Extracted $\Delta p/p$ = -0.00111, Horizontal emittance of off-momentum stable triangle = 7.16 π mm mrad, Vertical emittance of tracked particles equals zero]

3.2.3 First alternative calculation of the extraction in phase space

Figures 3.6 shows a picture equivalent to that of Figure 3.5 at the electrostatic septum only calculated according to the program FERMEX [2].

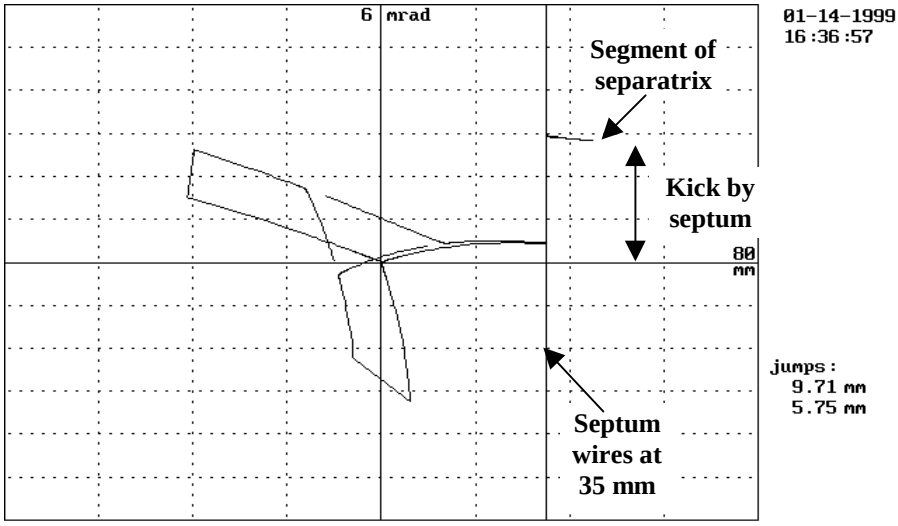

Figure 3.6 Horizontal phase-space picture of extraction at electrostatic septum
[Protons at 60 MeV, Extracted $\Delta p/p$ = -0.00111]

Figures 3.7 and 3.8 show additional outputs from FERMEX of the phase space at the magnetic septum and of the last stable triangle with its calculated emittance. The emittance of the stable triangle is a particularly sensitive parameter that is difficult to measure.

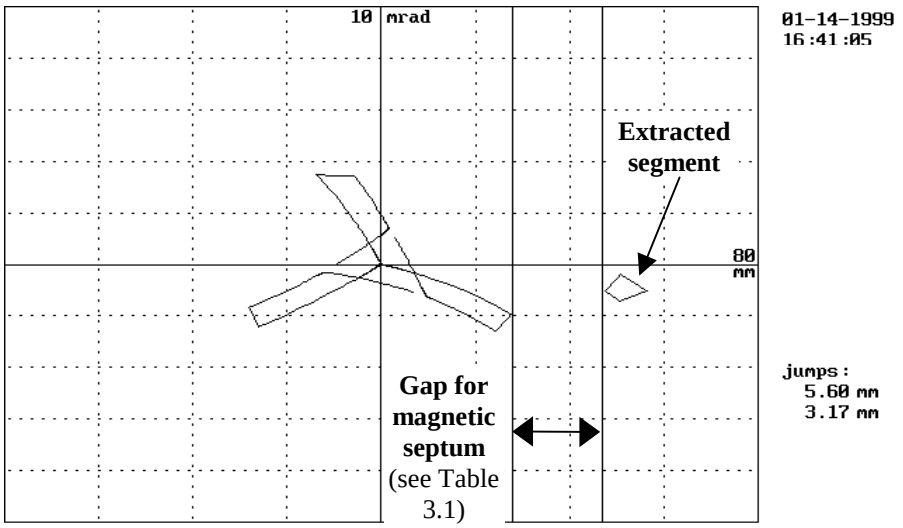

Figure 3.7 Horizontal phase-space picture of extraction at entry to magnetic septum
[Protons at 60 MeV, Extracted $\Delta p/p$ = -0.00111]

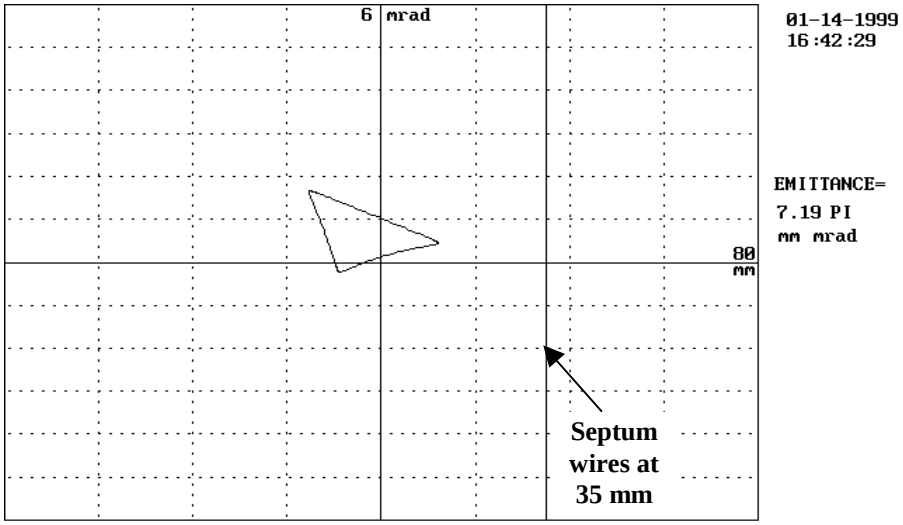

Figure 3.8 The last stable triangle seen at the electrostatic septum
[Protons at 60 MeV, Extracted $\Delta p/p$ = -0.00111]

3.2.4 Second alternative calculation of the extraction and comparison of results

Finally, Figure 3.9 shows the equivalent picture to Figures 3.5 and 3.6 of the phase space at the entry to the electrostatic septum using data calculated by the program MAD [3].

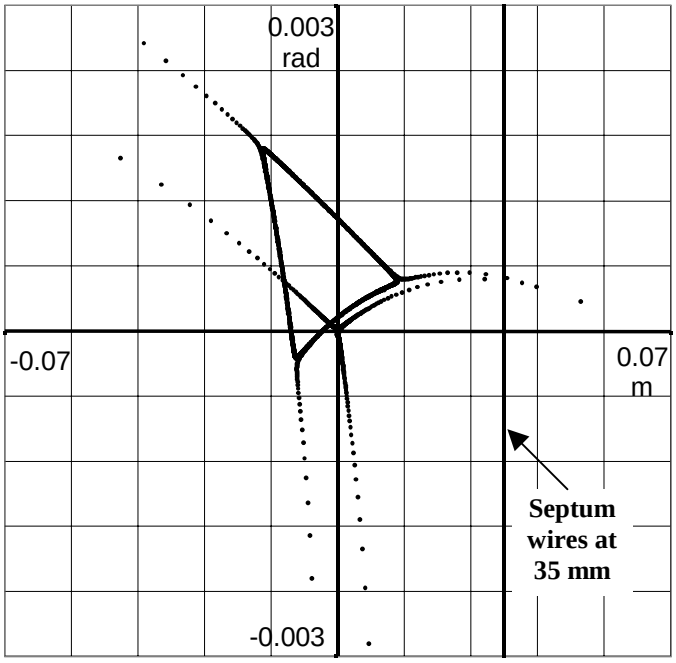

Figure 3.9 Horizontal phase-space picture of extraction at entry to electrostatic septum
[Protons at 60 MeV, Extracted $\Delta p/p$ = -0.00111, Horizontal emittance of off-momentum stable triangle = 7.24 π mm mrad, Vertical emittance of tracked particles zero]

Special care has been taken with the optimisation of the slow extraction since this is a crucial function of the synchrotron for hadron therapy. Table 3.1 tabulates the main parameters as calculated by the three different programs and shows that a good agreement has been obtained. It should be noted that each program uses a different tracking technique:

- AGILE creates a special lattice for the off-momentum particles that is derived from a dipole tracking in a hard-edge magnet model. It then applies first-order optics to this derived lattice for the focusing on this orbit.
- MAD applies field expansions around the central orbit in a second-order theory.
- FERMEX relies on the central-orbit optics calculated by an independent program and then applies some internal calculations to perform the off-momentum tracking.

Comparison of results from AGILE, FERMEX and MAD

Parameter		AGILE	FERMEX	MAD
Spiral step of on-momentum particles	[m]	0.01003	0.00971	0.01002
Spiral step of off-momentum particles	[m]	0.00571	0.00575	0.00592
Extracted momentum bite	$\Delta p/p$	-0.001107	-0.001107	-0.001107
Last stable triangle, emittance	[π mm mrad]	7.16	7.19	7.24
Position of septum wires	[m]	0.035	0.035	0.035
Separatrix angle at septum ($\Delta p/p = 0$)	[rad]	0.000449	0.000430	0.000464
Separatrix angle at septum ($\Delta p/p \neq 0$)	[rad]	0.000460	0.000450	0.000490
Gap for magnetic septum	[m]	0.0192	0.0201	0.0195

Table 3.1 Comparison of results from AGILE, FERMEX and MAD

3.2.5 Effect of coupling

In Figure 3.10, tracking is performed with the maximum vertical emittance ($E_{z,Total}$ = 7.14 π mm mrad) instead of zero vertical emittance as in Figures 3.5 to 3.9. The results appear almost identical, except that there is a slight widening of the lines in Figure 3.10 that is due to the coupling introduced via the sextupoles. The coupling is more visible in the relation between the extracted momentum bite and the emittance of the last stable triangle. Table 3.2 tabulates this small effect and shows an increase in the momentum bite of approximately 3%.

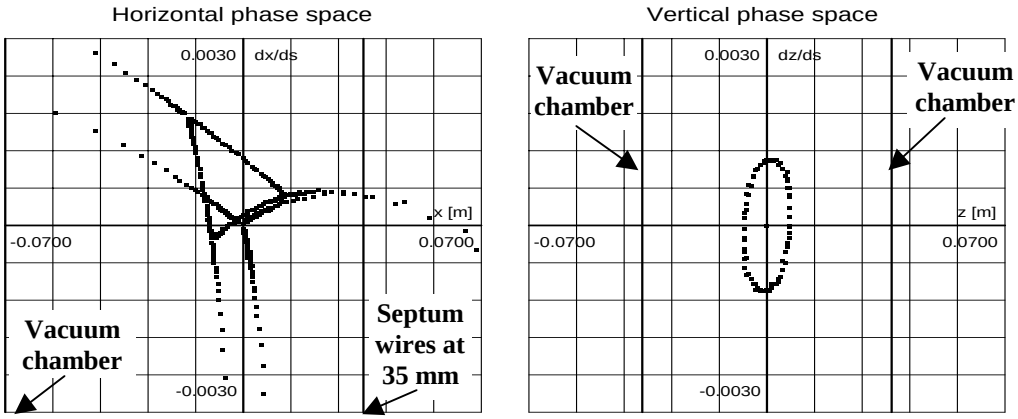

Figure 3.10 Phase-space picture of extraction at entry to electrostatic septum
[Protons at 60 MeV, Extracted $\Delta p/p$ = -0.00122, Horizontal emittance of off-momentum stable triangle = 7.14 π mm mrad, Vertical emittance of tracked particles = 7.14 π mm mrad]

Effect of coupling from the vertical plane on the extracted momentum bite					
Vertical emittance of circulating beam	[π mm mrad]	0	0.61	3.83	7.14
Horizontal emittance of stable triangle	[π mm mrad]	7.16	7.15	7.13	7.15
Extracted momentum bite	$\Delta p/p$	-0.001107	-0.001111	-0.001121	-0.001141
	(Design horizontal emittance of stable triangle = 7.143 π mm mrad)				

Table 3.2 Effect of coupling from the vertical plane on the extracted momentum bite

3.2.6 Optimisation of the spiral step

So far the spiral step of the on-resonance particles has been tacitly set to 10 mm. In practice, this choice has been guided by the following points.

- Assuming that the Hardt Condition is applied and the separatrices of different momenta are exactly aligned then the losses on the septum are due to the wire thickness. For a 10 mm step and a wire thickness of 0.1 mm the loss would be about 1%. This has the same order of magnitude as the other expected errors due to alignment and rectilinearity of the septum and the finite angular spread in the separatrix of about 0.1 mrad. Thus, the choice of a 10 mm spiral step is consistent with a policy of equalising the various loss mechanisms and aiming at a final overall loss of a few percent.

- A spiral step of 10 mm is comparable to the final spot size, which is an indication that no exotic optics will be needed in the transfer channel.

3.2.7 Optimisation of the radial positions of the septa

So far the radial position of the electrostatic septum wires has been set to 35 mm without any direct explanation. Although this is largely a question of creating a consistent scenario with other parameters, there are a number of underlying reasons.

The configuration of the electrostatic and magnetic septa with the separatrices is shown schematically in Figure 3.11. The circulating separatrix appears as a half-wave betatron oscillation in the outer half of the vacuum chamber. The electrostatic septum kicks the outermost layer of this separatrix at a point on the rising part of the oscillation and, a quarter wavelength later, the magnetic septum kicks the separated beam at a point on the falling part of the oscillation. Thus, the two septa sit, more or less, symmetrically astride the peak of the separatrix oscillation and centrally in the outer half of the aperture. The separation between the kicked beam and the circulating separatrix increases as much by virtue of the separatrix collapsing towards the central orbit as by the kicked beam moving outwards, which means a weak impact on the overall aperture. The beam that is waiting to enter the resonance sits mainly in the inner half of the vacuum chamber, but its betatron oscillations and closed-orbit distortion cause it to occupy the up to ~20 mm of the outer half of the chamber as well.

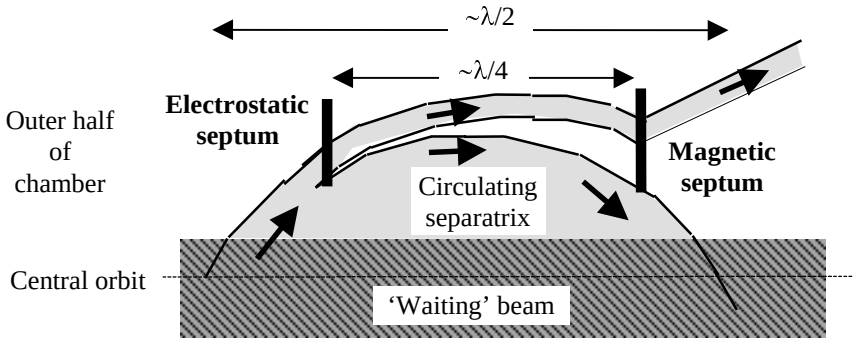

Figure 3.11 Schematic view of the extraction

Table 3.3 shows how the main parameters vary for different radial positions of the electrostatic septum over the range 27 to 45 mm.

The advantage gained by bringing the electrostatic septum closer to the central orbit is a reduction in the space needed for the separatrices. The absolute limit to this movement is the edge of the last-stable triangle of the off-momentum particles, which extends to ~14 mm from the central orbit, but in practice it is difficult to get numerical results below 27 mm from the central orbit. Moving the electrostatic septum inwards requires stronger sextupole fields (if the spiral step is kept constant) and the value rises rapidly as the distance is reduced. The production of the necessary fields is not a technical limit and a movement of say 5 to 10 mm would seem to be a possibility. The preference for the present value of 35 mm lies more with the off-momentum particles.

- The off-momentum particles have a different spiral step because the distance to the septum from the corner of the stable triangle is shorter and there are fewer turns in which the sextupole can act. In the nominal configuration (35 mm), the spiral step ranges from 5.7 to 10 mm. Bringing the electrostatic septum closer would increase this range and moving it further away would reduce it. It turns out that the present configuration is about optimum for the reasons exposed in Appendix C, but Appendix C is not a strong argument against a movement of say ±5 mm.

- A more serious reason is the formation of stable islands. Table 3.3 shows how the minimum aperture needed for stable islands to form for the off-momentum particles reduces as the electrostatic septum approaches the centre line. If the septum is at 35 mm, or more, the aperture for stable island formation is comfortably outside the physical aperture, but at 30 mm this limit falls inside the physical aperture.

Variation of extraction parameters with radial position of the electrostatic septum

ES position [mm]	Spiral step $\Delta p/p$=0 [mm]	Spiral step $\Delta p/p$=min.	Islands form within [mm]	$\Delta p/p$ extracted	Emittance of 'last triangle' π mm mrad	Resonance sextupole $k1$ [m-2]	Qx´ for Hardt Condition
27	10	3.4	±50	-0.00120	7.2	16.3×0.2	-5.1
30	10	4.4	±66	-0.00117	7.1	13.6×0.2	-4.5
35	10	5.7	±101	-0.00111	7.1	10.7×0.2	-3.75
40	10	6.5	±134	-0.00109	7.2	7.6×0.2	-3.1
45	10	7.3	±178	-0.00105	7.1	6×0.2	-2.7

Table 3.3 Variation of extraction parameters with radial position of the electrostatic septum

Figure 3.12 shows the formation of stable islands within an aperture of ±66 mm when the machine is tuned for operation with the electrostatic septum at 30 mm. In practice, the islands would never form because the electrostatic septum intercepts the particles, but it is an indication that the non-linearities are too strong and the dynamic aperture is less than the physical one.

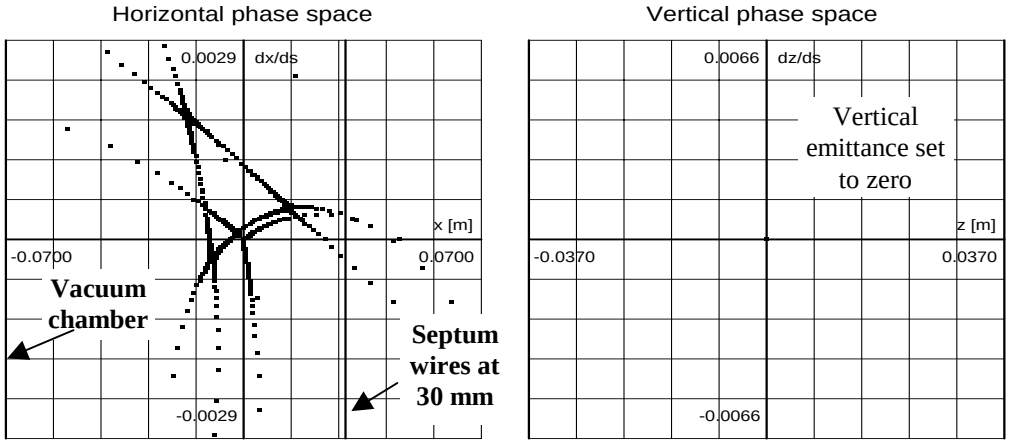

Figure 3.12 Formation of stable islands within an aperture of ±66 mm when the machine is tuned for operation with the electrostatic septum at 30 mm
[Vertical emittance of tracked particles equals zero]

3.3 MAIN MAGNET CYCLE

The choice of the magnet cycle is an important compromise. On the one hand, a rapid cycle shortens the treatment time and reduces the impact of cycles that have to be aborted. On the other hand, a long cycle time reduces the installed power and the size of the reactive-power compensator, which lowers cost. It also narrows the difference between the ramping voltage and the dc flat-top voltage, which improves performance, and it reduces the requirements imposed on the rf system. Indirectly, through the rf cycle, the momentum spread in the beam is also affected and this can influence the machine aperture.

The original specification required the machine to complete in 1 s a basic magnetic cycle that included the "round-in" and "round-out" sections, but not the duration of the treatment flat top, which was also nominally set at 1 s. After some discussion, the basic cycle has been relaxed to 1.2 to 1.4 s according to the situation. For a treatment of say 60 spills, this represents an increase of 12 to 24 s, but since many of the flat tops for the proximal slices will be terminated before the nominal 1 s spill time has elapsed, the overall treatment time is still likely to be close to the original request.

Figure 3.13 shows four extreme cycles (lowest and highest extraction energies for each type of particle) with a 200 ms flat-top for clarification. All cycles have the same extreme values. Only the positions of the injection flat bottoms, the extraction flat tops and the fine structure of the current forms change.

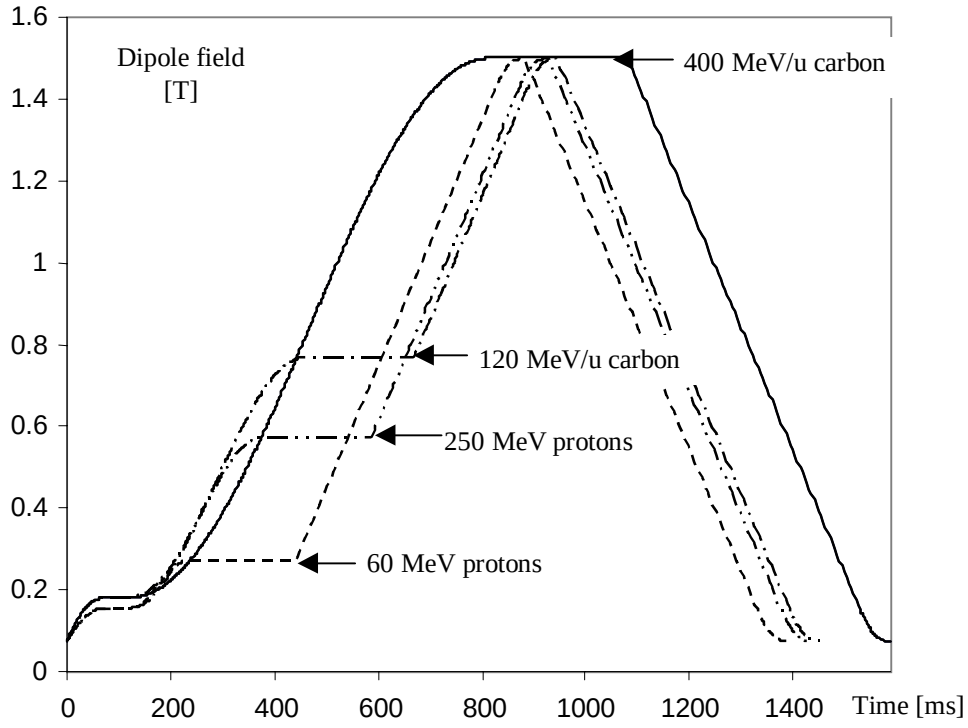

Figure 3.13 The four extreme cycles are shown, with 200 ms extraction plateaux
[Protons 20 to 60 MeV, Protons 20 to 250 MeV,
Carbon ions 7 to 120 MeV/u, Carbon ions 7 to 400 MeV/u]

Tables 3.4 to 3.7 summarise the time structures of the four cycles by listing the breakdown of the times for each feature in the cycles from left to right in Figure 3.13.

60 MeV proton cycle	
Parabola	70
Injection flat	50
Acceleration	110.78
Extraction flat	*200*
Start up-ramp	8
Linear Ramp	385.46
Smooth End	50
Start down-ramp	8
Linear Down	450.05
Smooth End	50
End	8
TOTAL [ms]	**1390.3**

Table 3.4 60 MeV proton cycle

120 MeV/u carbon cycle	
Parabola	70
Injection flat	50
Acceleration	340.05
Extraction flat	*200*
Start up-ramp	8
Linear Ramp	218.67
Smooth End	50
Start down-ramp	8
Linear Down	450.05
Smooth End	50
End	8
TOTAL [ms]	**1452.8**

Table 3.6 120 MeV/u carbon cycle

250 MeV proton cycle	
Parabola	70
Injection flat	50
Acceleration	258.99
Extraction flat	*200*
Start up-ramp	8
Linear Ramp	283.42
Smooth End	50
Start down ramp	8
Linear Down	450.05
Smooth End	50
End	8
TOTAL [ms]	**1436.5**

Table 3.5 250 MeV proton cycle

400 MeV/u carbon cycle	
Parabola	70
Injection flat	50
Acceleration	693.98
Extraction flat	*200*
Start up-ramp	8
Linear Ramp	0
Smooth End	50
Start down-ramp	8
Linear Down	450.05
Smooth End	50
End	8
TOTAL [ms]	**1588**

Table 3.7 400 MeV/u carbon cycle

The cycles detailed in Tables 3.4 to 3.7 assume that the main power supply will be under the control of a current loop acting at about 15 Hz, which encloses a voltage loop operating at about 150 Hz. To smoothly 'round-in' or 'round-out' from a precision flat bottom or top with an overshoot of less than 10^{-4} of the maximum current, a parabolic waveform has been used extending over 70 ms. When a ramp can be started quickly 8 ms have been allowed to smooth the transition from low to high voltage. The section of the cycle that accelerates the beam has a cosine waveform that is the basis of the rf cycle. There is a 50 ms stabilisation time at each extreme of the cycle. These times are adjusted so that the rate of field change never exceeds 3 T/s and the minimum acceleration time (for 60 MeV protons) is not shorter than 110 ms, which allows a smooth 'round-in' and 'round-out'.

The voltage cycles corresponding to Figure 3.13 are shown in Figure 3.14. All the cycles start with a high voltage to initiate the upward ramp, but this voltage quickly drops to the value needed to maintain the injection flat bottom (dc). The voltage then rises smoothly to near its maximum value and then falls back to the voltage needed to maintain the extraction flat top (dc). The rest of the cycle appears more 'rectangular' in character with the maximum positive and negative voltages being applied to complete the cycle quickly. The current for the minimum of the cycle is approximately 5% of maximum and the current on the injection flat bottoms is 10% and 12% for protons (20 MeV) and ions (7 MeV/u) respectively. Maintaining control of the current at such low values is not an easy task for the power converter that must work with a very small fraction of its maximum voltage.

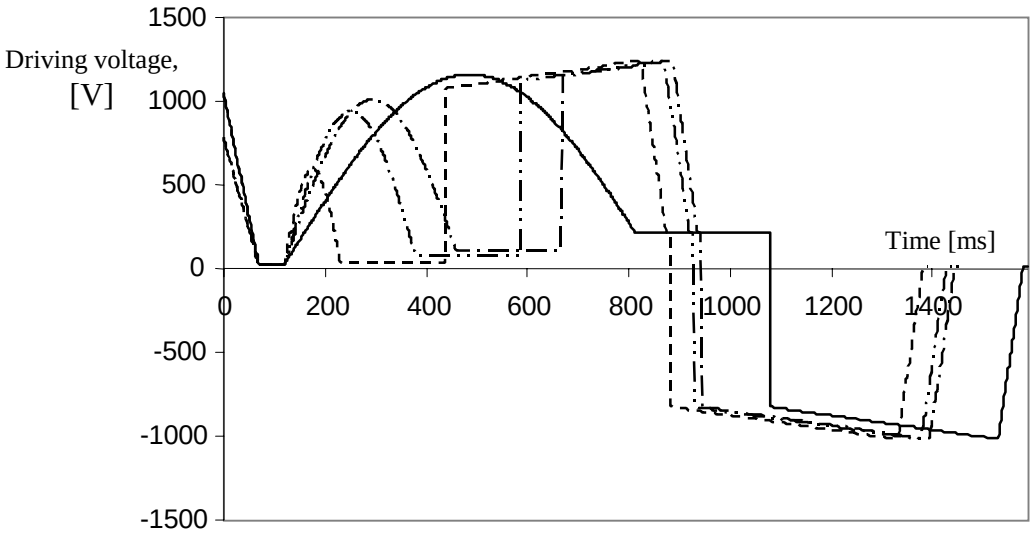

Figure 3.14 Voltage cycles for driving the main dipoles
[Compare to Figure 3.13]

Figures 3.15 to 3.18 show the active, reactive and apparent powers for each cycle separately.

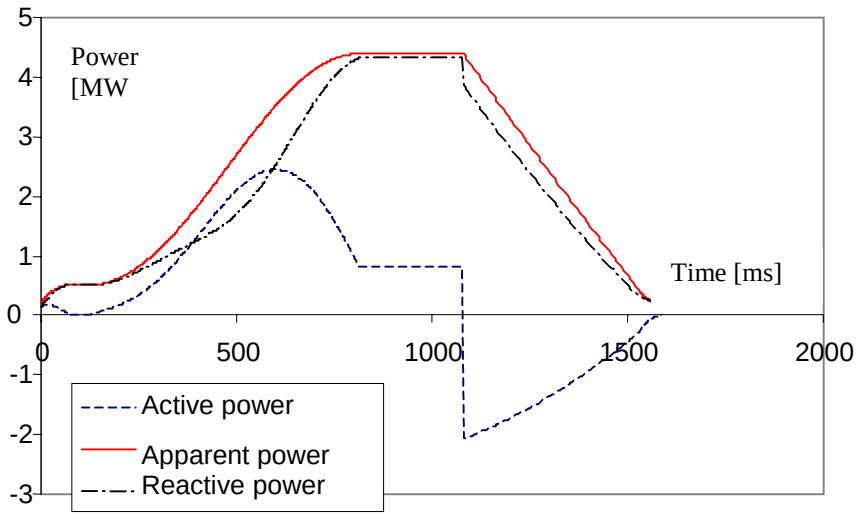

Figure 3.15 Power requirements for the main dipoles during 400 MeV/u carbon cycle

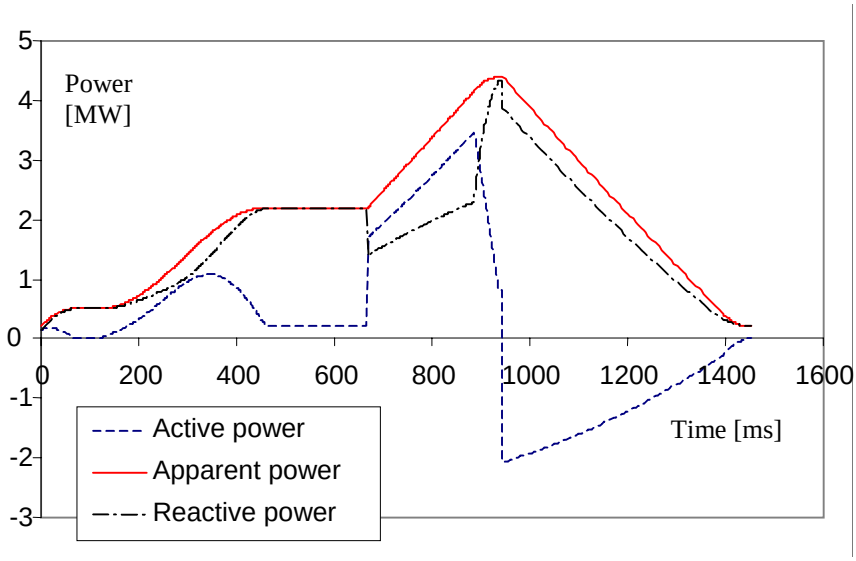

Figure 3.16. Power requirements for the main dipoles during 120 MeV/u carbon cycle

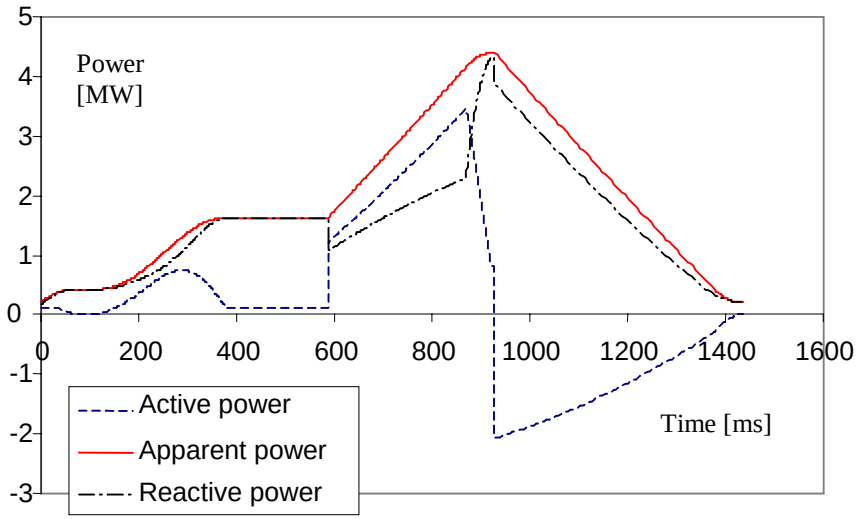

Figure 3.17 Power requirements for the main dipoles during 250 MeV proton cycle

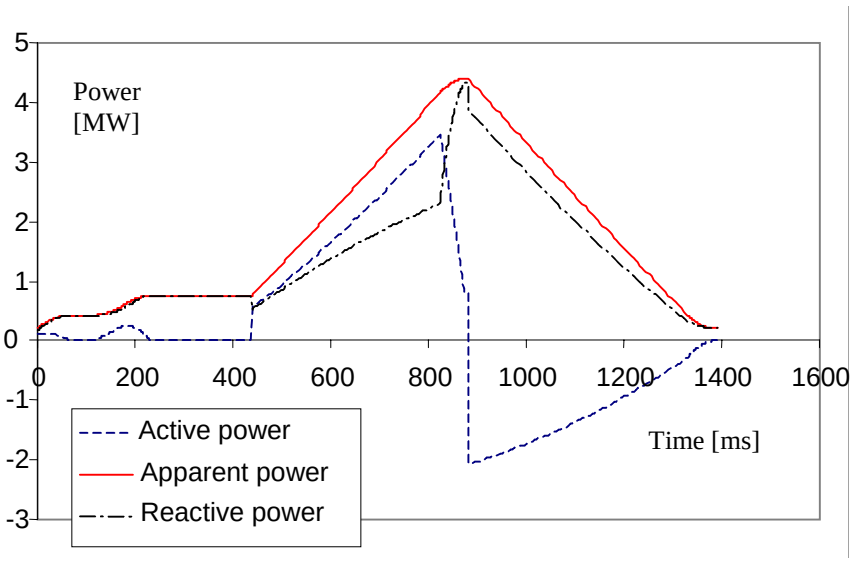

Figure 3.18 Power requirements for the main dipoles during 60 MeV proton cycle

The circuits considered in the above calculations include 17 dipoles (one for field measurements), 2×40 m of cable from the power supply to the ring and 2×100 m of interconnecting cable inside the ring. The cabling configuration has been foreseen to minimise inductance and stray field and to optimise the distribution of leakage current, by connecting first all the 'odd' dipoles and than all the 'even' ones on the return path. If losses prove to be more serious than expected, the upper coils could be connected in series around the ring and lower coils be connected in reverse order in the return path.

The above graphs are calculated by considering B and I as being proportional. When the $B(I)$ excitation curve (calculated by M. Giesch) is considered, saturation effects begin to be visible at high field levels (see Figure 3.19). This causes an increase in dB/dI of 14% at 1.4 T and 18% at 1.45 T. The final 'round-in' at the maximum of the current cycle starts at about 1.42 T. This implies that at around 1.4 T, the required voltage has to be 1240 × 1.14 = 1410 V to obtain the desired dB/dt. A maximum voltage of 1500 V has been foreseen to drive the main dipoles. This leaves a small margin to account for unforeseen changes in magnetic properties, additional cable lengths, adjustments in cycle parameters etc.

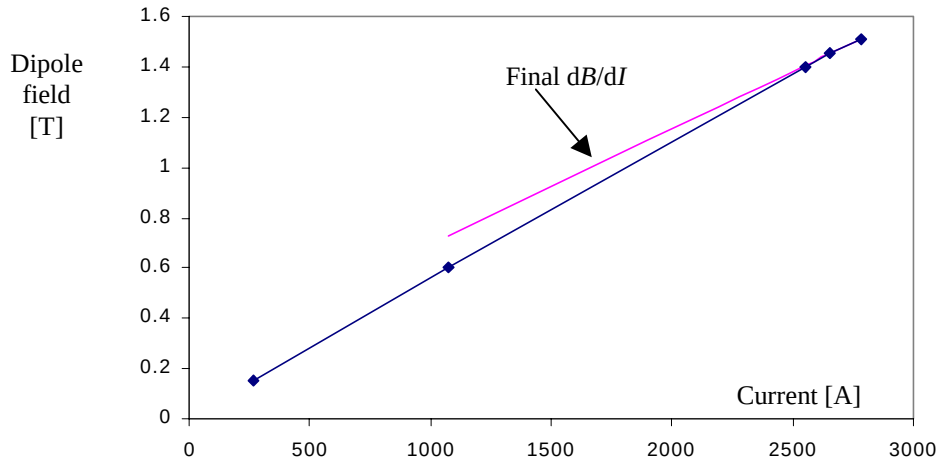

Figure 3.19 B-field as a function of the excitation current in the main dipoles

3.4 RF ACCELERATION PROGRAMMES

The rf acceleration cycles can be conveniently divided into 3 regions:

- The initial phase of adiabatic trapping,
- The start of acceleration that contains critical points for the maximum momentum spread and tune shifts.
- The closing phase of the acceleration up to the flat top.

The adiabatic trapping requires 30 to 40 ms. This is quickly followed by a critical period of about 40 ms during which the bunch turns in the bucket and suffers the maximum momentum spread and incoherent tune shifts. The peak in the momentum spread is of particular importance for the aperture, since the PIMMS design has a large dispersion function in the centre of the arcs. The final stage of the acceleration is not critical.

Three tools have been used for the computations:

- An analytical code RFAC [4] that was developed for this specific purpose.
- ESME [5], a multi-particle tracking code, well known in the accelerators community. However, it is only suitable for masses no heavier than the proton.
- TSC1D [6], Tracking with Space Charge 1D, a recently-developed multi-particle tracking code, which takes into account the longitudinal space-charge contribution.

For a perfect adiabatic cycle, the analytical code describes the evolution of the rf and the beam parameters during the cycle exactly, except that the beam emittance dilution due to the longitudinal space-charge force is not included. The non-adiabaticity is taken into account by ESME and TSC1D and the later also includes the longitudinal space-charge effect.

First the proton cycle was optimised with the analytical code and the results were checked with ESME. A limit for the adiabatic factor was established, below which the results were equivalent. Having thus verified the analytical code, the cycle for the carbon ions was calculated. The same cycles were then used in TSC1D to check the space-charge contribution and to revise the safety margins. Only a few iterations with the two codes are needed to minimise losses. This technique proved to be quicker than the direct use of multi particle codes.

3.4.1 Adiabatic trapping

The injected beam just before trapping contains up to 6.84×10^{10} protons or 7.90×10^{8} carbon ions. The beam is unbunched, occupies a rectangle in the longitudinal phase space and the distribution is considered to be uniform in phase and parabolic in energy (see Appendix-A). This beam is captured in an rf bucket ($h = 1$) by the method of adiabatic trapping [7]. A stationary rf bucket is created with a longitudinal phase-space area that is small with respect to the unbunched beam dimensions. The voltage is then progressively increased until the bucket acceptance is large enough to accommodate the entire beam. At the end of the process, the beam is bunched and ideally has suffered no longitudinal emittance dilution. The final ratio between the bunch and the bucket areas is called the *filling factor*. To make the capture process adiabatic, its duration must be long compared to the synchrotron period (T_s), which is considered as the typical time unit of the longitudinal dynamics (T_s is of the order of 1 ms for PIMMS). The bunch parameters at the end of adiabatic capture are only determined by the final bucket parameters and by the initial longitudinal emittance. A monitoring of the adiabaticity of the process is given by the so-called adiabatic factor α that can be defined as:

$$\alpha = \left| \frac{1}{A_B} \frac{dA_B}{dt} T_s \right| \tag{3.1}$$

where A_B is the bucket area. Acceptable values for an adiabatic process are $\alpha < 0.5$ [8]. The threshold value chosen for the PIMMS capture process is $\alpha = 0.1$. The iso-adiabatic law that describes the increase of the rf voltage, V_{rf} during the capture process is given by:

$$V_{rf}(t) = \frac{V_{final}}{\left[\sqrt{\frac{V_{final}}{V_{initial}}} - \frac{\alpha}{T_s}t\right]^2} \qquad (3.2)$$

where $V_{initial}$ and V_{final} are the voltages at the beginning and at the end of the trapping, respectively. The stable phase is maintained at zero and the variation of the rf voltage has the form shown in Figure 3.20. The bucket area is proportional to the square root of the final voltage and, at the end of the process, the bucket, A_B, and the bunch, A_b, areas are proportional (define $K_{AREA} = A_B/A_b$). The choice of K_{AREA} fixes this ratio, which, in the case of a perfectly adiabatic process, is the inverse of the filling factor. In practice, the bunch area increases more than expected due to non-adiabaticity. A safe margin is maintained by choosing $K_{AREA} \approx 1.6$. The ratio between final and initial voltage defines the bucket dimension at the beginning of the capture process. This ratio has been set $V_{final}/V_{initial} = 10$. The ratio, together with V_{final}, α and T_s, determines the trapping duration.

Thus, the trapping process is completely defined and has been chosen to satisfy the following criteria:

- Capture efficiency (i.e. the ratio between injected and captured particles) as close as possible to one.
- Dilution (i.e. increase of the longitudinal emittance) as small as possible.
- Bunching factor (i.e. the ratio between the longitudinal dimension of the bunch and the rf wavelength) as large as possible.

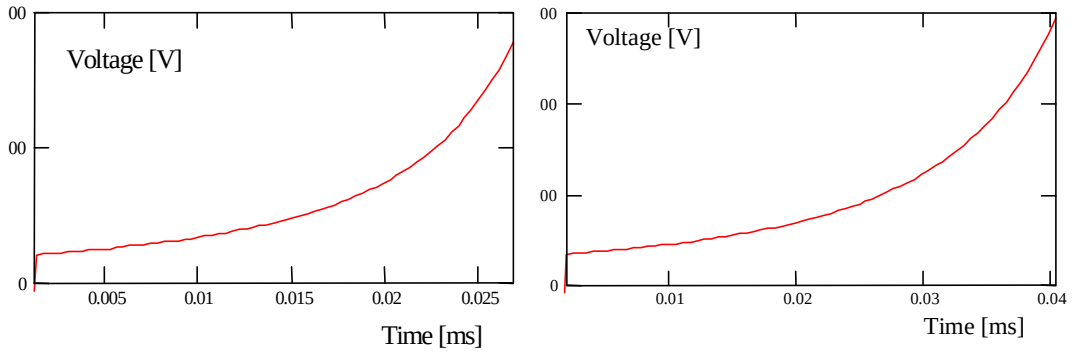

(a) 20 MeV protons (b) 7 MeV/u carbon ions

Figure 3.20 Voltage law for the adiabatic capture of the ions

The adiabatic trapping process inevitably produces an increase of the bunch momentum spread given by [9]:

$$\left(\frac{\Delta p}{p}\right)_{\text{After capture}} \geq \frac{\pi}{2}\left(\frac{\Delta p}{p}\right)_{\text{Before capture}} \qquad (3.3)$$

The momentum spread of the captured beam also depends on the choice of K_{AREA}. The main parameters are summarised in the Table 3.8.

Parameters for adiabatic trapping		
	Protons	**Ions**
Initial full $\Delta p/p$	$\pm 1.2 \times 10^{-3}$	$\pm 1.2 \times 10^{-3}$
Initial energy spread [keV]	±47.5	±201
Initial beam length [ns]	1235	2059
Injected beam emittance [eV s]	0.117	0.827
K_{AREA}	1.5	1.6
Final capture voltage [V]	350	291
Final full $\Delta p/p$	$\pm 2.441 \times 10^{-3}$	$\pm 2.534 \times 10^{-3}$
Final energy spread [keV]	±96.6	±424
Final beam length [ns]	819	1307
Capture time [ms]	26.8	40.4

Table 3.8 Parameters for adiabatic trapping

3.4.2 Acceleration cycle

After capture has been completed, the beam has to be accelerated to its extraction energy. The time needed to do this and the cosine form of the magnetic field ramp are described in Section 3.3. The magnets are always driven through the maximum cycle to establish stable hysteresis conditions whatever the particle type or extraction flat-top that is used. The cycles always contain the same sequence of functions, but since the partition between the ramping with and without beam changes so also does the overall cycle time (see Tables 3.4 to 3.7).

Since the main guide field is raised according to a cosine-like time law, the product $V_{RF}(t)\cdot\sin(\phi(t))$ is determined by the requirement that the beam energy must remain in synchronism with the field. The way in which the acceleration is shared between voltage and phase is the work of the optimisation of the rf programme. The goal of the rf programme is to perform this acceleration of the beam in the specified time, while keeping the bunch inside the aperture limits, minimising losses and keeping reasonable values for the rf voltage. A commonly used scheme is to rapidly reach a fixed rf voltage which is then kept constant. A cubic law for the voltage is satisfactory for the transition to the fixed value. Its boundary conditions are continuity of the function at the initial and final points and continuity of the first derivative at the end point. The continuity of the first derivative at the initial point has been dropped because it leads to an unacceptable increase of the momentum spread.

The cycles for the four extreme flat-tops are reported in Figures 3.21 to 3.24. Beneath each figure details are given of the critical points in the acceleration cycle at which the maximum space-charge tune shifts, the maximum momentum spread, the innermost excursion of the beam and the outermost excursion of the beam towards the electrostatic septum occur. Strictly speaking, the maximum horizontal and vertical tune shifts will also occur at different energies, but only one point is given since the differences are so small. Note that the beam is kept off-axis during injection, trapping and acceleration to make better use of the available aperture and to keep the beam away from the resonance.

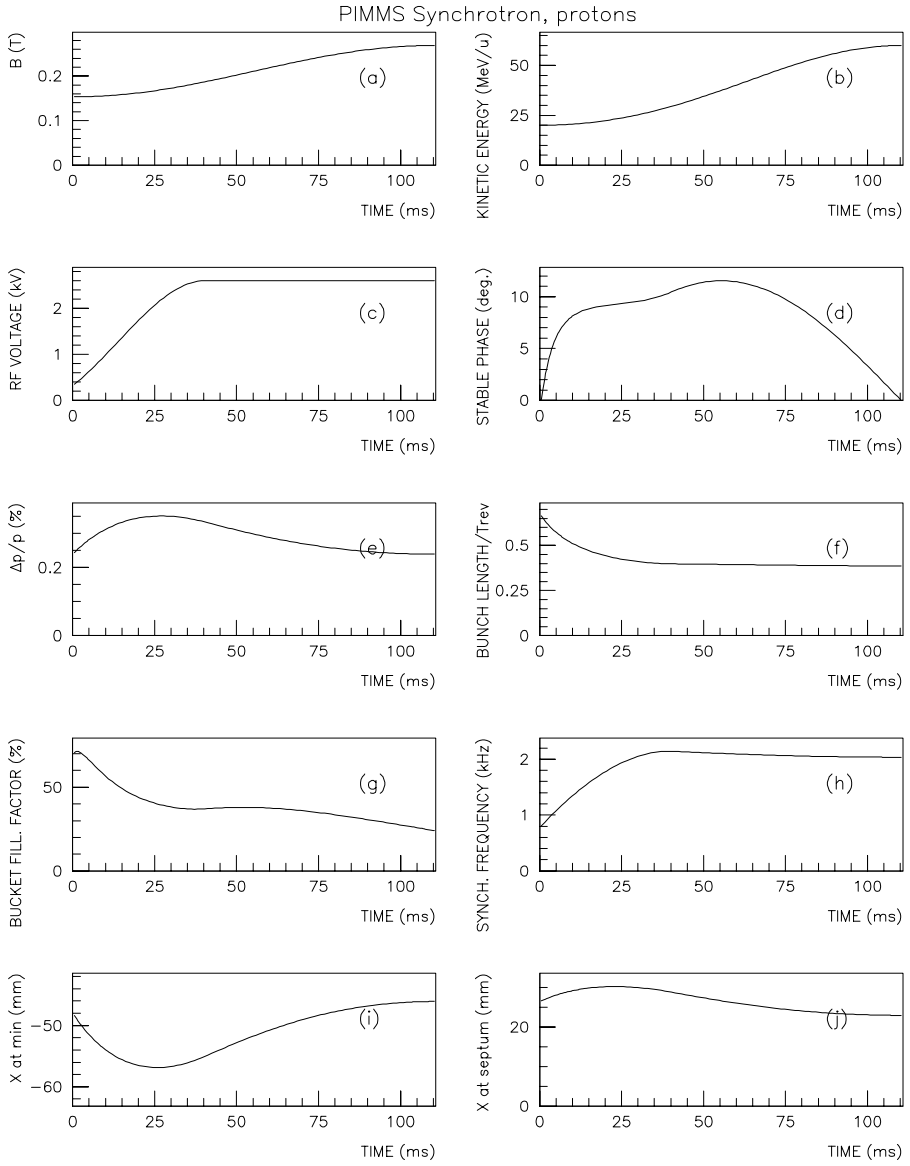

The acceleration time is 110.8 ms (see Table3.4). The maximum field ramp is 1.63 T/s.
The relevant parameters and their critical values during the acceleration cycle are:

Maximum $\Delta p/p$ = ±3.51‰ at:
t = 26.38 ms, K = 24.15 MeV, bunching factor = 0.41, innermost edge = -56.85 mm, edge at ES = 30.11 mm, synchrotron frequency = 1.97 kHz
Innermost excursion of the beam = -56.86 mm at:
t = 25.32 ms, K = 23.82 MeV, bunching factor = 0.42, edge at ES = 30.15 mm, synchrotron frequency = 1.95 kHz
Outermost excursion of the beam towards the ES = 30.19 mm at:
t = 22.16 ms, K = 22.93 MeV, bunching factor = 0.43, innermost edge = -56.74 mm, synchrotron frequency = 1.86 kHz

Figure 3.21 Proton acceleration to the lowest extraction energy of 60 MeV [10]

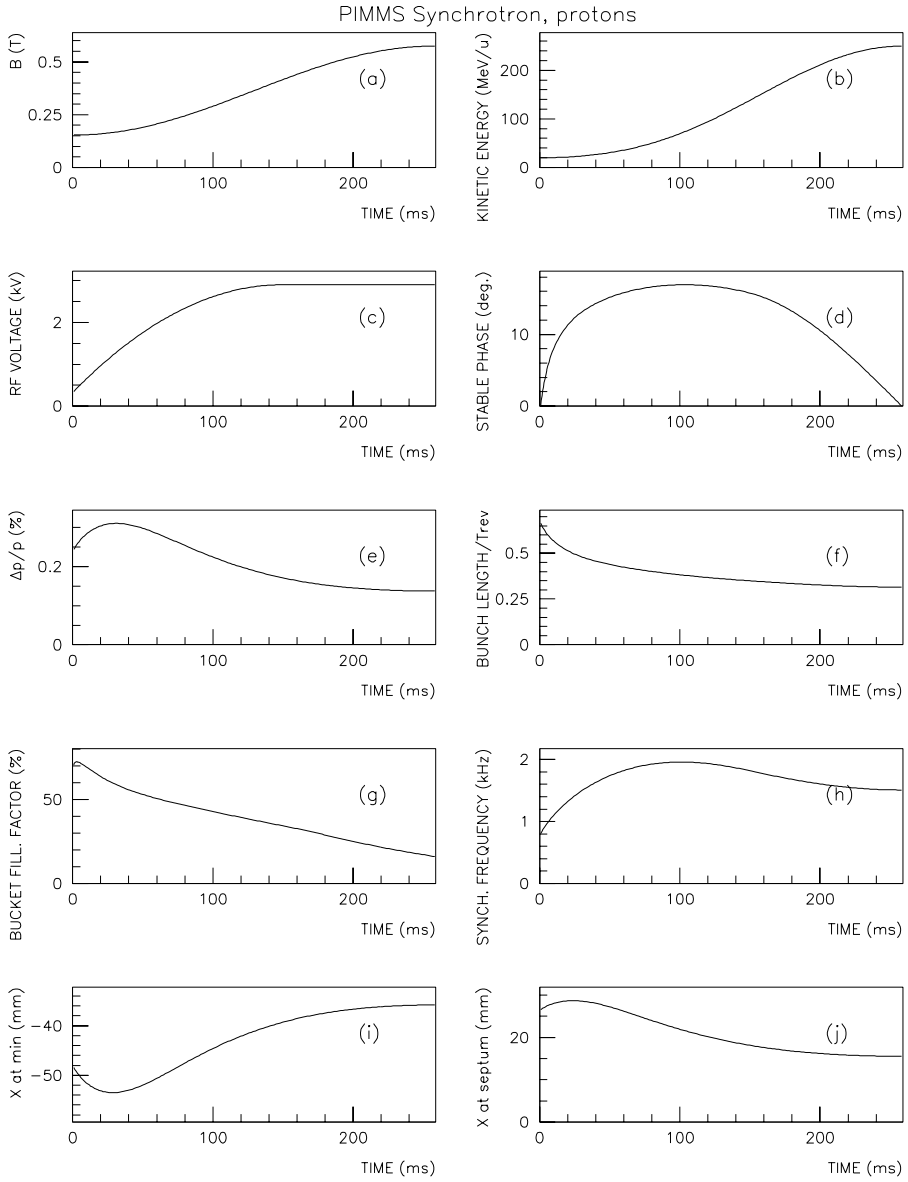

The acceleration time is 259.0 ms (see Table 3.5). The maximum field ramp is 2.55 T/s.
The relevant parameters and their critical values during the acceleration cycle are:

Maximum $\Delta p/p$ = ±3.10‰ at:
t = 30.49ms, K = 23.83 MeV, bunching factor = 0.47, innermost edge = -53.48 mm, edge at ES = 28.54 mm, synchrotron frequency = 1.51 kHz
Innermost excursion of the beam = -53.51 mm at:
t = 27.99 ms, K = 23.21 MeV, bunching factor = 0.48, edge at ES = 28.61 mm, synchrotron frequency = 1.47 kHz
Outermost excursion of the beam towards the ES = 28.67 mm at:
t = 22.97 ms, K = 22.14 MeV, bunching factor = 0.50, innermost edge = -53.39 mm, synchrotron frequency = 1.39 kHz

Figure 3.22 Proton acceleration to the highest extraction energy of 250 MeV [10]

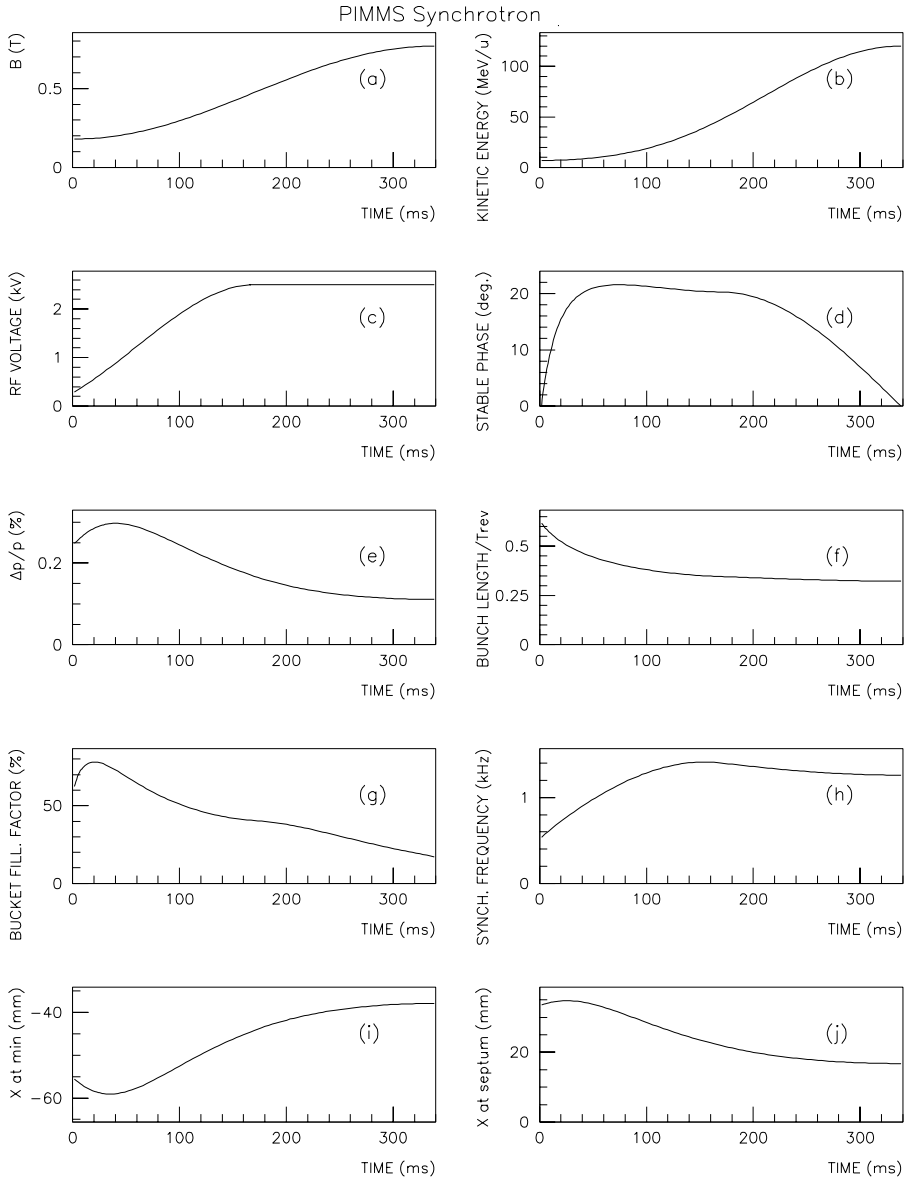

The acceleration time is 340.0 ms (see Table 3.6). The maximum field ramp is 2.72 T/s. The relevant parameters and their critical values during the acceleration cycle are:

Maximum $\Delta p/p$ = ±2.97‰ at:
t = 40.80 ms, K = 8.69 MeV/u, bunching factor = 0.46, innermost edge = -58.91 mm, edge at ES = 34.26 mm, synchrotron frequency = 0.92 kHz

Innermost excursion of the beam = -59.05 mm at:
t = 34.00 ms, K = 8.16 MeV/u, bunching factor = 0.48, edge at ES = 34.57 mm, synchrotron frequency = 0.86 kHz

Outermost excursion of the beam towards the ES = 34.74 mm at:
t = 23.8 ms, K = 7.55 MeV, bunching factor = 0.50, innermost edge = -58.79 mm, synchrotron frequency = 0.77 kHz

Figure 3.23 Carbon-ion acceleration to the lowest extraction energy 120 MeV/u [10]

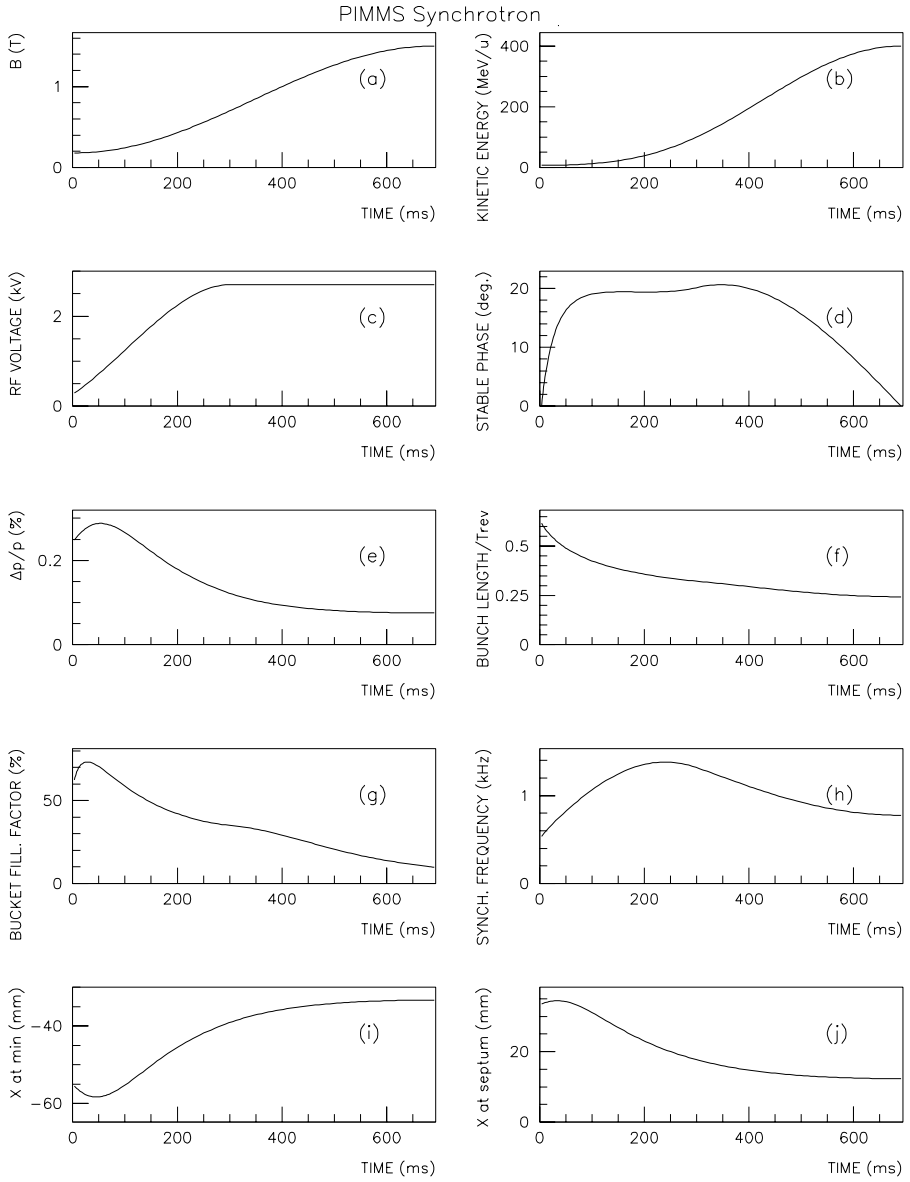

The acceleration time is 694.0 ms (see Table 3.7). The maximum field ramp is 2.98 T/s.
The relevant parameters and their critical values during the acceleration cycle are:

Maximum $\Delta p/p$ = ±2.88‰ at:
t = 48.58 ms, K = 8.28 MeV/u, bunching factor = 0.49, innermost edge = -58.28 mm, edge at ES = 34.14 mm, synchrotron frequency = 0.83 kHz

Innermost excursion of the beam = -58.33 mm at:
t = 41.64 ms, K = 7.93 MeV/u, bunching factor = 0.50, edge at ES = 34.33 mm, synchrotron frequency = 0.79 kHz

Outermost excursion of the beam towards the ES = 34.46 mm at:
t = 27.76 ms, K = 7.40 MeV, bunching factor = 0.53, innermost edge = -58.03 mm, synchrotron frequency = 0.71 kHz

Figure 3.24 Carbon-ion acceleration to the highest extraction energy 400 MeV/u [10]

3.4.3 Preparation of the beam for extraction

At the end of the acceleration, the bunch is shifted quickly in rf phase to the unstable fixed point and allowed to elongate along the separatrix before being debunched into a coasting beam with a total $\Delta p/p$ of ~4‰ and a distribution as uniform as possible. The technique is a relatively well-known rf gymnastic, but should take into account the following constraints:

- The time needed for the whole manipulation should be a few tens of milliseconds.
- The rf voltages should not exceed the values in the acceleration cycle.

The gymnastic is divided into two steps:

- **Step 1-RF phase jump:** At the end of the acceleration, the bucket is stationary ($\phi_s = 0$) and the rf voltage is maintained at its final value. In a few tens of nanoseconds, a phase jump of 180° is performed with the rf voltage. The bunch then elongates along the separatrix. The phase is maintained at the unstable fixed point until the desired $\Delta p/p$ is reached. For the parameters of the PIMMS cycle, this takes ~0.1 ms. The procedure is quick, simple to perform from the hardware point of view, and widens and flattens the final beam distribution.

- **Step 2-Debunching:** The rf voltage is switched off and the beam starts to fill the ring. The time needed until the head of the bunch reaches its tail is given by (3.4) from [6], which in the present case is less than 1 ms. However, a complete filamentation of the longitudinal phase space takes much longer and a period of 30 ms has been reserved for this.

$$T_{\mathrm{db}} = \frac{1}{\pi h f_{\mathrm{rev}} \eta \, \Delta p / p} \cdot \left(\pi - \frac{\Delta \phi_{\mathrm{bunch}}}{2} \right) \tag{3.4}$$

The debunching process is rapid and non-adiabatic. Simulations have been made with ESME with 10’000 macro-particles and are shown in Figure 3.25.

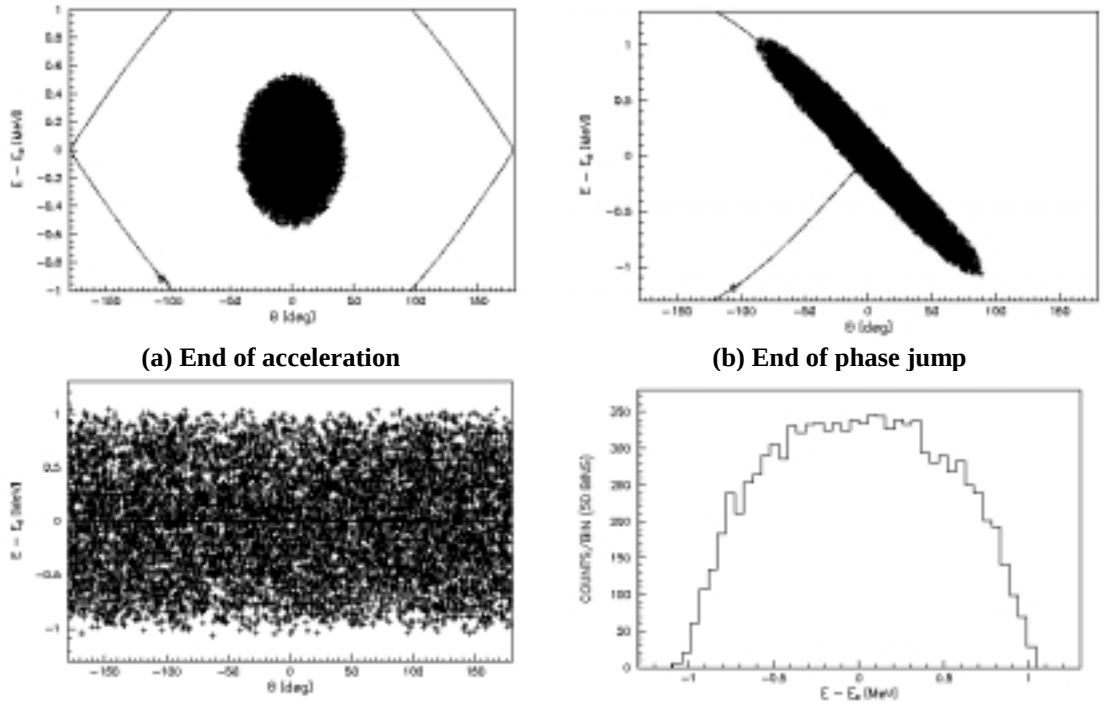

(a) End of acceleration **(b) End of phase jump**

(c) 20 ms after rf switch-off **(d) Final beam distribution in $\Delta E/E$**

Figure 3.25 RF manipulations after acceleration at the start of the flat-top

3.5 APERTURE

3.5.1 General considerations

Conventional machines

Most accelerators and storage rings have a single beam and the aperture can be determined by considering the basic space requirements for the betatron oscillations, the momentum spread, the estimated closed-orbit excursions and a collimation or chamber protection margin, as shown below.

$$\text{Chamber aperture} = \pm\left[\overbrace{\underbrace{n\sqrt{\beta E_{\sigma}/\pi}}_{\substack{\text{Betatron}\\ \text{envelope}}} + \underbrace{0.5D(\Delta p/p)_{\text{Full}}}_{\substack{\text{Momentum}\\ \text{envelope}}} + \text{Closed orbit}}^{\text{GOOD-field region}} + \overbrace{\text{Collimator margin}}^{\text{POOR}-\text{field region}}\right] \qquad (3.5)$$

where *n* refers to the number of RMS values to reach the edge of the beam.

The betatron oscillations, momentum spread and closed-orbit margin determine the 'good'-field region in the magnets while the collimation margin occupies the 'poor'-field region, since, in principle, the beam should not enter this space. In general, the largest beam occurs at injection and the smallest beam occurs at the top energy, due to adiabatic damping, making it possible to relax the 'good'-field specification at high field where the magnets saturate. Once the basic envelope is decided, any additional space that is required for injection, extraction etc. can be added.

In medical synchrotrons the situation is more complicated. The new and essential component is the space required by the separatrices, which is different to that required by the main beam. The separatrices are determined by tracking and do not follow the betatron envelope. They are not subject to adiabatic damping in the plane of extraction, but they are subject to it in the orthogonal plane. Since the separatrices have such a low density, it is unnecessary to consider a collimation margin. Finally, the main beam is accumulated and stored off-axis, which requires more aperture.

$$\text{Separatrix aperture} = \pm\left[\overbrace{\underbrace{\text{Separatrices}}_{\substack{\text{Based on}\\ \text{tracking}}} + \text{Closed orbit}}^{\text{GOOD-field region}}\right] \qquad (3.6)$$

PIMMS aperture

The calculation of the aperture depends on a number of compromises and somewhat arbitrary decisions concerning the definition of the total emittance, the closed-orbit margins and the collimation margins mentioned in (3.5) and (3.6). These decisions are summarised in Table 3.9.

Basic parameter choices for aperture calculations	
Maximum horizontal closed-orbit margin [mm]	±10
Maximum vertical closed-orbit margin [mm]	±7.5
Edges of the beam (2D elliptical beam model)	±√5 (RMS)
Collimation margin (~ half the closed-orbit margins) [mm]	±5

Table 3.9 Basic parameter choices for aperture calculations

The definition of the total emittance determines the beam edge for a given RMS emittance and this depends upon the model used (see Appendix A). The closed-orbit margins have been chosen to be consistent with the estimated orbit errors and operational requirements (see Section 3.6) In high-intensity machines, the collimation space should be at least equal to the maximum allowable closed-orbit distortion, but in a low-intensity machine, this space is useful, rather than essential, and a smaller margin is acceptable. The shadow behind the collimation block protects the chamber, pickup electrodes etc. and provides the space for the fast dumping. In any case, this shadow occupies the "poor" field region.

In the case of PIMMS, the separatrices determine the horizontal 'good-field' region and, since the separatrices occupy the same space (horizontally) at all times, this removes the usual bonus of being able to reduce the 'good-field' region at top energy. However, the proton beam determines the overall horizontal aperture, due to the additional space requirement for collimation in the 'poor-field' region. In the vertical plane, the aperture depends on the ion beam at injection (the proton beam has a smaller emittance). Because the main ion beam is accumulated off-axis and because the separatrices penetrate to the full extent of the horizontal aperture with the full vertical emittance, it necessary to move away from an elliptical chamber to a more rectangular shape.

3.5.2 Horizontal space requirements for the separatrices

Figure 3.26 shows a schematic view of the PIMMS aperture during extraction. The extraction is made to the outside of the chamber. The 'waiting' beam is in the inner half of the chamber and the resonance is positioned at the chamber centre so that the separatrices have a well-balanced aperture into which to grow. The radial position of the electrostatic septum wires is 35 mm and the spiral step is 10 mm.

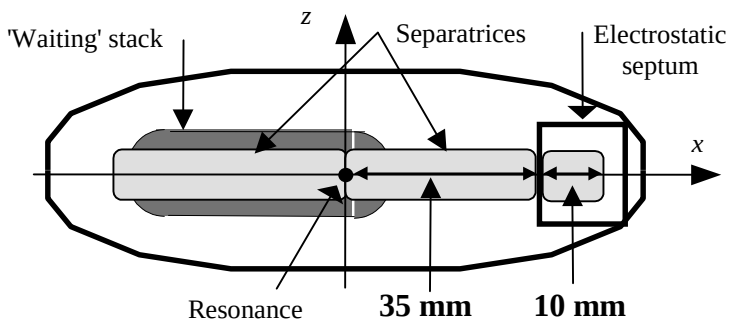

Figure 3.26 Schematic cross-section of the vacuum chamber at extraction

Figure 3.27 shows the limiting trajectories of the separatrices over the last three turns before they are extracted and the extracted beam segment between the electrostatic and magnetic septa. The figure appears rather complicated because all the distinct beam conditions are included (i.e. on-resonance ions and protons at all energies, off-resonance ions and protons at lowest extraction energy, off-resonance protons at top extraction energy and off-resonance ions at top extraction energy). The exact provenance of each curve is not important, the aim is to establish the overall space requirement for the separatrices at each position along the machine for all the possible operating conditions.

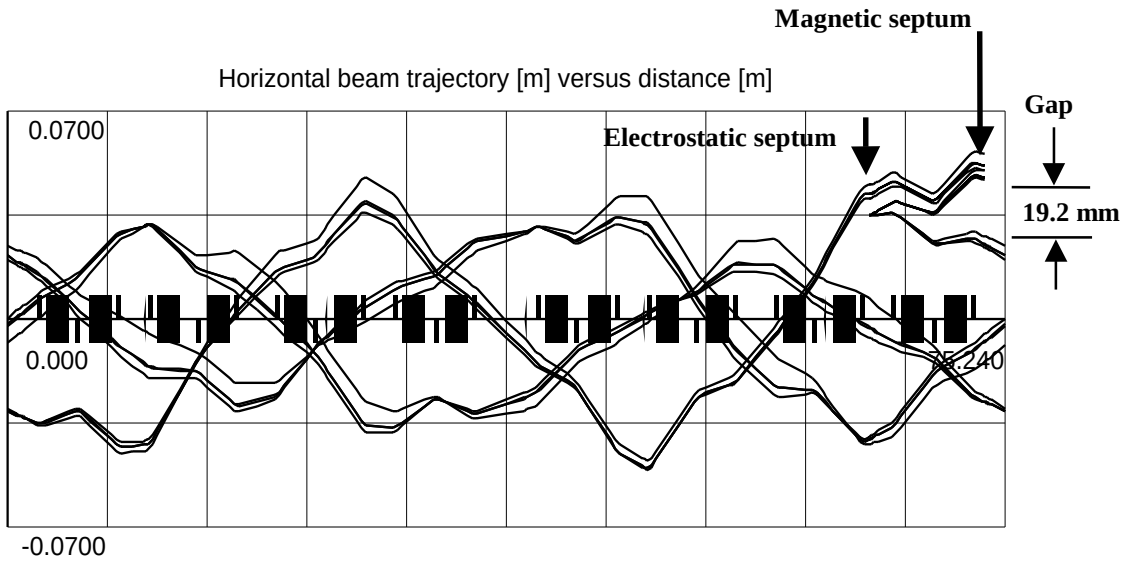

Figure 3.27 Limiting trajectories of the separatrices for the last three turns before extraction and the extracted segment between the electrostatic and magnetic septa

The extreme transverse excursions at each longitudinal position in Figure 3.27 are recorded in Table B1 in Appendix B. The bare excursions for the circulating separatrices fit within +47.4 mm (on-resonance protons) and -50.7 mm (off-resonance protons at lowest extraction energy). The segment of extracted beam passing between the electrostatic and magnetic septa has the outer limit of +56.6 mm (on-resonance protons). To these figures, it is necessary to add a closed-orbit margin (also recorded in Table B1 in Appendix B), but not a collimation margin. The segment of beam that passes between the two septa must be specially corrected by local bumps and a reduced, closed-orbit margin of 5 mm is applied in this region. However, for the rest of the machine, the normal, horizontal, closed-orbit margin of ±10 mm is maintained.

The addition of the full closed-orbit margin is justified as follows. Once the machine has reached extraction energy, the closed orbit will be corrected, but, in order, to make the machine operation tolerant of errors caused by missing monitors etc., orbit distortions up to ±5 mm peak-to-peak will be accepted. However, in certain elements (e.g. resonance sextupole, chromaticity sextupoles and extraction septa), a secondary set of orbit corrections must then be applied in the form of local bumps. The local bumps in this scenario can be up to ±5 mm and are likely to degrade the closed-orbit outside their central regions by about the same amount. For this reason,

the full closed-orbit margin has to be maintained for the rest of machine even though the closed orbit is, in principle, corrected for extraction.

Figure 3.27 also shows the extracted beam segment as it diverges from the circulating separatrices between the two septa and Table B2 in Appendix B lists the outermost edge of this beam segment with account being taken of all the possible beam conditions and with the addition of the closed-orbit margin.

3.5.3 Gap for the magnetic septum

The last feature of importance in Figure 3.27 is the 'gap' that is opened between the circulating separatrices and the extracted beam segment. The current 'wall' of the magnetic septum and the vacuum chamber walls must fit within this space. The trajectories that determine the minimum gap are the on-resonance particles in the circulating beam and the off-resonance particles in the extracted beam. The maximum available gap is 19.2 mm. Table 3.10 shows how this space will be allocated.

Allocation of the gap for the magnetic septum		
Clearance between circulating separatrix and vacuum pipe	[mm]	2.0
Main vacuum pipe*	[mm]	1.5
Magnetic shield	[mm]	1.0
Alignment tolerance and air gap	[mm]	0.7
Insulation of septum coil	[mm]	0.5
Septum coil	[mm]	9.5
Insulation of septum coil	[mm]	0.5
Alignment tolerance	[mm]	0.5
Extraction vacuum pipe*	[mm]	1.0
Clearance between vacuum pipe and extracted beam	[mm]	2.0
Total	[mm]	19.2

* The standard vacuum pipe wall thickness is 2mm, but, for walls against septa, the chamber can be machined up to 0.5 mm on the main chamber and 1 mm on the magnetic septum chamber so that the overall dimensions are respected.

Table 3.10 Allocation of the gap for the magnetic septum

3.5.4 Horizontal aperture for injected beam

Figures 3.28 and 3.29 show the horizontal envelope of the proton beam for passive spreading and the carbon ion beam shortly after injection at their so-called 'critical points'. In reality, a 'critical point' is a series of adjacent points near the start of the energy ramp, at which the space-charge tune shifts and the momentum spread in the beam reach their maximum values (due to the bunching action of the rf), but since the points are close and the maxima are rather flat, it is unnecessary in most cases to distinguish between them. In Figure 3.28, the proton beam is shown at 23 MeV and, in Figure 3.29, the carbon ion beam is shown at 8 MeV. These are the points at which each beam reaches its maximum horizontal size. The beams are off-centred to make the better use of the space between the inner chamber wall and the septa and they have the maximum momentum spread corresponding to the critical point (Proton beam: $\Delta p/p_{\text{average}} = -0.0018$, $\Delta p/p_{\text{full}} = 0.007$; Carbon-ion beam: $\Delta p/p_{\text{average}} = -0.0021$, $\Delta p/p_{\text{full}} = 0.006$).

For the protons in Figure 3.28, there is the added problem of space-charge induced incoherent tune shifts. Consequently, the unloaded working point has been displaced upwards in the tune diagram, so that once the full space-charge load is added the beam will occupy the nominal storage region (Q_x = 1.68, Q_z = 1.72) close to the resonance. The unloaded working point is closer to the integer resonance and, as a result, the oscillations of the betatron amplitude functions (and hence the beam size) are increased with respect to those at the nominal storage position. Since the synchrotron oscillations move particles through the length of the bunch from the extremities, where the space charge is quasi-zero, to the middle, where it is maximum, the beam will 'see' the perturbed Twiss functions and hence, for the aperture calculations in Figure 3.28, the unloaded working point is used. For simplicity, the unloaded working point (Q_x = 1.764; Q_z = 1.829) has been fixed according to the 'worst' case scenario of the passively spread proton beam at 23 MeV, the critical point in the rf cycle. It will be shown later that the proximity of the integer resonance is one of the effects that limits the lowering of the proton injection energy. The carbon ions have so little space charge that this consideration is of only academic interest.

Finally, for the purpose of determining the aperture, it is necessary to add the closed-orbit margin of 10 mm (scaled by $\sqrt{\beta}$) on both sides of the proton and carbon ion beams and, on the low-momentum (inner) side, an additional collimation margin of 5 mm (also scaled by $\sqrt{\beta}$) to protect the chamber and beam instrumentation. Unfortunately, it is not possible to add this margin on the high-momentum (outer) side, where it would protect the extraction septa, because the beam is far off axis and its outer edge is well inside the aperture required by the separatrices in virtually all positions. For this reason, it is possible that the electrostatic and magnetic septa may be hit by the 'waiting' beam in the event of a manipulation error. The apertures required by the proton and carbon beams are recorded with the closed-orbit and collimation margins in Tables B3 and B4 respectively in Appendix B. Comparing Tables B3 (protons) and Table B4 (carbon) with Tables B1 and B2 (separatrices) shows that the injected beams fit comfortably within the aperture of the separatrices.

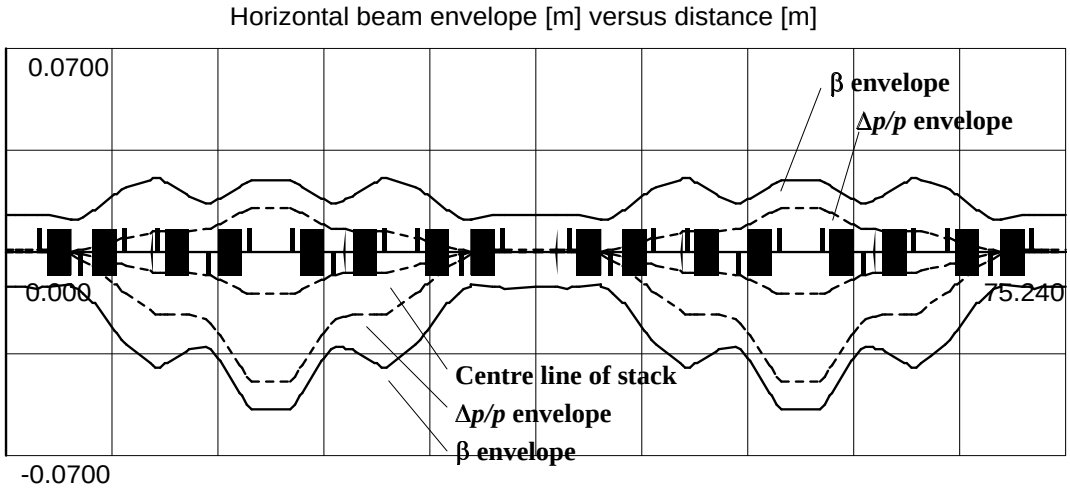

[At 23 MeV critical point; $\Delta p/p_{\text{ average}}$ = -0.0018; $\Delta p/p_{\text{ full}}$ = 0.007; $E_{x,RMS} = E_{z,RMS}$ = 2.2825π mm mrad; bunching factor = 0.4;
1-D parabolic distributions in all planes; 32.066 mA peak bunched current;
Unloaded tunes Q_x = 1.7642, Q_z = 1.8292; Loaded tunes Q_x = 1.6800, Q_z = 1.7200]

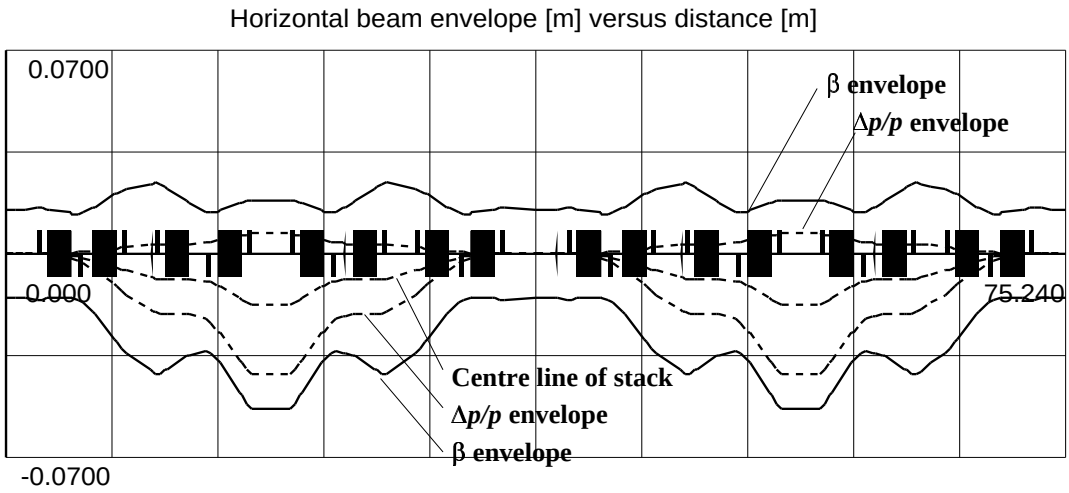

Figure 3.29 Horizontal beam envelope for the carbon-ion beam for active scanning
[At 8.5 MeV/u critical point; $\Delta p/p_{\text{average}} = -0.0021$; $\Delta p/p_{\text{full}} = 0.006$;
$E_{x,RMS} = E_{z,RMS} = 5.525\pi$ mm mrad; bunching factor = 0.4;
1-D parabolic distributions in all planes; 1.3705 mA peak bunched current]

3.5.5 Vertical aperture for the injected beam

Figure 3.30 shows the vertical envelopes at injection of the carbon-ion beam and the proton beam for passive spreading. However, only the carbon-ion beam needs to be considered in the context of the aperture, since its emittance is much larger ($E_{z,RMS} = 6.1\ \pi$ against $2.5\ \pi$ mm mrad for the proton beam).

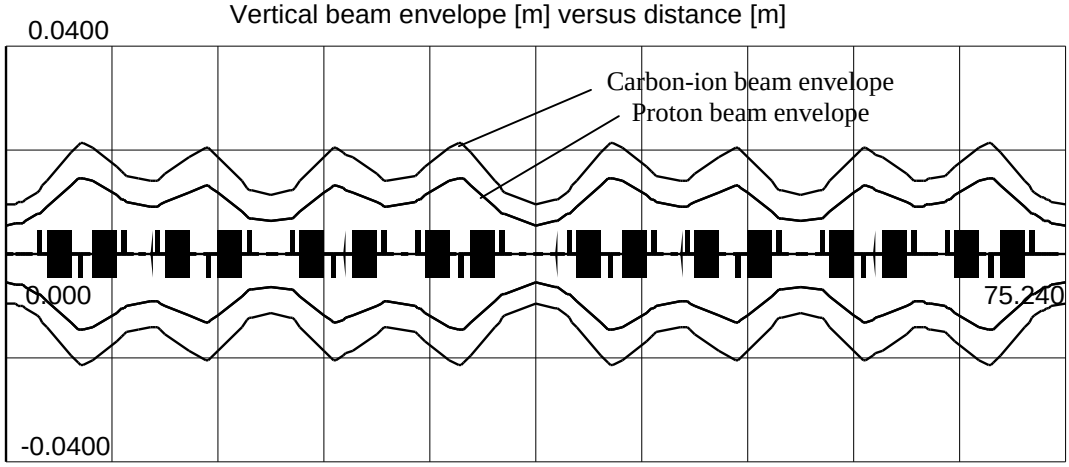

Figure 3.30 Vertical beam envelope of the carbon-ion beam at injection
[7 MeV/u and $E_{z,RMS} = 6.106\pi$ mm mrad]

The beam sizes in Figure 3.30 are tabulated in Appendix B in Table B5 and Table B6 with the extra margins for the closed orbit (±7.5 mm) and the collimation (±5 mm) both scaled with square root of the betatron amplitude.

3.5.6 Nominal dimensions of the aperture and 'good' field region

Based on the above considerations and the beam sizes tabulated in Appendix B, the nominal dimensions of the physical aperture (i.e. beam size + closed-orbit margin + collimation margin) and the 'good' field region (i.e. beam size + closed-orbit margin) have been decided and are recorded in Table 3.11. It can be noted that:

- Horizontally, the physical apertures have been interpreted liberally (140 mm aperture whereas 130 mm is technically sufficient). This means that the vacuum chamber occupies more of the 'poor' field region. This has been done to facilitate operation and to provide more aperture in the 'corners' of the aperture (see Section 3.2.8). This has been without affecting power consumption.
- Vertically, the physical aperture has been reduced to its minimum inside the main dipoles in order to reduce the magnet gaps and hence the power dissipation. Outside the main dipoles the vertical aperture is again interpreted liberally with 74 mm rather than the strict minimum of 68 mm.
- In general, the 'good' field regions have been interpreted as the minimum acceptable values.
- In certain vacuum chambers, for example next to septum magnets, it will be necessary to reduce the apertures below the nominal values in Table 3.11. In these cases, the local beam sizes will be used to determine the local requirements.
- Since the vertical plane is subject to adiabatic damping, the 'good' field region is reduced at high field according to $1/(\beta\gamma)$.

Nominal chambers, apertures and 'good' field regions

Parameter	Horizontal	Vertical	Comment
Chambers:			
Outside dipoles	144 (±72) mm	78 (±39) mm	2mm wall stainless steel
Inside dipoles	special	special	Thin-corrugated or ribs (See Section 4.11)
Physical aperture:			
Outside dipoles	140 (±70) mm	74 (±37) mm	Horiz. generous.
Inside dipoles	140 (±70) mm	64 (±32) mm	Vert. abs. min. in dipole.
'Good' field regions:			
At injection			
Outside dipoles	120 (±60) mm	60 (±30) mm	Horiz. set by separatrices
Inside dipoles	120 (±60) mm	56 (±28) mm	Vert. set by ion beam
At top field			
Outside dipoles	same as low field	22 (±11) mm	Horiz. has no damping
Inside dipoles	same as low field	20 (±10) mm	Vert. is damped

Table 3.11 Nominal chambers, apertures and 'good' field regions

3.5.7 Maximum beam sizes

The horizontal aperture has been decided with reference to the separatrices and, as a consequence, there is a small margin of security for the injected beams. Since the emittances are constant (set by the dilution), this margin is available for an increased momentum spread at the critical point in the rf cycle. Table 3.12

summarises the margins that are available calculated at the critical points in the rf cycles with reference to Figure 3.31.

Safety margins for injected beams calculated at critical points in rf cycle		
Scenario	**Nominal full width in $\Delta p/p$**	**Max. allowable full width in $\Delta p/p$**
High-intensity protons for passive spreading*	0.00728	0.0085 (mean $\Delta p/p$ = -0.0015
Carbon ions	0.00586	0.0062 (mean $\Delta p/p$ = -0.0021)

* Almost identical for the medium-intensity protons for active scanning.

Table 3.12 Safety margins for injected beam calculated at critical points in rf cycle
[Protons at 23 MeV on unloaded working point and $E_x = 2.2825\pi$ mm mrad.
Carbon ions at 8.5 MeV/u and $E_x = 5.525\pi$ mm mrad.]

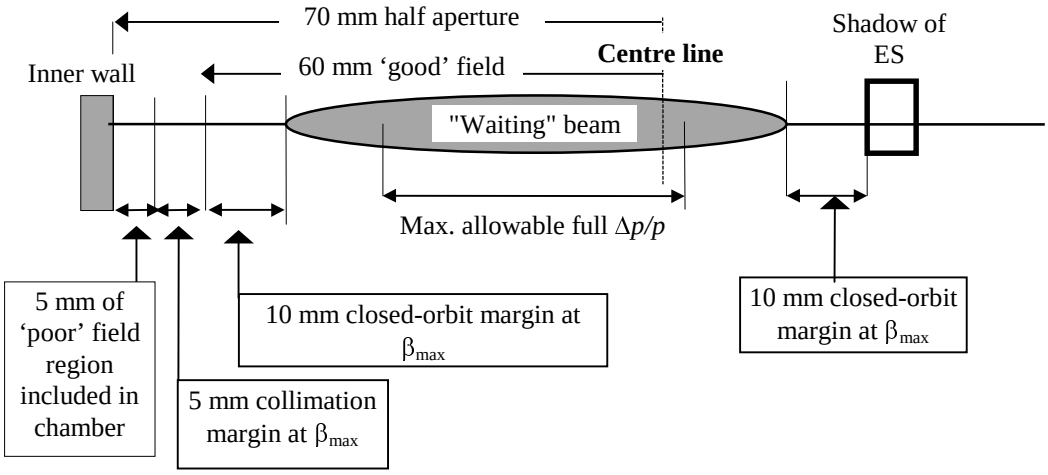

Figure 3.31 Layout of the aperture for the maximum 'waiting' beam size

3.5.8 Chamber cross-section

In most machines, it is accepted that the beam will have an elliptical cross-section and that any particles that start with large amplitudes in both planes will be lost somewhere along the injection chain. For this reason, it is usually unnecessary to insist on the full vertical aperture across the whole radial aperture. The separatrices and the off-centred stack in a medical synchrotron, however, do require a fuller vertical aperture than is usual. Fortunately, it has been possible to enlarge the chamber horizontally beyond what is strictly needed in the median plane and fortunately the separatrices, even at the lowest extraction energy, have shrunk considerably in the vertical plane due to adiabatic damping.

A rectangular vacuum chamber provides the best aperture, but it is not well adapted to withstanding the atmospheric pressure. From this point of view, a 'super'-

elliptical* or racetrack shape is preferable. Figures 3.32 and 3.33 show the locii of the 'corners of the maximum-sized beam at injection outside and inside the dipoles respectively. The smaller vertical aperture inside the dipoles is clearly visible in Figure 3.20 and in this case the beam exceeds the aperture by a very small margin. The maximum-sized beam that is used in Figures 3.32 and 3.33 is a carbon beam at injection that fills the full available radial aperture according to Section 3.5.7. Figure 3.33 shows that this beam indeed corresponds to the limit of the physical aperture.

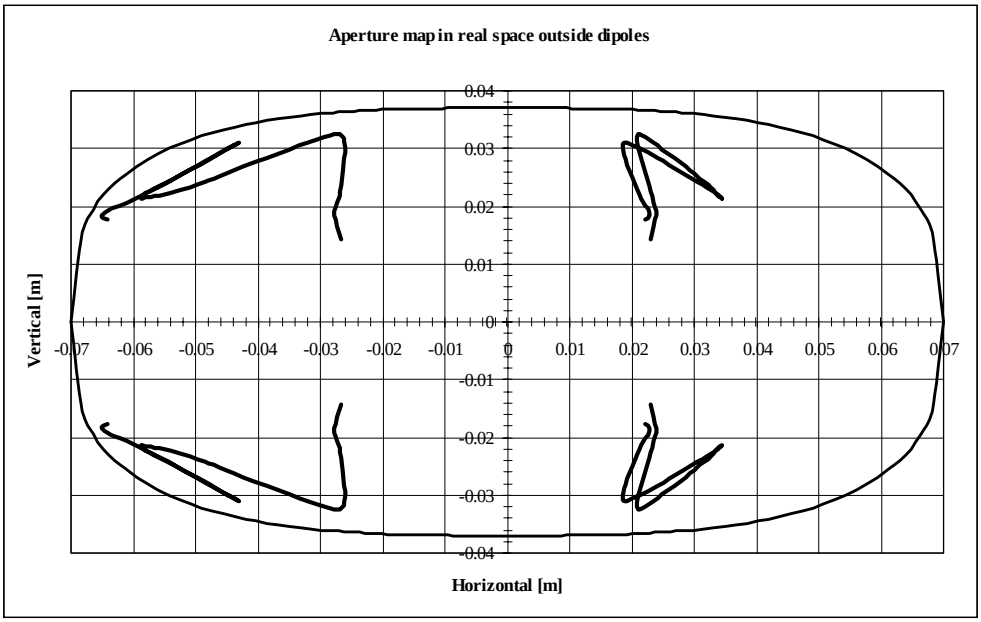

Figure 3.32 Locii of the 'corners' of the 'maximum beam' (according to Section 3.5.7) outside the dipoles

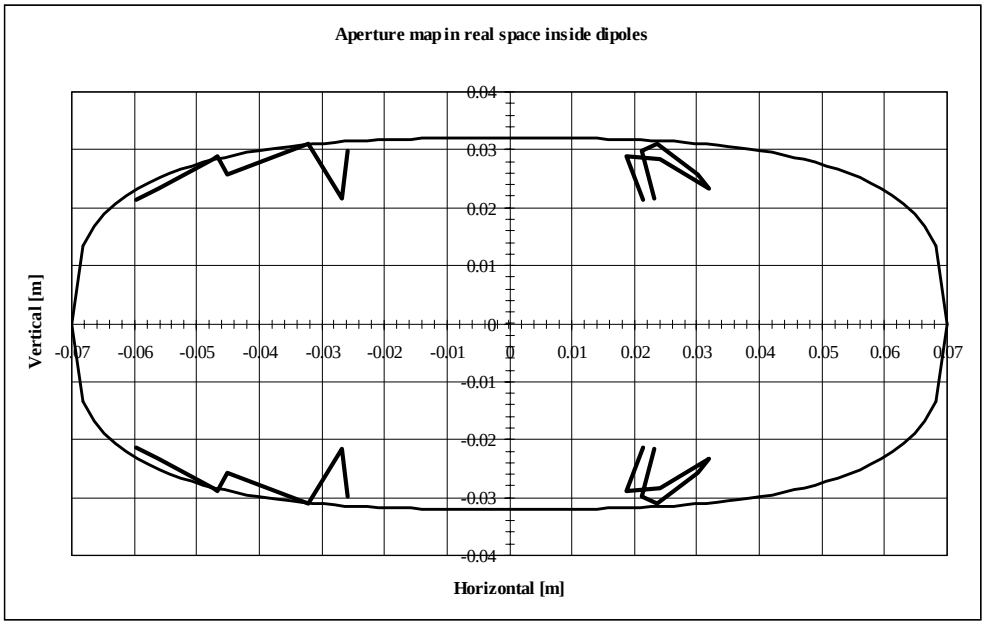

Figure 3.33 Locii of the 'corners' of the 'maximum beam' (according to Section 3.5.7) inside the dipoles

* The 'super'-ellipse of the form $(x/a)^n + (y/b)^n = 1$, where $n>2$. Coffee tables look pleasing with $n = 2.5$, but PIMMS is based on $n = 3$.

3.6 CLOSED-ORBIT PROGNOSIS AND CORRECTION [11]

The machine will inevitably contain many imperfections that will affect the closed orbit. These will include steel quality, manufacturing tolerances, alignment tolerances, thermal distortions and many others. The first step is to estimate the closed-orbit distortion to be expected in a freshly aligned machine and to compile statistics for the efficiency of the correction system. It is useful to estimate how quickly the closed orbit will degrade and to get some feeling for how frequently it will be necessary to realign. To determine the strength of the correctors, the demands for orbit manipulations other than the global orbit correction must also be evaluated. The basic guidelines for the closed-orbit correction and control are:

- For injection, the closed orbit must be within ±10 mm horizontally and ±7.5 mm vertically.
- For extraction, the basic closed orbit correction must be within ±5 mm in both planes.
- For extraction, local corrections are needed at the septa and sextupoles to better than ±1 mm.
- When adding a local correction the closed orbit may degrade elsewhere, but must never exceed the global limits of ±10 mm horizontally and ±7.5 mm vertically.

3.6.1 Closed-orbit distortion prognosis at injection

The closed orbit is most strongly affected by transverse alignment errors of quadrupoles, the longitudinal alignment errors of dipoles, tilts of dipoles and the random spread in integrated field in the dipoles (estimated in Section 4.1). The correctors, being weaker, are allowed a larger relative field error. The monitors have both alignment errors and reading errors. The latter are given a uniform distribution rather than the gaussian of all the other errors. It is assumed that the ring must be aligned with equipment and techniques that are standard and are not pushed to the limit of their performance. The tolerances to be expected from a standard alignment were established with expert help* and are given in Table 3.13.

Assumed tolerances for magnetic elements and monitors	
For a 'standard' alignment	**Tolerance**
Alignment tolerances: Δx_{RMS}, Δs_{RMS}, Δz_{RMS} [m]	0.3×10^{-3}
Tilt about all three co-ordinate axes, $\Delta\theta_{RMS}$ [rad]	0.3×10^{-3}
Cut-off for alignment and tilt errors	3 RMS
Monitor reading errors	
Uniform distribution [mm]	±0.1
Estimated magnet manufacturing tolerances	
Integrated relative dipole field error at low field*, $(\Delta BL/BL)_{RMS}$	1.2×10^{-3}
Integrated rel. dipole field error at high field*, $(\Delta BL/BL)_{RMS}$	1.2×10^{-3}
Integrated relative corrector field error**, $(\Delta BL/BL)_{RMS}$	1.0×10^{-2}
Cut off for all field errors	3σ

* Remanent field errors dominate at injection and packing factor errors dominate at top field. The packing factor tolerance has been adjusted to give approximately the same total error at all energies.
** Since correctors are much weaker than main dipoles they are allowed a larger relative error.

Table 3.13 Assumed tolerances for magnet elements and monitors

* M. Mayoud, Leader of the CERN Survey Group.

One thousand machines with random errors generated with gaussian distributions cut-off at three standard deviations according to Table 3.13 have been analysed before and after correction. The basic data is presented in Figures 3.34 (a) and (b) for the horizontal plane and Figures 3.35 (a) and (b) for the vertical plane. An analysis of this data is summarised in Table 3.14. The orbits have been calculated on the de-tuned working point (Q_x = 1.758, Q_z = 1.820) for a high-intensity proton beam for passive spreading at injection. This causes a slight degradation of the orbit compared to what would exist for a zero-intensity beam at the nominal injection tunes. The absolute maximum excursions are quoted, since these are of more direct interest for the aperture than the peak-to-peak values.

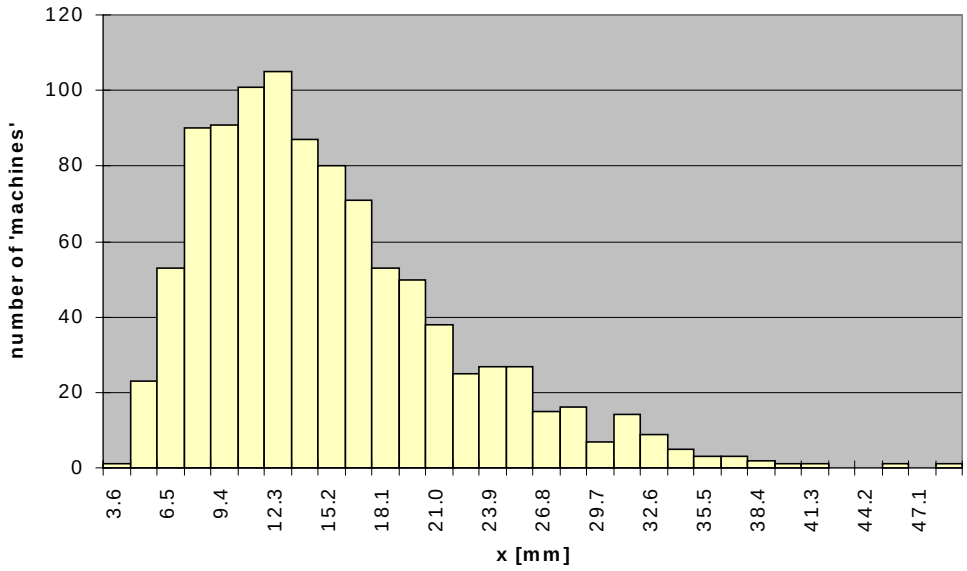

(a) Horizontal, maximum absolute excursions of the closed orbit before correction

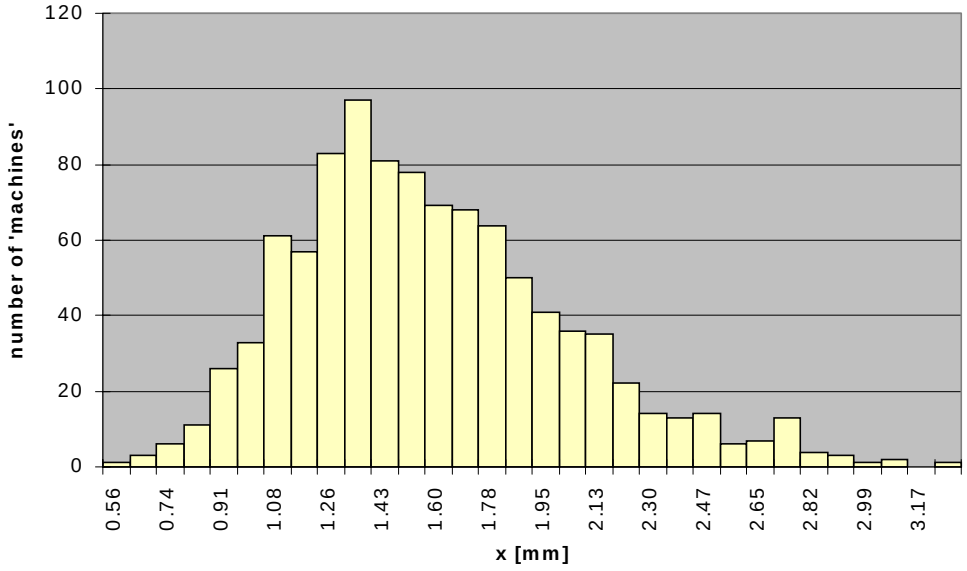

(b) Horizontal, maximum absolute excursions of the closed orbit after correction

Figure 3.34 Statistics for 1000 randomly generated, horizontal, closed orbits before and after correction at injection - Note the change of scale

[At injection 20 MeV (not critical point), De-tuned working point for the passively spread proton beam: Q_x = 1.758, Q_z = 1.820, Sextupoles are switched off, All correctors and monitors working]

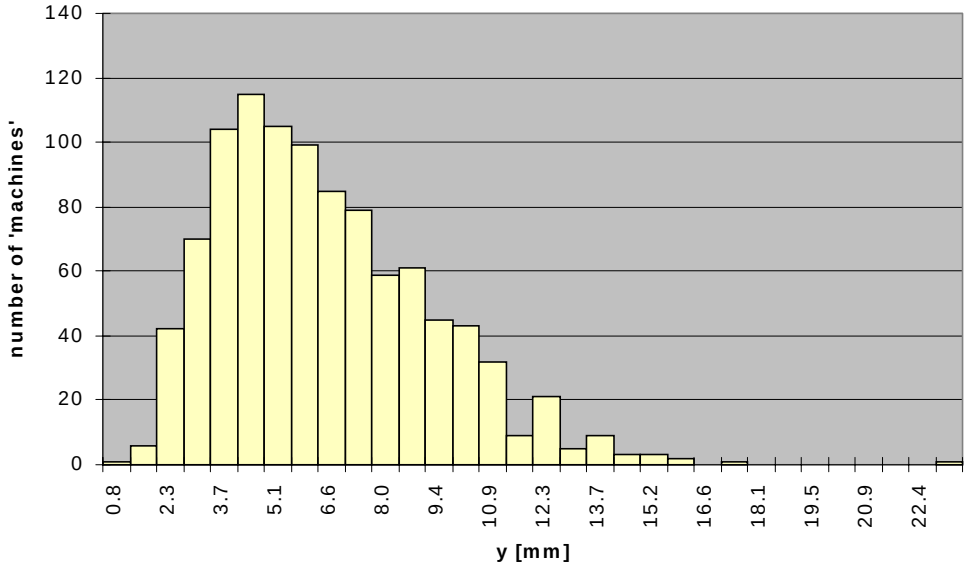

(a) Vertical, maximum absolute excursions of the closed orbit before correction

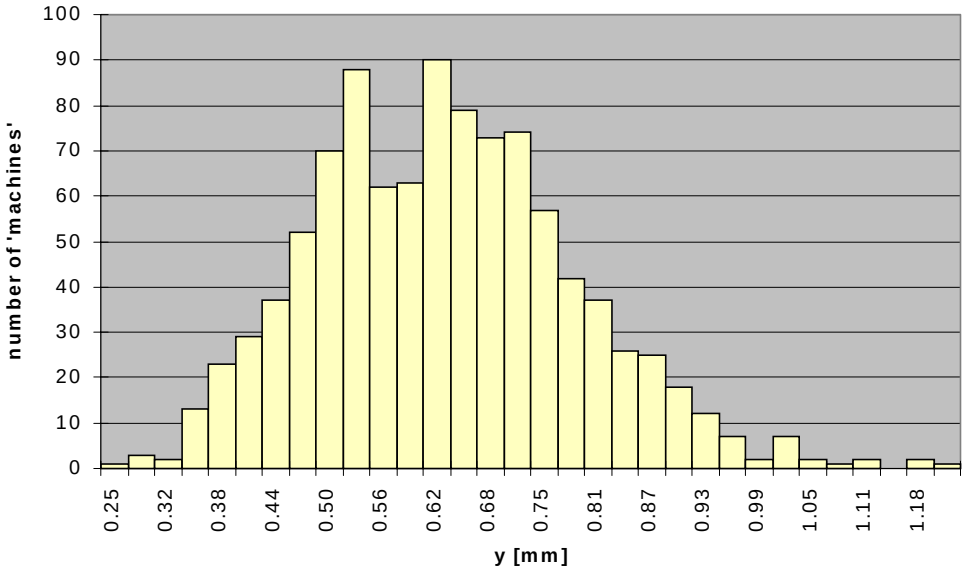

(b) Vertical, maximum absolute excursions of the closed orbit after correction

Figure 3.35 Statistics for 1000 randomly generated, vertical, closed orbits before and after correction at injection - Note the change of scale
[Injection 20 MeV (not critical point), De-tuned working point for the passively spread proton beam: Q_x = 1.758, Q_z = 1.820, Sextupoles are switched off, All correctors and monitors working]

Table 3.14 shows that the expected situation is quite comfortable for injection. With standard alignment techniques, 30% of the machines in the horizontal plane and 70% in the vertical plane would be within the allowed closed-orbit margins and could be injected with full intensity without any beam loss. After correction, all machines would be well within the tolerances for injection and also within the stricter tolerances for extraction.

Prognosis for closed orbits at injection and their correction				
	Before correction		**After correction**	
	Horizontal	**Vertical**	**Horizontal**	**Vertical**
Average of max. excursions [mm]	14.3	6.0	1.5	0.6
Max. absolute excursion [mm]	48.6	23.1	3.3	1.2
Average of max. kicks [mrad]	-	-	0.94	0.29
Max. corrector kick [mrad]	-	-	2.09	0.66
Closed-orbit tolerance [mm]	±10	±7.5	±10*	±7.5*
% of machines within tolerance	30	72	100	100

* For extraction, these limits are reduced to ±5 mm and certain sections of the orbit (e.g. at the septa and resonant sextupole) must be locally corrected to better than ±1 mm.

Table 3.14 Prognosis for closed orbits at injection and their correction
[On injection working point: $Q_x = 1.758$, $Q_z = 1.820$, 1000 machines]

Although the above graphs and table are based on the use of all monitors and correctors, it should be noted that a correction typically requires only 4 to 6 units to reach a satisfactory level (provided that the correctors are the most efficient for the chosen orbit), after which any additional correctors become less efficient and, in practice, may even lead to a degradation of the correction.

3.6.2 Sensitivity to errors and the effects of missing monitors

Figures 3.34 and 3.35 show the combined effect of all the random errors listed in Table 3.13. In order to determine the relative importance of the different errors, a series of runs were made with samples of 200 machines (see Table 3.15).

Sensitivity to the different errors		
	Average maximum excursions of the orbits:	
Error source	**Horizontal**	**Vertical**
Relative dipole field error (1.2×10^{-3})	12.5 mm	-
Transverse quadrupole shifts (0.3×10^{-3} m)	1.5 mm	1.9 mm
Longitudinal dipole shift (0.3×10^{-3} m)	0.6 mm	-
Tilt of dipoles (0.3×10^{-3} rad)	-	4 mm

Table 3.15 Sensitivity to the different field errors
[On extraction working point: $Q_x = 1.667$, $Q_z = 1.720$, samples of 200 machines]

In addition, the sensitivity to missing monitors was investigated in the horizontal plane, which is the more critical, by taking random samples of 200 machines and correcting orbits for various patterns of missing monitors. The quality of the correction was quantified by taking the ratio between the average of the absolute maximum excursions in the initial orbits and the average of the absolute maxima after correction (see Table 3.16).

Sensitivity to missing monitors	
Randomly chosen samples of 200 machines	**Ratio of average of maximum excursions of orbits before and after correction**
ALL monitors (11) and all correctors (10)	10.5
Selection of cases with one monitor missing*	9.5, 6, 10.1, 10.3, 3.8, 9.2, 4.6, 4.1, 3.7, 9.
Two consecutive monitors missing*	5.0, 3.8, 3.6, 3.0, 3.1
Two non-consecutive monitors missing*	9.2, 3.6,3.9,3.7,3.4
Three consecutive monitors missing*	2.0, 2.7, 2.5
Three non-consecutive monitors missing*	4.3

* The number of correctors used was always one less than the number of monitors, but these correctors were the most efficient chosen from the full complement.

Table 3.16 Sensitivity to missing monitors
[On injection working point: Q_x = 1.758, Q_z = 1.820, samples of 200 machines]

The reference calculation in Table 3.16 shows that with a full complement of monitors and correctors one can expect on average to reduce the beam excursions by a factor of 10.5. When removing a single monitor either the loss of efficiency is small with an improvement between 9 and 10, or much poorer with an improvement of only 3.7 to 6. This result correlates with the distance to neighbouring monitors. The three cases where pairs of monitors are close in betatron phase give the six high efficiencies and the intermediate monitors that are more isolated give the poorer results. When two consecutive monitors are missing, this nearly always results in a large gap in betatron phase and the efficiency drops directly, in all but one case, to between 3.4 and 3.9. With three consecutive monitors missing, there is, unsurprisingly, an even poorer improvement of only 2 to 2.7.

For the purpose of injection, two consecutive, missing monitors, or up to 3 non-consecutive monitors, would in the majority of the cases be acceptable. However, for extraction the orbit should be better corrected (±5 mm) and if one of the missing monitors should be needed for tuning the beam position in the septa or in the sextupoles, then the situation could be critical. Thus, with only a single missing monitor, it will be a question of luck whether the extraction can be adjusted correctly.

3.6.3 Distribution of correction strengths and effects of missing correctors

The simulations show that the correctors in both planes are used more or less uniformly. The only significant exception is a pair of horizontal correctors in the rf drift space that effectively share the load that would normally be applied to a single unit. Some tests made by selecting the best group of 2, 3, 4 etc. up to the maximum number of correctors did not show any significant changes in the average corrector strength, only an improvement in the orbit.

The sensitivity of the machine to missing correctors is investigated in Table 3.17 with randomly-generated groups of 200 machines on the extraction working point.

Sensitivity to missing correctors		
	Uncorrected	**Corrected**
Horizontal corrector HC31 (upstream) removed		
Average of absolute maximum excursions [mm]	11.7	1.7
Maximum absolute excursion [mm]	26.2	3.1
Average of maximum corrector kicks [mrad]	-	0.93
Maximum corrector kick [mrad]	-	1.80
Horizontal corrector HC36 removed		
Average of absolute maximum excursions [mm]	11.7	2.7
Maximum absolute excursion [mm]	26.2	7.7
Average of maximum corrector kicks [mrad]	-	1.74
Maximum corrector kick [mrad]	-	5.64
Vertical corrector VC08 removed		
Average of absolute maximum excursions [mm]	4.1	0.9
Maximum absolute excursion [mm]	9.7	2.0
Average of maximum corrector kicks [mrad]	-	0.29
Maximum corrector kick [mrad]	-	0.57
Horiz. correctors HC31 (upstream)+HC36 removed		
Average of absolute maximum excursions [mm]	11.7	3.3
Maximum absolute excursion [mm]	26.2	11.1
Average of maximum corrector kicks [mrad]	-	1.10
Maximum corrector kick [mrad]	-	2.67
Vertical correctors VC08+VC33 removed		
Average of absolute maximum excursions [mm]	4.1	1.1
Maximum absolute excursion [mm]	9.7	2.1
Average of maximum corrector kicks [mrad]	-	0.29
Maximum corrector kick [mrad]	-	0.59
HC31 (upstream)+HC36 & monitor PX31 (upstream) removed		
Average of absolute maximum excursions [mm]	11.7	2.9
Maximum absolute excursion [mm]	26.2	9.1
Average of maximum corrector kicks [mrad]	-	1.03
Maximum corrector kick [mrad]	-	2.28
VC08+VC33& monitor PY39 removed		
Average of absolute maximum excursions [mm]	4.1	1.6
Maximum absolute excursion [mm]	9.7	4.4
Average of maximum corrector kicks [mrad]	-	0.29
Maximum corrector kick [mrad]	-	0.60

Table 3.17 Sensitivity to missing correctors (see Table 3.14 for comparison)
[On extraction working point: $Q_x = 1.667$, $Q_z = 1.720$; samples of 200 machines]

In Table 3.17, the horizontal corrector HC31 is an example of a corrector with a nearby neighbour and corrector HC36 is a more typical case of a uniformly spaced corrector. Removing the former has little impact on the closed-orbit correction or the corrector strengths, whereas removing the latter approximately doubles the amplitude of the corrected closed orbit and the corrector strengths. As will be seen later, the

corrector strengths will not be able to satisfy such large increases even if the orbit is still technically good enough. Removing both of these correctors, leads to a stronger deterioration of the orbit to the point where the tail of the distribution is outside the tolerance. The poorer closed orbit requires weaker correction strengths but is still uncomfortably high. The same missing correctors with a missing monitor appears to improve the orbit correction and reduce the corrector strengths slightly. This means that the situation is essentially unchanged, but, by removing the constraint at one monitor, the correction has been modified for the overall good at positions between the monitors. This can happen, since the correction routine acts on the sum of the squares at the monitors and although the excursions between the monitors tend to follow, it is not impossible that one increases while the other decreases. The conclusion of Table 3.17 is that the loss of a horizontal corrector (apart from the few that have near neighbours) will have serious consequences for the operation.

The examples in Table 3.17 for the vertical plane are far less critical. The correctors are also more uniformly spaced in the vertical plane so that the examples given are very representative.

3.6.4 Degradation with time

Table 3.18 summarises the expectations for the growth of orbit distortion and corrector strengths after 2 and 5 years. It has been assumed that on average the standard deviation of alignment errors will increase by:

$$\Delta x_{RMS,0} = \Delta x_{RMS,n} + n\delta e,\ \Delta y_{RMS,0} = \Delta y_{RMS,n} + n\delta e\ ,\ \Delta z_{RMS,0} = \Delta z_{RMS,n} + n\delta e,$$

where n is the number of years and δe = 0.1 mm/year and

$$\Delta\theta_{RMS} = \Delta\theta_{RMS} + n\delta e, \text{ about any axis}, \quad \text{where } \delta e = 0.1 \text{ mrad/year.}$$

Natural growth of distortion and corrector strength with time

	Start	At 2 years	At 5 years
RMS alignment errors [mm]	0.3	0.5	0.8
RMS tilt errors [mrad]	0.3	0.5	0.8
Horizontal plane uncorrected			
Average of absolute maximum excursions [mm]	11.9	12.1	12.5
Maximum absolute excursion [mm]	37.7	37.3	36.9
Horizontal plane corrected			
Average of absolute maximum excursions [mm]	1.6	1.8	2.2
Maximum absolute excursion [mm]	3.5	3.8	4.4
Average of maximum corrector kicks [mrad]	0.94	1.02	1.21
Maximum corrector kick [mrad]	2.09	2.79	3.84
Vertical plane uncorrected			
Average of absolute maximum excursions [mm]	4.3	7.1	11.4
Maximum absolute excursion [mm]	13.4	22.4	36.1
Vertical plane corrected			
Average of absolute maximum excursions [mm]	0.63	1.04	1.66
Maximum absolute excursion [mm]	1.22	1.99	3.29
Average of maximum corrector kicks [mrad]	0.29	0.47	0.76
Maximum corrector kick [mrad]	0.66	1.09	1.75

Table 3.18 Natural growth of distortion and corrector strength with time
[On extraction working point: Q_x = 1.667, Q_z = 1.720, 1000 machines]

It is evident that the vertical plane, where the distortion and corrector strengths increase by almost a factor of three in 5 years, is the more strongly affected. Since the degradation with time will depend strongly on local conditions, Table 3.18 can only be considered as a general indication. However, the indication is that the corrected closed orbits in both planes will theoretically still be within tolerance after 5 years (i.e. ±5 mm), but the required increases in corrector strength to achieve this will mean that in more than 50% of the cases re-alignment will be necessary. Four to five-years between alignments appears to be a likely average.

3.6.5 Closed-orbit manipulations

The closed orbit control at extraction will contain two steps:

- Global correction to better than ±5 mm in both planes. If this cannot be achieved, then the machine should be re-aligned.
- Addition of local corrections at sextupoles, septa, etc. Although a local correction may degrade the orbit elsewhere, the overall distortion should not exceed ±10 mm horizontally and ±7.5 mm vertically.

Most local corrections will be made by pre-calculated 3- or 4-magnet bumps with an amplitude no bigger than 5 mm (see Appendix D).

Unfortunately, there is space for only one horizontal and one vertical corrector between the electrostatic and magnetic septa. This means that the 4-magnet bumps that would normally be used to control angle and position at these two elements overlap such that corrections at one septum would affect the other. In the horizontal plane, which is the more critical, this has been overcome by designing a 5-magnet bump that controls position and angle at the electrostatic septum and position at the magnetic septum. The magnetic septum must then adjust the angle of the extracted beam. For the circulating beam two correctors in the next arc close the bump. Since the extraction is of fundamental importance, the distributions of the angle errors at the two septa after a global obit correction have been calculated (see Figure 3.36 and 3.37). Table 3.19 summarises the main parameters from Figures 3.36 and 3.37. This data will be used in Section 3.6.6 to determine the corrector strengths. The expected position errors are assumed to have the same characteristics as the closed-orbit distortion after correction (from Table 3.14, maximum horizontal excursion after correction 3.3 mm). Based on these numbers, the 5-magnet bump will be designed to cover ±3.5 mm at the electrostatic and magnetic septa and ±0.25 mrad at the electrostatic septum. The magnetic septum will then have a residual angle to correct of less than ±0.2 mrad.

Angular distributions at the electrostatic and magnetic septa after global orbit correction

	Electrostatic septum	Magnetic septum
Maximum angle error [mrad]	1.15	0.93
Average angle error [mrad]	0.15	0.12
Angle for 75% of the distribution [mrad]	0.25	0.2

Table 3.19 Angular distributions at the electrostatic and magnetic septa after global orbit correction
[On extraction working point: Q_x = 1.667, Q_z = 1.720; 1000 machines]

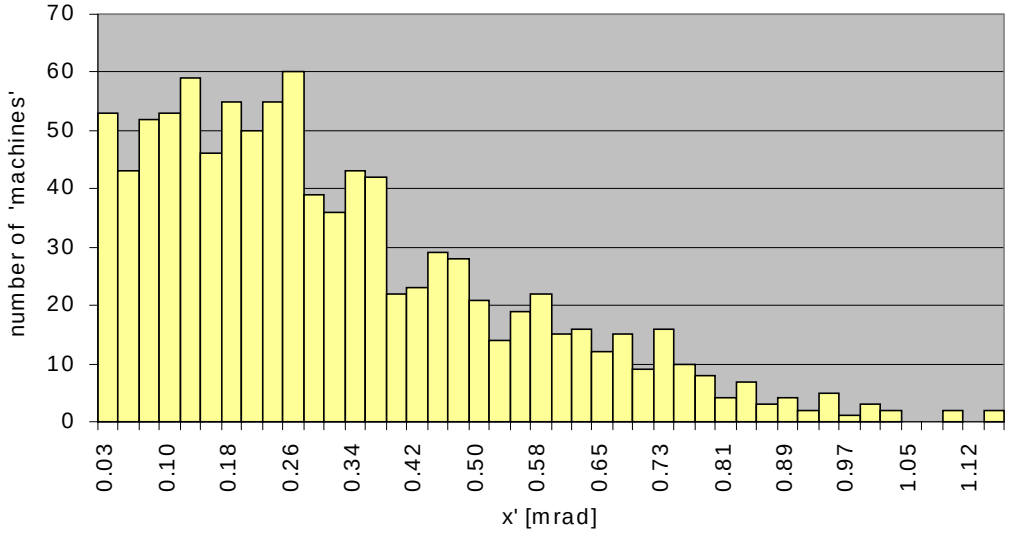

Figure 3.36 Expected distribution of the angle error at the electrostatic septum after a global closed-orbit correction
[On extraction working point: Q_x = 1.667, Q_z = 1.720; 1000 machines]

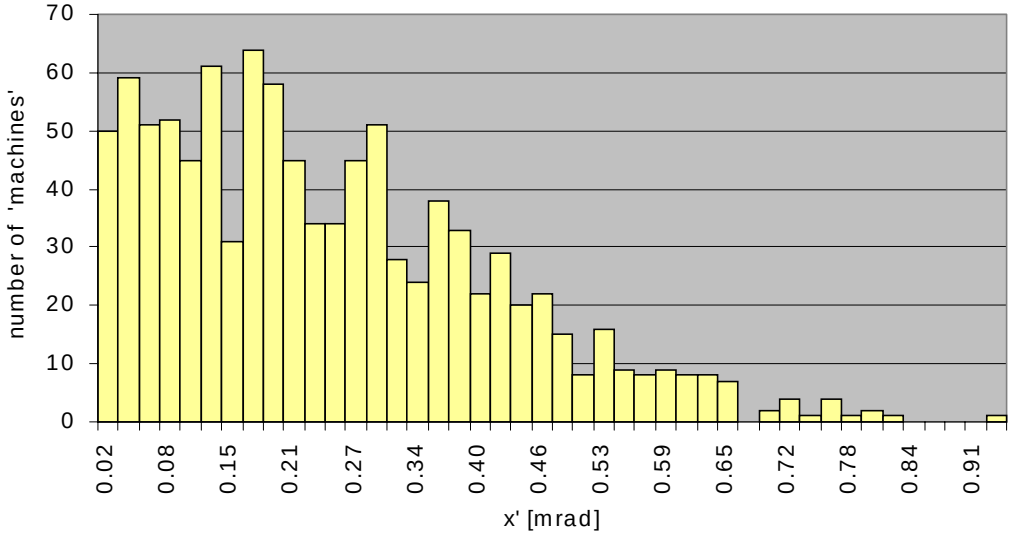

Figure 3.37 Expected distribution of the angle error at the magnetic septum after a global closed-orbit correction
[On extraction working point: Q_x = 1.667, Q_z = 1.720; 1000 machines]

The amplitude and angle at the electrostatic septum are controlled by two correctors upstream of the septum (see Figure 3.38), the excursion at the magnetic septum is controlled by a third corrector and, finally, the bump is closed by the last two correctors. In the PIMMS machine, there are a number of local considerations:

- Since the phase shift between the electrostatic and magnetic septa is only 51°, it would require an exceptional field error to cause the maximum orbit excursion (3.3 mm) to occur with opposite signs at the two septa. It is much more likely that the two excursions will have the same sign or be within the much smaller range (±1.5 mm).

- There are no sextupoles between the two septa. This means that the gap opened by the electrostatic septum between the circulating separatrix and the extracted segment should be independent of the orbit distortion and the bump height.

- There are two chromaticity sextupoles in the entry section of the bump. The first is just after the first correction where the amplitudes are quasi-zero, but the other may 'see' large amplitudes. Under extreme conditions, it may therefore be necessary to steer the bump slightly to account for the influence of this lens.

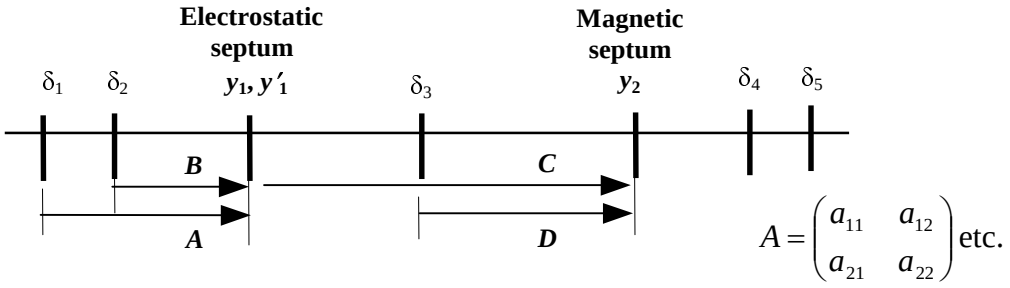

Figure 3.38 Layout of the 5-magnet bump for extraction

The first two correctors are set according to,

$$\begin{pmatrix}\delta_1\\ \delta_2\end{pmatrix}=\frac{1}{(b_{22}a_{12}-b_{12}a_{22})}\begin{pmatrix}b_{22} & -b_{12}\\ -a_{22} & a_{12}\end{pmatrix}\begin{pmatrix}y_1\\ y_1'\end{pmatrix} \tag{3.7}$$

and the third corrector is set according to

$$\delta_3=\frac{y_2-c_{11}y_1-c_{12}y_1'}{d_{12}}. \tag{3.8}$$

The angle at the magnetic septum will then be

$$y_2'=c_{21}y_1+c_{22}y_1'+d_{22}\left(\frac{y_2-c_{11}y_1-c_{12}y_1'}{d_{12}}\right). \tag{3.9}$$

Finally, the bump is closed by δ_4 and δ_5 in the same way as it is excited by δ_1 and δ_2.

Figure 3.9 shows some limiting cases for the 5-magnet bump and Table 3.20 lists the corresponding kick strengths.

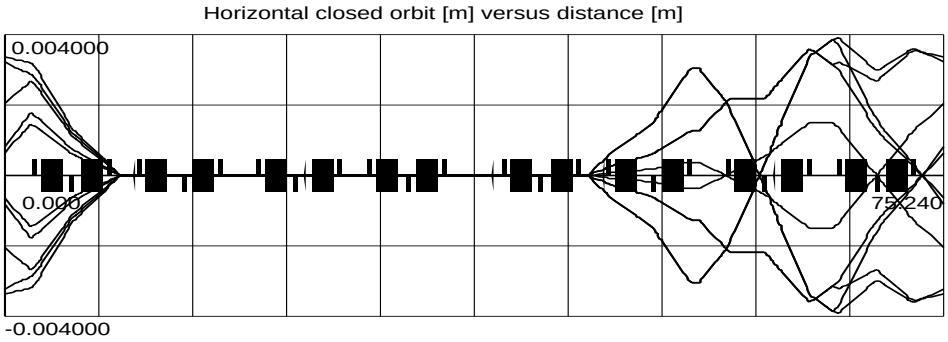

Figure 3.39 Some examples of the 5-magnet extraction bump

Some examples of the 5-magnet extraction bump

Electrostatic septum		Magnetic septum	δ1 HC 26	δ2 HC 31*	δ3 HC 36	δ4 HC 01	δ5 HC 06
3.5 mm	-0.25 mrad	3.5 mm	0.150 mrad	0.403 mrad	0.416 mrad	-0.192 mrad	0.387 mrad
3.5 mm	0.25 mrad	3.5 mm	-0.363 mrad	0.423 mrad	-0.142 mrad	-0.079 mrad	0.348 mrad
3.5 mm	-0.25 mrad	0.0 mm	0.150 mrad	0.403 mrad	-0.004 mrad	0.499 mrad	-0.174 mrad
3.5 mm	0.25 mrad	0.0 mm	-0.363 mrad	0.423 mrad	-0.562 mrad	0.612 mrad	-0.214 mrad
1.5 mm	0.0 mrad	-1.5 mm	-0.046 mrad	0.117 mrad	-0.302 mrad	0.534 mrad	-0.324 mrad

* Upstream HC-31

Table 3.20 Some examples of the 5-magnet extraction bump

3.6.6 Specifications for correctors

The correctors must be able to meet the demands of both the global orbit correction and the local corrections at top energy, as described in Section 3.6.5. The evaluation is therefore made on the extraction working point, which is the only working point used at top energy. Table 3.21 gives the prognosis for the correction efficiency on the extraction working point.

Prognosis for closed orbits at extraction and their correction

	Before correction		After correction	
	Horiz.	Vertical	Horiz.	Vertical
Maximum absolute excursion [mm]	37.7	13.4	3.5	1.2
Average of max. abs. excursions [mm]	11.9	4.3	1.6	0.6
Max. corrector kick [mrad]	-	-	2.09	0.65
Average of max. corrector kicks [mrad]	-	-	0.94	0.28
% of orbits corrected with kicks up to the average value	-	-	77	75
Closed-orbit tolerance [mm]	-	-	±5	±5
% of machines within tolerance	-	-	100	100

Table 3.21 Prognosis for closed orbits at extraction and their correction

Table 3.21 shows that correctors with a strength of 0.94 mrad kicks in the horizontal plane will correct 77% of the orbits and 0.28 mrad 75% in the vertical plane. A similar philosophy can be applied to the local bumps i.e. a maximum kick strength is chosen that will satisfy the maximum specified amplitude in more than 75% of the cases. Inspection of Table D1 (3-magnet bumps), Table D2 (4-magnet bumps) and Table 3.20 (5-magnet bump) indicates that 0.58 mrad is sufficient to fulfil this criterion in the horizontal plane and 0.47 mrad in the vertical. In the few cases that are not covered, the maximum kick is typically 0.75 mrad. Summing these requirements linearly implies strengths of 1.52 mrad in the horizontal plane and 0.75 mrad in the vertical plane. Table 3.21 also shows that there is some margin between the allowable closed-orbit tolerances in the two planes and the prognostics for the correction. This margin should make the above estimates rather safe and also help to absorb errors from missing monitors and/or correctors and degradation of the alignment with time. The proposal is therefore to build correctors with:

Proposed horizontal corrector strength = 1.5 mrad

Proposed vertical corrector strength = 0.75 mrad.

The lower value in the vertical plane fortuitously compensates for the need for a larger aperture. In principle, it is best to limit the corrector strengths as far as possible, since excessive strength will only contribute to imprecision when running the lower-rigidity proton beams.

3.7 GRADIENT ERRORS

In general, machines are less sensitive to fabrication and alignment errors in quadrupoles than to those in dipoles. In the case of dipoles, tolerances are set to what is feasible and then the closed orbit is corrected by a system of correctors to a level acceptable for operation. For quadrupoles, it is usually possible to specify the fabrication and alignment tolerances in order to be within the desired operational range directly. This situation exists for PIMMS and the tolerances are defined in Section 4.2.

However, it should be noted that in order to satisfy the tolerances specified in Section 4.2 for the low energy protons, the quadrupole design has to make use of the relatively unusual technique of lowering the packing factor in order to artificially increase the field level in the steel laminations. Secondly, the combined action of the tilt errors and the closed-orbit errors leads to a level of coupling that is close to acceptable limits. A possible coupling correction scheme is therefore discussed in the next section.

3.8 COUPLING FROM RANDOM ERRORS

Random quadrupole tilts, vertical misalignments of sextupoles and the vertical, closed-orbit distortion in sextupoles all contribute to betatron coupling. The coupling prognosis is given in Figure 3.40, Figure 3.41 and Table 3.22 (magnitudes and phases of the sum and difference coupling driving terms distributed over 1000 randomly generated machines). The assumed generating errors were:

- RMS quadrupole tilts = 0.0003 rad with cut-off at 3 RMS
- RMS vertical beam position in sextupoles = 0.0005 m with cut-off at 3 RMS

The RMS vertical beam position in the sextupoles is based on the limit of ±1 mm set for the local orbit correction and the alignment tolerance of 0.0003 m (RMS).

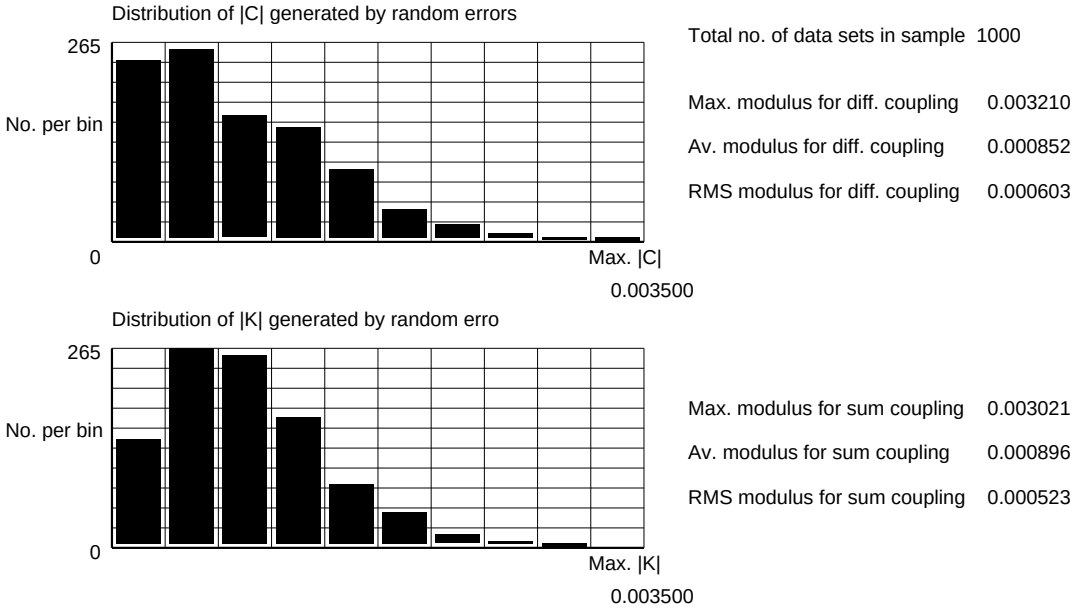

Figure 3.40 Distribution over 1000 randomly generated machines of the moduli of the difference and sum coupling coefficients

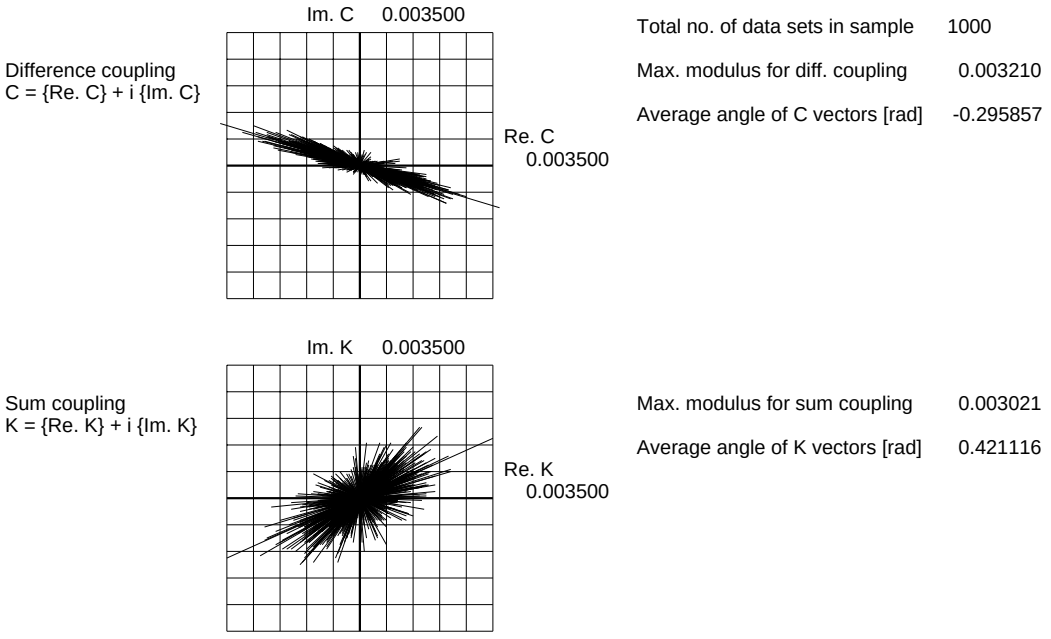

Figure 3.41 Distribution over 1000 randomly generated machines of the vectors of the difference and sum coupling coefficients with the average phase lines

Prognosis for coupling				
Observer at centre of injection drift (machine symmetry point in SS 01)	**Difference resonance**		**Sum resonance**	
	Modulus	**Phase**	**Modulus.**	**Phase**
Maximum modulus	0.00321	-	0.00302	-
Average modulus and phase [rad]	0.00085	-0.296	0.00090	0.421
RMS modulus	0.00060	-	0.00052	-

Table 3.22 Prognosis for coupling

To get some physical feeling for the situation in the PIMMS ring, the working point of the machine is relatively close to the difference resonance ($Q_x = Q_z$), far from the sum coupling resonance ($Q_x + Q_z = 3$) and the magnitude of the difference resonance driving term $|C|$ is equal to the resonance bandwidth in tune. With a maximum bandwidth of $\Delta Q = \pm 0.0032$ and an average bandwidth of ± 0.00085, the coupling is not strong, but it is considered to be prudent to make some provision for its correction.

The correction scheme proposed is approximate, but simple. The idea is to use a single skew quadrupole that is positioned so as to act along the average phase line of the difference resonance distribution in Figure 3.41. It is clear from the distribution that a correction magnet acting along the average phase line and with a maximum strength of 0.0035 would reduce the residual difference coupling well below 0.001. Figure 3.42 shows the coupling vector excited by a skew quadrupole positioned in the dispersion-free region close to the rf cavity (see Figure 3.43). A lens at this position, not only matches the average phase of the difference coupling resonance, it also matches the sum coupling resonance. However, the latter is both less important and more difficult to correct since the distribution is more symmetric. It is also extremely unlikely that a single magnet setting would be able to apply an efficient correction to both resonances.

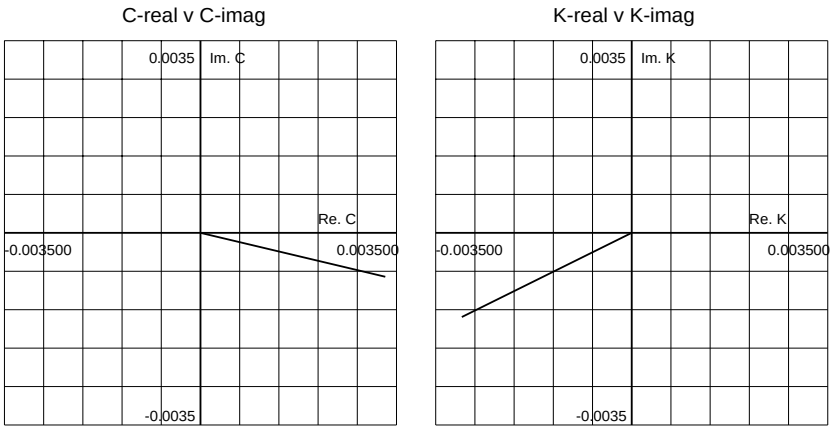

(a) Difference coupling vector (b) Sum coupling vector

Figure 3.42 Vectors excited by the compensation skew quadrupole (for positive gradient)
[Observer at symmetry point in SS MR 01 and skew quadrupole in SS MR 21]

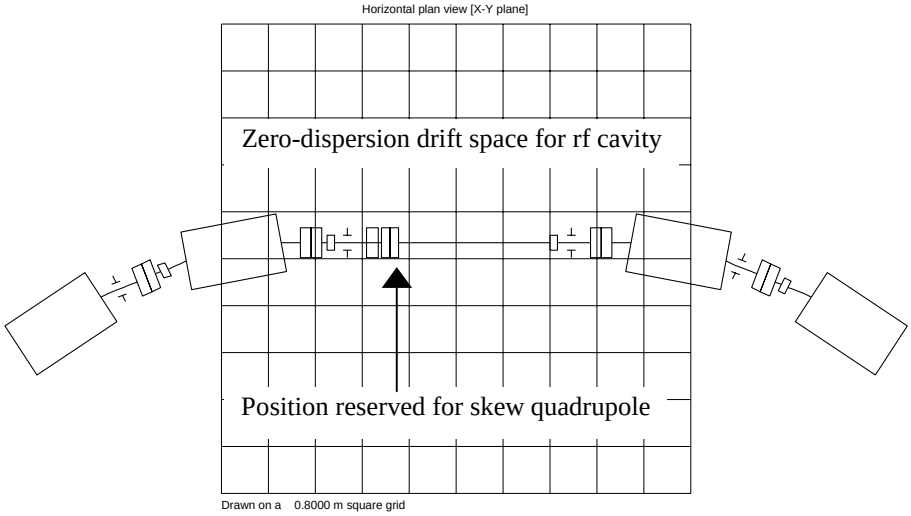

Figure 3.43 Position reserved for the compensation skew quadrupole in SS MR 21

If it is assumed that the effective magnetic length of the compensation skew quadrupole is 0.2 m then a pole tip field of 0.0105 T would excite a coupling vector with magnitude 0.0035 for the highest energy carbon ions. Thus this magnet is relatively weak and could be fabricated rather easily.

3.9 TUNING RANGE

The PIMMS lattice can be tuned over a range far beyond that needed operationally. For example, by using the three quadrupole chains, the tunes can be moved to any point in the region $1.05<Q_x<1.95$ and $1.05<Q_z<1.95$ with the zero dispersion condition maintained in the two long drift spaces between the arcs. When approaching the integer resonances, the influence of the stop bands drives the betatron amplitude functions up exponentially. At a tune distance of 0.05, the amplitude functions are of the order of 150 m. Once past the integer resonances, the betatron amplitude functions assume more reasonable values and the stability region continues beyond $Q_x = 2$ and $Q_z = 2$, but this is only of academic interest.

Operationally, the synchrotron is designed for slow extraction on the 5/3 integer resonance and the tuning requirements are limited to the fine-positioning of working lines and the pre-compensation of the space-charge tune shifts of the proton beam. The practical range of the power converters is decided by the highest energy carbon ions and what is considered a reasonable tuning around the extraction working point. Operationally, this will be the small region in the tune diagram defined by the third and fourth integer resonances $3Q_{x,z} = 5/3$ and $Q_{x,z} = 7/4$ and the diagonal $Q_x = Q_z$, inside which the beam needs to be maintained to prevent losses (see Figure 3.44). The highest gradients in this sub-region occur at $Q_{x,z} = 7/4$ and these will be taken for the determination of the power converter supplies. Note that although the space-charge dominated proton beam requires a larger tune range this only occurs at a very low rigidity and hence does not pose a problem for the power converters.

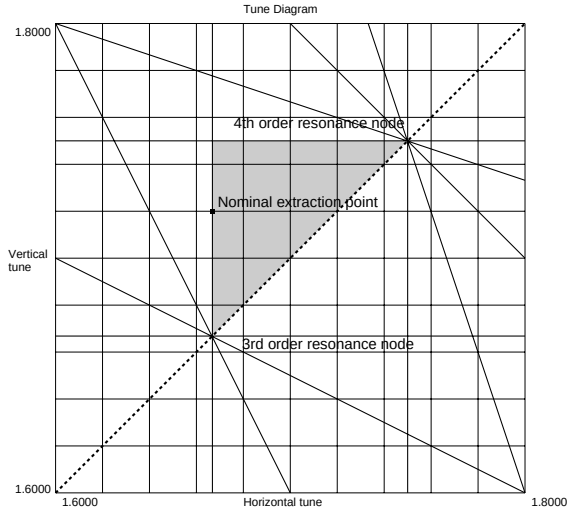

Figure 3.44 Tuning region around nominal extraction point

Based on Figure 3.44, the maximum normalised operational gradients will be $k_{F1} = 0.3517$, $k_{F2} = 0.5334$, $k_D = 0.5548$ and the overall maximum gradient for the magnet design will be 3.521 T/m ($B\rho = 6.346$ Tm). It is proposed that the F1-quadrupole family's power converter be designed with a lower maximum current than that of the F2 and D families that can be made equal. The justification for this is the extreme sensitivity of slow extraction to ripple and the fact that the ripple is proportional to the maximum current deliverable by a power converter independent of its actual setting.

The limited tuning range and the use of different maximum currents may seem like 'brinkmanship' and over-design, but it should be remembered that the ring will operate with both carbon ions and protons. This means that the lowest-energy protons will be extracted with less than 20% of the currents for the highest energy ions. In view of the sensitivity to tune ripple, it is important not to exaggerate the safety margins and to limit the maximum currents whenever possible.

3.10 CHROMATICITY AND RESONANCE CONTROL

There are two main functions for the sextupoles to fulfil, firstly, to tune the Hardt Condition and, secondly, to stabilise the space-charge dominated proton beam at injection. However, the latter task has no bearing on the maximum strength of the power converters, since this occurs only at low energy.

For the Hardt Condition, the proposal is to assume that the nominal spiral step of 10 mm will need adjustment over the range 10 ± 2.5 mm. This adjustment could be requested for spot size control, or simply because the optics model is imprecise. However, a tolerance of ±25% seems more than adequate. Over this range, the horizontal chromaticity ($dQ_x/dp/p$) would require a variation of approximately +0.7 to -0.5 with respect to the nominal value.

As with the main quadrupoles and dipoles, it is better to be as parsimonious as possible and not to add generous safety margins. This is done in order to limit the damage done by current ripple at the lower energies. The proposal therefore is to allow the resonance sextupole to tune up to a spiral step of 12.5 mm and for the

chromaticity sextupoles to tune up to $dQ_x/dp/p$ = -4.3 and $dQ_z/dp/p$ = -1.9. The maximum sextupole gradients corresponding to these settings are summarised in Table 3.23 for the top carbon ion energy of 400 MeV/u. Note a wider tuning range will automatically be available for stabilising space charge at injection.

The coincidence of minimum chromaticity in both planes leads to an inversion of sign in one sextupole chain (see Table 3.23). This is the most unlikely situation to be required and it is proposed to keep both sextupole chains uni-polar and to accept some loss in the tuning range. The maximum sextupole gradient for the chromaticity sextupoles will be 17.2 Tm^{-2} (k' = 2.71 m^{-3}, $B\rho$ = 6.346 Tm).

Maximum gradients for resonance and chromaticity* sextupoles

A) Resonance sextupole setting for maximum spiral step of 12.5 mm

k'_R	G'_R [Tm^{-2}]
13.4	85.0

B) Chromaticity sextupole settings for maximum spiral step of 12.5 mm

$dQ_x/dp/p$	$dQ_z/dp/p$	k'_F	k'_D	G'_F [Tm^{-2}]	G'_D [Tm^{-2}]
-4.3	-1.9	1.2	2.4	7.6	15.2

* Chromaticities were determined by tracking

Table 3.23 Maximum gradients for resonance and chromaticity sextupoles
[Carbon ions 400 MeV/u, $B\rho$ = 6.346 Tm]

Table 3.23 shows that the three sextupole families differ strongly in their maximum strengths and it is proposed that each of the three power converters be designed for the maximum current suited to its use. Normally, this would not be the case and, at least, the two chromaticity families would have identical supplies. The justification for this is the extreme sensitivity of slow extraction to ripple and the fact that the ripple is proportional to the maximum current deliverable by the power converter independent of its actual setting.

3.11 STANDARD WORKING LINES

Two standard working conditions have been used in this chapter. These are:

- **Nominal injection and first part of acceleration**
  Centre-line, working point: Q_x = 1.680, Q_z = 1.720
  Chromaticities: $\Delta Q_x/dp/p$ = -3.5, $\Delta Q_z/dp/p$ = -3.5

- **Nominal extraction and final part of acceleration**
  Centre-line, working point: Q_x = 1.6666, Q_z = 1.720
  Chromaticities: $\Delta Q_x/dp/p$ = -3.655, $\Delta Q_z/dp/p$ = -1.158

The nominal injection and acceleration line (see Figure 3.45 [a]) is meant for carbon ions at injection and during acceleration and for protons once the energy is high enough to ignore the effect of space charge. In these cases, the maximum-sized beam sits in a momentum bite of approximately $\Delta p/p$ = 0.002 to -0.006 (the exact values vary during the rf cycle, but the limits can be found in Table 3.12, which is evaluated at a critical point in the rf cycle where the beam's momentum spread is maximum).

For low-energy proton beams, the situation is more complicated. The principle is to de-tune the working point upwards in the tune diagram, so that once the space charge is added the line returns to the nominal position. The de-tuned working point at injection and during the early acceleration ($Q_x = 1.764$, $Q_z = 1.829$) is constructed for the maximum tune shifts that occur shortly after the start of the rf cycle when the beam is bunched (at 23 MeV for the proton beam for passive spreading)[1]. Figure 3.45[a] also shows the de-tuned working line for proton beams. For operational simplicity, this line will be used for all passively and actively scanned beams. The chromaticities of the injection and acceleration line in Figure 3.45[a] are made large and equal in order to stretch the working line and to place it approximately parallel to the diagonal. This is the best defence that can be provided against a transverse instability in the unbunched proton beam at injection caused by the space charge distortion of the working line (not calculated in Figure 3.45[a]). Once the beam is bunched, the space-charge 'necktie' is also displaced and stretched with momentum parallel to the diagonal and this keeps the beam clear of the diagonal (see Figure 3.46).

Once the acceleration is underway and the point of maximum tune shift (~23 MeV) is passed, the de-tuned working point is collapsed progressively onto the nominal line. Both particle species now follow the same procedure in which the line is rotated by changing the chromaticities to match the nominal line for extraction (see Figure 3.45[b]). Once acceleration has ended the beam has to be moved in horizontal tune until it enters the resonance.

The extraction working line (see Figure 3.45[c]) need only be defined for negative momentum deviations ($\Delta p/p = 0$ is at the resonance, $\Delta p/p = -0.005$ defines the region occupied by the beam that has a nominal $\Delta p/p = 0.004$). The horizontal chromaticity is defined by the Hardt Condition and the vertical chromaticity is reduced to limit the curvature of the separatrices and to make the slope of the separatrix quasi-independent of the radial position at the electrostatic septum ($\Delta Q_x/\mathrm{d}p/p = -3.655$, $\Delta Q_z/\mathrm{d}p/p = -1.158$). The effect of space charge is invisible at extraction.

It will be shown later that if the injection energy of the proton beam is lowered, then the de-tuned working point will move higher up in the tune diagram. This has the unfortunate effect of bringing the point closer to the integer resonance and causing larger fluctuations in the betatron amplitude function with a consequent reduction in the effective aperture.

[1] The decision to fix the de-tuned working point to a single point rather than changing it according to the space charge load simplifies the study, but may not be the best choice in a practical machine. This is part of a wider problem of how to set the injection lines and tune the multi-turn injection. This is discussed further in Sections 7.2.3 and 7.3.

(a) Unloaded working line and nominal injection line

The upper line is the unloaded line that is displaced downwards to the nominal line when space charge is added.
$Q_x = 1.764$, $Q_z = 1.829$

The lower line will also curve down at the centre due to the space-charge load, but this is not shown.
$Q_x = 1.680$, $Q_z = 1.720$

Carbon ions 'see' no space charge and will always be on the lower line.

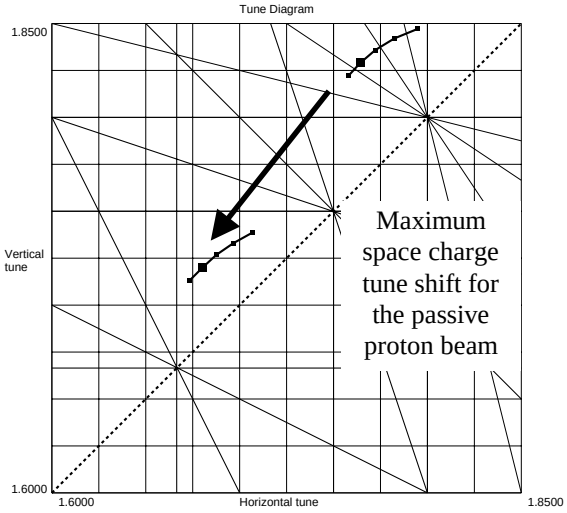

(b) Acceleration lines

The injection/acceleration line that is close to 45 degrees is rotated to the flatter acceleration/extraction line once space-charge effects are negligible.

Chromaticities change from
$\Delta Q_x/\mathrm{d}p/p = -3.5$, $\Delta Q_z/\mathrm{d}p/p = -3.5$
to
$\Delta Q_x/\mathrm{d}p/p = -3.655$, $\Delta Q_z/\mathrm{d}p/p = -1.158$

$Q_x = 1.680$, $Q_z = 1.720$

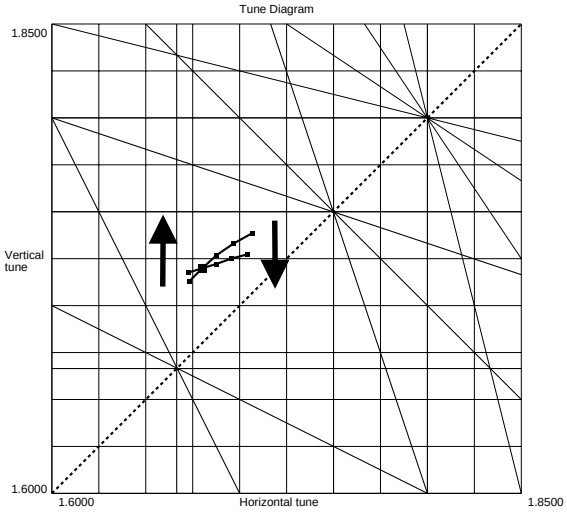

(c) Extraction line

For extraction a tune shift is made from the acceleration line to the extraction line which sits against the resonance.
$Q_x = 1.6666$, $Q_z = 1.720$

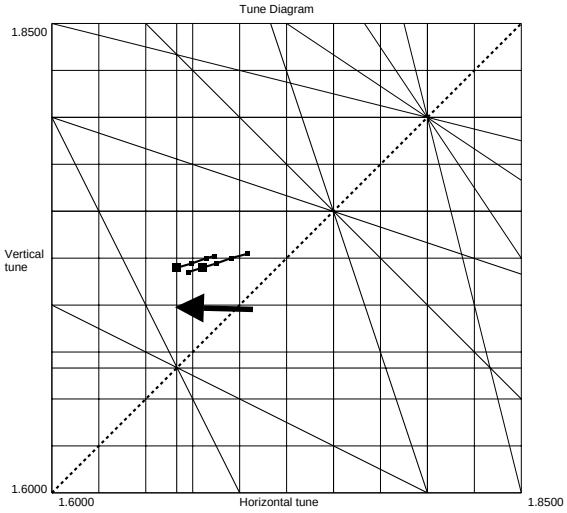

Figure 3.45 Standard working lines for injection acceleration and extraction
[For simplicity the unloaded working line is a single line adjusted for the highest intensity proton beam for passive spreading, but in an operational machine it could prove more useful to have many unloaded working points and intermediate working files for beams with different space-charge conditions.]

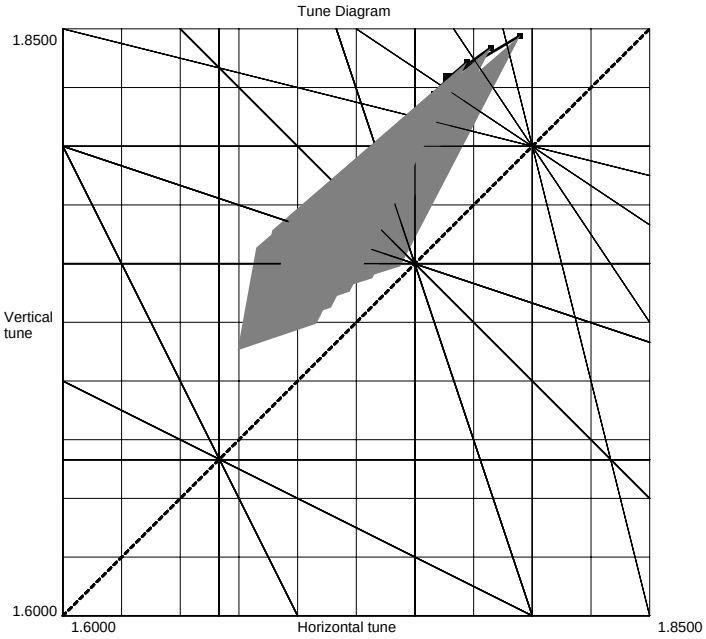

Figure 3.46 Estimation of the extended, space-charge 'necktie' at the critical energy of 23 MeV for the proton beam for passive spreading

3.12 VACUUM

The vacuum specifications are formulated with reference to:

- The needs of the carbon ions.
- The needs of the protons.
- The reliability needed for a medical environment.

3.12.1 Pressure

Carbon ions

The carbon ion beam is low intensity and the principal problem is losses due to electron capture from the residual gas. Assuming that the residual gas is nitrogen, Table 3.24 summarises the life expectancy of a carbon ion at injection (7 MeV/u), at the top extraction energy (400 MeV/u) and the expected survival from injection to the top extraction energy.

Lifetimes and survival estimates for fully stripped carbon ions

Pressure [Torr]	7 MeV/u lifetime (Injection) [s]	400 MeV/u lifetime (Top energy) [s]	Transmission (Injection to top energy) [%]
10^{-7}	0.043	34.8	61
10^{-8}	0.43	>100	95
10^{-9}	4.3	>100	99.5

Table 3.24 Lifetimes and survival estimates for fully stripped carbon ions

Protons

The proton beam is space-charge dominated at injection and the principal problem is one of electron capture in the potential well of the beam from the residual gas. The captured electrons partially neutralise the beam and affect the space charge

tune shifts. In the pressure range detailed in Table 3.25, this effect changes strongly and would lead to unstable injection conditions.

Electron production rates, neutralisation and tune shifts

Pressure [Torr]	Electron production rate [proton^{-1} s^{-1}]	Neutralisation after 10 ms [%]	Change in space-charge tune shift
10^{-7}	100	100	0.13
10^{-8}	10	10	0.013
10^{-9}	1	1	0.0013*

* Close to the usual tolerance for tune manipulations 0.001.

Table 3.25 Electron production rates, neutralisation and tune shifts

Specification

The ideal mean pressure in the main ring for carbon ions and protons would be 10^{-9} Torr. However, it is likely that pressures down to 10^{-8} Torr could be accepted, since the carbon ion losses are not serious and the capture of electrons in the proton beam is probably over-estimated due to the dynamic situation of debunching and rebunching that would tend to clear the beam. In the event of a permanently bad or fluctuating vacuum, clearing electrodes could be added, but these have not been foreseen in the present design. The final specification for the ring is:

10^{-9} Torr (mean pressure) with a upper limit for operation of 10^{-8} Torr.

3.12.2 Interventions

To maintain the validity of a cancer treatment plan, any interruption in machine operation should not exceed 24 h. For controlled interventions, the chamber must be vented to dry nitrogen and in this case the vacuum will recover to 10^{-9} Torr in less than 24 h. The vacuum recovery time after an accidental, or uncontrolled, intervention depends on the exposure time. Moist air causes a fast and persistent water vapour adsorption problem that builds up during two hours after which the exposure is largely irrelevant. The exact performance of a system is hard to predict, but Table 3.26 gives the most optimistic scenarios.

Minimum vacuum-recovery times after exposure to water vapour

Pressure [Torr]	Minimum recovery with NO heating	Minimum recovery with 120-150°C heating
10^{-8}	24 h	12 h
10^{-9}	48	24 h

Table 3.26 Minimum vacuum-recovery times after exposure to water vapour

Since operation is thought to be possible at 10^{-8} Torr, the question of whether a low-temperature baking system (120-150°C) for adsorbed gases is necessary is a delicate one. The final consensus is that the risk run by not installing such as system is minimal and the dipole gap has been reduced accordingly. However, it might still be possible to heat the dipole chamber by resistive heating and to introduce sufficient insulation to bake this chamber lightly if this proves to be really necessary.

3.12.3 Ring pumping system

Table 3.27 summarises the average, or characteristic, parameters of the ring vacuum system. The table also includes the pump ratings and the theoretical pump separation to achieve the target vacuum based on the average parameters. All elements are assumed to be stainless steel or ceramic and to have been vacuum fired at 450°C, or higher, before installation. The principal out-gassing will then be hydrogen diffusion from the bulk metal. Interventions must be made by venting the chambers to dry nitrogen to avoid contamination by water vapour. There are two safety margins in the calculated pumping speeds. Firstly, ion pumps are over twice as efficient when pumping hydrogen compared to oxygen, nitrogen or water vapour. Secondly, the pump size has been chosen so that the theoretical separation is always slightly larger than the nominal value. These reserves are maintained in order to account for the irregularities in pump spacing in a practical layout, the conductance of the pump connections and the additional surface area in position monitors etc. In addition to the basic scheme, dedicated 450 l/s ion pumps are installed for the vacuum tanks of the electrostatic septa and 3×100 l/s pumps for the isolation of the ring from the poorer vacuum in the lines. The practical layout is shown in Figure 3.47.

A general low-level bake-out system (~120°C for water vapour mainly) has been considered and rejected on the grounds that the system will always be vented to normal pressure with dry nitrogen as mentioned above and that catastrophic events are extremely rare. However, it will be essential to have an in situ bake-out system for the electrostatic septa. This can be done very simply by internally mounted infra-red lamps (a method used in the CERN PS septa).

Approximate characteristic parameters for ring vacuum system

Parameter	Main ring
Chamber form*	'Super' ellipse
Major half axis [m]	0.070
Minor half axis [m]	0.037
System length [m]	75.24
Specific surface area [$cm^2\ m^{-1}$]	3654
Specific out-gassing [Torr $l\ s^{-1}\ cm^{-2}$]	5×10^{-12}
Specific conductance [$l\ m\ s^{-1}$] for hydrogen at 25°C	446
Target average pressure [Torr]	10^{-9}
Ion pump speed [$l\ s^{-1}$]	100
Number of pumps	16
Theoretical pump separation [m]	5
Average pump separation [m]	4.7
Number of sectors	3
Roughing pumps (mechanical + turbo-molecular)	TM 80-450 l/s per sector
Additional dedicated pumps:	
Crossing of injection line and ring (in injection line) [l/s]	100
Extraction & injection lines (in the lines) [l/s]	2×100
For electrostatic septa [l/s]	2×450

* 'Super' ellipse is a flattened ellipse of the form $(x/a)^3+(y/b)^3 = 1$

Table 3.27 Approximate characteristic parameters for ring vacuum system

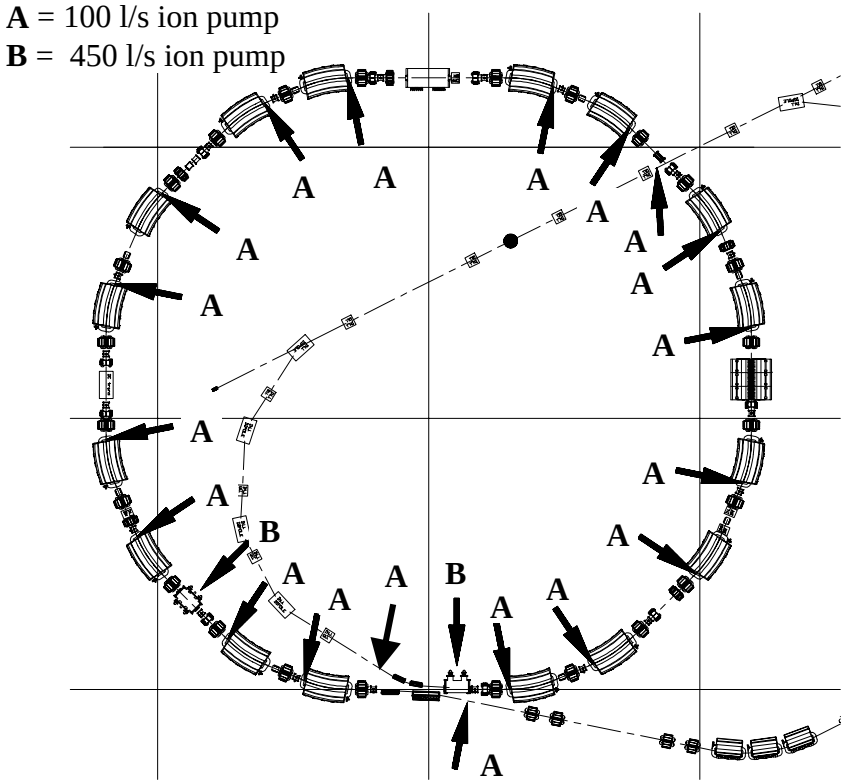

(a) Layout of ion pumps in the ring and the junctions with the lines

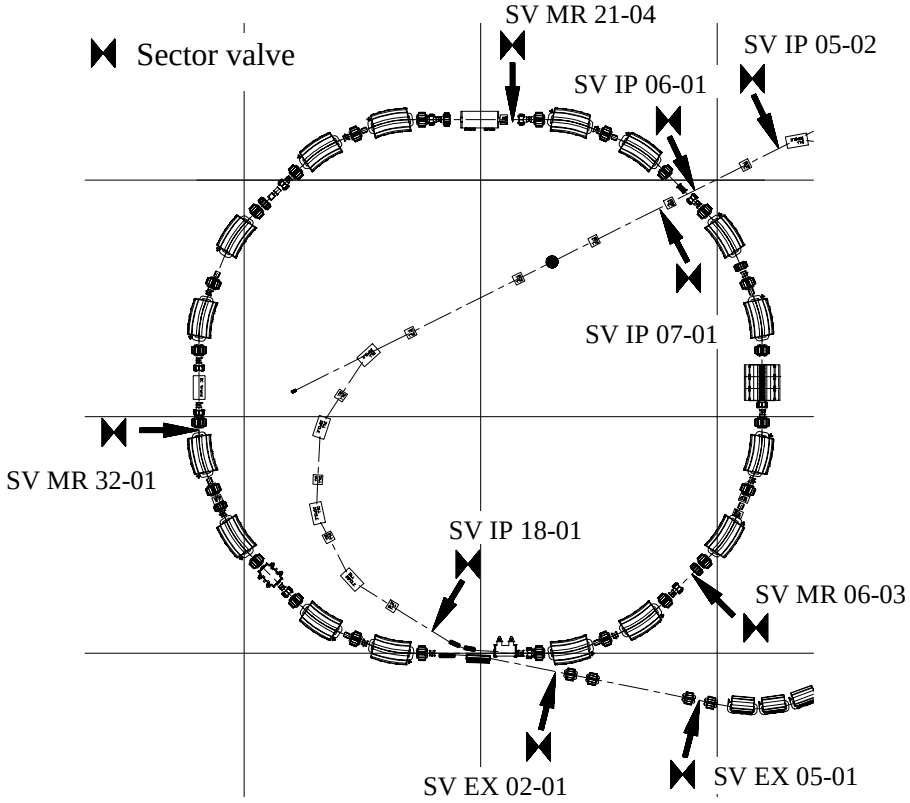

(b) Layout of vacuum sectors in the ring and the isolation valves in the lines

Figure 3.47 Schematic layout of the principal vacuum system elements

In Figure 3.47(a), each of the 16 dipole vacuum chambers in the ring is equipped with a 100 l/s ion pump with its port mounted between the dipole coils. An alternative to this solution would have been to design 'C'-shaped corrector magnets for the horizontal plane and to introduce the pump port on the open side. Figure 3.47(b) indicates the three approximately equal vacuum sectors. Each sector will also need a port where a mobile roughing station can be fixed and where gauges can be mounted.

3.13 TIME CONSTANTS

3.13.1 Eddy currents in the main ring magnets

The basic theory for the eddy currents in solid magnet yokes is given in [12]. The principles were extended for this study to the rectangular vacuum chambers in dipoles and circular chambers in quadrupoles in [13]. The combination of the eddy current effects in the laminations, the end plates and the vacuum chamber is given in [14]. How much the assumptions of rectangular and circular chambers alter the numerical results compared to the 'super' ellipse (flattened ellipse) of the PIMMS machine is unsure, but the effect is expected to be within the accuracy required.

The time constants of the magnets and vacuum chambers in the ring have two conflicting requirements:

- Small time constants for low field distortion during ramping.
- Large time constants to damp current ripple during extraction.

For the main ring magnets, the priority must lie with reducing the field distortion during ramping, but for the betatron core the priority can be placed more on the damping of the ripple and, in particular, the damping of the frequencies introduced by the DAC steps.

Dipole

To give some idea of the orders of magnitude involved, consider the principal sources of eddy current effects, in a dipole of the PIMMS dimensions:

- A solid yoke (normal carbon steel) would have a principal time constant of the order of 3.3 s.
- Solid endplates (normal carbon steel) of 25 mm would have a principal time constant of the order of 18.5 ms.
- A conventional non-magnetic, stainless steel chamber 2 mm thick would have a principal time constant of the order of 170 μs.
- Standard laminations (normal carbon steel) of 1.5 mm thickness would have a principal time constant of the order of 70 μs.

In approximate terms, the amplitude of the field distortion is given by the time constant [s] times the ramp rate [T/s]. At injection for 7 MeV/u carbon ions, the dipole field is 0.18 T, the maximum ramp rate is 3 T/s (see Section 3.3) and the approximate relative field errors would be:

- $\Delta B/B = 0.3$ within the end plates.
- $\Delta B/B = 2.8 \times 10^{-3}$ for the vacuum chamber.
- $\Delta B/B = 1.2 \times 10^{-3}$ for the laminations alone.

Thus, the end plates would be the main source of error and all the sources would be, for example, well outside the tolerance imposed on the field uniformity across the dipole aperture during extraction ($\pm 2 \times 10^{-4}$). It should be added, however, that this comparison is not strictly valid since extraction is particularly critical for other reasons and there are no field changes and eddy currents during extraction.

The present proposal is to bring the dipole as close as possible to the basic time constant imposed by the 1.5 mm laminations. This is done by:

- Gluing a 5 cm-stack of laminations together and then machining the composite block for the shim supports etc. This technique is often avoided because of radiation damage to the glue, but can be safely applied in the present case. Since the dipole is long and curved, it will be constructed with welded tie bars, which means that the glue will be damaged over a certain volume around the welds. However, the welding holds the laminations in these regions.
- Building a thin-walled vacuum chamber with a time constant no higher than that of the laminations. The chamber can either be corrugated in the longitudinal direction or supported by regularly-spaced vertical ribs. For the corrugated chamber, the proposal is to use stainless steel of resistivity $72 \times 10^{-8} \Omega$m (or better) and 0.4 mm thickness. Corrugations would have an amplitude of 3.2 mm and a period of 10 mm For the ribbed chamber, the proposal is to use stainless steel of resistivity $72 \times 10^{-8} \Omega$m (or better) and 0.3 mm thick, a rib spacing of 1.6 cm and a rib thickness of 2 mm. See Section 4.11.

Table 3.28 summarises the parameters relevant to the eddy current behaviour of the dipole with a corrugated chamber 0.4 mm thick, or an equivalent flat, ribbed chamber 0.3 mm thick. The principal time constants of the yoke and vacuum chamber are included with the residual field distortion and closed-orbit distortion variation across the chamber. The adverse effects are now quite acceptable during the ramp and the overall time constant (~100 μs) is still sufficient to introduce some smoothing of the ripple in the spill at kHz frequencies (i.e. 1.05 attenuation at 1 kHz rising to 6.4 at 10 kHz, which is the on-line dosimetry frequency).

Time response of the main ring dipole		
Yoke*:		**Time constant**
Length [m]	1.5530	
Pole width [m]	0.3400	
Half gap [m]	0.0360	
Lamination thickness [m]	0.0015	
Lamination resistivity [Ω m]	1×10^{-7}	
Av. iron path, pole face to pole face [m]	1.683	65 μs (yoke)
Vacuum chamber:		
Horizontal width [m]	0.1406	
Chamber thickness** [m]	0.0003	
Chamber resistivity [Ω m]	7.2×10^{-7}	30 μs (chamber)
Net response		
Overall time cosntant [μs]	95 μs	
Field lag at centre of chamber with the max. ramp of 3 T/s	0.00033 T	
Fractional field error at injection between the centre and edge of good field region	1.8×10^{-3}	
Change in closed-orbit distortion between centre and edge of good field region	1.5 mm peak to peak	

* No end plates ** The 0.4 mm corrugated chamber is assumed to be equivalent to 0.3 mm flat.

Table 3.28 Time response of the main ring dipole

Quadrupole and sextupole

The overall quadrupole and sextupole time constants should be of the order of the dipole, such that they do not over-perturb the ramp, but still provide some kHz-frequency smoothing for the spill. In both cases, end plates are suppressed and the complete yokes are laminated with 1.5 mm. The multi-pole geometry reduces eddy current effects and one consequence is that the yokes have lower time constants than the dipole. It is unnecessary therefore to install thin-walled vacuum chambers and depress the overall time constants still further. In fact, it is convenient to install normal 2 mm thick stainless steel chambers to increase the overall time constants and regain some of smoothing. Table 3.29 summarises the relevant parameters for the quadrupole. Since it is not possible, at present, to calculate sextupole geometries with eddy currents, the same conclusions are assumed to apply to both lenses.

Time response of the main ring quadrupole

Yoke *:		**Time constant**
Length [m]	0.2820	
Pole width [m]	0.1362	
Inscribed pole radius [m]	0.0850	
Lamination thickness [m]	0.0015	
Lamination resistivity [Ω m]	1×10^{-7}	
Av. iron path, pole face to pole face [m]	0.695	12 μs (yoke)
Vacuum chamber:		
Horizontal width [m]	0.144	
Chamber thickness [m]	0.002	
Chamber resistivity [Ω m]	7.2×10^{-7}	50 μs (chamber)
Net response		
Overall time constant [ms]	62 μσ	
'QD' gradient lag at the max. ramp rate**	0.0012 T/m	
'QD' relative gradient error at injection**	3.5×10^{-3}	
Tune shifts with errors in all quadrupole families: QF1, QF2 & QD	$\Delta Q_h = 0.001$; $\Delta Q_v = -0.001$	
Tune spreads with errors in all quadrupole families: QF1, QF2 & QD	$\Delta Q_h/\Delta p/p = 0.4$; $\Delta Q_v/\Delta p/p = -0.5$	

* No end plates. ** The 'QD' family is considered since it has the highest gradient.

Table 3.29 Time response of the main ring quadrupole

Correction magnets

The correction dipoles have low fields (0.03 T, horizontal corrector and 0.015 T, vertical corrector), but they should respond more quickly (say 50 times faster than the basic ramp rate of 1 s in order to follow the closed orbit manipulations). Thus, they are subjected to a maximum ramp rate of ~1.5 T/s, which is still relatively low. The geometry of these units leads to small time constants and the installation of the standard 2 mm thick vacuum chambers is acceptable. The standard lamination thickness of 1.5 mm is also adopted for convenience. Table 3.30 summarises the relevant parameters and time constants for the fields in these magnets.

Time response of the main ring correctors				
	Horizontal		Vertical	
Yoke *:		**Time const.**		**Time const.**
Length [m]	0.200		0.200	
Pole width [m]	0.164		0.098	
Half gap [m]	0.099		0.082	
Lamination thickness [m]	0.0015		0.0015	
Lamination resistivity [Ω m]	1×10^{-7}		1×10^{-7}	
Av. iron path, pole to pole [m]	0.45	13 μs (yoke)	0.40	7 μs (yoke)
Vacuum chamber:				
Horizontal width [m]	0.144		0.078	
Chamber thickness [m]	0.002		0.002	
Chamber resistivity [Ω m]	7.2×10^{-7}	6 μs (chamber)	7.2×10^{-7}	3 μs (chamber)
Net response				
Overall time constant [μs]	19 μs		10 μs	

* No end plates.

Table 3.30 Time response of the main ring correctors

Betatron core

The betatron core differs from the other magnets inasmuch as its field is never 'seen' directly by the beam and, consequently, the field quality within the core is of less concern. However, it would be impractical to make a massive core in order to get maximum smoothing for the spill, since the rapid cycling that is needed before and after the spill would cause considerable power loss in the core itself from eddy currents. The aim here is to keep the power losses tolerable, while providing a minimum attenuation of a factor of 10 (as defined in Part I Section 5.11) for the field ripple from DAC steps at 1 kHz, which is the lower limit accepted for low-energy protons.

Table 3.31 lists the time constants for different thickness lamination and the expected eddy current power losses. The power losses have been estimated with a simplified formula derived from first principles for the specific power loss, P_{eddy},

$$P_{\text{eddy}}[\text{W/m}^3] = \frac{1}{24}\frac{\omega^2[\text{s}^{-2}]\, d^2[\text{m}^2]}{\rho[\text{ohm m}]} B_{\text{AC}}^2[\text{T}^2]$$

where ω is the angular frequency, d is the lamination thickness (perpendicular to magnetic field direction), ρ is the resistivity of the laminations and B_{AC} is the amplitude of the sinusoidal field.

The time constants in Table 3.31 govern the response of the field to a given current change. There is a different time constant that governs the response of the current in the coil to a given voltage change from the power converter and this must be considered when designing the power converter. The two time constants can be considered as independent. In other words, the voltage needed to ramp the betatron core against its self-inductance will be much larger than the voltage needed to furnish the energy lost in eddy currents. A similar treatment can be found in Ref. [15] except that silicon steel with a resistivity of 4×10^{-7} ohm m was considered and the time constant used includes that of the coil.

To reach the minimum attenuation factor of 10 for field ripple at 1 kHz, the laminations need to be 1.0-1.5 mm thick. It is therefore convenient to standardise on the 1.5 mm iron sheet foreseen for the main ring units. The eddy current loss of 135 W is still very low and will have little effect on the 20.5 t iron core.

Comparison of laminations for the betatron core

Lamination thickness [mm]	Time constant [ms]	Attenuation of sinusoidal ripple at 1kHz and 10kHz	Eddy current power loss [W]
0.5	0.3	2.1, 18.9	15
1.0	1.1	7.0, 69.1	60
1.5	**2.5**	**15.7, 157**	**135**
2.0	4.4	27.7, 277	241
2.5	6.9	43.4, 434	377
3.0	9.9	62.2, 622	542

Note that time constants for the betatron core are much longer than those quoted earlier for the main dipole with the same lamination thickness. This is mainly due to the air gap in the dipole (72 mm) compared to the kapton sheet that separates the two halves of the betatron core (2×0.2 mm) and, to a lesser extent, to the differences in cross-section and path length in the iron yokes.

Table 3.31 Comparison of laminations for the betatron core
[Average path in iron = 2.6 m, air gap = 0.2 mm, yoke width = 0.67 m, resistivity = 10^{-7} ohm m, cycle rate for eddy current power loss = 1 Hz, volume of core = 2.6 m^3, average field in core = 1.187 T]

3.14 BEAM DUMPING AND COLLIMATION

3.14.1 Internal dump (vertical)

In the PIMMS ring, it is difficult to arrange a conventional beam dumping scheme operating in the vertical plane with a single fast kicker that removes the beam from the machine in one turn. Firstly, it is difficult to house the relatively large vacuum tank of the fast kicker in the lattice at a convenient position. Secondly, there is very little spare aperture in which the deflected beam can pass because the vertical aperture in the dipoles has been reduced to the minimum to limit the ampere-turns needed. With the single-kicker schemes that were tried, it was found that, with at least one of the many beam conditions, substantial particle losses were incurred outside of the dump block. The fast kicker is also a rather expensive item. Since the revolution time is short (2.1-0.35 μs), the kicker must be very fast or a substantial fraction of a coasting beam will be distributed around the ring during the upwards ramp of the kick. For these reasons, a dumping scheme based on a rapid bump that is excited over a few tens of turns has been adopted. In this way, microsecond technology is used rather than the more expensive nanosecond technology.

The rapid bump is excited by two bumper dipoles (in SS MR 08 and SS MR 21) powered in series. The two yoke can be identical, but the coils must be arranged so that the dipole in SS MR 08 gives half the kick of the other. Despite this complication, the bumper dipoles are simpler, smaller, and more reliable than a fast kicker and they avoid the complications of a vacuum tank with high-voltage

feedthroughs. Since the dumping action takes many turns, the voltages are lower and the power converter is simplified. Although the dumping action takes several turns, the beam is still removed in a short time (32 μs) and far quicker than the 200 μs usually quoted for the emergency interruption of the patient irradiation. The basic design concepts for the bumper dipoles are given in Appendix L.

Figure 3.48(a) indicates the positions of the bumpers, the dump blocks and the form of the closed orbit bump in the vertical plane. The dump blocks are set above and below the median plane after quadrupole QD MR 13. They are positioned according to the prescriptions in Section 3.5 and define the vertical limits of the 'good' field region as ±27.5 mm (i.e. theoretical maximum beam plus the closed orbit margin). All other elements in the vertical plane should be kept within the shadow of the dump block and leave at least the collimation margin free for halo particles and the passage of the dumped beam. Further details of the dump blocks are given in Appendix M. The bump in Figure 3.48(a) has a maximum height of 31.5 mm and passes at about 30 mm at the dump block. This corresponds to the extra kick needed if the closed orbit is displaced in the unfavourable direction by the maximum allowable amount at the dump block. When translated into kick strengths, this corresponds to 2.5 mrad and 5 mrad for the kickers.

The dump sits between two dipole chambers that limit the vertical aperture to ±32 mm. The dump blocks at ±27.5 mm therefore cast a protecting shadow on these chambers of about 4.5 mm. If the bump for dumping the beam grows by more than this margin in a single turn, then beam will be lost on the upstream dipole vacuum chamber rather than the dump block. The onset of this situation is shown in Figure 3.48(b), which shows the injected carbon-ion beam entering the dump block at about 31 mm. To allow for some error, the maximum growth rate of the bump will be set to 2 mm per turn. Thus, the bump can rise to its full height in a minimum of 16 turns. Based on the longest revolution time of 2 μs this corresponds to 32 μs for the rise time of the bump. If the figure of 32 μs is now used as a specification for the rise time under all conditions, the beam will be dumped over 16 to 90 turns and the bump increment per turn will correspondingly vary between 2 mm and 0.4 mm. To achieve this, the power converter must adapt its maximum voltage to the beam rigidity during the magnet cycle, so that the bump excited by the bumpers is always 31.5 ±2 mm in a rise time of 32 μs. Unless an abnormal situation occurs with a displaced vacuum chamber, or an exceptionally large orbit distortion, the dumping efficiency should be 100%. The vertical dump blocks also act as vertical collimators that protect the other machine elements from mis-steered beams or unstable beams.

3.14.2 Radial collimation

At the start of acceleration, any untrapped beam will spiral inwards onto the vacuum chamber wall. Similarly, after extraction, there will always be some beam left in the machine. If the extraction energy is below the peak of the magnet cycle, this beam will spiral inwards and be lost on the inner wall, but, if the extraction energy is at the peak of the magnet cycle, then the beam will spiral outwards and be lost on the outer wall during the down ramp of the field. These losses should be absorbed by radial collimators positioned in the centres of the arcs where the beam has

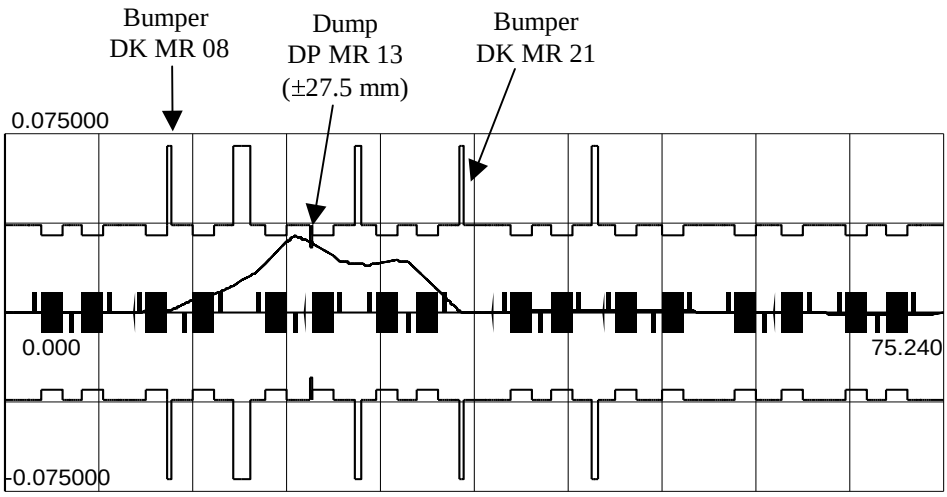

(a) Form of vertical closed-orbit bump for dumping, positions of elements and chamber wall

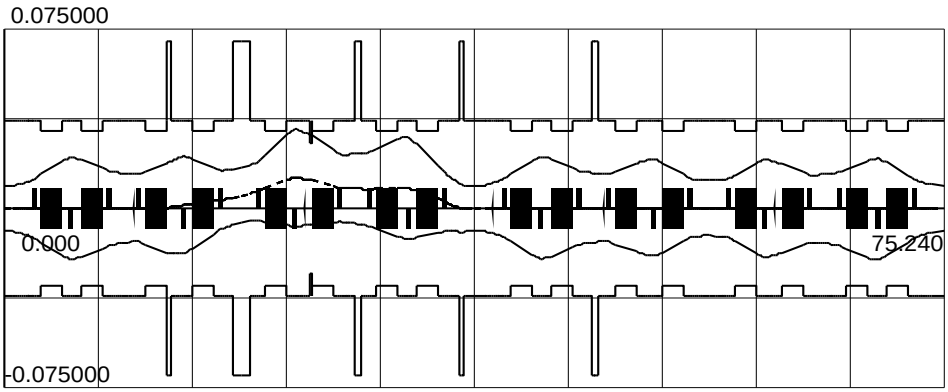

(b) Example of the carbon ion beam at injection entering the dump at a depth of ~31 mm.

Figure 3.48 Internal rapid dumping scheme (vertical plane)
[Example beam: Q_x = 1.6800, Q_z = 1.7200; 7 MeV/u and $E_{z,RMS}$ = 6.106π mm mrad]

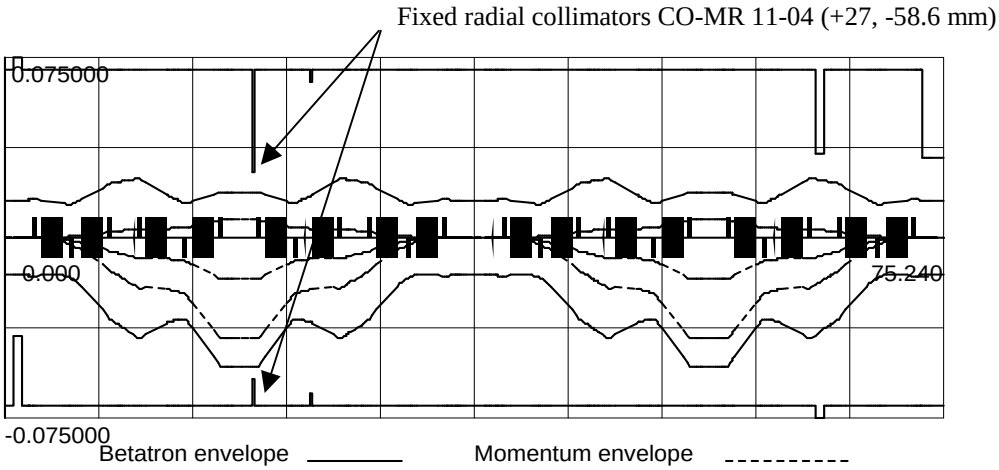

Figure 3.49 Radial collimation of beam
[Example beam: At 8.5 MeV/u critical point; $\Delta p/p_{\text{average}}$ = -0.0021; $\Delta p/p_{\text{full}}$ = 0.006;
$E_{x,RMS} = E_{z,RMS}$ = 5.525π mm mrad;]

its maximum horizontal size (Figure 3.49 shows the carbon ion beam at its critical point in the rf cycle ~8.5 MeV/u when its width is maximum).

The radial collimator blocks are set limit the inner aperture at -58.6 mm. This position is taken from the maximum beam size plus the closed-orbit margin recorded in Table B4 in Appendix B. A similar block is placed at +27 mm to limit the outer aperture. The position is taken from the excursions of the separatrices plus closed-orbit margin recorded in Table B1 in Appendix B. As was explained in Section 3.5.4, the electrostatic septum is not totally protected and may intercept beam that is moving outwards rather than the collimator. Unfortunately, there is nothing that can be done to improve this situation. Further details of the collimators are given in Appendix M.

References

[1] P.J. Bryant, *AGILE program for synchrotron lattice design*, http://nicewww.cern.ch/~bryant.

[2] C. Steinbach, Private communication, *FERMEX program for slow extraction optimisation*.

[3] H. Grote, F. Iselin *The MAD program, Users' Reference Manual*, CERN/SL/90-13 (AP), (1990).

[4] M. Crescenti, S. Rossi, Private communication, Analytical code RFAC for acceleration programmes, (1999).

[5] J. MacLachlan, *User's Guide to ESME v. 8.2*, (1996).

[6] P. Knaus, *Simulation of Space Charge Dominated Beams and Experimental Tests*, Ph.D. thesis, Inst. f. Exp. Kernphysik, Univ. Karlsruhe (TH), to be published.

[7] U. Bigliani, *Système HF du Booster, Capture dans l'espace de phase longitudinal*, SI/Int. EL/68-2 (1968).

[8] D. Boussard, *RF technique for pp-bar*, CERN 84-15, (1984), Vol. 1, 261-290.

[9] C. Bovet, R. Gouiran, I. Gumowski, K.H. Reich, *A Selection of Formulae and Data Useful for the Design of A.G. Synchrotrons*. CERN/MPS-SI/Int. DL/70/4.

[10] M. Crescenti, P. Knaus and S. Rossi, *The RF Cycle of the PIMMS Synchrotron*, CERN PS/DI Note, To be published.

[11] L. Badano, *Closed-orbit prognosis, correction and manipulation for the PIMMS synchrotron*, CERN-PS-99-059 (DI).

[12] P.J. Bryant, *Basic theory for magnetic measurements*, CERN 92-05, (Sept., 1992), p65-69.

[13] P.J. Bryant, Private communication, *Eddy currents in accelerator magnet vacuum chambers*, Extended PIMMS Meeting, (Dec., 1997).

[14] P.J. Bryant, *Eddy currents and their effects in the Split Field Magnet (SFM)*, Internal Note ISR-MA, (1972).

[15] L. Badano, S. Rossi, *Characteristics of a betatron core for extraction in a proton-ion medical synchrotron*, CERN/PS 97-19(DI).

* * *

II-4 MAIN RING HARDWARE

The magnetic cycle (see Section 3.3) has its maximum at the highest extraction energy for carbon ions and its minimum at 5% of the maximum field in the main dipoles. This leaves a small margin at the bottom of the cycle to establish the conditions for injection on the rising part of the hysteresis curve. The magnetic rigidities of the beams (see Table 4.1) determine the broad characteristics of the main ring hardware. In terms of rigidity, the operational range with beam is 1:10 from the proton injection to the highest extraction energy for carbon-ions. This is a fairly normal range for an accelerator. Extending the range upwards is limited by saturation and deteriorating field quality and extending it downwards is limited by remanent fields and setting precision. The range over which slow extraction is performed is more important for a medical synchrotron due to the extreme sensitivity of slow extraction to ripple. In PIMMS, this is 1:5.5 and is unusually wide due to the inclusion of two particle species (60 MeV protons to 400 MeV/u carbon ions). Since the relative current ripple depends on the maximum currents of the power converters, this means that on average the current ripple will be 3 times higher for the protons than for the carbon ions.

Beam rigidities

Situation	***B*ρ [Tm]**	**Comment**
Lower limit of magnetic cycle	0.3	Concern for converter stability
Proton injection (20 MeV)	0.65	Concern for field quality
Carbon-ion injection (7 MeV/u)	0.76	Concern for field quality
Lowest proton extraction (60 MeV)	1.14	Concern for current ripple
Highest proton extraction (250 MeV)	2.43	Concern for current ripple
Lowest carbon-ion extraction (120 MeV/u)	3.25	Good operating condition
Highest carbon-ion extraction (400 MeV/u)	6.35	Best operating condition
Upper limit of magnetic cycle	6.35	

Table 4.1 Beam rigidities

The standard approach to setting tolerances on machine components is to evaluate the effect of various errors on different aspects of performance and then to select the error conditions that impose the tightest restrictions. In cases where it is clear that tolerances cannot be met, it is necessary to impose 'reasonable' specifications and then to add a compensation scheme. This is, for example, the case of closed-orbit deviations that arise from errors in alignment and manufacture of the magnets.

When considering magnetic field quality, it is usually assumed that the betatron amplitude function is much greater than the length of the magnet (i.e. the phase advance is small, $\Delta\mu = \ell/\beta << 1$, where ℓ is the length of the magnet). In this case, the integral of the field through the magnet is the important quantity and the one that must satisfy the field quality criterion. This has the practical consequence that

there is no need to differentiate between field variations that are local (e.g. shims) or distributed (e.g. shaping of the pole profile) and either can be used to correct the magnet. For the PIMMS quadrupoles, sextupoles and other short magnets, this assumption is adequately satisfied. Thus, field errors arising from the transverse and longitudinal truncations of the pole can be corrected by introducing a shaping of the transverse pole profile at the design stage and, later during magnetic measurements, a further correction can be added with end-shims, if needed. The assumption is less true for the dipoles. The effective dipole length is 1.66 m and the minimum betatron amplitude functions are ~4 m (horizontal) and ~6 m (vertical). The betatron amplitude function also changes by up to a factor 2 within the length of some dipoles. This suggests that the correct design philosophy is to calculate the main dipole in 2-dimensions. This corrects the effect of the transverse truncation of the pole ONLY and corrects this uniformly along the magnet. The effect of the longitudinal truncation of the pole should then be corrected locally at the magnet ends by end-shims added according to the magnetic measurements. In this way, it does not matter if the lattice functions change along the length of the dipole as corrections are always made where the errors occur.

The current ripple would normally be included in the general determination of tolerances, but in the case of a machine using slow extraction this is an especially important topic and will be covered separately in Section 4.13.

4.1 MAIN DIPOLES

4.1.1 Field uniformity within individual dipoles

The tolerance on field uniformity across the aperture is based on the needs of the extracted beam while in transit between the electrostatic and magnetic septa. To avoid beam losses at the entry to the magnetic septum, it is necessary that the differential movement of the extraction orbit at the magnetic septum with respect to the central orbit, over the whole range from low to high field, is less than 1 mm (±0.5 mm). This tolerance is set to be of the same order of magnitude as the positional and straightness tolerances for the vacuum chamber.

The main concern is for the preservation of the gap of 19.2 mm that is opened between the extracted and circulating beams. This is particularly difficult to satisfy, since the extraction orbit between the septa passes at the very edge of the good-field region where the effects of saturation and multipole components are most evident, while the circulating beam is well inside the good-field region and “sees” a much smaller variation of the field with respect to central orbit. At low field, the edge of the aperture is over-compensated and the field level rises, so that at high field the loss of flux due to saturation is delayed as long as possible. Normal closed-orbit correction is of no help, since this is based on central-orbit measurement and acts as a constant correction for the whole aperture.

The significant error in this case is the systematic error across the main dipole aperture and how this error changes from low to high field. Although the section of lattice between the two septa is relative short, the trajectory is shifted by 1 mm (between low and high field) by a systematic error in the dipoles of

$\Delta(BL)/(BL)_0 = 4 \times 10^{-4}$. Thus, the systematic integrated field error across the main dipole aperture for all extraction energies must be less than $\pm 2 \times 10^{-4}$.

4.1.2 Field uniformity between dipoles

Remanent field errors

For the remanent field,

$$H_{\text{coercivity}}\,\ell_{\text{steel}} + \frac{B_{\text{remanent}}}{\mu_0}\,\ell_{\text{gap}} = 0 \tag{4.1}$$

where the flux path in the steel, $\ell_{\text{steel}} \approx 1.5$ m and the flux path in the air, $\ell_{\text{gap}} = 0.08$ m. If, for prudence, a medium to poor quality steel is assumed, then $H_{\text{coercivity}} = 100$ and $B_{\text{remanent}} = 24$ G. Superimposed on this remanent field will be a random fluctuation of approximately ±1.2 G (±5%) from unit to unit.

This leads to a tolerance of ±1.2 G for the random component in the remanent field between units. At the proton injection energy of 20 MeV, this corresponds to a relative integrated field error of $\Delta(BL)/(BL)_0 \le \pm 8 \times 10^{-4}$.

Model for packing factor and length tolerances

The magnetic circuit of the dipole can be simply represented by,

$$NI = \oint \boldsymbol{H}\cdot\boldsymbol{ds} = \oint \frac{\boldsymbol{B}}{\mu}\cdot\boldsymbol{ds} \approx \Phi \sum_i \left(\frac{\ell}{a\mu}\right)_i \tag{4.2}$$

where Φ is the magnetic flux in the circuit. In the ith section of the circuit, the length is ℓ_i the cross-sectional area is a_i and the permeability is μ_i. Thus, the main dipole can be represented by the simple circuit model of

$$\Phi = \frac{NI\mu_0}{\left(\dfrac{\ell_{\text{steel}}}{a_{\text{steel}}\mu_r} + \dfrac{\ell_{\text{air}}}{a_{\text{air}}}\right)} \approx \frac{aNI\mu_0}{\left(\dfrac{\ell_{\text{steel}}}{\mu_r} + \ell_{\text{air}}\right)} \tag{4.3}$$

where μ_r is the relative permeability of the steel. The second equation is based on the approximation $a \approx a_{\text{steel}} \approx a_{\text{air}}$.

Change in the packing factor

This leaves the overall dimensions of the magnet unchanged, but modifies the local cross-sectional area of the steel in the yoke. When the flux leaves the steel to enter the air gap, it spreads out across the gaps between the laminations so that the field is again uniform. The effect of the packing factor can be found by differentiating the flux expression with respect to a_{steel} to give,

$$\frac{\Delta\Phi}{\Phi} = \frac{\Delta a_{\text{steel}}}{a_{\text{steel}}}\,\frac{a_{\text{air}} l_{\text{steel}}}{a_{\text{steel}} l_{\text{air}}\mu_r}\left(1 + \frac{a_{\text{air}} l_{\text{steel}}}{a_{\text{steel}} l_{\text{air}}\mu_r}\right) \approx \frac{\Delta a_{\text{steel}}}{a_{\text{steel}}}\,\frac{l_{\text{steel}}}{l_{\text{air}}\mu_r} \approx 0.05\frac{\Delta a_{\text{steel}}}{a_{\text{steel}}} \tag{4.4}$$

where $\mu_r(\text{min}) = 400$, $a_{\text{steel}} \approx a_{\text{air}}$ and the other symbols are as defined above. Thus, the fractional field error is ~20 times less than the packing factor error. Since the remanent field error dominates at injection while the packing factor error dominates at high field, it would seem reasonable to specify tolerances so that these two errors are made equal in order to have approximately the same overall field error at all energies. This leads to a packing factor tolerance of $\pm 1.6 \times 10^{-2}$ between units for a random relative integrated field error at top energy of $\pm 8 \times 10^{-4}$.

Change in the length of the magnet

This affects equally the cross-sectional areas of the steel and the air gap such that,

$$\frac{\Delta\Phi}{\Phi} = \frac{\Delta(BL)}{BL} = \frac{\Delta L}{L}\left(\text{for constant width}\right) \qquad (4.5)$$

Thus a fractional error in the length of the magnet can be directly expressed as the same fractional error in the integrated field. Whereas a fractional error in the packing factor is ~20 times less effective. Unless special laminations are made, the length will be adjustable by ± one lamination thickness (~1.5 mm). Thus, for a length tolerance of $\pm 10^{-3}$ (i.e. ±1 lamination) the expected integrated field error from length errors will be also be $\pm 10^{-3}$ and will be independent of field level.

Closed orbit prognosis

The quadratic combination of the random errors from remanent fields and length variations at low fields and packing factor variations and length variations at high fields lead to the same net random error of $\Delta(BL)/(BL)_0 = \pm 1.2 \times 10^{-3}$. This has been interpreted pessimistically as an RMS value and used for the closed-orbit study made in Section 3.6.

Main Dipole construction

The dipole design is consistent with its use in a hospital environment as opposed to a high-energy physics laboratory. Its weight (~8 t) requires a modest crane capacity, the coil is a simple 'racetrack', the yoke is short enough to be curved by displacing laminations against a curved wall (rather than wedging) and the general dimensions are such that spare coils etc. can be easily stored. End plates are formed by gluing a stack of laminations to avoid the undesirable eddy current effects that thick end plates introduce. The discussion of eddy currents and lamination thickness is given in Section 3.13 Details of the mechanical and magnetic designs can be found in Appendix E.

4.1.3 Setting precision

The setting precision for the main field depends on the orbit stability at the proton injection energy and on the energy resolution (i.e. penetration depth) required for the extracted beam. In the PIMMS design, the main field is kept strictly constant during extraction, so there is no need to consider the size and smoothing of the DAC steps.

Orbit stability at injection

The precision and reproducibility of the injection closed orbit should be better than ±1 mm. The momentum compaction function can be used to estimate the required current precision for the protons at 20 MeV,

$$\frac{\Delta p}{p} = \gamma_t^2 \frac{\Delta C}{C} \quad \Rightarrow \quad \frac{\Delta I}{I} = \gamma_t^2 \frac{\Delta x}{R} \approx 4 \times \frac{0.001}{12} = 3.3 \times 10^{-4} . \tag{4.6}$$

Depth precision for treatment

The minimum thickness of a voxel will be a few millimetres. The precision of the penetration depth (i.e. energy) should be much better than 1 mm to maintain an overall sub-millimetre accuracy for the beam delivered by the machine. The values shown in Table 4.2 correspond to a setting precision of 0.2 mm for the penetration depth.

Precision of the main dipole current setting*		
	Protons	**Carbon ions**
Approx. energy step for penetration of 0.2 mm	~0.088 MeV	~0.2 MeV/u
Current precision, $\Delta I/I$	0.8×10^{-4}	5×10^{-4}

* Note that the precision of the energy setting is not the same as the energy steps needed for treatment planning. The precision should be finer than the steps for the treatment planning.

Table 4.2 Precision of the main dipole current setting

A 14-bit DAC satisfies the strictest of these criteria, i.e. the precision of energy setting required for the protons. This choice also leaves a margin of security for the stability of the injection orbit should the proton injection energy be lowered.(see Section 9.2). Since the dipoles are kept constant during the spill, there is no need to take into account the perturbation of their DAC steps.

4.1.4 Field ripple

In view of the importance of this topic, the considerations on ripple are gathered together in Sections 3.13 and 4.13

4.2 MAIN QUADRUPOLES

4.2.1 Gradient uniformity within individual quadrupoles

Shape of the working line

Gradient variations across the aperture of an individual unit and variations in this pattern with field level cause distortion of the working line in the tune diagram. This distortion should be within the tolerance of $\Delta Q = \pm 0.00075$[*] in either plane.

Table 4.3 summarises the sensitivity of the tunes to systematic gradient errors (i.e. errors that arise from the pole profile and saturation). For the PIMMS

[*] $\Delta Q = \pm 0.00075$ has been chosen, so that the quadratic addition with the random errors in Section 4.2.2 will lead to an overall position and distortion tolerance of the order of $\Delta Q = \pm 0.001$ in either plane.

quadrupole, the saturation effect is small, so all three families (QF1, QF2 and QD) will have almost the same fractional error, except that the QD-family will be of opposite sign. The maximum distortion in tune has been adjusted to $\Delta Q = \pm 0.0007$, which corresponds to a fractional gradient error of $\Delta(GL)/(GL)_0 = \pm 5 \times 10^{-4}$ that can be interpreted as the tolerance for the pole profile.

Sensitivity to systematic gradient errors				
Family	$k_{nominal}$	$\Delta k/k$	ΔQ_h	ΔQ_v
QF1	-0.3136	0.0005	0.00042	-0.00023
QF2	-0.5252	0.0005	0.00061	-0.00034
QD	0.5248	0.0005	-0.00031	0.00082
QF1+QF2-QD	as above	0.0005	0.00071	0.00026

Table 4.3 Sensitivity to systematic gradient errors

Stability of the extraction separatrix

The phase advance between the resonance sextupole and the electrostatic septum determines the angle of the separatrix as it reaches the septum wires. Any difference in this phase advance, between the low and high fields, changes the separatrix angle during a treatment and a change of ~0.1 mrad is equivalent to a 1% beam loss on the septum wires. The various sources of loss in the electrostatic septum have all been adjusted to be less than 1%, so ideally this should also be the case for the effect of systematic gradient changes between low and high field.

Figure 4.1 shows the configurations of the extraction separatrix at the resonance sextupole and at the electrostatic septum. Approximately half of the ring is contained in the intermediate lattice, so the horizontal tune shift from Table 4.3 can be divided by two and used to establish the relation between a gradient error and the change in horizontal phase advance, i.e. $\Delta k/k = 0.0005$ causes $\Delta\mu_x = 0.0022$ rad.

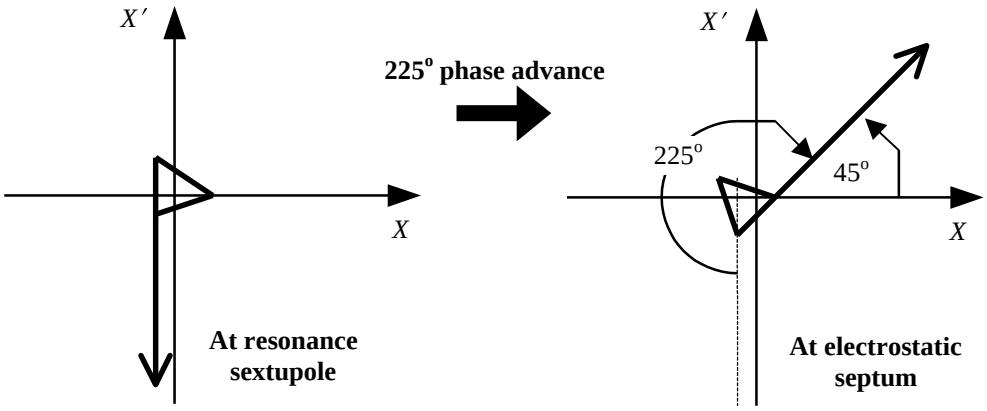

Figure 4.1 Configuration for the extraction separatrix

The movement of the separatrix, ΔS, in normalised phase space at the electrostatic septum for a small step in betatron phase, $\Delta\mu$, is,

$$\Delta S = \sqrt{(\Delta X)_{\mathrm{ES}}^2 + (\Delta X')_{\mathrm{ES}}^2} = \Delta\mu \sqrt{X_{\mathrm{ES}}^2 + X'^2_{\mathrm{ES}}} \,. \qquad (4.7)$$

Since the separatrix sits at ~45°, the changes in the normalised co-ordinates reduce to,

$$\Delta X_{\mathrm{ES}} = X_{\mathrm{ES}}\,\Delta\mu \quad \text{and} \quad \Delta X'_{\mathrm{ES}} = -X_{\mathrm{ES}}\,\Delta\mu \,. \qquad (4.8)$$

Conversion to real space yields an angular change of,

$$\Delta x'_{\mathrm{ES}} = \frac{(\Delta X' - \alpha\Delta X)}{\sqrt{\beta}} = -\frac{x_{\mathrm{ES}}}{\sqrt{\beta}}(1+\alpha)\Delta\mu = -0.035\times(1+0.36)\times 0.0022/\sqrt{16}$$

$$\Delta x'_{\mathrm{ES}} = 0.000026 \text{ rad} \,.$$

Thus the proposed tolerance on systematic gradient errors between low and high fields leads to a movement in the separatrix that is approximately 4 times smaller than the required stability of 0.0001 rad.

4.2.2 Gradient uniformity between quadrupoles

Variations in the integrated gradient between units lead to modulation of the betatron amplitude function and changes in the tune values. These errors will be random and due to mechanical tolerances and steel quality. Table 4.4 shows the sensitivity of the ring to random gradient errors.

Sensitivity to random gradient errors averaged over 1000 machines

Families	$(\Delta k/k)_{\mathrm{RMS}}$*	$(\Delta Q_h)_{\mathrm{RMS}}$	$(\Delta Q_v)_{\mathrm{RMS}}$
QF1+QF2-QD	0.0016	0.00069	0.00072

* $\Delta k/k$ is interpreted as the RMS value of a distribution with a cut-off at 1 RMS. This is close to a uniform random distribution in the band $\Delta k/k = \pm 0.0016$, which is the format of the tolerance that will be imposed on the quadrupoles when they are shimmed during magnetic measurements.

Table 4.4 Sensitivity to random gradient errors averaged over 1000 machines

Thus the quadrupoles should be shimmed so that the random error between units is $\Delta(GL)/(GL)_0 \le \pm 0.0016$. The working line then falls approximately in the band $\Delta Q = \pm 0.0007$, which is equal to the distortion in the working line expected from systematic errors within in a single unit (see Section 4.2.1). Combining the systematic errors and the random errors quadratically leads to an overall precision of the working line of $\Delta Q = \pm 0.001$.

Length and packing factor

The quadrupoles in PIMMS have relatively low excitation levels and there is a potential problem at the lowest field levels of random fluctuations between units from the remanent field. For this reason, the packing factor has been reduced to 0.7 to increase the field level in the steel artificially. The field enhancement is more pronounced at the magnet ends, since the air gaps between laminations makes it more difficult for the flux to distribute itself axially than in a solid magnet.

Since the PIMMS quadrupoles are short and have a low packing factor, it is better to ignore the conventional length tolerance and to substitute a fixed number of laminations plus a weight tolerance. The relative weight tolerance for a quadrant would be ±0.0016 in agreement with the gradient tolerance and would be adjusted by suitably selecting light and heavy laminations from the production. As with the dipole, the packing tolerance is less critical and would be $\pm 1.5 \times 10^{-2}$. Thus, the spaces between laminations would be 0.64±0.01mm, which becomes the tolerance on the spacers. According to the average thickness of the spacers, there would be 163 or 164 laminations per quadrant. Once this number is chosen, it must be respected in all quadrupoles in the production.

Main quadrupole construction

The construction uses the conventional approach of four individual quadrants that are bolted together, so that the magnet can be easily opened. Each quadrant is made from a stack of 1.5 mm thick laminations spaced by 0.64±0.01mm. The discussion of eddy currents and lamination thickness is given in Section 3.13 Details of the mechanical and magnetic designs can be found in Appendix F.

4.2.3 Setting precision

A precision of $\Delta Q = \pm 0.001$, is sufficient for general beam manipulations. Respecting this tolerance is most difficult at the injection energy for protons, where the gradients are approximately 10% of maximum and the required $\Delta G/G_{max}$ is approximately equivalent to $\Delta I/I_{max} = 6 \times 10^{-5}$.

A more strict tune requirement arises from the precise positioning of the beam against the resonance, before the betatron core starts its ramp. This avoids the core wasting a lot of time accelerating across a resonance-free region in search of the resonance. The positioning procedure should be delicate enough to position the beam to say 0.0002 in tune while measuring the beam loss. The step of 0.0002 represents ~12 ms of acceleration time by the core for a nominal 1 s spill (the "waiting" stack has a horizontal tune spread of $\Delta Q_x = 0.016$ i.e. $Q'_x \, \Delta p/p = 0.004 \times 4$). The time needed to engage the resonance also acts as a stabilisation time for the fields. Once the spill has started, there will be a further delay while the feedback circuit on the intensity adjusts the acceleration rate of the core.

The precision needed when engaging the resonance is the stricter of the two criteria and requires $\Delta I/I_{max} \approx 3.5 \times 10^{-5}$ for which a 16-bit DAC is needed. Note that since a betatron core 'feeds' the resonance, there are no auxiliary tuning quadrupoles. For this reason, the task of positioning the beam reverts to the main quadrupoles with the consequence of needing a precise DAC. Since the quadrupoles are kept constant during the spill, there is no need to take into account the perturbation of their DAC steps.

4.2.4 Gradient ripple

In view of the importance of this topic, the considerations on ripple are gathered together in Sections 3.13 and 4.13.

4.3 SEXTUPOLES

Table 4.5 summarises the functions of the different sextupoles and how these are affected for changes of 4×10^{-3} of the set excitation values. A brief inspection will show that none of the functions considered imposes a very tight tolerance on the pole profile and manufacture of these lenses. A blank tolerance of say $\pm 4 \times 10^{-3}$ is considered to be adequate for the field qualities. Since the protons work at much lower energy than the ions the setting precision needs to be say $\pm 10^{-3}$ (10-bit DAC), in order to be consistent with the mechanical tolerances.

In Table 4.5, the F-sextupole family affects principally the vertical plane and this is reflected in the fact that the angle of the separatrix and the spiral step are quasi-unaffected by changes in this family. The D-sextupole family affects mainly the horizontal plane and is important for the optimisation of the Hardt Condition. A few per mil precision when setting the D-family ensures that the precision of the separatrix is far better than 0.1 mrad (0.1 mrad corresponds to ~1% beam loss at the electrostatic septum).

Effects of systematic errors in sextupole gradients

Function and lenses	$\Delta k/k'$ of set		
Spiral step		**Changes in spiral step**	
Resonance sextupole	4×10^{-3}	0.084 mm	
F-family*	4×10^{-3}	0.000 mm	
D-family*	4×10^{-3}	-0.007 mm	
Chromaticity		**Changes in chromaticity**	
Resonance sextupole	4×10^{-3}	$\Delta Q'_x = 0.000$	$\Delta Q'_z = 0.000$
F-family*	4×10^{-3}	$\Delta Q'_x = 0.001$	$\Delta Q'_z = -0.003$
D-family*	4×10^{-3}	$\Delta Q'_x = -0.014$	$\Delta Q'_z = 0.006$
Separatrix angle		**Changes in separatrix angle**	
Resonance sextupole	4×10^{-3}	-0.003 mrad	
F-family*	4×10^{-3}	0.000 mrad	
D-family*	4×10^{-3}	-0.002 mrad	

* An F-type sextupole reinforces the gradient of an F-type quadrupole in the outer (positive) half of the aperture and similarly for the D-type.

Table 4.5 Effects of systematic errors in sextupole gradients

These magnets will have a laminated construction, but, unlike the quadrupoles, they will have a packing factor that is as close as possible to unity. The proposed blank manufacturing tolerance of $\pm 4 \times 10^{-3}$ implies a length tolerance of ±0.8 mm, since the lens is only 20 cm long. However, with such a short lens, it is more practical to specify an exact number of laminations, which with a practical stacking factor of 0.975 would be 143, and then to set a weight tolerance of $\pm 4 \times 10^{-3}$. As for the dipole and quadrupole, current ripple is of utmost importance and a discussion of eddy currents, lamination thickness and power converters is given in Sections 3.13 and 4.13 Further details are given in Appendix G.

4.4 CORRECTION DIPOLES

The horizontal orbit correctors have a maximum strength of 1.5 mrad and the vertical correctors 0.75 mrad (see Section 3.6.6) for the maximum energy carbon ions (400 MeV/u). There are 10 horizontal orbit correctors with a total integrated bending strength of 15 mrad and 8 vertical orbit correctors with a total integrated bending strength of 6 mrad. This represents 2.4×10^{-3} and 10^{-3} (horizontally and vertically respectively) of the total strength of the ring. Systematic and random errors in the field uniformity of these magnets (due to the pole profile and manufacturing tolerances) will be correspondingly less important (i.e. 500 to 1000 times less) than those in the main dipoles. Thus for systematic errors across the aperture (pole profile and saturation), a relative tolerance of $\pm 10^{-2}$ would be adequate assuming that the excitation of the magnets is scaled approximately with energy i.e. the maximum kicks do not exceed the 1.5 mrad horizontally and 0.75 mrad vertically. This low requirement on the field quality makes it possible to have a simple construction.

Random errors between units due to fabrication tolerances are simulated in Table 4.6. Based on the above, the effect of random errors with an RMS of 10^{-2} of the nominal strengths (1.5 mrad horizontally and 0.75 mrad vertically) have been evaluated and averaged over 500 machines. If it is assumed that the correctors will always be scaled approximately with energy, then Table 4.6 applies at all energies and a blank tolerance on the mechanical fabrication of $\pm 10^{-2}$ will be more than sufficient.

Sensitivity to random dipole kicks averaged over 500 machines

Correctors	δ_0, nominal max. kick [mrad]	$(\Delta\delta/\delta_0)_{RMS}$*	Distortion [mm]
10 horizontal	1.5	10^{-2}	$\|x\|_{maxRMS} = 0.06$
8 vertical	0.75	10^{-2}	$\|z\|_{maxRMS} = 0.12$

* $(\Delta\delta/\delta_0)_{RMS}$ is interpreted as the RMS value of a distribution with a cut-off at 1 RMS. This is close to a uniform random distribution in the band $\pm 10^{-2}$, which is the format of the tolerance that will be imposed on the dipoles.

Table 4.6 Sensitivity to random dipole errors averaged over 500 machines

The precision of setting needs to approximately 5 times better than the field quality tolerances in order that the low-energy protons are not outside the tolerance when the ions are just inside. This implies a precision of 2×10^{-3}, which would be on the limit for a 10-bit DAC and more than adequately satisfied by a 12-bit DAC.

A discussion of eddy currents, lamination thickness and time constants is given in Section 3.13 and the power converter ripple is examined in Sections 4.13. Further details of the mechanical and magnetic designs are given in Appendix H.

4.5 BETATRON CORE

4.5.1 Basic design considerations

The betatron core is the only element in the ring that changes during extraction. The quality of the spill depends directly on the action of the core and, for

this reason, the design of the core and its power converter merit special attention. The main practical points are:

- The core is laminated with 1.5 mm laminations. The lamination thickness is a compromise between the reduction of eddy current losses and a finite degree of eddy current smoothing of the field changes (DAC steps) during extraction (see Section 3.13).
- The halves of the yoke are mutually insulated by Kapton™ foil to prevent accidental conduction paths between laminations that could lead either to closed current paths that dissipate additional power, or earth return loops through the length of the core that might influence the beam via stray fields [1]. The Kapton™ foil and lamination irregularities introduce a total air gap of approximately 0.4 mm.
- The main coil is distributed in four symmetric windings that are placed close to the yoke, so that their fringe magnetic field in the central aperture is symmetric and weak.
- The yoke is split vertically so that the fringe field in the central aperture due to the small gap between the two halves is above and below the beam. In this way, the stray field 'seen' by the beam is the minimum possible.
- A ceramic vacuum chamber, or a ceramic gap in the chamber is required. The upstream and downstream ends of the chamber must be short-circuited by a conductor passing outside the core.

Appendix I gives further details on the mechanical and magnetic designs of the core.

4.5.2 Setting precision and DAC steps

The flux change in the core is designed for the full extraction of a carbon ion beam at 400 MeV/u by changing from -100% to +100%. The full extraction of the lowest energy proton beam requires only ±18% (in the ratio of the magnetic rigidities, see Table 4.1). The nominal time for the extraction is one second, but it is specified that the extraction must work down to at least 10% of this speed. Thus, in the most unfavourable case, the core will need to smoothly change only ±1.8% of the maximum flux in one second[*]. The 'granularity' of the DAC now becomes a problem. In this situation, a high-resolution DAC is absolutely essential. The change from -1.8% to +1.8% represents 2359 steps for a 16-bit DAC and 9437 steps for an 18-bit DAC. For a one second extraction, the 18-bit DAC almost brings the DAC frequency to 10 kHz, which is the clock frequency of the on-line dosimetry. The 16-bit DAC falls well short of this ideal. By virtue of the eddy current smoothing in the betatron core itself (× 10 at 1 kHz and × 100 at 10 kHz) the 16-bit DAC is probably acceptable. Thus a 16-bit DAC can be used, but an 18-bit DAC would be better if reliable units become available commercially. If only carbon beams were being extracted, then a 16-bit DAC would be sufficient, since it would always be operating above the on-line dosimetry frequency.

4.6 AIR-CORED QUADRUPOLE

Provision has been made for a feedback system operating via an air-cored quadrupole. Unfortunately the transit time (see Part I, Chapter 4) appears as a variable 'dead' time in the feedback loop, during which the particles in different time samples become mixed. This effect imposes a lower-than-normal cut-off frequency on the feedback. The frequency depends on the machine circumference, the horizontal emittance, the resonance strength etc.). In PIMMS, efficient operation is expected up

[*] Whenever possible, it is better to avoid changing around zero current by adding an offset.

to 1 kHz, but no detailed study has been made. Details of the air-cored quadrupole design can be found in Appendix J.

4.7 TUNE KICKERS

The ring will be equipped with one horizontal and one vertical tune kicker. These kickers are mounted outside the vacuum for simplicity. They are somewhat stronger than is strictly needed for tune measurements and can be used for other beam studies. Further details of the kicker design can be found in Appendix K.

4.8 BEAM DUMPING AND COLLIMATION

The beam is dumped in 32 μs by a rapid closed-orbit bump excited by two dipole bumpers in series (see Section 3.14). The concept design for the bumper dipoles can be found in Appendix L. The preliminary design ideas for the dump blocks and collimators blocks can be found in Appendix M.

4.9 RF SYSTEM

The single rf cavity is required to perform three separate functions:

- Acceleration of the beam to the extraction energy.
- Preparation of the beam for extraction by moving to the unstable fixed point to expand the momentum spread.
- Acceleration of the beam (by phase displacement around an empty rf bucket) into the resonance.

The frequency swing for the main acceleration is determined by operation with the carbon ions and is slightly less than 1:6. Although this is well within the capabilities of ferrite, a new material called VITROVAC6025F®[*] has been adopted. This material has a principal advantage of requiring far less bias power and the cavity itself is also slightly shorter than an equivalent ferrite design. The details of the cavity construction and its performance characteristics can be found in Appendix N.

The cavity will be equipped with the usual phase and radial position feedback loops. The signals for these loops will be taken from the standard pickups in the ring by adding additional electronics to the outputs. The phase signal can be taken from any monitor, but the adjacent PX MR 21-1 or PX MR 21-6 are the most convenient. The radial position signal must be taken from one or more monitors at positions with large dispersion values (e.g. PX MR 11 and PX MR 31).

4.10 MAIN RING DIAGNOSTICS

The main-ring diagnostics system will include the following measurements:

- Beam position.
- Beam current.
- Transverse and longitudinal beam profiles.
- Beam tune.
- Schottky instrumentation for the coasting beam on the flat-tops.
- Beam losses.

[*] The producer is VACUUMSCHMELZE GmbH, Grünen Weg 37, P.O. Box 2253, D-6450Hanau 1.

All monitors should be suitable for operation with the proton and carbon ion beams and should be able to cope with the wide intensity variation required by the treatment planning [2,3]. The diagnostic system is based on an expected average current variation in the synchrotron from 40 μA for carbon ions at injection to 25 mA for protons at extraction for passive scanning. Other beam parameters can be found in Tables 2, 3, 6 and 7 and in the Parameter List in Appendix DD. Additional information about the diagnostics equipment can be found in Ref. 4.

4.10.1 Position monitoring system

The beam position monitoring system consists of 18 single-plane, 20 cm-long electrostatic pick-ups (11 in the horizontal plane and 8 in the vertical) with an aperture of 140 mm × 74 mm. The distribution allows for at least four position measurements per betatron wavelength. The pick-ups are placed as evenly as possible in betatron phase and at local maxima of the betatron amplitude functions. With respect to the last point, the vertical plane is the more successful with monitors consistently at the maxima. Some additional pick-ups have been added in the horizontal plane close to critical regions (extraction septa, resonance sextupole and chromaticity sextupoles). The layout of the position monitors and the orbit correctors is shown in Figure 4.2.

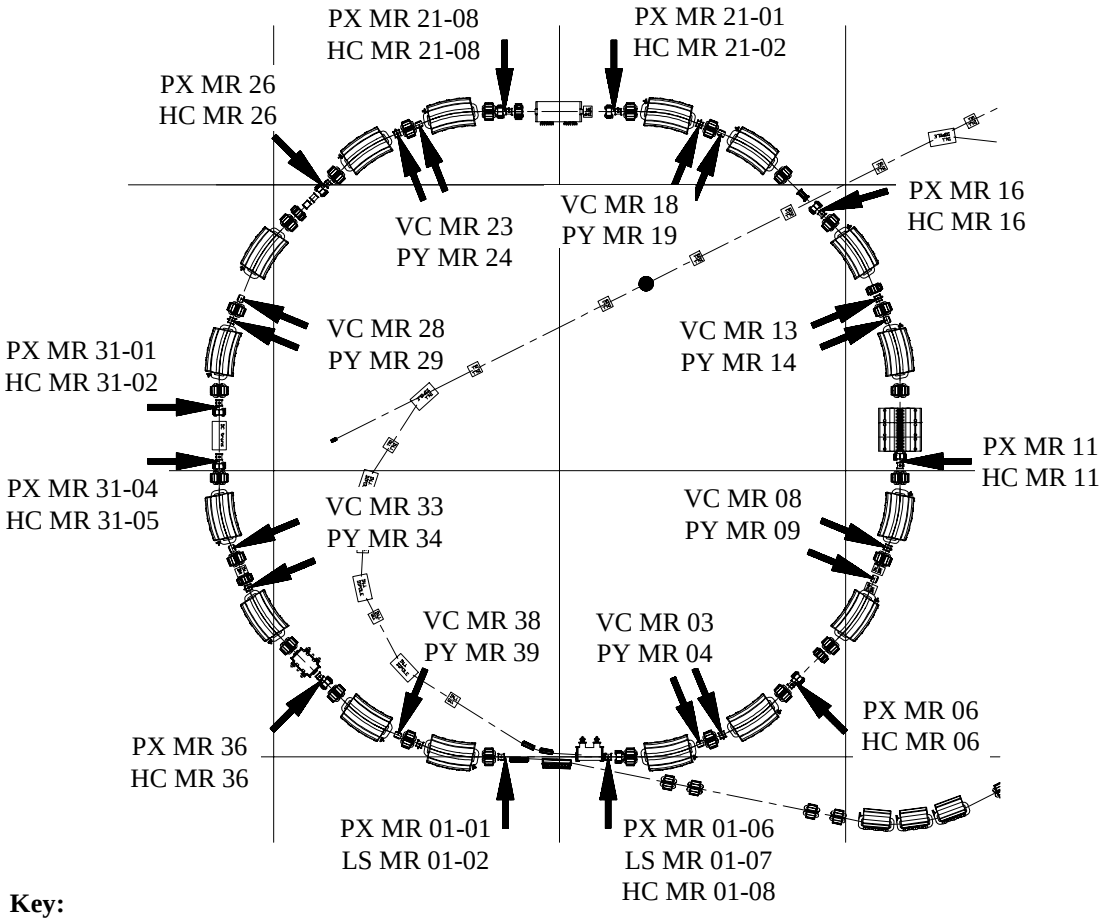

Key:
PX, PY are horizontal and vertical electrostatic pickups, respectively
HC, VC are horozontal and vertical dipole correctors, respectively
LS indicates scintillation screens. Grid is 10 m × 10 m

Figure 4.2 Layout of position monitors and correctors in the main ring

Electrostatic pick-ups were chosen because of their good low-frequency response and linearity. Both broad-band and narrow-band electronics have been considered.

Narrow-band

Two narrow-band solutions have been considered. Both systems have been studied and built at CERN and are listed in increasing order of cost, sensitivity and stability. The first, the 'normalizer', was used for the Antiproton Accumulator and the Antiproton Collector [5,6]. This device produces a dc signal, proportional to the voltage difference between the two plates divided by the sum of the plate voltages. The output from the 'normalizer' is then digitised and acquired by the control system. The second possibility, adopted for LEAR and AD [7], is the use of a network analyser, which provides the ratio between difference and sum signal and their phase relationship. The analyser outputs are also digitised and acquired by the control system. Due to the high cost of the network analyser, it would be necessary to scan several pickups with one unit using a multiplexer. The measurement time for a position resolution of 0.1 mm is of the order of 1 ms for both systems. In the case of the 'normalizer', one electronics module is foreseen for each pick-up and 1 ms corresponds to the total closed-orbit measurement time. In the second case, if one network analyser scans all 18 pick-ups, the closed-orbit measurement time will be of the order of 18 ms. As the PIMMS synchrotron is a pulsed machine, a measuring time of more than a few ms is a disadvantage and, to make this system acceptable, it would be necessary to have say two network analysers per plane. With present-day prices, the balance is firmly tipped in favour of the 'normalizer'. However, it is not excluded that one network analyser could be used with individual pickups for specific problems.

Broad-band

The proposed broad-band system is shown schematically in Figure 4.3.

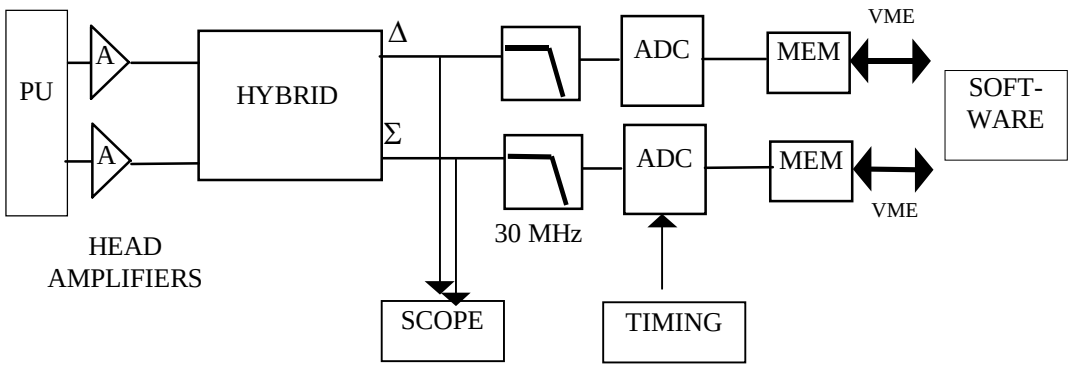

Figure 4.3 Broad-band beam position monitoring system

The voltages on the pick-up electrodes are amplified by a high-input impedance amplifier and then pass to a hybrid circuit, which produces the sum and difference signals that can be used for analogue observation on a wide-band oscilloscope or digitised with a 12 bit, 48 MHz ADC VME module, to guarantee a single-turn position resolution of 0.1 mm. As the system must cope with a revolution frequency variation from 0.5 MHz to 2.9 MHz, a 30 MHz low pass filter in front of the ADC has

been included to reduce the thermal noise level. After digitisation, the data is stored in a memory and processed at software level. Data treatment allows simultaneous calculation of the beam position for all the pick-ups as well as electronics chain calibration, base-line correction and averaging over many revolutions.

To achieve a single-turn position resolution of 0.1 mm over the whole aperture (the electrical half-aperture is effectively becomes 100 mm due to the capacitive coupling between the electrodes), the signal-to-noise ratio has been calculated under various conditions. The worst situation corresponds to carbon ion beams at injection and the best situation to proton beams for passive spreading at extraction. Assuming a head amplifier RMS noise of 1 nV/√Hz and a 70 pF single-electrode to ground capacitance, the difference (Δ) signal-to-noise ratio is ≈ 3 for ions and ≈ 65 for protons with 30 MHz bandwidth. The lower value is at the limit and becomes unacceptable with intensity reductions at the source. In these cases, a lower resolution must be accepted or the signal must be integrated over many revolutions via the software.

Choice of systems

The narrow-band solution with the 'normalizer' has been chosen for its speed, cost-effectiveness and accuracy for the principal position monitoring system. A wide-band oscilloscope looking at an individual pickup should also be provided for ad hoc measurements. Several factors determine the overall accuracy: pick-up fabrication tolerances, alignment in the vacuum chamber, alignment of the vacuum chamber, determination of the electrical centre, electronics calibration errors, attenuation and reflections in cables and electromagnetic interference. It is estimated that the absolute RMS position error can be limited to the order of 0.4 mm. The mechanical design of the position monitors is given in Appendix O.

Scintillation screens

Scintillation screens have been placed at each end of the long drift space used for injection and extraction (see Figure 4.2). The screen LS MR 01-07 will detect the incoming beam at the exit to the injection electrostatic septum (septum wall -41 mm wrt. central orbit). The second screen LS MR 01-02 detects the beam after one turn in the machine and is centred on the off-axis bump of the multi-turn injection scheme (see Section 7.5). These two screens are intended for establishing the first turn in the machine and visually checking the beam profile and position at injection with the multi-turn injection bump applied. They cannot be left in the aperture, if a circulating beam is to be established. The injection screen LS MR 01-07 could be incorporated in the vacuum tank of the electrostatic injection septum as has been done in some CERN-PS designs. This solution would be economical in space requiring only a few centimeters. In the lattice layout, however, both screens are in independent spaces, but a detailed design has not been made and this point remains open.

A third scintillation screen has been placed in the off-axis path of the extracted beam near the entrance to the thin extraction septum. It will probably be incorporated in the same vacuum chamber as LS MR 01-02, but care must be taken that it does not intercept the circulating beam or separatrices. An alternative solution would be to mount this screen separately in the extraction line after the thin magnetic septum. For the present, this choice remains open.

4.10.2 Beam current monitoring system

DC current transformer

A commercially available dc current transformer can be used to monitor the average circulating current. With a bandwidth of a few kHz, this device is insensitive to any rf structure on the beam. It will be possible to either monitor the circulating current or to normalise the signal with respect to the relativistic β and have the readout in units of charge, which is more useful during the acceleration cycle. Since this instrument is not vacuum compatible, it must be isolated from the vacuum by a ceramic tube that also interrupts the electrical continuity of the vacuum chamber. The main inconvenience is the extreme sensitivity of this type of monitor to stray magnetic fields. The sensor itself is only 0.15 m long, but with its magnetic shielding it has a total length of almost 1 m. This unit DC MR 31-03 has been installed in drift space 31 (see Figure 4.4). The principal data are listed in Table 4.7.

Principal data for the dc current transformer	
Bandwidth	0 to 20 [kHz]
Current scales	0-10 [mA] and 0-100 [mA]
Current resolution	5 μA RMS in 1 s
Sensitivity to stray fields	80 μA/G
Temperature coefficient	5 μA/degree C

Table 4.7 Principal data for the dc current transformer

Fast current transformer

A commercially available fast current transformer can be used for monitoring the longitudinal profile of the bunched current during acceleration. Typically such a device has a rise time of ~ 1 ns (bandwidth of ~ 160 MHz). In the first instance, a dc current transformer would probably be sufficient, but should a fast transformer prove to be necessary, it can be added in straight section 6, or possibly the equipment in straight section 31 can be re-arranged to install the two current transformers together.

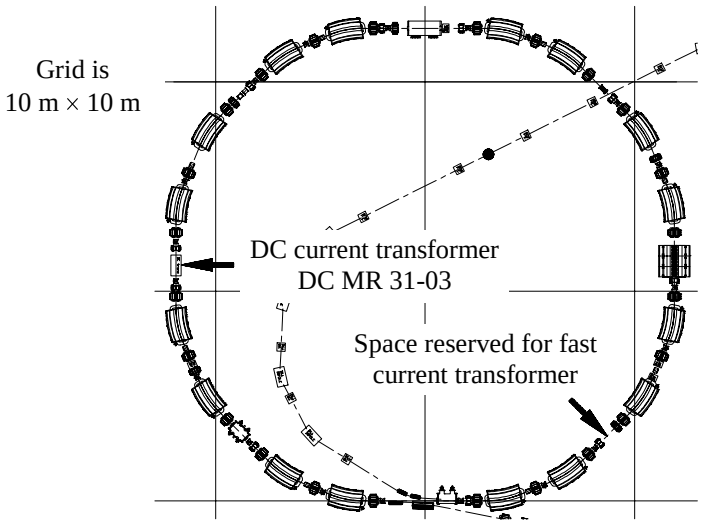

Figure 4.4 Positions of current transformers

4.10.3 Transverse and longitudinal profile monitors

Transverse profiles

The beam at the patient depends strongly on the ring emittances. The vertical emittance directly determines the spot size and the horizontal emittance determines the extracted momentum spread before the ridge filter. Thus, the measurement and quasi-continuous monitoring of the beam profile is an essential requirement. In many machines, this function is performed by flying-wire scanners with only minimal degradation of the beam. In the present case, however, flying-wire scanners have been discarded on the grounds that they are unsuitable for the low energy proton beam. At injection (20 MeV), a single scan using a carbon wire of 30 μm diameter with a scanning velocity of 10 m/s and $\beta = 4$ m at the monitor provokes an emittance blow-up of 200%. The solution that has been adopted is the residual-gas ionisation monitor. This non-destructive device is based on the detection of ions created by the interaction of the beam with the residual gas. The ions are collected with a high voltage and amplified with position sensitive micro-channel plates. The expected ion-production rates have been estimated for a residual gas pressure of 10^{-9} torr. Assuming a micro-channel plate length of 3 cm, with an integration time of 10 ms and an integrator capacitance of 10 pF, the minimum output voltage is 0.13 V, while the maximum is 0.64 V for nominal intensity beams. If one takes into account the intensity range factor, then longer integration times are needed to get sufficient signal strength at lower intensities. Assuming that the residual gas is mainly H_2 and that the collecting field is 5 kV over a distance of 5 cm, the maximum distortion in the beam 'image' is estimated to be 0.3 mm. This value is smaller than the distance between the strips of the multi-anode array (1 mm), which determines the monitor resolution. Additional sources of error are the channel to channel variation in the electronics and fluctuations in the beam position. The total measurement error, found by adding the individual contributions in quadrature, should not exceed 10% [8]. It is clear that the profile monitor cannot distinguish a single turn, but it provides a continuous measurement averaged over several turns.

The homogeneous electric field needed for the ion collection onto the micro-channel plate is of the order of 1 kV/cm. This gives a non-negligible deflection to the beam at the lower energies (see Table 4.8) and will have to be included in the closed-orbit correction.

Deflection given to beam by residual-gas profile monitor

Condition	Deflection [mrad]
Protons at injection 20 MeV	0.30
Carbon ions at injection 7 MeV/u	0.36
Protons at max. extraction 250 MeV	0.03
Carbon ions at max. extraction 400 MeV/u	0.01

Table 4.8 Deflection given to beam by residual-gas profile monitor

The calibration of these devices will need to be performed with either fixed beam scrapers used in combination with closed-orbit bumps and the dc current

transformer or movable scrapers and the dc current transformer. The positions of the monitors and scrapers are indicated in Figure. 4.5. All scrapers and monitors have zero-dispersion in the plane in which they are active. In the vertical plane, the monitor and scraper are well positioned with above average values of the vertical betatron amplitude function. In the horizontal plane, the constraint of requiring zero dispersion has led to a compromise where both monitor and scraper have average values of the betatron amplitude function.

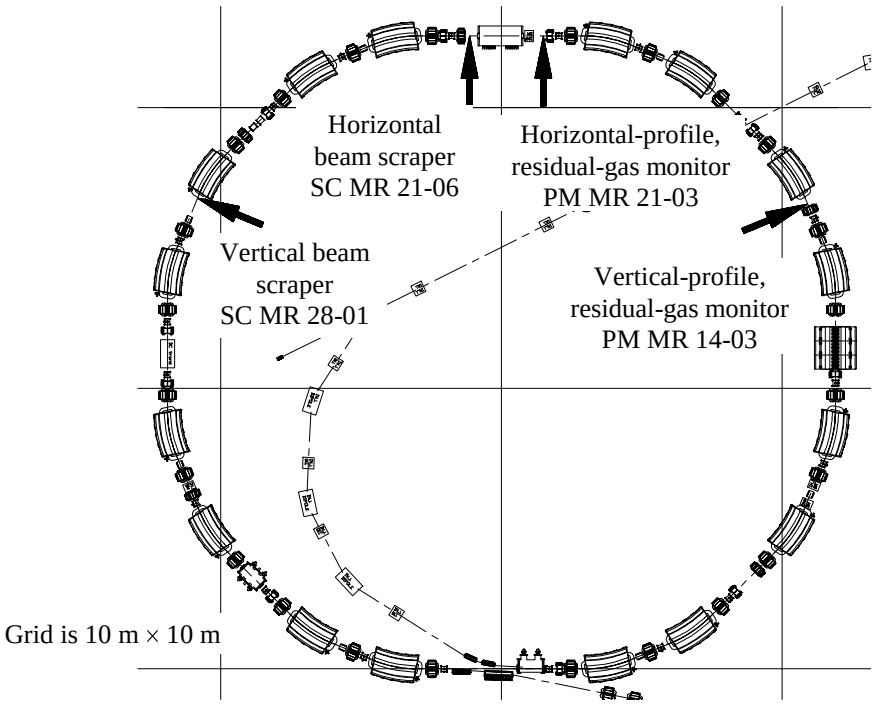

Figure 4.5 Positions of profile monitors and scrapers

The scrapers require to introduce enough material into the beam that the energy loss on traversal causes the particles to be lost after one or a few traversals. A tungsten foil or blade is commonly used because of its high stopping power and high melting point. Spaces of 10 cm have been allowed in the lattice. Fixed scrapers, could be mounted rigidly inside a 10 cm length of chamber as proposed in Appendix M. In this case, a substantial thickness of tungsten (say 0.5 cm) would be advisable as this would be mechanically reliable. Mobile scrapers could use the 'rocking' bellows principle, also described in Appendix M. For the mobile scraper, the tungsten blade must be a lightweight foil and under extreme circumstances might be damaged by melting. Whether the scattered beam from a thin foil can be collected after several traversals on the vertical beam dump ($\beta_z > \beta_x$ at the scraper) or whether the beam must be lost around the whole machine has not been studied. The mobile scraper is to be preferred as it is more flexible for machine operation.

Longitudinal profiles

In the present design, it is thought to be sufficient to equip one of the standard position monitors with broadband electronics (30 MHz).

4.10.4 Tune measurement

As the synchrotron is a pulsed machine, swept-frequency techniques are inappropriate and the ring is equipped with a fast kicker magnet in each plane for the excitation of coherent oscillations (see Figure 4.6). In order that the system is fast enough to follow rapid tune changes, a fast signal processor acquires and digitizes the coherent oscillation from a single pick-up, which is one of the standard units equipped with special electronics to record the beam position at each revolution over 1000 or more turns. Subsequent analysis of the data by fast Fourier transform provides the fractional tune and the tune spread from the decoherence time. The tune can be measured with kicks of the order of 0.03 mrad giving rise to an oscillation amplitude at the pick-ups of about 0.5 mm. The pick-up signals are recorded at revolution frequency with a fast, 12-bit digitizer in such a way to have a 0.1 mm resolution. The precision of the tune measurement is proportional to the measurement time, which is limited by chromaticity and momentum spread. In the PIMMS, under optimum machine conditions, an accuracy of some 10^{-4} in tune is expected. The kick method for tune measurement leads to emittance growth. With kicks of ~0.03 mrad, the emittance blow-up is of the order of 5% at injection and 10 % at extraction. The tune kickers are powerful enough to investigate tune dependence with amplitude up to the aperture limit.

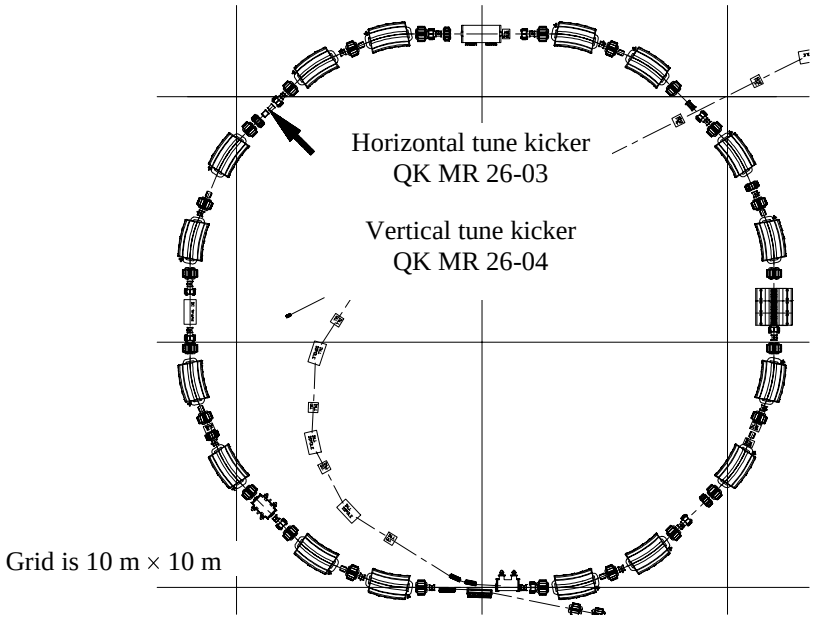

Figure 4.6 Positions of tune kickers

4.10.5 Schottky monitors

During the critical phase of extraction, the beam is unbunched, the electrostatic pick-ups are blind and it is not permissible to kick the beam for tune measurements. In this situation, Schottky monitors can provide vital diagnostic information on the transverse and longitudinal beam distributions and the tunes. Due to the very small signals expected, the measurements will be performed with a narrow bandwidth to improve the signal-to-noise ratio and, when necessary, with the help of resonant electrodes.

The most difficult case (poorest signal-to-noise ratio) corresponds to the lowest flat-top for extraction (60 MeV) of the actively-scanned proton beam. A directional coupler pickup of 0.5 m, 50 Ω single-electrode line impedance and a harmonic number of 27, have been chosen to give the maximum response at the passage of the beam and to avoid the overlap of the Schottky side-bands and of the transverse and longitudinal bands. The spectral power density in the longitudinal plane (considering the sum signal of the electrode pair) is $dP/df = 4\times10^{-19}$ W/Hz for a longitudinal Schottky band of 93.8 kHz. With low-noise preamplifiers, this corresponds to a signal-to-noise ratio of ~80. Thus, the longitudinal Schottky band will be clearly visible on the spectrum analyser, provided the flat-top is long enough for time averaging of the statistical signals. For the transverse planes, where the Schottky signals are obtained from the difference outputs of the electrode pair of the horizontal and vertical pick-up respectively, the situation is more delicate. In the horizontal plane, the power density is 19% of the amplifier noise level. After spectral power addition with the noise level, the signal will emerge from the noise by only 9%. In the vertical plane, due to the smaller vacuum chamber, the power density is 60% of the amplifier noise level and after quadratic addition with the noise level the signal will rise above the noise by 22%. To improve the signal-to-noise ratio, resonant pick-ups seem imperative for transverse scans. A sufficient signal enhancement for the transverse profiles should be obtainable with values of Q, the merit factor of the resonant circuit, around 10, resulting in an increase of the spectral signal power by the same factor. The electric circuit proposed consists of electrodes short-circuited at one extremity and at the other extremity connected to a piece of low-loss cable (see Figure. 4.7). The cable is also short-circuited so that the ensemble constitutes a half-wave resonator (the electrode being approximately a quarter wavelength long). This circuit has then a Q-value much higher than the nominal one of 10, but can be loaded down to the desired level by connecting the amplifier input to the inner conductor of the low-loss cable at an appropriate distance from the short-circuited end. The hybrid combiner should be situated after the pre-amplifiers. This method has been extensively used in the CERN antiproton complex. Various cables with different lengths and pre-amplifiers can be switched by means of relays onto the electrode in order to obtain resonance at the various desired frequencies.

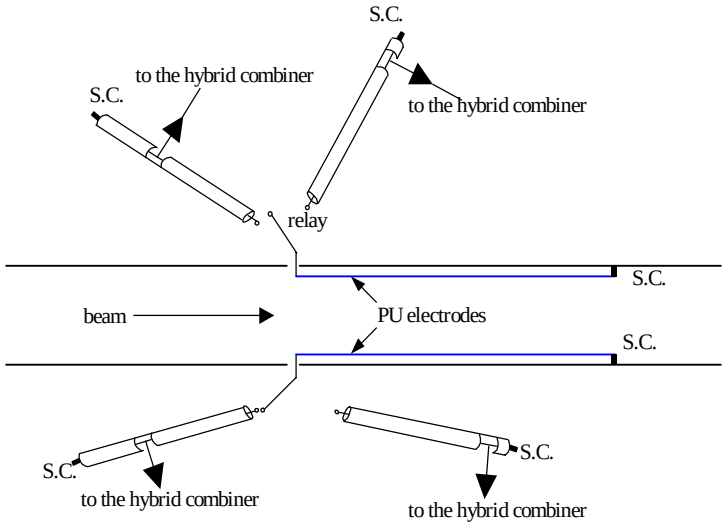

s.c.=short-circuit

Figure 4.7 Resonant Schottky pickup

A better estimate of the Schottky power density is obtained by averaging several spectra taken successively. The degree of confidence in the measurement increases with the number of averaged spectra, at the expense of the total analysis time. With a typical fast fourier transform bandwidth of 100 kHz, a sampling rate of 200 kHz, and 800 data points, the acquisition time for a single spectrum is 4 ms. For example, in 1 s for the horizontal tune, 120 averages on each sideband can be performed. From ref. [9], the true spectrum differs from the measured one by less than 10 % with a 90% confidence level.

The locations of the horizontal and vertical Schottky monitors in the ring are shown in Figure 4.8. The longitudinal Schottky signal can be obtained as the sum of the signals from either the horizontal or the vertical pick-up electrodes. For smaller spectral power densities in the transverse planes, an alternate solution is the use of the beam transfer function method (BTF). This is an important diagnostic tool for coasting particle beams, complementary to Schottky diagnostics and superior to it in situations where the Schottky noise is weak. This is not included in the present design, but could be of interest later.

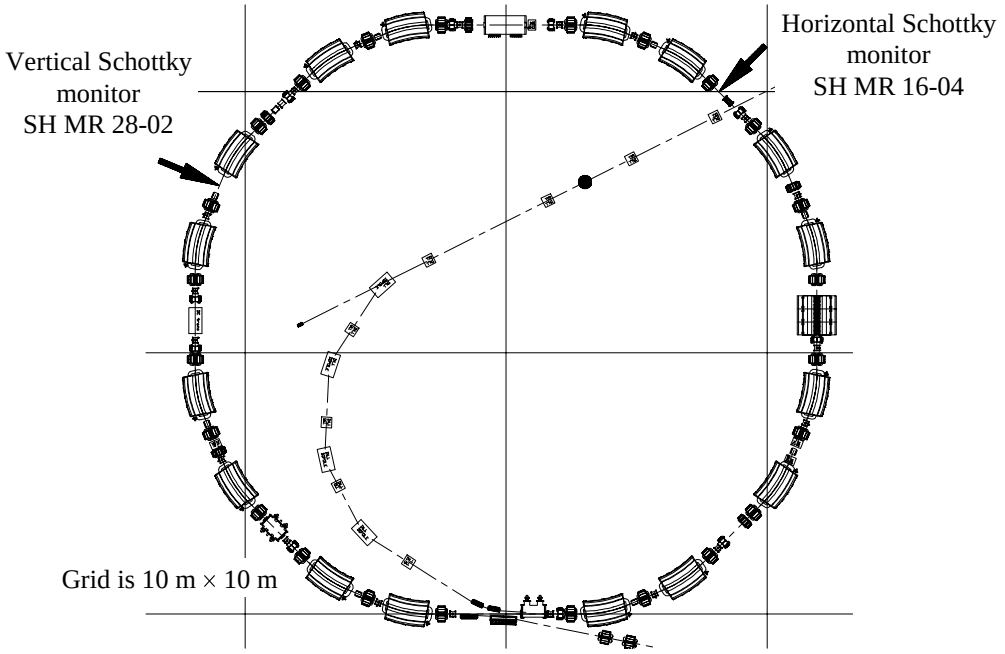

Figure 4.8 Locations of transverse Schottky monitors

4.10.6 Beam loss monitors

In absolute terms, the radiation levels will be low and of little danger to equipment, but owing to the proximity of large numbers of people working in and visiting the centre, it will be necessary to have a well developed system for loss detection and radiation protection. Losses are also one of the first indications that the machine is operating incorrectly. The primary signature of lost protons in the PIMMS energy range is the neutron yield and this rises roughly quadratically with the energy. Thus, loss monitors must be neutron sensitive and must have a very large dynamic range. Two possible solutions have been considered: scintillators coupled to photo-tubes or ionisation chambers. The first possibility is very sensitive (100 μA per rad

for 0.5 litre scintillator oil) and has the ability to observe beam losses with rise times in the 10 ns range but, due to unstable gain, require to be calibrated often. The second possibility is a factor 100 to 1000 less sensitive for the same useful volume (0.1 to 1 μA per rad), but the gains of the individual monitors are very stable albeit rather slow (~ 1 μs rise time) and cannot therefore resolve fractional turn losses.

It is planned to distribute ten monitors along the ring circumference and to group them more densely at the extraction kicker and septa, where beam losses are more critical. It is also foreseen to provide a mobile device with long cables that can be positioned according to specific needs. Since the monitor type does not impose any constraint on the accelerator design, the final choice between the two possible solutions is left open until detailed simulations of the beam losses have been made.

4.10.7 Main ring diagnostics summary

- 18 electrostatic pick-ups (10 horizontal, 8 vertical),
- 3 scintillation screens, (1 in the extraction line)
- 1 dc current transformer,
- space reserved for 1 fast current transformer,
- 2 residual gas monitor (1 horizontal, 1 vertical),
- 2 scrapers for calibration purposes,
- 2 fast kickers for the tune measurement (1 horizontal, 1 vertical),
- 2 directional couplers for Schottky noise measurements.

4.11 VACUUM SYSTEM

The main dipole vacuum chamber has been studied in some detail. Two constructions meet the mechanical and magnetic (eddy current) requirements. A thin-walled, stainless steel chamber with transverse supporting ribs [10] and a corrugated, thin-walled, stainless steel chamber based on the CERN Booster dipole chamber [11]. Figure 4.9 shows the two designs and gives the main dimensions. In either case, the chamber would need a thicker section in the weak field region under the dipole coils at one end so that a pumping port could be added.

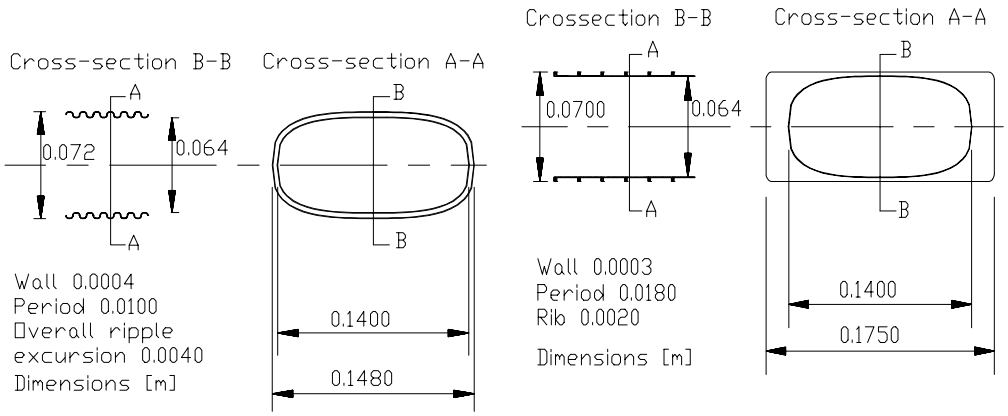

(a) Corrugated chamber (b) Ribbed chamber

Figure 4.9 Thin-walled vacuum chamber designs for the main dipole

The rest of the vacuum system is conventional in its design, but the dimensions of the chambers in the injection/extraction straight section (SS MR 01) are somewhat complicated. Figure 4.11 shows a preliminary design for this region. The central chamber has to accommodate both the injection and extraction lines. The outer wall of this central chamber (i.e. outer wrt the centre of the ring and lower wall in the figure) is only 29.75 mm from the centre line of the synchrotron. This is possible because the 'waiting' stack is in a zero dispersion region (see Figure 3.28 and 3.29) and the separatrices are either of small amplitude or in the inner half of the chamber (see Figure 3.27).

The standard vacuum chamber dimensions are given in Section 3.5.6 and wall thicknesses can be found in Section 3.13 where the effect of eddy currents are estimated for the different elements. When ceramic chambers are needed, this is mentioned either in Section 3.13 or in the Appendix devoted to the mechanical design of the element in question. Overall views of the vertical and horizontal apertures can be seen in the Figure 4.10.

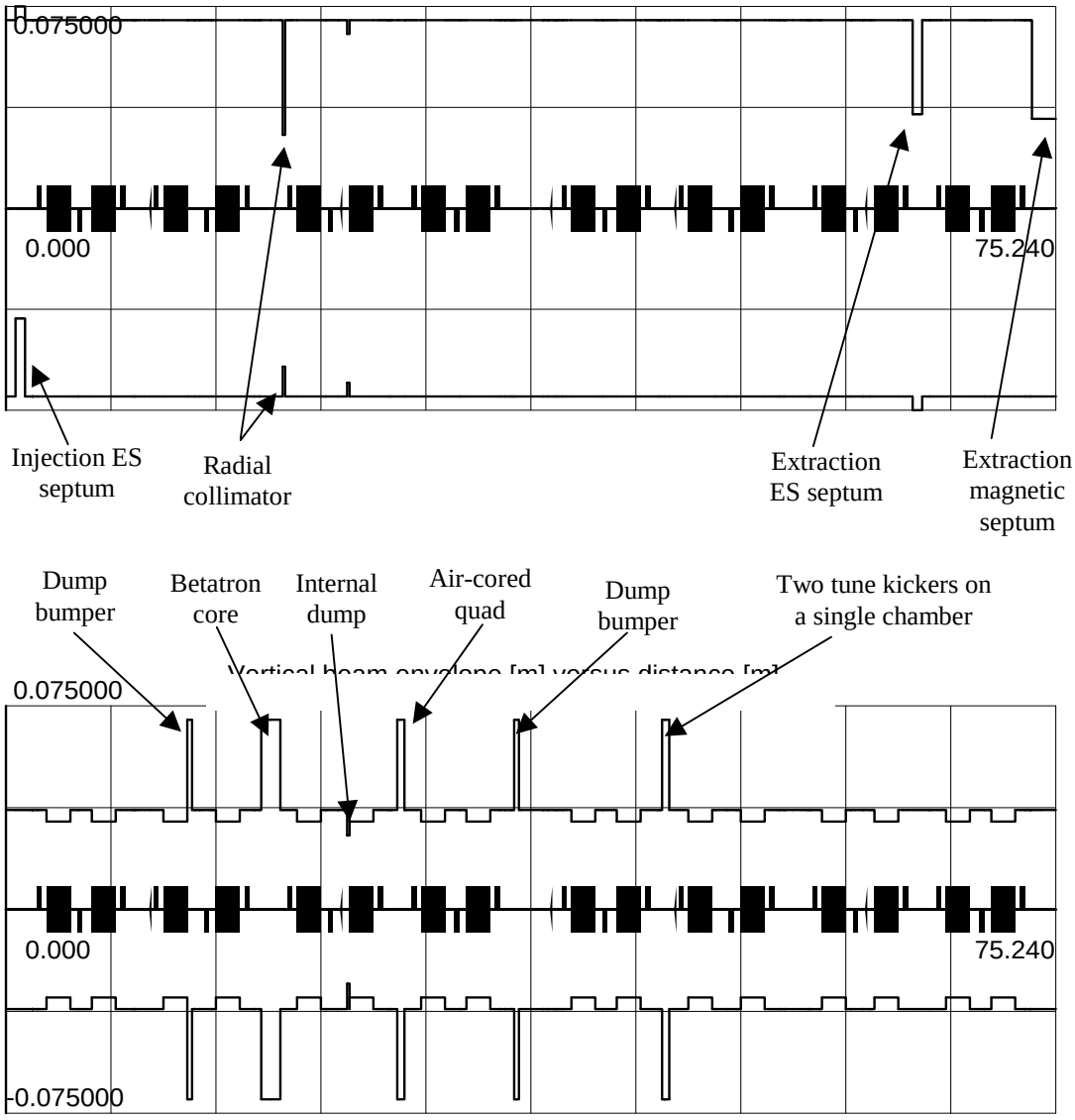

Figure 4.10 The physical apertures in the horizontal and vertical planes

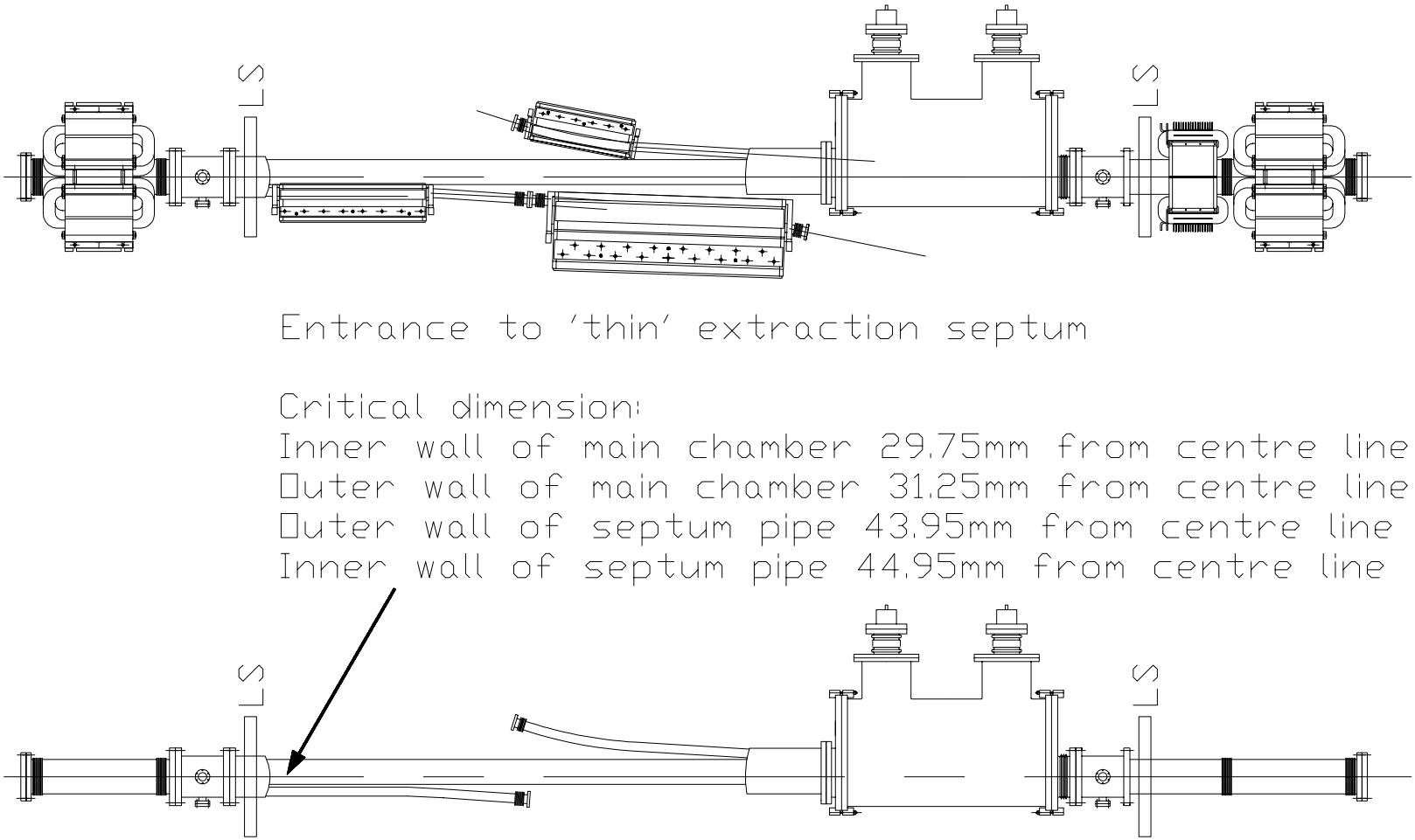

Figure 4.11 Preliminary vacuum chamber design in the injection/extraction region (SS MR 01)

4.12 STANDS AND ALIGNMENT

The beam height above floor level is 1.2 m. The supports for the units are chosen according to the situation. The stands have not been designed in detail. The guide lines are:

- Transversally, the largest element in the ring is the betatron core and it is convenient to stand this unit on three independent adjustable supports.
- The main dipoles stand on three-adjustable point supports with a low-profile frame linking the three stands.
- The main quadrupoles, electrostatic septa and resonance sextupole have single-column stands with sliding plates and screw adjustments for alignment.
- Whenever possible, the smaller elements have been grouped and are first mounted and aligned on a rigid frame before entering the ring. The frame carrying the elements is then placed on an adjustable 'table' support in the ring and the whole module is aligned.
- Certain elements such as position monitors, collimators and scrapers will be aligned by means of their vacuum chamber.
- The vacuum chamber is not free to move in the main dipole.
- The vacuum chamber is movable in the straight sections by virtue of bellows.
- In the straight sections there is a clearance between the vacuum chamber and units such as quadrupoles, sextupoles, correction dipoles, betatron core, rf cavity etc. and the chamber can be aligned independently.

4.13 POWER CONVERTER RIPPLE

The ripple specifications for the main ring power converters are determined in two stages:

- Determining the permissible ripple in the spill rate.
- Converting this to the permissible ripple in the power converter currents taking into the account the tools available for smoothing and desensitising the machine.

4.13.1 Permissible ripple in the spill

The permissible ripple in the spill is set by the tolerance of the scanning and on-line diagnostic systems to irregularities. This has been discussed for pure voxel scanning with up to 9 frequencies superimposed and a preliminary specification is summarised at the end of Section 5.12.2 in Part I. It has been done for mini-voxel scanning with single-frequency errors and the result is summarised in Figure 11.12 in Part I. Finally, the exercise has also been done for true raster scanning with single-frequency errors and the result is summarised in Figure 11.22 in Part I.

For the present exercise, the specification defined in Figure 4.12 for the spill quality will be used. This specification is based on a general appreciation of the above studies and reflects the needs of voxel and mini-voxel scanning more than the true raster scanning presented in Section 11.2 of Part I. True raster scanning requires further development to filter the velocity compensation so that it acts only on the lower frequencies. If this could be done, then its error specification would probably look very similar to Figure 4.12.

The choice of Figure 4.12 is meant more as an example rather than a definitive judgement. The premise is that if each error frequency in the spill obeys the specification in Figure 4.12, then the combined effect of say 5 errors at different frequencies will be tolerable.

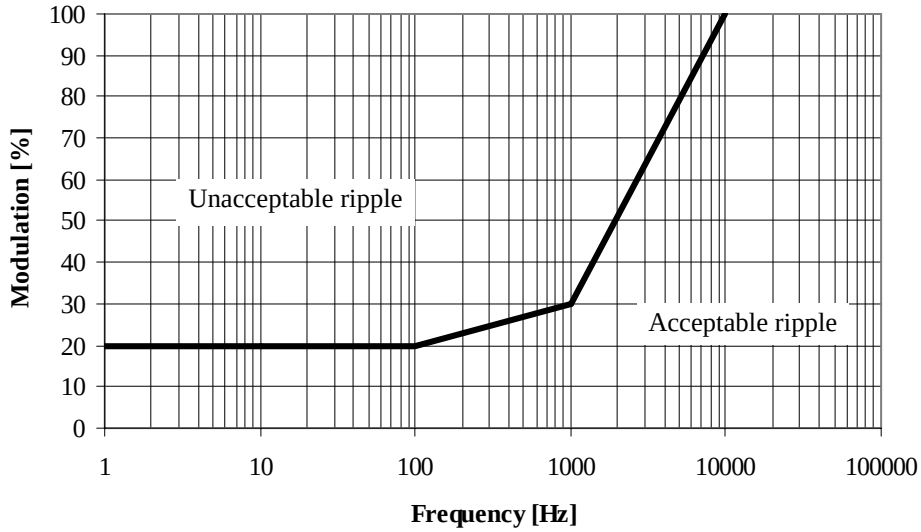

Figure 4.12 Specification for tolerable ripple in spill (up to 5 frequencies can be combined)

4.13.2 Conversion to permissible tune ripple in the instantaneous transfer model

The instantaneous transfer model is described in Section 5.5 in Part I [13]. This model effectively describes the worst possible situation in the spill for a given tune ripple at the input to the resonance. The relation between ripple in the spill and ripple in the tune is given by,

$$\frac{\Delta(\mathrm{d}N/\mathrm{d}t)}{(\mathrm{d}N/\mathrm{d}t)_0} = \frac{\omega\Delta Q}{(\mathrm{d}Q/\mathrm{d}t)_0} \tag{4.9}$$

where $\Delta(\mathrm{d}N/\mathrm{d}t)$ is the amplitude of the ripple in the spill, $(\mathrm{d}N/\mathrm{d}t)_0$ is the nominal spill rate, ω is the angular tune ripple frequency, ΔQ is the amplitude of the tune ripple and $(\mathrm{d}Q/\mathrm{d}t)_0$ is the nominal tune velocity of the particles entering into the resonance. For a spill time of one second and the nominal tune spread in the beam of 0.0144, the nominal tune velocity is $0.0144\ \mathrm{s}^{-1}$. For the numerical calculations that follow it is convenient to re-express (4.9) as,

$$\frac{\Delta(\mathrm{d}N/\mathrm{d}t)}{(\mathrm{d}N/\mathrm{d}t)_0} \approx 116\omega\frac{\Delta Q_x}{Q_x} \tag{4.10}$$

where $Q = 1.666$, the tune of the extraction. The more advanced features of the non-instantaneous transfer model will be included later in the form of ripple attenuation functions.

4.13.3 Conversion of power converter ripple to tune ripple

The power converters in the synchrotron that need to be included are:

- Quadrupole chains (3),
- Main dipole chain (1),
- Sextupole chains (3),
- Betatron core (1),
- Horizontal dipole correctors (10).

It should be noted that all power converters, apart from the betatron core, are rigorous constant during extraction. The main dipole and quadrupole chains are potentially the strongest sources of ripple. The horizontal corrector dipoles account for only 2.4×10^{-3} of the total bending power in the ring and their specification can be relaxed considerably. However, owing to their large number there is a greater chance that a faulty supply will inject abnormally high ripple and not be detected by the control system. The problem of ripple for the betatron core is more to do with the height and frequency of the DAC steps as the magnet is ramped than ripple arising from the converter itself (see Section 4.5.2).

Approximate relationships are needed linking the current ripple from the converters to the tune ripple in the horizontal (extraction) plane. These relations are first calculated for the maximum energy and later scaled for operation at lower energies.

- ***Quadrupole chains***

Incremental changes in the quadrupoles give: $\Delta I_{F1}/I_{set} = 0.5\ \Delta Q_x/Q_x$, $\Delta I_{F2}/I_{set} = 0.7\ \Delta Q_x/Q_x$ and $\Delta I_D/I_{set} = 0.4\ \Delta Q_x/Q_x$. If all the chains are incremented by the same fractional amount then $\Delta I/I_{set} = 0.9\ \Delta Q_x/Q_x$, It is unnecessary to be so precise for ripple specification, so it will be assumed that each one of the quadrupole chains affects the horizontal tune at top energy according to:

$$\Delta I/I_{max} \approx 0.5\ \Delta Q_x/Q_x \qquad (4.11)$$

and all chains together according to:

$$\Delta I/I_{max} \approx \Delta Q_x/Q_x, \qquad (4.12)$$

- ***Main dipole chain***

If the whole machine is set to a momentum that is slightly different to that of the beam then the tune difference is calculable via the horizontal chromaticity (= -3.6[*]) according to $\Delta Q_x/Q_x = (Q_x'/Q_x)(\Delta p/p)$ where $\Delta p/p \equiv \Delta B/B \equiv \Delta I/I$. If only the dipoles are set differently, then the effect of the quadrupoles (calculated above) should be subtracted, so that:

$$\Delta I/I_{max} = \{(Q_x/Q'_x)-1\}\ \Delta Q_x/Q_x \approx -1.5\ \Delta Q_x/Q_x. \qquad (4.13)$$

- ***Sextupole chains***

Sextupoles have no effect on the central orbit tunes, so that relative positions in tune of the zero amplitude particles and the resonance are unaffected by sextupole ripple. Large amplitude particles, however, are affected and, for the purpose of the calculation, the whole beam will be assumed to have the nominal maximum offset in momentum i.e. $\Delta p/p = -0.0011$.

The sextupoles fall into three categories. Of the two chromaticity chains, only the D-type sextupoles affect the horizontal plane significantly and for this chain $\Delta Q'_x/Q'_x = 0.8\ \Delta I/I$. Hence for $\Delta p/p = -0.0011$ and $Q'_x = -3.6$

$$\text{D-type sextupole chain,} \qquad \Delta I/I_{max} \approx 500\ \Delta Q_x/Q_x. \qquad (4.14)$$

The third type of sextupole drives the resonance. Ripple in this sextupole will change the resonance bandwidth[**]. From equation (3.1) in Part I [13], the sextupole strength is directly proportional to the bandwidth, which is $\sim 4 \times 10^{-3}$, so that,

$$\text{Resonance sextupole,} \qquad \Delta I/I_{max} \approx 420\ \Delta Q_x/Q_x. \qquad (4.15)$$

[*] This value has been found by tracking.

[**] The chromaticity sextupoles have been arranged to have a weak effect on the resonance.

Betatron core

At top energy, the betatron core changes from -100% to +100% to change the beam momentum by $\Delta p/p = 0.005$. This represent a tune shift of $\Delta Q_x = -0.018$. Thus,

$$\Delta I/I_{max} \approx 100\ \Delta Q_x/Q_x. \qquad (4.16)$$

- ***Horizontal dipole correctors***

An individual horizontal corrector can excite 2.4×10^{-4} of the total bending power of the full ring. Its maximum effect on the tune compared to that of the main dipole chain will therefore be correspondingly reduced to:

$$\Delta I/I_{max} \approx -6250\ \Delta Q_x/Q_x, \qquad (4.17)$$

but 10 units must be added quadratically for the full effect.

4.13.4 Mechanisms that smooth the ripple, or its effect

The effect of the tune ripple, or tune changes induced by the current ripple can be smoothed by a number of active and passive techniques.

- ***Partial smoothing***

This effect is due to overlap of the plateaux (see Section 5.6 Part I [13]). It depends on the storage time in the resonance and, for the PIMMS machine, it is not effective below 1 kHz. Above 1 kHz, the plateaux overlap and this reduces ripple in the spill by factor of $\sqrt{2}$.

- ***Intrinsic smoothing***

This effect is due to the overlap of peaks (see Ref. [14] and Section 4.5 Part I [13]). The width of the peak depends on the initial beam distribution. For the PIMMS parameters, the series of extended peaks just touch at 4 kHz and the ripple is compensated. At 8 kHz, the extended peaks should just overlap once and the frequencies of 4 and 8 kHz should be compensated. At 12 kHz, the extended peaks should just doubly overlap and the frequencies of 4, 8 and 12 kHz should be compensated and so on. Between multiples of 4 kHz, the modulation should rise to some fraction of the uncompensated effect. The theory for the peaks and plateaux is very detailed and the simulations of a few specific cases have been made, but a simple function describing the gain over the useful frequency range has not yet been derived. Since the mechanism is complex (the particular shape of the peaks, the beam distribution, etc.), this may require considerable work. For this reason, the simple attenuation curve described below will be assumed. The curve is thought to be pessimistic on average, but the true gain from intrinsic smoothing at all frequencies has yet to be established.

Intrinsic smoothing model:

14 kHz (quadruple partial overlap)	Attenuation by a factor 6
12 kHz (triple partial overlap)	Attenuation by a factor 5
10 kHz (double partial overlap)	Attenuation by a factor 4
6 kHz (single partial overlap)	Attenuation factor 3
2 kHz (no overlapping)	No effect

- ***RF empty bucket channelling***

This effect is actively induced by the rf cavity and increases the tune velocity of the particles as they enter the resonance. Table 4.9 has been adapted from Ref. 15 for the multiplying factor for the increase of tune velocity. Note that the efficiency decreases with increasing ripple frequency.

***K*-factors for the velocity multiplication obtained by an empty channelling bucket**								
Particle	**Energy [MeV/u]**	**Spill [s]**	**$\Delta p/p$**	**Multiplying factors for increasing ripple frequency**				
				K_0	**$K_{10\ Hz}$**	**$K_{100\ Hz}$**	**$K_{1\ kH}$z**	**$K_{10\ kHz}$**
Proton	300	1	0.005	55.7	50.8	32.2	12.1	3.9
$_{12}C^{6+}$	425	1	0.005	35.5	32.4	20.5	7.7	2.5

Table 4.9 *K*-factors for the velocity multiplication obtained by an empty channelling bucket

- ***Eddy current damping***

Eddy current damping reduces the field seen by the beam (see Section 5.11 in Part I [13]). Table 4.10 summarises the attenuation obtained.

Eddy current smoothing				
Ripple frequency [Hz] =	**100**	**1000**	**5000**	**10000**
Dipole: Time const.= 95 μs				
Attenuation factor	1.0	1.2	3.2	6.1
Quadrupole: Time const.= 62 μs				
Attenuation factor	1.0	1.1	2.2	4.0
Sextupole: Time const.= 62 μs				
Attenuation factor	1.0	1.1	2.2	4.0
Betatron core: Time const. = 2500 μs				
Attenuation factor	1.9	15.7	78.5	157
Correctors: Time const. = 10 μs				
Attenuation factor	1.0	1.0	1.1	1.2

Table 4.10 Eddy current smoothing

4.13.5 Relation between the ripple in the spill and the power converters

The ripple in the spill can be related to the ripple in the power converters at any one frequency, ω, by combining quadratically all the tune ripple sources divided by their appropriate attenuation factors and applying the net tune ripple to equation (4.10). The various tune ripple sources are listed in equations (4.11) to (4.17) and the attenuation factors for each source are tabulated in Section 4.13.4. This can be written in the form,

$$\frac{\Delta(\mathrm{d}N/\mathrm{d}t)}{(\mathrm{d}N/\mathrm{d}t)_0} \approx 116\omega \sqrt{\left(\sum_{\mathrm{js}} \left[\left(\prod_{\mathrm{i}} \frac{1}{A_{\mathrm{i}}} \right) S_{\mathrm{j}} \left(\frac{\Delta I}{I} \right)_{\mathrm{j}} \right]^2 \right)} \qquad (4.18)$$

where A_i are the attenuation factors given by the smoothing mechanisms and S_j are the scaling factors that relate $\Delta I/I$ to $\Delta Q_x/Q_x$ for each converter. Note that eddy current attenuation is the only mechanism that is different for each converter. Equation (4.18) does not uniquely determine the $\Delta I/I$ for each converter and there is some freedom to distribute the allowable ripple between the different converters.

An approximate idea of the sensitivity of the PIMMS machine can be found by assuming that there is no smoothing ($A_i = 1$) and that the scaling factors are unity ($\Delta Q_x/Q_x = \Delta I/I$), which is approximately true for the quadrupoles and main dipole. For the main contributors (3 quadrupole chains and the main dipole chain), equation (4.18) simplifies to,

$$\frac{\Delta(\mathrm{d}N/\mathrm{d}t)}{(\mathrm{d}N/\mathrm{d}t)_0} \approx 116\omega\sqrt{4}\,\frac{\Delta I}{I}. \qquad (4.19)$$

This yields, for 20% ripple in the spill, a specification for each power converter of $\Delta I/I$ of 1.4×10^{-5} at 10 Hz, 1.4×10^{-6} at 100 Hz, 1.4×10^{-7} at 1 kHz, 1.4×10^{-8} at 10 kHz. Taking into account the spread of 2 in magnetic rigidity of the extracted carbon ions, this simplified specification must be improved to $\Delta I/I$ of 7×10^{-6} at 10Hz, 7×10^{-7} at 100Hz, 7×10^{-8} at 1 kHz, 7×10^{-9} at 10 kHz. This illustrates why specifications of 10^{-8} and even 10^{-10} are sometimes quoted and the importance of introducing smoothing mechanisms.

4.13.6 Determination of the power converter specifications

It is assumed in Section 4.13.1 that power converter ripple will consist of up to five sinusoidal oscillations at different frequencies. Typically these would be multiples of 50 Hz and 300 Hz from the power converters themselves and frequencies in the range 1-10 kHz from the DACs. Equation (4.18) has been used to construct a solution for the PIMMS power converter specifications for carbon ions at the top extraction energy of 400 MeV/u. This specification has then been scaled by a factor of 1.95 to satisfy the carbon ions at the lowest extraction energy of 120 MeV/u and the results are recorded in Figure 4.13. The betatron core has the only power converter that changes during the extraction and in this case, the ripple specification is more relevant to the DAC steps. The recommended 16-bit DAC (see Section 4.5.2) produces steps of 1.5×10^{-5} of I_{max}, which is consistent with Figure 4.13. The results in Figure 4.13 will be taken as the PIMMS specification.

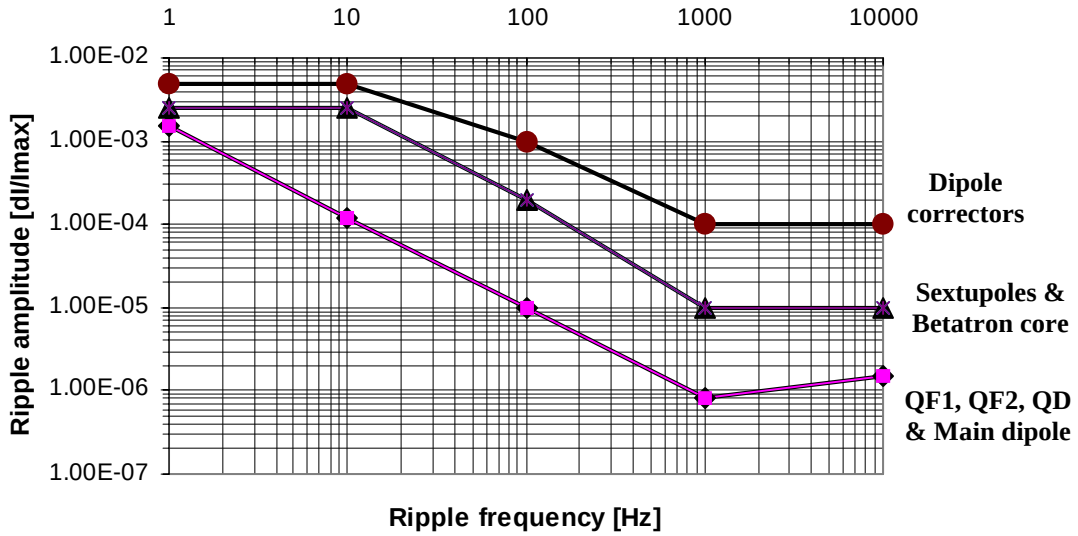

Figure 4.13 Specifications for power converter ripple at the lowest extraction energy for carbon ions (120 MeV/u)

When evaluating equation (4.18), it is clear that the quadrupole and main dipole chains are the most important. It is also clear that there is a problem around 1 kHz, where the smoothing mechanisms are weak and the specification is still strict. However, the extremely tight specifications of 10^{-8} to 10^{-10} that are some times quoted for current ripple have been avoided, although the specifications are still far from being lax.

4.13.7 Operation with protons

Operation with protons poses a more serious problem, since they work with beam rigidities up to 2.85 times lower than the lowest carbon-ion beam. This implies a further tightening of the ripple specifications by a factor of ~3. This is especially difficult for the quadrupoles and main dipole around 1 kHz. There are a number of possible ways of tackling this problem:

- Sufficient investment could possibly develop power converters with a much improved and reliable performance.
- PIMMS will be equipped with an air-cored quadrupole for a feedback system. This is regarded somewhat as a safety factor. The quadrupole has been designed (see Appendix J) and a place in the lattice has been reserved (QA MR 16-03), but the feedback has not been studied. Feedback systems work best at low frequencies and are limited in the kHz range by the variable storage time in the resonance, but it is hoped that the factor of 3 will still be available a 1 kHz.
- The air-cored quadrupole can also be used in a feed-forward mode for repeatable ripple patterns. This has been used in the CERN with mixed degrees of success.
- The spill rate can be reduced for proton treatments so that a higher ripple amplitude can be accepted by the scanning and dosimetry systems. Since, in most cases, only a fraction of the stored beam is used, this could result in an acceptable compromise for operation.
- Drop operation of protons in the actively scanned mode and keep only the passively spread proton operation which is less critical concerning spill quality.

4.14 FIELD DISPLAY

The *field display* provides a direct and independent check on how the magnetic fields in the machine are behaving. This is important for the security of the patient. The field display uses signals from measuring coils in additional magnet units put in series with the ring (main dipole chain, the three quadrupole chains and the resonance sextupole). The additional units can be placed close to the power converters and it can be arranged such that the units would be accessible during operation. This arrangement provides an independent measurement of what the beam 'sees' during the magnet cycle and can be an extremely useful diagnostic tool.

References

[1] C. Ellert, D. Habs, E. Jaeschke, T. Kambara, M. Music, D. Schwalm, P. Sigray, A. Wolf, An *induction accelerator for the Heidelberg Test Storage Ring TSR*, Nucl. Instr. and Meth. A314, (1992), 399-408.

[2] U. Amaldi ed., *Il Centro Nazionale di Adroterapia Oncologica a Mirasole – The Red Book*, INFN-LNF, Frascati (1997).

[3] U. Amaldi and Sandro Rossi eds, *Il Centro Nazionale di Adroterapia Oncologica a Mirasole – Sincrotrone e linee di trasporto, Addendum to The Red Book*, INFN-LNF, Frascati (1998).

[4] L. Badano, *Beam diagnostics and monitors for the PIMMS synchrotron*, CERN/PS 99-037 (DI).

[5] M. Le Gras, *Performance du Module Normalisateur pour le Mesure de la position du Faisceau au AA*, CERN/PS/BR/Note 81-4, CERN (1981).
[6] G. Gelato et al., *The Closed-Orbit Observation System of the CERN Antiproton Accumulator*, CERN/PS/AA/BR/81-19, CERN (1981).
[7] L. Bernard et al., *Wide Dynamic Range (7 Decades) Beam Position and Profile Measurement for the CERN LEAR*, IEEE Trans. Nucl. Sci., NS-30 (1983).
[8] W.S. Graves, *Error Analysis and Correction in a Beam Profile Monitor*, Nucl. Instr. and Meth, A364 (1995).
[9] D. Boussard, *Schottky noise and beam transfer function diagnostics*, CERN/SPS 86-11 ARF, CERN (1988).
[10] G. Brianti, V.Chimenti, A. Clozza, G. Delle Monache, S. Rossi, C. Sanelli, F. Sgamma, *Design of the dipole vacuum chamber for the CNAO Synchrotron (Based on the PIMM Study)*, PS/DI/Note 99-23(Tech), 17 Nov. 1999.
[11] G. Brianti, K. Schindl, *Computation of stress and deflections of elliptical vacuum chambers with corrugated thin-wall profile of variable amplitude*. SI/Int. DL/69-5 (1969).
[12] PIMMS Group, *Parameter List*, to be published.
[13] PIMMS Group, *Proton-Ion Medical Machine Study (PIMMS), Part I*, CERN-PS/99-010 (DI).
[14] M. Pullia, *Dynamique de l'éjection lente et son influence sur les lignes de transfert*, Ph.D. thesis, Université Claude Bernard - Lyon 1, 25 October 1999.
[15] Private communication, M. Crescenti, *Empty bucket stabilisation of the spill*, Minutes of the 2nd Meeting on Slow Extraction from Synchrotrons for Cancer Therapy, CERN 2nd-3rd September 1996, p187-204.

* * *

II-5 EXTRACTION

The extraction transfer lines are based on a modular design that takes into account the strong asymmetry between the beam's two transverse emittances and the near-rectangular distribution of the beam in the horizontal phase space. The general design philosophy and explanations of the modules can be found in Part I in Chapter 9. In the engineering design, the start of the extraction line is defined as the entry to the electrostatic septum in the ring. The lattice of the extraction line falls naturally into three sections:

- The off-axis passage in the ring from the electrostatic septum to the magnetic septum.
- The matching of the beam from the ring to the modular transfer line.
- The modular layout of the beam distribution to the different treatment rooms.

The first two points are specific to the PIMMS design, but the third point is universal. It appears feasible to have one design of dipole and one design of quadrupole.

5.1 BOUNDARY CONDITIONS FOR EXTRACTION

5.1.1 Twiss functions and geometry

At the entry to the extraction line, the beam has the vertical phase-space characteristics of the ring and therefore has the vertical emittance and Twiss functions of the ring. At each fixed beam-line exit or gantry exit, the beam is defined by the medical specifications and there is a definite range of vertical Twiss functions (β_z = 2.02 m to 27 m, $\alpha_z = 0$) that has already been discussed in Section 1.3. At the 'hand-over' planes between modules in the line, there is some freedom. Upstream of the 'stepper' module, the values of $\beta_z = 3$ m, $\alpha_z = 0$ have been chosen, but, downstream of the 'stepper' module, it is logical to adopt the current vertical Twiss functions as at the exit to the gantry, or, when telescopic modules are used, a simple multiple of these values.

In the horizontal plane, the beam is a segment of the extraction separatrix that is represented as a 'diameter' of an unfilled ellipse. The value of this emittance and the corresponding Twiss functions are, to a certain degree, *free parameters*. The underlying requirement is that the maximum horizontal spot size at the patient (10 mm) occurs when the 'bar' of charge is horizontal in the 'unfilled' ellipse and that it is minimum (<4 mm) when it is upright ($\alpha_x = 0$ at the patient). Since the 'bar' is uniformly filled, the product ($E_x[\pi$ mm mrad] $\times \beta_x$[m]/π) needs to be 25 at the patient, which makes the full width of the spot 10 mm. In the PIMMS design, the length of the 'bar' at the electrostatic septum is also 10 mm, so the extraction β_x must therefore be set to same value as at the patient to be consistent with the emittance of the 'unfilled' ellipse. At the 'hand-over' planes between modules in the line, there is again some freedom and the values of $\beta_x = 3$ m, $\alpha_x = 0$ have been chosen. As in the vertical plane, these values may be changed by a simple multiple if telescopic modules are in use. The next step is to fix the emittance of the 'unfilled' ellipse. The 'bar' of charge should appear clearly as a 'diameter' line and be dominated by the height of the ellipse. This situation should be insensitive to say a doubling or trebling of the divergence (width) of the 'bar'. Changes of this order can easily occur because the

'bar' is very narrow and sensitive to changeable parameters such as the closed orbit. This reasoning led to an emittance of the 'unfilled' ellipse of 5π mm mrad (increased from 1.65π mm mrad in Part I), so that when the 'bar' is upright in the ellipse its width falls well below 4 mm.

The dispersion vector at the entry to the extraction line is determined by the disposition of the 'bars' of charge for different momenta. Table 5.1 summarises the data for the lowest extraction energy and shows how the dispersion and its derivative are calculated. The values for higher extraction energies differ slightly, but these differences are not significant and will be ignored as far as the dispersion vector is concerned and the values as calculated in Table 5.1 will be applied universally when matching the lines.

Finally, a central orbit for the extracted beam must be defined. Taking into account the small variation in the extracted momentum spreads ($\Delta p/p = -1.1 \times 10^{-3}$at lowest extraction energy to -0.825×10^{-3} for protons at the top extraction energy), the central momentum for the extracted beam in all cases will be defined with the 'round' value of $\Delta p/p = -0.5 \times 10^{-3}$ with respect to particles exactly on resonance. The position of this orbit has been found by tracking and is recorded in Table 5.1 with its survey co-ordinates at the entry point. The definition of $\Delta p/p = -0.5 \times 10^{-3}$ as the central orbit means that the different extracted beams will be asymmetric in the dispersion regions at the sub-millimetre level. However, at the gantry exit, dispersion is zero and these minute effects will disappear.

Dispersion and central orbit of extracted beam at entry to electrostatic septum

	On-resonance particles $\Delta p/p$ = 0.0		**Off-resonance particles $\Delta p/p$ = -0.001107**	
	Position [m]	**Angle [rad]**	**Position [m]**	**Angle [rad]**
Inner edge of segment	0.0350	0.000449	0.0350	0.000460
Outer edge of segment	0.0450	0.000338	0.0407	0.000383
Average radial position/angle	0.0400	0.0003935	0.03785	0.0004215
Shift of average position due to momentum [m]			-0.00215	
Shift of average angle due to momentum [rad]			0.000028	
Dispersion, D_x = {Radial shift / ($\Delta p/p$)} [m]			**D_x = 1.942**	
Derivative of dispersion D'_x = {Angular shift / ($\Delta p/p$)} [rad]			**D'_x = -0.025**	
Momentum of the central orbit of the extracted beam wrt the on-resonance particles (definition)			**$\Delta p/p$ = -0.0005**	
Radial position of central orbit of extracted beam [m]			**x = 0.039324**	
Angle of central orbit of extracted beam [rad]			**x′ = 0.0004255**	
Survey co-ordinates of : extraction beam centre line	**X = -9.195740 m** **Z = 1.200000 m**		**Y = 3.554285 m** **Θ_H = 5.497362 rad**	

Table 5.1 Dispersion and central orbit of extracted beam at entry to electrostatic septum

Table 5.2 summarises the boundary conditions for the extraction lines including the principal values from Table 5.1.

Boundary conditions for extraction		
Survey co-ordinates of entry point (ES in ring)		
X = -9.195740	Y = 3.554285	
Z = 1.200000		Floor defined as Z = 0.0 m.
Θ_h = 5.497362	Φ = 0.000000	
Twiss functions at entry (ES in ring)		
β_x = 5 m	α_x = 0	'Free' parameter.
Ex = 5π mm mrad		'Unfilled' ellipse - 'free'.
β_z = 6.5229 m	α_z = -0.1708	Values from ring.
$E_{z,RMS}$ = 1.4286 to 0.7324 π mm mrad		Carbon range from ring.
$E_{z,RMS}$ = 1.4286 to 0.6679 π mm mrad		Proton range from ring.
D_x = 1.942	D'_x = -0.025	Determined by extraction.
D_z = 0	D'_z = 0	
'Hand-over' Twiss values between modules		
β_x = 3 m	α_x = 0	'Free' parameters.
β_z = 2 to 27 m	α_z = 0	Range from 'stepper'.
D_x = 0	D'_x = 0	'Free' parameters.
D_z = 0	D'_z = 0	
Twiss functions at exit (all beam exits)		
β_x = 5 m	α_x = 0	According to medical
β_z = 2 to 27 m	α_z = 0	specifications and earlier
D_x = 0	D'_x = 0	choice of 'free' parameters.
D_z = 0	D'_z = 0	

Table 5.2 Boundary conditions for extraction

5.1.2 Correction to the horizontal beam shape and size

So far, the extracted beam has been described by a simple model with a 'near-rectangular' horizontal beam distribution. This is true for mono-energetic samples of the beam, but, from Table 5.1, it can be seen that the spiral step varies from 10 mm at high $\Delta p/p \approx +0.5 \times 10^{-3}$ to 5.7 mm at low $\Delta p/p \approx -0.5 \times 10^{-3}$. This corresponds to particles with zero and maximum betatron amplitudes respectively in the ring. Since the circulating beam is approximately gaussian, the particle distribution will be zero at zero and maximum betatron amplitudes and maximum at 1σ. The 1σ point will correspond to a spiral step of ~8.3 mm. The horizontal projected beam distribution in the extracted beam will therefore be 'near-trapezoidal' rather than 'near-rectangular' and the full width at half height will be ~8.3 mm, that is the spiral step at the 1σ point. For this reason, in order to reach the specified 10 mm spot size at FWHH, the final horizontal betatron amplitude at the patient has to be increased from the 5 m of the simple model to 7.2 m.

5.2 EXTRACTION OPTICS INSIDE THE RING

5.2.1 Between the septa

Using the data in Table 5.1, the central orbit of the extracted beam has been tracked from the electrostatic septum to the magnetic septum. Since the beam has a momentum deviation, passes close to the edge of the 'good' field region and crosses elements at larger angles than normal, the characteristics of the magnetic elements have been re-calculated to correspond exactly to this beam (see Distorted Orbits in

WinAGILE [1]). In the new lattice, for example, quadrupoles appear as dipoles with edge angles and a strength that has been modified for the momentum deviation. This technique makes it possible to describe the focusing forces accurately and to incorporate the section of the extraction that is inside the ring as a simple extension of the lattice of the main extraction line. Table 5.3 lists the modified lattice to show the order of magnitude of the changes that occur in the parameters. Figure 5.1 shows the Twiss functions. The divergent β_x and D_x at the exit of the ring is unavoidable and cannot be 'trapped' until the beam is well clear and there is space for a quadrupole.

Modified lattice* for extracted beam in the ring between septa

Name	Type	Length [m]	H-bend [rad]	Edge-1 [rad]	Edge-2 [rad]	*k*-value [m^{-2}]
ES MR 36	SBEND	0.8	-0.00250013	0.0	0.00250013	0.0
SS MR 36	DRIFT	0.9500041	0.0	0.0	0.0	0.0
QF MR 36	SBEND	0.35000038	0.00479606	0.00292675	0.00186931	-0.31372741
SS MR 37	DRIFT	0.37054475	0.0	0.0	0.0	0.0
MB MR 37	SBEND	1.66101406	0.39289799	0.19448023	0.19841776	0.0
SS MR 38	DRIFT	0.66991166	0.0	0.0	0.0	0.0
QD MR 38	SBEND	0.35000110	-0.00706571	0.00206822	0.00499749	0.52507311
SS MR 39	DRIFT	0.57030492	0.0	0.0	0.0	0.0
MB MR 39	SBEND	1.66103077	0.39289794	0.20134703	0.19155096	0.0
SS MR 40	DRIFT	0.34187872	0.0	0.0	0.0	0.0
QF MR 40	SBEND	0.35000115	0.00568213	0.00479858	0.00088355	-0.31372741
SS MR 01	DRIFT	0.55600022	0.0	0.0	0.0	0.0

* Sign and naming conventions for WinAGILE.

Table 5.3 Modified lattice for extracted beam in the ring between septa

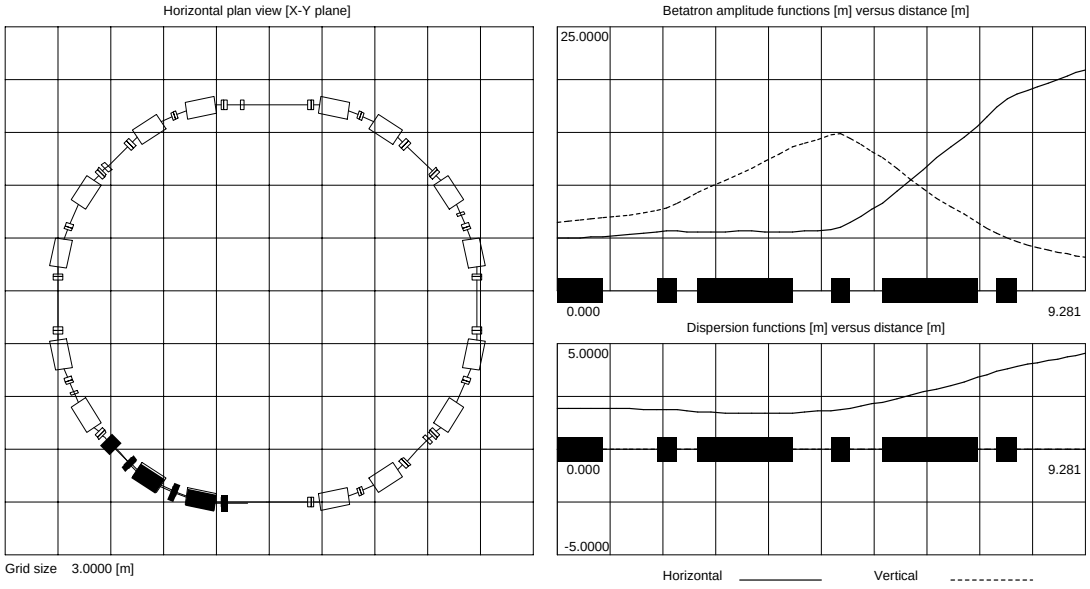

(a) Section of ring with extracted beam (b) Twiss functions

Figure 5.1 Extracted beam characteristics inside the ring

Note that in the vertical plane, the Twiss functions in Figure 5.1 can be used to represent the beam envelope, but, in the horizontal plane, the Twiss functions represent the 'unfilled' ellipse and the true beam size is determined by the angle of the

'bar' of charge within the ellipse. The true beam shape must therefore be found by tracking.

5.2.2 Alignment of the extraction electrostatic septum

The wires at the entry to the electrostatic septum (0.1 mm diameter) should be positioned radially at $(35\pm0.1) \times 10^{-3}$ m (outwards) with respect to the central orbit of the ring and its angle set according to the Hardt condition, which refers to the inner edges of the extracted beam segments for the different momenta. The Parameter List in Appendix DD shows that the Hardt Condition is not perfectly respected and that the angles of the inner edges of the different separatrices are spread over some 30×10^{-6} rad (449×10^{-6} to 481×10^{-6} rad). This spread theoretically represents an additional thickness of the septum wires of 24 microns and an additional beam loss of 0.24%. In practice, the alignment tolerance for the septum will be $\pm 100 \times 10^{-6}$ rad, which corresponds to 0.8% beam loss, and the small spread can be ignored. The septum will therefore be aligned at $(450\pm100) \times 10^{-6}$ rad with respect to the central orbit in the ring. This angle corresponds to the principal separatrix (since it does not change with energy).

Note that the ideal septum angle (449×10^{-6} rad) does not coincide exactly with the central orbit of the extracted beam (442×10^{-6} rad) as defined above in Table 5.1, but it is equivalent for all practical purposes. The electrostatic septum is a straight 'rectangular' unit and will be represented in the optics with a zero entry-edge angle and an exit-edge angle equal to the full bending angle.

5.3 COMMON SECTION OF EXTRACTION LINE

5.3.1 Matching from the ring to the line

To match from the ring to the extraction line, the Twiss functions must be brought to the 'handover' values in Table 5.2 and the dispersion function must be reduced to zero. In addition, the overall layout of the complex has the injection and extraction lines parallel, which requires that the bending in the matching insertion brings the beam to horizontal survey angle of $\Theta_H = 0.464093$ rad.

After the second septum there is an obligatory drift space in order to pass the main ring units and, at the end of this drift space, the horizontal betatron amplitude and dispersion functions reach their peak values. The matching insertion has been adapted to include an empty straight section close to the ring, from which the vacuum pipe can be removed to provide a vehicle track. The final straight section of the matching insertion will be used later to house a module called the 'chopper'. Figure 5.2 shows the Twiss functions and the geometry with respect to the ring.

5.3.2 Alignment of the magnetic extraction septa

There are two magnetic extraction septa. They are both straight units ('rectangular' bends) that have been designed to run in series from a single power converter. The first septum is the smaller ('thin' septum) with an angle of 0.050 rad and the second is larger ('thick' septum) with a bend of 0.150 rad. The physical edge of the current wall of the 'thin' septum should be positioned radially at 0.03295 ±0.0001 m (outwards) with respect to the central orbit of the ring and aligned parallel to the central orbit of the ring. Both the vacuum chamber of the ring and the

septum have a nominal thickness of 2 mm, but the critical walls against the septum can be machined up to 0.5 mm for the main ring chamber and 1.0 mm for the septum chamber to ensure that the overall dimensions are respected (see Table 3.10).

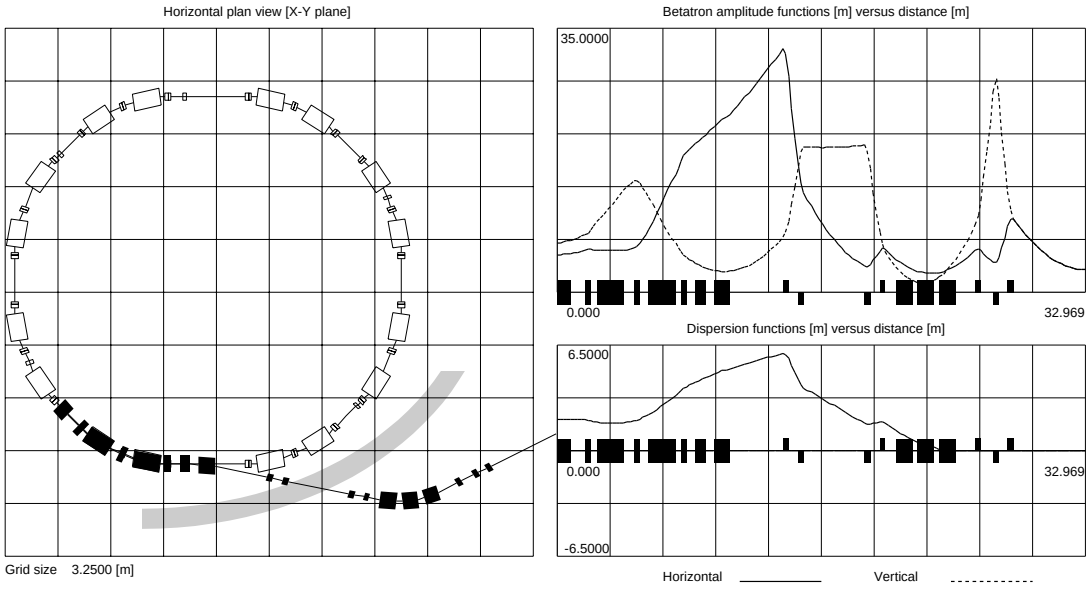

(a) Section in ring and matching insertion (b) Twiss functions

Figure 5.2 Lattice functions and geometry of the extraction matching insertion

Since the extracted beam has a small slope towards the axis, this appears as an entry-edge angle to the 'thin' septum. The exit-edge angle is then the septum's bending angle less the initial entry angle. Due to lack of space, the following 'thick' septum is aligned with a small entry-edge angle (0.0257 rad) and the remainder of its bending angle in the exit-edge angle (0.1243 rad). Table 5.4 lists the optical parameters for the lattice program for these septa. The rest of the insertion has no special features.

Optical representation of the magnetic septa*

Name	Type	Length [m]	H-bend [rad]	Edge-1 [rad]	Edge-2 [rad]	*k*-value [m^{-2}]
MS MR 01	SBEND	0.65	-0.050	0.00131	0.04869	0.0
SS EX 01	DRIFT	0.50	0.0	0.0	0.0	0.0
MS-EX-01	SBEND	1.00	-0.150	0.0257	0.0.1243	0.0

* Sign and naming conventions for WinAGILE.

Table 5.4 Optical representation of the magnetic septa

Note that the circulating separatrices in the ring and the 'bar' of charge in the septum can, in neither case, be calculated from the Twiss functions. The Twiss functions of the extracted beam (see Figure 5.2) define the beam envelope of the 'unfilled' ellipse in which the 'bar' of charge is turning. In fact, this envelope passes through the walls of the septa, but there is no loss because the 'bar' is angled sufficiently to avoid them. Figure 5.3 indicates the real space distribution of the extracted beam calculated by tracking at the entry to the first magnetic septum. The beam is represented by two groups of particles that correspond to the extreme

momentum deviations. The distribution is gaussian in the vertical phase space, but the rectangular distribution in the horizontal phase space is clearly visible in the sharp edges to the beam.

Figure 5.3 shows the nominal clearance of just 2 mm between the beam and the vacuum chamber. It will be possible in practice to increase this gap by kicking harder with the electrostatic septum and correcting the orbit later in the line. The beam would then pass through the edge of the 'poor' field region, but the extraction should be less difficult to set up. The optimum balance remains a question for operational experience with the final machine.

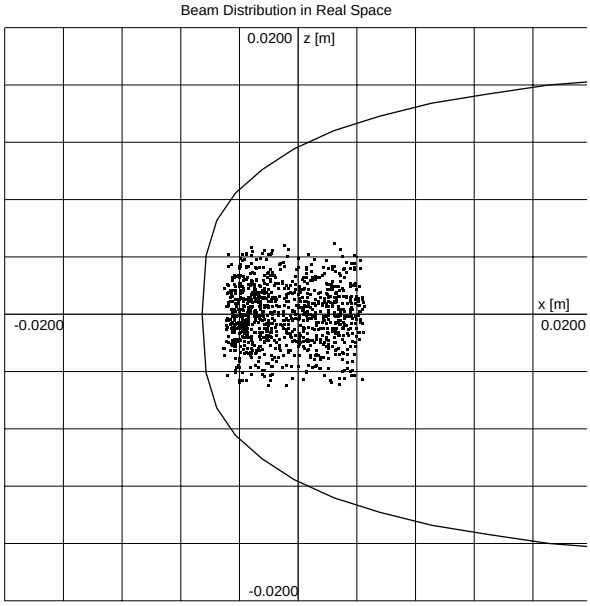

Figure 5.3 Real-space beam distribution at the entry to the first magnetic extraction septum
[The beam is represented by two groups of particles with the extreme values of $\Delta p/p$ = 0.0005 and $\Delta p/p$ = -0.0006. Note the gaussian tails vertically and the rectangular distribution horizontally]

5.3.3 Phase shifter and stepper

The phase shifter and stepper serves all beam delivery rooms and for this reason appears in the common part of the extraction line. The module proposed for PIMMS is shown in Figure 5.4 with a sample number of settings. This unit has been matched to shift the horizontal betatron phase from 1.83 - 5.76 rad while delivering the full range of vertical betatron amplitude functions from 2 - 27 m. This is beyond what is actually necessary and less than what is possible. For the larger phase advances, the betatron amplitude functions inside the module become large and eventually this would limit the tuning range in this direction. The module has six independent quadrupoles to control five variables (β_x, α_x, μ_x, β_z and α_z), which introduces some flexibility in the matching. With just five quadrupoles, the solutions would be unique and it could be that the desired parameter space would have regions with no solutions, or ones that were extreme in character. The sixth variable guarantees a solution and makes it possible to adapt those solutions that are impractical, for example, due to high excitations or large betatron amplitude functions. Note that the insertion is also capable of producing a wide range of aspect ratios in the beam spot.

The exercise of matching the module ($\Delta\mu_x$ = 1.83 - 5.76 rad; β_z = 2 - 27 m) was carried out in order to confirm that the solution range was indeed possible. The results are recorded in Appendix CC and, as an example, Figure 5.5 shows the surface in μ_x-β_z space that defines the *k*-value of the first quadrupole. Since the vertical phase advance was not controlled, the solutions are not unique and the 2-D surfaces for the quadrupole excitations are not always perfectly smooth. However, it is clear that there are no major disruptions that would lead to non-solution areas. For a practical machine, there would be two ways to proceed, either an on-line matching routine working from a 'seed' solution could calculate an exact solution when required, or some extra work could be done to control the vertical phase advance such that it changes smoothly across the parameter space while selecting the best behaved solution sets. This would take some time to perform, but once done the quadrupole currents could be fitted and only the polynomials stored.

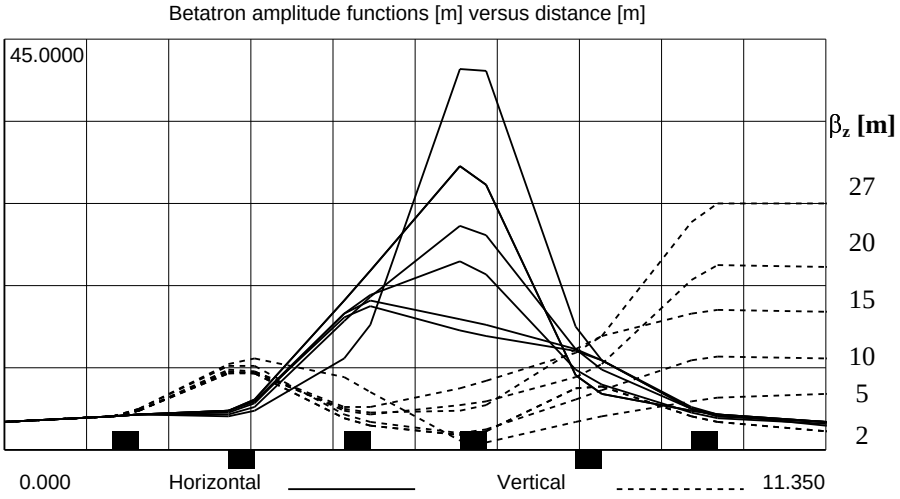

Figure 5.4 A sample set of lattice functions in the phase shifter-stepper [β_z = 2 to 27 m for $\Delta\mu_x$ = 2.1 rad,]

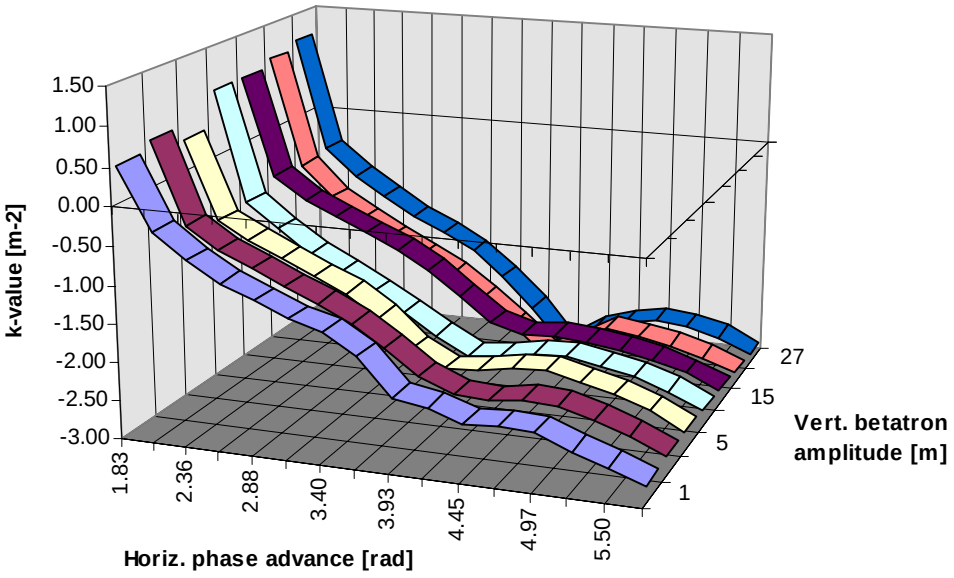

Figure 5.5 *k*-value surface for the first quadrupole in the phase shifter-stepper defined over the range $\Delta\mu_x$ = 1.83 to 5.75 rad and β_z = 2 to 27 m

5.3.4 Chopper

All treatment rooms will be able to switch the beam on and off for routine operational reasons and in emergencies by means of the beam chopper. In particular, the beam chopper will:

- Switch the beam on or off rapidly (<200 μs)
- Switch the beam on and off without perturbing its position at the patient.
- Be fail safe in that the power-off state is also the beam-off state.

The chopper, shown schematically in Figure 5.6, requires ~6 m of free space. This can be found between the last quadrupole of the matching insertion from the ring and the phase shifter and stepper. In this region, there are equal waists in both betatron amplitude functions and, in addition, the 'bar' of charge is close to being vertical making the horizontal beam size the smaller of the two (less than 4 mm). The chopper works by making a closed-orbit bump that bypasses a dump block mounted inside the vacuum chamber. The extra narrow beam and the absence of tails on the 'bar' of charge makes the horizontal plane the preferred choice for the bump that is excited by four equal bumper dipoles in series. Since the four dipoles sit in a common drift space, the bump is perfectly closed and the downstream trajectory of the beam is unaffected at all times. For this reason, the stability and over-shoot of the power converter are not critical issues. The dump block is mounted inside the vacuum chamber (see Appendix M) and obscures more than half of the aperture with its edge beyond the centre line by the amount of:

• 1 × half beam width	2 mm
• 1 × closed-orbit margin	4 mm
• Alignment safety margin	1 mm
Block edge is beyond centre line by:	**7 mm.**

If the bumper magnets fail, the beam should hit the block under all operating conditions. The total movement of the beam across the edge of the dump block is calculated as:

• 1 × full beam width	4 mm
• 2 × closed-orbit margin	8 mm
• 2 × alignment safety margin	2 mm
Total beam movement	**14 mm.**

The width of the 'bar' of charge and the closed orbit margin have been rounded up to convenient numbers. Equally, the safety margin that includes the dump block alignment is generous. The central pair of bumpers are radially displaced by 14 mm to be centred on the therapy beam to get the best field quality. The straight through beam that hits the dump is then 14 mm off-axis, but this is of no importance.

From the beam movement of 14 mm and the separation of the units shown in Figure 5.6, the chopper dipoles must provide kicks of 6.6 mrad. For the highest rigidity beam, this represents an integrated field of 0.0418 Tm. The concept design of the chopper dipole can be found in Appendix Z. The maximum rise time (i.e. 400 MeV/u carbon ions) has been set at 180 μs. The horizontal aperture of the bumper is relatively large and no problem should be encountered concerning field quality.

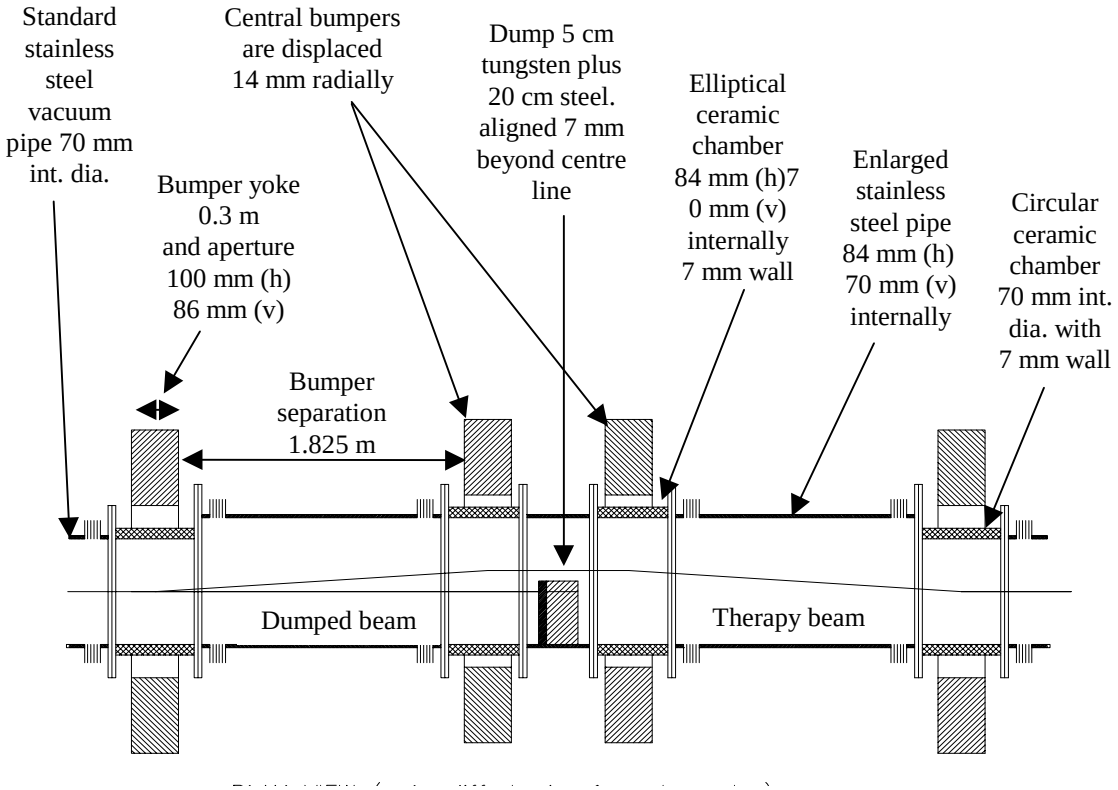

Figure 5.6 Plan view of the chopper module showing horizontal deflection of beam [Note that longitudinal and transverse scales are different]

5.4 CUSTOMISED PART OF LINE

A characteristic feature of the PIMMS layout is the alternation of fixed-beam rooms with gantry rooms. This leads to a basic spacing of 13 m between the first four beam switching points. However, due to the layout of the preparation rooms, the fifth switch to the carbon-ion gantry is shifted and this distance is considerably increased. The basic modules are described first followed by the various lines in the PIMMS example layout. The gantry types have been chosen as examples of active versus passive delivery systems, closed versus open dispersion bumps, 'barrel' versus 'conical' and 'Riesenrad' and not as a recommended set of units for a final centre.

5.4.1 Extension modules

Extension modules provide the lattice in which a beam switching point is embedded. PIMMS has two designs of extension module:

- A basic 13 m module that is used for all proton lines and the fixed carbon-ion line (see Figure 5.7 for geometry and lattice functions).
- A longer 16 m module used for the 'Riesenrad' carbon-ion gantry (see Figure 5.8 for geometry and lattice functions).

There is no unique structure for extension modules, but they must respect certain requirements to:

- Provide sufficient space for the introduction of dipoles for switching the beam into a secondary line
- Be a one-to-one structure in the vertical plane to transport the β_z from the stepper.

- Transport $\beta_x = 3$ m and $\alpha_x = 0$ at the entry to $\beta_x = 3$ m and $\alpha_x = o$ at the exit in the horizontal plane. A one-to-one structure ($\Delta\mu_x = \pi$) is ideal, but not absolutely essential, for this. The 13 m module is a one-to-one structure in both planes but the 16 m module is not.

Figures 5.7 and 5.8 show the extension modules with the standard 3 m 'hand-over' value for β_x and the two extreme values of 1 m and 27 m for β_z from the stepper.

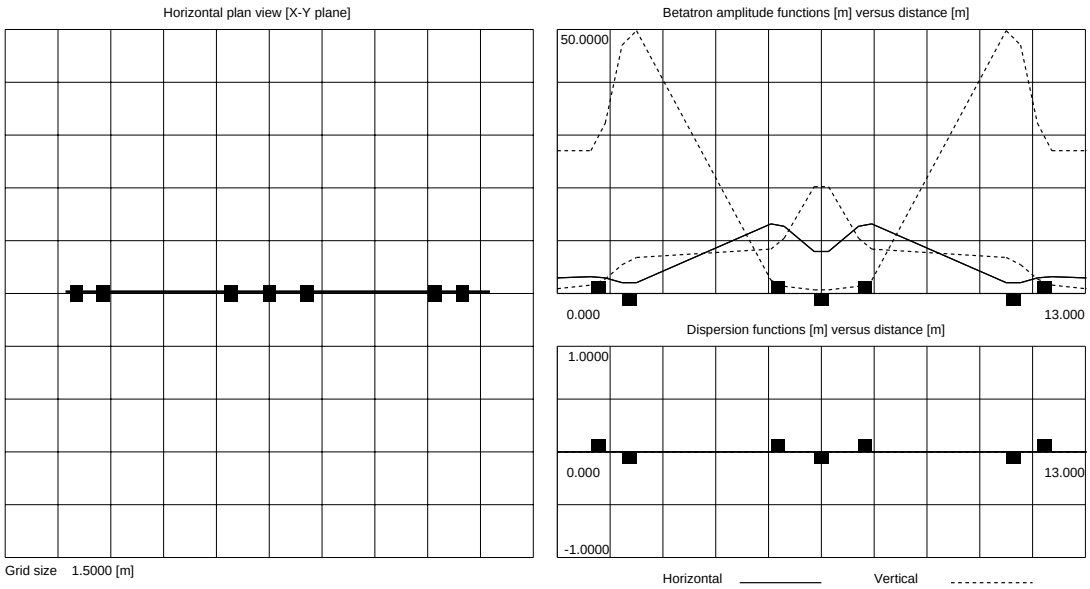

(a) Geometry (b) Twiss functions

Figure 5.7 Basic extension module

[$\Delta\mu_x = \Delta\mu_z = \pi$, At entry and exit, $\beta_x = 3$ m, $\beta_z = 1$ m and 27 m, $\alpha_x = \alpha_z = 0$, $D_x = D_z = 0$, $D'_x = D'_z = 0$]

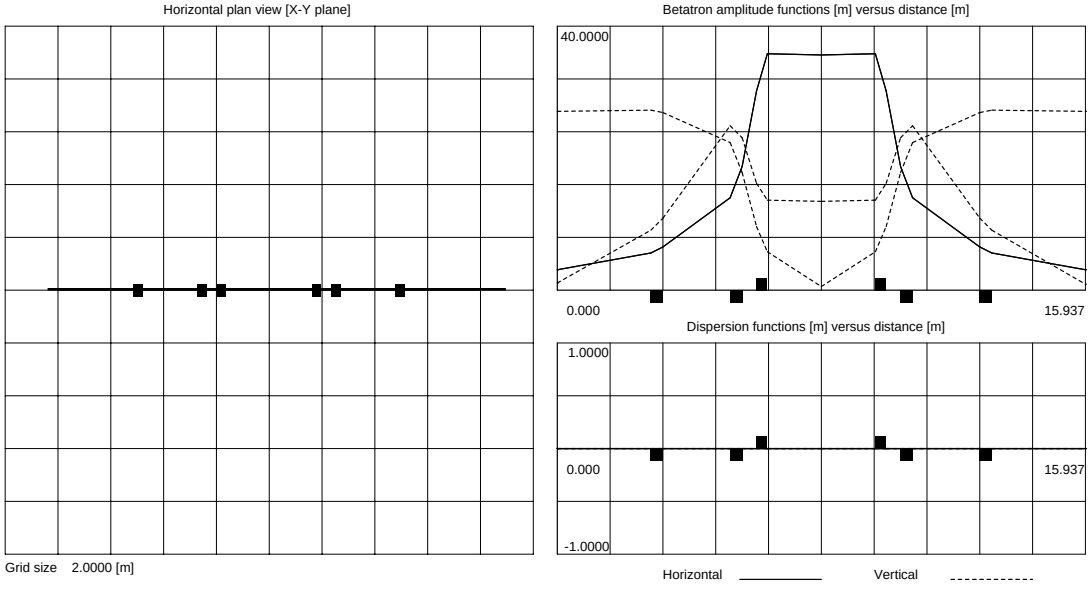

(a) Geometry (b) Twiss functions

Figure 5.8 'Riesenrad' extension module

[$\Delta\mu_z = \pi$, At entry and exit, $\beta_x = 3$ m, $\beta_z = 1$ m and 27 m, $\alpha_x = \alpha_z = 0$, $D_x = D_z = 0$, $D'_x = D'_z = 0$]

5.4.2 Deflection module with closed dispersion bump

Figure 5.9 shows how a deflection module can be embedded in the standard extension module and shows the Twiss functions in the deflection branch. In the present example, the dispersion excited by the bend is trapped in a closed bump and the module is transmitting the standard 'hand-over' value of 3 m for β_x and the extreme values of 1 m and 27 m for β_z from the stepper.

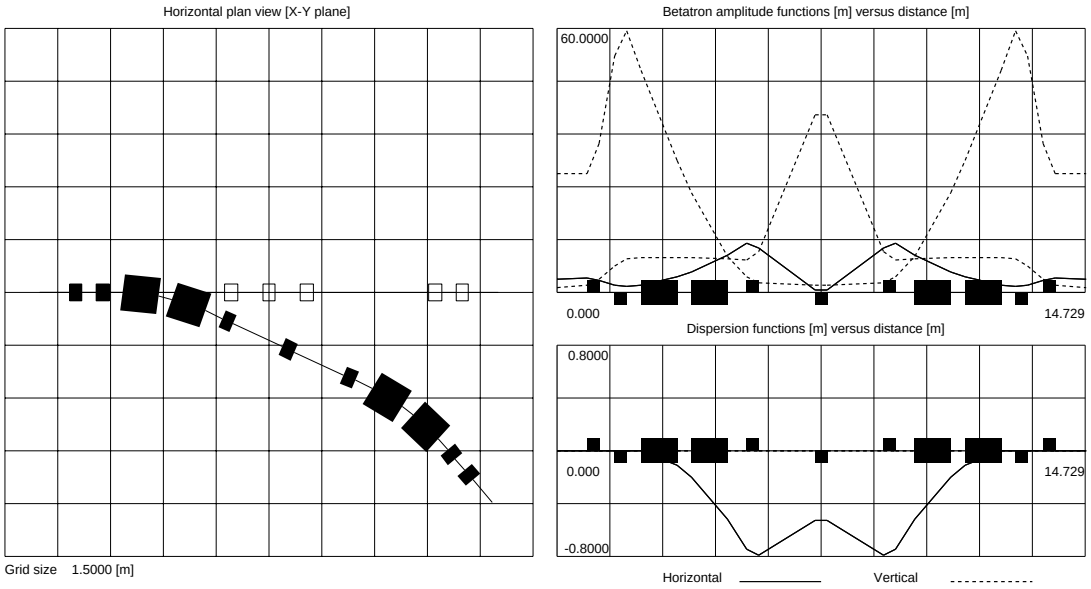

(a) Geometry (b) Twiss functions

Figure 5.9 Closed deflection module

[$\Delta\mu_x = 2\pi$, $\Delta\mu_z = \pi$, At entry and exit, $\beta_x = 3$ m, $\beta_z = 1$ m and 27 m, $\alpha_x = \alpha_z = 0$, $D_x = D_z = 0$, $D'_x = D'_z = 0$]

The extension and deflection modules are essentially universal designs that can be scaled for use anywhere. A deflection module, in which the dispersion bump is not closed, has to be designed with its gantry and is therefore unique to a certain degree, although the basic idea is unchanged. An examples of an open dispersion bend will be given later with the 'Riesenrad' gantry (see Section 5.4.7)

5.4.3 Rotator

The rotator is a short string of quadrupoles that is turned on its axis by half of the angle of the gantry and has the effect of rotating the phases spaces to match the gantry angle. The theory and general design are covered in Part I Sections 8.5 and 8.6. The specific design foreseen for PIMMS is the same for all gantries and is shown in Figure 5.10. This figure corresponds to the rotator in the 'zero-angle position' and shows the standard 'hand-over' $\beta_x = 3$ m and the stepper values $\beta_z = 1$ m and 13.5 m. However, the rotator will accept and transmit this range of values at any angle. Note the maximum vertical betatron amplitude function is only 13.5 m in this case, because all the PIMMS gantry lines are designed with telescopes to limit the values inside the rotator. The analysis of the beam sizes during rotation can be found in Part I, Section 8.8. Note that Figure 5.10 has zero dispersion, but, for an open-dispersion bend, the dispersion presented to the rotator would be non-zero and would be rotated to the angle of the gantry in the same way as the Twiss functions. The ability of the rotator to accept and rotate the dispersion vector opens the way towards more flexible optical

design in which the dispersion bump from the gantry is closed in the deflection module. This is essential in the case of the 'Riesenrad' gantry.

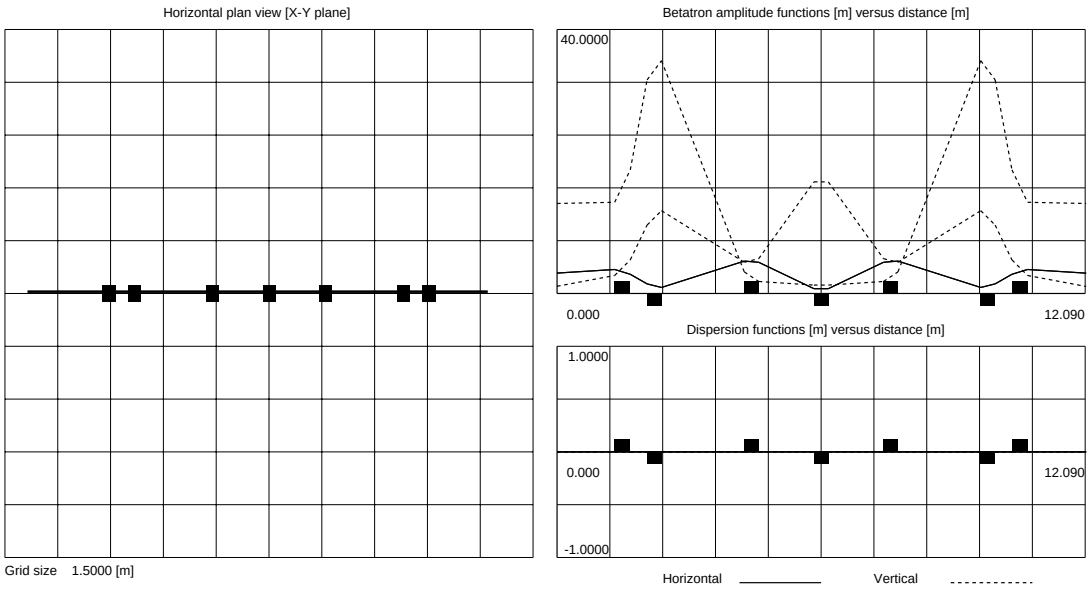

(a) Geometry (b) Twiss functions

Figure 5.10 Rotator at zero angle position
[$\Delta\mu_x = 2\pi$, $\Delta\mu_z = \pi$, At entry and exit, $\beta_x = \beta_z = 1$ m and 13.5 m , $\alpha_x = \alpha_z = 0$, $D_x = D_z = 0$, $D'_x = D'_z = 0$]

5.4.4 Proton gantry for parallel active scanning

The first exit from the main extraction line serves a proton gantry foreseen for active beam scanning. This gantry is an isocentric, 'barrel' design in which the dispersion bump is closed within the gantry itself. The deflection module must therefore also close its own dispersion bump as described in Section 5.4.2. The 'barrel' construction has been chosen to accommodate the scanning magnets inside the gantry in order to have parallel scanning. The more classical (and commercially available) 'conical' shape is better suited to passive spreading (see Section 5.4.6), although there are proposals for to add scanning magnets to 'conical' gantries after the last dipole. Figure 5.11 shows the geometry from the main extraction line, through the deflection module and rotator to the exit of the gantry and the geometry of the gantry by itself in the horizontal position. The lattice functions are shown for the standard 'hand-over' value of 3 m for β_x and the values of 1 m and 13.5 m for β_z from the stepper. The optics in the horizontal plane is constant as the beam size is adjusted by rotating the 'bar' of charge.

The gantry has been designed as a 1:2 telescope in the vertical plane in order to limit the betatron amplitude function in the rotator. In this scheme, the phase-shifter stepper delivers vertical betatron amplitude functions over the reduced range of 1 to 13.5 m and the gantry magnifies these values to 2 to 27 m. These two cases are shown in Figure 5.11 and the vertical betatron amplitude function can be seen to rise to around 40 m. At intermediate values it is comparable to the horizontal amplitude function. In the horizontal plane, the gantry provides a $\beta_x = 7.2$ m as explained in Section 5.1.2. Note that the gantry is assumed to be on its side (zero angle) in order that the rotator can be represented with the normal Twiss functions.

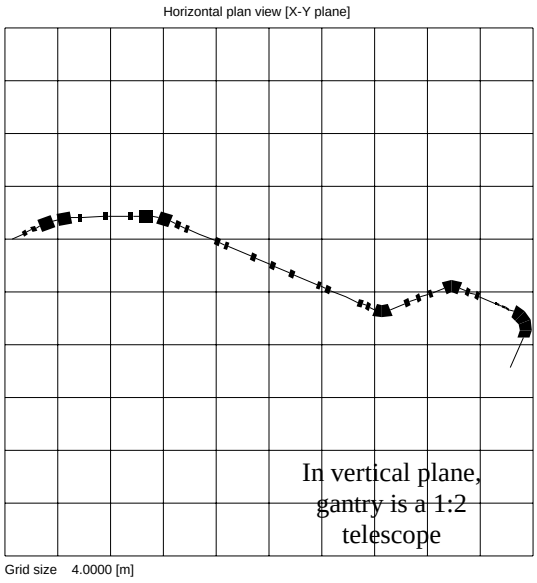

(a) Geometry of line T1 with proton gantry

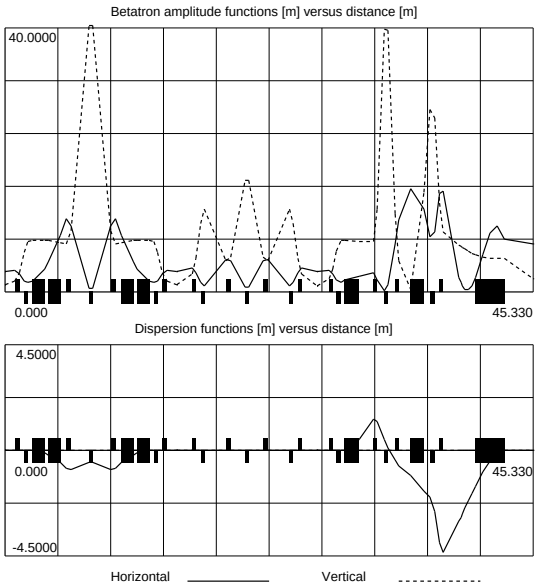

(b) Optics for β_x = 3 m and β_z = 1 m at entry

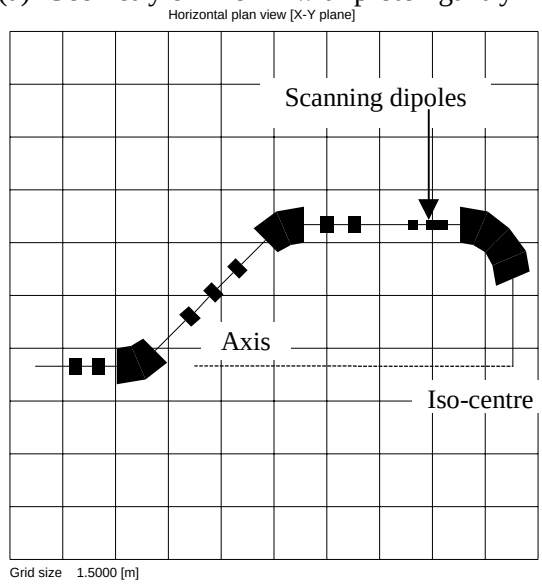

(c) Geometry of the gantry alone

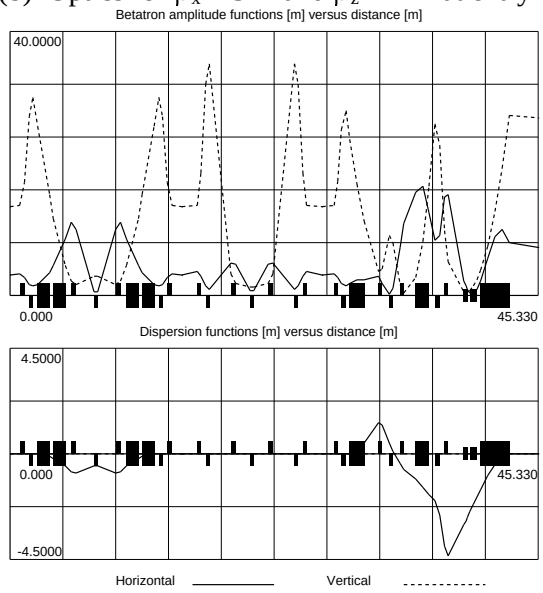

(d) Optics for β_x = 3 m and β_z = 13.5 m at entry

Figure 5.11 Transfer line T1 and its proton gantry in the horizontal position
[At entry, $\beta_x = 3$, $\beta_z = 1$ and 13.5, $\alpha_x = \alpha_z = 0$, $D_x = D_z = 0$, $D'_x = D'_z = 0$;
At exit, $\beta_x = 7.2$, $\beta_z = 2$ and 27, $\alpha_x = \alpha_z = 0$, $D_x = D_z = 0$, $D'_x = D'_z = 0$]

This proton gantry is intended for parallel scanning as illustrated in Figure 5.12. In the horizontal plane, the envelope represents the 'unfilled' emittance ellipse that corresponds to the maximum beam size. The phase shifter can be used to rotate the 'bar' of charge within this envelope to get any beam size down to ~2 mm. In the vertical plane, the envelope represents the beam size directly and in the example shown corresponds to the 10 mm beam at FWHH. The vertical beam appears to be slightly larger than the horizontal because its distribution slopes more at the edges. To scan ±0.1 m in both planes requires approximately ±0.025 rad in the vertical plane and ±0.062 rad in the horizontal plane. The scanning dipoles are positioned such that parallel scanning is performed in both planes. This requires a large aperture in the last

dipole approximately equal to the area to be scanned. The full details of the optics can be found in the Parameter List [2].

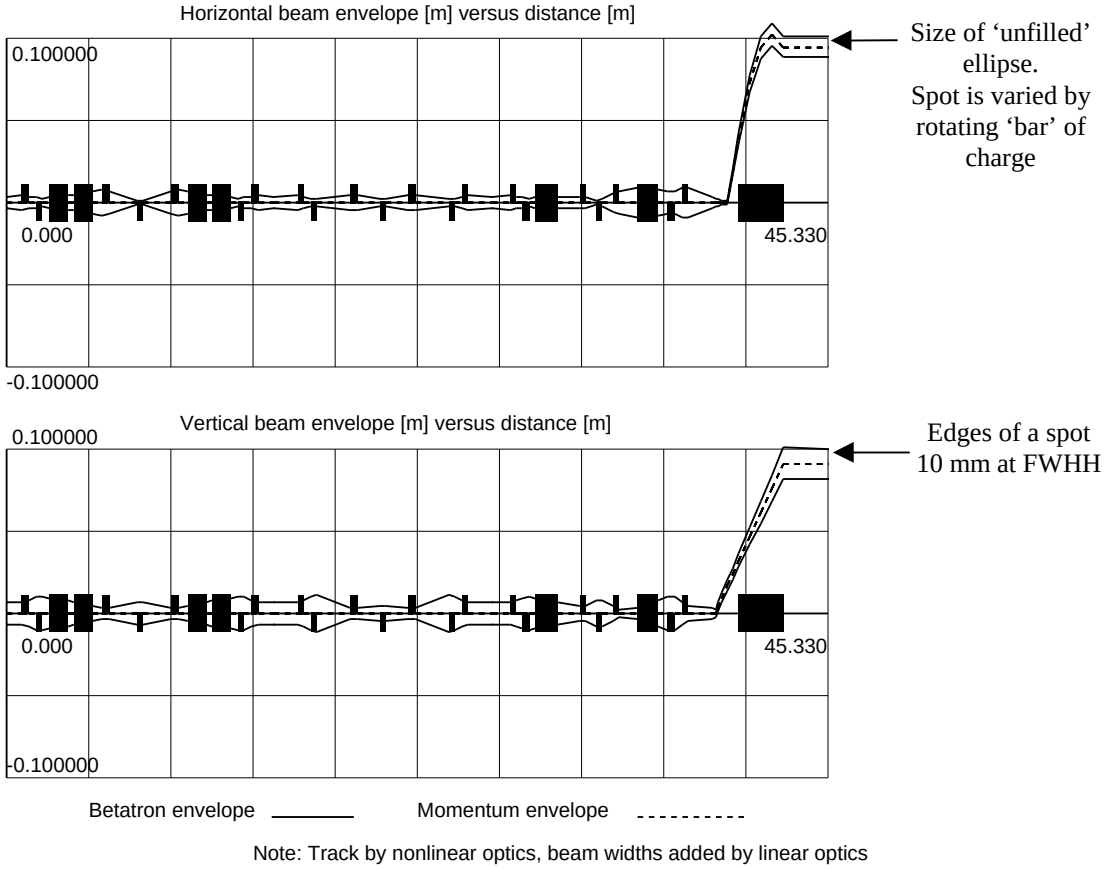

Figure 5.12 Envelopes of beams steered off-axis for scanning

Since PIMMS is concerned mainly with carbon-ion therapy and since proton gantries already exist, it was not felt to be necessary to go deeply into the design details. Consequently no study has been made of the mechanical and magnetic designs of the gantry elements nor of the effect of the mechanical deflections on the beam optics.

5.4.5 Proton and ion deliveries via fixed beam lines with active scanning

The second and fourth exits from the main extraction line serve fixed-beam treatment rooms for protons and ions respectively. The same optics has been adopted for both cases to limit the number of different types of magnets that will be needed. After the last quadrupole, there is a long drift space before the beam reaches its 'waist' where the patient will be positioned. A single scanning dipole for each plane is placed at the start of this drift space, so that the scanning angles are minimised. The same design of scanning magnet is proposed for both of these lines and for the 'Riesenrad' gantry. This means that the proton line and scanning magnets may appear somewhat over-dimensioned. In this example, the deflection and scanning modules do not give any magnification. Consequently, the lattice functions in the deflection module are somewhat larger than those in the previous line, T1 (see Section 5.4.4) where the vertical betatron amplitude function is magnified by a factor of 2 at the end of the line by the gantry. Figure 5.13 shows the geometry of a fixed beam line and the lattice

functions are shown for the standard 'hand-over' value of 3 m for β_x and the 2 m and 27 m for β_z from the stepper. The optics in the horizontal plane is constant as the beam size is adjusted by rotating the 'bar' of charge.

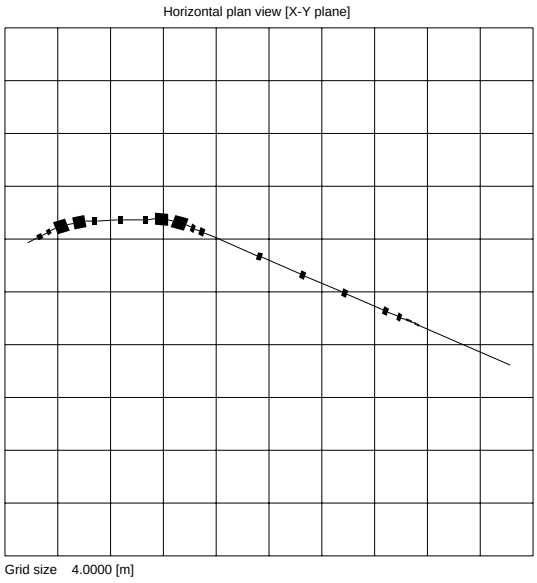

(a) Geometry of the fixed lines T2 and T4

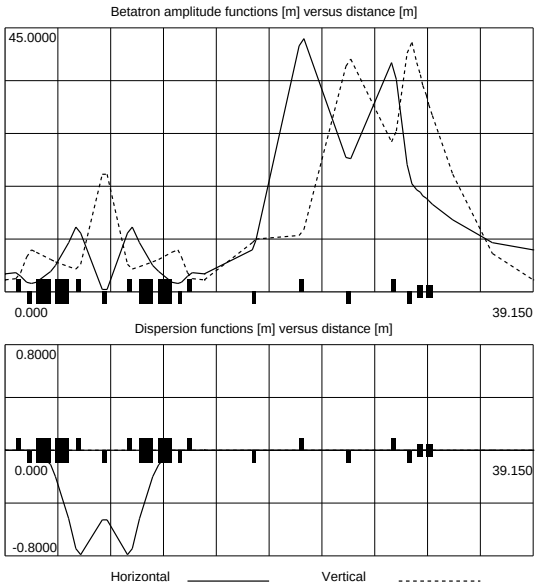

(b) Optics for β_x = 3 m and β_z = 2 m at entry

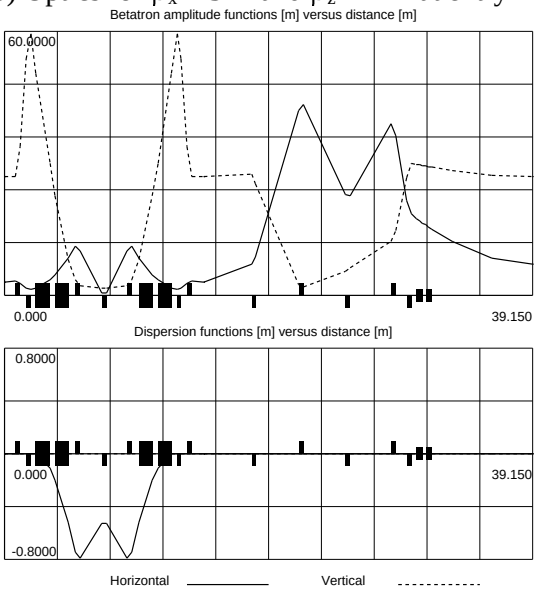

(c) Optics for β_x = 3 m and β_z = 27 m at entry

Figure 5.13 Transfer lines T2 and T4 for fixed beam scanning
[At entry, $\beta_x = 3$, $\beta_z = 2$ and 27, $\alpha_x = \alpha_z = 0$, $D_x = D_z = 0$, $D'_x = D'_z = 0$;
At exit, $\beta_x = 7.2$, $\beta_z = 2$ and 27, $\alpha_x = \alpha_z = 0$, $D_x = D_z = 0$, $D'_x = D'_z = 0$]

To scan ±0.1 m in both planes requires approximately ±0.012 rad. The scanning is divergent and at the edge of the scan (10 cm from the axis) the beam has an angle of approximately 0.07°. This fits comfortably inside the limit of 1° that is often quoted as a medical specification. The full details of the optics can be found in the Parameter List [2].

5.4.6 Proton gantry for passive spreading

The third exit from the main extraction line serves a proton gantry foreseen for a passive spreading delivery system. This gantry is an isocentric, 'conical' design in which the dispersion bump is closed within the gantry itself. The deflection module must therefore also close its own dispersion bump as described in Section 5.4.2. The 'conical' construction has been chosen, since it leads to a relatively compact gantry when there are no scanning magnets to be included. This type of design is commercially available, but with different optics to those shown here[*].

Figure 5.14 shows the geometry from the main extraction line, through the deflection module and rotator to the exit of the gantry and the geometry of the gantry by itself in the horizontal position. The beam envelopes[**] are shown for the maximum values required. The optics in the horizontal plane corresponds to the maximum beam size (i.e. the 'bar' of charge is horizontal). Note that the 'waist' at which the nominal beam parameters appear is not on the axis at the isocentre, but 20 cm after the last dipole where the double scatterer is mounted to passively spread the beam uniformly over a 20 cm × 20 cm area. The double scatterer for this gantry has not been designed, but it is assumed that the largest beam spot would be suitable. The beam distribution is near-gaussian in the vertical plane and 'near-trapezoidal' in the horizontal plane with a very low divergence, whereas to date double scatters have been designed for symmetric beams with equal emittances and lattice functions. The scattering in a double scatterer is very strong and the initial asymmetry between the angles in the two transverse planes may not have a strong effect on the final distribution. The assumptions made here are that either the system is insensitive to the initial angular distribution or the double scatterer can be redesigned to account for the differences. It may be necessary to adjust beam sizes for different scatterers and at different energies, but this is done in the same way as in the other gantries. This particular design is a 1:3 telescope in the vertical plane and delivers the values of 7.2 m for the horizontal betatron amplitude function as described in Section 5.4.4. Full details of the optics can be found in the Parameter List [2].

Since the passive spreading takes place after the last dipole, all the magnets in the gantry can all have a small aperture, which reduces weight and power consumption and makes the mechanical construction easier. Since this type of gantry is commercially available, it was not felt to be necessary to go deeply into the design details or to make an error analysis of the effects of mechanical deformations on the beam optics.

---

[*] Commercially available gantries of the 'conical' and 'corkscrew' designs have optics that accept beams with equal Twiss functions and emittances in the two transverse planes. Since the PIMMS beam is asymmetric, the optics has to be modified.

[**] When the beam passes through a rotator, there is in general coupling and the normal Twiss functions are no longer valid. One possibility is to consider the gantry only when it is on its side so that the optics can be described normally (as was done in Figure 5.11 for the first proton gantry). The alternative is to switch to beam envelopes as is done in Figures 5.14 and 5.15, but strictly speaking beam envelopes are then needed for all angles. Since the rotators have been designed to avoid large perturbations to the beam envelopes during rotation, the former representation or a single envelope is sufficient for aperture purposes.

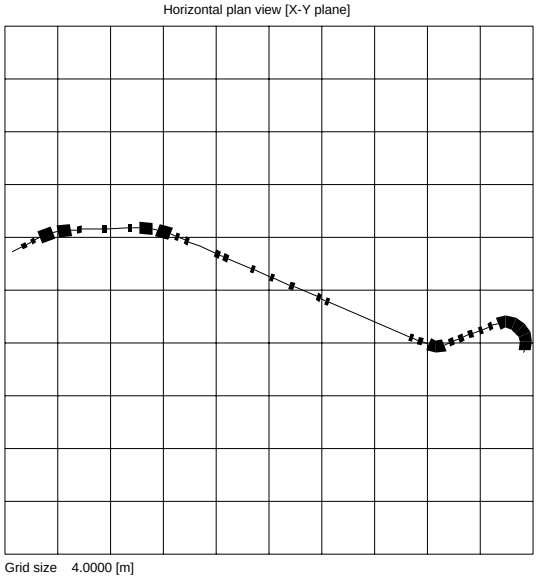

(a) Geometry of line T3 with proton gantry

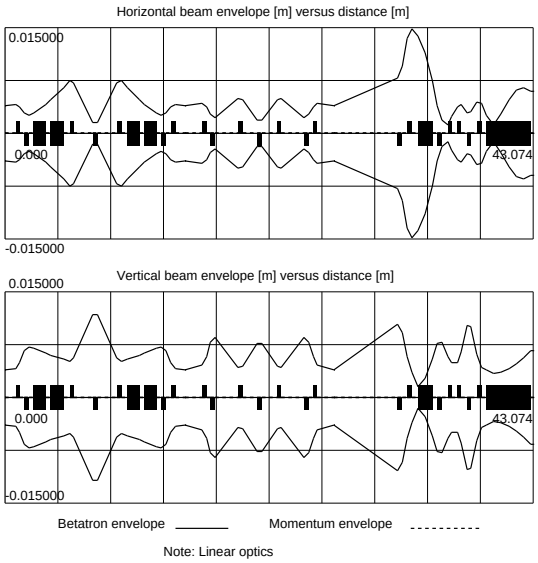

(b) Optics for $\beta_x = 3$ m and $\beta_z = 9$ m at entry

Note that the vertical beam size appears slightly larger than the horizontal in the above figure. This is because the figure shows the beam edges for beams of equal FWHH, but different distributions. The longer tails of the vertical distribution make the beam look larger.

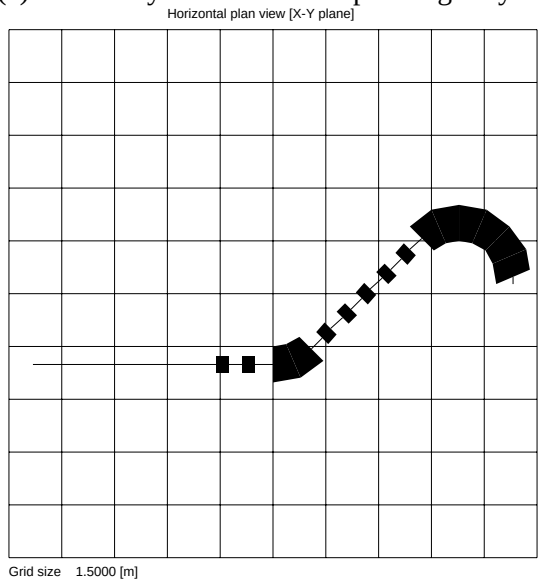

(c) Geometry of the gantry alone

Figure 5.14 Transfer line T3 and its proton gantry in the horizontal position
[At entry, $\beta_x = 3$, $\beta_z = 9$, $\alpha_x = \alpha_z = 0$, $D_x = D_z = 0$, $D'_x = D'_z = 0$;
At exit, $\beta_x = 7.2$, $\beta_z = 27$, $\alpha_x = \alpha_z = 0$, $D_x = D_z = 0$, $D'_x = D'_z = 0$;
'Bar' of charge would be horizontal for largest beam size.]

5.4.7 'Riesenrad' gantry for carbon ion active scanning

The fifth exit from the main extraction line serves a carbon ion gantry foreseen for active beam scanning[*] . This gantry is an exocentric design known as the 'Riesenrad'. The 'Riesenrad' uses a single 90-degree dipole that rotates about the incoming beam axis. The patient is positioned exocentrically on a circle of a few

[*] Passive spreading is not proposed for carbon ions because (a) to get sufficiently large scattering angles the losses would be high and the particle intensity from the accelerator is too low, (b) the scattering causes fragmentation and neutron background, (c) this would ignore one of the principal advantages of carbon ions, that is the small, high-precision beam spots preserved by the low scattering.

meters radius such that the beam impinges on the tumour from any desired direction. With carbon ions, it is not possible to put the scanning magnets after the main dipole while maintaining reasonable parameters for the scanning magnets and a reasonable radius for the machine. Thus these units are positioned just before the main dipole such that the phase advances are suitable for parallel scanning. With the scanning magnets upstream of the main dipole, it is necessary to construct the dipole with an aperture approximately equal to the area to be scanned. Since the main dipole is a single unit, this large aperture is required over the complete length of the magnet. Furthermore, it is not possible to close the dispersion bump within the gantry itself and for this reason the gantry, rotator and deflection module must be designed as an integral unit. The main design constraints are:

- The dispersion must be closed between the deflection module and the gantry.
- The modules are made telescopic to keep beams sizes within reasonable limits.
- Edge angles on the main dipole are needed to help adjust the phase advances to the scanning magnets for parallel scanning.

Figure 5.15 shows the geometry from the main extraction line, through the deflection module and rotator to the exit of the gantry and the geometry of the gantry by itself in the horizontal position. The lattice functions are shown for the standard 'hand-over' value of 3 m for β_x and the 1 m and 13.5 m for β_z from the stepper. The optics in the horizontal plane is constant as the beam size is adjusted by rotating the 'bar' of charge. In order to keep beam envelopes well within the aperture and to help the matching, the deflection module de-magnifies the vertical betatron amplitude function by 1:0.7 and then the gantry re-magnifies it from 0.7:2 giving an overall magnification of 1:2.

Figure 5.16 shows the 10 mm beam envelopes for scanning ±0.1 m. In the horizontal plane, the envelope represents the 'unfilled' emittance ellipse that corresponds to the maximum beam size. The phase shifter can be used to rotate the 'bar' of charge within this envelope to get any beam size down to ~2 mm. In the vertical plane, the envelope represents the beam size directly and in the example shown corresponds to the 10 mm beam at FWHH. The vertical beam appears to be slightly larger than the horizontal because its distribution slopes more at the edges. To scan ±0.1 m in both planes requires approximately ±0.0125 rad in the vertical plane and $\pm(2 \times 0.0125)$ rad in the horizontal plane. The scanning dipoles are positioned such that parallel scanning is performed in the horizontal plane and near-parallel scanning in the vertical plane. This requires a large aperture in the dipole equal to area to be scanned. The full details of the optics can be found in the Parameter List [2]. The mechanical and magnetic design of the 'Riesenrad' dipole can be found in Appendix X. A concept design of the raster scanning dipoles can be found in Appendix Y. Chapter 6 gives further details of the mechanical design of the gantry and its alignment. An error analysis of the systematic and random errors in the gantry and rotator structures and the impact of these errors on the beam optics is also included in Chapter 6.

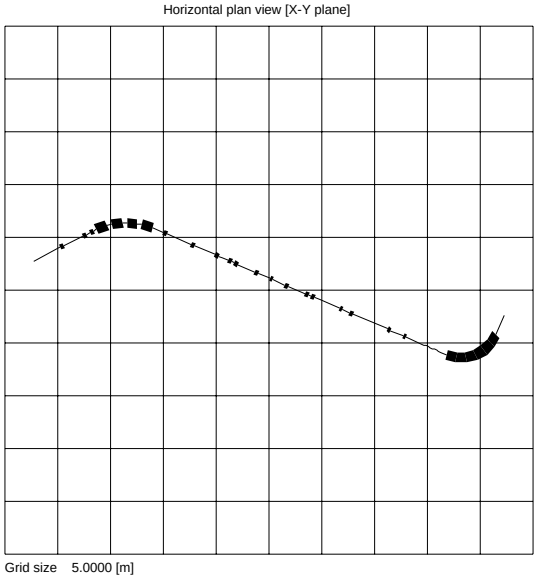

(a) Geometry of line T5 with gantry

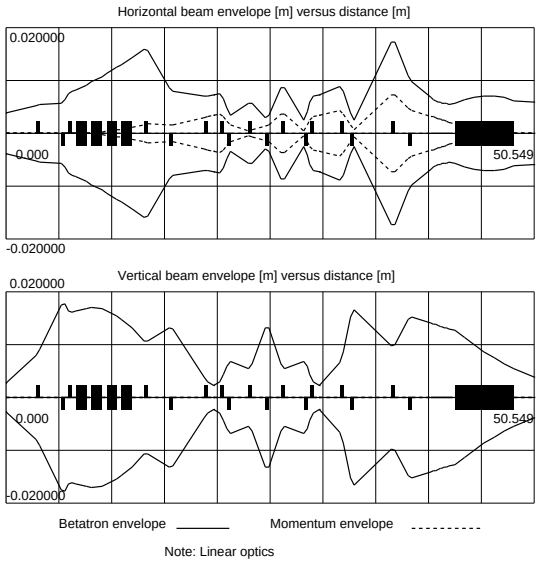

(b) Optics for β_x = 3 m and β_z = 1 m at entry

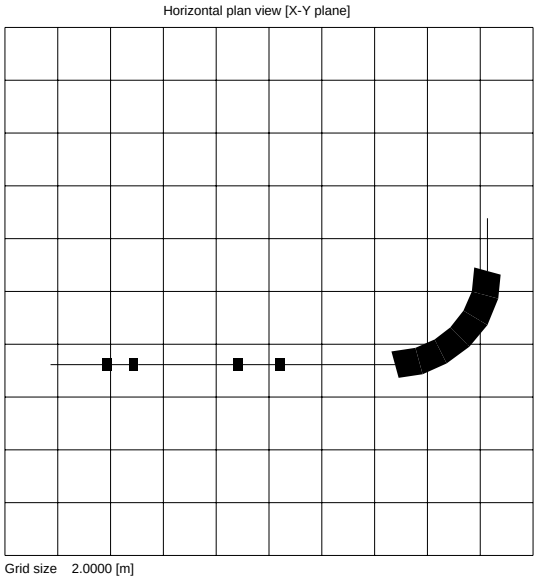

(c) Geometry of the gantry alone

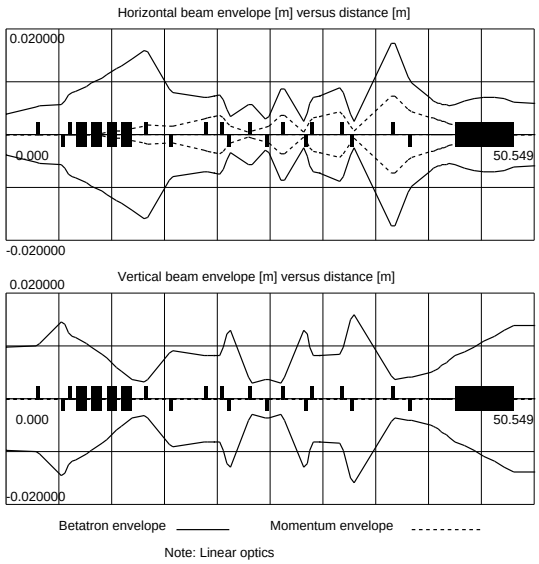

(d) Optics for β_x = 3 m and β_z = 13.5 m at entry

Figure 5.15 Transfer line T5 and its 'Riesenrad' gantry in the horizontal position
[At entry, $\beta_x = 3$, $\beta_z = 1$ and 13.5, $\alpha_x = \alpha_z = 0$, $D_x = D_z = 0$, $D'_x = D'_z = 0$;
At exit, $\beta_x = 7.2$, $\beta_z = 2$ and 27, $\alpha_x = \alpha_z = 0$, $D_x = D_z = 0$, $D'_x = D'_z = 0$]

5.4.8 Overall view of extraction line with dump

Figure 5.17 shows the extraction complex from the exit of the phase shifter and stepper to the different beam delivery points. The reference points F, G, H and I indicate the starting points of the first four beam delivery lines and are regularly spaced at 13 m. The derivation point, J, of the fifth line is much further along the line to match the layout of the treatment rooms. This extra distance is provided by two structures: a standard extension module that serves only to prolong the line and a special extension module for the 'Riesenrad' gantry. If further gantries, or fixed beam lines, were to be added then this would be done with additional standard extension

modules for proton lines and special extension modules for ‘Riesenrad’ gantry lines. Finally, the line is terminated with a module that brings the beam to a dump block. The individual sections are described in more detail in the preceding sections.

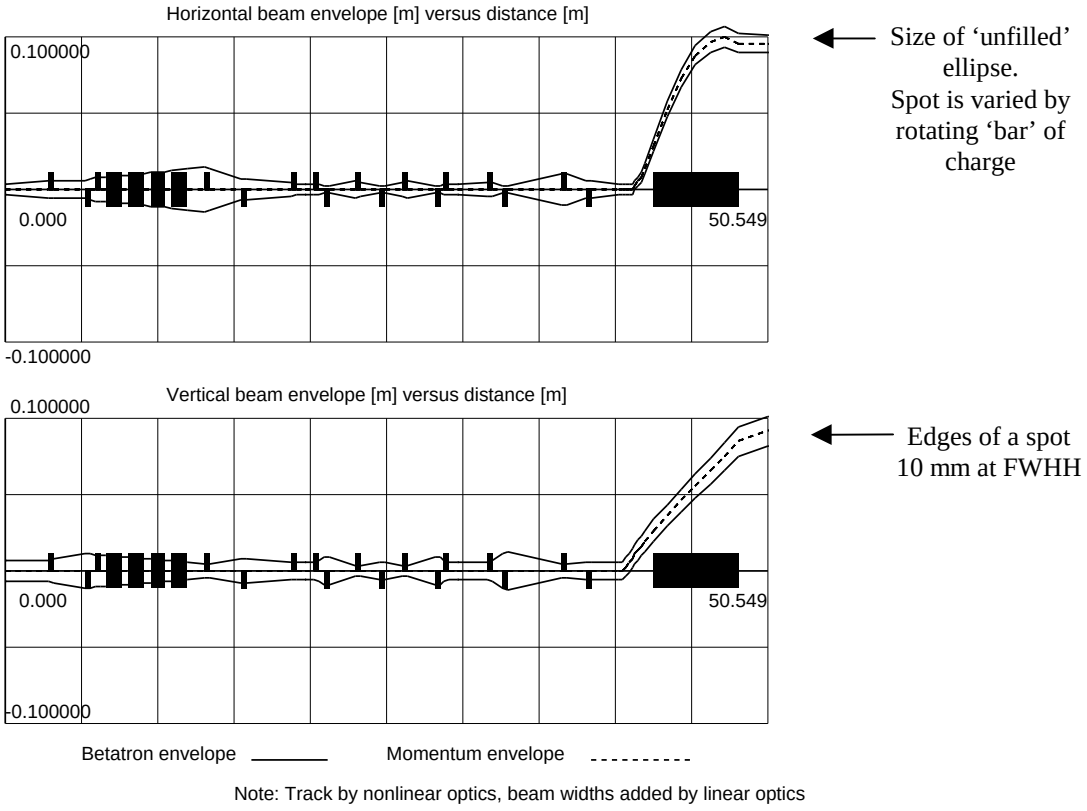

Figure 5.16 Envelopes of beams steered off-axis for scanning in the ‘Riesenrad’
[At entry, $\beta_x = 3$, $\beta_z = 1$ and 13.5, $\alpha_x = \alpha_z = 0$, $D_x = D_z = 0$, $D'_x = D'_z = 0$;
At exit, $\beta_x = 7.2$, $\beta_z = 2$ and 27, $\alpha_x = \alpha_z = 0$, $D_x = D_z = 0$, $D'_x = D'_z = 0$]

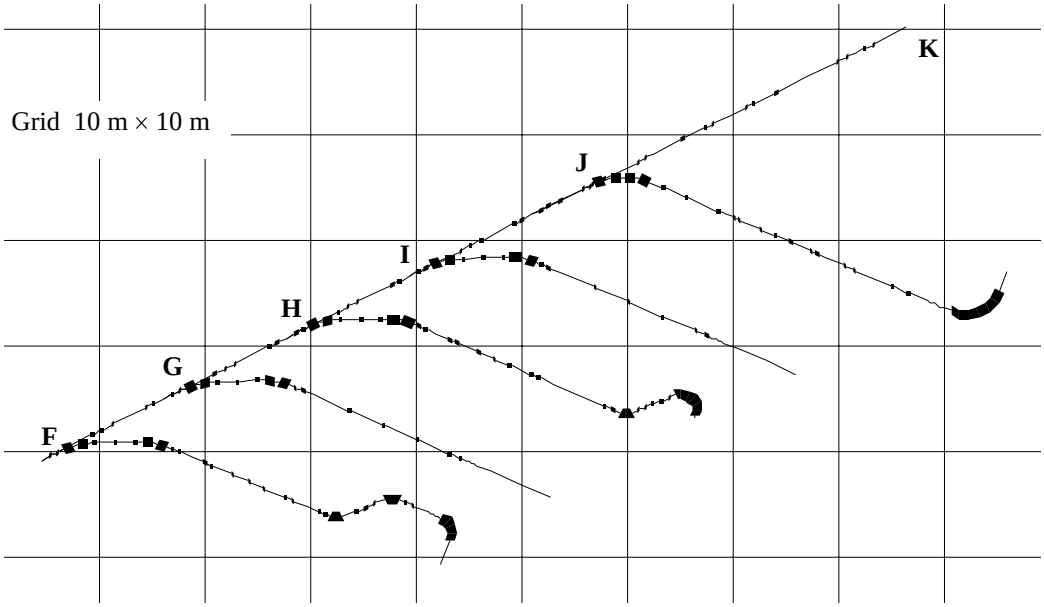

Figure 5.17 Geometry of the delivery complex from the exit of the phase-shifter-stepper
[**F** proton gantry line for active scanning, **G** fixed proton line, **H** proton gantry line for passive spreading, **I** carbon-ion gantry line for active scanning, **K** beam dump.]

One important operational aspect of the extraction complex is the rotation of the 'bar' of charge at each delivery point and the requirements this imposes on the phase-shifter-stepper. Figure 5.18 shows the 'bar' of charge tracked to the patient position in the lines T1, T2, T4 and T5 and to the double scatterer in line T3 with the phase-shifter-stepper set to the phase advance of 1.83 rad (i.e. the minimum that has been matched, see Appendix CC). In all cases, the 'bar' is close to horizontal and hence near to the maximum projected horizontal beam size. A further phase shift of ~105° (~1.8 rad) would bring all 'bars' to the vertical position (accounting for the small spread in angles) and hence to the minimum projected size. This additional phase shift is less than half of the known capability of the module.

5.5 APERTURE

The most critical condition for the vertical aperture in the extraction lines corresponds to the creation of the smallest beam spot (4 mm FWHH) in the vertical plane from the largest emittance (7.1429π mm mrad). This slightly unusual situation occurs because the vertical betatron amplitude function tends to large values when the 'hand-over' value is forced down to the minimum value of 1 m. The counter situation of the largest spot size (10 mm FWHH) from the smallest emittance (0.6679π mm mrad) is almost as critical, but the worst cases are avoided by the use of de-magnifying telescopes. The horizontal plane is more simple since the emittance is constant and the largest beam sizes occur when the betatron amplitude function and the dispersion combine unfavourably.

Figure 5.19 (from the ring to the phase-shifter-stepper) and Figure 5.20 (from the exit of the phase-shifter-stepper to the delivery points) show the beam envelopes for the lowest extraction energy (i.e. the largest emittance 7.1429π mm mrad). In the horizontal plane, the envelope is that of the 'unfilled' ellipse. Upstream of the phase-shifter-stepper the orientation of the 'bar' of charge does not change and the envelope as shown is an over-estimate of the horizontal beam size at many positions. However, this consideration is needed only for the magnetic septa where the chamber has been positioned according to the true beam edge (see Figure 5.3) For all other units the 'unfilled' emittance ellipse is used. Downstream of the phase-shifter-steeper the 'bar' of charge will occupy all orientations at different times, so the unfilled ellipse is the correct measure of the beam size for horizontal aperture purposes. In the vertical plane, from the ring to the phase-shifter-stepper (Figure 5.19), the envelope is the true beam envelope and the largest that will occur. In Figure 5.20 the situation downstream of the phase-shifter-stepper is represented in the vertical plane by the smallest beam spot (4 mm) combined with the largest emittance as explained above.

The affect of turning the rotator has been tacitly ignored in the above. This has been studied in Part I in Section 8.8 and the rotators have been designed accordingly to avoid large perturbations to the beam envelopes during rotation. To avoid a situation that is extremely complex but brings very little change to the final result, the apertures will be determined with the gantries and rotators set at zero angle.

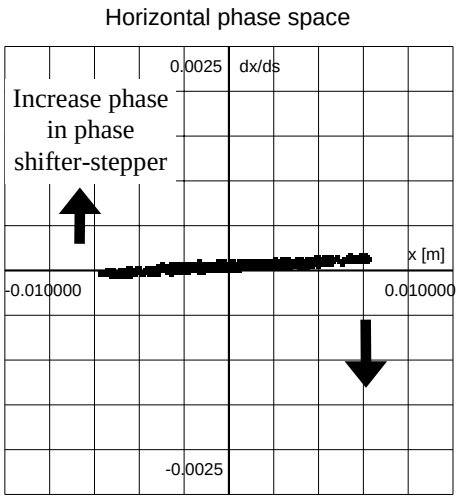

(a) T1 proton gantry with active scanning

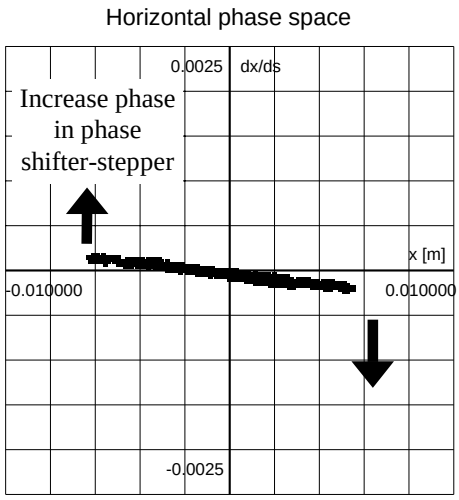

(b) T2 fixed proton beam line

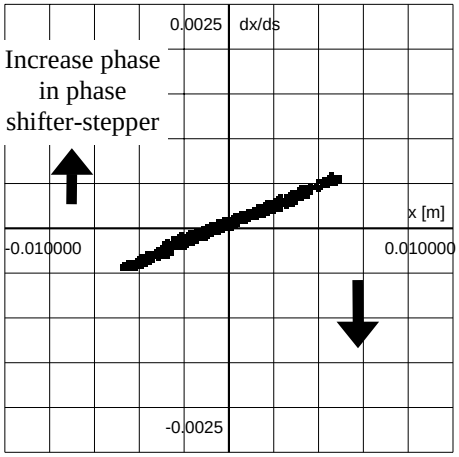

(c) T3 proton gantry with passive spreading

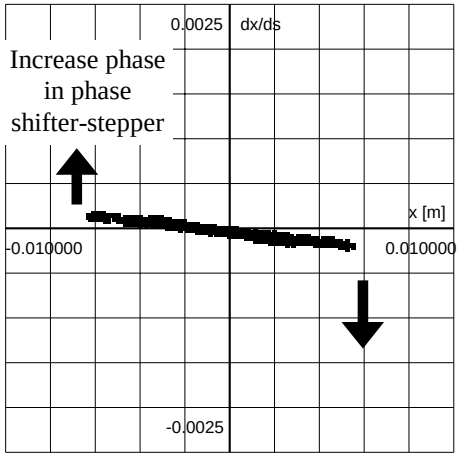

(d) T4 fixed carbon-ion line

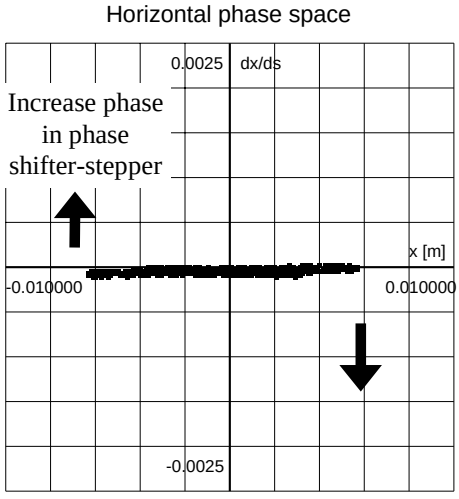

(e) T5 ‘Riesenrad’ carbon-ion gantry

Figure 5.18 Orientation of the ‘bars’ of charge in each line with minimum phase advance (1.83 rad) in the phase-shifter-stepper
[Arrows show motion of ‘bar’ when increasing phase shift from the phase-shifter-stepper]

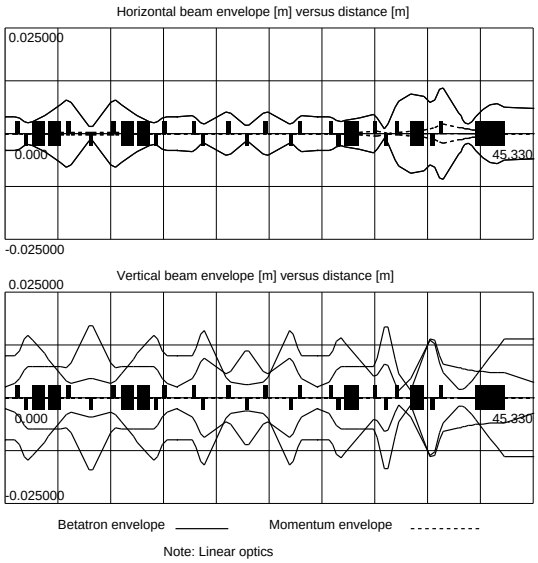

Figure 5.19 Extraction beam envelopes from the ring to the phase-shifter-stepper [Horizontal envelope corresponds to the 'unfilled' emittance ellipse, vertical envelope correspond ring emittance]

Envelopes, 'good-field' regions, apertures and vacuum pipes		
	Horizontal	**Vertical**
General		
Maximum beam sizes [mm]	±17.2	±17.8
Closed orbit margin [mm]	±10	±7.5
Sagitta in dipoles	±13.8	0
Quadrupoles		
Good field region (rounded) [mm]	±27	±26
Vacuum pipe internal diameter* [mm]	70	
Vacuum pipe external diameter [mm]	73	
Drift space (same as quadrupoles)		
Vacuum pipe internal diameter (circular) [mm]	70	
Vacuum pipe external diameter (circular) [mm]	73	
Dipoles		
Good-field region [mm]	±41	±26
Internal vacuum pipe (super ellipse) [mm]	70 (curved)	52
External vacuum pipe (super ellipse) [mm]	73 (curved)	55

* Typically 30% of the aperture in a quadrupole is 'poor'-field region, but it is an advantage for vacuum conductance and beam steering to include this space inside the vacuum.

Table 5.5 Envelopes, 'good-field' regions apertures and vacuum pipes

In Figures 5.19 and 5.20, the horizontal beam envelopes reach ±17.2 mm (in the 'Riesenrad' due to the dispersion) and the vertical envelopes reach ±17.8 mm (also in 'Riesenrad'). The standard aperture for the entire extraction complex will be based on these values with the addition of closed orbit margins of ±10 mm horizontally and ±7.5 mm vertically (as used in the ring) and a sagitta of 27.6 mm in the transfer dipoles, see Table 5.5. These values are used as the basis for a single quadrupole design and a single dipole design for use throughout the extraction complex.

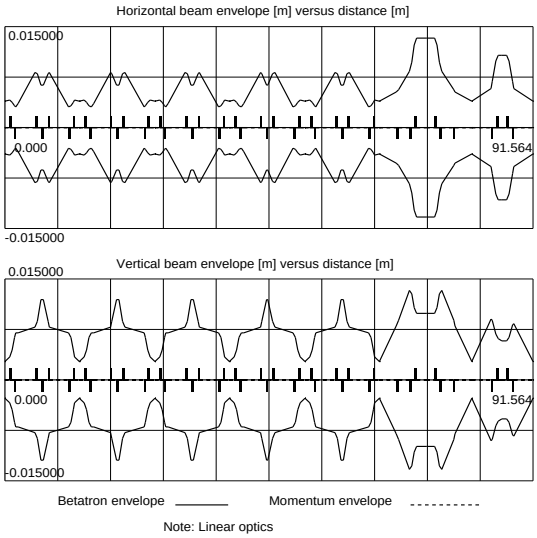

(a) Exit phase-shifter-stepper to dump

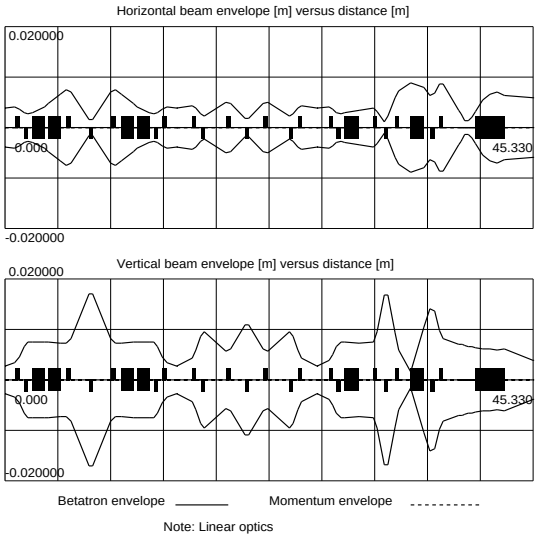

(b) T1 line to 1st proton gantry

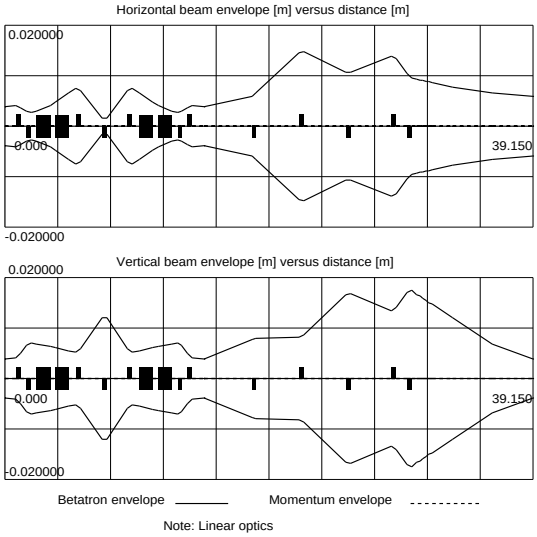

(c) T2 fixed proton line

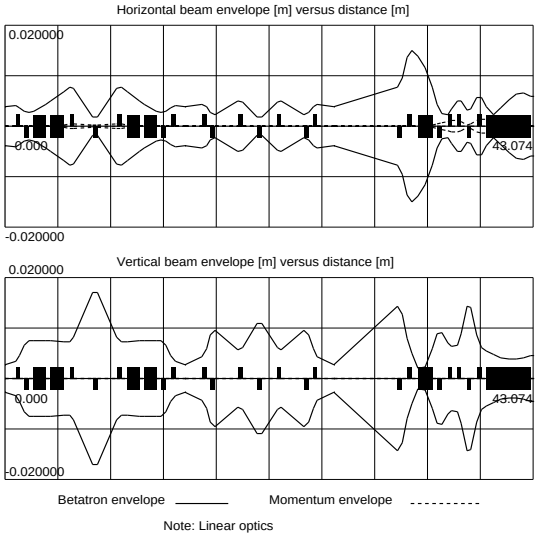

(d) T3 line to 2nd proton gantry

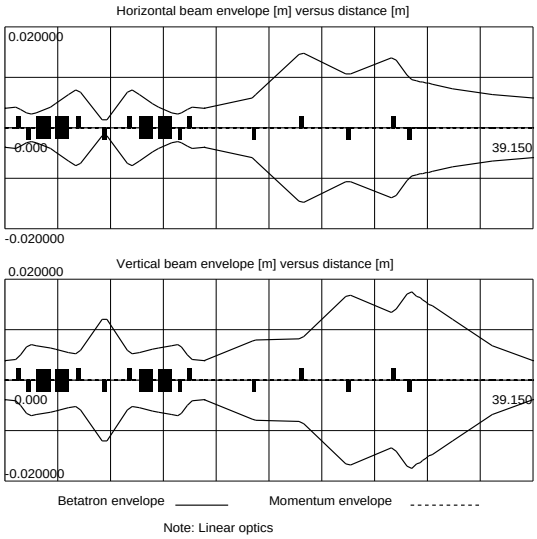

(e) T4 fixed carbon-ion line

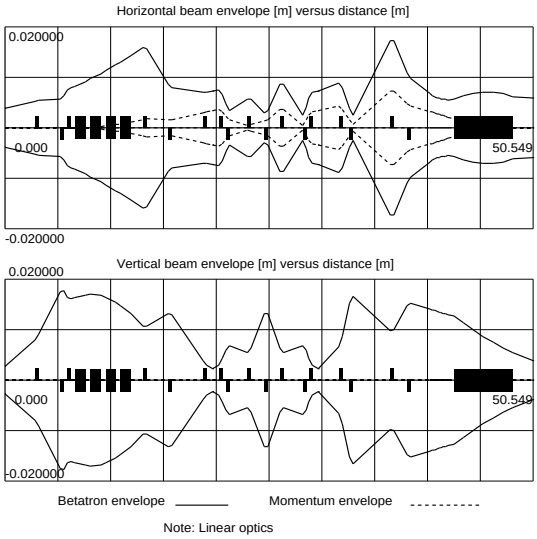

(f) T5 line to carbon-ion gantry

Figure 5.20 Beam envelopes in the extraction lines
[Horizontal envelopes correspond to the 'unfilled' emittance ellipse, vertical envelopes correspond to the smallest spot (4 mm) with the largest emittance (7.1429π mm mrad)]

In addition to the general situation for the aperture in the transfer lines, there are also some special situations that require individual attention and will be discussed in the following sections. These are:

- Aperture limits in the phase-shifter-stepper.
- Chambers in the switching dipoles.
- Chambers in the chopper dipoles.
- Chambers in the raster scanning dipoles.
- Chambers in the final dipoles in gantries with active scanning.

5.5.1 Aperture in the phase-shifter stepper

The phase-shifter-stepper is ultimately limited by beam size. While the betatron amplitudes remains everywhere below ~55 m there is adequate aperture with the largest emittance beam (7.1429π mm mrad). If the closed orbit is well behaved, then betatron amplitudes can technically increase to a maximum of ~95 m before there is beam loss. The performance of the phase-shifter-stepper, as proposed in Section 5.3.3 and specified in Appendix CC, is summarised in Figure 5.21. For the full range of horizontal phase shifts that has been tabulated and for β_z values from 1 to 13.5 m, the beam remains small and comfortably within the 'good-field' region. This covers twice over the needs of all the gantries proposed. The fixed beam lines have been calculated without magnifying telescopes and they require the extended range of β_z values from 2 to 27 m. In this case, there is a corner of the parameter space where, for large β_z and large horizontal phase advance, the β_z-value inside the module can exceed acceptable limits. In practice, this is not a limitation. The useful region up to $\pi/2$ phase shift is very well behaved and adequate. The region up to π phase shift that could conceivably be used, is only affected for large β_z and large emittance, which is the least likely parameter combination. In addition, β_z inside the module still does not exceed the absolute limit of 95 m and it is not excluded that either the range of the module could be extended downwards or the out-of tolerance points could be re-matched with different vertical phase advances. The phase-shifter-stepper can therefore be equipped with the standard extraction line vacuum chamber and quadrupoles.

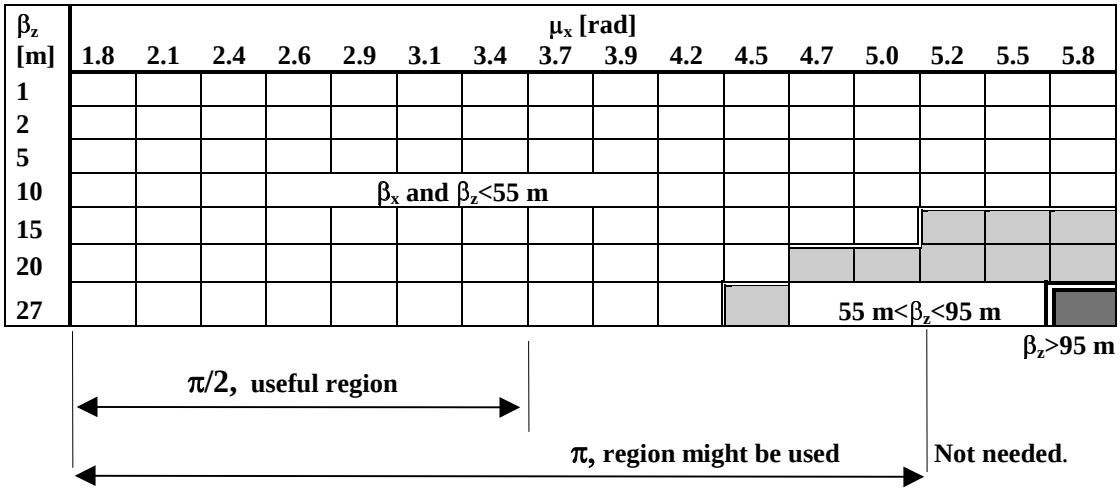

Figure 5.20 Lattice functions in the β_z - μ_x phase space of the phase-shifter-stepper

5.5.2 Aperture in chopper dipoles

The chopper dipole aperture will be based on the general prescription given in Table 5.5 that define a pipe of 70 mm internal diameter in straight sections and quadrupoles. The horizontal beam movement of 14 mm must then be added to this basic dimension in the horizontal plane to give an internal elliptical aperture of 84 mm (horizontal) × 70 mm(vertical). The vacuum chamber must be ceramic, which implies a thick wall of ~7 mm. Allowing for some clearance, the magnet aperture should be a minimum of 100 mm × 86 mm. All four chopper dipoles must be identical with the enlarged aperture, but the chambers in the outer pair of bumpers can be simple ceramic tubes with an internal diameter of 70 mm (as drawn in Figure 5.6).

The chopper magnets will have window-frame yokes with saddle coils. A field quality of a few 10^{-3} will be obtainable over the full aperture. Allowing for the thick vacuum chamber, the alignment clearance and the fact that the beam is rather small at this position, the field quality over the beam region will, in fact, be better than 10^{-3}.

5.5.3 Aperture in the 'Riesenrad' raster scanning dipoles

The raster scanning dipoles are slower than the bumpers for the chopper and can be equipped with thin-walled stainless steel vacuum chambers rather than thick-walled ceramic ones. They will also have laminated iron yokes rather than ferrite yokes and will require a somewhat better field quality. To rationalise the design work, storage of spares etc., a single design for all scanning magnets is proposed (see Appendix Y). The aperture is based on the configuration in the 'Riesenrad' gantry, where three scanning magnets are mounted in the short space of 1.75 m. The maximum beam sizes at the exit to this group of magnets (one vertical and two horizontal) are given below and used to determine the aperture in Table 5.6.

Apertures in the third raster-scanning dipole in the 'Riesenrad'

	Horizontal	**Vertical**
Full beam width* [mm]	±5.8	±8.0
Maximum deflection** [mm]	±13.8	±19.1
Security*** margin [mm]	±5	±5
Aperture for beam [mm] (rounded)	±25	±32
Vacuum chamber (corrugated or ribbed) [mm]	2 × 10	2 × 4
Additional 'poor' field region [mm]	2 × 25	-
Alignment tolerance [mm]	2 × 1	2 × 1
Magnet aperture [mm] (rounded)	±60	±40

* Maximum horizontal beam width calculated with 5π mm mrad 'unfilled' emittance ellipse and full momentum spread of $\Delta p/p = 0.0011$. Maximum vertical beam width calculated at lowest extraction energy $E_z = 7.143\pi$ mm mrad, which is the same for both protons and carbon ions.

** Deflection in last magnet after ±12.5 mrad (vertical) in first magnet and a total of ±25 mrad (horizontal) in the second and third magnets.

*** During set up, the scanning dipoles will be off so that there will be adequate space for closed orbit deviations. In principle, the closed orbit will be made perfect before scanning starts so only a small security margin is needed.

Table 5.6 Apertures in the third raster-scanning dipole in the 'Riesenrad'

The second and third scanning dipoles in the 'Riesenrad' are configured according to Table 5.6. The first dipole kicks vertically and will therefore be turned on by 90°. However, in this magnet the beam deflections are still zero, so the magnet gap height of 80 mm is still more than adequate for the horizontal beam dimension.

5.5.4 'Riesenrad' main dipole

The physical aperture in the 'Riesenrad' dipole is 0.261 m × 0.208 m. During a beam spill, the magnet has a constant field, so the vacuum chamber can be made from non-magnetic, stainless steel and be sufficiently thick to withstand the atmospheric pressure. The chamber has not been studied and the final aperture for the beam can only be nominally set to 0.2 m (horizontal) × 0.18 m (vertical). Whether this aperture is maintained along the whole length of the magnet or whether it is tapered is undetermined and remains an open question for the future design.

5.6 TOLERANCES

Tolerances for beam transfer line magnets are generally less strict than for the ring units. For the basic transfer lines, the field uniformity has been set to $\pm 5 \times 10^{-4}$ for the dipoles and the gradient uniformity has been set at $\pm 10^{-3}$ for the quadrupoles.

The situation is different for the final dipole in a gantry that performs active scanning. If, for example, the distance to the patient is 2.0 m, then an angular error of 0.2 mrad causes a positional error of 0.4 mm (i.e. 10% of the smallest spot size). Since the bending angle in the final dipole is large (90° or 135°) an angular error of ±0.2 mrad implies that the integrated field should not deviate from its ideal value by more than $\pm 10^{-4}$. For such a large dipole, this is felt to be impractical and, consequently, the problem has to be solved in two stages:

- First, set attainable tolerances for the magnet to limit the errors. Calculate the 2D profile to give a good transverse field quality ($\Delta B/B = \pm 2 \times 10^{-4}$), then correct 3D end-fields by measuring the integrated field through the magnet and shimming ($\Delta BL/BL = \pm 4 \times 10^{-4}$).
- Finally, calibrate the magnet with beam and create a correction map that can be applied via the scanning magnets (expected position corrections at edge of aperture ±1 mm).

There is no fundamental reason why these and other errors should not be corrected on-line by the scanning magnets. However, the principle should always be to reduce such errors to an absolute minimum first, in order that the correction to be applied becomes small and relatively unimportant.

5.7 MAGNETIC ELEMENTS

5.7.1 Extraction line dipoles

Switch dipole

There is a single design for the extraction line dipoles. Since they are used as switching magnets in many instances, they have a 'C'-shaped yoke so that the straight-through beam can be easily accommodated. A preliminary design is presented in Appendix W. The dipoles are laminated with 1.5 mm laminations and constructed with end plates. Although eddy current losses and field distortion are not critical problems, the laminations will ensure rapid stabilisation after cycling and field changes. It also standardises the construction of the magnets with the same steel sheet

as will be used for the main ring units. The construction technique with laminations also has the advantage that the steel sheets can be shuffled to ensure uniform magnetic quality.

Gantry dipoles

The Riesenrad gantry dipole is the only gantry dipole that has been studied (see Appendix X). It will be laminated with 2 mm and will be the one exception to the use of 1.5 mm laminations. This choice has been made to limit the elastic deformations of the dipole. Due to the low elasticity- and shear-modulus of the glue between two laminations (compared to steel), the joints are responsible for a softening of the entire dipole causing higher deformations. This weakening is proportional to the number of joints. Increasing the lamination thickness reduces the number of joints and increases the mechanical stiffness. Increasing the mechanical stiffness makes it possible to reduce the dimensions (and weight) of the tie bars and cover-plates that ultimately determine the overall deformation of the structure. The average shear modulus of a dipole made out of 1.5 mm and 2 mm laminations is 2200 kN/mm^2 and 2700 kN/mm^2 respectively (compared to 8100 kN/mm^2 for a solid steel yoke). From the mechanical point of view even higher lamination thicknesses are desirable provided that the same manufacturing quality during the punching/cutting process can be met.

Correction dipole

No study has been made for these units. It is assumed that a scaled version of the main ring correction dipole will be used.

5.7.2 Extraction line quadrupole

Initially, a single design has been proposed for the 130 extraction line quadrupoles (see Appendix V). This preliminary design has straight poles with long roots to accommodate large coils for the high field requirements. The yokes are laminated with 1.5 mm laminations and constructed with end plates. Although eddy current losses and field distortion are not critical problems, the laminations will ensure rapid stabilisation after cycling and field changes. It also standardises the construction of the magnets with the same steel sheet as will be used for the main ring units. The construction technique with laminations also has the advantage that the steel sheets can be shuffled to ensure uniform qualities.

This solution, however, is not ideal. For high fields, the quadrupoles would be better with tapered poles and, when used at lower fields, the yoke appears oversized. A series of 2 or 3 different coils would already be an advantage. More ideally, a second quadrupole with a smaller yoke and coils is needed to satisfy the many low field cases. Fortunately, there is the strong possibility that the injection line quadrupole can be used for this, but a final decision must await the detailed design of all of these units.

5.7.3 Extraction septa

Electrostatic septum

Although the electrostatic extraction septum is in the synchrotron, it forms part of the extraction line from an optical point of view. Fortunately the maximum voltage

is below 100 kV and the power converter is a standard, commercially available item. A first draft of the design of the septum is presented in Appendix U.

'Thin' and 'thick' magnetic extraction septa

The mechanical and magnetic designs for these units are presented in Appendices R and S respectively.

5.8 DIAGNOSTICS

The exceeding low intensities of the beam in the extraction lines make diagnostics difficult and makes this a prime field for the development of new monitors. For the moment, it is assumed that scintillation screens will be installed for general diagnostics and ionisation and multi-wire proportional chambers will be installed in the 'nozzle' just before the patient. However, the exact description of these devices is sure to change over the next few years. Only the instruments in the 'nozzle' will remain permanently in the beam during treatment.

The extraction lines are characterised by many similar modules with big phase advances and it will not be practical to apply criteria of the type applied in synchrotrons (i.e. 5-6 pickups per betatron wavelength). Instead, monitors and correctors for each plane should be positioned in pairs to perform position and angle measurements and position and angle steering at the entry to each module. In addition, it will be necessary to add two correctors per plane in the gantries. In principle, the raster scanning magnets in active scanning gantries could also take account of systematic corrections, but it is better to decouple scanning and steering as far as this is possible. On the assumption that a single monitor can measure in both planes, the total number of monitors and correctors can be estimated as 22 and 40 (respectively). A further and more detailed discussion can be found in Ref 2.

5.9 VACUUM

The vacuum system for the extraction lines requires an average vacuum between 10^{-7} and 10^{-8} Torr. To allow some margin for the extra surface area in monitors etc. and the conduction of pump manifolds, the stricter value of 10^{-8} Torr will be used for the calculations. It is preferable to use several small pumps rather than a few large ones to introduce some tolerance of failure into the system and to limit the excursion between the average and maximum pressures. As for the synchrotron, it is assumed that all elements are vacuum fired at 450°C before installation. The principal out-gassing will then be hydrogen from the bulk metal. No in situ baking will be needed. Additional vacuum pumps will be needed to ensure a good vacuum in the two gantries and two fixed-beam lines that have enlarged chambers for active scanning. Additional pumps will also be to isolate the poorer vacuum of the lines from the ring, to absorb any out-gassing from the chopper dump and to combat the leaks in the rotational joints of the rotators. Seven sector valves will make it possible to isolate each of the five beam delivery lines from main extraction line, to isolate the short section of line that can be removed for the vehicle track around the outside of the ring and to isolate the entire extraction system from the synchrotron. The only non-standard components are five thin windows of large dimension (~20 cm × 20 cm) at the ends of the treatment lines and a total of six rotating joints for the three gantry lines. Table 5.6 summarises the details.

Extraction lines' vacuum system	
Cross-section of the standard chamber	Circular
Average chamber radius [m]	0.035
Length of the line from ring to dump (EX-line) [m]	136
Length of the first gantry line (T1-line) [m]	45
Length of the first fixed line (T2-line) [m]	39
Length of the second gantry line (T3-line) [m]	43
Length of the second gantry line (T4-line) [m]	39
Length of the third gantry line (T5-line) [m]	50
Specific surface area [$cm^2\ m^{-1}$]	2200
Specific out-gassing [Torr $l\ s^{-1}\ cm^{-2}$]	5×10^{-12}
Specific conductance [$l\ m\ s^{-1}$] (H_2 at 25°C)	160
Target average pressure [Torr]	10^{-8}
Ion pump speed [$l\ s^{-1}$]	30
Theoretical pump separation [m]	20.6
Nominal number of pumps	17
Sector valves (exit to synchrotron, vehicle track and entry to each beam delivery line)	7
Additional pumps	
Isolation of poorer vacuum of lines from ring [ls^{-1}]*	1×100
Rotating joints (in T1, T3 and T5 at entry to rotator and between rotator and gantry) [$l\ s^{-1}$]	6×100
Dedicated to active scanning delivery lines [$l\ s^{-1}$]	4×100
Chopper [$l\ s^{-1}$]	100
Mobile roughing pump	TM 80-450 $l\ s^{-1}$

* Already mentioned in Table 3.25 for the vacuum requirements of the ring.

Table 5.6 Extraction lines' vacuum system

5.10 MAGNETIC CYCLE

The magnetic extraction septa, the extraction line and gantries will all be operated on a simpler and slower magnetic cycle than that used in the synchrotron. The synchrotron cycle (see Section 3.3) is of the order of 0.5 Hz and corresponds to the spill repetition rate. All the precision settings are on the upward branch of the hysteresis curve. The extraction line cycle is far slower and corresponds to the treatment time that is measured in minutes. All the precision settings occur on the downward branch of the hysteresis curve. Figure 5.21 schematically compares the two cycles.

When first switched on, the ring and lines should be cycled several times to stabilise their hysteresis loops. In the ring, once treatment starts, the cycle must always be completed before the next injection occurs. In the extraction lines the magnets move incrementally downwards in field level before the next injection occurs. The adoption of this extraction line cycle imposes on the treatment plan that the tumour slices must be irradiated in the strict order of decreasing energy. The incremental changes in the extraction settings from one slice of the tumour to the next make it much easier to change and precisely set the large gantry dipoles. Magnets can be constructed with thick end plates and no thin-walled or ceramic vacuum chambers are needed (except for the chopper and scanning dipoles). This type of cycle would be

compatible with the use of superconducting magnets in the gantries*. Whatever, the cycle, it is important that the magnetic elements are measured on the same cycle that are to execute operationally

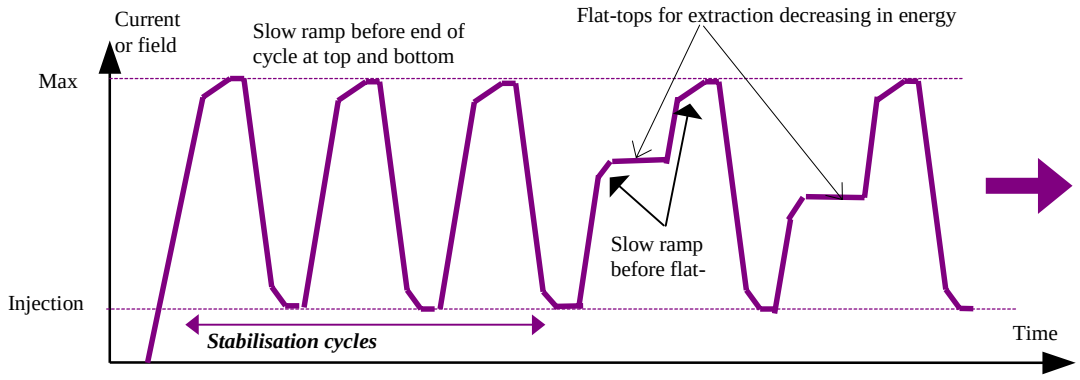

(a) Main ring cycle (precision settings on upwards branch of the hysteresis curve)

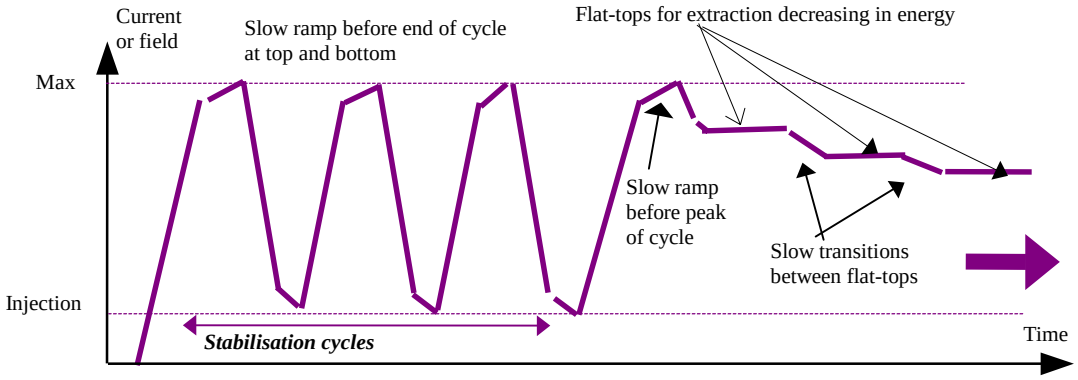

(b) Extraction line cycle (precision settings on downward branch of hysteresis curve)

Figure 5.21 Schematic comparison of the synchrotron and extraction line magnetic cycles

5.11 SECURITY

The security system for irradiating patients will need to be carefully planned. To ensure the efficient use of the centre, it will be necessary to authorise entry to treatment rooms when another treatment room is working with beam. This implies:

- Full shielding between the accelerator complex and the treatment rooms.
- Full shielding between adjacent treatment rooms.
- Double security systems for preventing beam entering a branch line to a treatment room (i.e. T1, T2, T3, T4 and T5)
    1. Interlock on the switching magnets for T1, T2, T3, T4 and T5
    2. Beam stoppers at the entries to T1, T2, T3, T4 and T5 (see Appendix M).
- Hard-wired activation of the beam chopper to cut off the beam in an emergency.

* Superconducting magnets have not been considered because: a) this introduces a totally different technology into an otherwise conventional centre, b) the cooling must be run dc, but the saving in magnet power is only for infrequent 2 minute periods, c) a large iron yoke will still be needed to limit stray fields, d) the liquid helium supply to a rotating magnet is not trivial, e) in the case of a quench, the vent pipe to the exterior presents a problem, f) in the case of a quench, the patient will be subjected to an acoustic shock.

- Hard-wired activation of the internal dump in the ring to dump the beam in an emergency.
- Fail safe chopper and stoppers (i.e. beam is cut off if the power is cut to the safety equipment).

Although the absolute radiation levels are not high, the proximity of staff and visitors to the equipment and the long exposure of the staff require strict radiation security. It will be necessary to have permanent radiation monitoring equipment throughout the complex as well as the individual monitoring of staff members with film badges. This has not been studied in detail, but should not present any fundamental problems.

Proton hazard

The synchrotron is design for carbon-ions of high rigidity (6.35 Tm) and it would be possible for the synchrotron to accelerate protons to about 1.2 GeV. However, such high-energy protons are not needed for therapy. The proposal therefore is to hardware limit the rf cavity frequency to 2.85 MHz. This will allow the carbon ions to reach their highest extraction energy while limiting the protons to 405 MeV. However, it should be realised that the shielding needs to be designed for 405 MeV protons and not the nominal 250 MeV mentioned in the specifications for therapy.

References

[1] P.J. Bryant, AGILE program for synchrotron lattice design, http://nicewww.cern.ch/~bryant.

[2] L. Badano, *Injection and extraction lines instrumentation for PIMMS*, PS/DR/Note 2000-011 (Tech.).

* * *

II-6 MORE ABOUT THE 'RIESENRAD' GANTRY

The optics of the 'Riesenrad' gantry have been described in Part I [1] and Section 5.4.7. The design of the main dipole is described in Appendix X. The quadrupoles are assumed to be the standard quadrupole from the extraction lines. The present chapter looks at the mechanical construction of the gantry and its rotator. An analysis is made of alignment and mechanical deformation errors and their impact on the beam optics. The issues of alignment and safety are discussed.

6.1 MECHANICAL CONCEPT

The principle of the 'Riesenrad' gantry is shown in Figure 6.1 and compared to the conventional isocentric gantry. In the 'Riesenrad', a 90° dipole is placed at the end of the transfer line and rotated around the incoming beam axis. The magnet can be set at any angle and the beam will be deflected in the corresponding direction. The patient must, in this case, be placed eccentrically and follow the dipole rotation.

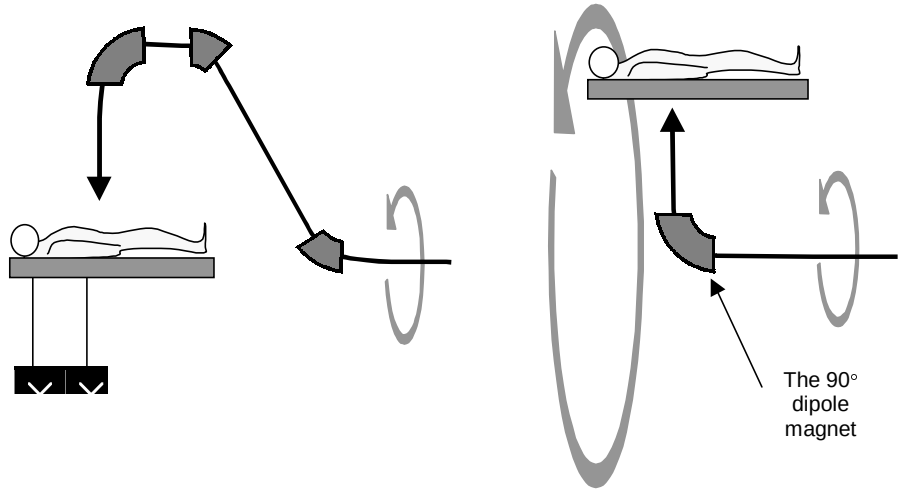

(a) Conventional isocentric gantry (b) Exocentric 'Riesenrad' gantry

Figure 6.1 Principles of the isocentric and exocentric gantries

There are several technical concepts of the 'Riesenrad' principle [2]:

- ***Wheel gantry***, in which the counter-balance weight, magnet and the patient cabin are rigidly encased in a large wheel, but the patient room can rotate within its support.
- ***Centrally supported gantry***, in which the counter-balance weight, magnet and patient cabin are rigidly fixed along a centrally-supported girder and the patient cabin can rotate within its support.
- ***Cantilever gantry,*** which is an extreme approach to the centrally-supported gantry.
- ***Independent-cabin gantry***, in which the counter-balance weight and magnet are in a smaller structure and the patient cabin has an independent telescopic support.

The key issues are related to the weight of the gantry:

- The design of the gantry is driven by the desire to minimise elastic deformations. Consequently, for a steel structure, the self weight represents a major part of the total load on the structure. There is a point where additional material does not lead to an increase in rigidity.

- ***Support rings*** and rollers have high specific loads and some gantry types will require sophisticated designs. Very large rings, as needed in the wheel gantry are difficult and expensive to produce.

Assuming that a mechanically viable design exists, there are secondary issues such as access in emergencies, space around the patient couch, total volume of the gantry room with shielding and so on. The preferred mechanical solution with respect to all of these issues is the *independent-cabin gantry*. This design, which is schematically shown in Figure 6.2, has the advantageous features of:

- The central cage containing only magnets and counter-balance weight is relatively light (support structure 40 t, counterweight 23 t, the dipole 62 t and scanning magnets 1.5 t making a total of ~127 t) and elastic deformations along the beam trajectory are kept below 0.1 mm.
- The front support ring is 4.3 m outer diameter and the rear support is a commercially available bearing ~ 0.7 m internal diameter.
- Radial loads on the support are acceptable (front ring 2 × 480 kN and rear bearing 1 × 400 kN).
- The patient cabin is spacious and essentially unlimited in size (compared to the situation in say the wheel gantry) and in a practical design would probably not exceed 25 t.
- The patient cabin is a low-precision lift structure with a telescopic floor. Only the patient couch requires precision alignment and this is done photogrammetrically with respect to the dipole.
- The inner volume of the gantry room is 1700 m^3.
- The patient cabin has continuous contact with the lateral wall of the gantry room and, by virtue of this, has permanent emergency access by a staircase at all times.

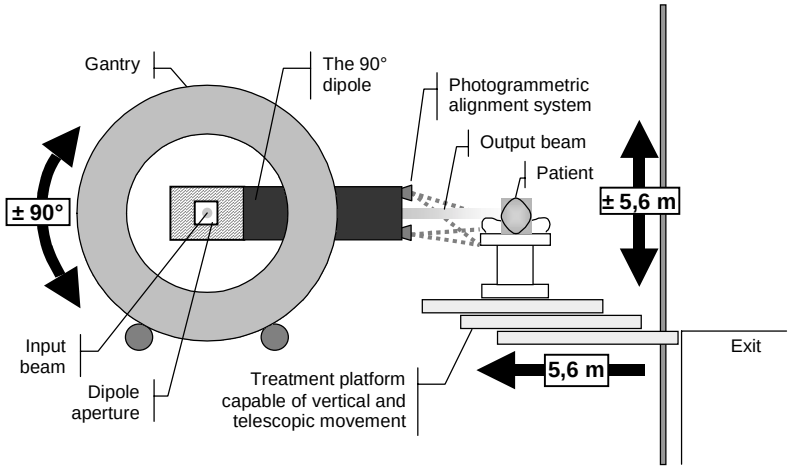

Figure 6.2 'Riesenrad' gantry with movable treatment platform
[The patient is positioned corresponding to a particular dipole angle by vertical and horizontal translations of the treatment platform. The dipole can rotate ±90° and the patient couch can rotate 360° around its vertical axis so as to achieve effectively any treatment angle.]

6.2 STRUCTURAL DESIGN

6.2.1 The main 90° dipole

The structural studies were based on the initial assumptions for the 90° dipole of a field of 1.8 T, a bending radius of 3.6 m, a cross-section of 1.5 m × 1.0 m and a weight of 60 t. The details of the final magnet are in very close agreement and can be found in Appendix X. Figure 6.3 shows the cross-section of the final design with the additional side and top 'cover' plates that have been added for extra rigidity.

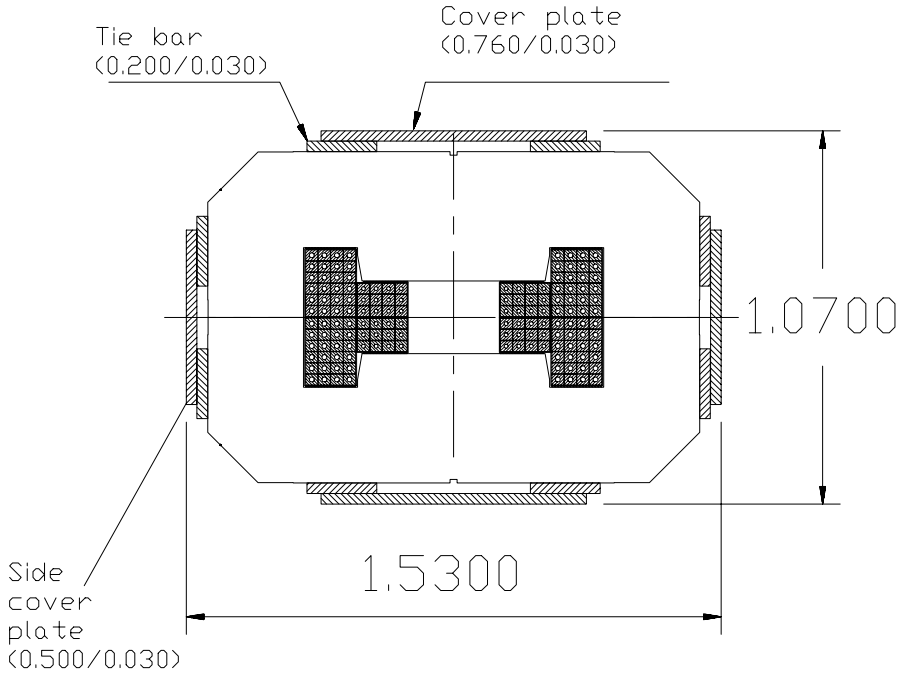

Figure 6.3 Cross section of the 90° dipole

The 90° dipole is made out of two half-yokes. Each half-yoke comprises several laminated segments (2 mm thick laminations). A segment is constructed by gluing the laminations and then machining the block to the correct 'wedge' angle. When assembling a half-yoke, the segments are first glued and then welded between thick end plates by tie bars. The low mechanical stiffness of the glue is responsible for the comparatively low shear and Young's moduli of the iron yoke (for instance shear modulus = 27000 N/mm^2 compared to 81000 N/mm^2 for a solid iron yoke). The dipole is reinforced by a 'corset' of tie bars and cover plates to hold the two halves together and increase rigidity (see Figure 6.3). This 'corset' adds ~5 t to the weight of the dipole, while taking approximately one third of its bending and shear force. Varying the two supports of the dipole inside the gantry structure showed that the optimum support positions were around 1 m from the two faces of the dipole. Supported at these positions, the reinforced dipole could be regarded as being rigid (maximum deformations smaller than 0.03 mm) and performing rigid body movements only.

6.2.2 Support structures

Central cage

The central cage (see Figure 6.4) supports the three scanning magnets (1.5 t maximum) and the large 90° dipole (62 t). The total weight is ~127 t, of which 23 t are due to the counterweight. The design of the central cage is driven by the desire to minimise sagging of the dipole no matter what gantry position is considered.

Approximately half of the dipole's weight is taken directly by the front *ring*. Unlike conventional isocentric gantries, this ring does not have to provide a large aperture to accommodate the treatment area. Instead, it is an extremely rigid cylindrical box (outer diameter 4.3 m) with a comparatively small 'window' to allow

the dipole to enter the cage. Depending on the gantry rotation, the other half of the dipole load is taken by the two *transverse shear walls* (vertical gantry position) or a pair of *'balancing tongs'* (horizontal gantry position). Each of the truss-like tongs transfers its balanced load (dipole on one side, counterweight on the other) via the central diagonals and the inner girder onto the *main shear wall*. The outer girder is free to glide over the main shear wall (i.e. no mechanical connection). As a consequence, a relatively low force, which is applied via the *stiffening struts*, is sufficient to compensate elastic deformations on the dipole-side of the structure and keep the magnet in the desired horizontal position. The front ring rests on two pairs of *rollers* of diameter 0.6 m that withstand a normal force of 240 kN each. The *rear bearing* provides a second support that is a standard tapered roller bearing unit. Consoles guide the forces to the (diaphragm) walls of the building. A *front structure* cantilevered out from the front ring towards the incoming transfer line supports the scanning magnets.

Patient cabin

The patient cabin is an independent structure (see Figure 6.4) with no mechanical connection to the central cage. The central cage therefore avoids an equivalent increase in its counterweight and is relieved of the task of holding the treatment room rigidly at a large radius. This affords a considerable reduction in the total weight and moment of inertia of the central cage, which is consequently more rigid and easier to build.

The exact alignment of the patient couch and the control of the 'gantry radius' (5.527 m) is guaranteed by a photogrammetric system that automatically and actively moves the patient table with four degrees of freedom (*x y, z* and rotation about vertical axis). Reflectors on the patient couch are monitored by four cameras attached to the face of the dipole, which calculate the relative position with an accuracy better than 0.1 mm (σ). Only a moderate positioning accuracy of the cabin itself is required. The patient cabin travels vertically up to $\pm$5.6 m with respect to the entrance level by using two guide rails on each side of the cabin that are fixed to the building walls. The lateral movement is assured by a horizontal telescopic motion of the treatment platform by a maximum of 5.6 m. Access to the treatment platform is possible at all times by a lift. The telescopic action of the treatment platform keeps it in constant contact with the back wall of the shielded enclosure on which a staircase is mounted for emergency access.

Rotator

From the mechanical point of view, the 'rotator' is a trussed girder, 10 m long with a square cross-section (1.2 m diagonal) supporting seven quadrupoles. A similar structure holds the four quadrupoles between the rotator and the gantry. Each of these structures is supported by sets of rollers. The maximum elastic deformations are lower than 0.05 mm (vertically downward). The weight is about 2.5 ton each (not taking into account the quads, which are ~170 kg each).

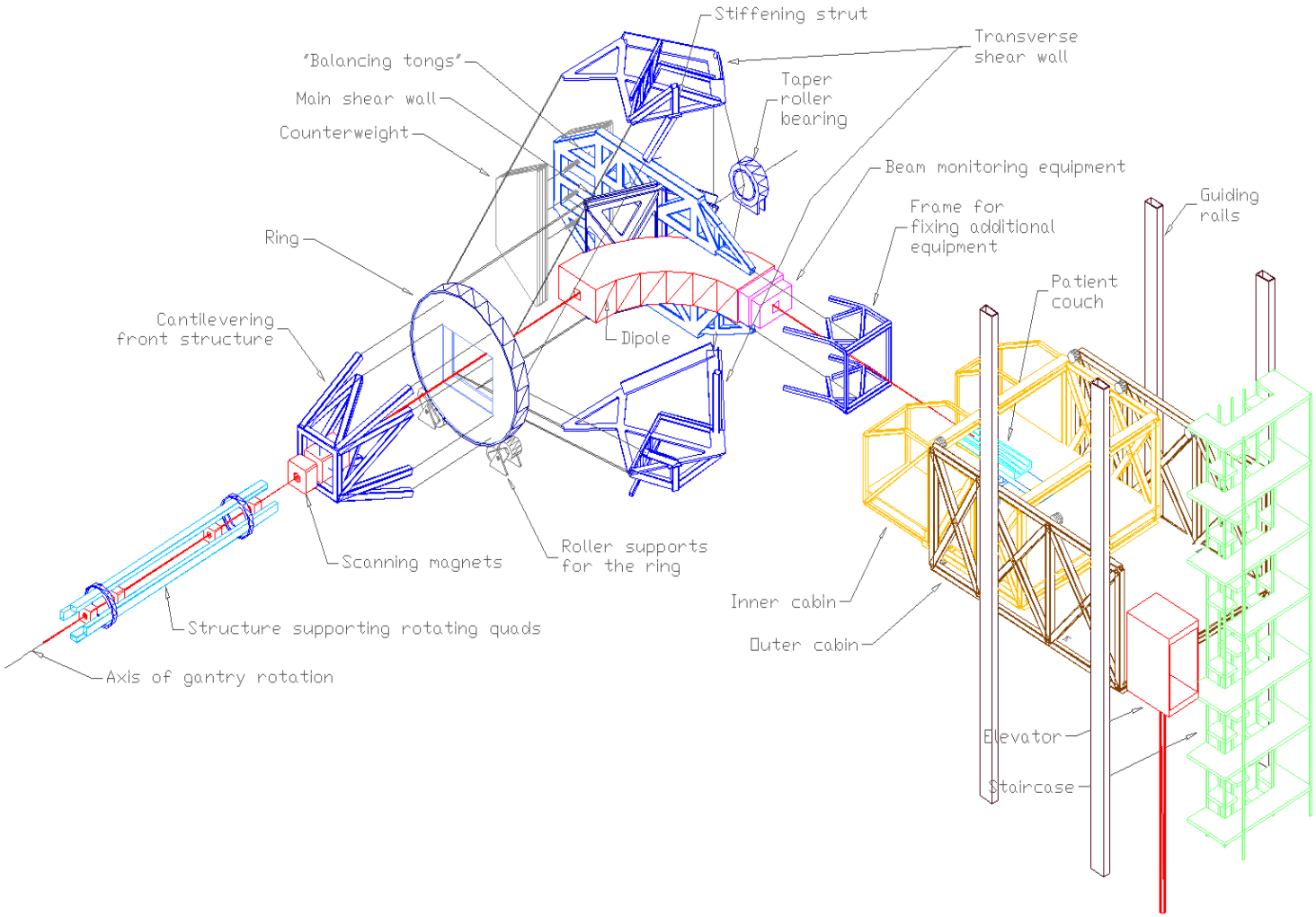

Figure 6.4 Principal elements of the gantry structure

6.3 OPERATIONAL PROCEDURE

Figure 6.6 shows the gantry in several characteristic positions during a standard treatment with a lateral field. The patient will find himself on a specially prepared couch that can be shifted in all three dimensions and rotated around the vertical axis. The beam can be directed into the treatment room at any angle over 180 degrees from pointing vertically downwards to vertically upwards. The different kinetics of the 'Riesenrad' gantry (compared to conventional gantries) affect treatment procedures. Opposed fields do not require the rotation of the gantry, but instead the rotation of the patient couch horizontally around the (local) isocentre. Vertex fields are achieved when the patient bed is aligned in the beam direction. As can be seen from Figure 6.5 the gantry virtually supports 4π-irradiation.

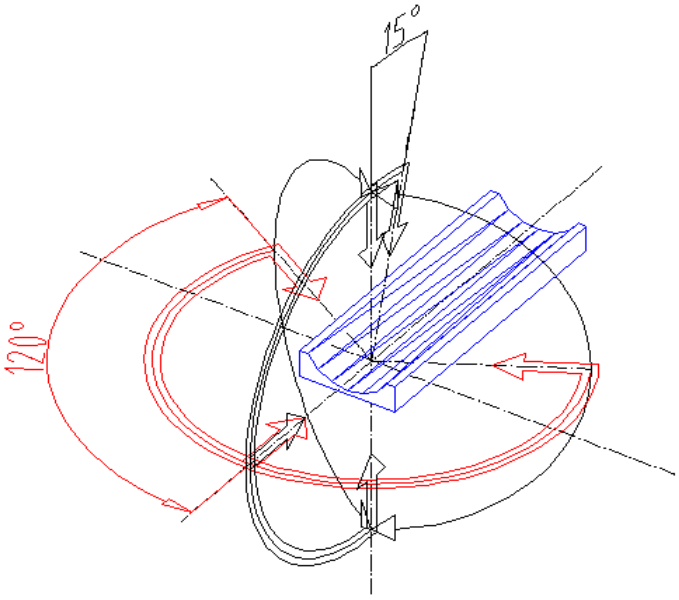

Figure 6.5 Range of possible treatment angles
[Cabin and patient positioning system allow a 360° table rotation. In combination with a gantry rotation of +/-90° the theoretical 4π-irradiation is limited only by the need to avoid collisions between the 'nozzle' and patient table]

6.4 FLEXIBILITY

Changing the dipole is possible without dismantling the gantry. For this purpose, the central cage is moved to the horizontal position, the front structure is dismounted, and the dipole is horizontally moved (rotated) out of the structure into a small hall between switchyard and the gantry, where there is a removable lateral wall. Initial installation will also be done in this way.

The large surface area in the patient cabin guarantees maximum flexibility for the positioning of medical equipment, facilitates the setting-up of the patient and provides a generous working space for handling devices (in particular, the bulky patient moulds). A CT scanner that is directly accessible by the patient positioning system can be placed inside the cabin. Cabin loads can be increased without affecting the alignment procedure and precision. The 2 m drift between the dipole and patient facilitates collision prevention. Up to 0.8 m of this drift can be used to mount instruments for beam position monitoring and dose verification.

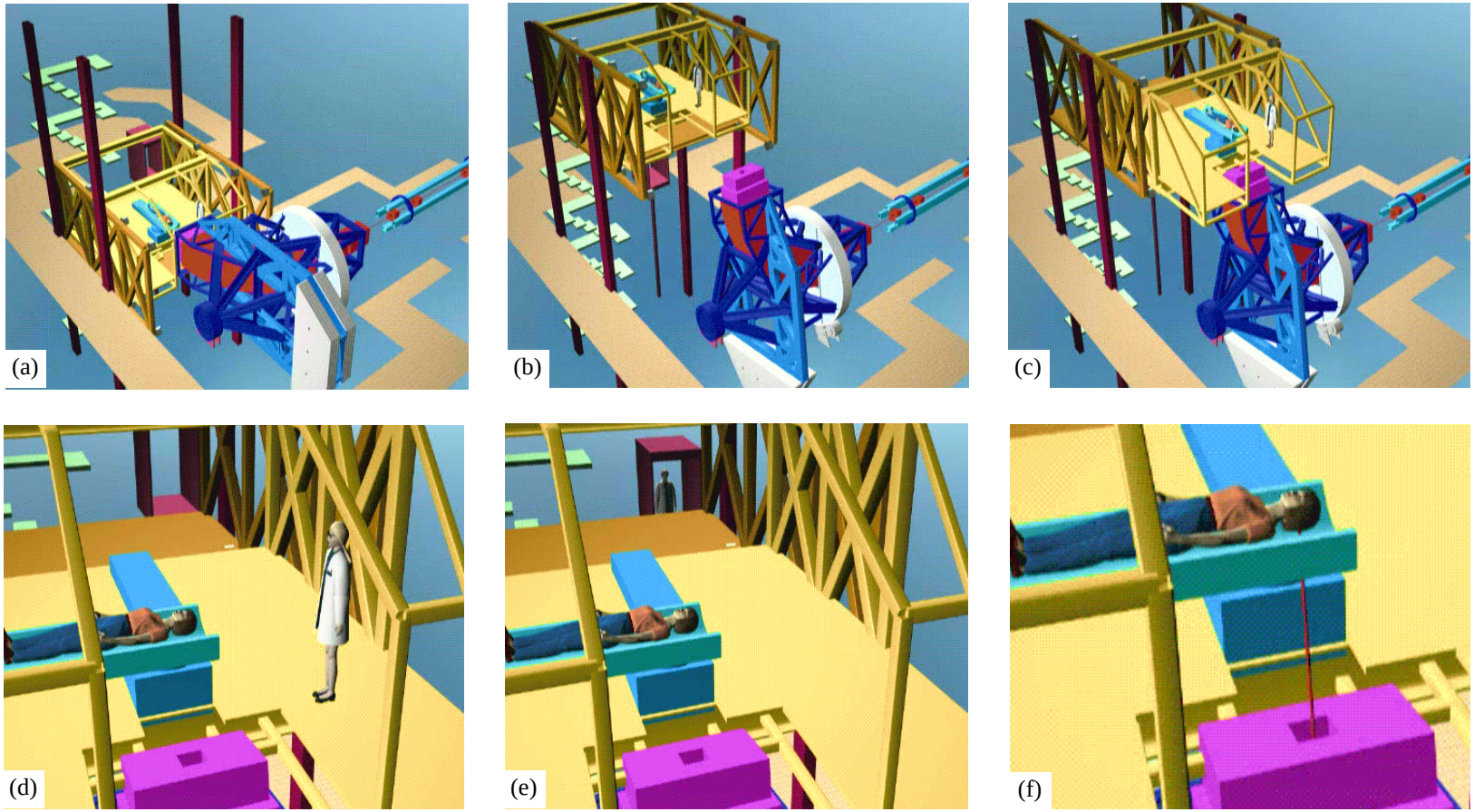

Figure 6.6 Standard treatment with a lateral field
[(a) Gantry in reference position. (b) Central cage in treatment position and cabin with patient and personnel lifted. (c) Patient cabin telescoped forward. (d) Patient couch rotated into treatment position. (e) Personnel leave the room by the rear lift. (f) Irradiation starts.]

Since the rotator, gantry quadrupole structure, central cage and patient cabin are independent structural systems, they can, to a certain degree, be optimised, installed and tested separately. The design offers, at a later stage, the possibility of having a second patient cabin mounted diametrically opposite the first one provided that the gantry enclosure is made big enough. The gantry would then serve the two treatment cabins alternately.

6.5 SAFETY

For any gantry system, two safety aspects are of crucial importance:

- Quick access to the patient during all modes of operation.
- Avoidance of collisions between movable parts and the patient.

These issues are particularly decisive for exocentric gantries where the patient is moved in space to the final treatment position before irradiation. The 'Riesenrad' gantry guarantees constant access by providing two independent active systems to connect the entrance level (chicane) and the treatment position. First, the patient cabin with a maximum travelling time of ~60 s and, second, the elevator with a maximum of 5.6 m to travel in ~15 s. In the event of a complete system breakdown, access via the staircase is always possible and emergency procedures do not have to rely on the availability of any mechanically-driven system.

Collision between the cabin (including the patient table) and the gantry has to be avoided calling for the possibility of rapid gantry stops. The situation can be ameliorated by the following guidelines:

- The central cage and the fully retracted patient cabin can be moved independently (requiring a minimum free drift without any monitoring equipment of 1.2 m in front of the isocentre.
- The central cage is only rotated when the patient cabin is in the fully retracted position.
- The patient cabin and/or central cage are only moved when the patient positioning system is in its reference (backward) position (highest priority).

Since the gantry rotation is restricted to ±90°, the gantry speed (and therefore the angular momentum to be absorbed) can be relatively low.

6.6 STRUCTURAL ANALYSIS

The structural analysis was performed with the software CUBUS [3], using the modules Statik-3 (analysis of space trusses) and Fagus-3. The steel grade is S355, the joints of the analysed static model were assumed to be rigid, shear deformations were taken into account (increasing the deflections by approx. 10%). Because of the slow rotation of a gantry, the structure was analysed as being static. A massless beam cantilevering perpendicularly from the 90° dipole aperture indicated the movements of the local isocentre.

Due to the high-precision requirements, the structural and mechanical design of the ion gantry is governed by the permissible deflections and, generally, no problems concerning maximal stress and stability were encountered (i.e. deformation-driven design). Actual stress levels in the members rarely exceed 10 N/mm^2, only a few highly-loaded struts of the tongs show maximum stresses of about 20 N/mm^2.

Consequently, the analysis was carried out applying safety factors of 1.0 for resistances and loads.

6.6.1 Elastic deformation

Based on the results of the structural analysis, one can get an idea of the mechanical misalignment at the isocentre (Figure 6.7) and the deformed beam path inside the gantry (Figure 6.8).

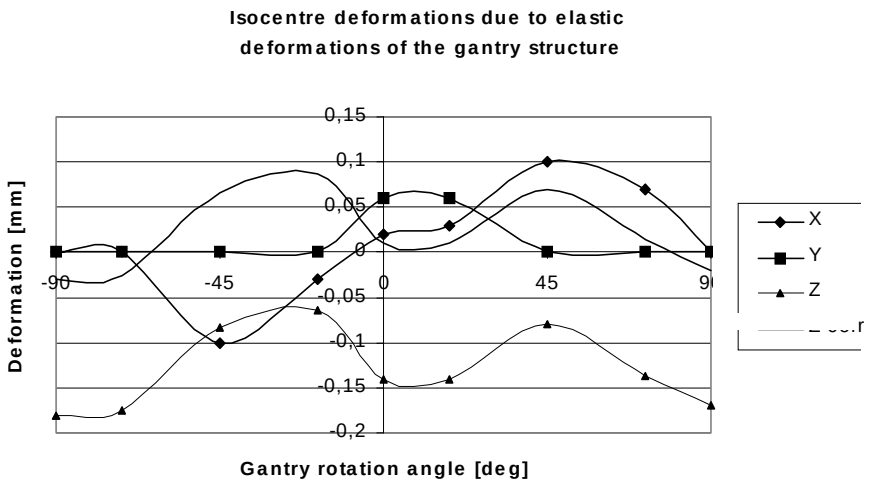

Figure 6.7 Mechanical misalignment of the isocentre due to elastic deformations of the gantry structure (in global room co-ordinates)

Figure 6.8 plots the calculated vertical deflection (*Z*) along the beam line due to elastic deformation of the gantry structure at various gantry angles. Note that this mechanically deformed path represents the sagging of the beam transport elements and does not take into account any ion-optical consequences of these deformations. This is studied separately and reported in Section 6.7. The comparatively uniform vertical displacement of the whole beam line in the gantry and its relative independence of angular position yields the opportunity to slightly lift the whole structure (by 0.15 mm) at the bearings in order that only the differential deformations of about ±0.1 mm become visible (compare *Z-corr* in Figure 6.7). The comparatively large deformations (up to -0.25 mm vertically and 0.03 mrad rotationally around the horizontal axis) occurring at the scanning magnets, are non-critical, as their influence on the eventual misalignment of the particle beam is negligible provided that the beam stays in the 'good-field' region of the scanning magnets.

Deformations in the two other directions (*X* and *Y*) also show values below ±0.1 mm, hence, from a mechanical point of view, one can suggest that elastic deformations in any direction and at any point along the beam trajectory inside the gantry will barely exceed ±0.1 mm.

Deformations of the treatment-platform are irrelevant because the patient positioning system and the photogrammetric alignment system will ensure their correction before treatment starts.

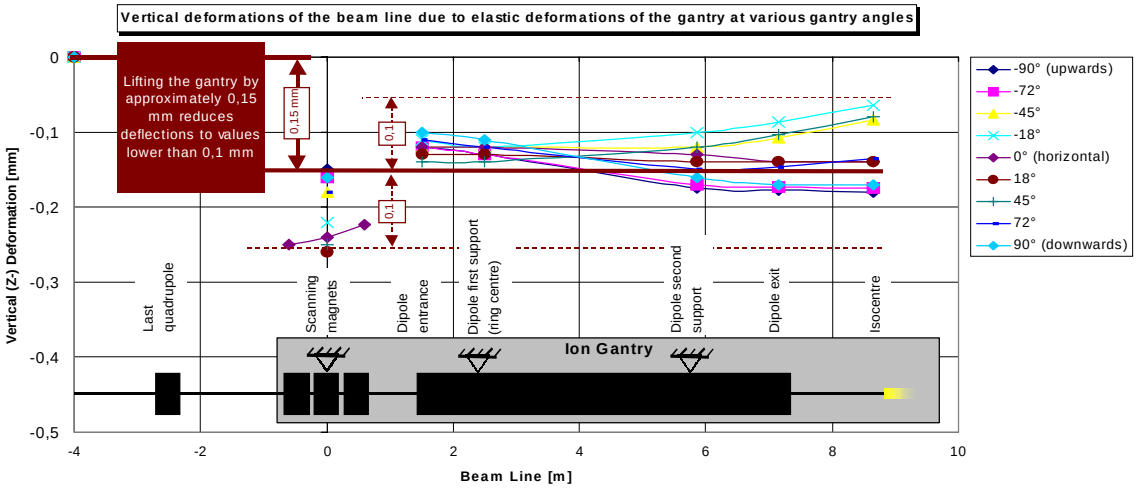

Figure 6.8 Vertical elastic deformation of the beam line inside the gantry
[The deformed shape of the dipole and the sagging of the central scanning magnet are indicated for nine different gantry angles, the position of the other two scanning magnets is only shown for the horizontal gantry position]

6.6.2 Temperature effects

It is foreseen to maintain the temperature in the gantry room within ±1 K. On this basis, the following temperature-related effects were investigated:

- ***Uniform temperature rise by 1 K in the gantry room***. This lifts the centre of the front ring by approximately 0.05 mm, the isocentre rises about one third of this value.
- ***A temperature gradient of 2 K from the lower (-1 K) towards the upper part (+1 K) of the gantry room***. Depending on the gantry angle the effects vary, however, they are of the same order of magnitude as for the uniform temperature rise (maximum deformation 0.03 mm, maximum rotation 0.01 mrad).
- ***A heating of 1 K of the dipole relative to the gantry structure***. The resulting effect is quite sensitive to the design (elasticity) of the dipole fixations. Maximum values are 0.04 mm/0.005 mrad.

6.6.3 Other sources of alignment errors

The calculated elastic deformations affecting the quadrupoles, the scanning magnets and the main dipole positions can be used to adjust the transfer matrices and calculate the actual (mis)alignment of the beam spot at the isocentre for every gantry angle (see Section 6.7). Ultimately, these systematic errors will be measured and listed in a correction map and can be fully compensated via the patient positioning system or the scanning magnets. This principle, called ‘mapping’, also applies for the correction of other systematic errors such as manufacturing errors, initial alignment errors and the imperfections of the magnetic field inside the main dipole. Long-term (systematic) effects like differential settlement of the building (to be detected by a system of water levels) or wear of the mechanics will call for a ‘re-mapping’ from time to time. Unfortunately, such a feed-forward correction is not feasible for random errors. The main random error contributor will be temperature effects. Other sources of random errors (which are smaller and were therefore not taken into account) are backlash of drive mechanics, free-play in bearings and ripple in the power supplies.

6.7 BEAM POSITION ERROR ANALYSIS

6.7.1 Beam transport system of the 'Riesenrad' gantry

The lattice functions and geometry of the beam transport to and in the 'Riesenrad' gantry are described in Section 5.4.7. The part that concerns the present analysis starts at the entry to the rotator and continues to the local isocentre at the patient (see Figure 6.9). Upstream of this point, the magnets are all static and mounted on individual stands directly on the floor. Downstream of this point, the magnetic elements are supported in three different rotatable structures that suffer elastic deformations and other errors. It is assumed that the monitors and steering units in the upstream line will guide the beam into the rotator perfectly on axis.

Neither the gantry nor the rotator is involved in the control of the beam size at the isocentre. This task is accomplished by the dedicated phase-shifter-stepper in the upstream transfer line (see Section 5.3.3). This means that changing the beam size will not affect the position of the beam spot because the optical settings are constant. However, the overall transfer matrix from the rotator entrance to the isocentre is a function of the gantry angle α, because an angle $\alpha/2$ appears between the exit of the rotator and the entrance of the gantry. Thus, rotation can affect the sensitivity of the optical system to position errors.

6.7.2 Error analysis

General considerations

The present analysis has been restricted to errors leading to a wrong beam position at the gantry isocentre, which is the most critical aspect of the gantry beam transport system. The effects causing focusing errors such as deviations from an exact beam size or deformations of a round beam spot have been neglected. Only the misalignment of beam transport elements that causes a deviation of the beam from the optical axis has been considered. The beam transport elements are assumed to be perfectly manufactured, correctly powered, having an ideal field quality, but displaced along and/or rotated about each of the local co-ordinate system axes *x, y,* and *z* (see Figure 6.9).

The misalignments have been classified into two categories: *systematic* and *random*. *Systematic misalignments* are caused by deformations of the gantry and rotator support structures. The main feature of systematic misalignments is their short-term reproducibility as a function of the gantry angle. Long-term effects like building or ground movements are not considered and must be compensated by periodic re-alignment of the whole system. *Random misalignments* represent all possible effects with no reproducibility as a function of the gantry angle. A source of random misalignments could be temperature fluctuations, fabrication imperfections of the gantry supporting ring[*], backlash of bearings and motors, etc. These misalignments are expected to have a gaussian distribution which is superimposed on the systematic misalignments. The position of each beam transport element is therefore characterised by a particular value of the systematic misalignment (element-specific) and a standard deviation of the random misalignment distribution. The situation is illustrated in Figure 6.10.

[*] It could happen due to slippage that the support rollers and ring will not have the same relative positions each time a particular gantry angle is set.

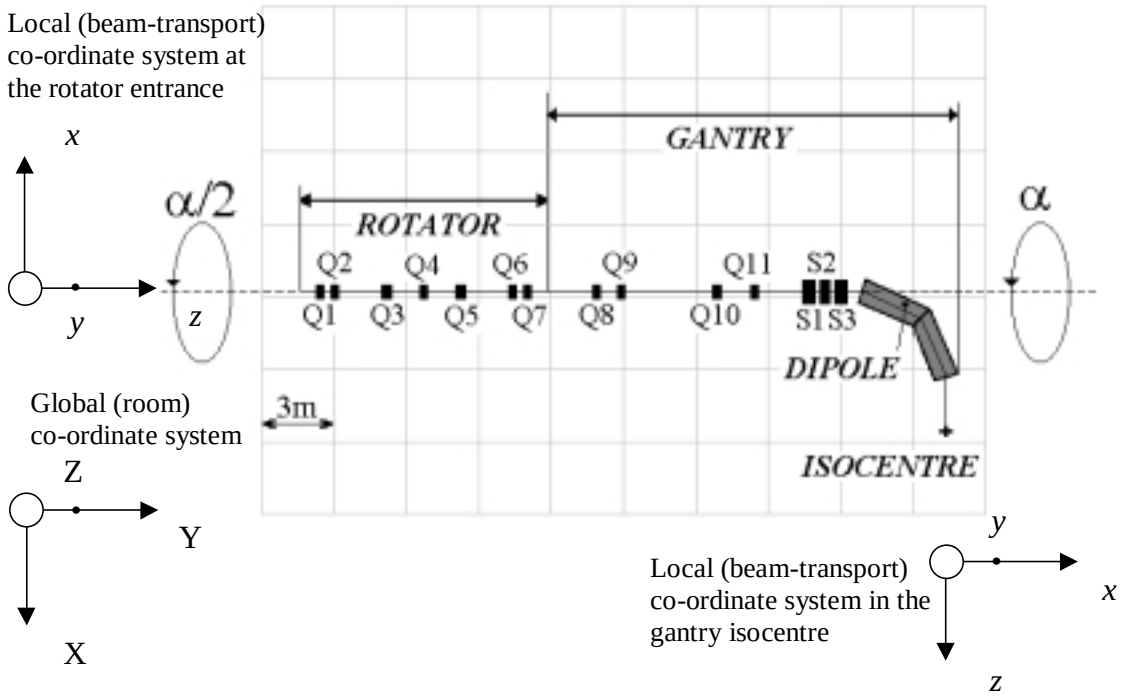

Figure 6.9 Beam transport system of the 'Riesenrad' gantry including the rotator [Rotator = 7 quadrupoles (Q1-Q7) in one rotating structure, Gantry = 4 quadrupoles (Q8-Q12) in one rotating structure, Scanning magnets (S1, S2, S3) and main dipole are in the central cage. Global (room) and local (beam-transport) co-ordinate systems are indicated.]

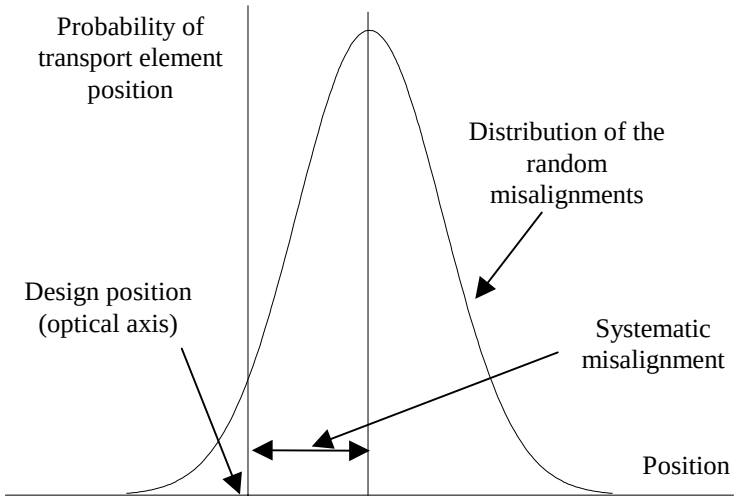

Figure 6.10 Position probability distribution of a beam transport element showing the systematic and random misalignment components

Effects of misalignments

A misaligned quadrupole causes a transverse 'kick' to the beam, which can be calculated from the transfer matrix of the quadrupole:

$$\begin{pmatrix} x_1 \\ x_1' \\ y_1 \\ y_1' \end{pmatrix} = \begin{pmatrix} \cos\sqrt{k}L & \frac{1}{\sqrt{k}}\sin\sqrt{k}L & 0 & 0 \\ -\sqrt{k}\sin\sqrt{k}L & \cos\sqrt{k}L & 0 & 0 \\ 0 & 0 & \cosh\sqrt{k}L & \frac{1}{\sqrt{k}}\sin\sqrt{k}L \\ 0 & 0 & \sqrt{k}\sin\sqrt{k}L & \cosh\sqrt{k}L \end{pmatrix} \cdot \begin{pmatrix} x_0 \\ x_0' \\ y_0 \\ y_0' \end{pmatrix} \qquad (6.1)$$

for a quadrupole which focuses in the (x, z) plane, where x_0, x_0', y_0, y_0' are the particle co-ordinates at the entrance, x_1, x_1', y_1, y_1' are the co-ordinates at the exit, L is the quadrupole effective length [m] and k is the strength [m^{-2}] defined as $k = g/(B\rho)$ where g is the gradient [T/m] and $B\rho$ is the magnetic beam rigidity [Tm]. For a transverse misalignment Δx, Δy one gets for the kick, by putting $x_0 = -\Delta x$, $x_0' = 0$, $y_0 = -\Delta y$ and $y_0' = 0$, (see Figure 6.11(a)).

$$x_1' - x_0' = \left(\sqrt{k}\sin\sqrt{k}L\right)\cdot \Delta x \qquad (6.2)(a)$$

for the focusing plane and

$$y_1' - y_0' = \left(-\sqrt{k}\sinh\sqrt{k}L\right)\cdot \Delta y \qquad (6.2)(b)$$

for the defocusing plane of the quadrupole. Note that the misalignment of a magnet which is positive in the local beam co-ordinate system causes the reference particle to be negatively displaced with respect to the optical axis of the misaligned magnet, hence $x_0 = -\Delta x$ and $y_0 = -\Delta y$.

When tilting the magnet by angles R_x (about x-axis) and R_y (about y-axis), then x_0=0, x_0'=$-R_y$, $y_0 = 0$ and $y_0' = +R_x$ (see Figure 6.11(b)). The kicks are given:

$$x_1' - x_0' = \left(-\cos\sqrt{k}L\right)\cdot R_y - (-R_y) = (1 - \cos\sqrt{k}L)\cdot R_y \qquad (6.3)(a)$$

for the focusing plane and

$$y_1' - y_0' = \left(\cosh\sqrt{k}L\right)\cdot R_x - R_x = (\cosh\sqrt{k}L - 1)\cdot R_x \qquad (6.3)(b)$$

for the defocusing plane. Similarly, the effects of dipole misalignments, which are basically geometrical focusing and/or trigonometric transformations between the local co-ordinate systems at the dipole entrance and the dipole exit, can be calculated.

Systematic and random misalignments must be treated differently. The systematic misalignments represent the situation when all elements are misaligned by a known amount. For each gantry angle, the elements have definite positions different from the ideal design positions and the whole beam line represents a certain particular combination of element misalignments. The position of the beam in the gantry isocentre is obtained by tracing the beam through this misaligned beam line by a computer code.

The random misalignments are interpreted as an uncertainty of the actual element position. In other words, the element position is given a certain probability distribution, which is assumed to be gaussian. All misalignments in all elements are

assumed to be independent and their individual contributions to the beam displacement are added quadratically. If the parameters of the element misalignment are taken as representing one standard deviation of the misalignment distribution, then the calculated beam position represents one standard deviation of a beam position probability distribution.

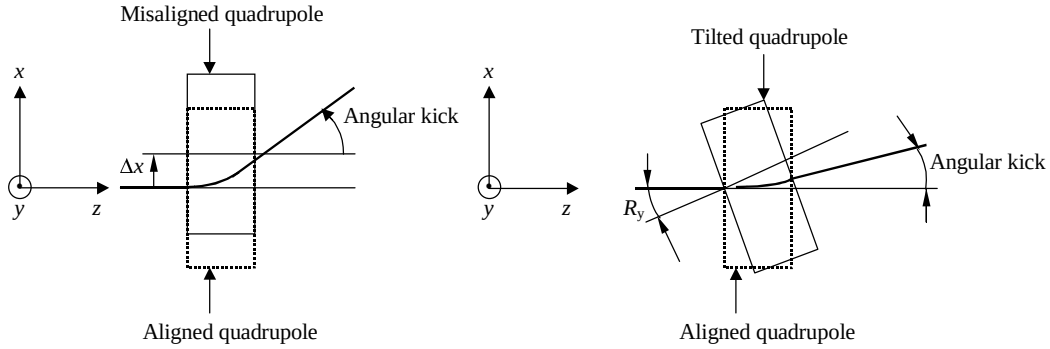

(a) Transverse shift (b) Transverse tilt

Figure. 6.11 Effects of a misaligned quadrupole lens
[Note that the outputs given by the transfer matrix of the quadrupole are in fact related to the optical axis of the misaligned element and have to be properly converted to the co-ordinate system following a design trajectory.]

6.7.3 Beam transport calculations

The beam transport calculations were performed by two computer codes using different strategies for simulating the misalignment effects. TRANSPORT [4] calculates first all individual contributions for all elements and then sums them. WinAGILE [5] generates many lattices each representing a certain particular combination of misalignments and traces the beam through each lattice. The beam positions at a specified point of interest are collected and statistically evaluated. An excellent agreement between the two computer codes has been observed.

Systematic misalignments

Typical, and probably the dominating component, of the systematic misalignments are the elastic deformations of the gantry support structure. The elastic deformations were calculated by the computer code CUBUS [3] and converted from the global (room) co-ordinate system to the local (beam-transport) co-ordinate system that follows the bends and rotations of the beam line. In the local co-ordinate system, the *z*-axis always points in the beam direction and the [*x*-*z*] and [*y*-*z*] planes at the dipole exit are identical with the bending and non-bending planes, respectively, independent of the angle of gantry rotation (see Figure 6.9). The global (room) co-ordinate system is fixed and does not follow the gantry rotation.

The results of the beam transport calculations showing the response of the system to the elastic deformation misalignments are shown in Figure 6.12. The position of the beam-centre in the gantry isocentre is given in the local (beam-transport) co-ordinate system for different angles of gantry rotation from –90° to +90° in 10° steps. Three sets of data are presented corresponding to the misalignment of the quadrupoles alone, the gantry dipole alone and all elements together.

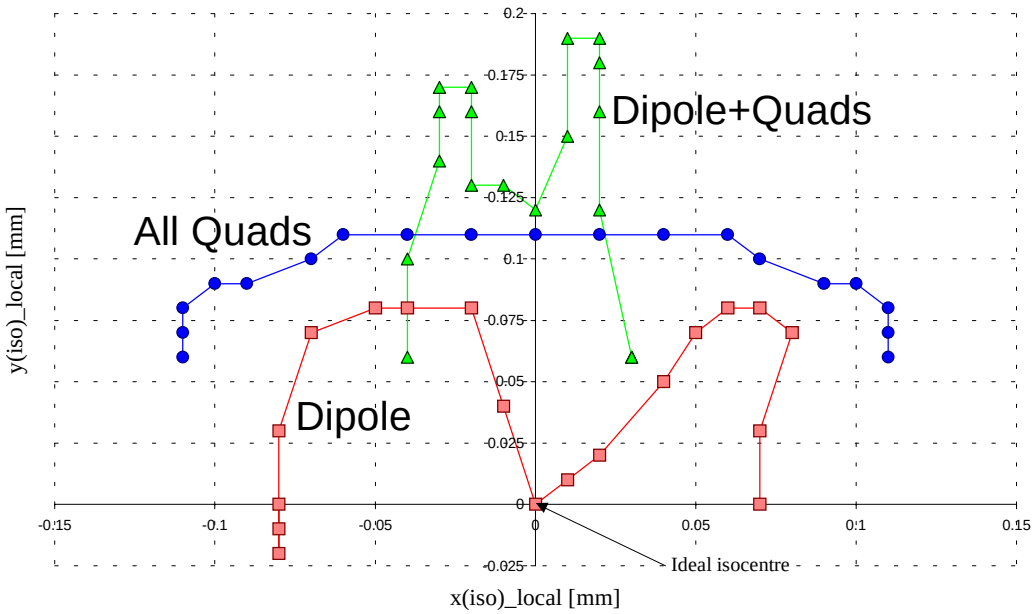

Key		
	Circles	Only quadrupoles have been misaligned
	Squares	Only the dipole has been misaligned
	Triangles	Quadrupoles and dipole have been misaligned

Figure. 6.12 Beam position in the gantry isocentre for different angles of gantry rotation [Deviations from the ideal isocentre are caused by elastic deformations of the support structures]

Random misalignments

It is difficult to assess the random misalignments in the same way as the systematic ones and a different strategy has been chosen. The sensitivity of the gantry beam transport system has been investigated thus giving the possibility to specify 'backwards' the necessary tolerances on the element positions. For this purpose, some approximations have been introduced into the model. The first approximation is to express the effect of a misaligned quadrupole as an angular kick with zero displacement at the exit to the quadrupole (thin-lens approximation). The angular kicks are given by (6.2) and (6.3). The kicks then cause beam displacements at the gantry isocentre according to the transformation:

$$\begin{pmatrix} x \\ x' \\ y \\ y' \end{pmatrix} = \begin{pmatrix} t_{11} & t_{12} & t_{13} & t_{14} \\ t_{21} & t_{22} & t_{23} & t_{24} \\ t_{31} & t_{32} & t_{33} & t_{34} \\ t_{41} & t_{42} & t_{43} & t_{44} \end{pmatrix} . \begin{pmatrix} x_0 \\ x_0' \\ y_0 \\ y_0' \end{pmatrix} \qquad (6.4)$$

where x, x', y, y' are parameters of the reference trajectory (beam centre) in the gantry isocentre, x_0 , x_0', y_0 , y_0' are parameters of the reference trajectory at the exit to the misaligned element and t_{ij} are elements in the transfer matrix from the exit of the misaligned element to the gantry isocentre. The thin-lens approximation gives $x_0 = y_0 = 0$ and x_0' and y_0' will be called H_{kick} and V_{kick} for the horizontal and vertical planes, respectively. Note that there is a coupling between the horizontal and the vertical planes due to the fact that the gantry is rotated by an angle $\alpha/2$ with respect to

the rotator, α being the angle of gantry rotation. The terms in the off-diagonal sub-matrices are therefore not zero. The final beam displacement due to the quadrupole shift is:

$$x = t_{12} \cdot H_{\text{kick}} + t_{14} \cdot V_{\text{kick}} \text{ (horizontal plane)}$$
$$y = t_{32} \cdot H_{\text{kick}} + t_{34} \cdot V_{\text{kick}} \text{ (vertical plane)} \quad (6.5).$$

After evaluating the kicks using (6.2), one obtains:

$$x = t_{12} \cdot \sqrt{k} \sin\sqrt{k}L \cdot \Delta x - t_{14} \cdot \sqrt{k} \sinh\sqrt{k}L \cdot \Delta y = C_1 \Delta x + C_2 \Delta y$$
$$y = t_{32} \cdot \sqrt{k} \sin\sqrt{k}L \cdot \Delta x - t_{34} \cdot \sqrt{k} \sinh\sqrt{k}L \cdot \Delta y = C_3 \Delta x + C_4 \Delta y \quad (6.6)$$

where C_1, C_2, C_3 and C_4 are constants depending only on the angle of gantry rotation. For analysis of random errors, the misalignments Δx and Δy are taken as representing a standard deviation of the position probability distribution of a misaligned element and their effects – supposing independent random misalignments in any direction – must be added quadratically:

$$\sigma(i)_H = \sqrt{\left(x(\Delta x, \Delta y = 0)\right)^2 + \left(x(\Delta x = 0, \Delta y)\right)^2} = \sqrt{C_1(i)^2 (\Delta x)^2 + C_2(i)^2 (\Delta y)^2}$$
$$\sigma(i)_V = \sqrt{\left(y(\Delta x, \Delta y = 0)\right)^2 + \left(y(\Delta x = 0, \Delta y)\right)^2} = \sqrt{C_3(i)^2 (\Delta x)^2 + C_4(i)^2 (\Delta y)^2} \quad (6.7)$$

where $\sigma(i)_H$ and $\sigma(i)_V$ now represent a standard deviation of the beam position probability distribution corresponding to the misalignment of the i-th quadrupole and indexes H and V assign the horizontal and vertical planes, respectively.

The second approximation in the model is a physically reasonable assumption that the position uncertainty for all quadrupoles in all directions is the same, that is $\Delta x = \Delta y = \Delta z \equiv \Delta_{\text{shift}}$ where Δ_{shift} is now introduced as representing the random misalignment of a quadrupole in any direction. Equation (6.7) then looks like:

$$\sigma(i)_H = \sqrt{C_1(i)^2 + C_2(i)^2} \cdot \Delta_{shift} = C(i)_H \Delta_{shift}$$
$$\sigma(i)_V = \sqrt{C_3(i)^2 + C_4(i)^2} \cdot \Delta_{shift} = C(i)_V \Delta_{shift} \quad (6.8).$$

Equation (6.8) demonstrates that the beam displacement in the gantry isocentre caused by a random quadrupole shift is simply proportional to the shift. The proportionality constants are different in the horizontal and vertical plane $C(i)_H \neq C(i)_V$. If all quadrupoles are independently misaligned, the standard deviation of the beam position probability distribution in each plane will be given by:

$$\sigma_{shift} = \sqrt{\sum_i \left(\sigma(i)\right)^2} = \sqrt{\sum_i \left(C(i)^2 \Delta_{shift}^2\right)} = \sqrt{\sum_i \left(C(i)^2\right)} \cdot \Delta_{shift} \propto \Delta_{shift} \quad (6.9)$$

where indexes for horizontal and vertical planes are no longer indicated keeping in mind that equation (6.9) differs for the different planes by only the proportionality constant.

The same strategy can be applied for effects of quadrupole tilting, dipole shift and dipole tilt yielding the final expression for the standard deviation of the beam position probability distribution in a given plane, σ_{total}:

$$\sigma_{total} = \sqrt{\left(\sigma(\text{quads})_{shift}\right)^2 + \left(\sigma(\text{quads})_{tilt}\right)^2 + \left(\sigma(\text{dipole})_{shift}\right)^2 + \left(\sigma(\text{dipole})_{tilt}\right)^2} \qquad (6.10)$$

where each contributing effect is proportional with a different proportionality constant to the corresponding misalignment. This enables a proportional scaling of results and to specify 'backwards' the tolerable misalignments from the requirements on the beam position accuracy. In principle, calculations have to be done for all gantry angles, because the proportionality constants depends on the angle of gantry rotation.

The input data used in the random misalignment analysis were $3\sigma_{shift}$ = 0.1 mm and $3\sigma_{tilt}$ = 0.1 mrad for all quadrupole and dipole magnets. Specifying the 3σ-value means practically that the elements are always expected to be within -3σ to +3σ tolerances. The calculations have been done for gantry angles from -90° to +90° with 10° step. Figure 6.13 shows the results for two significant angles of gantry rotation +90° and 0°. The values for other gantry angles were in-between these two extreme cases. The individual contributions listed in (6.10) were (horizontal plane/vertical plane):

- $3\sigma\ (\text{quads})_{shift}$ = 0.93/1.23 mm,
- $3\sigma\ (\text{quads})_{tilt}$ = 0.16/0.22 mm,
- $3\sigma\ (\text{dipole})_{shift}$ = 0.1/0.06 mm
- $3\sigma\ (\text{dipole})_{tilt}$ = 0.14/0.63 mm for $\alpha = 90°$.

The 3σ-regions of the beam position probability distribution corresponding to the above values are depicted in Figure 6.14. The maximum overall values $3\sigma_{total}$ = 0.96/1.4 mm were obtained for $\alpha = 90°$.

In Figure 6.15, the results obtained for the 'reference' misalignments are scaled to the expected random misalignments due to temperature fluctuations (reported in Section 6.6.2), which are considered as the main contributor to random errors.

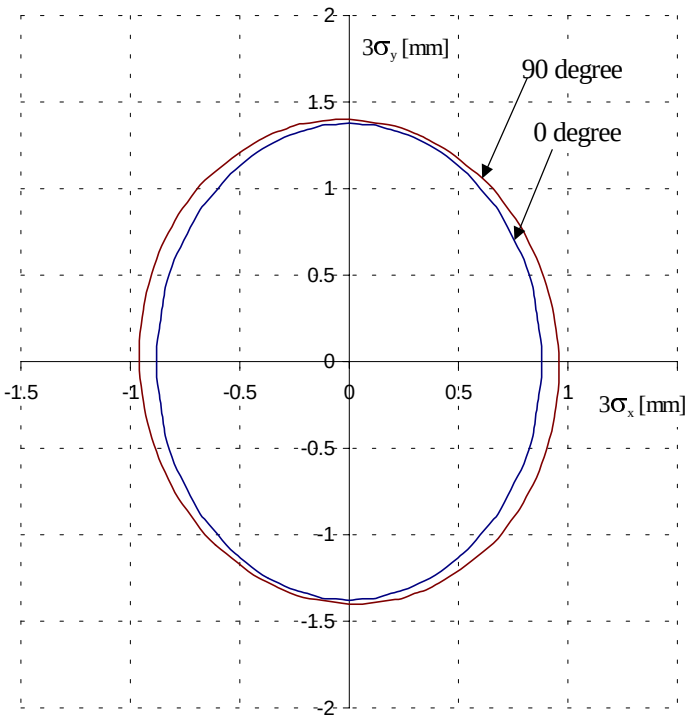

Figure 6.13 Uncertainty of the beam position in the gantry isocentre expressed as a 3σ-value of the beam position probability distribution for two angles of gantry rotation (0° and 90°) and the 'reference' random misalignments of all elements of 0.1 mm and 0.1 mrad

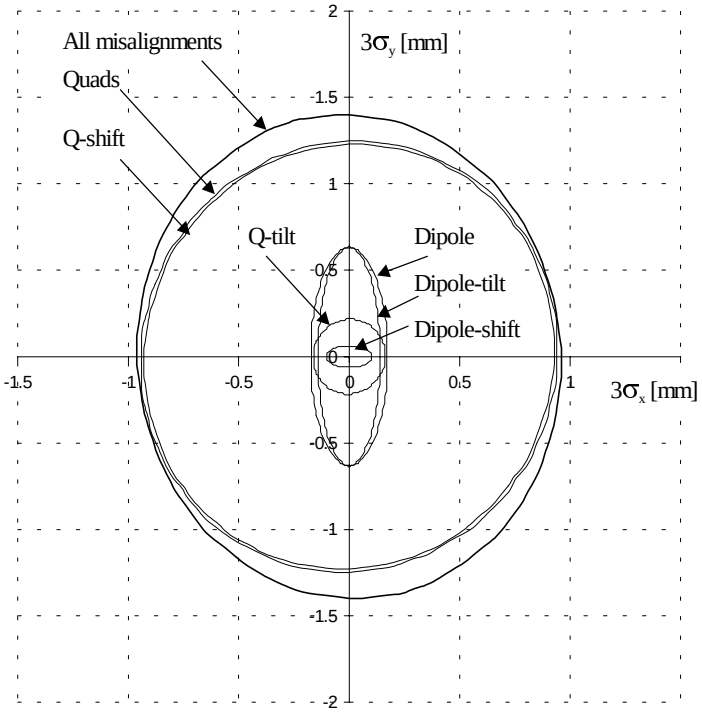

Figure. 6.14 Individual random misalignment contributions corresponding to shifting and tilting of the quadrupoles and the dipole for the angle of gantry rotation of 90° and the 'reference' random misalignments of all elements of 0.1 mm and 0.1 mrad

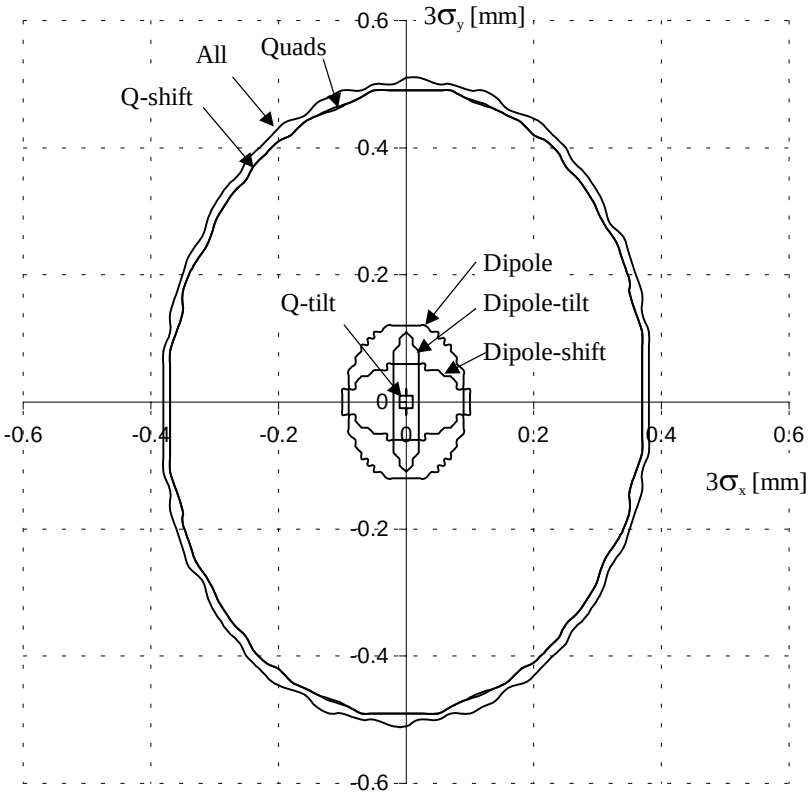

Figure 6.15 Beam position uncertainty due to temperature fluctuations. 3σ-regions are always indicated

6.7.4 Summary

The systematic misalignments caused by elastic deformations of the gantry structure lead to excursions of the beam from the gantry isocentre less than 0.2 mm, which is within the required precision. However, there will be other components of the systematic misalignments, for example fabricating errors, which are presently not included in the calculations because their exact values are not yet known. Nevertheless, the systematic errors are considered not to be critical for routine gantry operation. By virtue of their reproducibility (as a function of the gantry angle), they can be compensated by a set of fixed corrections that can be realised, for example, as an off-set of the scanning magnets or as a kick from dedicated corrector magnets (mapping). The second alternative is preferred in order to keep the scanning and the corrections as two orthogonal functions.

The sensitivity of the beam position accuracy to random misalignments has been calculated using the 'reference' values of 0.1 mm and 0.1 mrad for misalignments in all elements independently. The response of the beam position can now be scaled proportionally to correspond to other input misalignment values. In the case of different values for different effects (quadrupole-shift, quadrupole-tilt, dipole-shift, dipole-tilt), the scaling must be done separately for each effect and the resulting contributions must be added quadratically.

The random misalignment effects have been particularly assessed for temperature fluctuations and finally a contribution from the photogrammetric

alignment system of the patient couch (3σ = 0.3 mm) was added (see Figure. 6.16). The main results are collected in Table 6.1.

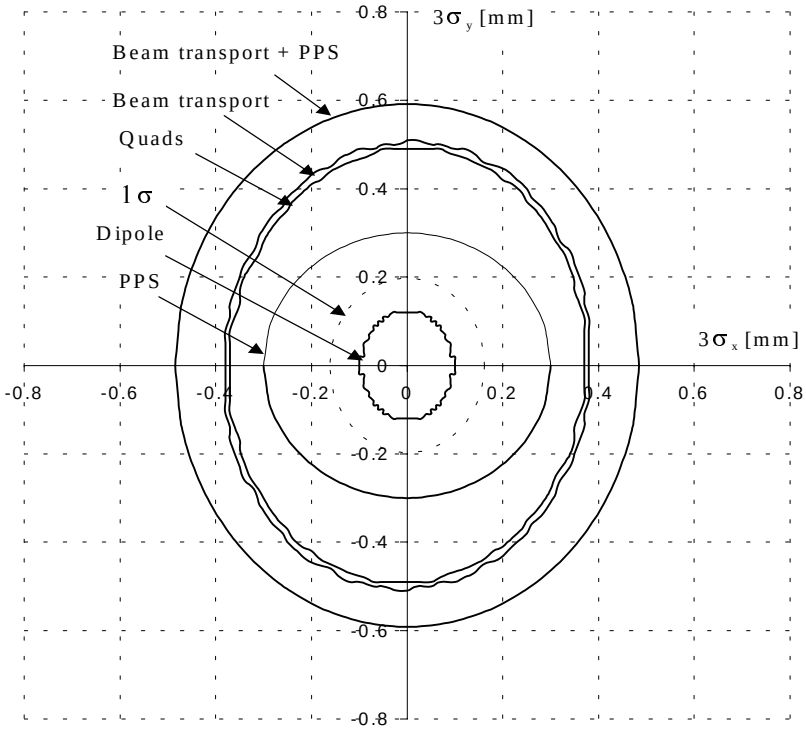

Figure 6.16 Beam position uncertainty due to temperature fluctuations and the resolution error of the photogrammetric alignment system

Summary of the effects of random misalignments

Source of error	3σ–region of the beam position probability distribution for the 'reference' misalignments of 0.1 mm and 0.1 mrad H/V plane [mm]	3σ-region of the beam position probability distribution for the misalignments due to temperature fluctuations H/V plane [mm]
Dipole-shift	0.10 / 0.06	0.09 / 0.06
Dipole-tilt	0.14 / 0.63	0.02 / 0.11
Dipole	0.17 / 0.64	0.10 / 0.12
Quadrupole-shifts	0.93 / 1.23	0.37 / 0.49
Quadrupole-tilts	0.16 / 0.22	0.01 / 0.02
Quadrupoles	0.94 / 1.25	0.37 / 0.49
Beam transport, quadrupoles + dipoles	0.95 / 1.40	0.38 / 0.51
Beam transport + patient positioning system	1.00 / 1.43	0.48 / 0.59

Table 6.1. Summary of the effects of random misalignments

The results show that the sensitivity of the beam transport to the element misalignments is rather high. In order to achieve sub-millimetre precision (interpreted so that the 3σ value of the beam position probability distribution is lower than 1 mm), the misalignments have to be kept below 0.1 mm and 0.1 mrad. However, not all

misalignments are that critical. The dominating contribution comes from the shifting of quadrupoles, which is equally true for the 'reference' situation as well as for the temperature effects. A precision of ± 0.08 mm (3σ) would be required for the transversal position of the quadrupoles. The effect of quadrupole tilt is about a factor of 6 lower and can be practically neglected. For the dipole, the angular misalignments are more critical compared to the shifts, especially in the vertical plane. The tolerances 0.1 mm and 0.1 mrad are acceptable.

It would also be possible to reduce the quadrupole contribution by steering magnets located downstream of the gantry quadrupoles and upstream of the scanning magnets. These correctors would be to direct the beam into the centre of the scanning system and hence remove the position and angular errors of the incoming beam caused by the upstream misalignments. These corrector magnets could be controlled on-line by a permanent beam position monitoring system at the entrance to the scanning dipoles. A similar strategy is applied at the GSI fixed therapy beam-line, where the correction action is performed directly by the scanning system [6].

A further conclusion of the study is the fact that the angular dependence (gantry angle) of the beam position uncertainty at the isocentre is practically negligible, which reduces drastically the calculations that have to be done in the future to refine the study of the gantry. There are two reasons for this very weak angular dependence. The first reason is that the width of the overall beam position probability distribution is given as a quadratic sum of many contributions, namely three independent shifts and tilts of each element, all elements being further independently misaligned with respect to each other. Each individual contribution has its own angular dependence which may be increasing or decreasing with the gantry angle, so that in the quadratic sum the decrease of one contribution is well balanced by an increase in another. The second reason is that there are also contributions from elements that are downstream of the rotator-to-gantry coupling point. These contributions are independent of the angle of gantry rotation. The situation is illustrated in Figure 6.17, that shows the response of the beam position at the gantry isocentre as a function of the gantry angle separately for horizontal and vertical misalignments (0.1 mm) of the first quadrupole. The quadratic sum of these two effects are indicated as "Sum I" while "Sum II" is a quadratic sum of these effects AND contributions from the elements downstream of the rotator-to-gantry coupling point. The overall angular dependence becomes practically negligible.

6.8 ERROR DETECTION AND ALIGNMENT

In this analysis, the position of each beam transport element is characterised by a particular systematic misalignment and a standard deviation of the random misalignment distribution. The systematic misalignments can be compensated by the mapping strategy mentioned in Section 6.6.3, the random misalignments should be kept within the tolerances derived above.

During the treatment, the actual beam position must be measured permanently by an on-line beam position monitor placed as close as possible to the patient. In the case of intolerable beam excursions from the planned position, an interlock signal is sent to a dedicated beam-stopper and the treatment is interrupted. The current practice

in radiotherapy is to mount the monitoring equipment in the so-called "nozzle" on the supporting frame of the beam line or the gantry. The information so obtained is the relative position of the beam with respect to the nozzle and not with respect to the patient.

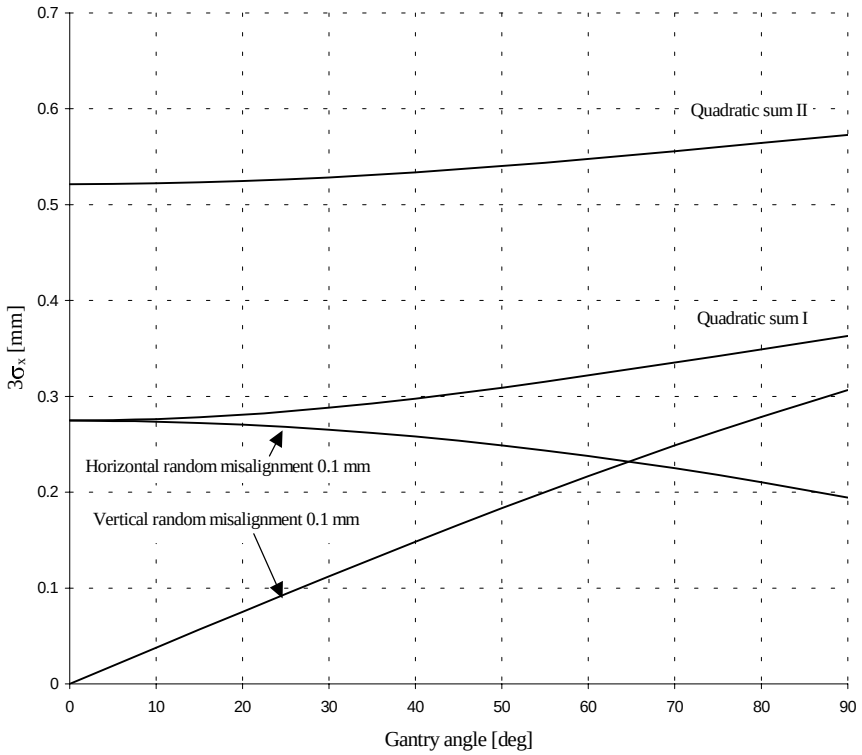

Figure 6.17 Demonstration of the summation of different random misalignment contributions leading to 'vanishing' of the angular dependence of the beam position accuracy

This method is suitable for passive beam spreading techniques where the irradiated area is in fact defined by the collimators in the nozzle and not directly by the beam position. It may also be accepted for fixed beam lines where the relative position between the nozzle and the patient couch is fixed. For a gantry equipped with an active pencil-beam scanning, a different strategy is recommended. An optimum would be to attach the beam monitoring system to the patient couch, so that it measures the absolute position of the beam with respect to the patient. A comparatively small monitoring unit would be sufficient. The concept of a diagnostic ring mounted around the patient couch and lockable at any angle is schematically shown in Figure 6.18. Any remaining source of uncertainty is related to the position of the tumour relative to the patient couch. Information about this can be obtained by placing the patient together with the couch in a CT scanner. Fortunately, the treatment platform in the 'Riesenrad' provides adequate space to accommodate this equipment and the same robot arm that holds the patient couch over the beam can reposition the couch in the scanner. The CT should be combined with a PET camera [7] that would monitor the deposited dose immediately after the treatment.

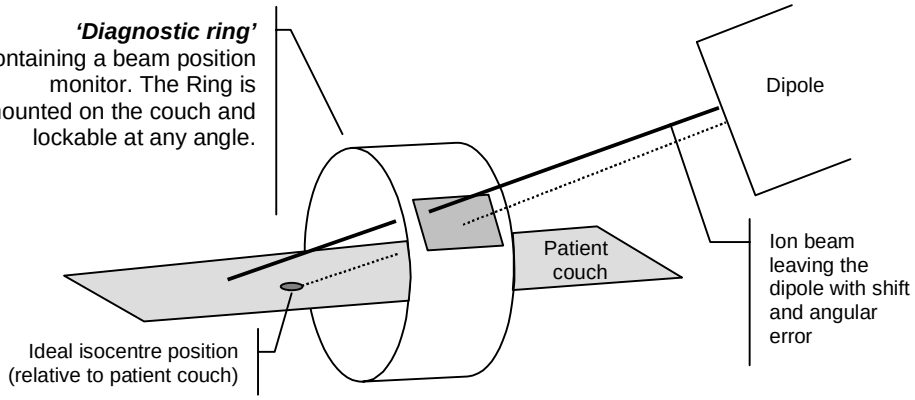

Figure 6.18 Schematic principle of the 'diagnostic ring' for quality assurance checking the position of the actual incoming beam relative to the patient table

[As the ideal isocentre relative to the patient couch is known from the treatment plan, a theoretical beam path can be calculated (depending on the treatment angle and the couch rotation) and the centre of the beam monitoring device will be moved to the expected location. From the difference between expected hit and the actual passing point of the beam a positioning error is calculated]

In addition to the alignment errors discussed so far, other, "accidental" errors, may happen during routine gantry operation. They may be caused for instance by the sudden breakage of equipment, impacts on the structure and cameras etc. and would lead to a sudden, and probably large, deviation of the beam from the desired position. Basically, an accidental error can be interpreted as an excessive random misalignment occurring with low probability outside the 3σ-region of the random misalignment probability distribution. In order to detect an accidental error before treatment starts, an alignment control system for the rotator and the gantry is proposed (see Figure 6.19). Two laser beams are running along the line of quadrupoles, whose relative positions towards the laser beams are obtained from retro-reflectors. By turning the quadrupoles, a different set of retro-reflectors becomes visible for the laser beams. Such an alignment control system, it is certainly capable of detecting misalignments in excess of ± 0.3 mm (3σ), however, depending on the effort that is invested in the system, an even better performance can be expected. Another reason for this system is its ability to identify the element responsible for the beam displacement, which is not the case for the beam monitoring system measuring just the final beam position in front of the patient.

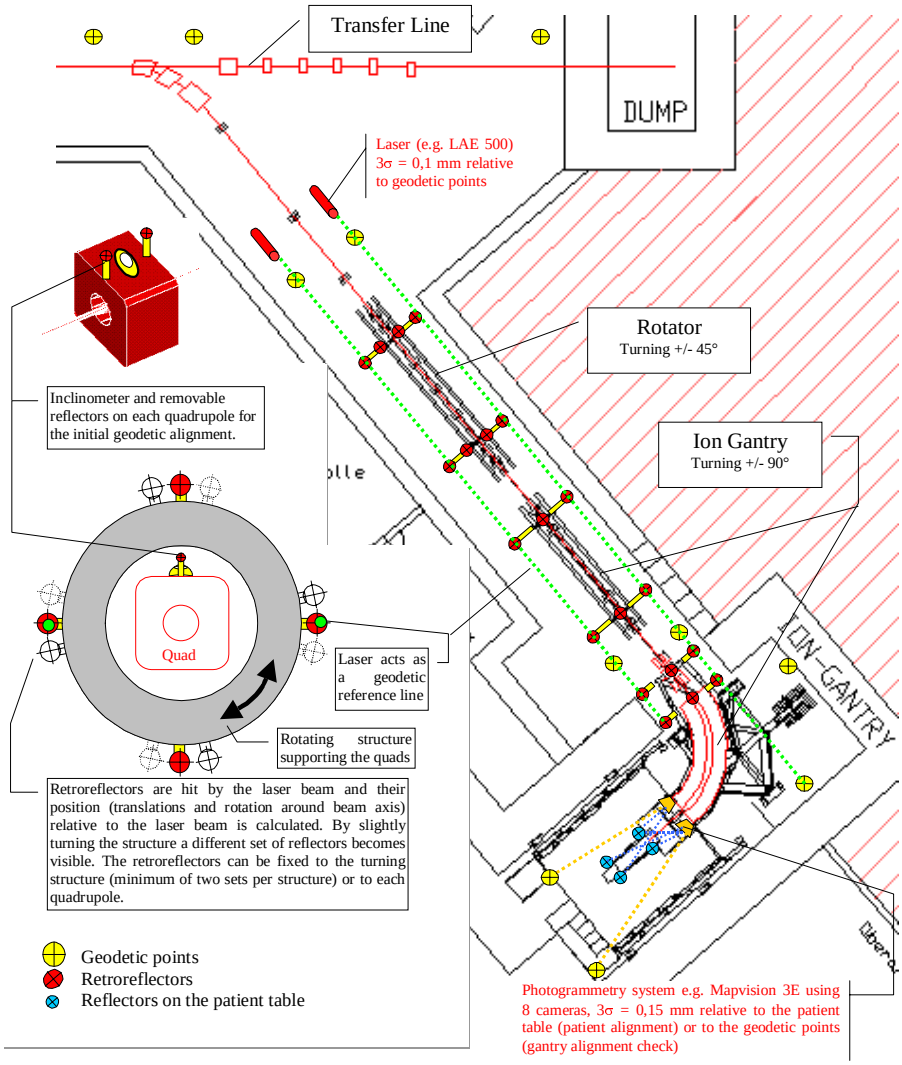

Figure 6.19 Functions of the different alignment systems in the 'Riesenrad' gantry

Figure 6.20 summarises the process of gantry alignment and alignment control. A correction map acts as a feed forward loop to compensate systematic errors. Long-term effects (settlements, wear, etc.) will alter the system and introduce 'long term systematic errors' (which must be compensated by a regular re-calibration of the correction map). The alignment control system sees excessive (accidental) errors before treatment. The beam monitoring system fixed to the patient couch checks whether the beam position follows the desirable pattern listed in the treatment plan with a pre-defined precision.

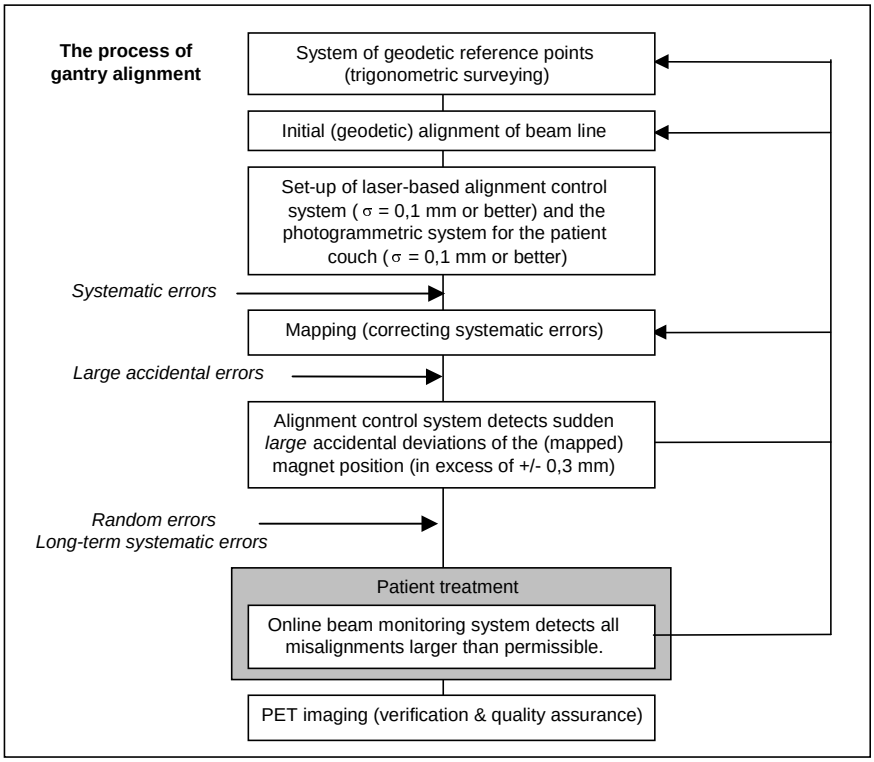

Figure 6.20 Principal steps in the alignment process of the ion gantry

6.9 CONCLUSION

Patient and staff will hardly realise that they are not in a fixed room, but in a patient cabin guiding them smoothly into the treatment position. An elevator provides quick and redundant access and there is always the possibility of using a conventional staircase for a maximum of two floors vertical distance. The exocentric 'Riesenrad', or 'independent-cabin', gantry yields a high efficiency in terms of structural weight to supported load. The elastic deformations are calculated to be lower than for any existing proton gantry. The future treatment procedures have been partly anticipated by the large area of the patient cabin.

References

[1] PIMMS Group, Proton-Ion Medical Machine Study (PIMMS), Part I, CERN-PS/99-010 (DI).
[2] S. Reimoser, Variants for a Riesenrad Ion Gantry, CERN-ST-99-002, April 1999.
[3] CUBUS Software, Statik-3 Benutzeranleitung, Berechnung von ebenen und raumlichen Stabtragwerken, 1998, Zurich.
[4] D. C. Carey et al., *Third-Order Transport. A Computer Program for Designing Charged Particle Beam Transport Systems*, SLAC-R-95-462, Fermilab-Pub-95/0, UC-414, May 1995.
[5] P. J. Bryant, *WinAGILE*, http://nicewww.cern.ch/~bryant.
[6] W. Enghardt et al., *Heavy-Ion Therapy at GSI: Progress Report*, GSI Scientific Report 1998, GSI Report 99-1, May 1999, 138.
[7] University of Pittsburgh Medical Center and CTI PET Systems Inc., *The PET/CT tomograph project*, http://www.pet.upmc.edu/~tbeyer/pet_ct/PETCT.html#functional.

* * *

II-7 INJECTION

Since there is a controlled emittance blow-up at injection, the injection chain is partially decoupled from the rest of the complex. For this reason, it is not a serious problem to change linacs or to propose different layouts for the injection lines. The layout presented here is based on separate carbon-ion and proton linacs with separate dumps for testing and all sensitive equipment outside the ring for ease of access. The carbon-ion linac accelerates C^{4+} ions that are stripped to C^{6+} directly at the exit to the linac. The design of the lines must take care of two problems. The first is the positioning of de-bunching cavities for each particle type and the second is the optics for the space-charge dominated proton beam. More compact and cheaper solutions are probably possible and a combined RFQ and linac for two species operation is being studied [1] for just these reasons

7.1 BOUNDARY CONDITIONS

The exact beam parameters at the exits to the carbon-ion and proton linacs are unknown, since these devices have not been designed. Consequently, some assumptions have had to be made, but fortunately, this is non-critical in the present instance. The transverse emittances are based on the assumption that the total normalised emitance in either case will be about 1π mm mrad and the blow-up of the carbon ion beam in the stripping foil is estimated to be about 10%. This can be neglected at the level of accuracy used for these assumptions, especially since the emittances are, in any case, diluted at injection. At the entries to the carbon-ion and proton injection lines, a doublet has been added which can, with gradient and position matching, assure matched liaisons between the lines and the whatever linacs are finally chosen. Table 7.1 summarises the assumed parameters of the two linacs. This table can be interpreted as a specification, although in practice there would be considerable flexibility.

Assumed parameters of the proton and carbon-ion linacs

	Proton linac	**Carbon-ion linac***
Frequency [MHz]	200	200
Current [emA]	≥ 4.4	≥ 0.11
Pulse width [μs]	≤ 200	≤ 200
Repetition rate [Hz]	≤ 1	≤ 1
E_x, E_y [π mm mrad] 5 RMS normalised	1	1
E_x, E_y [π mm mrad] 5 RMS unnormalised	5.0	8.0
E_z [π deg keV] 5 RMS unnormalised	807	1364
α_x, β_x [m]	0.0, 0.6	0.0, 0.6
α_y, β_y [m]	0.0, 1.0	0.0, 1.0
RMS relative momentum spread $\Delta p/p$	10^{-3}	1.5×10^{-3}
Nominal energy [MeV/u]	20	7
ΔT [keV]	± 60	± 250
$B\rho$ [Tm]	0.649	0.763

* After stripping foil, before debunching cavities

Table 7.1 Assumed parameters for the proton and carbon-ion linacs
[Based on multi-turn injection for carbon-ion active scanning and proton passive spreading]

It will be necessary to control the debunching of the beams, so as to minimise the momentum spreads, especially for the carbon-ion beam after the stripping foil. Table 7.2 summarises the results of the studies and the main parameters of the cavities.

Debunching cavities for the proton and carbon-ion beams

	Proton	**Carbon-ion**
Required drift [m]	38	15
Initial RMS $\Delta p/p$	10^{-3}	1.5×10^{-3}
Final RMS $\Delta p/p$	0.5×10^{-3}	0.5×10^{-3}
Debuncher cavity type	$\lambda/4$, 2 gaps	$\lambda/4$, 2 gaps
Nominal energy [MeV/u]	20	7
Frequency [MHz]	200	200
Length [m]	0.6	0.4
Max. effective voltage per gap [kV]	50	50
RF amplifier power (solid state) [kW]	2	2

Table 7.2 Debunching cavities for the proton and carbon-ion beams

Table 7.3 summarises the Twiss boundary conditions at the entries and exit to the injection lines. The Twiss parameters at the injection into the ring are different for the two species and contain intentional mismatches in the vertical plane (see the multi-turn injection studies in Section 7.3). The Twiss parameters and survey co-ordinates at the various intermediate reference points are listed Appendix DD.

Boundary conditions for injection

Twiss functions at exit to both linacs (Ref. points N and P)		
$\beta_x = 0.6$ m	$\alpha_x = 0$	Estimated parameters
$\beta_z = 1.0$ m	$\alpha_z = 0$	
$D_x = 0$ m	$D'_x = 0$	
$D_z = 0$ m	$D'_z = 0$	
Survey co-ordinates of end point (Ref. point B at exit to ES in ring)		
$X = 1.350000$	$Y = 0.047600$	Floor defined as $Z = 0.0$ m
$\Theta_h = 0.000100$	$\Phi = 0.000000$	
Twiss functions at exit to ES in the ring for proton injection		
$\beta_x = 7.0310$ m	$\alpha_x = -0.19966$	Space-charge, de-tuned
$\beta_z = 3.7000$ m	$\alpha_z = 0$	working point*. Mismatch
$D_x = 0$	$D'_x = 0$	in vertical plane for dilution.
$D_z = 0$	$D'_z = 0$	
Twiss functions at exit to ES in the ring for carbon ion injection		
$\beta_x = 8.5278$ m	$\alpha_x = -0.16248$	Nominal working point.
$\beta_z = 5.7000$ m	$\alpha_z = 0$	Mismatch in vertical plane.
$D_x = 0$	$D'_x = 0$	for dilution.
$D_z = 0$	$D'_z = 0$	

* The de-tuned lattice for protons is adjusted so that at the maximum tune shift during the acceleration cycle, the lowest point of the necktie ends at the nominal working point of the 'waiting' beam (Qx = 1.68, Qz = 1.72).

Table 7.3 Boundary conditions for injection

7.2 LATTICE

7.2.1 General layout

Figure 7.1 shows the layout of the injection lines with the main ring. Both lines have basically the same sequence of modules, i.e. ion source, RFQ, linac, matching section, FODO transport line and matching section to ring. The principal difference is that the carbon-ion line has a matched "S" bend or "dog leg" insertion inside the FODO section in order to set the two linacs side by side. The 'dog leg' is placed in the carbon line in order that the space-charge-dominated proton line is made as simple as possible. The basic FODO cell used in both lines is 7.15 m long with a phase advance of 82.4°.

Injection is made into the ring from the inside with a multi-turn injection scheme. A single-turn injection appears to be possible and might even be preferred, but in order to be sure that the carbon ion source will not present any intensity problems the multi-turn injection has been adopted. It is also easier to fit into the available space an electrostatic septum with all its electrode controls on one side of the vacuum tank (see Appendix T) than the symmetric tank of a fast kicker magnet. The lattice has been adjusted so as to require only one design of dipole and one design of quadrupole. Since the injection is from the inside and since it has been decided to position the linacs outside of the ring, the injection line must cross the main ring. The geometry has been adjusted so as to make this crossing in the long straight section SS-MR-16 at approximately 90 degrees. The vehicle track around the ring has also been maintained although there is less space than at the extraction point.

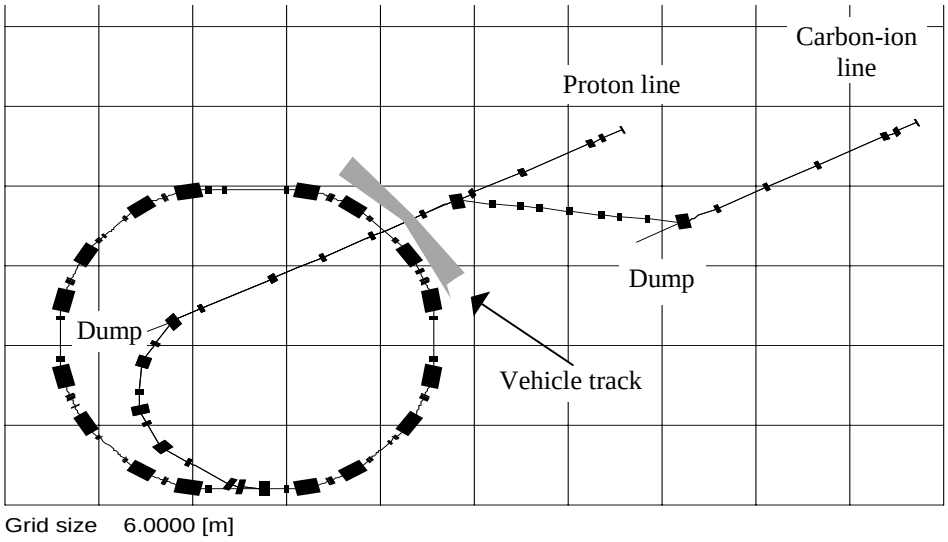

Figure 7.1 Layout of the injection lines and main ring

7.2.2 Injection optics for the carbon beam

Figure 7.2 shows the geometry and lattice functions of the carbon injection line. The short extension of the straight line from the linac goes to a dump.

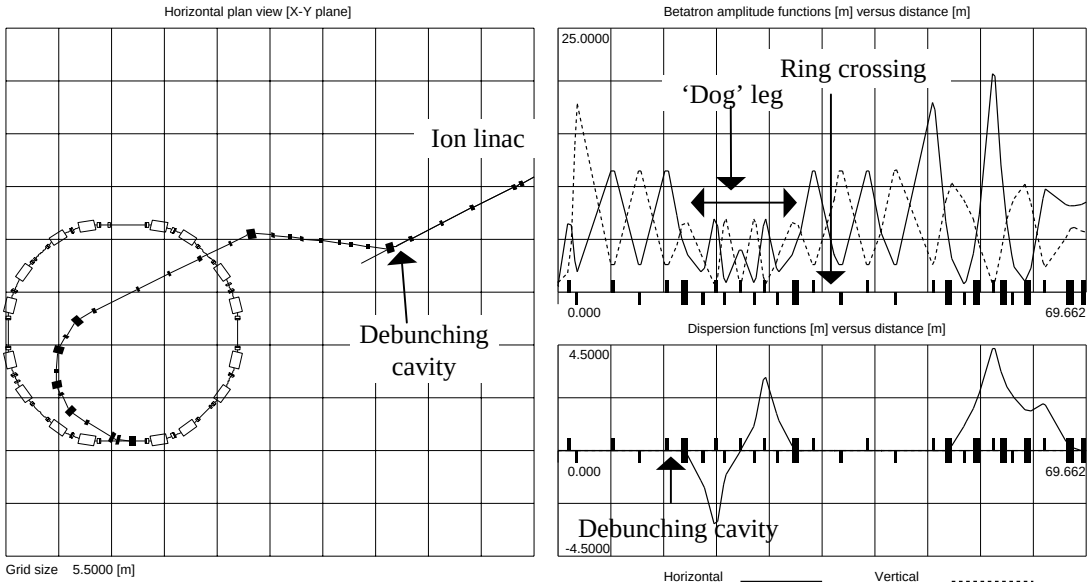

(a) Geometry (b) Lattice functions

Figure 7.2 Geometry and lattice functions in the carbon injection line

7.2.3 Injection optics for the proton beam

Figure 7.2 shows the geometry and lattice functions of the proton injection line for zero space charge conditions. The short extension of the straight line from the linac goes to a dump.

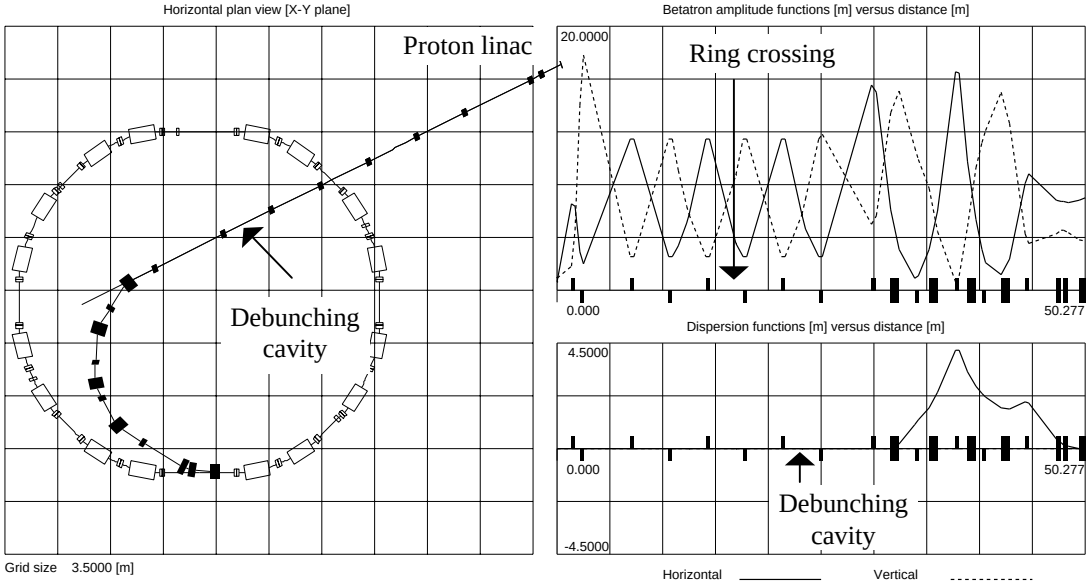

(a) Geometry (b) Lattice functions

Figure 7.3 Geometry and lattice functions in the proton injection line

Figures 7.2 and 7.3 show the non-space-charge design of the injection complex. However, the proton line will be used, in most cases, with a beam that is strongly affected by space charge. For the purposes of the study, it has been decided to simplify the injection and the number of working conditions in the ring by:

- Having only one space-charge optics condition for the injection chain.

- Always de-tuning the working point of the ring to account for the maximum space-charge tune shift possible.
- Adjusting the intensity in the ring by changing the injection time.
- Correcting the tune values during the acceleration of the beam.

This is a quite complicated situation because:

- The intensity range required in the ring is large 1:65 (see Section 1.1).
- The injection time for each intensity depends on the profile of beam losses during the multi-turn injection. This can be simulated, but will need to checked experimentally.
- The main ring quadrupoles may need to be programmed for each intensity to avoid that low-space-charge beams spend too much time on the non-linear resonances between the de-tuned working point and the nominal working point.

The alternative, which may be the more practical, but for the study requires too many optical conditions to be calculated, would be to

- Vary the intensity at the level of the ion source.
- Adjust the matching in the transfer line as a continuous function of the space charge.
- Adjust the de-tuning of the ring as a continuous function of the space charge.
- Keep the multi-turn injection process and any beam scraping constant.
- Linearly correct the de-tuning during the acceleration.

For the present study, just one example of the space-charge matching will be given. The calculation has been made with the TRACE3D program [2] for a space-charge dominated proton beam (Figure 7.4(a)) and a non-space-charge carbon-ion beam (Figure 7.4(b)). The proton beam corresponds to the maximum intensity assumed from the source for a passively spread beam. Note that there are small differences in the geometry of these examples compared to Figures 2 and 3 and the total emittance of the beam has been taken as 8π rather than 5π as given in Table 7.1.

7.2.4 Alignment of the magnetic injection septa

There is a pair of identical magnetic septa at the end of the injection line. Each unit is a rectangular-type dipole providing 250 mrad (seee Appendix Q). There is sufficient space that both units can be aligned symmetrically with respect to the central orbit of the beam (i.e. equal edge angles) and the 14 mm sagitta can be shared equally between the inner and outer halves of the aperture.

7.2.5 Alignment of the electrostatic injection septum

The electrostatic injection septum provides the final kick of 60 mrad (see Appendix T). The unit is bent (simulating a curved unit) and is treated as a sector bending element (i.e. zero edge angles). The last section of the bent septum wall is set 41 mm from the central orbit of the ring towards the inside of the ring and parallel to the central obit of the ring.

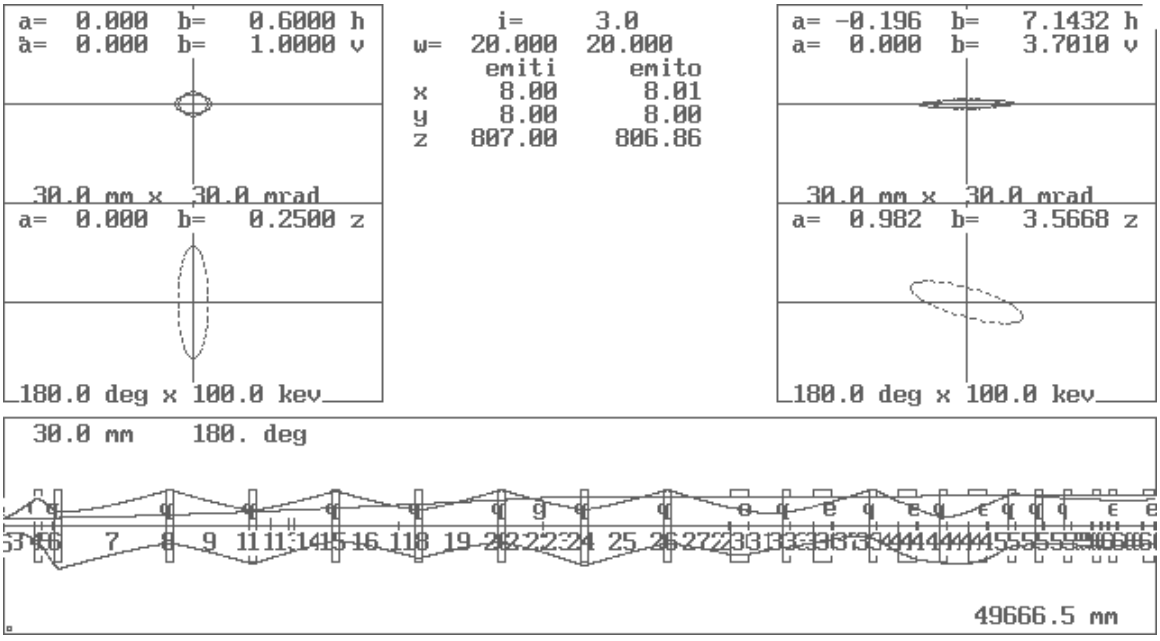

(a) Beam envelopes and emittances in the proton injection line

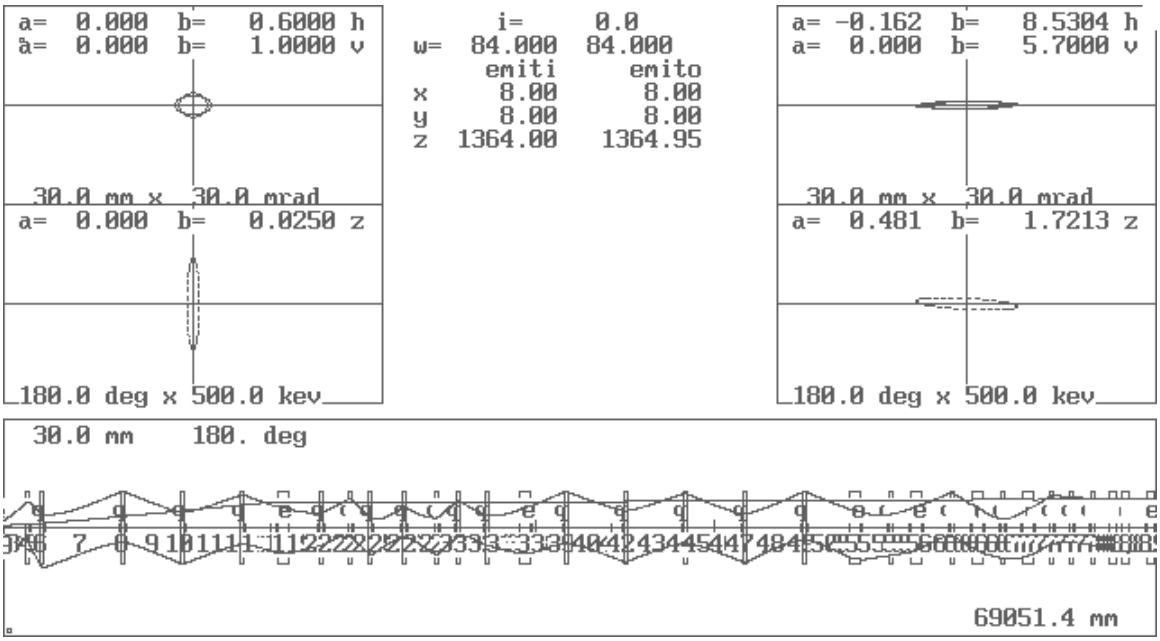

(b) Beam envelopes and emittances in the carbon-ion injection line

Figure 7.4 Output of TRACE3D showing emittances and envelopes in the 3 phase planes

7.3 MULTI-TURN INJECTION

The multi-turn injection scheme has two objectives:

- To obtain the diluted emittances mentioned in Chapter 1 for both the protons and the carbon ions.
- To reduce the intensity requirements for the carbon ion source.

The diluted emittances required at injection are calculated from the design emittance at the minimum extraction energy, which is equal for both types of particles. The relevant parameters are summarised in Table 7.4 that is based on Tables 1.2 and 7.1.

Geometric emittance evolution from the source to the extraction flat tops			
		Energy [MeV/u]	**Total emittance [π mm mrad]**
Protons			
Source		20	5
Dilution	**× 2.5**		
At start of acceleration		20	12.502
At lowest extraction energy		60	7.143
At highest extraction energy		250	3.339
Carbon ions			
Source		7	8
Dilution	**× 3.8**		
At start of acceleration		7	30.530
At lowest extraction energy		120	7.143
At highest extraction energy		400	3.662

Table 7.4 Geometric emittance evolution from the source to the extraction flat tops

All the particles surviving the injection, but outside these limits will be scraped away before acceleration starts. In the vertical plane, scraping ensures the correct beam size at the patient and in the horizontal plane it ensures the design momentum spread. Moreover it concentrates the principal beam losses at low energy. The scraping may be done in different ways. If the scrapers SC MR 21-06 (horizontal) and SC MR 28-01 (vertical) are of the mobile type (this choice is still open, see Section 4.10.3), it will be relatively simple to experimentally establish the movement of the scrapers to achieve the correct emittances and the scraping action will be very rapid. If fixed scrapers are installed, then closed-orbit bumps will be needed, which is less convenient.

To find the best combination of parameters, extensive simulations of the injection process have been made using the de-tuned lattice for a passively spread proton beam, but neglecting the space-charge effects during the multi-turn injection to keep the time needed for tracking the macro-particles within practical limits. . The de-tuned lattice for protons is adjusted so that at the maximum tune shift during the cycle, the lowest point of the necktie ends at (Q_x = 1.68, Q_z = 1.72), as shown in Figure 7.5. For carbon ions, the space charge is negligible and the lattice is tuned directly to (Q_x = 1.68, Q_z = 1.72) in order to stay clear of the resonance lines. For both particle species, the efficiency of the multi-turn injection has been studied as a function of:

- Number of turns for the injection bump to collapse.
- Injection angle with respect to central orbit of the ring
- Kick of the injection bumpers (bump height).

The aim of the simulations was to maximise the beam trapped within the specified emittances of Table 7.4 and not to maximise the beam trapped in the full aperture.

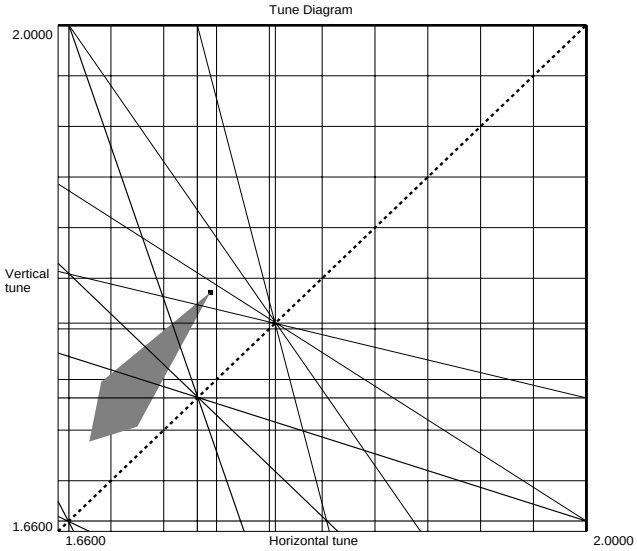

Figure 7.5 Tune diagram for 20 MeV protons with space-charge for passive spreading.

The simulation results have been organised in graphs corresponding to a fixed number of collapsing turns. Figure 7.6 contains the two graphs in which the maximum injection efficiency was attained. In Figure 7.7 the maximum efficiency is plotted as a function of the number of turns.

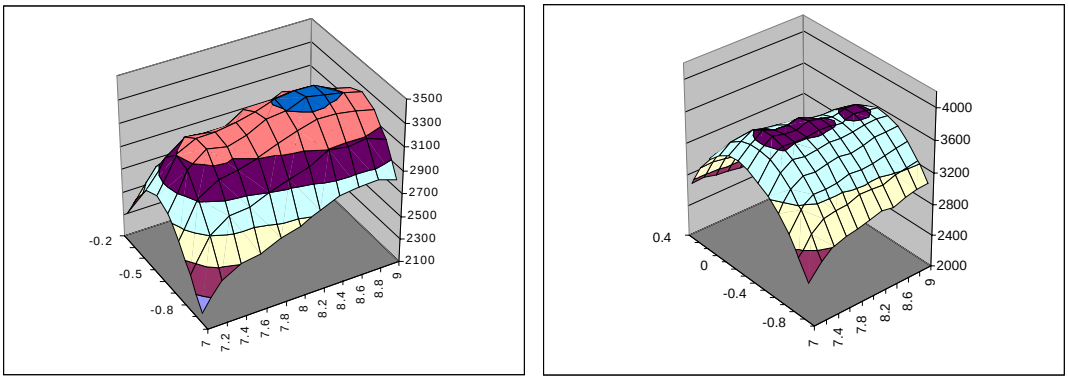

Figure 7.6 Injection efficiency versus injection angle and bumper kick
[Protons left, bump collapses in 28 turn; Carbon ions right, bump collapses in 16 turn]

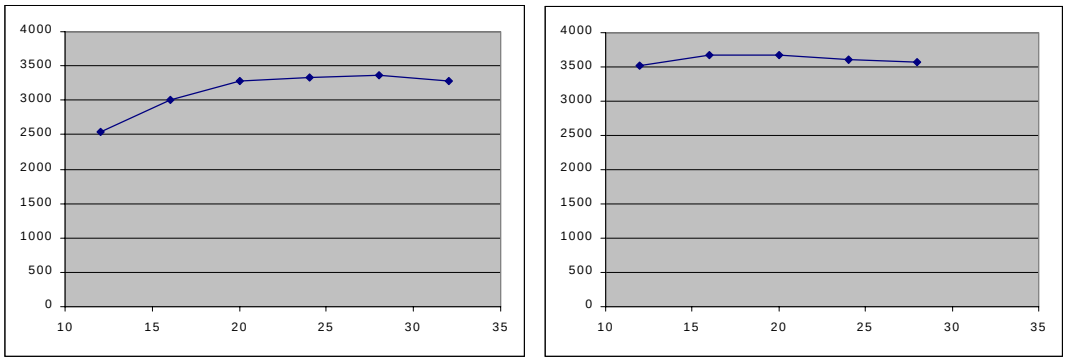

Figure 7.7 Maximum injection efficiency versus number of collapsing turns
[Protons left; Carbon ions right]

The maximum equivalent number of injected turns is 3.4 for protons and 3.7 for carbon ions. These results correspond, respectively, to 28 turns with -0.6 mrad initial injection angle and 8.4 mrad kick in the bumper magnets and to 16 turns with -0.1 mrad initial angle and 7.4 mrad kick in the bumper magnets. Inspection of the data shows that the injection efficiency varies only slowly with the parameters, tolerating .errors of ±0.5 mrad on both the initial angle and bumper kick with an efficiency reduction of less than 10%.

When only the number of turns is considered, the two particle species require different schemes, but when the bump collapse time is considered a fortunate situation occurs in which the time is approximately the same for both species:

$$T_{\text{proton}} = 28\ T_{\text{rev}} = 35\ \mu\text{s};\quad T_{\text{carbon}} = 16\ T_{\text{rev}} = 33\ \mu\text{s}.$$

Thus, a unique circuit for the injection bump can be foreseen, in which the bump collapse in ~34 μs.

The emittance dilution is obtained in the horizontal phase space as a by-product of the multi-turn injection. In the vertical plane, the dilution is obtained by a mixture of a betatron function mismatch and a vertical beam offset. Since the medical specifications are given in terms of FWHH, this is the quantity that has been considered rather than the RMS value that would require a specification of the distribution as well. The FWHH values that must result in the vertical plane after injection are:

7 MeV/u carbon ions: FWHH = 10.8 mm (vertical)
20 MeV protons: FWHH = 6.6 mm (vertical).

The injected beam has been assumed to have a total geometric emittance of 5π mm mrad for carbon ions and the same normalised emittance for protons, that corresponds to 2.95π mm mrad total geometric emittance[1].

Exploiting the fact that the injection electrostatic septum is the element where the losses occur and the fact that it is situated in a dispersion-free region, the simulations have been performed using a mono-energetic beam. This saves simulation time and allows the use of a reasonably low number of macro-particles. At the end of the simulation, each surviving particle was replaced by a set of 30 particles randomly distributed in momentum. This enabled the final distribution to be obtained after filamentation. The filamentation during the multi-turn injection has been neglected using the argument that a few per mil momentum spread would yield a negligible phase advance difference in the few turns of the injection process.

In the following sub-sections, three sets of multi-turn parameters and their resulting beam distributions are reported. One scheme is proposed for the carbon ions and two schemes for the protons. The first proton scheme maximises the injection

[1] Note that these figures vary with respect to Table 7.1 and Figure 7.4. Once the linacs are definitely decided it will be necessary to repeat all of these calculations.

efficiency. Its main drawback is that a partially hollow beam results in the horizontal phase plane. Having a low number of particles with small amplitudes has the undesirable result that there is less intrinsic smoothing of the ripple during extraction [Part. I Sections 4.4 and 4.5 and Ref. 3]. At the price of a slightly lower injection efficiency this problem is solved by the second scheme. Since intensity is not a major problem for the proton source, the optimisation of the distribution takes preference.

7.3.1 Injection parameters for carbon ions

Table 7.5 contains the simulation parameters for the carbon-ion injection and Figures 7.8-10 show the simulation results.

Carbon ion injection parameters		
Incoming beam		
Nominal energy {MeV/u]	7	
$\Delta p/p$ wrt to central orbit of ring*	-0.0021	
Horizontal lattice functions (matched to ring)	β_x = 8.53 m	α_x = -0.162
	D_x = 0 m	D'_x = 0
Vertical lattice functions (mismatched to ring)	β_z = 5.7 m	α_z = 0
	D_z = 0 m	D'_z = 0
Injected beam at exit of ES in local ring co-ordinates:	x = -47.6 mm	x' = -0.01 mrad
	z = 4.5 mm	z' = 0 mrad
Total emittance (5 RMS unnormalised)	E_x = 5π mm mrad	E_z = 5π mm mrad
Injection conditions in ring		
Septum wall [m]	-41×10^{-3}	
Initial kick in injection bumper dipoles [rad]	7.4×10^{-3}	
Injection bump collapse [turn]	16	
Injection efficiency	3.6 effective turns	

* The beam in the ring is off-centre towards the inner half of the aperture.

Table 7.5 Simulated carbon-ion injection parameters

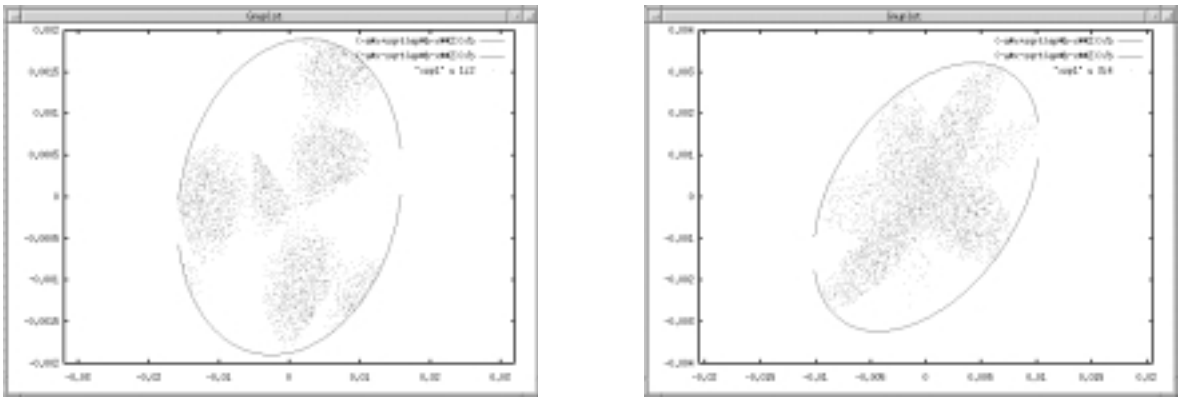

Figure 7.8 Phase-space distributions of the multi-turn injected beam before filamentation and the ellipse of the theoretical diluted-beam
[Left x-x' plane, Right z-z' plane]

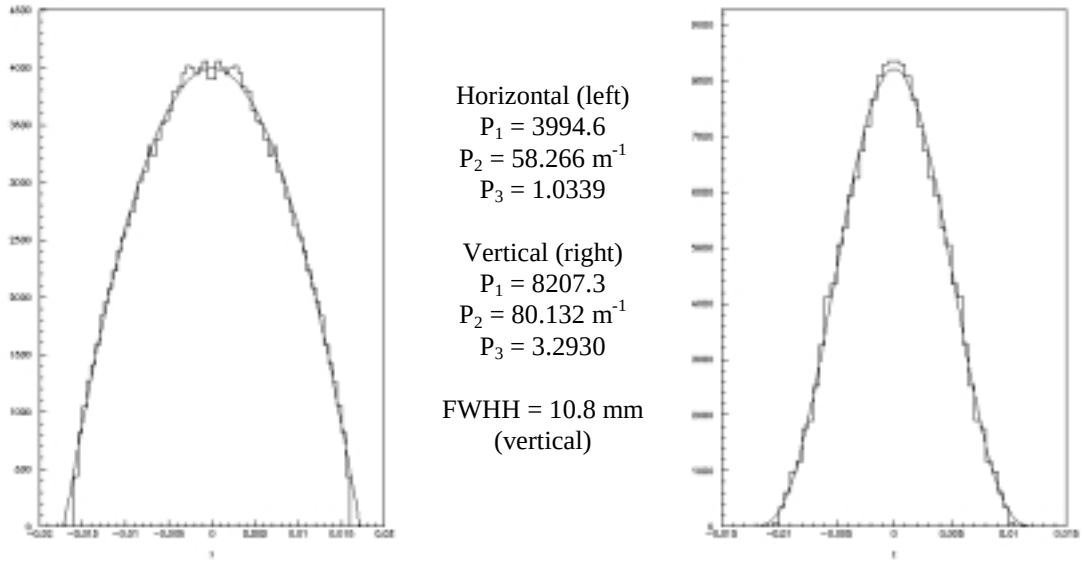

Figure 7.9 Projections of diluted beam on *x* (left) and *z* (right) axes.
[Histograms are fitted with a curve of the family $P_1 (1–y^2 \times P_2^2)^{P3}$.]

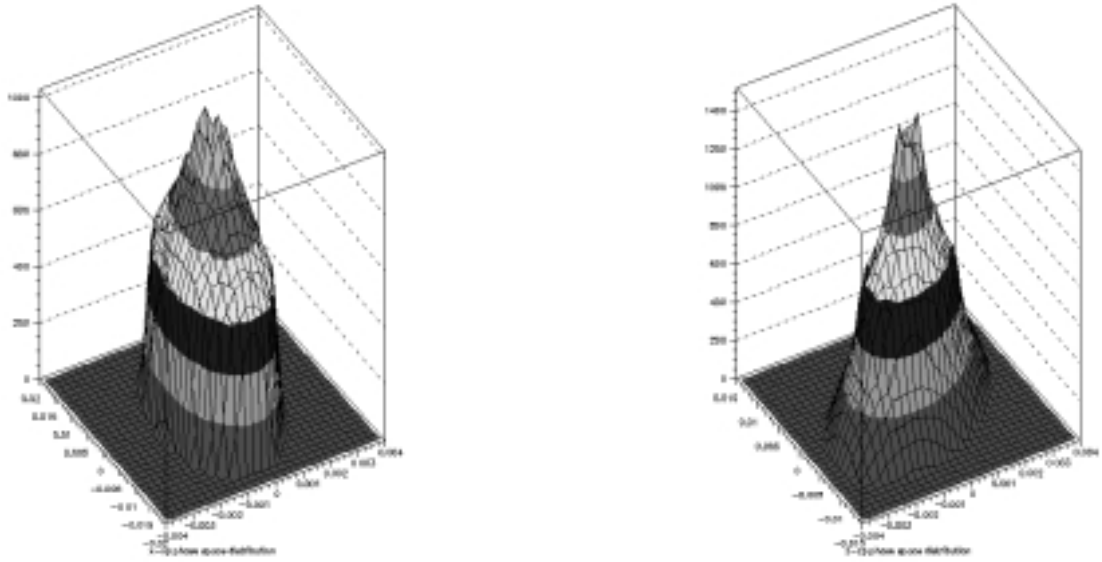

Figure 7.10 Phase-space distributions of diluted beam
[Left *x*-*x′* plane, Right *z*-*z′* plane]

7.3.2 First set of injection parameters for protons

Table 7.6 contains the first set of simulation parameters for proton injection and Figures 7.11-13 show the simulation results. The drawback of this particular simulation is the central hole in the beam distribution. This means that small amplitude particles will be scarce and this reduces the intrinsic smoothing of ripple that can be expected during extraction.

First set of proton injection parameters		
Incoming beam		
Nominal energy [MeV]	20	
$\Delta p/p$ wrt to central orbit of ring*	-1.8×10^{-3}	
Horizontal lattice functions (matched to de-tuned ring)	β_x = 7.0310 m	α_x = -0.19966
	$D_x = 0$	$D'_x = 0$
Vertical lattice functions (mismatched to ring)	β_z = 3.8000 m	$\alpha_z = 0$
	$D_z = 0$	$D'_z = 0$
Injected beam at exit of ES in local ring co-ordinates:	x = -45.6 mm	x' = -0.6 mrad
	z = 2.6 mm	z' = 0 mrad
Total emittance (5 RMS unnormalised)	$E_x = 3\pi$ mm mrad	$E_y = 3\pi$ mm mrad
Injection conditions in ring		
Septum wall [m]	-41×10^{-3}	
Initial kick in injection bumper dipoles [rad]	8.4×10^{-3}	
Injection bump collapse [turn]	28	
Injection efficiency	3.3 effective turns	

* The beam in the ring is off-centre towards the inner half of the aperture. The proton and carbon ion beams have different offsets (see Section 3.5.7)

Table 7.6 First set of proton injection parameters

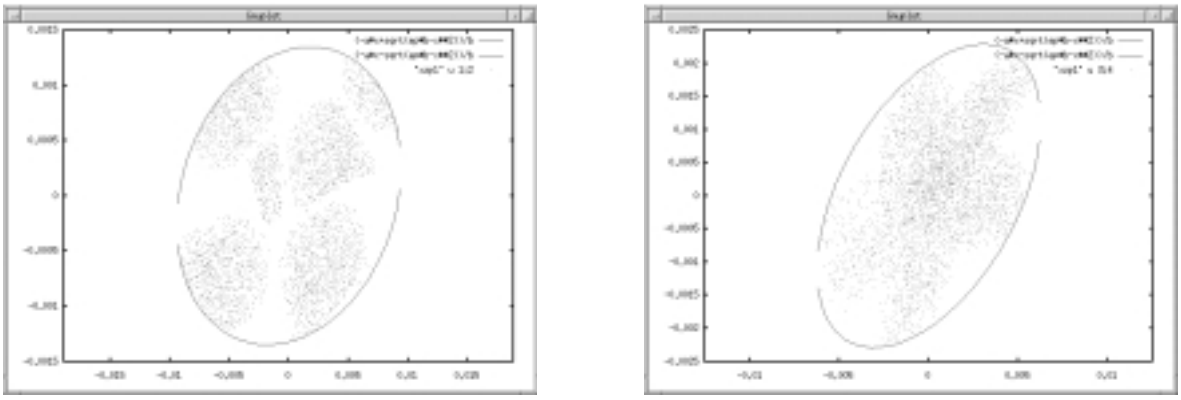

Figure 7.11 Phase-space distributions of the multi-turn injected beam before filamentation and the ellipse of the theoretical diluted-beam
[Left x-x' plane, Right z-z' plane]

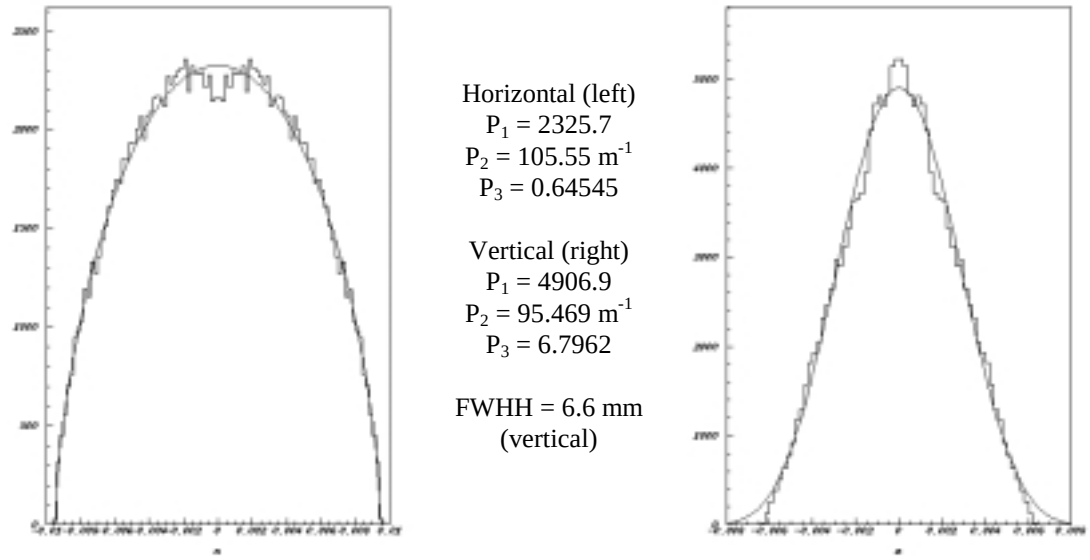

Figure 7.12 Projections of diluted beam on *x* (left) and *z* (right) axes.
[Histograms are fitted with a curve of the family $P_1\,(1–y^2\times P_2^2)^{P3}$.]

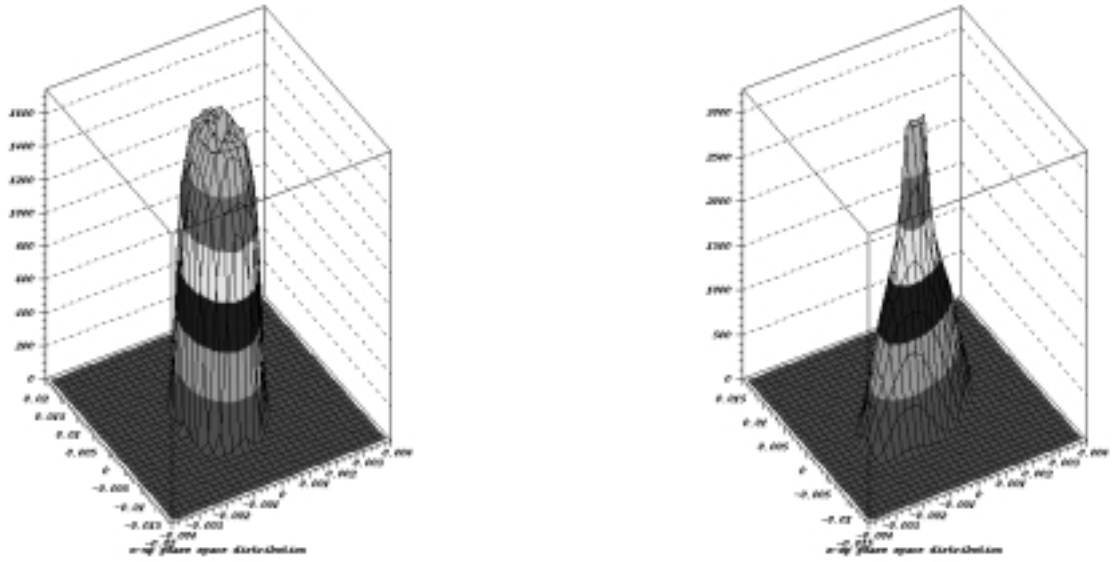

Figure 7.13 Phase-space distributions of diluted beam
[Left *x*-*x*′plane, Right *z*-*z*′plane]

7.3.3 Second set of injection parameters for protons

Table 7.7 contains the second set of simulation parameters for proton injection and Figures 7.14-16 show the simulation results. This simulation shows an improved beam distribution in the *x*-*x*′ plane. Since intensity is not a major problem for the proton source the optimisation of the distribution takes preference.

Second set of proton injection parameters		
Incoming beam		
Nominal energy {MeV]	20	
$\Delta p/p$ wrt to central orbit of ring*	-1.8×10^{-3}	
Horizontal lattice functions (matched to de-tuned ring)	β_x = 7.0310 m $D_x = 0$	α_x = -0.19966 $D'_x = 0$
Vertical lattice functions (mismatched to ring)	β_z = 3.7000 m $D_z = 0$	$\alpha_z = 0$ $D'_z = 0$
Injected beam at exit of ES in local ring co-ordinates:	x = -45.6 mm z = 2.6 mm	x' = -0.4 mrad z' = 0 mrad
Total emittance (5 RMS unnormalised)	$E_x = 3\pi$ mm mrad	$E_y = 3\pi$ mm mrad
Injection conditions in ring		
Septum wall [m]	-41×10^{-3}	
Initial kick in injection bumper dipoles [rad]	8.2×10^{-3}	
Injection bump collapse [turn]	28	
Injection efficiency	3.1 effective turns	

* The beam in the ring is off-centre towards the inner half of the aperture. The proton and carbon ion beams have different offsets (see Section 3.5.7)

Table 7.7 Second set of proton injection parameters

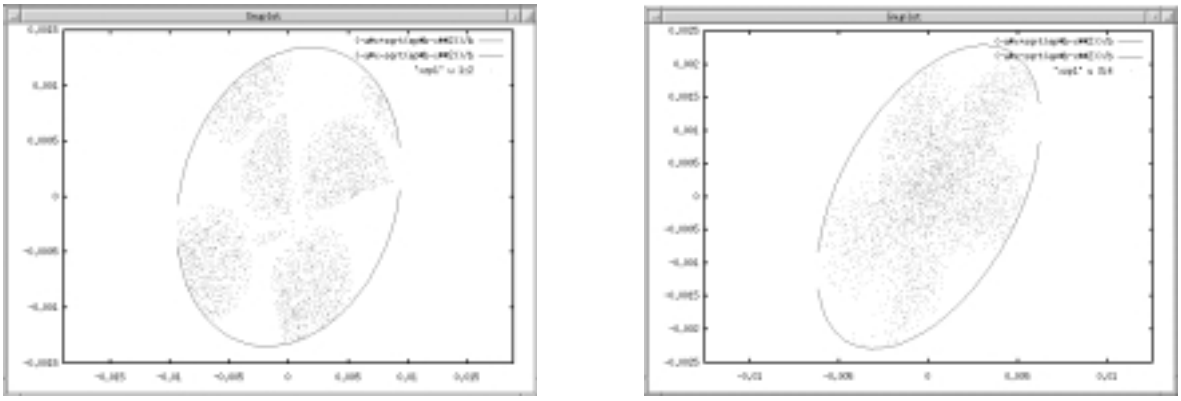

Figure 7.14 Phase-space distributions of the multi-turn injected beam before filamentation and the ellipse of the theoretical diluted-beam
[Left x-x' plane, Right z-z' plane]

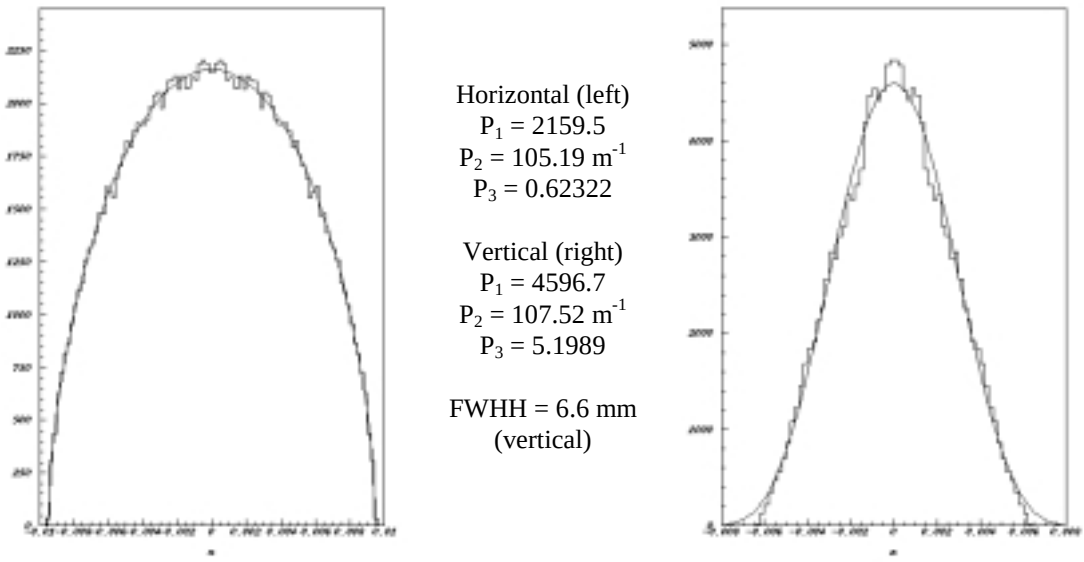

Horizontal (left)
P_1 = 2159.5
P_2 = 105.19 m^{-1}
P_3 = 0.62322

Vertical (right)
P_1 = 4596.7
P_2 = 107.52 m^{-1}
P_3 = 5.1989

FWHH = 6.6 mm
(vertical)

Figure 7.15 Projections of diluted beam on *x* (left) and *z* (right) axes.
[Histograms are fitted with a curve of the family $P_1 (1–y^2 \times P_2^2)^{P3}$.]

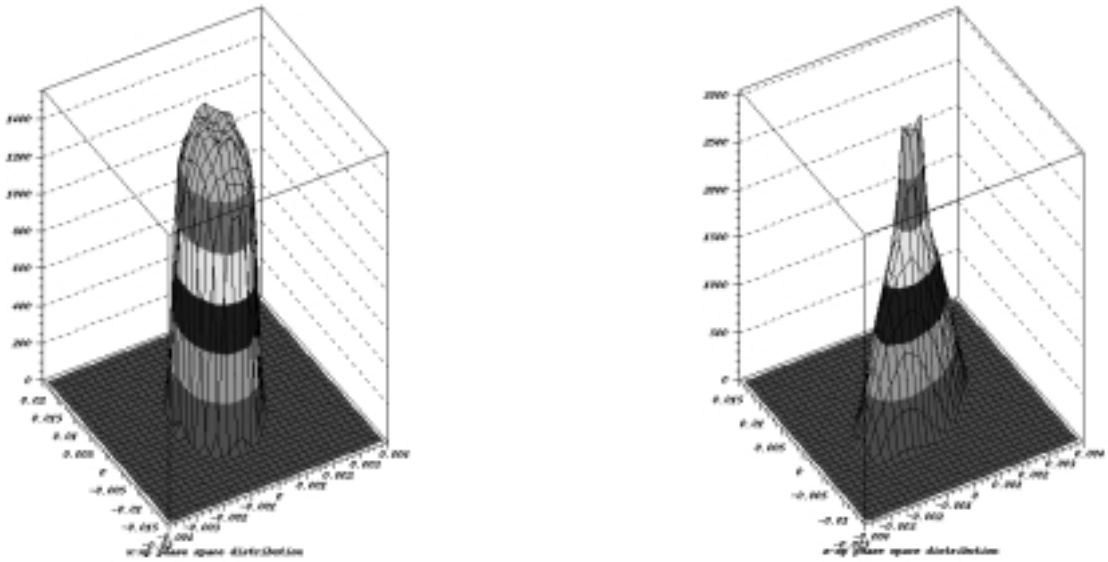

Figure 7.16 Phase-space distributions of diluted beam
[Left *x*-*x*′plane, Right *z*-*z*′plane]

7.3.4 Summary and source requirements

Since multi-turn injection is primarily meant to relax the requirements on the carbon-ion source, the injection has been configured according to the simulation parameters of the carbon injection in described Section 7.3.1 and Table 7.5. In particular, the geometry of the injection orbit at the exit to the electrostatic injection septum recorded in Table 7.5 is that adopted for the line and has already been presented in the boundary conditions for injection in Table 7.3. The proton injection is best served by the parameter set given in Section 7.3.3, but the slightly different

geometry at the exit to the electrostatic septum has to be created by steering in the injection line.

Now that the effective number of turns are known for the injection scheme, it is possible to define the current requirements for the particle sources (and to retrospectively provide the data for the space-charge calculation of the proton transfer line in Figure 7.4). For specification purposes, the higher intensity proton beam for passive spreading is used. Tables 1.6 and 1.7 in Chapter 1 give the number of particles required after injection and just before acceleration in order to have the specified number of particles at the patient. Tables 7.5 and 7.7 gives the number of turns for the injection and the effective number of turns injected. Table 7.8 summarises this information and specifies the sources. The efficiency of the stripping foil has been assumed to be 95%. However, stripping foils do vary widely in quality and the published data is not always consistent.

Specification of current sources

	Proton beam	**Carbon-ion beam**
Nominal energy [MeV/u]	20	7
No. of particles to inject (Tables 1.6 & 1.7 resp.)	7.20×10^{10}	8.31×10^{8}
Revolution time [μs]	1.235	2.063
No. of turns for injection (Tables 7.5 & 7.7 resp.)	28	16
No. of effective turns injected	3.1	3.6
Filling time [s]	34.58×10^{-6}	32.9×10^{-6}
Repetition rate [Hz]	<1	<1
Current in transfer line [emA]	**3.01 (H^+)**	**0.108 (C^{6+})**
Loss in stripping foil 5% Current before stripping foil [emA] (C^{4+})		0.0681
Current from source [emA] (Losses in linac, RFQ, LEBT and contingency according to Tables 1.6 & 1.7 resp.)	**4.4 (H^+)**	**0.11 (C^{4+})**

Table 7.8 Specification of current sources

7.4 C^{4+} SOURCE, STRIPPING FOIL AND SINGLE-TURN INJECTION

7.4.1 C^{4+} source

The multi-turn injection requirement of 120 eμA C^{4+} in Table 7.8 appears to fall within the range of commercially available permanent-magnet ECR sources [4]. The permanent magnet design is both reliable and economical to run, which is well suited to the application of a medical synchrotron.

Initially the PIMMS design considered a single-turn injection. In this case, the currents required from the sources increased sharply to 20.4 mA for the proton source and 538 eμA for the C^{4+} ion source. Although no commercial source at that time was actually producing the C^{4+} current, confidence was felt that it would be possible to

deliver 600 eμA C^{4+} ions [5]. However, the source would be more complicated, more expensive and have a higher power consumption. The fast kicker needed for the single-turn injection was also an expensive item, but it is largely balanced by the electrostatic septum and two bumper dipoles for the multi-turn scheme. However, the electrostatic septum fitted the available space much more easily than the fast kicker and, for all these reasons, the single-turn injection was abandoned.

More recently, an EBIS source has been proposed for hadron therapy [6]. This source is capable of high currents and offers the possibility of working directly with C^{6+} and injecting at 2-3 MeV/u from an RFQ alone. There is, however, a technical problem with impurities in the beam, but these may well be soluble.

7.4.2 Stripping foil

For stripping, a carbon foil between 50 and 200 μ-gm/cm^2 can be used. The equilibrium stripping thickness is near the lower end of the range. Foils with less than 50 μ-gm/cm^2 become hard to handle and foils thicker than 200 μ-gm/cm^2 will unnecessarily perturb the beam. In practice, there can be considerable variation in density across individual foils and between different production batches. The data presented in Table 7.8 has been calculated for a stripping foil of 200 μ-g/cm^2 in order to have pessimistic, but practical, values.

Stripping foil characteristics	
Foil material	Carbon
Foil thickness* [μ-gm/cm^2]	200
Beam energy [MeV/u]	7
Stripping efficiency	0.95
Energy loss [MeV]	0.034
Momentum spread due to stripping [$\Delta p/p$]	0.14×10^{-3}
Temperature rise [K]	< 40
Assuming: $\beta_x = \beta_z = 2$ m; $\alpha_x = \alpha_z = 0$; $E_x = E_z = 0.7\pi$ mm mrad RMS norm	
Then emittance blowup [%]	14

* Thickness can be as low as 50 μg/cm^2, but for practical purposes the calculations are made with the thickest acceptable foil.

Table 7.9 Stripping foil characteristics

7.4.3 Single-turn injection

Although the single-turn injection will not be used, it is interesting to note the design constraints on such a scheme. The choice of energy for single-turn injection depends on two factors:

- The stripping efficiency from C^{4+} to C^{6+} that increases with energy.
- The injection time (revolution period) that decreases with energy.

The compromise between a higher injection energy to improve stripping efficiency and a lower injection energy to benefit from a longer injection time appears to have an optimum between 5 and 7 MeV/u for C^{4+} ions stripping to C^{6+} ions in the PIMMS

ring. For the multi-turn scheme, the time becomes less important and this favours the current choice of the higher energy of 7 MeV/u.

7.5 MULTI-TURN INJECTION BUMP

The horizontal injection bump is excited by two identical dipoles that, by virtue of the symmetry in the lattice, provide a parallel displacement starting at -44.7 mm (for carbon) and -49.6 mm (for protons) of the closed orbit at the injection septum. Figure 7.17(a) shows the -44.7 mm bump in local beam co-ordinates with a carbon-ion beam of emittance 8π mm rad (5 RMS) and full $\Delta p/p = 0.0024$. Figure 7.17(b) shows the -49.6 mm bump in local beam co-ordinates with a proton beam of emittance 5π mm mrad (5 RMS) and full $\Delta p/p = 0.0024$. The positioning of the dipoles is not quite ideal and a residual distortion of about 10% is excited outside the bump, but the form of the bump is good, as, it has no side lobes that could lead to beam loss. The carbon-ion bump collapses in 16 turns and the proton bump collapses in 28 turns.

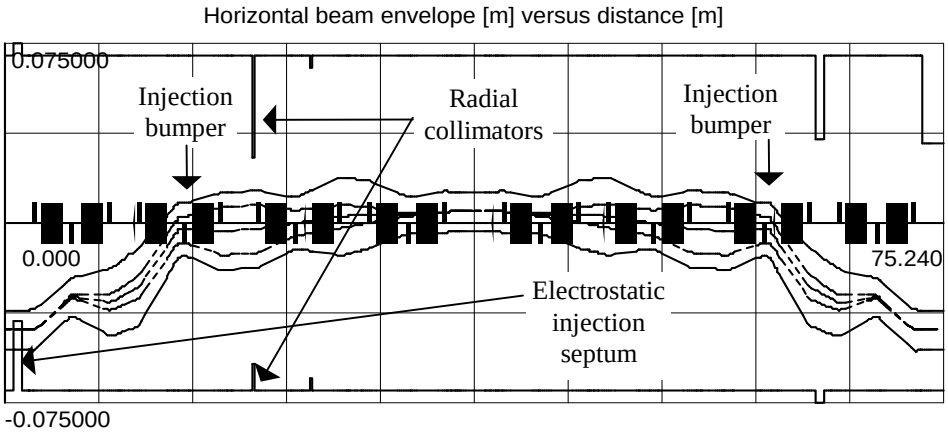

(a) Carbon ion beam at start of injection (8π mm mrad, $\Delta p/p = 0.0024$, bump -44.7 mm)

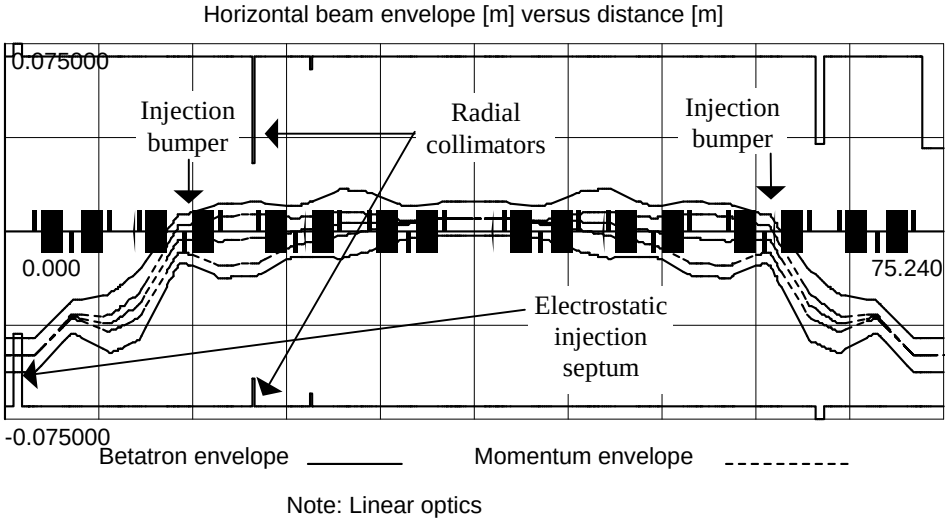

(b) Proton beam at start of injection (5π mm mrad, $\Delta p/p = 0.0024$, bump -49.6 mm)

Figure 7.17 Closed-orbit bumps for multi-turn injection

Multi-turn injections are very lossy, but the losses occur at low energy. In this case, the majority of the losses occur on the foil wall of the electrostatic injection septum. A concept design of the bumpers is given in Appendix P.

7.6 APERTURE

7.6.1 General aperture

Figures 7.18 and 7.19 show the beam envelopes from the two linacs to the ring. The proton line in Figure 7.18 is calculated without space charge.

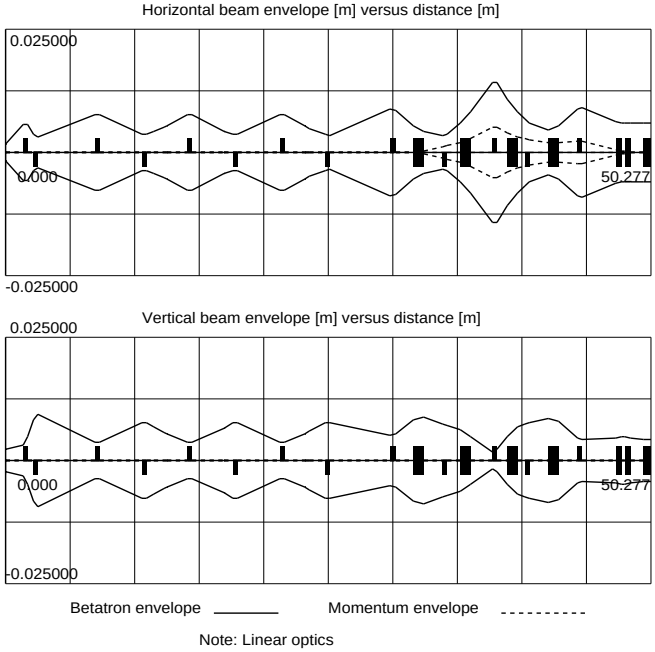

Figure 7.18 Beam envelopes in the proton injection line
[$E_x = E_z = 5\pi$ mm mrad (5 RMS), $\Delta p/p = 0.0024$ ($2\sqrt{5}$ RMS after debunching)]

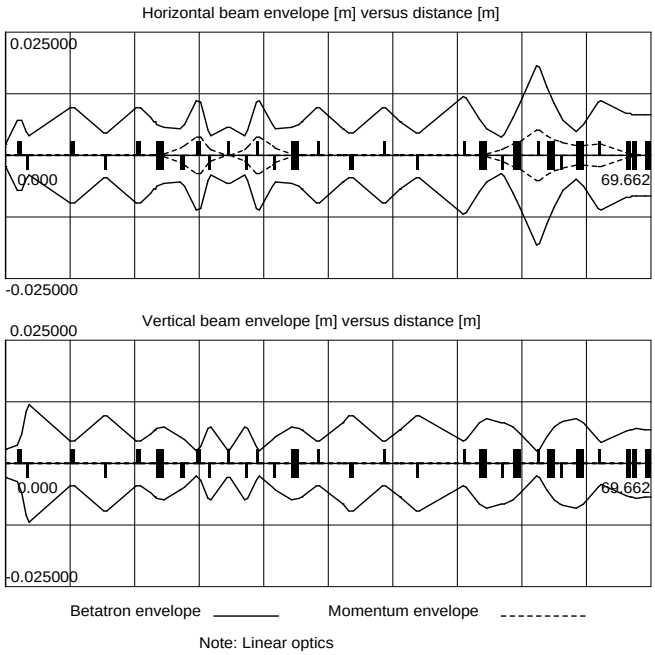

Figure 7.19 Beam envelopes in the carbon-ion injection line
[$E_x = E_z = 8\pi$ mm mrad (5 RMS), $\Delta p/p = 0.0024$ ($2\sqrt{5}$ RMS after debunching)]

In Figures 7.18 and 7.19, the horizontal beam envelopes reach ±18 mm and the vertical envelopes reach ±12 mm. The standard aperture for both injection lines will be based on these values with the addition of closed orbit margins of ±10 mm horizontally and ±7.5 mm vertically (as already done in the extraction lines). The dipole also needs to take into account an addition 57.6 mm for the maximum beam sagitta. A summary of the aperture calculation is made in Table 7.10 and the values are used as the basis for a single quadrupole design and a single dipole design for all the injection lines.

Envelopes, 'good-field' regions, apertures and vacuum pipes

	Horizontal	**Vertical**
General		
Maximum beam sizes [mm]	±18	±12
Closed orbit margin [mm]	±10	±7.5
Max. sagitta in dipoles ('dog-leg') [mm]	57.6	0
Quadrupoles		
Good field region (rounded) [mm]	±28	±19.5
Vacuum pipe internal diameter* [mm]	70	
Vacuum pipe external diameter [mm]	73	
Drift space (same as quadrupoles)		
Vacuum pipe internal diameter (circular) [mm]	70	
Vacuum pipe external diameter (circular) [mm]	73	
Dipoles**		
Good-field region [mm]	±28	±19.5
Internal vacuum pipe (super ellipse) [mm]	70 (curved)	50
External vacuum pipe (super ellipse) [mm]	73 (curved)	53

* Typically 30% of the aperture in a quadrupole is 'poor'-field region, but it is an advantage for vacuum conductance and beam steering to include this space inside the vacuum.
** Sagitta is so large that it is better to curve the dipole and its vacuum chamber.

Table 7.10 Envelopes, 'good-field' regions apertures and vacuum pipes

7.6.2 Septa

The aperture in the pair of magnetic septa in the injection line and the electrostatic injection septum in the ring have apertures tailored to the local beam sizes. The aperture of the magnetic septa is 0.0697 m (horiz.) × 0.0296 m (vert.). The injection channel in the electrostatic septum has a horizontal aperture of 0.030 m and the vertical aperture is equal to that of the main ring.

7.7 MAGNETIC ELEMENTS

Concept designs for the injection line quadrupole and dipole are given in Appendices AA and BB. The quadrupole has the same physical aperture and length as the extraction quadrupole, but requires fewer ampere-turns per pole. It may be possible to use the injection quadrupole (or a slightly strengthed version) for both the injection line and those quadrupoles that have low gradients in the extraction line. The extraction quadrupole could then be designed more specifically for high-field use.

The design of the magnetic injection septa are given in Appendix Q. The electrostatic injection septum is described in Appendix T and a concept design of the injection bumper dipole is given in Appendix P. The details of tolerances etc. have not been evaluated but should be identical to the extraction line.

7.8 DIAGNOSTICS

A discussion of the injection line optics can be found in Ref. 7. The lines will require position, current and profile monitoring and steering dipoles as usual. Fortunately, the line has adequate beam intensities, unlike the extraction lines. The injection lines are based on a strings of FODO cells with matching sections at entry and exit, an embedded 'S' bend in the carbon line and a main bend in the common line before the ring. The monitoring and steering philosophy will be similar to that of the extraction lines. Monitors and correctors for each plane should be positioned in pairs to perform position and angle measurements and position and angle steering at the entry to each long string of FODO cells, before the 'S' bend, before the main bend and before the injection into the ring. On the assumption that a single monitor can measure in both planes, the total number of monitors and correctors can be estimated as 10 and 20 (respectively).

7.9 VACUUM

The requirements for the injection lines' vacuum system can be considered as the same as for the extraction lines. The same basic layout of 25-30 l/s ion pumps spaced at ~20 m (as calculated for the extraction lines in Table 5.6) should be more than sufficient. Two additional vacuum pumps will isolate the poorer vacuum of the lines at the point where the injection line crosses the ring and at injection. A total of six sector valves are used to isolate the ring crossing point, the pipe that can be removed for the vehicle track, the injection into the ring and each of the linacs. Table 7.11 summarises the data.

Injection lines' vacuum system	
Cross-section of the standard chamber	Circular
Average chamber radius [m]	0.035
Length of the proton line [m]	50
Addition length of line for the carbon beam [m]	31
Specific surface area [$cm^2\ m^{-1}$]	2200
Specific out-gassing [Torr $l\ s^{-1}\ cm^{-2}$]	5×10^{-12}
Specific conductance [$l\ m\ s^{-1}$] (H_2 at 25°C)	160
Target average pressure [Torr]	10^{-8}
Ion pump speed [$l\ s^{-1}$]	30
Theoretical pump separation [m]	20.6
Nominal number of pumps	4
Sector valves (exits to linacs, vehicle track, ring crossing and entry to ring)	6
Additional pumps	
Isolation of poorer vacuum of lines from ring [ls^{-1}]*	2×100
Mobile roughing pump	80-450 $l\ s^{-1}$

* Already mentioned in Table 3.25 for the vacuum requirements of the ring.

Table 7.11 Injection lines' vacuum system

The linacs, RFQs and ion sources will require substantial vacuum pumps, but these units should be designed and supplied with the equipment they serve.

7.10 MAGNET CYCLE

The same cycle must always be used for setting the magnets and it must be the same cycle as that used for the magnetic measurements. When starting, all elements should be taken several times around the standard cycle from a minimum value that is well below their operating level to their maximum value in order to stabilise their hysteresis loops. The operating value should be set on the upward branch of the hysteresis curve*. The individual lines can then be left to run d.c. The common section of the injection lines will need to operate at two field levels (protons, $B\rho = 0.496$ Tm; carbon ions, $B\rho = 0.761$ Tm) and will be required to change from one level to the other in a matter of seconds. If the change is in the direction of the cycle on the hysteresis curve (i.e. upwards as proposed here) then the units can be simply moved up in current to the new level. However, if the change is against the direction of cycling (i.e downwards in the case proposed here), then all the units must be taken around the full cycle and set on the upward branch of the next cycle. The magnets will be laminated, but will have thick end plates for convenience of construction. A cycle time of say 10 s with a few hundred milliseconds for stabilisation will be more than adequate and will not require additional ramping voltages.

References

[1] K.D. Gross, M. Pavolvic (editors), Proposal for a dedicated ion beam facility for cancer therapy, (Sept. 1998) available from GSI, Darmstadt. Dual species linac is based on: U. Ratzinger, B. Schlitt, *Design of a carbon injector for a medical acccelerator complex,* Proc. 6th EPAC, Stockholm (1998).

[2] K.R. Crandall, *TRACE3D Documentation*, Los Alamos National Laboratory, LA-UR-90-4146.

[3] M. Pullia, *Time profile of the slowly extracted beam*, CERN/PS 97-50 (DI).

[4] Supernanogan source, Pantechnik S.A., 4, rue Alfred Kastler, F-14000 CAEN.

[5] C. Bieth, Private communication, Hypernanogen source, Pantechnik S.A., 4, rue Alfred Kastler, F-14000 CAEN.

[6] R. Becker, H. Hoeltermann, M. Kleinod, A. Schempp, B. Zipfel, *The EBIS option for hadron therapy*, Proc. EPAC-98, Stockholm 22-26 June 1998, (IOP Institute of Physics Publishing, UK) ISBN: 0 7503 0580 0, (1998), 2345-7.

[7] L. Badano, *Injection and extraction lines instrumentation for PIMMS*, PS/DR/Note 2000-011 (Tech.).

* * *

* The downward branch could equally be used (as in the extraction lines), but the same decision should be applied to all units and at all times.

II-8 OTHER ASPECTS

PIMMS is not tailored to any particular site and it contains a selection of gantries and fixed beam lines that are meant to illustrate the different possibilities rather than fulfil particular requirements. It may therefore not be very representative of a practical project. The low-ripple power converters, the extraction line diagnostics and the gantries stand out as rather special items that cannot be bought easily off the shelf. The RF cavity is also unique, but could be replaced by a conventional ferrite cavity. However, the only truly problematic items as far as cost estimates are concerned are the gantries and especially the ion gantry. For this reason, an estimate is made for the basic elements of the 'Riesenrad' gantry.

8.1 TEMPERATURE AND HUMIDITY

The air temperature in the accelerator complex is assumed to be 22 to 25°C, (the exact value is not important) and should be maintained constant to better than ±4°C throughout the complex during operation. The steel magnet supports (1.2 m) will move differentially by the alignment tolerance of 0.1 mm for a temperature gradient of 8°C across the ring. Aluminium supports expand about twice as much.

The temperature uniformity within and between magnet yokes should be better than ±3°C in order that the field uniformity between yokes and within a yoke is within $\pm 2 \times 10^{-4}$ (temperature effect on permeability). Since there is virtually no eddy current heating in the yokes and the coils are adequately cooled this should not present a problem. The high thermal capacity of the yokes will protect them from larger temperature changes in the air.

The humidity must be adjusted so that the dew point is lower than the incoming cooling water temperature. If this is not the case, then the magnet coils will become coated in condensation and an electrical breakdown may occur.

The gantry rooms are more critical as regards temperature gradients and must be kept within ±1°C.

The linacs are critical concerning the incoming water temperature that will require to be controlled to ±0.5°C (to be checked with final linac design).

8.2 COOLING WATER

The cooling water is assumed to enter at 20°C and leave at no more than 40°C. In most cases, the upper temperature will be far lower than this limit. Ideally, the incoming and outgoing cooling water temperatures should be equally balanced around the room temperature in order to be neutral with respect to the air conditioning. However, this is difficult in a machine that operates at so many different power levels and cycles. It would also require chilled water at the input, which is more expensive. The pressure delivered to all magnets is 7 bar, which implies a system pressure of 8 or 9 bar. The total installed water consumption for the magnets, excluding the proton gantries, is 2.25 m^3/min. To this figure must be added the requirements for the ventilation system, power converters, etc.

8.3 POWER

The principal power converters for the synchrotron are somewhat special in that they have a tight ripple tolerance that implies the use of active filters. This will be an important factor in the cost and will require considerable design work. It may not be possible, or cost effective, to contract to this design work to industry. A specialised design team would be desirable.

8.4 COST ESTIMATES

The most difficult aspects of the cost estimate for the therapy centre are the gantries and the low-ripple power converters. The remaining items are more or less standard, or similar examples can be found. The gantries will vary widely in cost according to whether a specialised design team is set up by the project, or whether the gantry is ordered on the basis of a performance contract from industry. The former is to be preferred. The optics designs are now well understood. The mechanical deformations and their effect on the optics for the 'Riesenrad' have been calculated and this could be repeated for the isocentric proton gantries relatively quickly with the present design team.

To give some help with the costs, some estimates are made below for the 'Riesenrad' gantry, which is the principal unknown in the whole complex. On the basis that the project sets up a specialised design team, then the execution design of the basic gantry with its rotator could be made, specified to industry, built and tested according to Table 8.1. This leaves the 'nozzle' diagnostics, power converters, vacuum system, control system and civil engineering unaccounted for in the estimate, but these could be considered as part of the overall costs of the centre.

Man-year and cost estimate for basic elements of the 'Riesenrad' gantry and rotator

Item	Design effort in project team [man year]	Cost of industrial procurement [MCHF]
Main dipole	2	1.25
Quadrupoles (11)	0*	0.06
Scanning dipoles (3)	1	0.06
Central cage	1.0	1.5
Quadrupole cage	0.25	0.25
Rotator cage	0.25	0.25
Alignment system	0**	0.5
Treatment platform, lift	0**	3.0
Treatment couch with diagnostic ring	1***	1.0
Overall project	2	-
Total	7.5	7.87

* The extraction quadrupole is used. This will be produced in a medium-sized series of 130 units plus spares and the cost is based on the series price.

** Commercially available.

*** Treatment couch is commercially available, but not the diagnostic ring.

Table 8.1 Man-year and cost estimate for basic elements of the 'Riesenrad' gantry and rotator

8.5 ASPECTS NOT STUDIED

No detailed study of shielding has been made for the PIMMS layout. Radiation zones have not been defined. Security has been mentioned, for example, for the hardware frequency limit imposed on the rf cavity to prevent the production of high-energy protons, but it has not been discussed in detail.

A lot of general mechanical engineering problems such as supports, cranes and access for large equipment need to be considered. The power and ventilation services, and especially the reactive power compensator, have not been looked at in detail. The space for storage of spares, maintenance workshops etc. also has to be evaluated more carefully. Services such as fire fighting would be best sub-contracted to the local authorities.

The control system is a major, but intentional, omission. Since controls and computing evolve so quickly and the building of a therapy centre may be several years away, it was felt to be too early to define this system in any detail. If there is a worrying factor in this area, it is not so much the control system, it is more the programming of the control system. Since the cancer treatment will be totally under computer control, this item could be very expensive, unless carefully planned.

The next problem is the cost of manpower, first for the project design and secondly for the measurements, assembly and installation. The practical scenario would probably be somewhat mixed. Some items can be simply bought, while others would need a design team. Activities such as the magnetic measurements, survey, diagnostics and dosimetry could be sub-contracted to national accelerator laboratories and might even be obtained as contributions to the project.

Finally, all non-accelerator aspects have been ignored.

* * *

II-9 OTHER SCENARIOS

During the study, there were often competing ideas and a choice had to be made for what should be adopted. Since the main study is generic and pedagogic in character, it is very possible that these choices will not correspond to the realities of the practical designs and budgets. To try and bridge this gap some of the alternative ideas are presented below.

9.1 COMBINING THE CARBON-ION AND PROTON LINACS

The adoption in PIMMS of an injection chain with two separate linacs and RFQs delivering beams of comparable rigidities is perhaps too ideal. When there are limitations on space and funding a dual species injection chain looks very attractive. The possible advantages are:

- Injection equipment could be installed inside the ring (if the drifts spaces for the debunching cavities are considered this is rather unlikely).
- A minimum of equipment is needed.

The disadvantages are:

- More time is needed to change particle species. This is difficult to evaluate without a design, but 20 min is the estimated time.
- The linac would be designed primarily for 7 MeV/u carbon ions. Unless the structure included additional sections for boosting the proton energy, which would partially destroy the cost advantages, the protons would also be 7 MeV.

The possibility of combining the linacs is under study [1] so this is more than an academic question. The value of 7 MeV is felt to be rather low. However, this raises the more general question, discussed in the next section, of whether the cost advantage (even with separate linacs) of lowering the proton energy is viable in terms of operational reliability.

9.2 LOWERING THE PROTON INJECTION ENERGY

9.2.1 Available aperture versus injection energy

The determination of the vacuum chamber aperture in the PIMMS synchrotron is described in Section 3.5. The situation can be summarised as the horizontal aperture is determined by the separatrices, the vertical aperture is determined by the emittance of the carbon-ion beam at injection and the cross-section of the chamber is affected by the off-centred beam and the separatrices. To these basic conditions are added closed-orbit and collimation margins to determine a minimum aperture. The minimum aperture is then interpreted, generously where possible, to define two standard vacuum chamber cross-sections.

The above procedure has left some flexibility for the injection of the proton beam. At the nominal injection energies, the proton beam has a smaller total geometric emittance (12.5 π mm mrad-diluted at 20 MeV) than the carbon ion beam (30.5 π mm mrad-diluted at 7 MeV/u). Consequently, the proton injection energy can be lowered considerably without the adiabatic expansion causing an aperture limitation. To see where this aperture limitation finally occurs, the maximum horizontal and vertical half beam sizes (from the emittance) of the protons have been plotted in Figures 9.1(a) and (b) against the proton injection energy. The injection

beam sizes for the 7 MeV/u carbon ions are shown as dotted lines in the same figures for comparison. Once the proton beam exceeds the injected carbon-ion beam dimensions, the proton beam is too large to be able to respect the allowed margins.

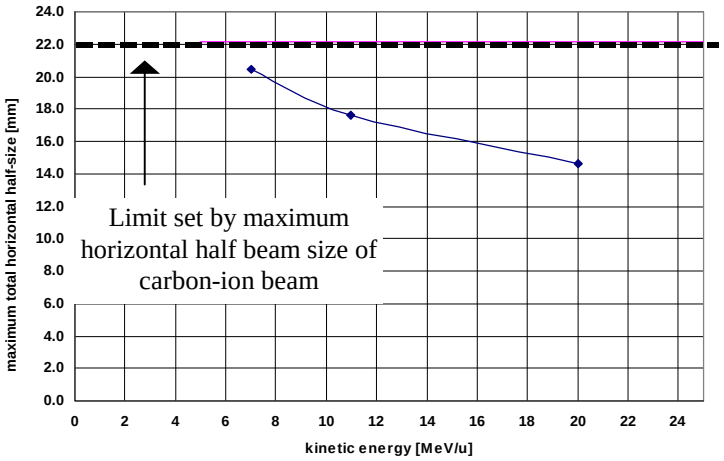

(a) Maximum horizontal half-beam size for the proton beam versus injection energy

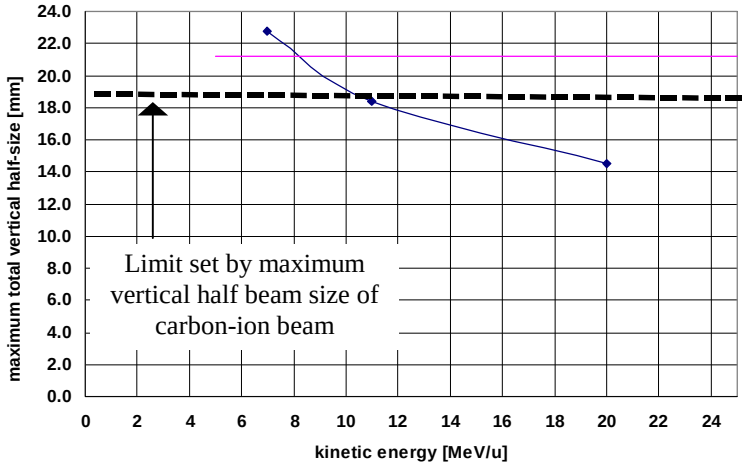

(a) Maximum vertical half-beam size for the proton beam versus injection energy

Figure 9.1 Proton maximum beam half-sizes versus injection energy

At 7 MeV in Figure 9.1, the beam is still smaller than the carbon ion beam horizontally but slightly larger vertically. The figure of 7 MeV appears to be an acceptable compromise for the minimum proton injection energy. It should be remembered that the 7 MeV/u for the ions was chosen to give ~100% efficient stripping of the C^{4+} to C^{6+} and the emittances (diluted) have been chosen to equate the geometrical emittances of the two particle species at the lowest extraction energies for reasons of spot size at the patient. Thus, the dual species linac proposed in Section 9.1 for 7 MeV/u ions and protons fits a consistent parameter set for the machine design. An intermediate solution could be 11 MeV for the proton injection since this fits a commercially available proton linac that would be considerably cheaper than the proposed 20 MeV proton linac.

The main reservation against lowering the proton injection energy arises from the deterioration of the closed orbit. This deterioration arises from two sources. The first is the increasing influence of the spread in the remanent fields in the magnets.

This is a common problem in all accelerators. The second is due to space charge. As the energy is lowered the 'unloaded' working point has to be detuned upwards in the tune diagram. This brings the 'unloaded' working point closer to the integer resonance and causes the betatron amplitude functions (mainly the vertical) to become more and more strongly modulated, affecting apertures and closed orbits. Although the addition of the space charge load corrects the working line back to the nominal position for centre of the beam bunches, the ends of the bunches see quasi-zero space charge and are subject to the distorted conditions. Figure 9.2 shows quantitatively how the situation degrades as the injection energy is lowered. Starting at 20 MeV with normal alignment techniques, there is a 30% probability in the horizontal plane and a 70% probability in the vertical plane that the machine will be within the closed-orbit tolerances without correction and could be injected with full intensity without beam loss. At 11 MeV, 16% of the machines in the horizontal plane and 40% in the vertical plane would be within the allowed closed-orbit margins and, finally, at 7 MeV, only 12% of the machines in the horizontal plane and 24% in the vertical plane would be within the allowed closed-orbit margins. This does not mean that it will be impossible to run. It is a measure of the increasing sensitivity to errors. It means an increasing level of operational difficulty, more frequent adjustments and less tolerance of events such as broken monitors. After correction (assuming that all correctors and monitors are operational), all machines at all energies would be within the closed-orbit tolerances for injection and also within the stricter tolerances for extraction.

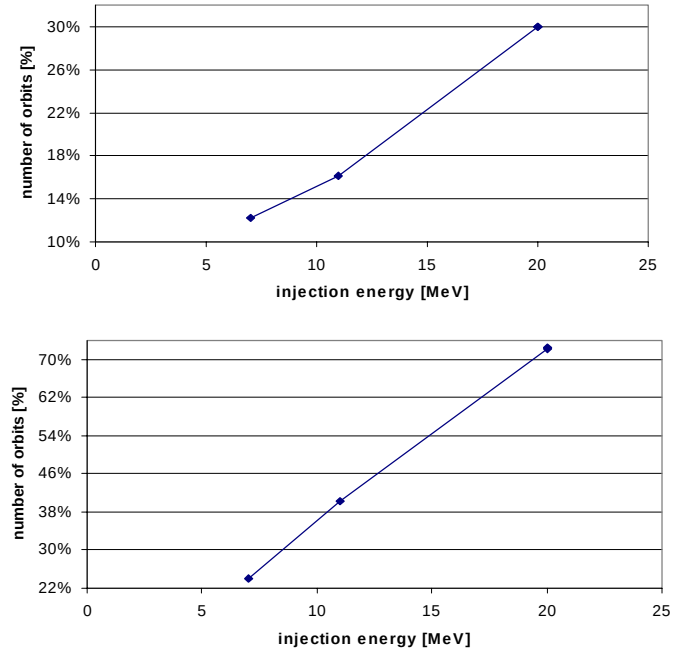

Figure 9.2 Percentage of closed orbits before correction that are within the allowed closed-orbit margins versus energy.

9.3 REMOVING PROTON OPERATION

Treatments tend to be divided into larger tumours in soft parts of the body that cannot be easily immobilised and smaller tumours in hard parts of the body that can be immobilised. The former are ideally treated by a proton beam that is spread passively and administered in short spills that are respiration gated. The later are ideally treated by carbon-ion beams that are less affected by multiple scattering in the

body and can be administered with 'pencil' beams in a very precise manner. Passively-spread proton beams are well suited to a cyclotron-based facility, while the treatment with an actively-scanned, carbon-ion beam requires a larger synchrotron. To these two main categories, a third possibility can be added that of an actively scanned proton beam provided either by a cyclotron or synchrotron.

Putting the passively-spread protons in the same synchrotron as the actively-scanned carbon ions (as done in PIMMS) is not ideal, but possible. It complicates the operation at injection due to the high space charge (see Chapter 7). If the injection energy of the protons is lowered, then the reservations made in Section 9.2 also apply.

Putting actively-scanned protons into the same synchrotron as the actively-scanned carbon ions (as done in PIMMS) runs into the problem of stability of the spill. This is evaluated in Section 4.13 where the specifications for the power converter ripple are evaluated. For proton operation, the specifications go beyond $\Delta I/I_{max} < 10^{-6}$ for the current ripple, which is felt to be difficult in a hospital environment. The stability of 10^{-6} is already very strict and requires active filters that are not normally commercially available. Section 4.13.7 discusses ways of approaching this problem. However, it should be borne in mind that protons scatter more in the patient's body than carbon ions at therapy energies, which destroys some of the potential precision that active scanning offers.

The above reservations suggest that a practical centre might be better served by a dedicated cyclotron for passively-spread proton treatments, a dedicated synchrotron for high-precision carbon ion treatments only and to drop completely the actively-scanned proton treatment.

9.4 ROTATOR OPTIONS

The rotators occupy a lot of space and constitute a mechanical complication. Replacing them with solenoids has been studied [2], but no practical solutions have been found. The possibility of introducing a scatterer into the extracted beam to convert the 'bar' of charge to a near gaussian distribution has been discussed but no design proposals have been made.

References

[1] K.D. Gross, M. Pavolvic (editors), *Proposal for a dedicated ion beam facility for cancer therapy*, (Sept. 1998) available from GSI, Darmstadt. Dual species linac is based on:
U. Ratzinger, B. Schlitt, *Design of a carbon injector for a medical accelerator complex*, Proc. 6th EPAC, Stockholm (1998).

[2] G. Hadinger, *Transport d'un faiseau de particules à travers un solénoïde*, Institut de physique nucléaire de Lyon, Université Claude Bernard, Internal Note, LYCEN RI 9883 (Oct. 1998).

* * *

II-10 CONCLUSIONS

The four-years devoted to this study started with a concentrated effort on the theoretical aspects that are presented in the Part I published in CERN-PS/99-010 (DI). In addition to a general improvement in understanding, fundamental advances were made in the theory of slow extraction and how to smooth the beam spill. The analytical descriptions of 'strip' and 'band' spills and the use of these concepts to compare different classes of slow extraction and the optimisation of what was baptised as the 'intrinsic smoothing' form part of this work. The analytical analysis of 'empty-bucket' channelling provided another tool for smoothing. The theory made it possible to optimise and predict the performance in detail. 'Empty-bucket' channelling also has the advantage that is easy to apply and control. For some topics, the theoretical work continued until almost the end of the study. Here the analytical analysis of the errors in voxel, mini-voxel and true raster scanning can be mentioned. As the study progressed, more and more practical topics were introduced. This started very early with the adoption of a betatron core to drive the extraction, attention then passed to the adoption of 'rotators' to overcome the matching problems to the gantries with beams of unequal emittance. An innovative design was proposed that took into account the rather special phase-space distributions in the extracted beam and controlled the beam sizes at the patient. As the study drew to a close, the practical design that is presented in this volume absorbed most of the available effort. In particular, the design and error analysis of the ion gantry was a major part of this work.

The PIMMS team is also pleased to be able to offer its work in an interactive form on the accompanying CD-ROM. On this disk, not only the files of all the PIMMS publications can be found, but also many of the AUTOCAD[1] drawings, the input files for MERMAID[2] magnet calculations, an EXCEL[3] parameter list and the WinAGILE[4] lattice files. The parameter list and lattice files form truly interactive tools for future design.

II-11 ACKOWLEDGEMENTS

The PIMMS team would like to thank the CERN Directorate and the national organisations of Med-AUSTRON, Onkologie-2000 and TERA, who have supported this study. The warm hospitality and logistic help given by the CERN PS Division during the period from 1996 to 2000 are gratefully acknowledged. Many people have contributed in many ways during this time and their support has been of tremendous value to the study team. In particular, the guidance given by the experts at GSI, Darmstadt has been much appreciated.

* * *

[1] Registered trademark, program from Autodesk Inc.
[2] SIM Ltd., *Mermaid, Magnet design in two and three dimensions*, Novosibirsk, (1994).
[3] Registered trademark, program from Microsoft Inc.
[4] P.J. Bryant, *AGILE program for synchrotron lattice design*, http://nicewww.cern.ch/~bryant.

APPENDIX II A

BEAM MODELS AND EMITTANCE

The primary definition of transverse, geometric emittance uses a single standard deviation, or RMS value, of the projected particle distribution,

$$E_{\mathrm{RMS}} = \pi\sigma_y{}^2 / \beta_y \qquad \text{(A1)}$$

where β_y is the betatron amplitude, σ is the standard deviation and *y* represents either of the transverse co-ordinates *x* or *z*. All emittances will be expressed in the units of [mm mrad] with the π apparent, e.g. 2.5π mm mrad.

For the practical purposes of the design, it is necessary to adopt certain beam models in order to define the vacuum chamber aperture, the space-charge tune shifts, the debunching forces and so on. This may appear restrictive and even arbitrary at times, but providing the model and the RMS emittance are known, it is not difficult to translate the results to other models.

Linac beam in the injection line

For space-charge and aperture calculations, a linac bunch is assumed to be a uniformly-filled 3-D ellipsoid (see Figure. A1).

$$\rho(x,s,z) = \rho_0 \quad \text{over the volume} \quad \left(\frac{x}{a}\right)^2 + \left(\frac{s}{b}\right)^2 + \left(\frac{z}{c}\right)^2 \le 1 \qquad \text{(A2)}$$

where ρ is the particle density and (*a*,*b*,*c*) are the half widths on the axes (*x*, *s*, *z*). The projection of the uniformly-filled ellipsoid onto the *x*-*z* plane yields a 2-D elliptic distribution and a 1-D parabolic distribution when projected onto a single axis.

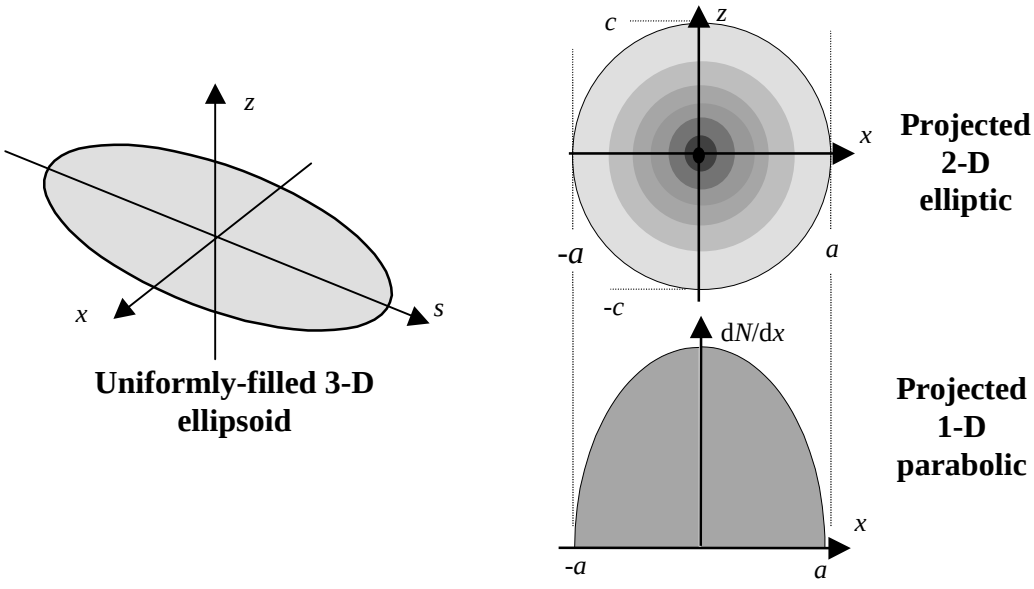

Figure A1 Uniformly-filled ellipsoid beam model

The 2-D elliptic distribution is given by

$$\rho(x,z) = 2b\rho_0\sqrt{\left(1-\left[\frac{x}{a}\right]^2-\left[\frac{z}{c}\right]^2\right)} \qquad \text{(A3)}$$

and the 1-D parabolic distribution by

$$\rho(x) = \pi bc\rho_0\left(1-\left[\frac{x}{a}\right]^2\right). \qquad \text{(A4)}$$

The beam edges are given by

$$a = \sigma_x\sqrt{5}, \quad b = \sigma_s\sqrt{5} \quad \text{and} \quad c = \sigma_z\sqrt{5}\,. \qquad \text{(A5)}$$

The peak density over the average density for the projected 1-D distribution is needed for calculating the peak current and has the value,

In 1-D $$\frac{\text{Peak density}}{\text{Average density}} = 1.5\,. \qquad \text{(A6)}$$

For space-charge calculations, the peak density of the 2-D distribution compared to the density of the uniform distribution that has the same RMS value is needed. This is usually denoted by *G* and has the value,

In 2-D $$G = 6/5\,. \qquad \text{(A7)}$$

Main ring beam model

It has been assumed for space-charge and aperture calculations that all beams in the main ring will also have a 2-D elliptic distribution in transverse space, which transforms to a 1-D parabolic distribution when projected onto a single transverse co-ordinate (see Figure A1). No distinction in the transverse distributions will be made between the bunched and unbunched beams. This simplification is possible since the single beam bunch (h = 1) is long.

The choice of the 2-D elliptic distribution for the injection line and the main ring is a somewhat arbitrary, but convenient, choice from the binomial family that has finite beam edges and has the sequence 2-D uniform, 2-D elliptic, 2-D parabolic and so on to still more 'peaked' distributions. In the case of the main ring, the beam will be diluted at injection this will tend to flatten the beam distribution. A 2-D uniform distribution is not attainable in practice, but the 2-D elliptic is expected to be a good approximation for the diluted beam.

For space-charge calculations, it is necessary to estimate the peak current caused by the bunching. For this purpose, the bunching factor and the longitudinal

beam distribution are needed and for the latter a 1-D parabolic distribution has been assumed in accordance with the earlier models.

For such calculations as the particle density against collimators, it is necessary to assume a beam model with tails for which the truncated gaussian, with the same RMS emittance, is the preferred choice.

Extracted beam in the transfer line

The slow-extracted beam in the plane perpendicular to the extraction is taken to be the same as in the main ring. In the plane of the extraction, however, it has an entirely different form. Its phase-space area is small and almost rectangular in shape and the particle density is quasi-constant over the surface. At the entrance to the electrostatic septum, the on-resonance particles have a phase-space 'footprint' 10 mm full width with 0.05 mrad full divergence. This gives a phase-space area of 0.16 π mm mrad. This is not a very convenient formulation and instead the beam 'footprint' is considered as a 'bar' in an unfilled ellipse of emittance 5π mm mrad (see Figure A2). The exact divergence of the extracted beam is difficult to specify, but providing this divergence is small compared to the height of the unfilled ellipse, the optics is not very sensitive to this value.

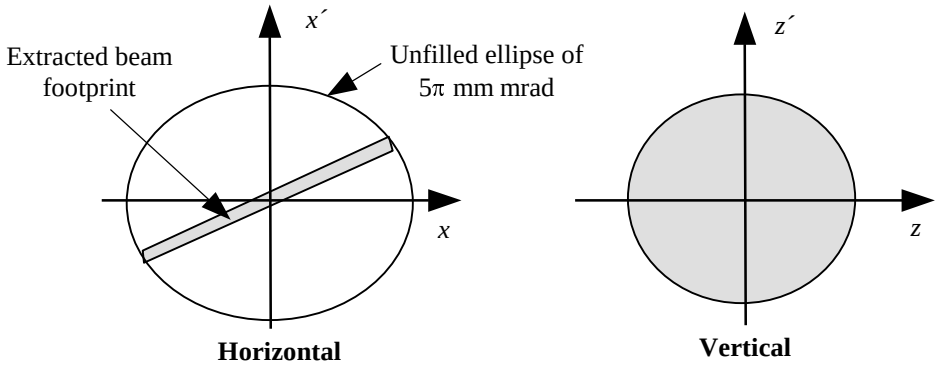

Figure A2 Extracted beam model

* * *

APPENDIX II B

NOMINAL BEAM SIZES IN THE MAIN RING

The beam sizes with closed-orbit and collimation margins in the following tables correspond to the nominal operation conditions, which is based on injecting the protons at 20 MeV and the carbon ions at 7 MeV/u. These tables are used to determine the nominal physical aperture and the 'good' field region. It is shown in Chapter 9 that the proton injection energy can be lowered to ~7 MeV without altering the aperture.

Horizontal aperture required by the resonance separatrices

Table B1 summarises the aperture requirements of the separatrices at all positions along the machine for all the foreseen machine conditions. Columns 4 and 5 contains the innermost and outermost positions of the separatrices and columns 6 and 7 contain these positions plus a closed-orbit margin of 10 mm that has been scaled with the square root of the local betatron amplitude function normalised by the maximum value. The overall maximum excursions for all cases and all positions are +57.4 mm and -60.7 mm.

Horizontal aperture requirement of the separatrices

			Excursion of separatrices		Excursion + closed-orbit margin	
Element name	**Type**	**Length [m]**	**Outside [m]**	**Inside [m]**	**Outside [m]**	**Inside [m]**
SS MR 01-03	Drift	2.3000	0.0244	-0.0309	0.0317	-0.0382
QF MR 01	Quadrupole	0.3500	0.0201	-0.0358	0.0277	-0.0434
SS MR 02	Drift	0.3320	0.0190	-0.0359	0.0265	-0.0434
MB MR 02	Dipole	1.6610	0.0177	-0.0354	0.0250	-0.0427
SS MR 03	Drift	0.5620	0.0137	-0.0331	0.0203	-0.0397
QD MR 03	Quadrupole	0.3500	0.0148	-0.0322	0.0212	-0.0386
SS MR 04	Drift	0.6620	0.0160	-0.0327	0.0225	-0.0392
MB MR 04	Dipole	1.6610	0.0192	-0.0357	0.0264	-0.0429
SS MR 05	Drift	0.3620	0.0267	-0.0429	0.0357	-0.0519
QF MR 05	Quadrupole	0.3500	0.0283	-0.0445	0.0377	-0.0539
SS MR 06-01	Drift	0.8000	0.0293	-0.0452	0.0389	-0.0548
SS MR 06-01	Drift	0.8000	0.0303	-0.0448	0.0401	-0.0546
XC MR 06-01	Sextupole	0.2000	0.0313	-0.0444	0.0412	-0.0543
SS MR 06-02	Drift	0.2000	0.0317	-0.0443	0.0417	-0.0543
QF MR 06	Quadrupole	0.3500	0.0320	-0.0441	0.0420	-0.0541
SS MR 07	Drift	0.3620	0.0318	-0.0424	0.0416	-0.0522
MB MR 07	Dipole	1.6610	0.0307	-0.0392	0.0399	-0.0484
SS MR 08	Drift	1.2120	0.0255	-0.0249	0.0322	-0.0316
QD MR 08	Quadrupole	0.3500	0.0215	-0.0199	0.0266	-0.0250
SS MR 09	Drift	0.5620	0.0211	-0.0206	0.0260	-0.0255
MB MR 09	Dipole	1.6610	0.0215	-0.0227	0.0263	-0.0275
SS MR 10	Drift	0.3620	0.0226	-0.0292	0.0279	-0.0345
See next page						

QF MR 10	Quadrupole	0.3500	0.0228	-0.0307	0.0283	-0.0362
SS MR 11	Drift	1.3500	0.0223	-0.0312	0.0278	-0.0367
SS MR 11	Drift	1.3500	0.0176	-0.0292	0.0229	-0.0345
QF MR 11	Quadrupole	0.3500	0.0215	-0.0272	0.0270	-0.0327
SS MR 12	Drift	0.3620	0.0227	-0.0258	0.0282	-0.0313
MB MR 12	Dipole	1.6610	0.0232	-0.0235	0.0285	-0.0288
SS MR 13	Drift	0.5620	0.0253	-0.0134	0.0301	-0.0182
QD MR 13	Quadrupole	0.3500	0.0260	-0.0135	0.0309	-0.0184
SS MR 14-01	Drift	0.5000	0.0273	-0.0153	0.0324	-0.0204
XC MR 14-01	Sextupole	0.2000	0.0304	-0.0185	0.0362	-0.0243
SS MR 14-02	Drift	0.5120	0.0316	-0.0199	0.0376	-0.0259
MB MR 14	Dipole	1.6610	0.0347	-0.0232	0.0414	-0.0299
SS MR 15	Drift	0.3620	0.0446	-0.0342	0.0538	-0.0434
QF MR 15	Quadrupole	0.3500	0.0468	-0.0367	0.0566	-0.0465
SS MR 16	Drift	2.0000	0.0474	-0.0379	**0.0574 Peak**	-0.0479
QF MR 16	Quadrupole	0.3500	0.0423	-0.0381	0.0519	-0.0477
SS MR 17	Drift	0.3620	0.0405	-0.0374	0.0499	-0.0468
MB MR 17	Dipole	1.6610	0.0380	-0.0359	0.0470	-0.0449
SS MR 18	Drift	0.6620	0.0264	-0.0297	0.0336	-0.0369
QD MR 18	Quadrupole	0.3500	0.0216	-0.0273	0.0281	-0.0338
SS MR 19	Drift	0.5620	0.0198	-0.0269	0.0262	-0.0333
MB MR 19	Dipole	1.6610	0.0189	-0.0279	0.0255	-0.0345
SS MR 20	Drift	0.3320	0.0251	-0.0324	0.0324	-0.0397
QF MR 20	Quadrupole	0.3500	0.0263	-0.0333	0.0338	-0.0408
SS MR 21-01	Drift	2.3000	0.0270	-0.0337	0.0346	-0.0413
SS MR 21-02	Drift	1.3350	0.0285	-0.0319	0.0358	-0.0392
XR MR 21-02	Sextupole	0.2000	0.0294	-0.0308	0.0368	-0.0382
SS MR 21-03	Drift	0.7650	0.0296	-0.0305	0.0370	-0.0379
QF MR 21	Quadrupole	0.3500	0.0310	-0.0292	0.0386	-0.0368
SS MR 22	Drift	0.3320	0.0310	-0.0280	0.0385	-0.0355
MB MR 22	Dipole	1.6610	0.0305	-0.0263	0.0378	-0.0336
SS MR 23	Drift	0.5620	0.0288	-0.0216	0.0354	-0.0282
QD MR 23	Quadrupole	0.3500	0.0283	-0.0231	0.0347	-0.0295
SS MR 24	Drift	0.6620	0.0288	-0.0248	0.0353	-0.0313
MB MR 24	Dipole	1.6610	0.0316	-0.0295	0.0388	-0.0367
SS MR 25	Drift	0.3620	0.0385	-0.0412	0.0475	-0.0502
QF MR 25	Quadrupole	0.3500	0.0400	-0.0440	0.0494	-0.0534
SS MR 26-01	Drift	1.6000	0.0407	-0.0457	0.0503	-0.0553
XC MR 26-01	Sextupole	0.2000	0.0404	-0.0498	0.0503	-0.0597
SS MR 26-02	Drift	0.2000	0.0404	-0.0503	0.0504	-0.0603
QF MR 26	Quadrupole	0.3500	0.0404	-0.0507*	0.0504	**-0.0607 Peak**
SS MR 27	Drift	0.3620	0.0391	-0.0498	0.0489	-0.0596
MB MR 27	Dipole	1.6610	0.0365	-0.0472	0.0457	-0.0564
SS MR 28	Drift	1.2120	0.0247	-0.0359	0.0314	-0.0426
QD MR 28	Quadrupole	0.3500	0.0159	-0.0277	0.0210	-0.0328
SS MR 29	Drift	0.5620	0.0138	-0.0262	0.0187	-0.0311
MB MR 29	Dipole	1.6610	0.0146	-0.0252	0.0194	-0.0300
SS MR 30	Drift	0.3620	0.0230	-0.0226	0.0283	-0.0279
QF MR 30	Quadrupole	0.3500	0.0249	-0.0221	0.0304	-0.0276
SS MR 31	Drift	1.3500	0.0259	-0.0209	0.0314	-0.0264
SS MR 31	Drift	1.3500	0.0266	-0.0201	0.0319	-0.0254
QF MR 31	Quadrupole	0.3500	0.0273	-0.0256	0.0328	-0.0311
See next page						

SS MR 32	Drift	0.3620	0.0266	-0.0262	0.0321	-0.0317
MB MR 32	Dipole	1.6610	0.0250	-0.0259	0.0303	-0.0312
SS MR 33	Drift	0.5620	0.0178	-0.0251	0.0226	-0.0299
QD MR 33	Quadrupole	0.3500	0.0153	-0.0249	0.0202	-0.0298
SS MR 34-01	Drift	0.5000	0.0162	-0.0256	0.0213	-0.0307
XC MR 34-01	Sextupole	0.2000	0.0204	-0.0277	0.0262	-0.0335
SS MR 34-02	Drift	0.5120	0.0221	-0.0286	0.0281	-0.0346
MB MR 34	Dipole	1.6610	0.0265	-0.0308	0.0332	-0.0375
SS MR 35	Drift	0.3620	0.0402	-0.0389	0.0494	-0.0481
QF MR 35	Quadrupole	0.3500	0.0433	-0.0411	0.0531	-0.0509
SS MR 36-01	Drift	0.2500	0.0449	-0.0419	0.0549	-0.0519
ES MR 36-01	Septum	0.2000	0.0450	-0.0415	0.0549	-0.0514
ES MR 36-01	Septum	0.2000	0.0351	-0.0412	0.0450	-0.0511
ES MR 36-01	Septum	0.2000	0.0352	-0.0409	0.0451	-0.0508
ES MR 36-01	Septum	0.2000	0.0353	-0.0406	0.0451	-0.0504
SS MR 36-02	Drift	0.9500	0.0354	-0.0403	0.0452	-0.0501
QF MR 36	Quadrupole	0.3500	0.0358	-0.0389	0.0454	-0.0485
SS MR 37	Drift	0.3620	0.0353	-0.0377	0.0447	-0.0471
MB MR 37	Dipole	1.6610	0.0341	-0.0356	0.0431	-0.0446
SS MR 38	Drift	0.6620	0.0284	-0.0264	0.0356	-0.0336
QD MR 38	Quadrupole	0.3500	0.0261	-0.0227	0.0326	-0.0292
SS MR 39	Drift	0.5620	0.0257	-0.0214	0.0321	-0.0278
MB MR 39	Dipole	1.6610	0.0264	-0.0204	0.0330	-0.0270
SS MR 40	Drift	0.3320	0.0285	-0.0244	0.0358	-0.0317
QF MR 40	Quadrupole	0.3500	0.0289	-0.0259	0.0364	-0.0334
SS MR 01-01	Drift	0.5560	0.0288	-0.0270	0.0364	-0.0346
MS MR 01-01	Septum	0.1625	0.0284	-0.0273	0.0359	-0.0348
MS MR 01-01	Septum	0.1625	0.0280	-0.0278	0.0355	-0.0353
MS MR 01-01	Septum	0.1625	0.0275	-0.0282	0.0349	-0.0356
MS MR 01-01	Septum	0.1625	0.0270	-0.0286	0.0344	-0.0360
SS MR 01-02	Drift	1.0940	0.0265	-0.0290	0.0339	-0.0364

Table B1 Horizontal aperture required by the separatrices
[All values are quoted at the entries to the elements]

Horizontal aperture required by the extracted beam segment between the septa

Table B2 summarises the overall aperture requirement of the extracted beam segment at all positions between the electrostatic and magnetic septa for all of the foreseen machine conditions. Column 4 contains the outermost excursions and column 5 contains these positions plus a closed-orbit margin of 5 mm that has been scaled with the square root of the local betatron amplitude function normalised by the maximum value in the machine. The overall maximum excursion for all cases is +60.3 mm, which occurs at the exit to the focusing quadrupole in front of the magnetic septum.

Horizontal aperture required by the extracted beam between septa

Element name	Type	Length [m]	Excursions of separatrices + closed-orbit margin to the outside [m]	Excursions of extracted segment + closed-orbit margin to the outside [m]
ES MR 36-01	Septum	0.2000	0.0549*	0.0500*
ES MR 36-01	Septum	0.2000	0.0450	0.0501
ES MR 36-01	Septum	0.2000	0.0451	0.0503
ES MR 36-01	Septum	0.2000	0.0451	0.0507
SS MR 36-02	Drift	0.9500	0.0452	0.0512
QF MR 36	Quadrupole	0.3500	0.0454	0.0538
SS MR 37	Drift	0.3620	0.0447	0.0537
MB MR 37	Dipole	1.6610	0.0431	0.0526
SS MR 38	Drift	0.6620	0.0356	0.0476
QD MR 38	Quadrupole	0.3500	0.0326	0.0455
SS MR 39	Drift	0.5620	0.0321	0.0459
MB MR 39	Dipole	1.6610	0.0330	0.0490
SS MR 40	Drift	0.3320	0.0358	0.0578
QF MR 40	Quadrupole	0.3500	0.0364	0.0596
SS MR 01-01	Drift	0.5560	0.0364	**0.0603 Peak**
MS MR 01-01	Septum	0.1625	0.0359	0.0597

*The separatrices have a closed-orbit margin of 10 mm whereas the segment has only 5 mm. This causes an apparent mismatch at the entry to the table.

Table B2 Horizontal aperture required by the extracted beam between septa
[All values are quoted at the entries to the elements]

Horizontal aperture required by the 'waiting' proton beam

The horizontal aperture requirements of the 'waiting' proton beam are maximum at the critical point at 23 MeV when the momentum spread in the bunched beam nears its maximum. The beam is strongly influenced by space charge and the unloaded working point of the machine has to be displaced upwards in the tune diagram towards the integer resonance. The envelopes are calculated on the unloaded

working point because the proximity of the integer resonance increases the beam sizes (this is stronger in the vertical plane) and the particles in the beam 'see' this condition during a part of the synchrotron oscillation. Table B3 summarises the beam sizes, the beam sizes with the closed-orbit margin and, on the low-momentum side, the beam size with the closed-orbit margin and the collimation margin. Only quarter of the machine is recorded in Table B3. The remainder can be found by symmetry.

Horizontal aperture required by the 'waiting' proton beam

			Beam edge		Beam edge + closed-orbit		Inner edge + closed orbit + collimation
Element name	**Type**	**Length [m]**	**Inside [m]**	**Outside [m]**	**Inside [m]**	**Outside [m]**	**Inside [m]**
SS MR 01-03	Drift	2.3000	-0.0092	0.0099	-0.0154	0.0161	-0.0185
QF MR 01	Quadrupole	0.3500	-0.0096	0.0104	-0.0162	0.0170	-0.0195
SS MR 02	Drift	0.3320	-0.0096	0.0103	-0.0162	0.0169	-0.0194
MB MR 02	Dipole	1.6610	-0.0094	0.0100	-0.0158	0.0164	-0.0190
SS MR 03	Drift	0.5620	-0.0092	0.0086	-0.0150	0.0144	-0.0180
QD MR 03	Quadrupole	0.3500	-0.0103	0.0089	-0.0161	0.0146	-0.0190
SS MR 04	Drift	0.6620	-0.0115	0.0094	-0.0174	0.0154	-0.0204
MB MR 04	Dipole	1.6610	-0.0145	0.0111	-0.0212	0.0179	-0.0246
SS MR 05	Drift	0.3620	-0.0238	0.0162	-0.0326	0.0250	-0.0370
QF MR 05	Quadrupole	0.3500	-0.0263	0.0175	-0.0356	0.0268	-0.0402
SS MR 06-01	Drift	0.8000	-0.0281	0.0184	-0.0377	0.0280	-0.0425
SS MR 06-01	Drift	0.8000	-0.0309	0.0195	-0.0407	0.0292	-0.0455
XC MR 06-01	Sextupole	0.2000	-0.0338	0.0206	-0.0437	0.0305	-0.0486
SS MR 06-02	Drift	0.2000	-0.0345	0.0209	-0.0445	0.0309	-0.0494
QF MR 06	Quadrupole	0.3500	-0.0352	0.0212	-0.0452	**0.0312 Peak**	-0.0502
SS MR 07	Drift	0.3620	-0.0353	0.0210	-0.0451	0.0308	-0.0499
MB MR 07	Dipole	1.6610	-0.0342	0.0201	-0.0433	0.0293	-0.0479
SS MR 08	Drift	1.2120	-0.0310	0.0166	-0.0376	0.0233	-0.0409
QD MR 08	Quadrupole	0.3500	-0.0302	0.0148	-0.0351	0.0197	-0.0376
SS MR 09	Drift	0.5620	-0.0311	0.0149	-0.0358	0.0195	-0.0381
MB MR 09	Dipole	1.6610	-0.0345	0.0160	-0.0391	0.0206	-0.0414
SS MR 10	Drift	0.3620	-0.0469	0.0205	-0.0519	0.0256	-0.0544
QF MR 10	Quadrupole	0.3500	-0.0502	0.0218	-0.0554	0.0271	-0.0580
SS MR 11	Drift	1.3500	-0.0517	0.0224	-0.0570	0.0277	**-0.0596 Peak**
Centre Arc	Drift	0.0	-0.0514	0.0221	-0.0564	0.0271	-0.0590

Table B3 Horizontal aperture required by the 'waiting' proton beam
[At 23 MeV critical point; $\Delta p/p_{\text{average}}$ = -0.0018; $\Delta p/p_{\text{full}}$ = 0.00728;
$E_{x,RMS} = E_{z,RMS}$ = 2.2825π mm mrad. On the unloaded working point for a bunching factor = 0.4; 1-D parabolic distributions in all planes; 32.066 mA peak bunched current.
Unloaded tunes Q_x = 1.7642, Q_z = 1.8292; Loaded tunes Q_x = 1.6800, Q_z = 1.7200.
All values are quoted at the entries to the elements and only quarter of the machine is given.]

Horizontal aperture required by the 'waiting' carbon-ion beam

The horizontal aperture requirements of the 'waiting' carbon-ion beam are maximum at the critical point at 8.5 MeV/u when the momentum spread in the bunched beam nears its maximum. Table B4 summarises the beam sizes, the beam sizes with the closed-orbit margin and, on the low-momentum side, the beam size with the closed-orbit margin and the collimation margin. Only quarter of the machine is recorded in Table B4. The remainder can be found by symmetry.

Horizontal aperture required by the 'waiting' carbon-ion beam

			Beam edge		Beam edge + closed-orbit		Inner edge + closed orbit + collimation
Element name	**Type**	**Length [m]**	**Inside [m]**	**Outside [m]**	**Inside [m]**	**Outside [m]**	**Inside [m]**
SS MR 01-03	Drift	2.3000	-0.0151	0.0152	-0.0222	0.0223	-0.0258
QF MR 01	Quadrupole	0.3500	-0.0157	0.0158	-0.0231	0.0232	-0.0268
SS MR 02	Drift	0.3320	-0.0156	0.0156	-0.0229	0.0230	-0.0266
MB MR 02	Dipole	1.6610	-0.0152	0.0152	-0.0223	0.0224	-0.0259
SS MR 03	Drift	0.5620	-0.0152	0.0139	-0.0217	0.0204	-0.0249
QD MR 03	Quadrupole	0.3500	-0.0160	0.0137	-0.0223	0.0201	-0.0254
SS MR 04	Drift	0.6620	-0.0170	0.0141	-0.0235	0.0206	-0.0267
MB MR 04	Dipole	1.6610	-0.0202	0.0159	-0.0273	0.0230	-0.0309
SS MR 05	Drift	0.3620	-0.0298	0.0207	-0.0388	0.0296	-0.0433
QF MR 05	Quadrupole	0.3500	-0.0324	0.0219	-0.0418	0.0312	-0.0465
SS MR 06-01	Drift	0.8000	-0.0343	0.0226	-0.0439	0.0322	-0.0487
SS MR 06-01	Drift	0.8000	-0.0370	0.0233	-0.0468	0.0330	-0.0516
XC MR 06-01	Sextupole	0.2000	-0.0398	0.0240	-0.0497	0.0339	-0.0547
SS MR 06-02	Drift	0.2000	-0.0405	0.0242	-0.0505	0.0342	-0.0554
QF MR 06	Quadrupole	0.3500	-0.0412	0.0244	-0.0512	**0.0344 Peak**	-0.0562
SS MR 07	Drift	0.3620	-0.0411	0.0240	-0.0509	0.0337	-0.0558
MB MR 07	Dipole	1.6610	-0.0397	0.0227	-0.0489	0.0319	-0.0535
SS MR 08	Drift	1.2120	-0.0350	0.0176	-0.0417	0.0244	-0.0451
QD MR 08	Quadrupole	0.3500	-0.0332	0.0145	-0.0383	0.0196	-0.0408
SS MR 09	Drift	0.5620	-0.0339	0.0142	-0.0387	0.0190	-0.0412
MB MR 09	Dipole	1.6610	-0.0369	0.0146	-0.0417	0.0194	-0.0441
SS MR 10	Drift	0.3620	-0.0485	0.0173	-0.0538	0.0226	-0.0564
QF MR 10	Quadrupole	0.3500	-0.0516	0.0182	-0.0571	0.0237	-0.0599
SS MR 11	Drift	1.3500	-0.0531	0.0185	-0.0586	0.0241	**-0.0614 Peak**
Centre Arc	Drift	0.0	-0.0526	0.0180	-0.0579	0.0234	-0.0606

Table B4 Horizontal aperture required by the 'waiting' carbon-ion beam
[At 8.5 MeV/u critical point; $\Delta p/p$ $_{\text{average}}$ = -0.0021; $\Delta p/p$ $_{\text{full}}$ = 0.00586;
$E_{x,RMS} = E_{z,RMS} = 5.5253\pi$ mm mrad. On the unloaded working point for a bunching factor = 0.4; 1-D parabolic distributions in all planes; 1.3705 mA peak bunched current. All values are quoted at the entries to the elements and only quarter of the machine is given.]

Vertical aperture required by the 'waiting' carbon-ion beam at injection

The vertical aperture requirements of the 'waiting' carbon-ion beam are maximum at injection (7 MeV/u). Table B5 summarises the beam sizes, the beam sizes with the closed-orbit margin and the beam size with the closed-orbit margin and the collimation margin. Only quarter of the machine is recorded in Table B5. The remainder can be found by symmetry.

Vertical aperture required by the 'waiting' carbon-ion beam at injection

			Beam edge		Beam edge + closed-orbit		Beam edge + closed-orbit + collimation	
Element name	**Type**	**Length [m]**	**Bottom [m]**	**Top [m]**	**Bottom [m]**	**Top [m]**	**Bottom [m]**	**Top [m]**
SS MR 01-03	Drift	2.3000	-0.0094	0.0094	-0.0127	0.0127	-0.0149	0.0149
QF MR 01	Quadrupole	0.3500	-0.0120	0.0120	-0.0162	0.0162	-0.0191	0.0191
SS MR 02	Drift	0.3320	-0.0130	0.0130	-0.0176	0.0176	-0.0206	0.0206
MB MR 02	Dipole	1.6610	-0.0142	0.0142	-0.0192	0.0192	-0.0225	0.0225
SS MR 03	Drift	0.5620	-0.0196	0.0196	-0.0265	0.0265	-0.0311	0.0311
QD MR 03	Quadrupole	0.3500	-0.0210	0.0210	-0.0284	0.0284	-0.0333	0.0333
SS MR 04	Drift	0.6620	-0.0212	0.0212	-0.0287	0.0287	**-0.0337**	**0.0337**
							Outside dipoles	
MB MR 04	Dipole	1.6610	-0.0203	0.0203	-0.0275	0.0275	**-0.0323**	**0.0323**
							Inside dipoles	
SS MR 05	Drift	0.3620	-0.0168	0.0168	-0.0227	0.0227	-0.0267	0.0267
QF MR 05	Quadrupole	0.3500	-0.0158	0.0158	-0.0214	0.0214	-0.0251	0.0251
SS MR 06-01	Drift	0.8000	-0.0152	0.0152	-0.0205	0.0205	-0.0241	0.0241
SS MR 06-01	Drift	0.8000	-0.0145	0.0145	-0.0197	0.0197	-0.0231	0.0231
XC MR 06-01	Sextupole	0.2000	-0.0141	0.0141	-0.0191	0.0191	-0.0224	0.0224
SS MR 06-02	Drift	0.2000	-0.0140	0.0140	-0.0190	0.0190	-0.0223	0.0223
QF MR 06	Quadrupole	0.3500	-0.0140	0.0140	-0.0189	0.0189	-0.0222	0.0222
SS MR 07	Drift	0.3620	-0.0144	0.0144	-0.0194	0.0194	-0.0228	0.0228
MB MR 07	Dipole	1.6610	-0.0153	0.0153	-0.0206	0.0206	-0.0242	0.0242
SS MR 08	Drift	1.2120	-0.0186	0.0186	-0.0251	0.0251	-0.0295	0.0295
QD MR 08	Quadrupole	0.3500	-0.0202	0.0202	-0.0274	0.0274	-0.0321	0.0321
SS MR 09	Drift	0.5620	-0.0201	0.0201	-0.0272	0.0272	-0.0319	0.0319
MB MR 09	Dipole	1.6610	-0.0188	0.0188	-0.0255	0.0255	-0.0299	0.0299
SS MR 10	Drift	0.3620	-0.0140	0.0140	-0.0189	0.0189	-0.0222	0.0222
QF MR 10	Quadrupole	0.3500	-0.0128	0.0128	-0.0173	0.0173	-0.0203	0.0203
SS MR 11	Drift	1.3500	-0.0121	0.0121	-0.0163	0.0163	-0.0192	0.0192
Centre Arc	Drift	0.0	-0.0115	0.0115	-0.0156	0.0156	-0.0183	0.0183

Table B5 Vertical aperture required by the 'waiting' carbon-ion beam at injection
[At 7 MeV/u and $E_{z,RMS}$ = 6.106π mm mrad.]

Vertical aperture required by the 'waiting' proton beam at injection

The high-intensity proton beam for passive spreading is considered at injection (20 MeV) on the unloaded working point, which is high in the tune diagram. The proximity of the integer resonance perturbs the betatron amplitude functions and the maximum β_z increases from 14.81 m on the nominal working point to 17.38 m. However, the proton beam is still smaller than the carbon-ion beam, which has a larger emittance. Table B6 summarises the beam sizes, the beam sizes with the closed-orbit margin and the beam size with the closed-orbit margin and the collimation margin. Only quarter of the machine is recorded in Table B6.

Vertical aperture required by the 'waiting' proton beam at injection

			Beam edge		Beam edge + closed-orbit		Beam edge + closed-orbit + collimation	
Element name	**Type**	**Length [m]**	**Bottom [m]**	**Top [m]**	**Bottom [m]**	**Top [m]**	**Bottom [m]**	**Top [m]**
SS MR 01-03	Drift	2.3000	-0.0054	0.0054	-0.0082	0.0082	-0.0101	0.0101
QF MR 01	Quadrupole	0.3500	-0.0076	0.0076	-0.0114	0.0115	-0.0140	0.0140
SS MR 02	Drift	0.3320	-0.0083	0.0083	-0.0126	0.0126	-0.0154	0.0154
MB MR 02	Dipole	1.6610	-0.0093	0.0093	-0.0140	0.0140	-0.0171	0.0171
SS MR 03	Drift	0.5620	-0.0134	0.0134	-0.0202	0.0202	-0.0247	0.0247
QD MR 03	Quadrupole	0.3500	-0.0145	0.0145	-0.0218	0.0219	-0.0267	0.0267
SS MR 04	Drift	0.6620	-0.0146	0.0146	-0.0221	0.0221	**-0.0270**	**0.0270**
							Outside dipoles	
MB MR 04	Dipole	1.6610	-0.0139	0.0139	-0.0210	0.0211	**-0.0258**	**0.0258**
							Inside dipoles	
SS MR 05	Drift	0.3620	-0.0113	0.0113	-0.0171	0.0171	-0.0209	0.0209
QF MR 05	Quadrupole	0.3500	-0.0106	0.0106	-0.0159	0.0160	-0.0195	0.0195
SS MR 06-01	Drift	0.8000	-0.0101	0.0101	-0.0152	0.0153	-0.0187	0.0187
SS MR 06-01	Drift	0.8000	-0.0096	0.0096	-0.0145	0.0146	-0.0178	0.0178
XC MR 06-01	Sextupole	0.2000	-0.0093	0.0093	-0.0140	0.0140	-0.0172	0.0172
SS MR 06-02	Drift	0.2000	-0.0092	0.0092	-0.0139	0.0139	-0.0170	0.0170
QF MR 06	Quadrupole	0.3500	-0.0092	0.0092	-0.0138	0.0138	-0.0169	0.0169
SS MR 07	Drift	0.3620	-0.0094	0.0094	-0.0141	0.0142	-0.0173	0.0173
MB MR 07	Dipole	1.6610	-0.0099	0.0099	-0.0150	0.0150	-0.0184	0.0184
SS MR 08	Drift	1.2120	-0.0120	0.0120	-0.0181	0.0181	-0.0222	0.0222
QD MR 08	Quadrupole	0.3500	-0.0130	0.0130	-0.0196	0.0196	-0.0240	0.0240
SS MR 09	Drift	0.5620	-0.0128	0.0128	-0.0193	0.0194	-0.0237	0.0237
MB MR 09	Dipole	1.6610	-0.0118	0.0118	-0.0178	0.0179	-0.0218	0.0218
SS MR 10	Drift	0.3620	-0.0082	0.0082	-0.0124	0.0124	-0.0152	0.0152
QF MR 10	Quadrupole	0.3500	-0.0074	0.0074	-0.0111	0.0111	-0.0136	0.0136
SS MR 11	Drift	1.3500	-0.0068	0.0068	-0.0103	0.0103	-0.0126	0.0126
Centre Arc	Drift	0.0	-0.0063	0.0063	-0.0095	0.0095	-0.0116	0.0116

Table B6 Vertical aperture required by the 'waiting' proton beam at injection
[At 20 MeV and $E_{z,RMS}$ = 2.5π mm mrad.]

* * *

APPENDIX II C

CHANGE IN SPIRAL STEP WITH MOMENTUM IN THE EXTRACTED BEAM

Particles entering the resonance with different betatron amplitudes exhibit different spiral steps in the extracted beam (see Section 3.2 and Table 3.1). The largest spiral step at the electrostatic septum occurs for the zero-amplitude particles that are exactly on-resonance. For PIMMS, this has been adjusted to 10 mm. Smaller spiral steps occur for the particles that are off-resonance and have finite betatron amplitudes. The smallest spiral step in the PIMMS design is 5.7 mm and corresponds to particles that have an emittance of 7.15π mm mrad and a momentum deviation from the resonance of $\Delta p/p = -1.107 \times 10^{-3}$. This causes the extracted beam to vary 'trapezoidally' in width with momentum when viewed on a scale of less than one per mil momentum spread and to have a 'trapezoidal' distribution when projected onto a plane.

However, the variation in range that would occur in the patient due to an extracted momentum spread of one per mil is small. Table C1 shows approximate ranges, calculated with the help of the Bethe-Block equation for energy loss.

Range loss for a one per mil decrease in momentum		
Range loss due to $\Delta p/p = -0.001$ for :	60 MeV protons	~ 0.11 mm
	200 MeV protons	~ 0.85 mm
	250 MeV protons	~ 1.2 mm
	120 MeV/u carbon	~ 0.12 mm
	400 MeV/u carbon	~0.79 mm

Table C1 Range loss for one a per mil decrease in momentum

To be suitable for therapy, the beam needs a much wider momentum spread, so that the Bragg peak is spread out over 5 to 10 mm. This requires the use of a ridge-filter. Assuming that the ridge filter spreads the Bragg peak over 5 mm, the effect of say 1 mm from the intrinsic momentum spread summed in quadrature is entirely negligible. Thus, there will be no memory of the initial correlation between width and momentum in the final beam.

Once the correlation between the transverse distribution and momentum has been randomised by the ridge filter, the transverse beam distribution will be trapezoidal and equal for all momenta. Recalling that the medical specifications require the lateral fall at the edge of the beam to occur within 2 mm (for 80% to 20% intensity reduction), the maximum allowable slope width S_w is 2 mm/0.6 = 3.3 mm, which is larger than will be obtained with the trapezoidal shape and hence consistent with requirements.

The lateral slopes of the beam spot have a positive effect on the overlapping of nearby voxels in an active scanning system by making the system less sensitive to

alignment errors. If the transverse beam distribution were exactly rectangular, no error could be allowed, since any misalignment would yield patches of a double, or null, doses (neglecting the smoothing effect of scattering in the patient's body). On the other hand, the usual overlapping of gaussian distributions is more tolerant. When compared to a gaussian distribution, the trapezoidal one behaves slightly worse, by a factor of about 2. In PIMMS the maximum S_w is 2.15 mm, which requires a positional precision of 0.043 mm (in the relative movement from one voxel to the next, not the absolute position) to achieve the 2% uniformity. At higher extraction energies, S_w reduces, but the scattering in the patient's body increases and homogenises the dose at the tumour.

* * *

APPENDIX II D

THREE AND FOUR MAGNET BUMPS

Sets of 3- and 4-magnet, closed-orbit bumps have been prepared for general orbit manipulations. Tables D1 and D2 list the excitations and Figures D1 and D2 summarise the distribution and forms of the bumps (standardised to 5 mm amplitude at the appropriate beam monitor).

Excitations for 3-magnet bumps (see Figure D1)

Horizontal		Vertical	
Corrector or Monitor	**Kick [mrad] or Deflection [mm]**	**Corrector or Monitor**	**Kick [mrad] or Deflection [mm]**
HC MR 01	0.62	VC MR 03	0.48
PX MR 06	5	VC MR 08	-0.37
HC MR 06	-0.39	**PY MR 09**	5
HC MR 11	0.62	VC MR 13	0.41
HC MR 06	0.60	VC MR 08	0.42
PX MR 11	5	VC MR 13	-0.35
HC MR 11	-0.001	**PY MR 14**	5
HC MR 16	0.59	VC MR 18	0.46
HC MR 11	0.59	VC MR 13	0.45
PX MR 16	5	VC MR 18	-0.04
HC MR 16	-0.22	**PY MR 19**	5
HC MR 21 (upstream)	0.55	VC MR 23	0.41
HC MR 16	0.56	VC MR 18	0.42
PX MR 21 (upstream)	5	VC MR 23	-0.04
HC MR 21 (upstream*)	-0.69	**PY MR 24**	5
HC MR 26	0.47	VC MR 28	0.46
HC MR 21 (upstream*)	0.47	VC MR 23	0.47
PX MR 26	5	VC MR 28	-0.35
HC MR 26	-0.17	**PY MR 29**	5
HC MR 31 (upstream)	0.61	VC MR 33	0.41
HC MR 26	0.60	VC MR 28	0.45
PX MR 31 (upstream)	5	VC MR 33	0.51
HC MR 31 (upstream*)	0.08	**PY MR 34**	5
HC MR 36	0.61	VC MR 38	0.51
HC MR 31 (upstream*)	0.60	VC MR 33	0.45
PX MR 36	5	VC MR 38	0.04
HC MR 36	0.04	**PY MR 39**	5
HC MR 01	0.45	VC MR 03	0.41
HC MR 36-3	0.46	VC MR 38	0.42
PX MR 01-7	5	VC MR 03	-0.06
HC MR 01-8	-0.76	**PY MR 04**	5
HC MR 06-2	0.62	VC MR 08	0.49

* When two correctors exist in the same drift space a choice has been made to minimise the total correction strength.

Table D1 Excitations for 3-magnet bumps (see Figure D1)
[On extraction working point: $Q_x = 1.667$, $Q_z = 1.720$]

Excitations for 4-magnet bumps (see Figure D2)			
Horizontal		**Vertical**	
Corrector or Monitor	**Kick [mrad] or Deflection [mm]**	**Corrector or Monitor**	**Kick [mrad] or Deflection [mm]**
HC MR 01	-0.03	VC MR 03	0.41
HC MR 06	0.62	VC MR 08	0.36
PX MR 11	5	**PY MR 09**	5
HC MR 11	-0.03	VC MR 13	-0.21
HC MR 16	0.59	VC MR 18	0.74
HC MR 06	-0.15	VC MR 08	-0.38
HC MR 11	0.59	VC MR 13	0.31
PX MR 16	5	**PY MR 14**	5
HC MR 16	-0.37	VC MR 18	-0.36
HC MR 21 (upstream)	0.55	VC MR 23	0.57
HC MR 11	0.38	VC MR 13	0.42
HC MR 16	0.41	VC MR 18	0.40
PX MR 21 (upstream)	5	**PY MR 19**	5
HC MR 21 (upstream)	-0.32	VC MR 23	0.33
HC MR 26	0.46	VC MR 28	0.48
HC MR 16	0.30	VC MR 18	0.38
HC MR 21 (upstream)	0.12	VC MR 23	0.53
PX MR 26	5	**PY MR 24**	5
HC MR 26	0.04	VC MR 28	-0.01
HC MR 31 (upstream)	0.60	VC MR 33	0.50
HC MR 21 (upstream)	-0.02	VC MR 23	0.42
HC MR 26	0.61	VC MR 28	0.34
PX MR 31 (upstream)	5	**PY MR 29**	5
HC MR 31 (upstream)	0.05	VC MR 33	-0.21
HC MR 36	0.61	VC MR 38	0.74
HC MR 26	-0.02	VC MR 28	0.37
HC MR 31 (upstream)	0.60	VC MR33	0.30
PX MR 36	5	P**Y MR 34**	5
HC MR 36	0.20	VC MR 38	0.36
HC MR 01	0.45	VC MR 03	0.57
HC MR 31 (downstream)	0.43	VC MR 33	0.42
HC MR 36	0.32	VC MR 38	0.40
PX MR 01	5	**PY MR 39**	5
HC MR 01	-0.42	VC MR 03	0.32
HC MR 06	0.61	VC MR 08	0.51
HC MR 36	0.31	VC MR 38	0.38
HC MR 01	0.09	VC MR 03	0.53
PX MR 06	5	**PY MR 04**	5
HC MR 06	0.04	VC MR 08	-0.01
HC MR 11	0.60	VC MR 13	0.50

* When two correctors or monitors exist in the same drift space a choice has been made to minimise the total correction strength.

Table D2 Excitations for 4-magnet bumps (see Figure D2)
[On extraction working point: $Q_x = 1.667$, $Q_z = 1.720$]

Figures D1 and D2 are drawn to the same scale and standardised to an amplitude of 5 mm at the principal monitor for the bump. The 3-magnet bumps and the horizontal 4-magnet bumps are all well behaved, but certain of the vertical, 4-magnet bumps have large peaks that go beyond the excursion at the monitor and these bumps are unfortunately less useful as a consequence.

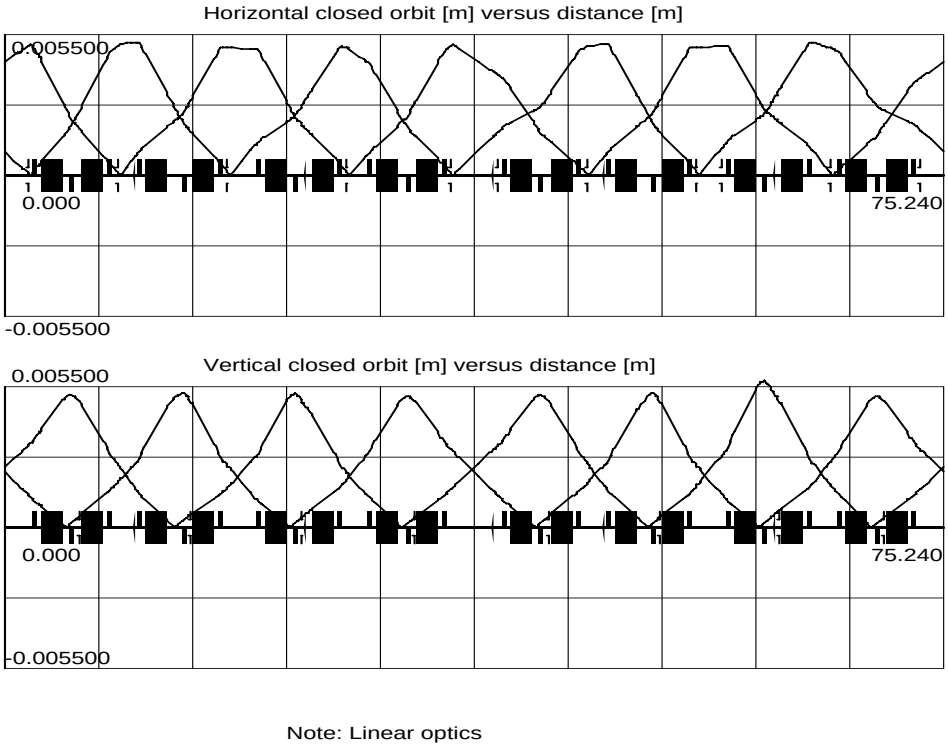

Figure D1 3-magnet bumps set to 5 mm at an intermediate beam monitor
[On extraction working point: Q_x = 1.667, Q_z = 1.720]

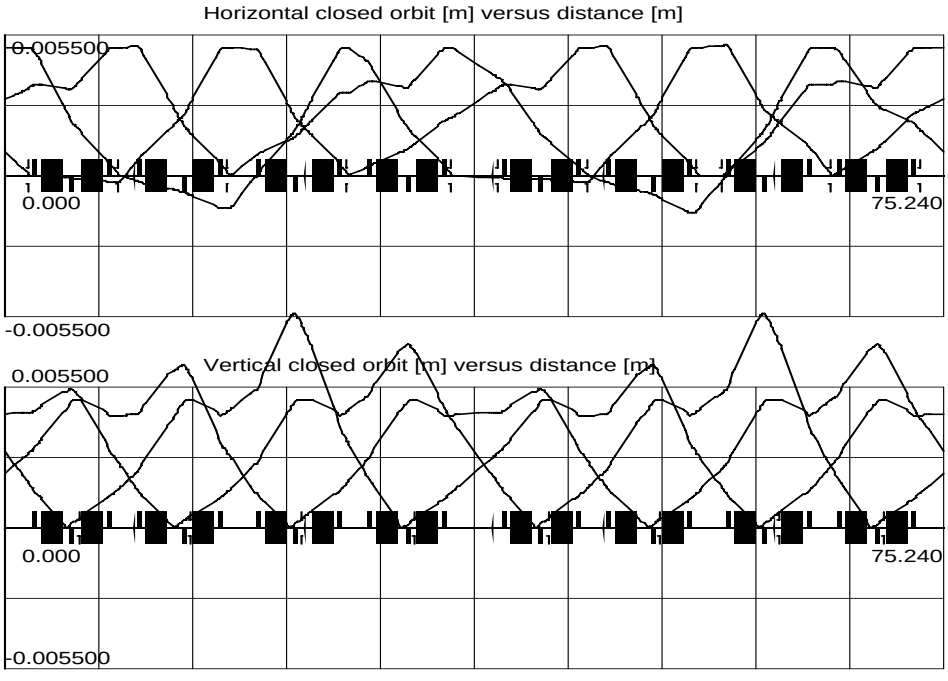

Figure D2 4-magnet bumps set to 5 mm at an intermediate beam monitor
[On extraction working point: Q_x = 1.667, Q_z = 1.720]

* * *

APPENDIX II E

MECHANICAL AND MAGNETIC DESIGN OF THE MAIN DIPOLES

The main dipole is an H-type design [1]. A C-type design would have been ~40% bigger, while its advantages (direct access to vacuum chamber and beams can be injected and extracted at small angles) were not needed. A window-frame design, although providing excellent field quality, would have required a more expensive and complicated saddle coil. The dipole has been curved to account for the 81 mm beam sagitta. A straight unit, although simpler to build, would have required a 25% increase in the volume of the gap that would have added inductance (expensive reactive power) during ramping, 4% to the resistive power and a heavier yoke. Since the curvature is small, it is obtained by pushing the laminations against a curved reference wall. The half yokes are stacked, put under compression and welded with external tie bars. The two halves can then be welded or bolted to form the complete yoke. The pole profile is calculated in two dimensions and the end fields will be compensated by shims added at the time of the measurements. This is preferred to a uniformly-distributed correction of the pole profile because the lattice functions change appreciably along the magnet. End plates are fabricated by gluing a stack of laminations and then machining the composite block with a recess in which to mount shims. This avoids the undesirable eddy current effects that thick end plates introduce. The laminations are insulated by 'blue-steaming' the steel roll at the time of fabrication. The sheets have to be shuffled to randomise magnetic properties. The main characteristics are summarised in Table E1 and in Figures E1, E2, E3 and E4. For further details see Ref. 1.

Main ring dipole: principal parameters*	
Overall length [m]	1.8930
Yoke length [m]	1.5530
Width of cross-section [m]	1.0080
Overall width [m]	1.0893
Overall height [m]	0.7060
Gap height on central orbit [m]	0.0720
Packing factor	>0.97
Weight [t]	8
Nominal maximum field [T]	1.5
Current for maximum field[A]	2778
Effective magnetic length at max. field [m]	1.661
'Good-field' region (all field levels)	At least ±60 mm horizontal; ±28 mm vertical
Field quality, $\Delta B/B$ (all field levels)	$\leq \pm 2 \times 10^{-4}$
Beam follows centre line of aperture	Yoke is curved
Resistance (magnet) [Ω]	0.00408
Inductance (magnet) [H]	0.011
Number of coils	2 (1 per pole)
Number of turns	32 (16 per coil)
Number of water circuits	4 (2 per coil) All in parallel
Average turn length [m]	4.252
Length of a single water circuit [m]	34.02
Temperature rise in a single circuit [°C]	10.2
Water flow (magnet) [l/min]	44.2 (11.05 per circuit)
Pressure drop [bar]	7

* There are small differences with respect to Ref. 1. In Ref 1, the coil resistance and temperature rise are slightly higher and the water flow is slightly lower.

Table E1 Main ring dipole: principal parameters

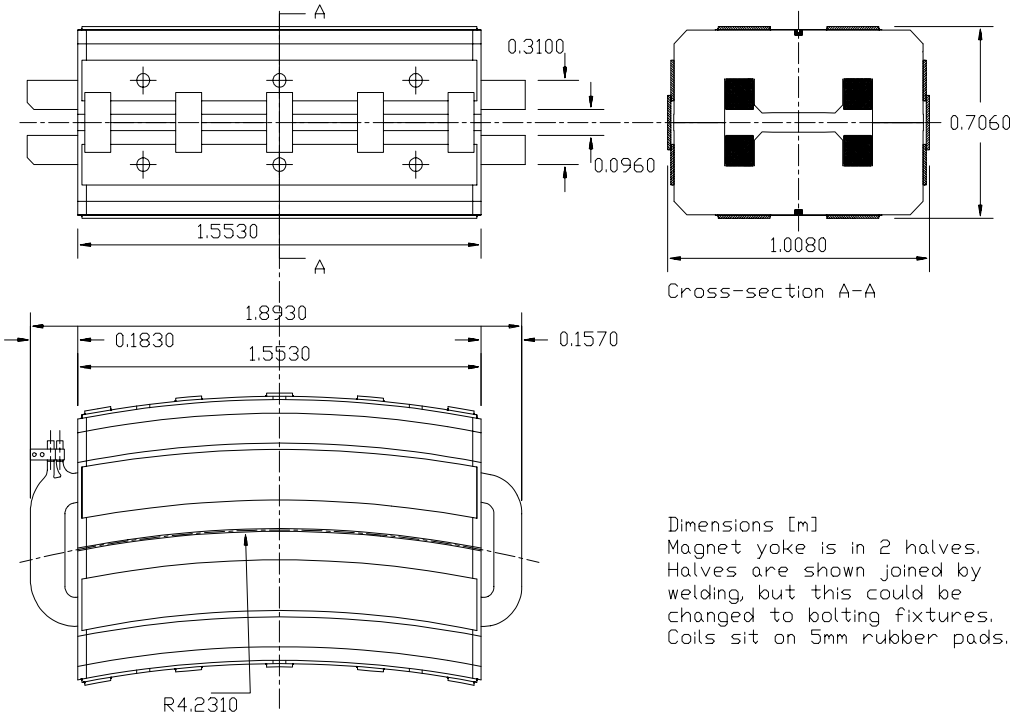

Figure E1 Main ring dipole

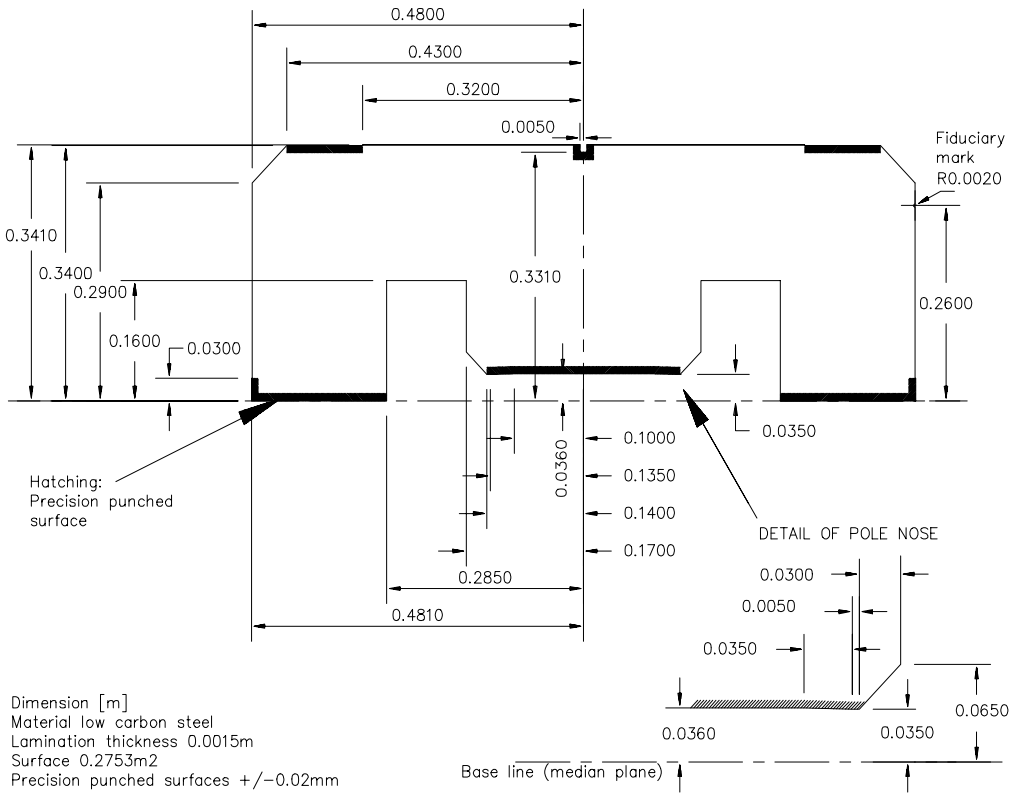

Figure E2 Main ring dipole lamination

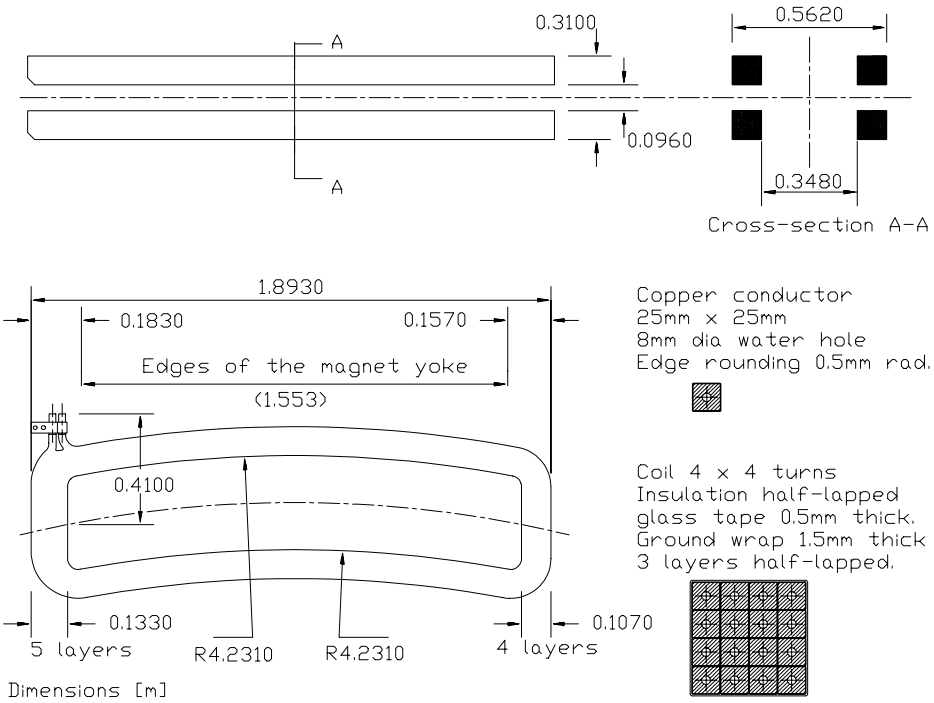

Figure E3 Main ring dipole coil

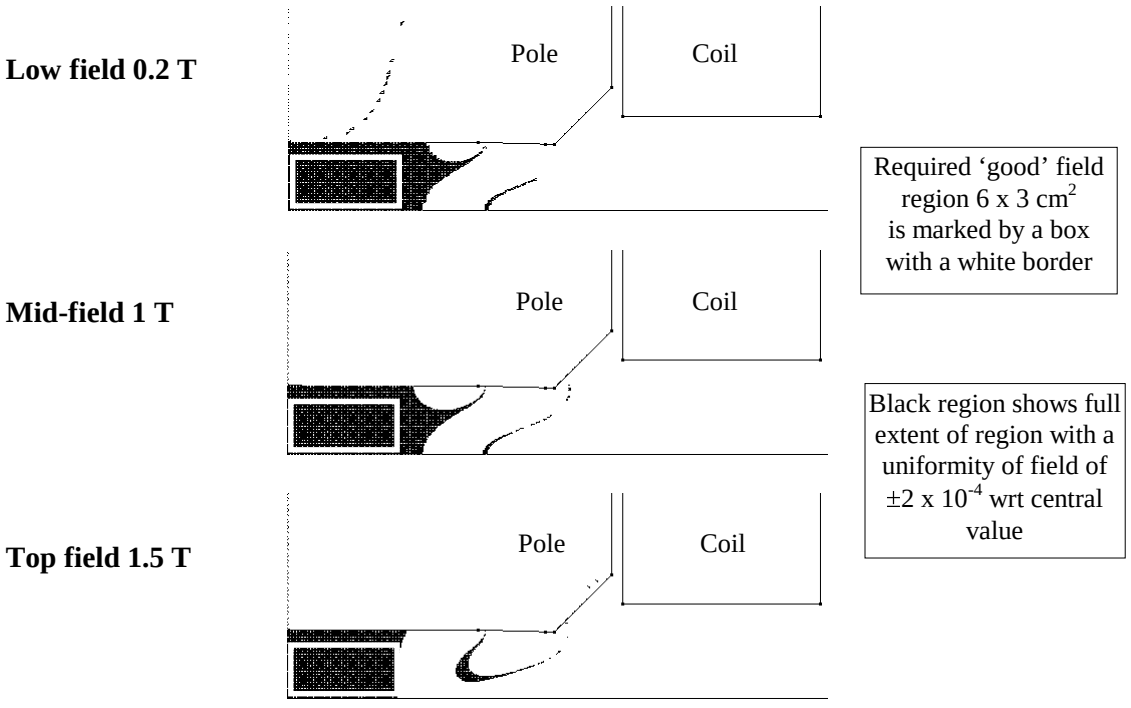

Figure E4 Main ring dipole field uniformity

References

[1] G. Brianti, M. Giesch, S. Rossi, *Dipole of the CNAO synchrotron (based on the PIMM Study)*, PS/DI/Note 98-15 (Tech.).

* * *

APPENDIX II F

MAGNETIC AND MECHANICAL DESIGN OF THE MAIN QUADRUPOLES

The main quadrupole has been designed with a packing factor of 0.7 that increases the field level in the steel with the aim of improving the low-field performance. The pole profile is based on a three-dimensional calculation [1], since the large aperture and short yoke make two-dimensional calculations inaccurate. The construction uses four individual quadrants made from a spaced stack of 1.5 mm thick laminations (packing factor of 0.7) without end plates. The quadrants are bolted together, so that the magnet can be easily opened. Two possible constructions of the quadrants are presented:

- In this Appendix, the individual quadrants are bolted longitudinally (bolts are non-magnetic and insulated). The laminations are spaced by washers (0.64 mm thick) on the longitudinal bolts. The washers can be ceramic and will require a tolerance of 0.64 ±0.01 mm. The quadrants are potted in epoxy resin to prevent 'ringing'.

- In Ref. 1, the laminations are spaced by punching depressions into the laminations. The quadrants are then welded by external tie bars.

The number of laminations per quadrant must be fixed for the magnet series production (depending on the exact thickness of the steel sheet production this should be 163 or 164). To ensure similar field integrals, the laminations must be selected so that the quadrant weights are distributed within ±0.002 of the average. The main characteristics are summarised in Table F1 and in Figures F1, F2 and F3. Further details can be found with the 3D-field calculations in Ref 1.

Main ring quadrupoles (QF1, QF2, QD): principal parameters	
Overall length [m]	0.4620
Yoke length [m]	0.2820
Overall width and height [m]	0.6206
Inscribed circle radius [m]	0.0850
Packing factor	0.70
Weight [t]	0.39
Nominal maximum gradient [T/m]	3.65
Current for maximum gradient[A]	540
Effective magnetic length at max. gradient [m]	0.350
'Good-field' region (all field levels)	At least ±60 mm horizontal; ±30 mm vertical
Int. gradient quality, $\Delta Gl/Gl$ (all field levels)	$\leq \pm 5 \times 10^{-4}$
Resistance (magnet) [Ω]	0.0166
Inductance (magnet) [H]	0.00475
Number of coils	4 (1 per pole)
Number of turns	80 (20 per coil)
Number of water circuits	2 (0.5 per coil)
Average turn length [m]	1.093
Length of a single water circuit [m]	42.3
Temperature rise in a single circuit [°C]	12.6
Water flow (magnet) [l/min]	5.5 (2.75 per circuit)
Pressure drop [bar]	7

Table F1 Main ring quadrupoles (QF1, QF2, QD): principal parameters

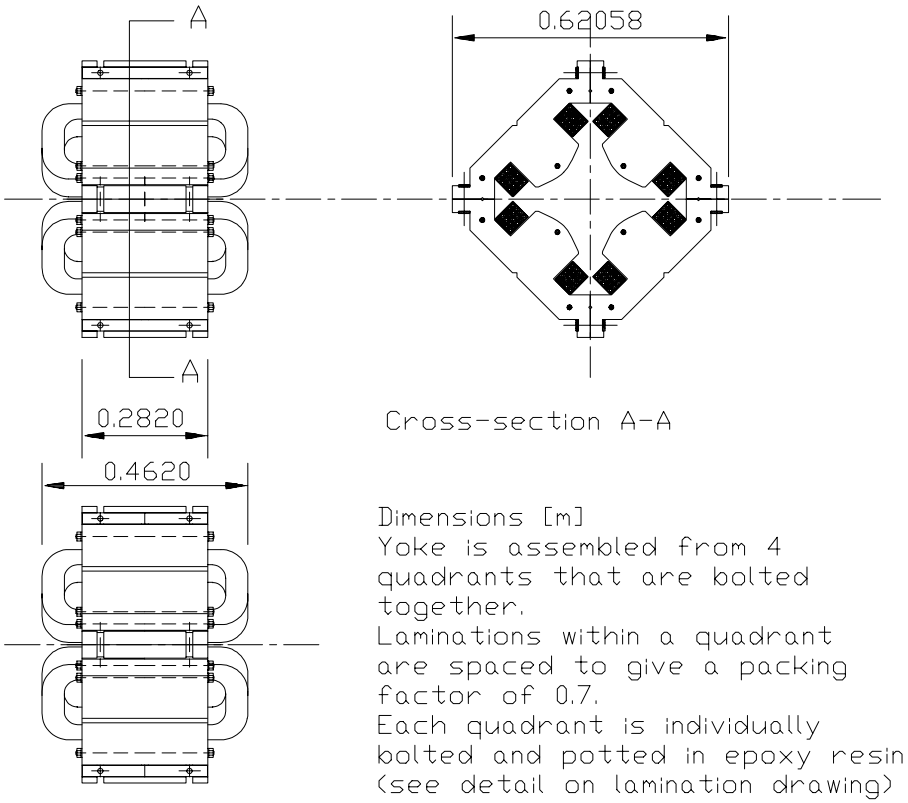

Figure F1 Main ring quadrupole

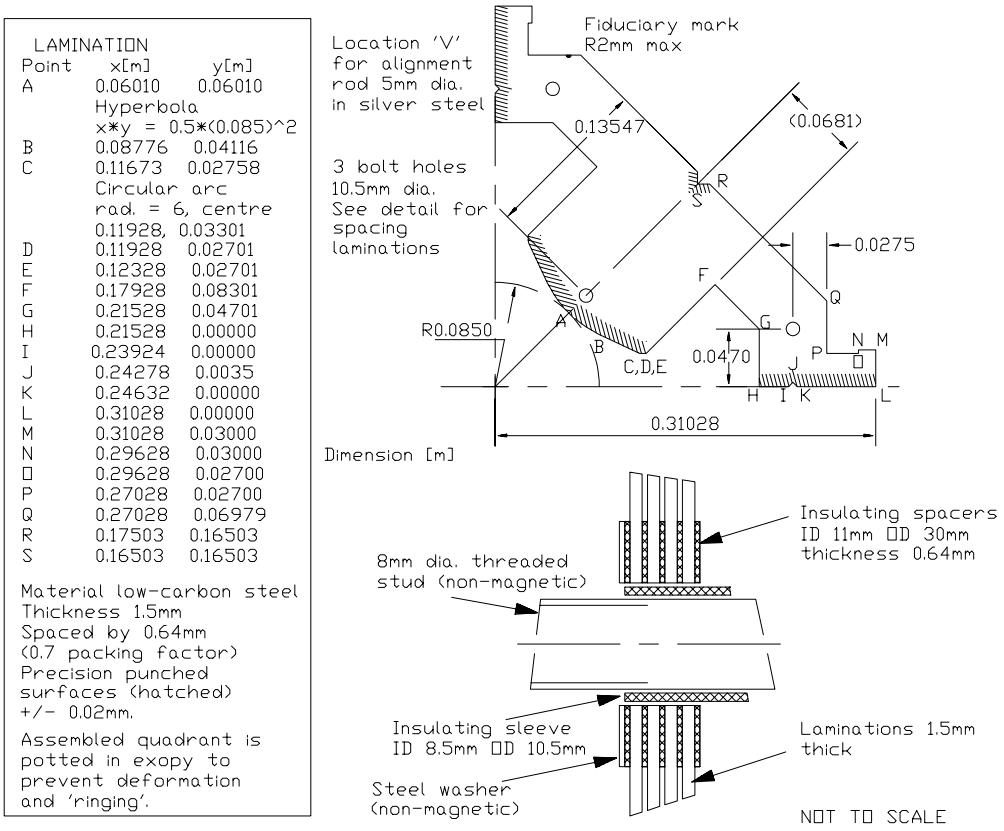

Figure F2 Main ring quadrupole lamination

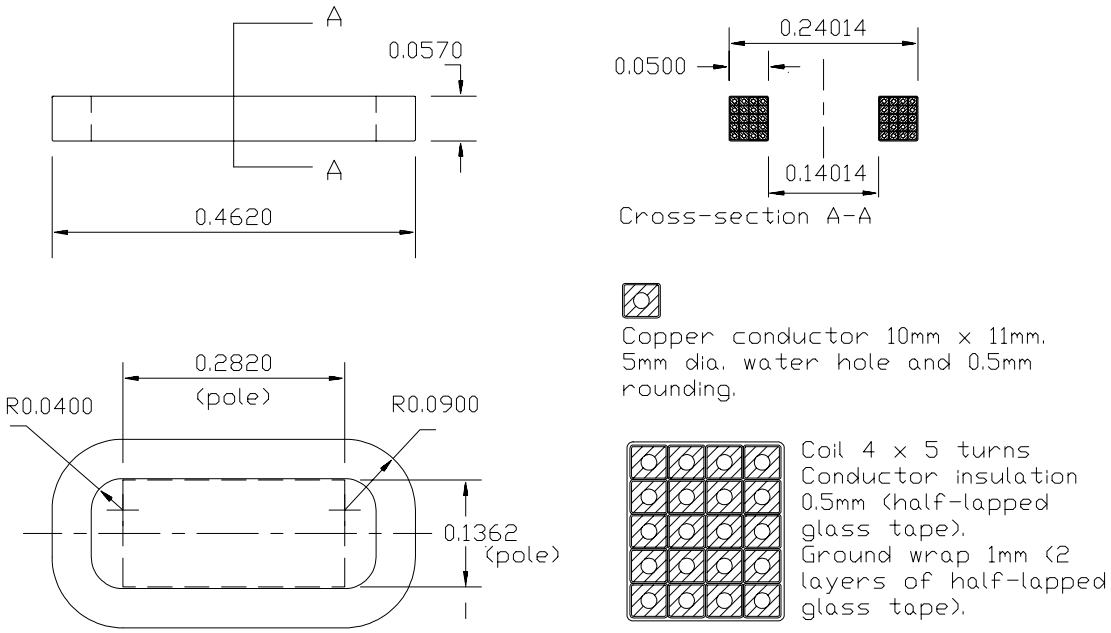

Figure F3 Main ring quadrupole coil

References

[1] G. Borri, *Main quadrupole of the CNAO synchrotron (Based on the PIMM Study)*, PS/DI/Note 99-10(Tech).

* * *

APPENDIX II G

MAGNETIC AND MECHANICAL DESIGN OF THE MAIN SEXTUPOLES

The main sextupole has its pole profile based on a three-dimensional calculation [1], since the large aperture and short yoke make two-dimensional calculations inaccurate. The construction uses six individual sextants built from 1.5 mm thick laminations without end plates. The sextants are bolted together, so that the magnet can be easily opened. Two possible constructions of the sextants are presented:

- In this Appendix, the individual sextants are glued to prevent 'ringing' and bolted longitudinally (bolts are magnetic and insulated).
- In Ref. 1, the sextants are glued to prevent 'ringing' and then welded by external tie bars.

With such a short lens, it is practical to specify an exact number of laminations per sextant, which with a practical stacking factor of 0.975 would be 143, and then to set a weight tolerance of $\pm 4 \times 10^{-3}$. The main characteristics are summarised in Table G1 and in Figures G1, G2 and G3. Further details can be found in Ref. 1.

Main ring sextupoles (F-type, D-type, Resonance): principal parameters	
Overall length [m]	0.3000
Yoke length [m]	0.2200
Overall width [m]	0.5600
Overall height [m]	0.5050
Inscribed circle radius [m]	0.1000
Packing factor	>0.975
Weight [t]	0.27
Nominal maximum gradient [T/m^2]	54.3
Current for maximum gradient[A]	500
Effective magnetic length at max. gradient [m]	0.25
'Good-field' region (all field levels)	At least ±60 mm horizontal; ±30 mm vertical
Int. gradient quality, $\Delta Gl/Gl$ (all field levels)	$\pm 4 \times 10^{-3}$ required*
Resistance (magnet) [Ω]	0.0275
Inductance (magnet) [H]	0.0472
Number of coils	6 (1 per pole)
Number of turns	84 (14 per coil)
Number of water circuits	3 (0.5 per coil)
Average turn length [m]	0.83
Length of a single water circuit [m]	23.24
Temperature rise in a single circuit [°C]	16.5
Water flow (magnet) [l/min]	6.13 (2.04 per circuit)
Pressure drop [bar]	7

* The calculations in Ref. 1 were terminated before the specified precision was obtained. The strengths of the chromaticity and resonance sextupoles differs by about a factor of 10 and it seems likely that different chains will need to be shimmed independently according to the field range over which they will be used. Similarly, the single sextupole used for driving the resonance reaches a current density of 10.35 A/mm^2. The current density in the chromaticity sextupoles does not exceed 1.75 A/mm^2. However, it is not cost effective to design totally different magnets.

Table G1 Main ring sextupoles (F-type, D-type, Resonance): principal parameters

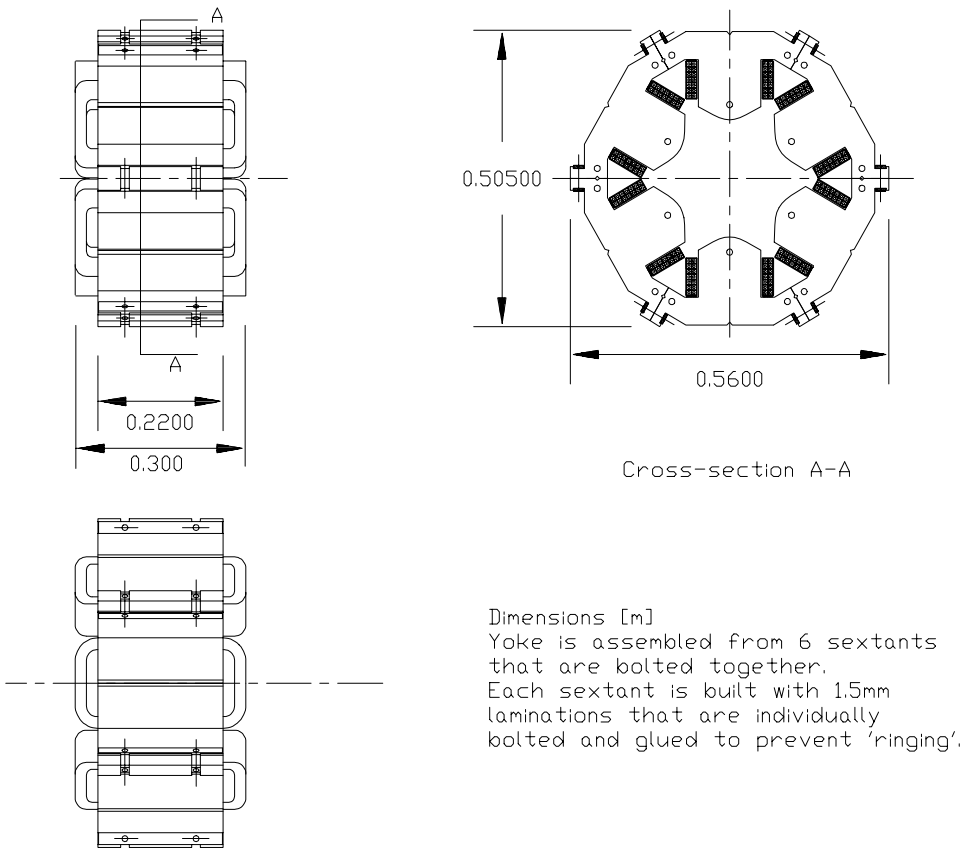

Figure G1 Main ring sextupole

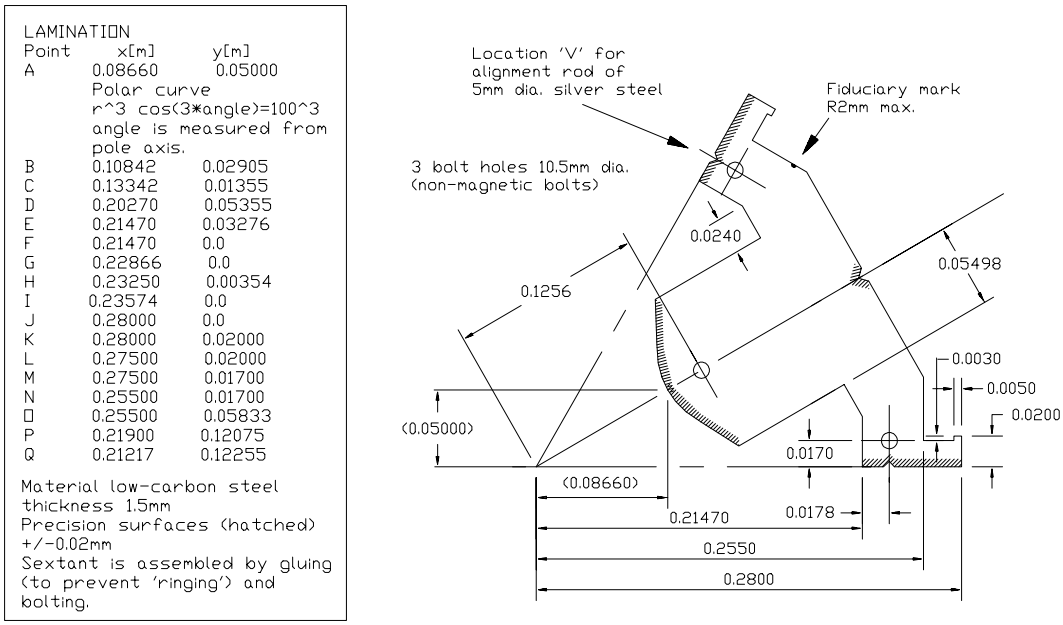

Figure G2 Main ring sextupole lamination

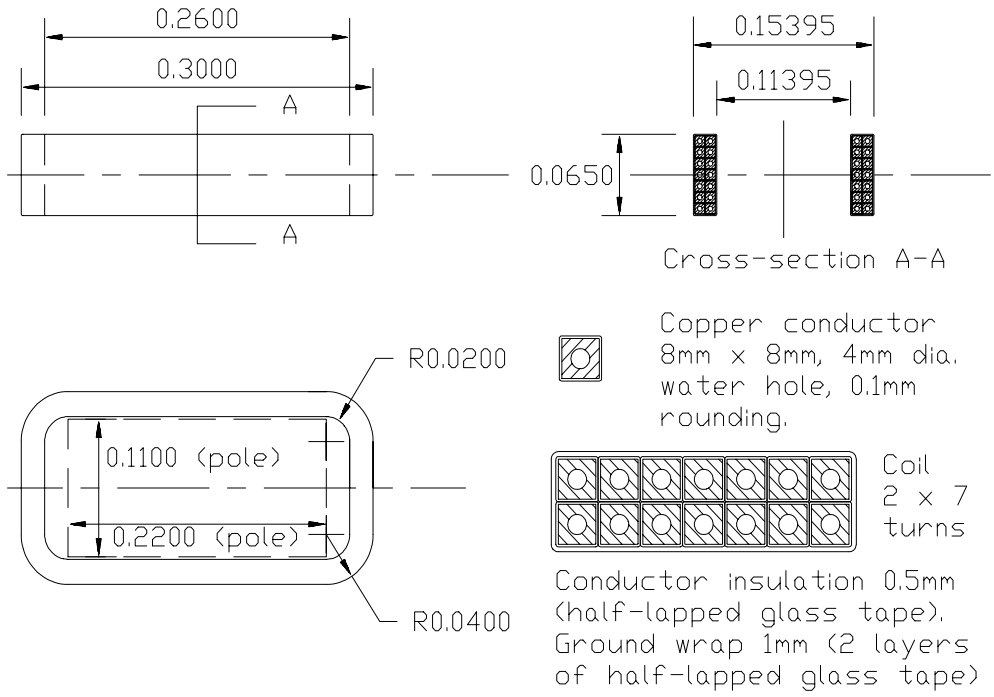

Figure G3 Main ring sextupole coil

References

[1] S. Rossi, *The sextupole of the CNAO synchrotron*, PS/DI/Note 99-11.

* * *

APPENDIX II H

MAGNETIC AND MECHANICAL DESIGN OF THE CORRECTION DIPOLES

The horizontal and vertical dipole correctors for the main ring are simple window-frame units with laminated cores that are bolted with end plates. The present design assumes 1.5 mm-thick laminations and 15 mm-thick end plates, but these dimensions are not critical and are not marked on the drawings. In both units, the poles have been shaped with two shallow rectangular recesses into which the coils sit. The depth of the recess is adjusted for the best field uniformity. Both units have air-cooled coils and the horizontal unit that has a more compact and higher powered coil has been equipped with cooling fins to ensure that the centre of the coil cannot overheat. The cooling fins are mounted by including a sheet of aluminium in the mid-plane of the coil (see detail in Figure H2) on the long outer side. The sheet is bent into a 'U' shape and has the fins mounted on the outer face.

The main characteristics are summarised in Table H1 and in Figures H1 to H4 for the mechanical design and H5 to H10 for the magnetic field maps. Figures H5 and H6 show the improvements in the 2D field quality due to the pole shaping for the horizontal and vertical magnets respectively. The horizontal magnet is well within ±0.001 and the vertical magnet is almost within this limit. Figures H7 and H8 show the integrated field through both magnets. The horizontal corrector has an excellent integrated field quality within ±0.003, which is well within the required ±0.01 tolerance. The vertical magnet is less good. Most of its aperture is within ±0.01, but the corner drops to -0.025 giving an error range of -0.025 to +0.007. This is due to the unfavourable aspect ratio of the gap. Finally, Figures H9 and H10 show the longitudinal distribution of the fields to give an idea of the levels at nearby equipment.

Main ring dipole correctors: principal parameters

	Horizontal	**Vertical**
Overall length [m]	0.290	0.244
Yoke length [m]	0.2000	0.2000
Overall width [m]	0.4540	0.2280
Overall height [m]	0.1600	0.224
Packing factor	>0.975	>0.975
Weight [t]	0.065	0.045
Nominal maximum field [T]	0.0293	0.0158
Effective magnetic length at max. field [m]	0.03137	0.03513
Current for maximum field [A]	11.60	25.75
Maximum current ramp [A/s]	600	1200
'Good-field' region (all field levels)	±60 mm hor.; ±30 mm vert.	±60 mm hor.; ±30 mm vert.
Integrated field quality	$\Delta B/\!/B/\!/ = \pm 0.003$	$\Delta B/\!/B/\!/ =$ -0.025,+0.007
Resistance (magnet) [Ω]	0.36 (0.18 per coil)	0.0667 (0.0333 per coil)
Inductance (magnet) [H]	0.0041	0.0030
Number of coils	2	2
Number of turns	400 (200 per coil)	160 (80 per coil)
Cooling	Air-cooling with fins	Air-cooled

Table H1 Main ring correction dipoles: principal parameters

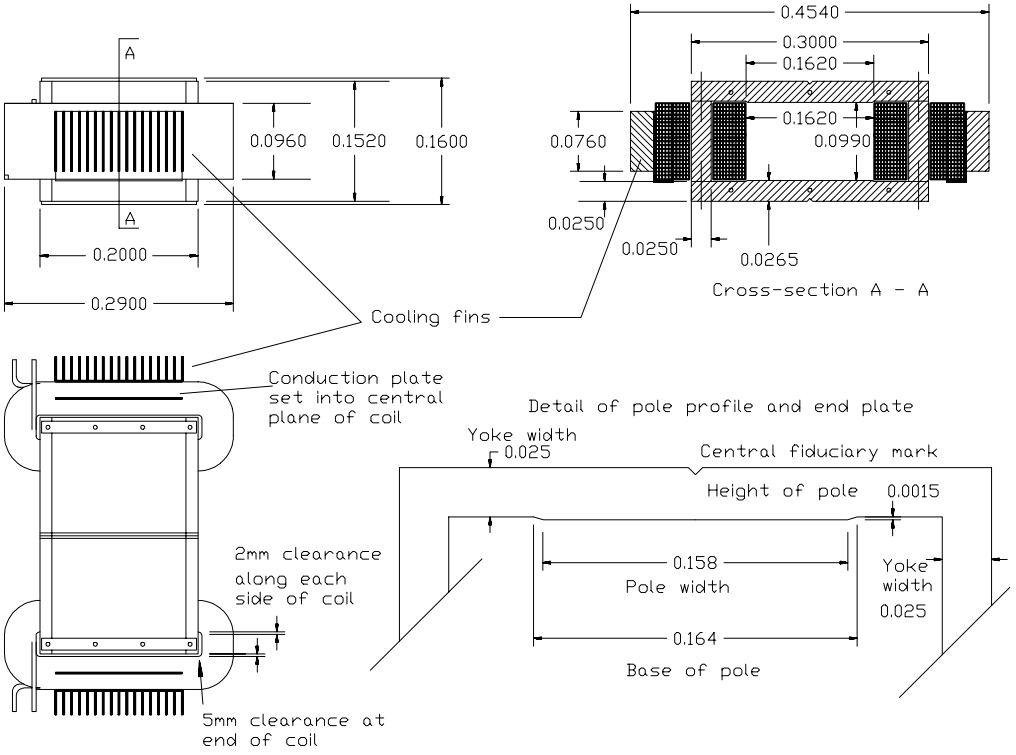

Figure H1 Main ring horizontal dipole corrector

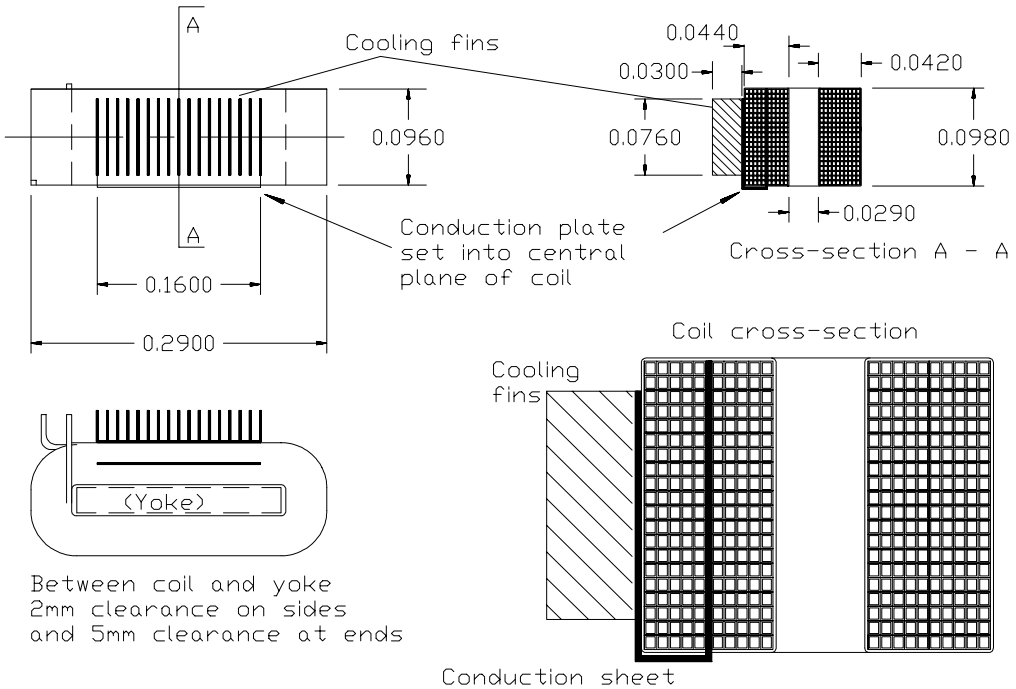

Solid copper conductor 3mm x 3.8mm with 0.5mm insulation and 1mm ground wrap. Coil has 200 turns and is air-cooled. The cooling is aided by fins mounted on a conduction sheet 2mm thick (Al) in the shape of a "U" with one side embedded in the coil.
Dimensions [m]

Figure H2 Main ring horizontal dipole corrector coil

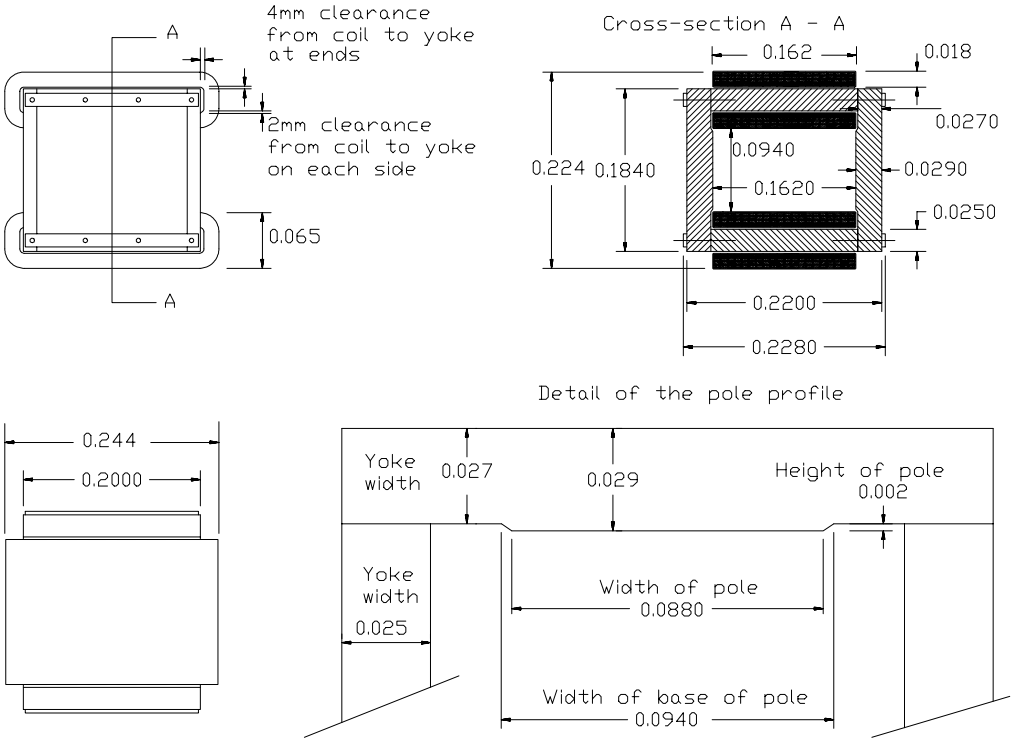

Figure H3 Main ring vertical dipole corrector

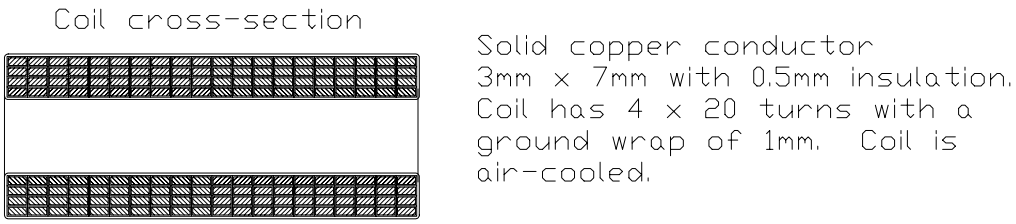

Figure H4 Main ring vertical dipole corrector coil

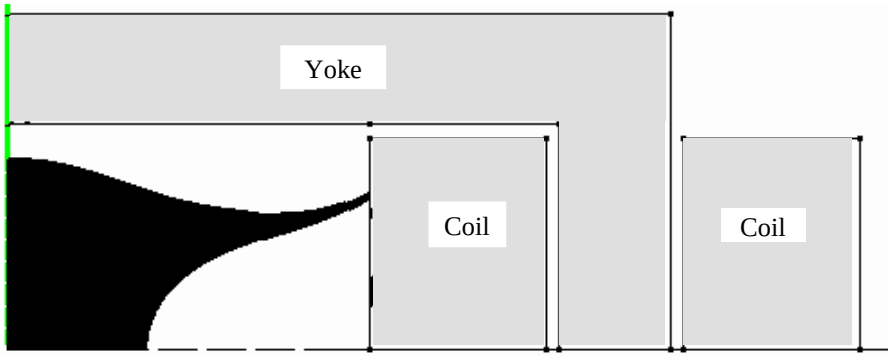

(a) Flat pole field quality

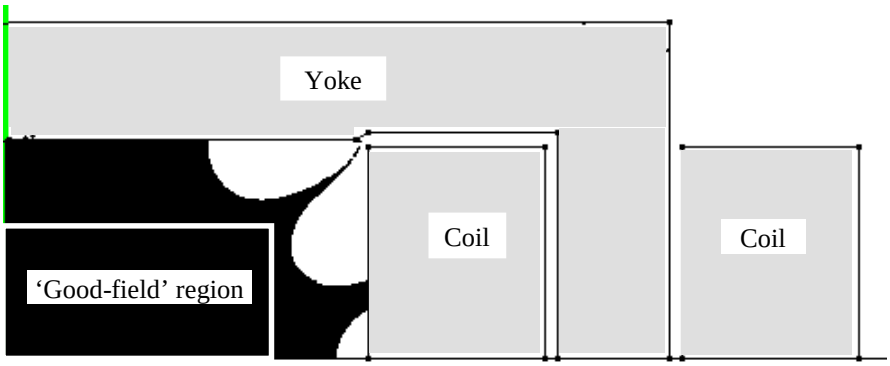

(b) Shaped pole field quality

Figure H5 Horizontal corrector 2D field qualities with flat pole and shaped pole over a quarter of the aperture at top field 0.0293 T
[Black region is within the tolerance $\Delta B/B = \pm 10^{-3}$, the required 'good-field region is marked by a white box at +60 mm,+30 mm]

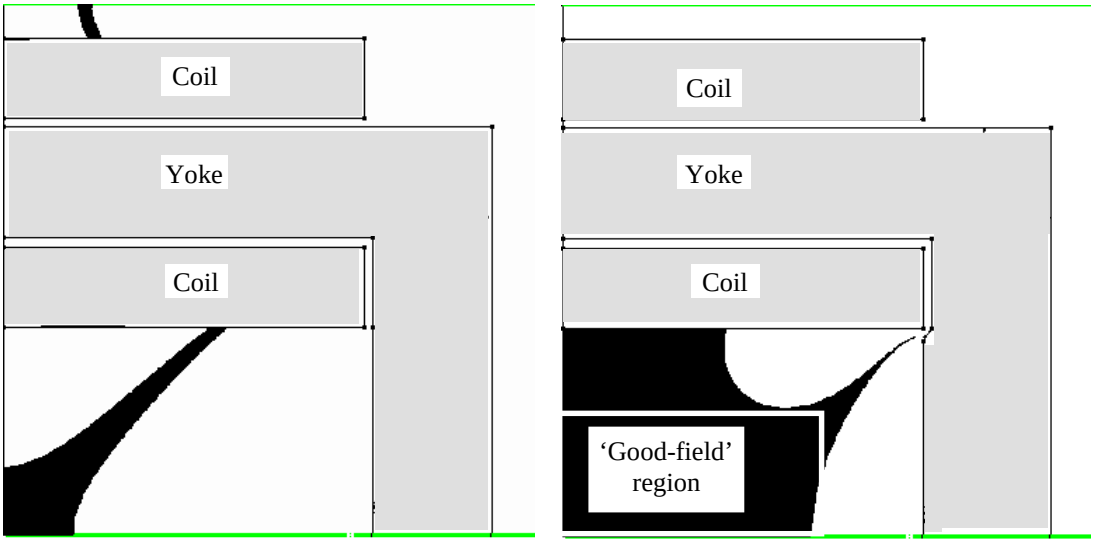

(a) Flat pole field quality (b) Shaped pole field quality

Figure H6 Vertical corrector 2D field qualities with flat pole and shaped pole over a quarter of the aperture at top field 0.0158 T
[Black region is within the tolerance $\Delta B/B = \pm 10^{-3}$, the required 'good-field region is marked by a white box at +60 mm,+30 mm]

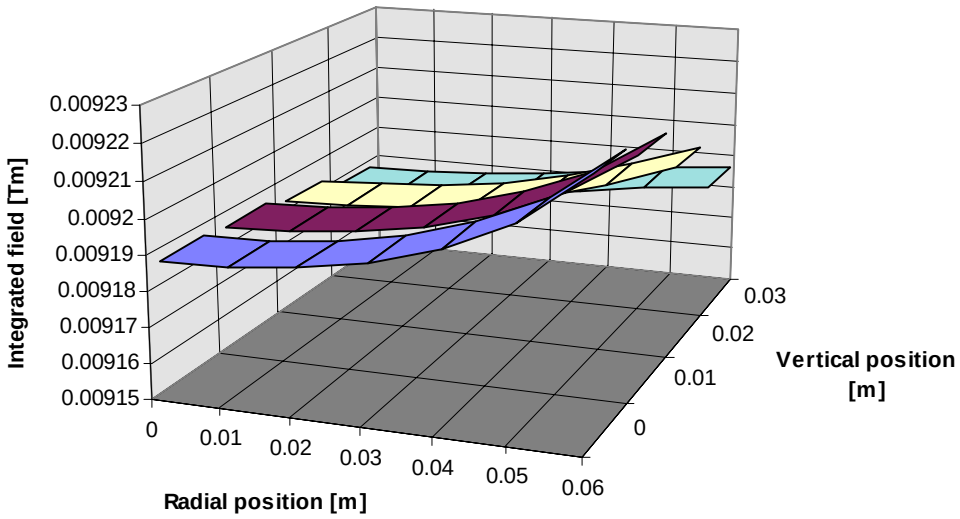

Integrated field through full magnet over a quarter of the aperture at top field

Vertical posn [m]	Radial position [m] 0.00	0.01	0.02	0.03	0.04	0.05	0.06
0	0.009186	0.009187	0.009189	0.009192	0.009198	0.009207	0.009221
0.01	0.009186	0.009186	0.009188	0.009191	0.009196	0.009204	0.009216
0.02	0.009183	0.009183	0.009185	0.009187	0.009191	0.009197	0.009204
0.03	0.009178	0.009178	0.009179	0.009181	0.009183	0.009186	0.009188

Figure H7 Horizontal corrector integrated field quality at top field 0.0293 T

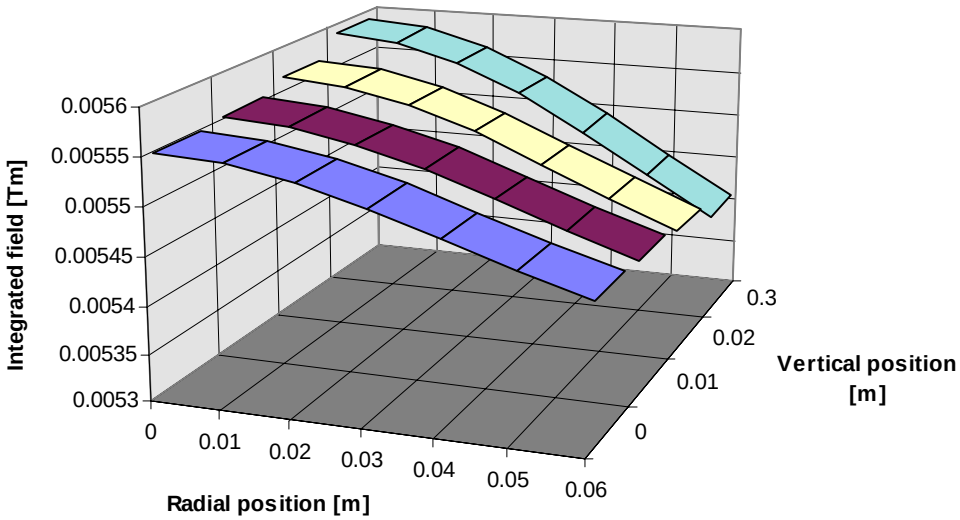

Integrated field through full magnet over a quarter of the aperture at top field

Vertical posn [m]	Radial position [m] 0	0.01	0.02	0.03	0.04	0.05	0.06
0	0.005549	0.005545	0.005533	0.005514	0.005492	0.005468	0.005447
0.01	0.005553	0.005549	0.005536	0.005516	0.005492	0.005467	0.005444
0.02	0.005567	0.005561	0.005546	0.005523	0.005493	0.005461	0.005433
0.3	0.00559	0.005584	0.005565	0.005535	0.005495	0.005451	0.005411

Figure H8 Vertical corrector integrated field quality at top field 0.0158 T

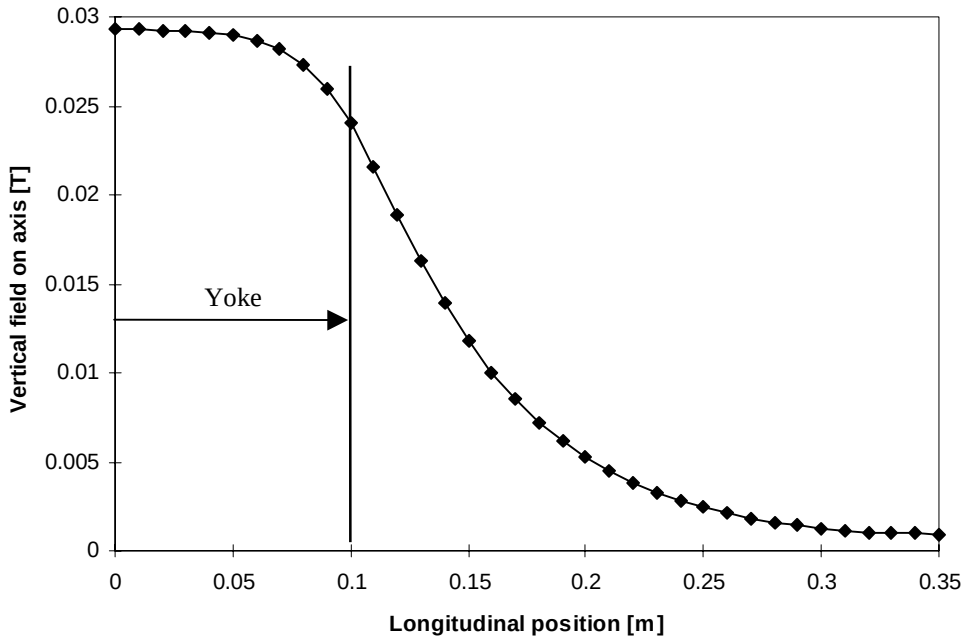

Figure H9 Horizontal corrector vertical field distribution along axis (at top field)

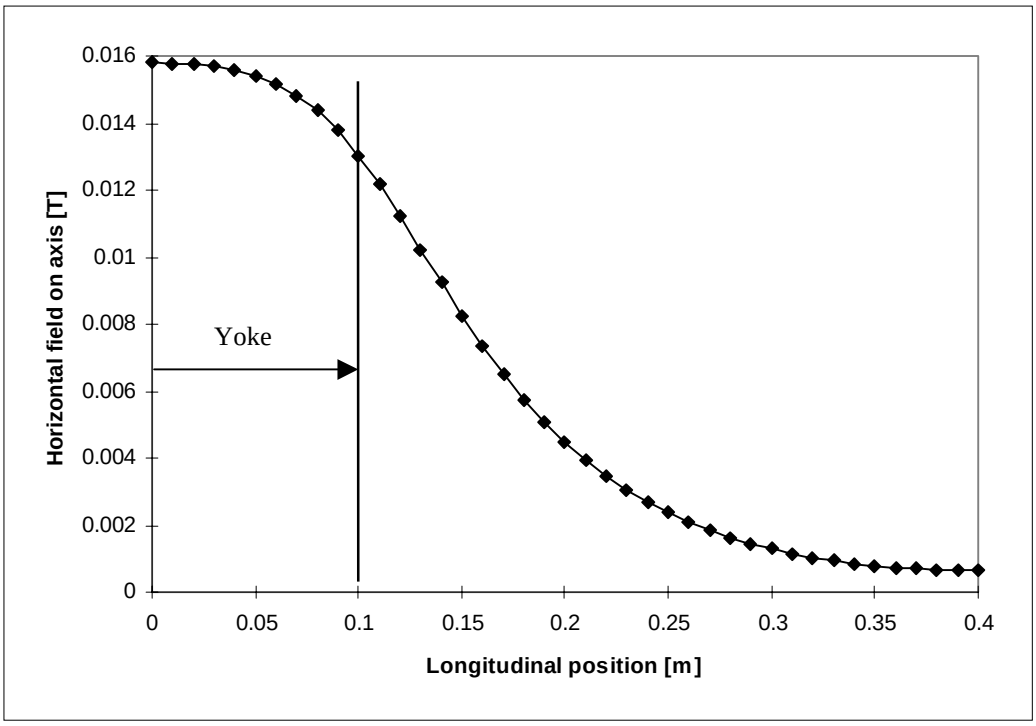

Figure H8 Vertical corrector horizontal field distribution along axis (at top field)

* * *

APPENDIX II I

MAGNETIC AND MECHANICAL DESIGN OF THE BETATRON CORE

The betatron core is the only element in the ring that changes its current level during extraction. It has 1.5 mm laminations to impose a pre-calculated degree of smoothing on field changes, without causing excessive eddy current power losses. The main parameters are given in Table I1.

The yoke is made in two halves that are opened laterally rather than vertically (see Figure I1). This is done because the small gap between the half-yokes creates a fringe field (see Figures I2 and I3) that extends along the full 1.5 m length of the core. It is prudent to keep this perturbation as far from the beam as possible. Each half-yoke comprises three 50 cm long blocks of glued laminations. The steel is 'blue-steamed' to ensure a high inter-lamination resistance. Three blocks are bolted with insulated bolts to form a half-yoke. The laminations (see Figure I4) are stamped with lugs that allow the two half-yokes to be bolted together. Periodically sets of ten laminations have the lugs removed from one side to allow the bolts to be mounted. The two half-yokes are insulated with a sheet of 200 μm Kapton™. The field map inside the core is shown in Figure I5 and a graph of the distribution across the lamination is shown in Figure I6. The coil is wound in four symmetric sections of ten turns each to keep the fringe field to a minimum. The coil is wound from 4×4 mm^2 copper conductor and is both air-cooled and conduction-cooled to the yoke (see Figure I1). The alignment of the coil is not critical, except that it is advantageous to keep the conductor as close as possible to the yoke to limit fringe fields. The vacuum chamber must be ceramic over at least part of the yoke length. From a structural point of view, the chamber is best made circular in cross-section. Reference 1 contains further details, but the design differs inasmuch as it requires approximately half the ampere-turns because the insulation sheets (2×200 μm) have not been included.

Betatron core: principal parameters	
Overall length (with coil but excl. bolts and pressure pads) [m]	1.5200
Yoke length [m]	1.500
Overall width [m]	1.500
Packing factor	1.700
Weight [t]	21.6
Nominal maximum mean field in core [T]	1.187
Maximum flux change in core [Weber]	±1.193
Current for maximum field [A]	45
Self-inductance [H]	0.4476
Coil	4 sets of 5 turns with 4x4mm^2 copper
Cooling	Air and conduction to yoke
Maximum current density [A/mm^2]	2.8
Average turn length [m]	4.365
Resistance (full coil at 40°C) [Ω]	0.1
Maximum fringe field inside beam aperture ±70 mm (H) × ±37 mm (V) [T]	0.001

Table I1 Betatron core: principal parameters

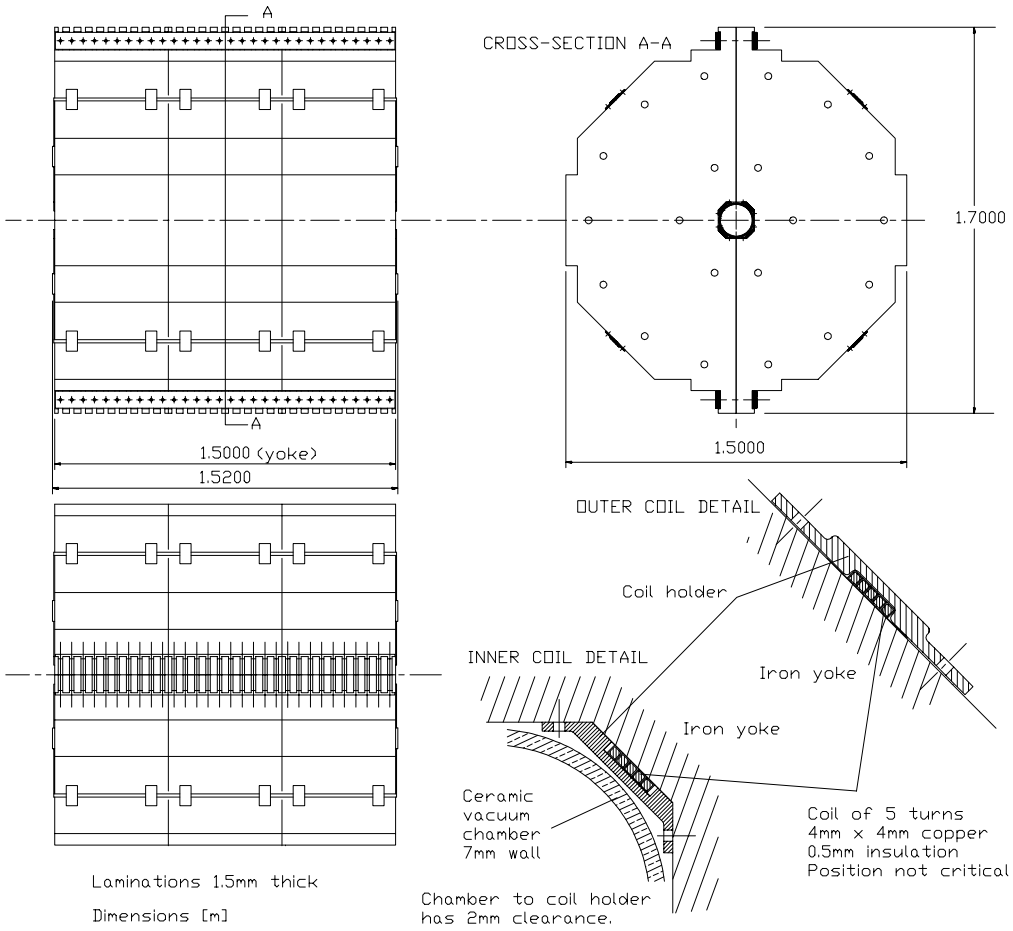

Figure I1 Betatron core

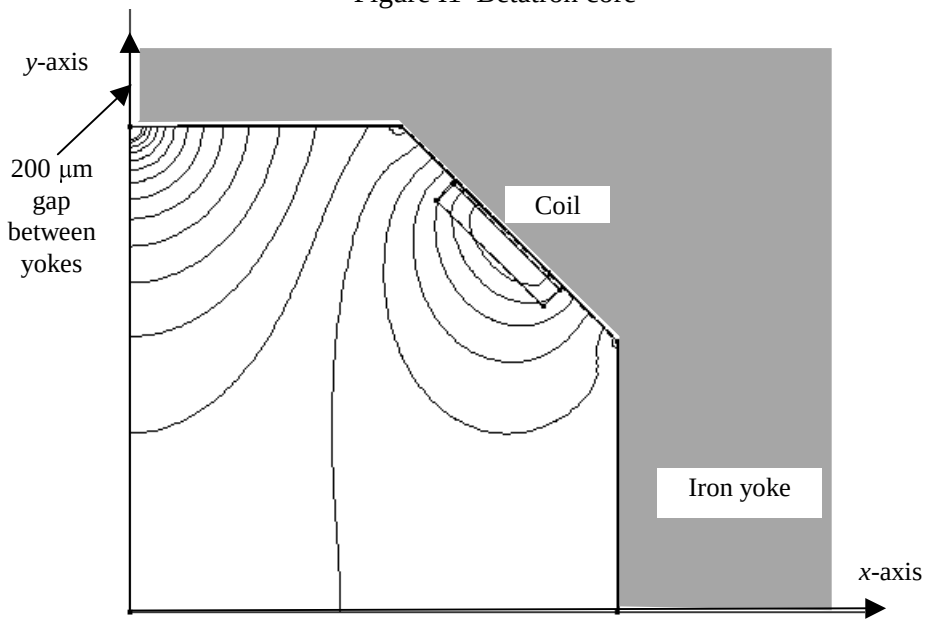

Figure I2 Fringe-field map inside the central aperture of the betatron core

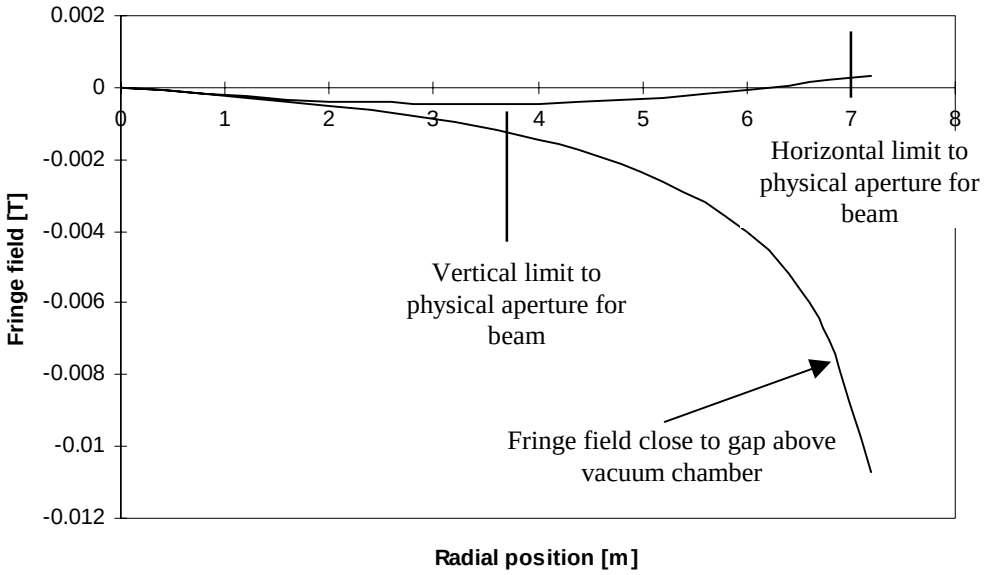

Figure I3 Fringe-field in central aperture of the betatron core
[B_x along y-axis and B_y along x-axis]

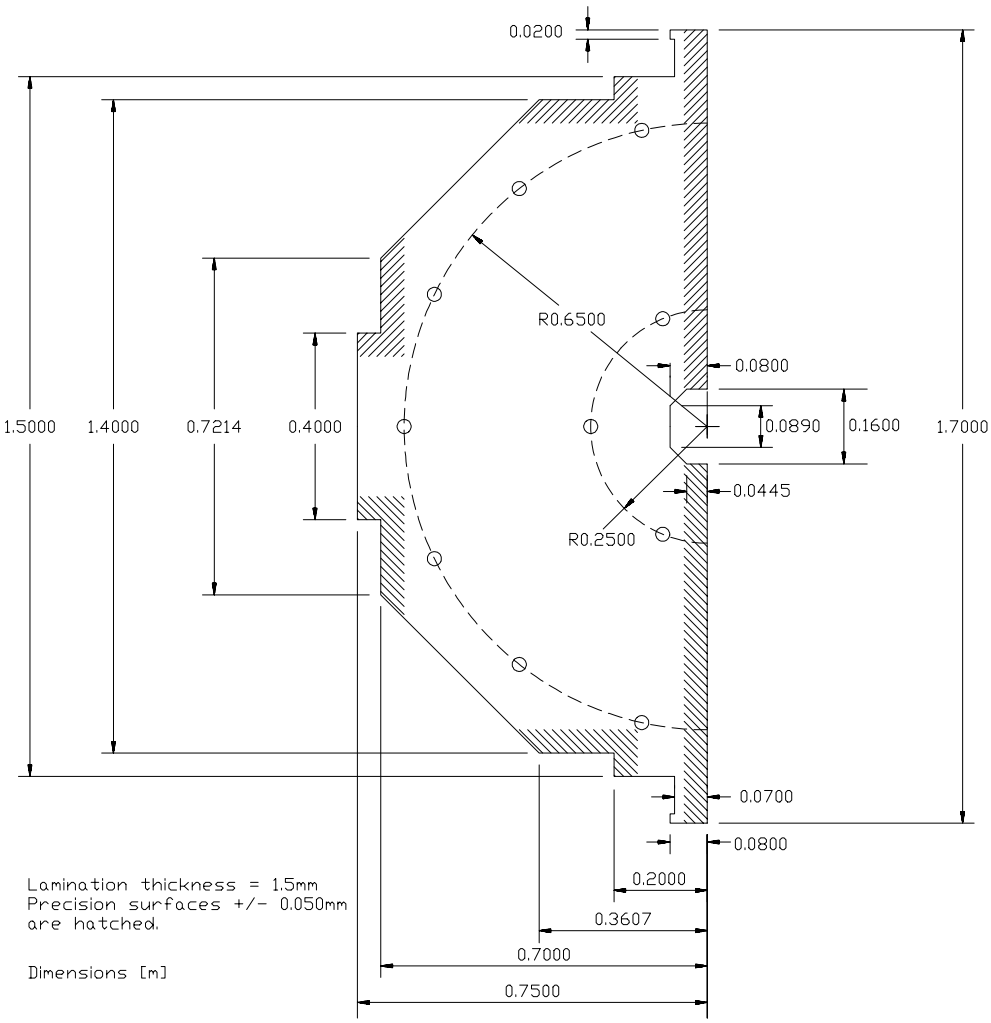

Figure I4 Betatron core lamination

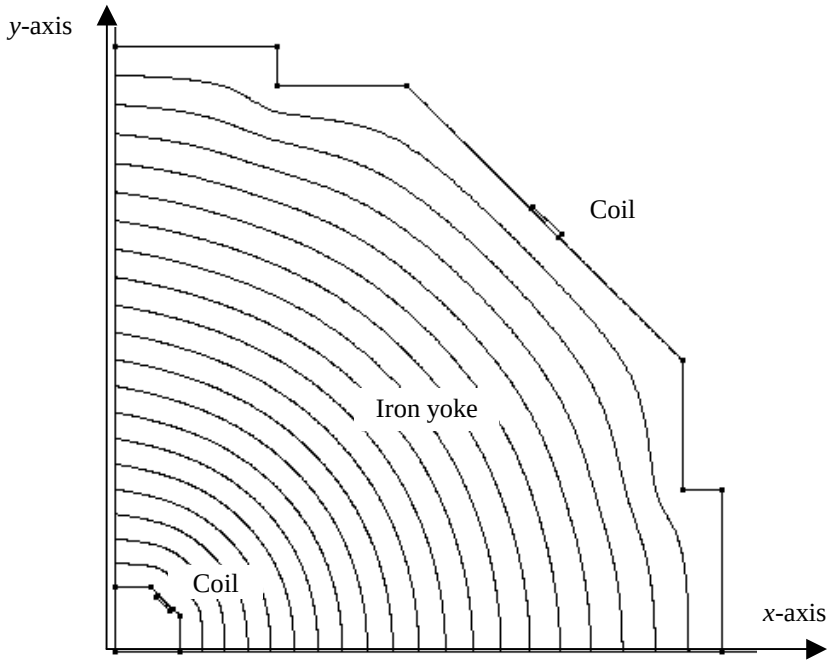

Figure I5 Field map inside core

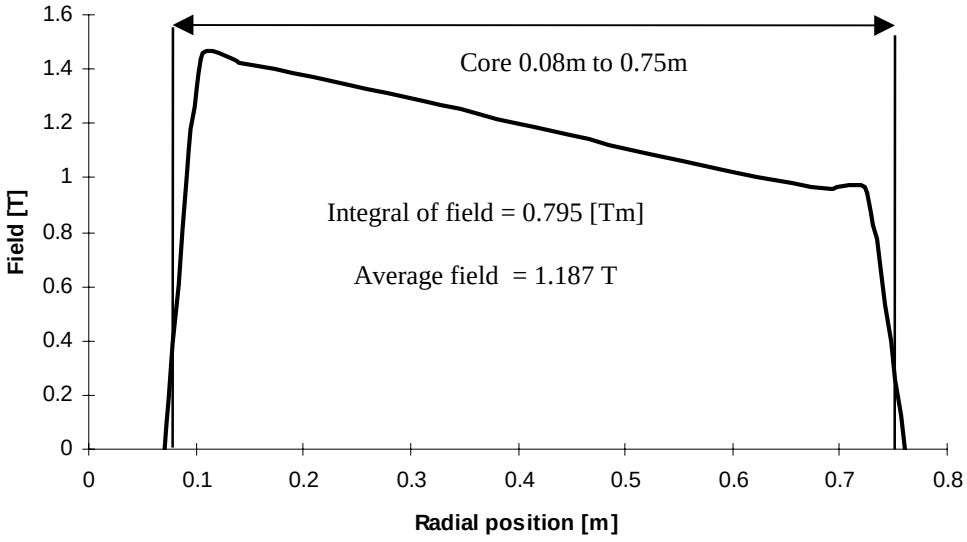

Figure I6 Field distribution across core

References

[1] L. Badano, S. Rossi, *Characteristics of a betatron core for extraction in a proton-ion medical synchrotron*, CERN/PS 97-19(DI).

* * *

APPENDIX II J

MAGNETIC AND MECHANICAL DESIGN OF THE AIR-CORED QUADRUPOLE

The air-cored quadrupole comprises four loops of copper conductor (16 mm^2) that are air-cooled and supported on a fibre-glass frame. The unit is separable into two halves for mounting around a circular ceramic vacuum chamber. Alignment tolerances of ±0.5 mm and ±1 mrad will be sufficient. Table J1 summarises the main parameters and the mechanical design is shown in Figure J1. Figure J2 shows the field map on the central plane, Figure J3 shows the results of 2-D calculations for the gradient field over the aperture of ±6 cm (horizontal) × ±3 cm (vertical) and Figure J4 shows the uniformity of the integrated gradient over the same aperture. Further details are given in Ref 1.

The effective magnetic length of the coil is very close to its physical length and the 2-D gradient uniformity at the centre of the coil is very similar to the integrated gradient uniformity. As can be seen from Table J1, the gradient uniformity degrades rapidly towards the edge of the aperture, but this is not of concern. The air-cored quadrupole is meant to apply extremely small tune corrections to the particles that are in the vicinity of the resonance at the centre of the chamber and the fact that the 'waiting' beam sees a slightly distorted correction has no effect since the resonance is then far away.

Air-cored quadrupole: principal parameters	
Overall length [m]	0.4100
Overall width [m]	0.2400
Overall height [m]	0.2400
Nominal maximum gradient [T/m]	0.0132
Current for maximum gradient[A]	80
Effective magnetic length [m]	0.4045
Integrated gradient quality ±40 mm (H); ±30 mm (V)	+2%, -1.7%
Integrated gradient quality ±50 mm (H); ±30 mm (V)	+9%, -7%
Integrated gradient quality ±60 mm (H); ±30 mm (V)	+37%, -30%
Cooling	Air-cooled
Resistance (magnet) [Ω]	0.0042
Inductance (magnet) [H]	3.5×10^{-6}

Table J1 Air-cored quadrupole: principal parameters

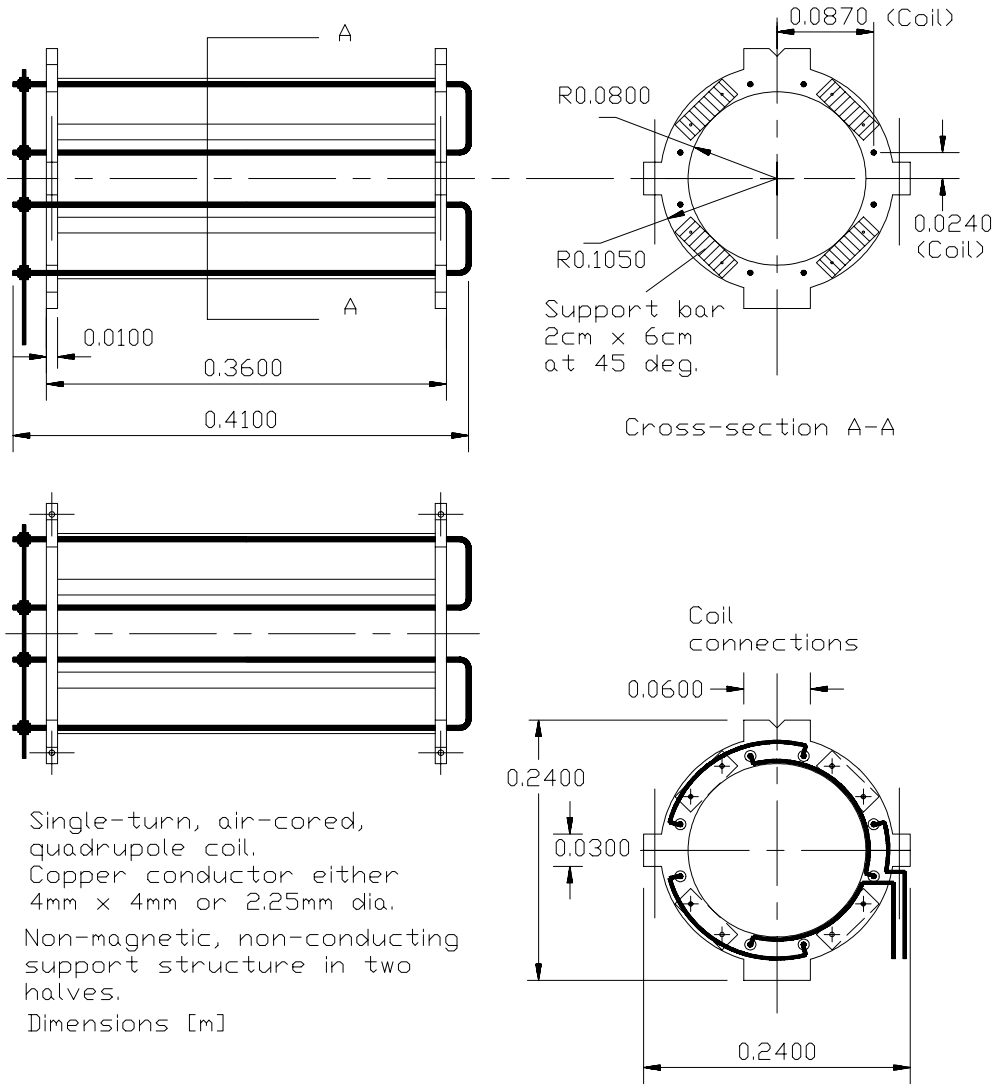

Figure J1 Air-cored quadrupole construction and coil connections

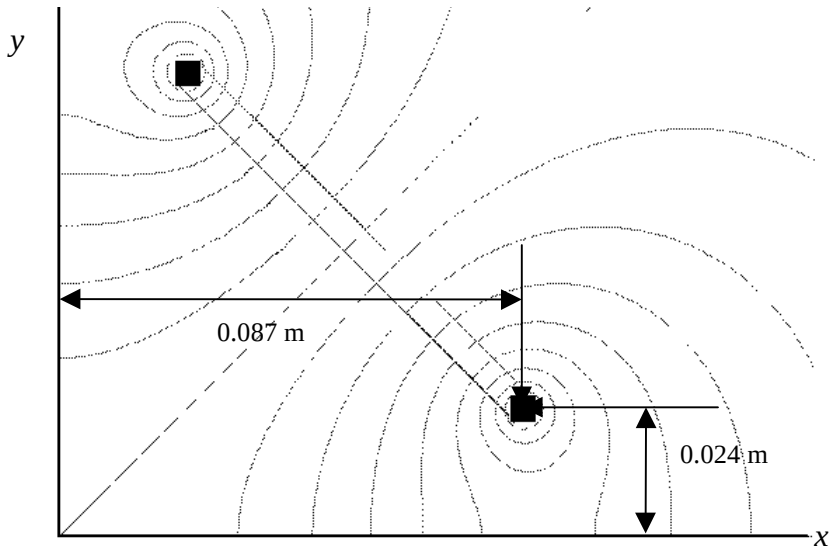

Figure J2 Field map in one quadrant on the central plane

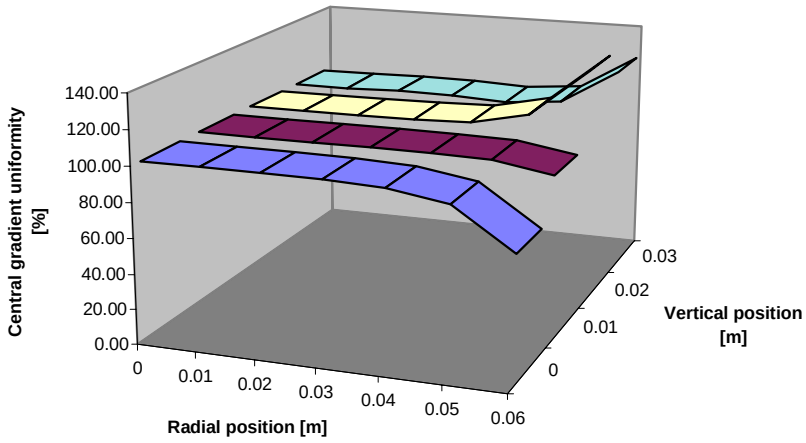

Gradient on central x-y plane [T/m] over aperture for maximum current of 80 A							
x, y [m]	*x* = 0.0	*x* = 0.01	*x* = 0.02	*x* = 0.03	*x* = 0.04	*x* = 0.05	*x* = 0.06
y = 0.0	0.0132	0.0132	0.0132	0.0132	0.0130	0.0123	0.0094
y = 0.01	0.0132	0.0132	0.0132	0.0132	0.0132	0.0132	0.0124
y = 0.02	0.0132	0.0132	0.0133	0.0133	0.0135	0.0144	0.0181
y = 0.03	0.0132	0.0133	0.0133	0.0133	0.0131	0.0134	0.0162
Gradient with respect to the central orbit value [%]							
x, y [m]	*x* = 0.0	*x* = 0.01	*x* = 0.02	*x* = 0.03	*x* = 0.04	*x* = 0.05	*x* = 0.06
y = 0.0	100.0	100.0	100.0	99.7	98.3	93.2	70.8
y = 0.01	100.0	100.0	100.8	100.1	99.9	99.4	93.8
y = 0.02	99.9	99.9	100.2	100.5	101.7	108.8	136.7
y = 0.03	99.6	99.6	100.5	100.2	98.7	101.6	122.4

Figure J3 Gradient uniformity at centre of quadrupole over one quadrant

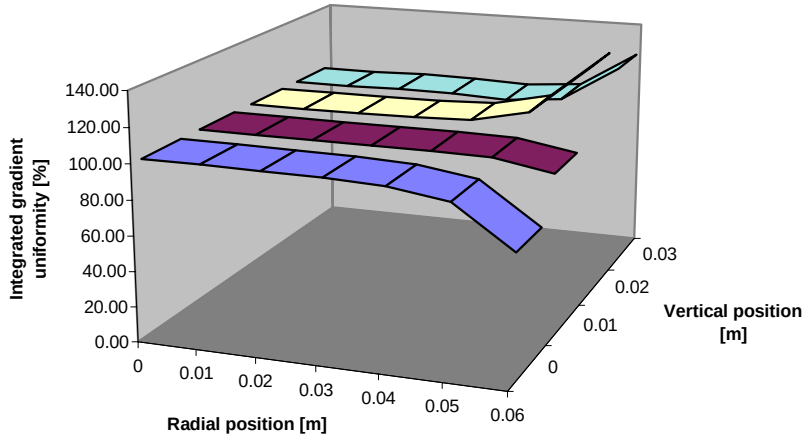

Integrated gradient [T] over aperture							
x, y [m]	*x* = 0.0	*x* = 0.01	*x* = 0.02	*x* = 0.03	*x* = 0.04	*x* = 0.05	*x* = 0.06
y = 0.0	0.00534	0.00534	0.00533	0.00531	0.00524	0.00497	0.00374
y = 0.01	0.00534	0.00534	0.00533	0.00533	0.00532	0.00530	0.00499
y = 0.02	0.00534	0.00534	0.00534	0.00536	0.00543	0.00582	0.00733
y = 0.03	0.00532	0.00532	0.00536	0.00534	0.00527	0.00543	0.00657
Integrated gradient with respect to the central orbit value [%]							
x, y [m]	*x* = 0.0	*x* = 0.01	*x* = 0.02	*x* = 0.03	*x* = 0.04	*x* = 0.05	*x* = 0.06
y = 0.0	100.0	100.0	99.7	99.5	98.1	93.1	70.1
y = 0.01	100.0	100.0	99.9	99.9	99.8	99.2	93.5
y = 0.02	99.9	99.9	100.1	100.3	101.7	109.0	137.3
y = 0.03	99.6	99.6	100.4	100.1	98.7	101.7	123.1

Figure J4 Integrated gradient uniformity over one quadrant of aperture

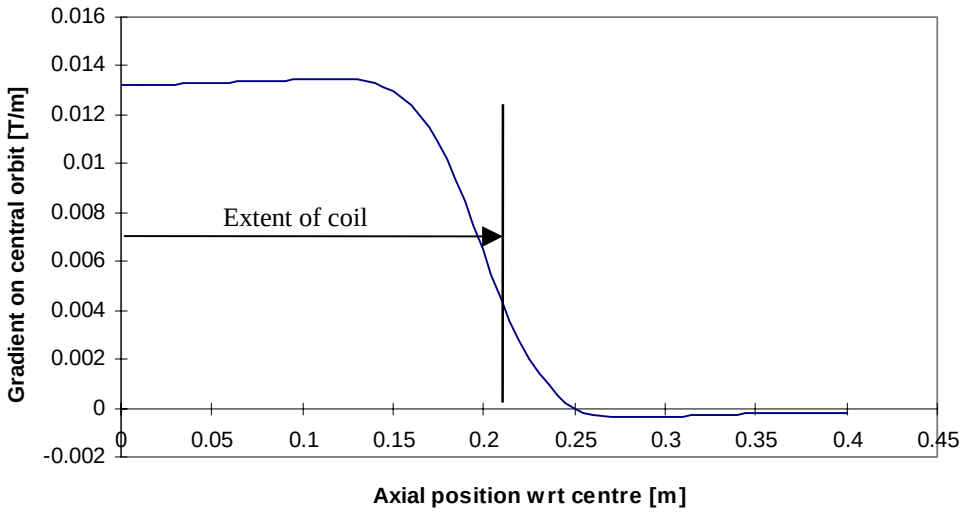

Figure J5 Axial profile of the field plotted from the magnet centre

References

[1] S. Rossi, *An air core quadrupole for the PIMMS synchrotron*, PS/DI/Note.99-12 (Tech).

* * *

APPENDIX II K

MAGNETIC AND MECHANICAL DESIGN OF THE TUNE KICKERS

The two tune kickers (horizontal and vertical) are identical with a rectangular aperture of 160×170 mm^2. The yoke is a simple box structure made from ferrite. The coil is air-cooled and a single turn made from copper sheet. The kicker has to be assembled with the circular ceramic vacuum chamber (outer diameter 156 mm and wall 8 mm) in place. Table K1 summarises the main parameters and the basic mechanical design is shown in Figures K1 and K2. In the final magnets, it would be necessary to add an outer frame to hold the ferrite yoke-pieces firmly together. Figure K3 shows the field uniformity on the central transverse plane and Figure J4 shows the uniformity of the integrated field over the same aperture. Figure J5 shows the axial profile of the field to give a first indication of how the field will interact with nearby equipment. For further details see Ref 1.

The field integration has been made over the effective magnetic length plus two apertures on either side (±45 mm). This causes a small underestimate of the integrated field for a magnet standing in free space, but in the machine the more distant fringe field is short-circuited by adjacent magnet yokes.

Tune kickers: principal parameters		
Overall length [m]	0.2460	
Overall width [m]	0.2500	
Overall height [m]	0.2400	
Yoke length [m]	0.2100	
Yoke thickness [m]	0.015	
Yoke material	Ferrite Philips BC11	
Nominal maximum field [T]	0.0179	
Effective magnetic length [m]	0.320	
Current for maximum field [A]	2450	
Field quality over 'good field' region:	**2-Dimension**	**3-Dimension**
Horizontal ±60 mm, Vertical ±30 mm	+2.17%, -0%	+2.14%, -0.33%
Number of turns	1	
Cooling	Air-cooled	
Resistance (magnet) [Ω]	90×10^{-6}	
Inductance (magnet) [H]	0.45×10^{-6}	

Table K1 Tune kickers: principal characteristics

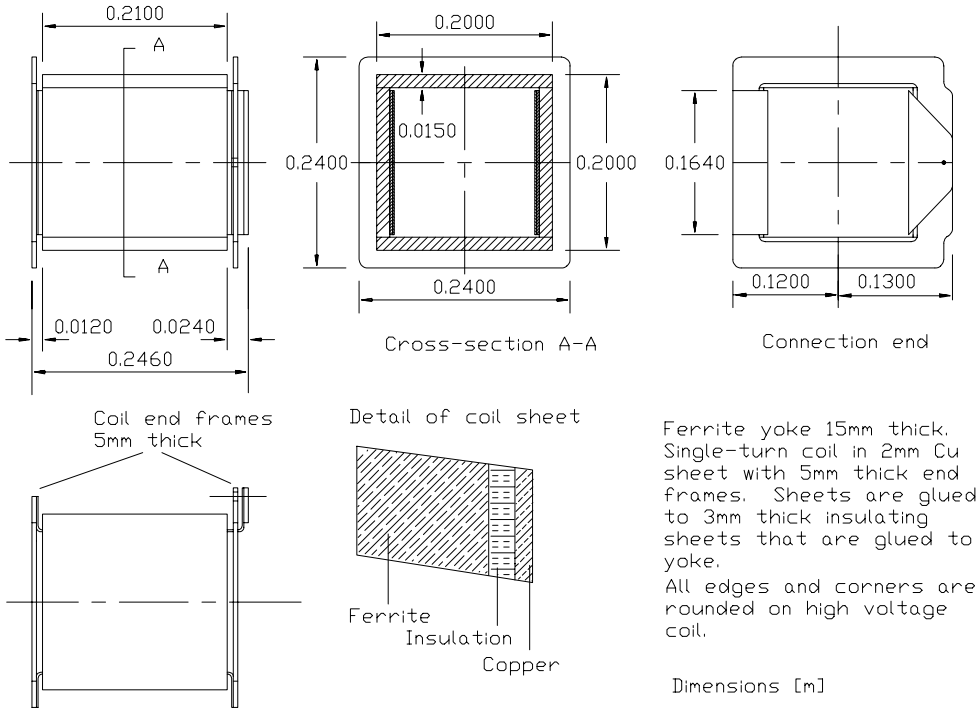

Figure K1 Tune kicker assembly

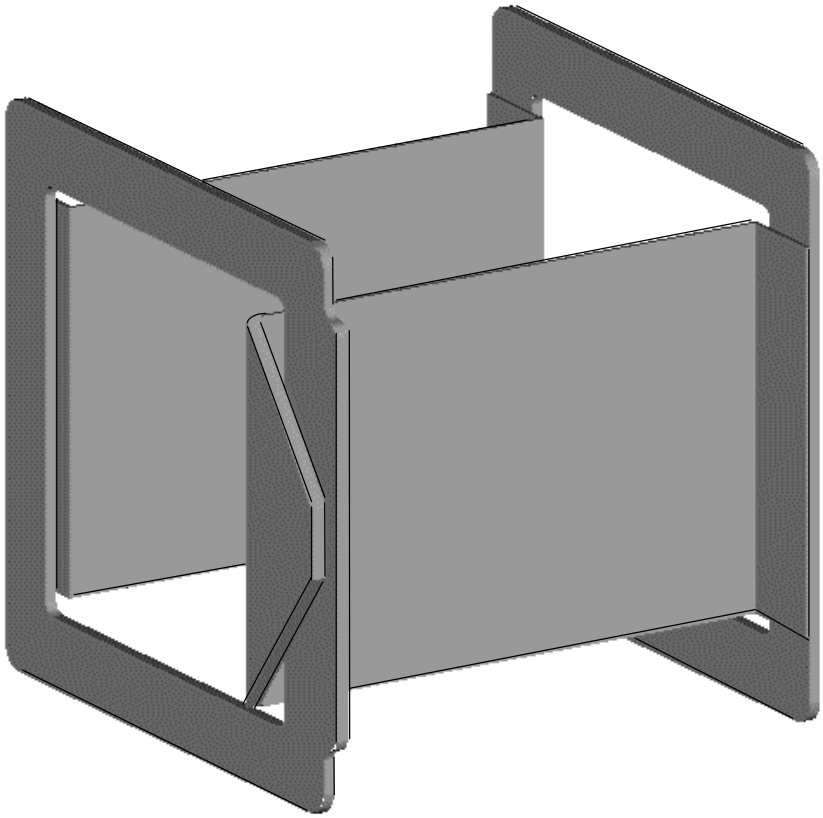

Figure K2 Tune kicker coil

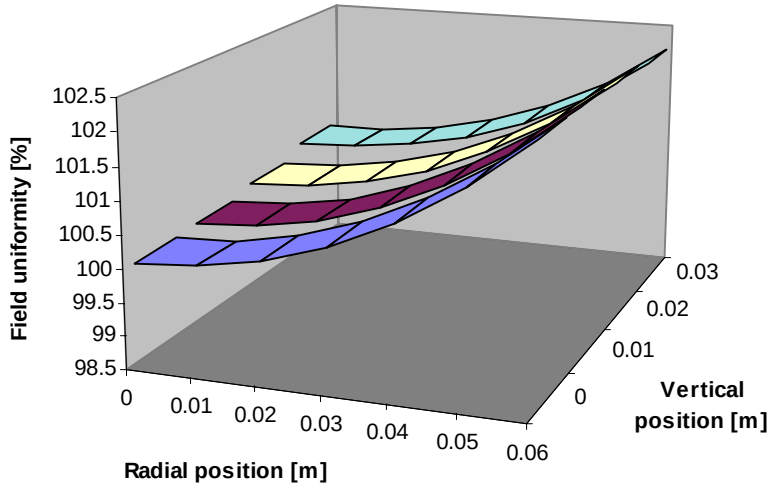

Field on central x-y plane [T] over aperture for maximum current of 2450 A							
x, *y* [m]	*x* = 0.0	*x* = 0.01	*x* = 0.02	*x* = 0.03	*x* = 0.04	*x* = 0.05	*x* = 0.06
y = 0.0	0.01789	0.01790	0.01793	0.01799	0.01807	0.01817	0.01830
y = 0.01	0.01790	0.01791	0.01794	0.01800	0.01807	0.01817	0.01830
y = 0.02	0.01792	0.01793	0.01796	0.01800	0.01807	0.01817	0.01829
y = 0.03	0.01796	0.01796	0.01798	0.01802	0.01808	0.01816	0.01828
Field with respect to the central orbit value [%]							
x, *y* [m]	*x* = 0.0	*x* = 0.01	*x* = 0.02	*x* = 0.03	*x* = 0.04	*x* = 0.05	*x* = 0.06
y = 0.0	100.00	100.06	100.24	100.55	100.99	101.58	102.31
y = 0.01	100.05	100.10	100.28	100.57	101.01	101.59	102.31
y = 0.02	100.18	100.23	100.38	100.64	101.04	101.58	102.27
y = 0.03	100.38	100.42	100.53	100.74	101.05	101.52	102.17

Figure K3 Field uniformity at centre of kicker over one quadrant

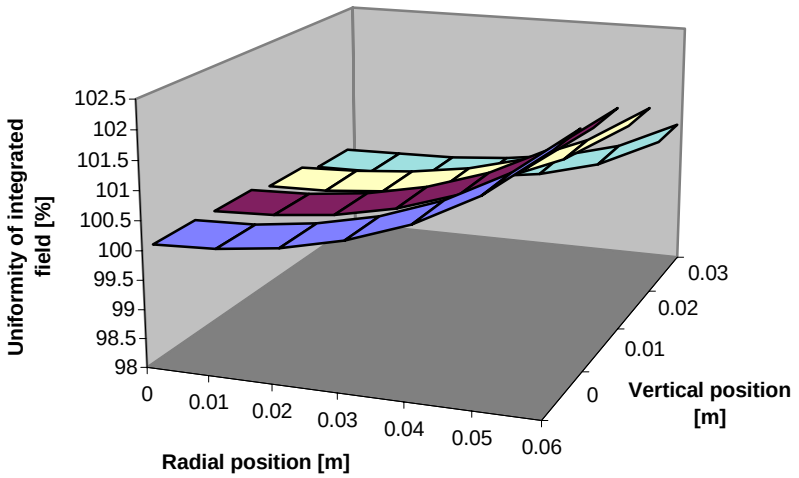

Integrated field [Tm] through magnet for maximum current of 2450 A							
x, *y* [m]	*x* = 0.0	*x* = 0.01	*x* = 0.02	*x* = 0.03	*x* = 0.04	*x* = 0.05	*x* = 0.06
y = 0.0	0.0057167	0.0057190	0.0057263	0.0057397	0.0057612	0.0057933	0.0058393
y = 0.01	0.0057145	0.0057167	0.0057233	0.0057358	0.0057559	0.0057863	5.8306
y = 0.02	0.0057076	0.0057092	0.0057140	0.0057235	0.0057395	0.0057648	5.8037
y = 0.03	0.0056977	0.0056984	0.0056996	0.0057039	0.0057127	0.0057290	5.7582
Integrated field with respect to the central orbit value [%]							
x, *y* [m]	*x* = 0.0	*x* = 0.01	*x* = 0.02	*x* = 0.03	*x* = 0.04	*x* = 0.05	*x* = 0.06
y = 0.0	100.00	100.04	100.17	100.40	100.78	101.34	102.14
y = 0.01	99.96	100.00	100.12	100.33	100.69	101.22	101.99
y = 0.02	99.84	99.87	99.95	100.12	100.40	100.84	101.52
y = 0.03	99.67	99.68	99.70	99.78	99.93	100.22	100.73

Figure K4 Integrated field uniformity of kicker

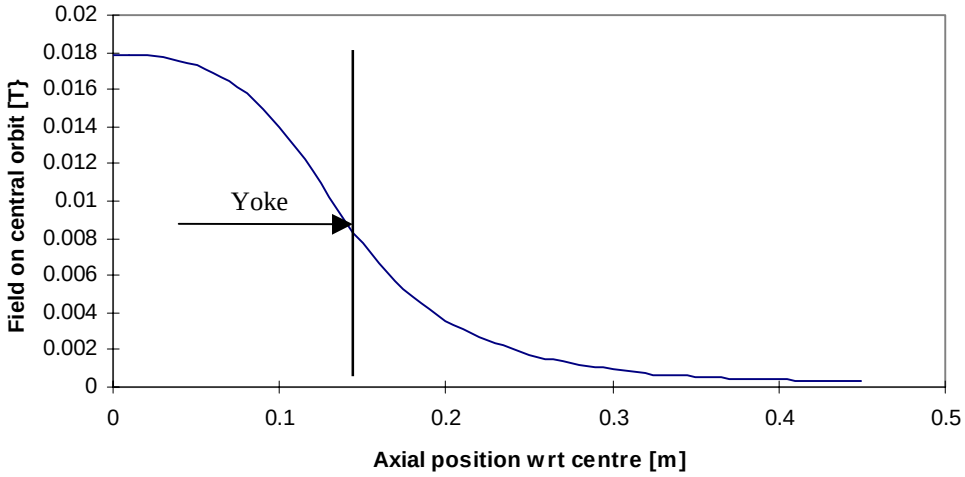

Figure K5 Axial profile of the field plotted from the magnet centre

References

[1] R. Maccaferri, K. Metzmacher, S. Rossi, *Preliminary design of a tune kicker for the PIMMS synchrotron*, PS/DI/Note 98-19 (Tech.).

* * *

APPENDIX II L

CONCEPT DESIGN OF THE DUMP BUMPERS

The dump bumpers have not been designed in any detail and the following parameters are meant only as a rough guide to what is needed. The effective magnetic length has been set to 0.3 m. The overall dimensions with coil and covers will be longer, but should still fit the available space. To get half the kick in the first unit the number of turns in the coil of that unit has been halved. Table L1 summarises the main parameters of the bumpers based on these assumptions and the maximum kick of 5 mrad required for the highest rigidity beam. There is no need for water cooling of the coil since the dumping cycle takes <100 μs with a repetition rate of <1 Hz.

To ensure efficient dumping at all times, the maximum voltage of the power converter must track the beam rigidity during the magnet cycle, so that the bump excited by the bumpers is always 31.5 ±2 mm with a rise time of 32 μs.

Dump bumper parameters		
	Bumper in SS MR 08	**Bumper in SS MR 21**
Required kick [rad]	0.0025	0.005
Maximum rigidity [Tm]	6.3464	6.3464
Eff. magnetic length [m]	0.3	0.3
Maximum field [T]	0.053	0.106
Pole gap [m]	0.15	0.15
Space between coils [m]	0.15	0.15
Field quality	$\pm 5 \times 10^{-3}$	$\pm 5 \times 10^{-3}$
Yoke design	Ferrite, window-frame	Ferrite, window-frame
Coil design	Saddle	Saddle
Vacuum chamber design	Ceramic, circular, 5mm	Ceramic, circular, 5mm
Maximum current [A]	1265	1265
No. of turns	5	10
Estimated inductance* [H]	9.5×10^{-6}	38×10^{-6}
Cooling	Air-cooled	
	Bumpers in series	
Total inductance [H]	47.5×10^{-6}	
Maximum current [A]	1265	
Rise time for kick [s]	32×10^{-6}	
Max. ramp voltage [V]	1900	
Power converter	Capacitor discharge into half-wave resonant circuit with 3rd harmonic for flat top ~30×10^{-6}s	
Max. repetition rate [Hz]	1	
Duty cycle	$<10^{-4}$	

* Saddle coil has low stray field. Stored energy based on field in aperture.

Table L1 Dump bumper parameters

* * *

APPENDIX II M

BEAM DUMPS, COLLIMATORS, STOPPERS AND SCRAPERS

Table M1 lists some approximate ranges for protons and carbon ions in common materials. For carbon ions, there is appreciable nuclear fragmentation and it is necessary to add up to 20% to the range to absorb these particles. Fortunately, the average stored beam power in PIMMS is not high and thermal effects can therefore be ignored. After traversing 3 cm of tungsten 400 MeV/u reach scattering angles of up to 15° and after 4 cm of tungsten 250 MeV protons reach scattering angles of up to 35°. With such large angles, it is necessary to add shielding transversally for the residual low-energy radiation and especially neutrons.

Approximate ranges for the highest energy particles

Material	250 MeV proton range [cm]	400 MeV/u carbon ion range [cm]
Water	38	27
Carbon	19	14
Iron	7.25	5
Lead	7	4.75
Copper	6.5	4.5
Tungsten	4	3

Table M1 Approximate ranges for the highest energy particles

About 5 cm of tungsten will adequately stop the primary beam making a compact dump or collimator. Some additional shielding is then necessary to deal with:

- Particles that are scattered out of the longitudinal faces of the block and emerge from the vacuum chamber further downstream.
- Low-energy radiation that diffuses out at large angles.
- Induced activity over longer periods.

Copper is the next best absorber among the common metals for use inside vacuum systems. It is not used in dumps because of its activation products. However, it is used for beam stoppers. A beam stopper is a safety device that blocks the vacuum pipe and, in principle, never 'sees' beam except under fault conditions. In this case, the high stopping power is an advantage and the activation is unimportant. Steel has about half the stopping power of tungsten, but being cheaper and easily machined, it is often used in dumps. Carbon is often used at low energies, e.g. in linacs, but its stopping power is still lower.

Internal dump in the ring

The beam dump scheme for the ring (see Section 3.14.1), requires a dump block to be placed in the vicinity of quadrupole QD MR 13. Ideally, the dump block should be inside the quadrupole, but this excludes all materials with any conductivity (eddy currents) or permeability. To make the best use of the remaining space, the

dump has been mounted in the last section of vacuum chamber of the straight section SS MR 14. This avoids particle showers in the sensitive monitors and the following dipole MB MR 14 will provide some shielding. To keep the block small it is made from tungsten (7 × 1 cm plates). For the strict purpose of dumping, only an upper (or a lower) of block is needed. In this case, both the upper and lower blocks are installed. They are fixed and are aligned as part of the vacuum chamber. Thus, they also serve the purposes of defining the vertical aperture and collimating the beam. Figure M1 shows the proposed construction.

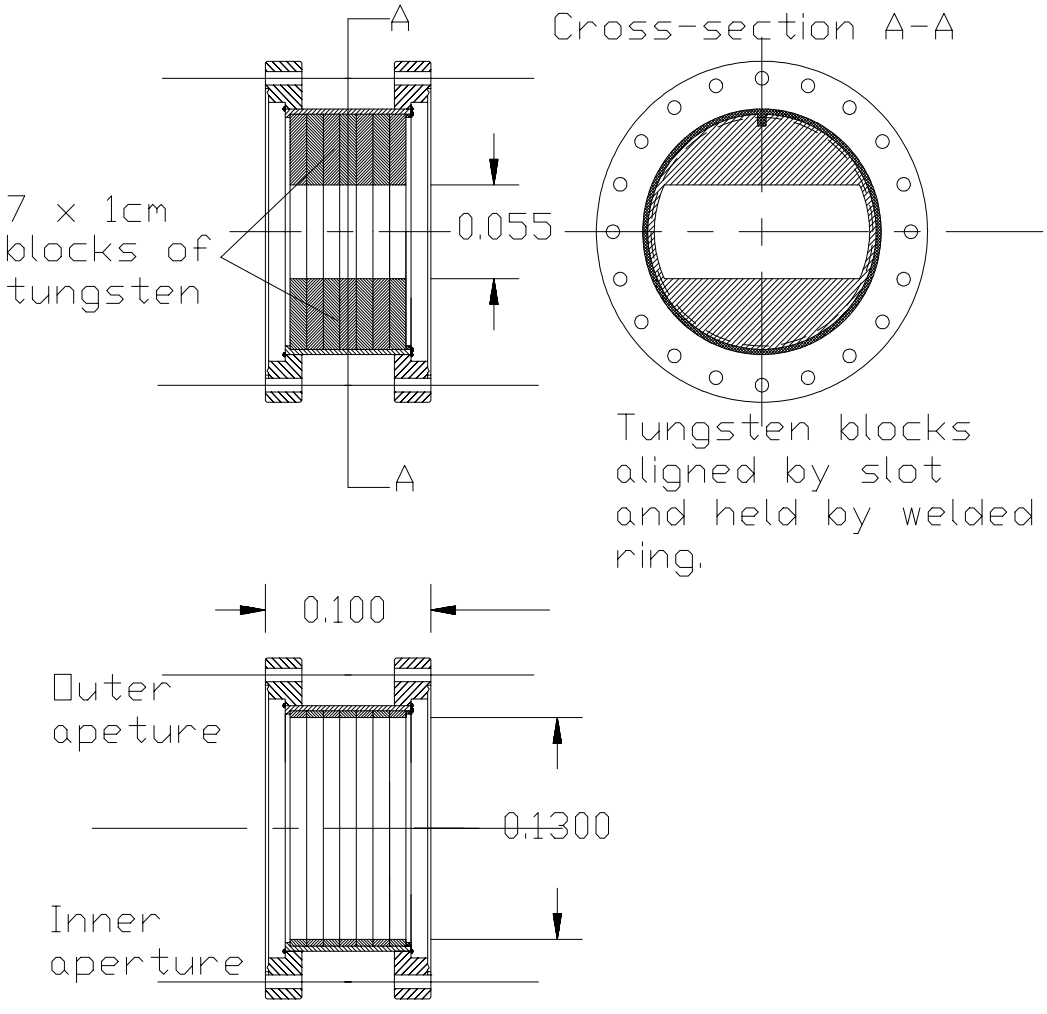

Figure M1 Vertical internal dump for the synchrotron
[Also acts as the vertical collimator]

Radial collimators in the ring

Although there is no equivalent of dumping in the horizontal plane, it is still necessary to trap the radial beam losses. The collimator blocks are similar to the vertical dump/collimator blocks described above. They comprise stacks of five 1 cm tungsten plates that are rigidly fixed to the vacuum chamber and aligned with it. Since the collimator is relatively short (5 cm) the problem of axial alignment is made less critical. Figure M2 shows the construction.

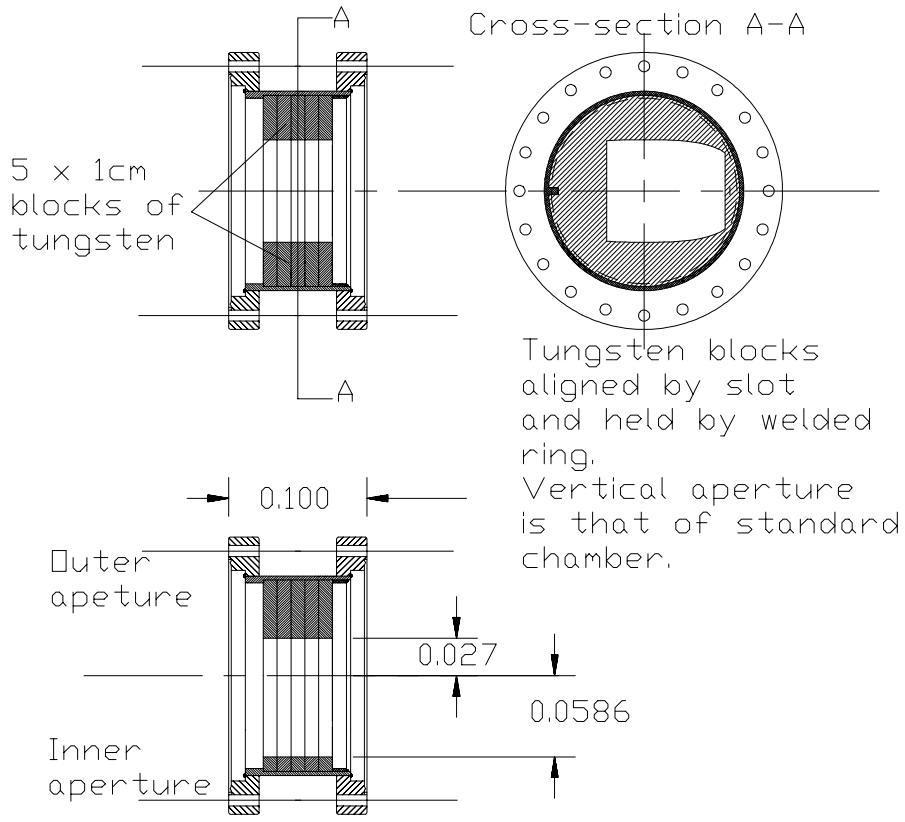

Figure M2 Radial collimator for the synchrotron

Chopper dump

As with ring dump and collimators, the main element for stopping the beam is a stack of five 1 cm tungsten plates. However, the chopper dump is expected to have regular pulse-to-pulse use and since there is adequate space 20 cm of steel has been added longitudinally to provide additional shielding. It is also important to add shielding transversally downstream of the block. The chopper dump will have the same basic construction as shown in Figures M1 and M2, but the dimensions will be different. Figure M3 shows the chopper dump schematically. The special geometry is explained in Section 5.3.4.

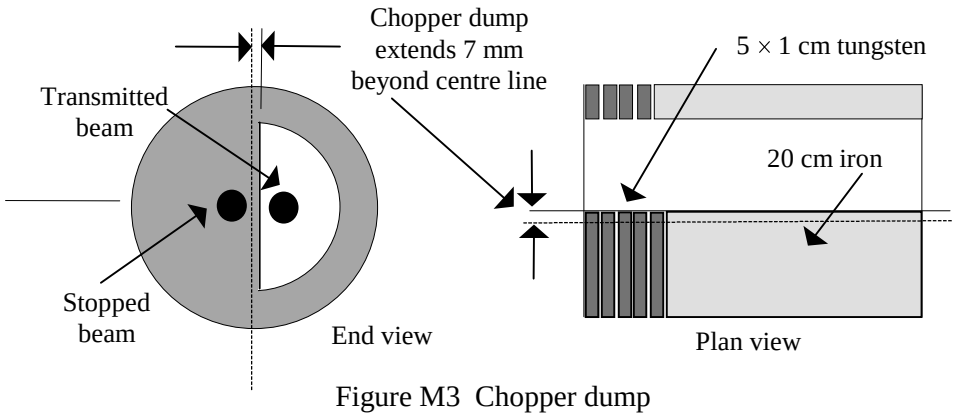

Figure M3 Chopper dump

Beam line dumps

For the extraction line, the same basic design using 5 × 1 cm plates of tungsten with an additional 20 cm of steel in the beam direction and additional concrete shielding enclosing the dump block would be a conventional solution. The injection lines operate at much lower energies and, since space is not so critical, alternative materials with lower stopping powers could be considered.

Fixed beam scrapers

Fixed scrapers would have the same form as the vertical dump in Figure M1, except that in the beam direction they would be much thinner, say 0.5 cm of tungsten. However, mobile scrapers would be more useful.

Mobile beam scrapers

Mobile scrapers would have a lightweight arm carrying a tungsten foil. One possible design is the 'rocking bellows' design shown schematically in Figure M4.

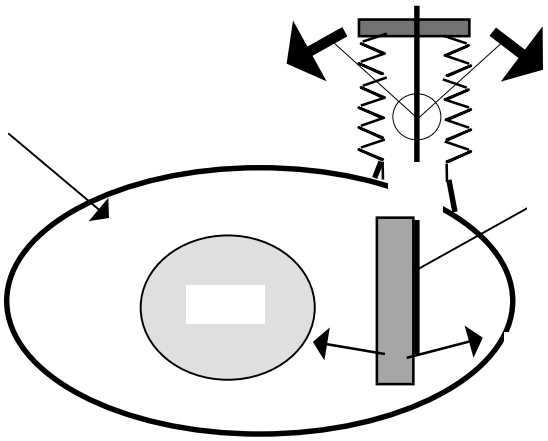

Figure M4 Schematic design of a 'rocking' scraper

Beam line stoppers

The beam stopper is a safety device that, in principle, should never 'see' beam. A schematic design is shown in Figure M5. If the power fails, the copper block must be fail safe and fall down to block the chamber.

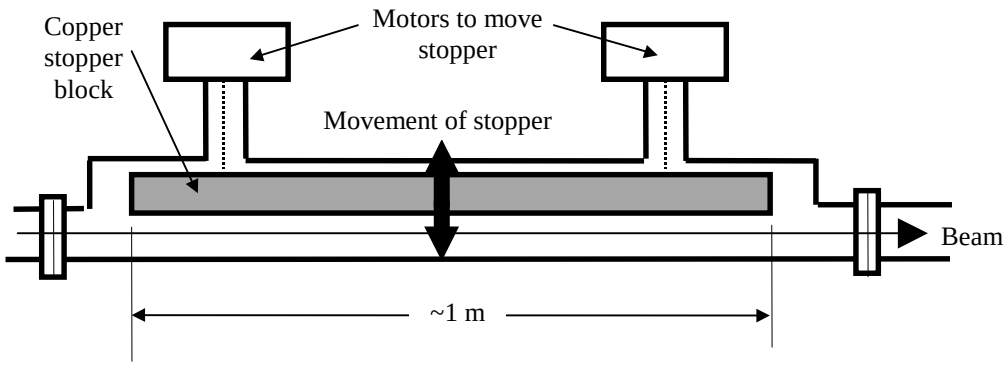

Figure M5 Schematic design of a beam stopper

* * *

APPENDIX II N

GENERAL DESIGN OF THE RF CAVITY

The construction of the rf cavity and its amplifier are described in Refs 1 and 2 respectively and the performance results from the first tests are given in Ref. 3.

A schematic presentation of the cavity is given in Figure N1. The reels of VITROVAC6025F® tape and the power amplifiers are water cooled. The power amplifiers are mounted in the space between the floor and the cavity. Gap voltages of 5 kV have been reached, which fully satisfies the PIMMS requirements. The frequency swing is also beyond what is actually needed for the synchrotron. The bias current for the frequency swing is a few tens of amperes, far below what would be needed for a conventional ferrite cavity.

RF cavity: principal parameters	
Overall length [m]	1.6400
Overall width [m]	0.8150
Overall height [m]	0.6640
Weight of cavity [kg]	600
Installed power (2 tetrodes in push-pull) [kW]	2 × 50
Gap voltage peak [kV]	5
Maximum frequency swing [MHz]	0.15-10
Bias current for a swing of 0.5-4 MHz [A]	32
Shunt impedance at 0.5 MHz [Ω]	~450
Shunt impedance at 4.0 MHz [Ω]	~350
Water cooling:	
Power dissipated in magnetic modules [kW]	35 (26 ×1.35)
Power dissipated by rf power tubes [kW]	70 (2 × 35)
Total water flow [l/min]	105
Water pressure [bar]	5 max.
Air cooling:	
Power amplifiers and electronics [m^3/min]	0.6

Table N1 RF cavity: principal parameters

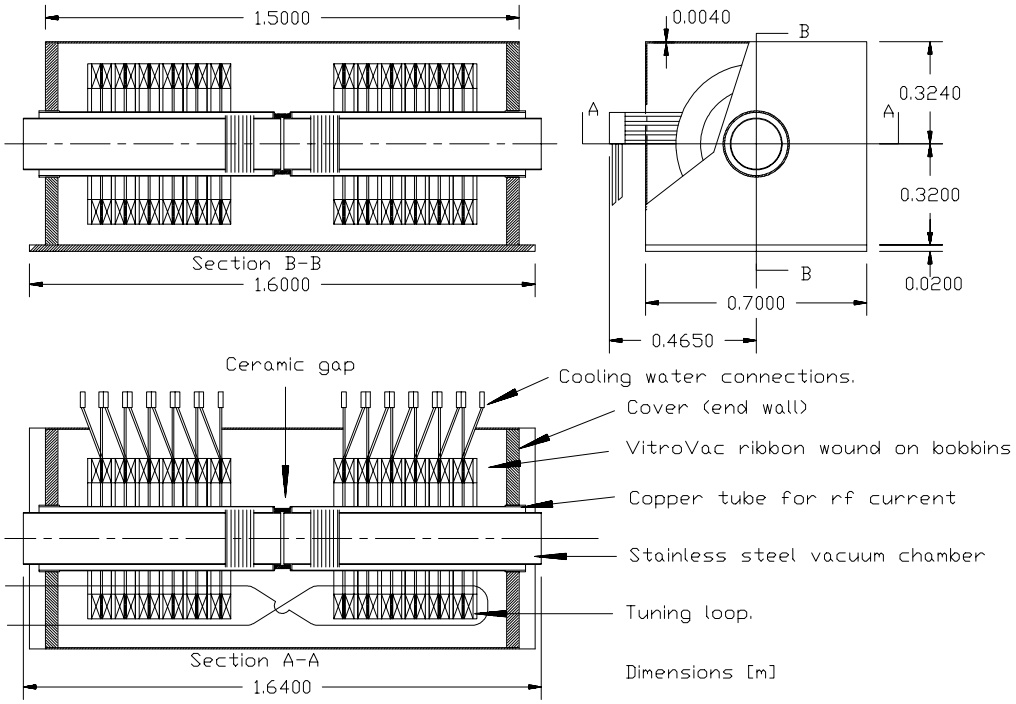

Figure N1 RF cavity

References

[1] M. Crescenti, G. Primadei, A. Susini, *Mechanical design of the rf cavity for TERA/PIMMS medical synchrotron*, PS/DI/Note 99-13 (Tech).

[2] M. Crescenti, G. Primadei, A. Susini, *Preliminary design of the rf amplifer for TERA/PIMMS medical synchrotron*, PS/DI/Note 99-14 (Tech).

[3] M. Crescenti, G. Primadei, A. Susini, *A new compact large frequency swing rf system for hadron acccceleration: Test results*, CERN/PS 97-60 (DI).

* * *

APPENDIX II O

MECHANICAL DESIGN OF THE MAIN RING POSITION MONITORS

For ease of manufacture and of signal analysis, linear-cut rectangular electrodes have been adopted (see schematic view in Figure O1). The width (140 mm) and height (74 mm) of the electrodes equal the major and minor diameters of the standard vacuum chamber to prevent the pick-ups becoming aperture limitations. The head amplifier is mounted directly on the feed through from the pick-up in order to locate the electronics as close as possible to the source of the signal. This is possible since the radiation levels will be very low. The electrodes are mounted in a rectangular box called the 'body' and the 'body' is mounted in the vacuum chamber. The capacitance of the 'body' to the electrodes can be adjusted by cutting holes in the 'body'. The vacuum chamber has two ports and is the same for both the horizontal monitor (see Figure O2) and the vertical monitor (see Figure O3). The only difference is that the blank flange and the feed through are interchanged.

The choice of parameters and expected performance are discussed in Ref. 1.

Position monitors: principal parameters

	Horizontal	**Vertical**
Overall length (flange-flange) [m]	0.2250	0.2250
Overall width [m]	0.2440	0.2480 excl. amplifier
Overall height [m]	0.2480 excl. amplifier	0.2400
Electrode length [m]	0.2000	0.2000
Vertical aperture [m]	0.7400	0.7400
Horizontal aperture [m]	0.1400	0.1400
Electrode material	stainless steel	stainless steel
Electrode thickness [m]	0.0010	0.0010
'Body' length	0.2040	0.2040
'Body' material	stainless steel	stainless steel
'Body' thickness [m]	0.0020	0.0020
Electrode to 'body' separation [m]	0.0070	0.0070
Vacuum chamber	Rounded rectangular form, stainless steel 3 mm	

Table O1 Position monitors: principal parameters

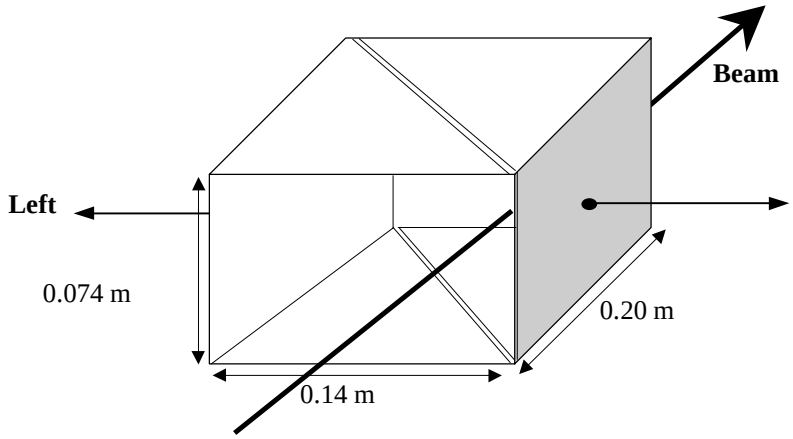

Figure O1 Schematic view of a single-plane, linear-cut pick-up

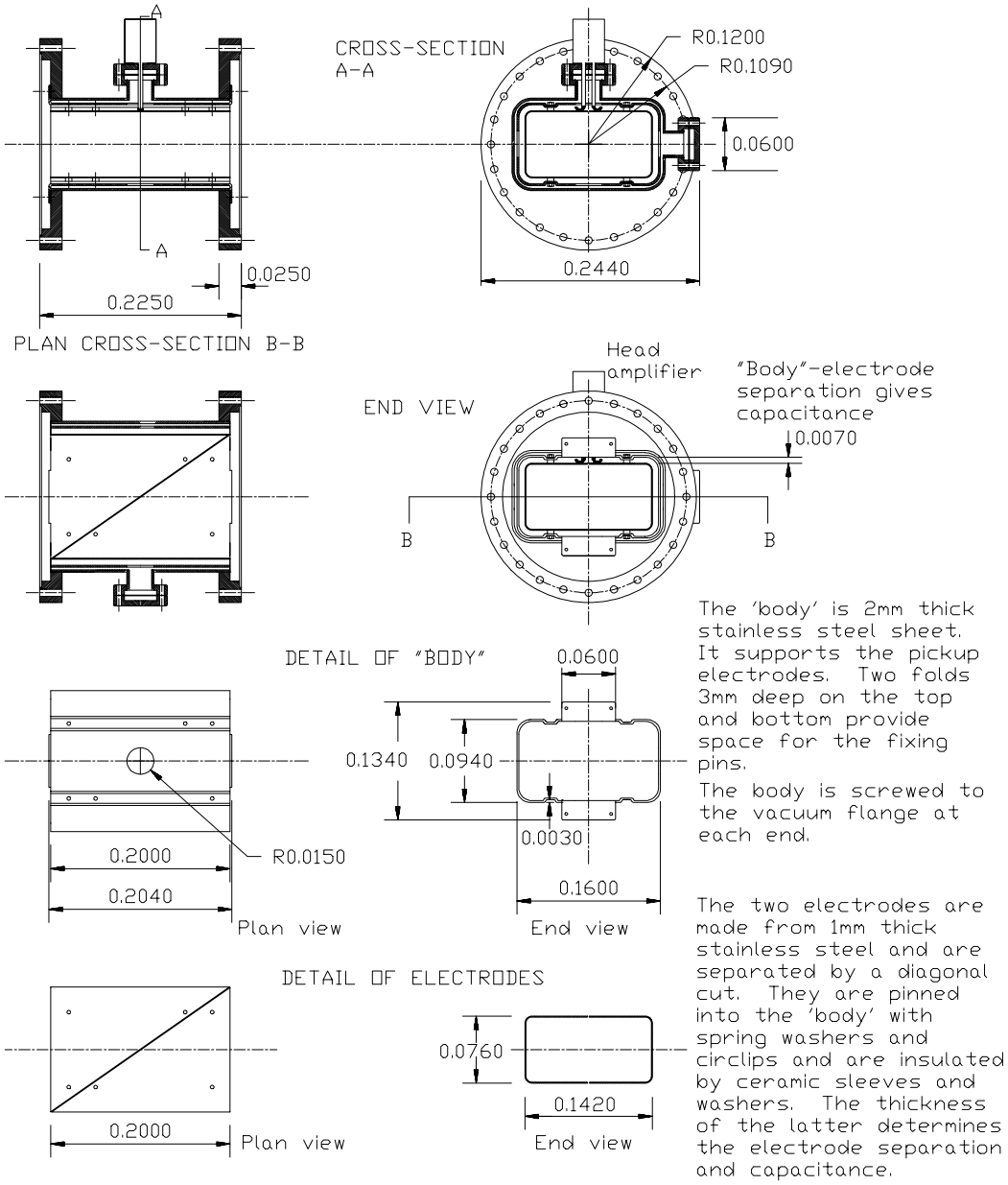

Figure O2 Horizontal monitor

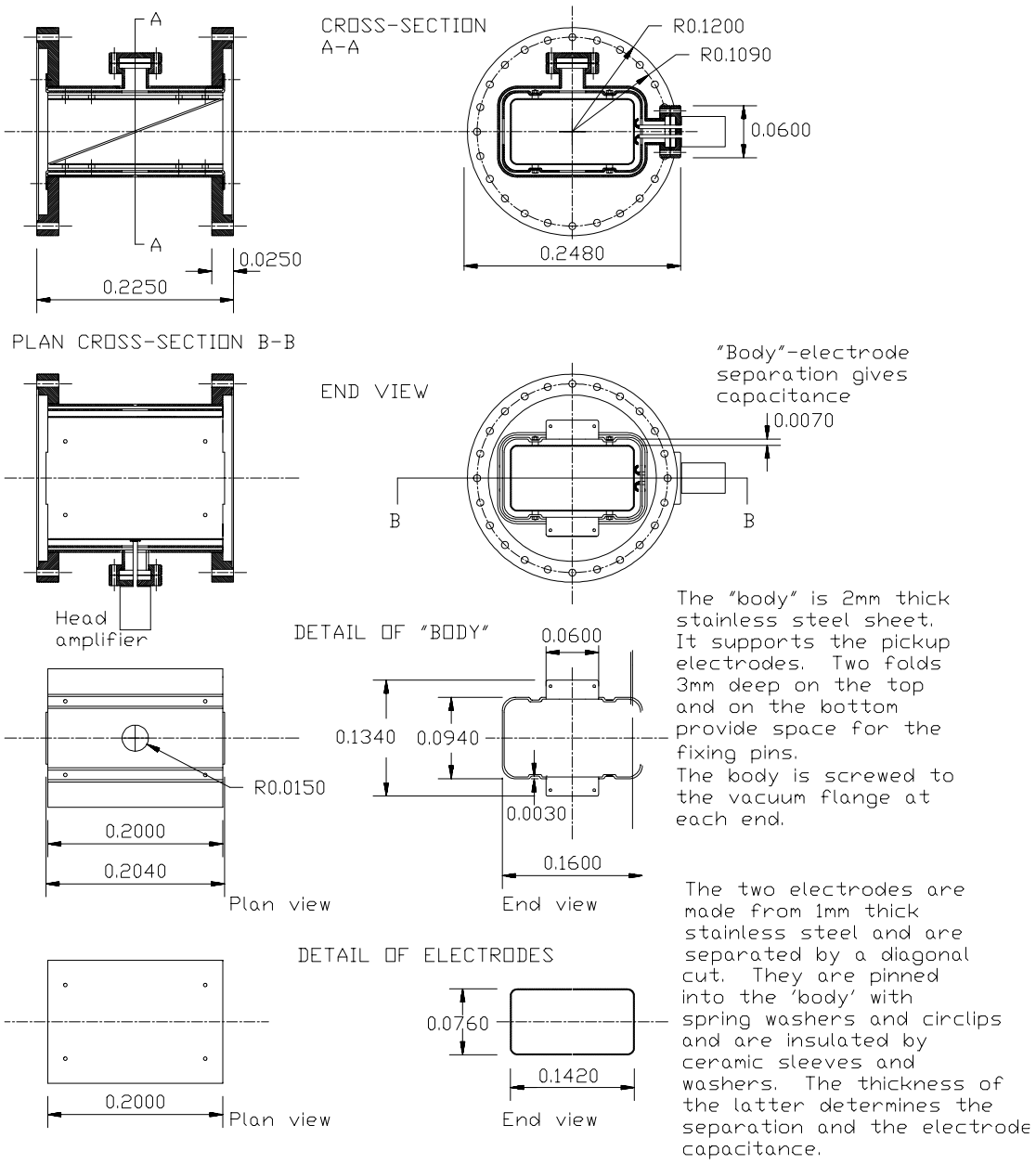

Figure O3 Vertical monitor

References

[1] L. Badano, *Beam diagnostics and monitors for the PIMMS synchrotron*, CERN/PS 99-037 (DI).

* * *

APPENDIX II P

CONCEPT DESIGN OF THE INJECTION BUMPERS

The injection bumpers have not been designed in detail, but the CERN-LEAR multi-turn injection bumper [1] is close to what is required except that its aperture is marginally too small once the thick ceramic chamber is taken into account. Table P1 summarises the main parameters of the injection bumper for the maximum field requirement of 0.0056 Tm for the carbon-ion. There is no need for water cooling of the coil since the injection cycle takes <100 μs with a repetition rate of <1 Hz.

Injection bumper parameters	
	Bumper in SS MR 08
Kick [rad] (carbon-ion beam*)	0.0074
Magnetic rigidity [Tm]	0.7613
Eff. magnetic lgth [m]	0.3
Maximum field [T]	0.01878
Pole gap [m]	0.09
Space between coils [m]	0.16
Field quality	$\pm 10^{-3}$
Yoke design	Ferrite, window-frame
Coil design	1 coil on each leg of yoke
Vacuum chamber design	Ceramic, elliptical, 7 mm
Maximum current [A]	336.25
No. of turns	4 per coil
Estimated inductance* [H]	17×10^{-6}
	2 units in series**
Total inductance [H]	21×10^{-6}
Maximum current [A]	336.25
Rise time for kick [μs]	33
Max. ramp voltage [V]	214
Power converter	Capacitor discharge into half-wave resonant circuit with 3rd harmonic for flat top ~30 μs. Beam at end of cycle
Max. repetition rate [Hz]	1
Duty cycle	$<10^{-4}$

* Having one coil on each leg of the yoke increases the stray field. The stored energy is estimated as 1.6 times the energy in magnet aperture, i.e.
$E_{total} = 1.6 \times 0.5 \times (\text{Central field})^2 \times (\text{Inter-coil gap}) \times (\text{Gap height}) \times (\text{Eff. lgth})/\mu_0 = 0.97$ J
** Note 2nd magnet has half the number of turns and hence half the field and quarter of the energy.

Table P1 Injection bumper parameters

References

[1] M. Chanel, S. Maury, D. Möhl, *Specification of a LEAR bump for multi-turn injection*, PS/AR/Note 96-04(Spec.).

* * *

APPENDIX II Q

MAGNETIC AND MECHANICAL DESIGN OF THE INJECTION SEPTA

The injection to the main ring will make use of two current-wall septa powered in series. Although these septa will be dc and will only have their fields changed during setting-up and when the particle species is changed, it is preferable, both for operation and construction, to laminate them with 1.5 mm laminations. However the half yokes have thick end plates and each individual half yoke is held by welded tie bars. The two half yokes are then bolted to form the final magnet. Because the beam will be subjected to a controlled emittance dilution once in the ring, the required field quality in these septa is only in the percent range. However, it is proposed to build the best magnet that is reasonably possible. For this reason, the pole is shaped with two shallow rectangular regions into which the coils sit. Basically, the poles act as parallel mirrors making two infinite series of images of the coil conductors. The disturbance to the field due to the insulation gaps between turns is minimised, if the mirrors sits at approximately half the thickness of this gap from the top and bottom turns. This is done by recessing the poles.

Table Q1 summarises the main parameters and the mechanical design is shown in Figures Q1 to Q4. Figure Q5 shows the field uniformity on the central transverse plane and the integrated fields through the magnet at low middle and top field levels. The axial truncation of the magnet and the saddle-ended coil degrade the quality of the magnet, but saturation has a negligible effect. In theory, it would be possible to shape the pole further, or shim the magnet, to improve the field, but this is not required for the present application and is, in fact, rarely attempted for septa. Figure Q6 shows the stray field comparison with and without a magnetic shield. Finally, Figure Q7 shows the axial profile of the field to give a first indication of the field level at nearby equipment.

Magnetic injection septum: principal parameters	
Overall length [m]	0.4700
Yoke length [m]	0.4200
Overall width [m]	0.1670
Overall height [m]	0.1620
Packing factor	>0.975
Weight [t]	0.071
Nominal maximum field [T]	0.4218
Current for maximum field [A]	2541
Effective magnetic length at max. field [m]	0.4561
Aperture (width [m] × height [m])	0.0697 × 0.0296
Resistance (magnet) [Ω]	1.19×10^{-3}
Inductance (magnet) [H]	24×10^{-6}
Number of turns	4
Number of water circuits	4
Pressure reduction required from the nominal 7 bar (details to be decided)	-
Probable water flow [l/min]	~7.5

Table Q1 Magnetic injection septum: principal parameters

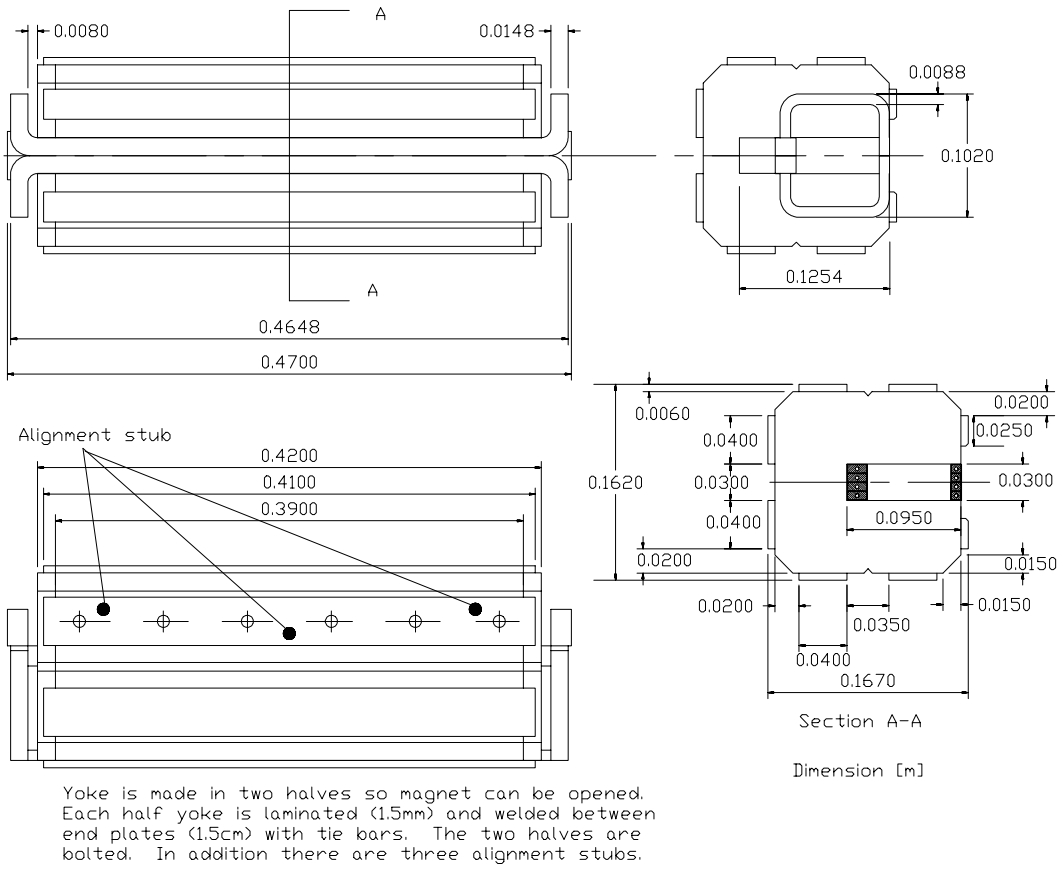

Figure Q1 Injection magnetic septum assembly

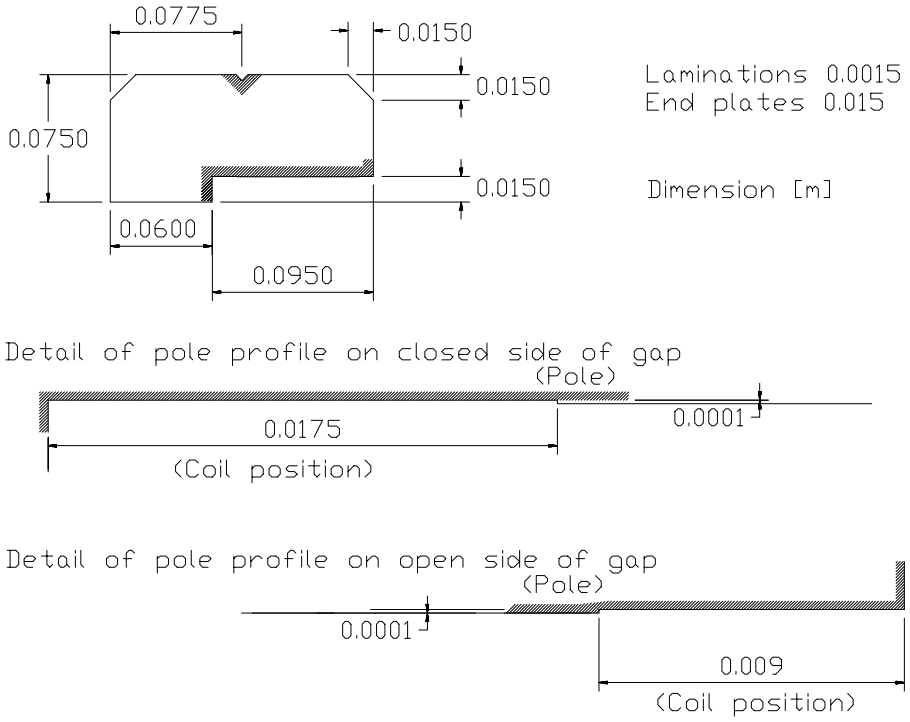

Figure Q2 Injection magnetic septum lamination and end plate

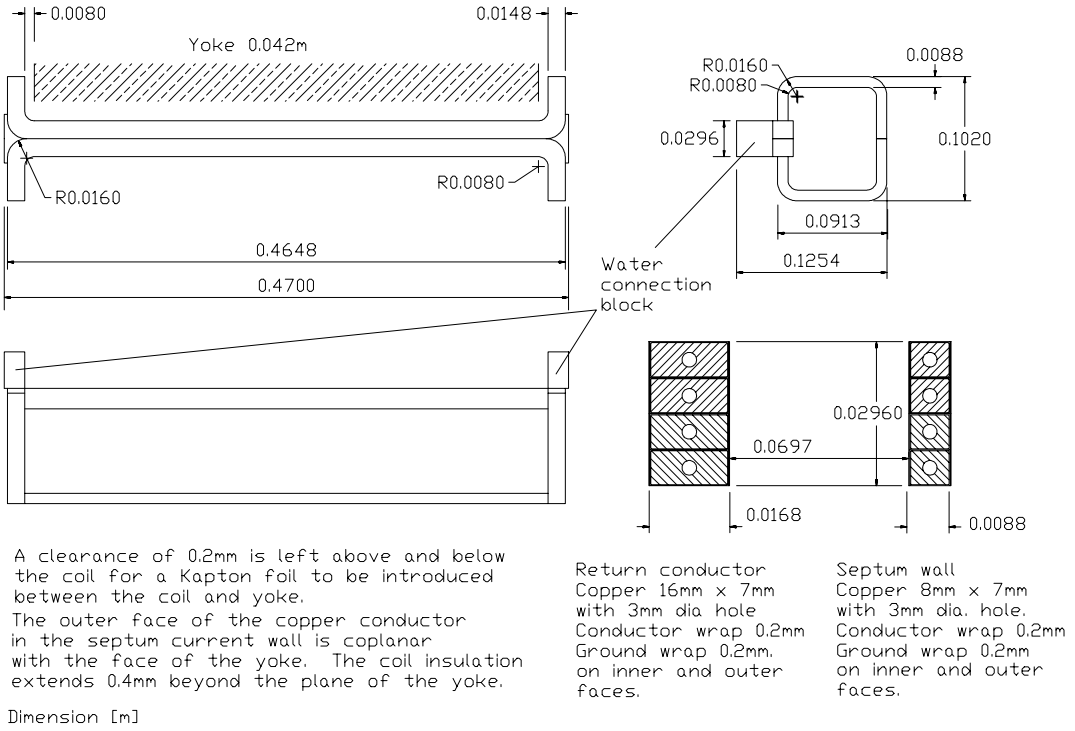

Figure Q3 Injection magnetic septum coil

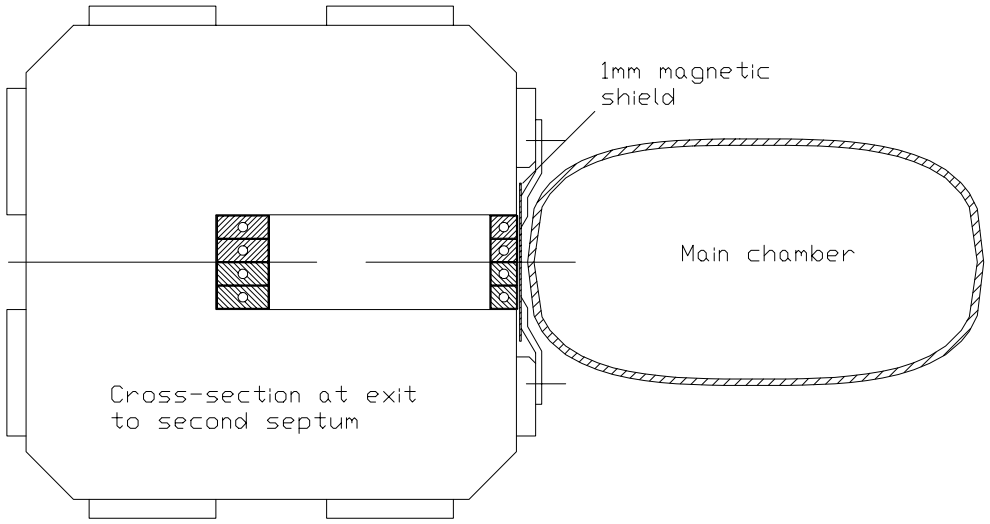

Figure Q4 Injection magnetic septum with shield

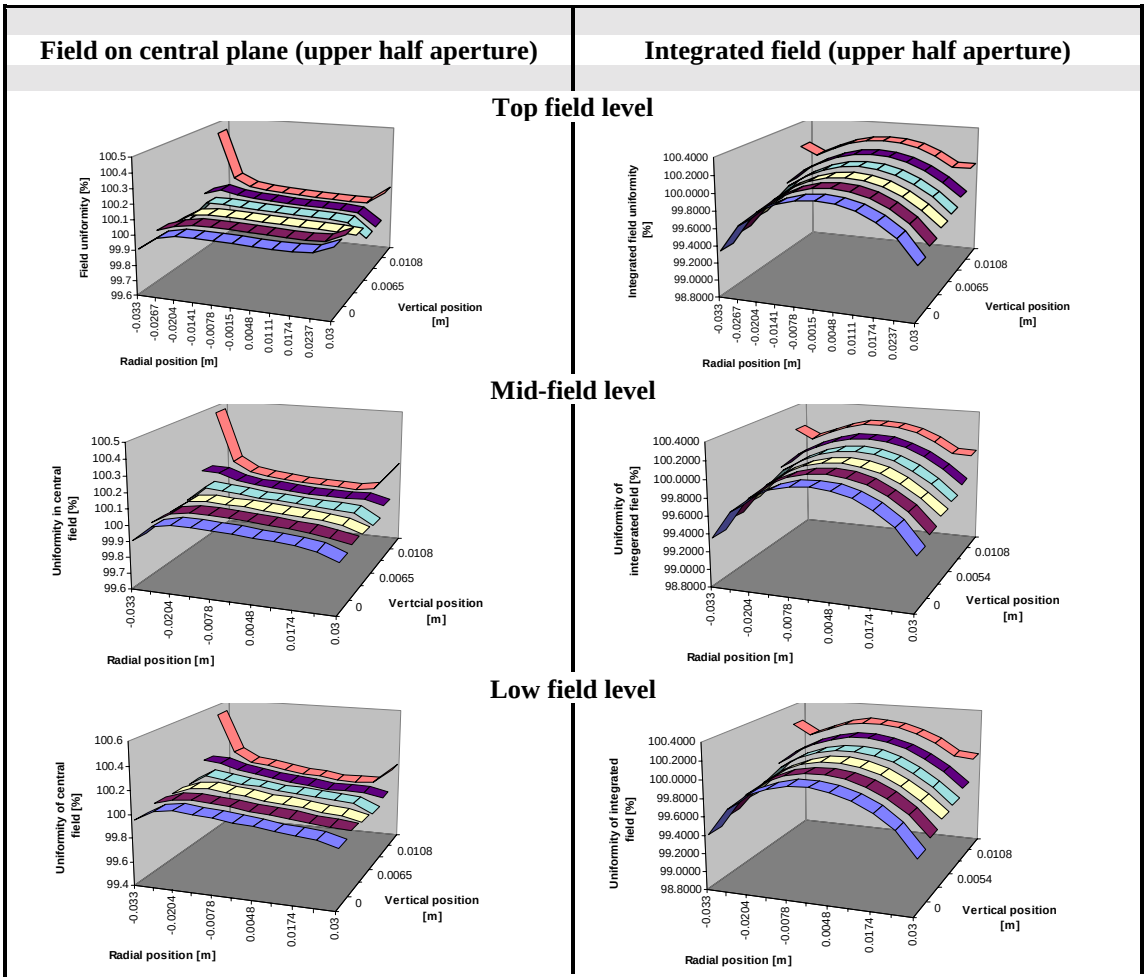

[Central orbit at x = 0, current wall on right-hand side]

Field on central x-y plane [T] for maximum current of 2541 A							
x, y [m]	x = -0.033	x = -0.0204	x = -0.014	x = -0.0015	x = 0.0111	x = 0.0174	x = 0.03
y = 0.0	0.4241	0.4247	0.4247	0.4247	0.4246	0.4246	0.4243
y = 0.0065	0.4243	0.4247	0.4247	0.4247	0.4246	0.4246	0.4244
y = 0.0108	0.4249	0.4248	0.4247	0.4247	0.4246	0.4246	0.4246
y = 0.0135	0.4265	0.4248	0.4247	0.4247	0.4246	0.4246	0.4254
Field with respect to the central orbit value [%]							
x, y [m]	x = -0.033	x = -0.0204	x = -0.014	x = -0.0015	x = 0.0111	x = 0.0174	x = 0.03
y = 0.0	99.90	100.00	100.01	100.00	99.99	99.99	100.05
y = 0.0065	99.93	100.01	100.01	100.00	99.99	99.99	99.97
y = 0.0108	100.01	100.03	100.01	100.00	99.99	99.98	99.89
y = 0.0135	100.42	100.03	100.01	100.00	99.99	99.98	100.07

Integrated field [Tm] for maximum current of 2541 A							
x, y [m]	x = -0.033	x = -0.0204	x = -0.014	x = -0.0015	x = 0.0111	x = 0.0174	x = 0.03
y = 0.0	0.19536	0.19632	0.19653	0.19670	0.19655	0.19636	0.19553
y = 0.0065	0.19566	0.19644	0.19664	0.19679	0.19666	0.19646	0.19584
y = 0.0108	0.19508	0.19666	0.19684	0.19698	0.19685	0.19667	0.19611
y = 0.0135	0.19686	0.19685	0.19702	0.19715	0.19703	0.19686	0.19662
Integrated field with respect to the central orbit value [%]							
x, y [m]	x = -0.033	x = -0.0204	x = -0.014	x = -0.0015	x = 0.0111	x = 0.0174	x = 0.03
y = 0.0	99.32	99.81	99.92	100.00	99.93	99.83	99.41
y = 0.0065	99.47	99.87	99.97	100.05	99.98	99.88	99.56
y = 0.0108	99.69	99.98	100.07	100.15	100.08	99.99	99.70
y = 0.0135	100.08	100.08	100.17	100.23	100.17	100.08	99.96

Figure Q5 Field uniformity of injection septum
(Since the field level has little effect only the top field values are recorded)

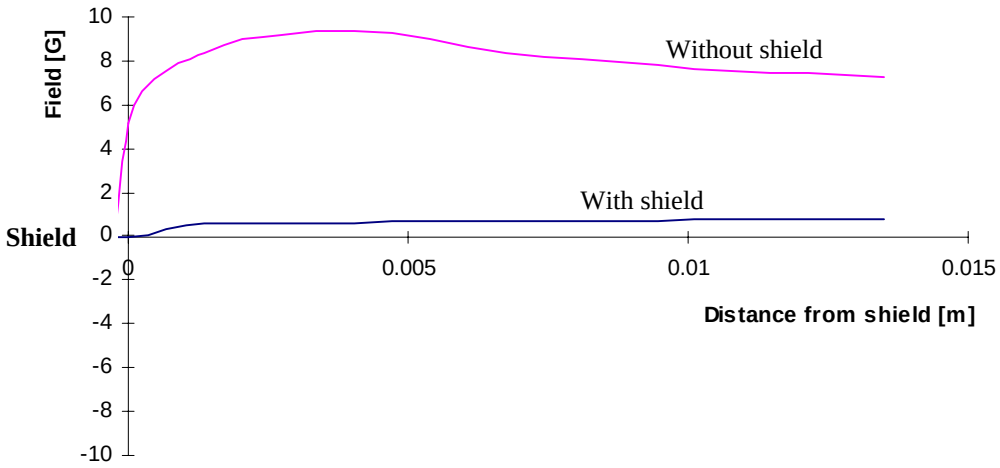

Figure Q6 Fringe field with and without magnetic shield
[Magnetic shield is 1 mm thick and set 0.5 mm away from the yoke and coil faces.]

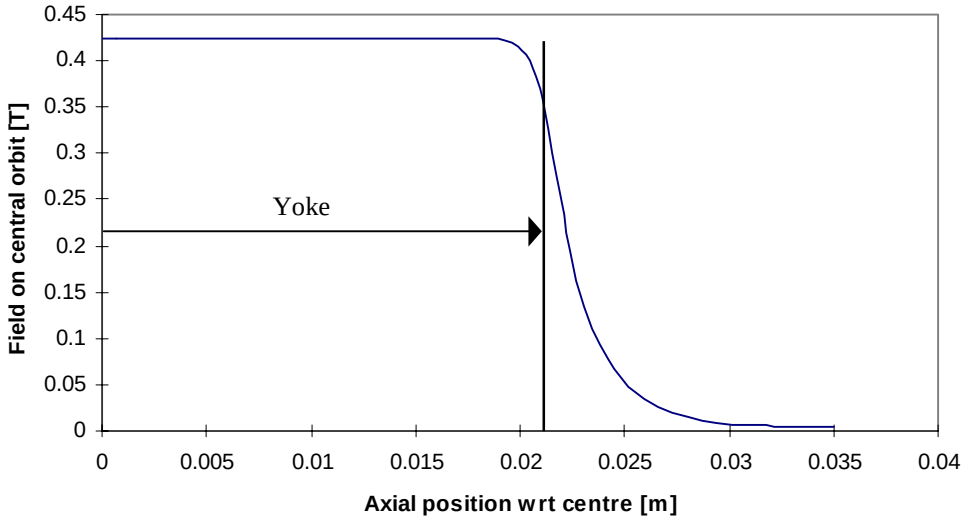

Figure Q7 Axial profile of the field plotted from the magnet centre

References

[1] M. Thivent, Private Communication, *Prédétermination septum magnétique*.

* * *

APPENDIX II R

MAGNETIC AND MECHANICAL DESIGN OF THE 'THIN' EXTRACTION SEPTUM

The extraction from the main ring starts with an electrostatic septum followed by first a 'thin' and then a 'thick' magnetic septum. Figure R1 shows the construction of the 'thin' magnetic septum. This unit and the following 'thick' septum are design to be run in series. Both are laminated with 1.5 mm laminations, but, since the field changes will be relatively slow, they are constructed using thick end plates (1.5 cm). The yokes are made in two equal halves. Each half is welded with tie bars between the thick end plates. The two halves are then assembled by bolts through the back yoke, so that the magnet can be easily opened. Because the beam will pass extremely close to the current wall of the thin septum and errors will directly distort the beam spot at the patient, the pole of the 'thin' septum has been shaped to improve the 2D field uniformity.

Table R1 summarises the main parameters and the mechanical design is shown in Figures R1 to R3

'Thin' magnetic extraction septum: principal parameters	
Overall length [m]	0.6736
Yoke length [m]	0.6100
Overall width [m]	0.1620
Overall height [m]	0.1620
Packing factor	>0.975
Weight [t]	0.1
Nominal maximum field [T]	0.4892
Current for maximum field [A]	3897
Effective magnetic length at max. field [m]	0.6541
Aperture (width [m] × height [m])	0.0546 × 0.0396
Resistance (magnet) [Ω]	860×10^{-6}
Inductance (magnet) [H]	22.9×10^{-6}
Number of turns	4
Number of water circuits	4
Pressure reduction required from the nominal 7 bar (details to be decided)	-
Probable water flow [l/min]	~12.5

Table R1 Thin magnetic extraction septum: principal parameters

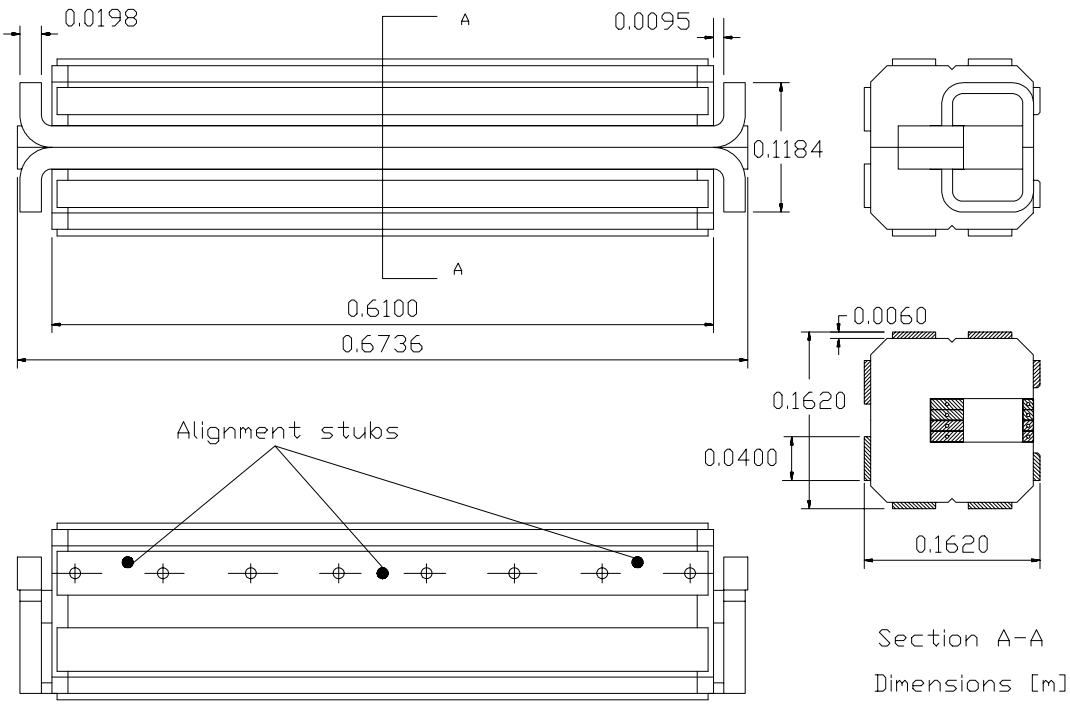

Yoke is made in 2 parts, so that septum can be opened.
Each half is laminated (1.5mm) and welded with tie bars
between end plates (1.5cm). The 2 halves are bolted.
In addition there are three alignment studs.
Kapton foil of 200 micron is introduced above and below
the coil between the coil and yoke.

Figure R1 'Thin' extraction magnetic septum assembly

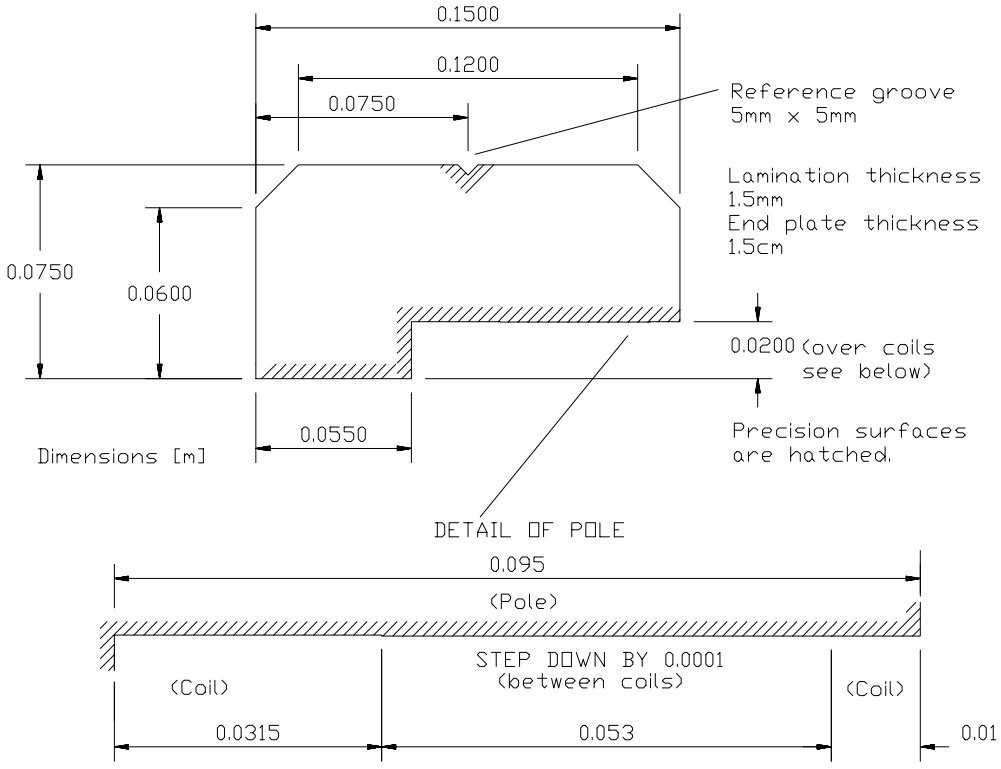

Figure R2 'Thin' extraction magnetic septum lamination and end plate

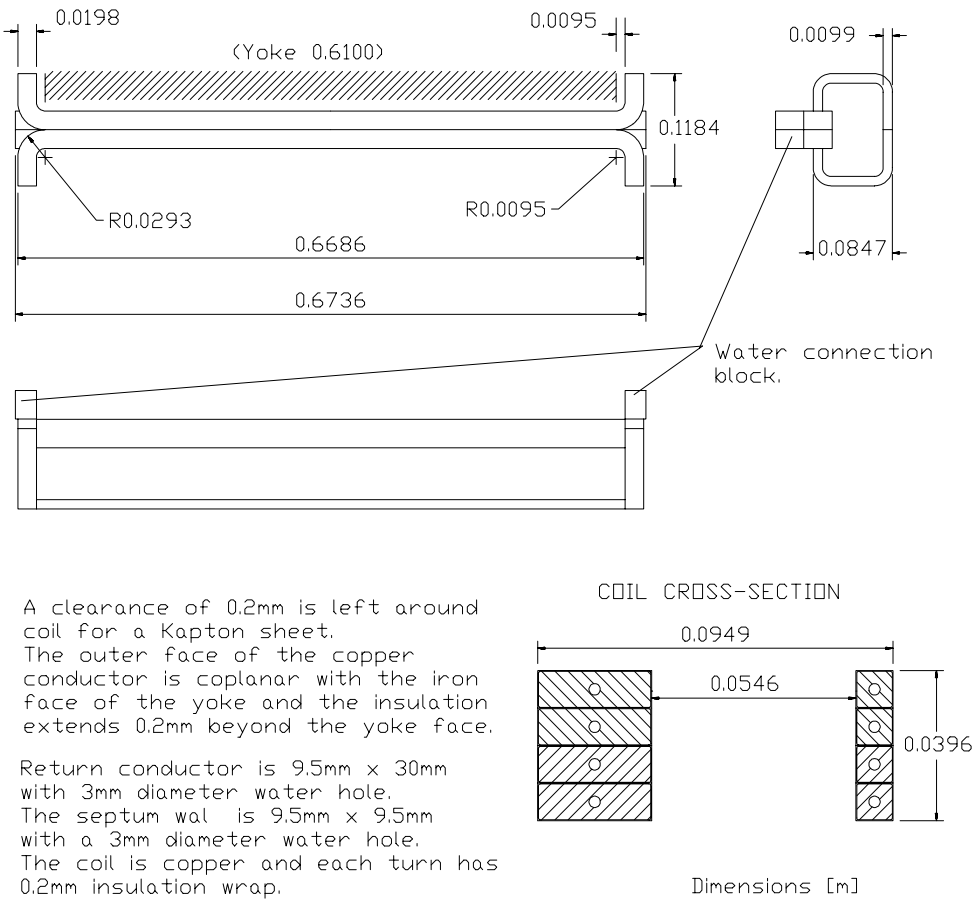

A clearance of 0.2mm is left around coil for a Kapton sheet.
The outer face of the copper conductor is coplanar with the iron face of the yoke and the insulation extends 0.2mm beyond the yoke face.

Return conductor is 9.5mm x 30mm with 3mm diameter water hole.
The septum wal is 9.5mm x 9.5mm with a 3mm diameter water hole.
The coil is copper and each turn has 0.2mm insulation wrap.

Figure R3 'Thin' extraction magnetic septum coil

Figure R4 shows the stray field comparison with and without a magnetic shield 1 mm thick set at 0.5 mm from the yoke and coil at top field level of 0.49 T. Figure R5 shows how shaping the pole can improve the 2D-field quality. The figure shows the boundary of the region of field uniformity ($\pm 5 \times 10^{-3}$) on the central transverse plane, first with a flat pole and then with a shaped pole. Since the beam passes very close to the septum current wall and distortions directly affect the beam spot at the patient, it was decided to adopt the shaped pole. Figure R6 shows in more detail the 2D field uniformity. Figure 7 gives the equivalent data for the integrated field through the magnet the top field level. The axial truncation of the magnet and the saddle-ended coil degrade the quality of the magnet, but the effect is surprisingly small. Saturation has a negligible effect and the lower field levels are very similar. In theory, it would be possible to shape the pole further, or shim the magnet, to improve the field, but this is not required for the present application and is, in fact, rarely done for septa. Finally, Figure R8 shows the axial profile of the field to give a first indication of the field level at nearby equipment.

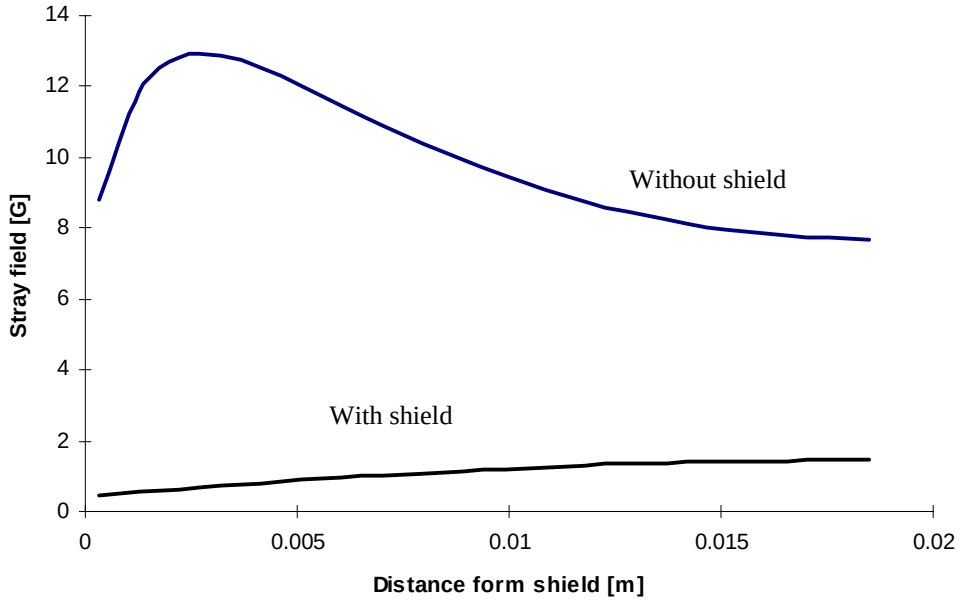

Figure R4 Comparison of the stray field with and without a magnetic shield 1 mm thick
[See Table 3.10 for clearances and thicknesses of shield, chamber etc.]

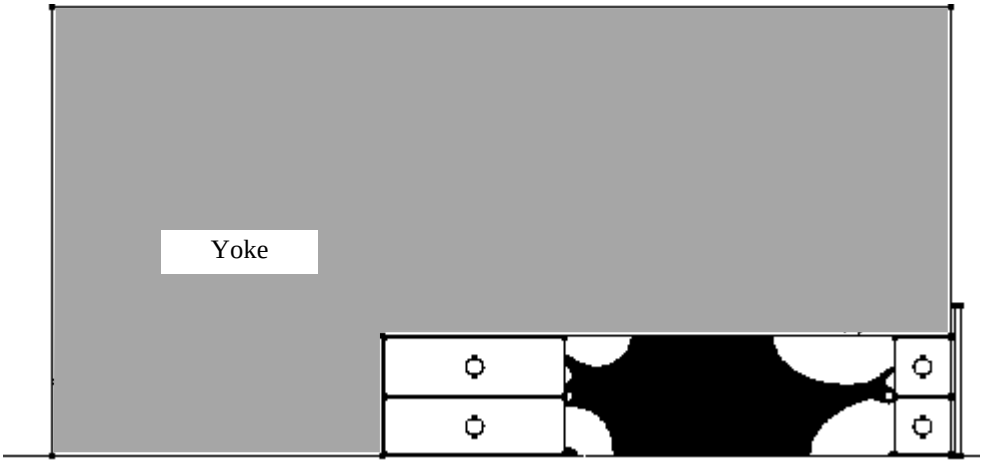

(a) Flat pole (large, out-of-tolerance region near septum wall)

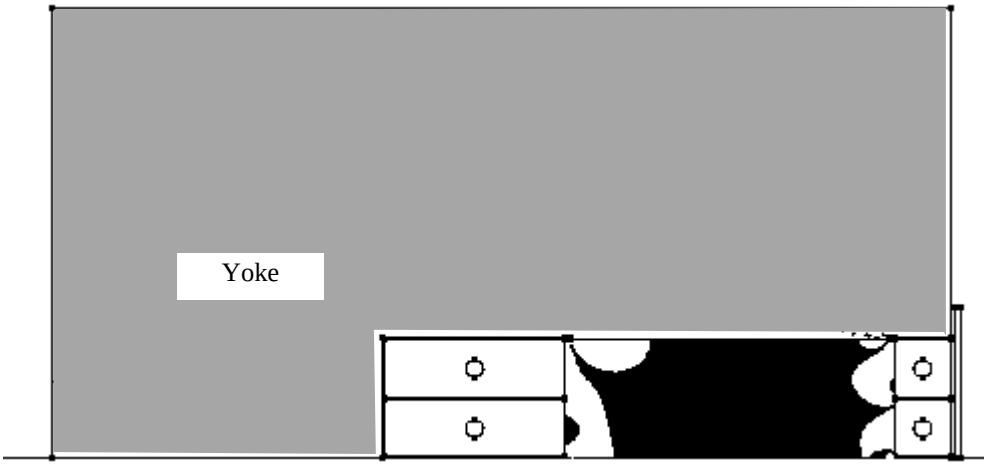

(b) Shaped pole (better field uniformity near current wall)

Figure R5 Effect of pole shaping
[Region of field uniformity $\pm 5 \times 10^{-3}$ at top field 0.49 T : (a) Flat pole, (b) Shaped pole]

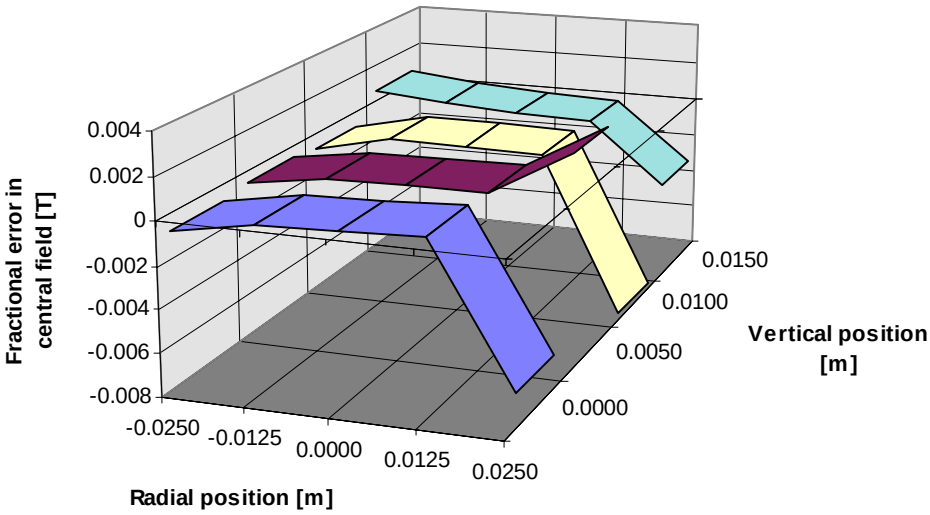

Figure R6 2D field quality at centre of magnet at top field 0.49 T

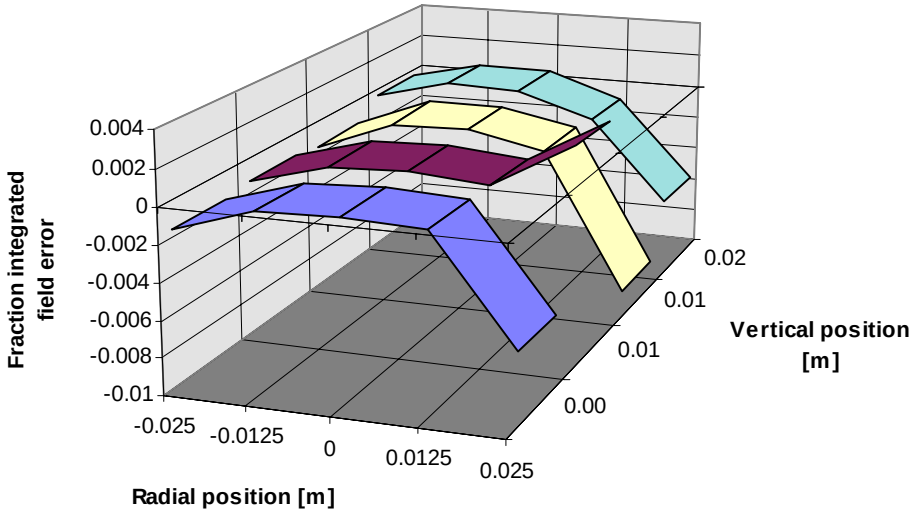

Figure R7 3D field quality at top field 0.49 T

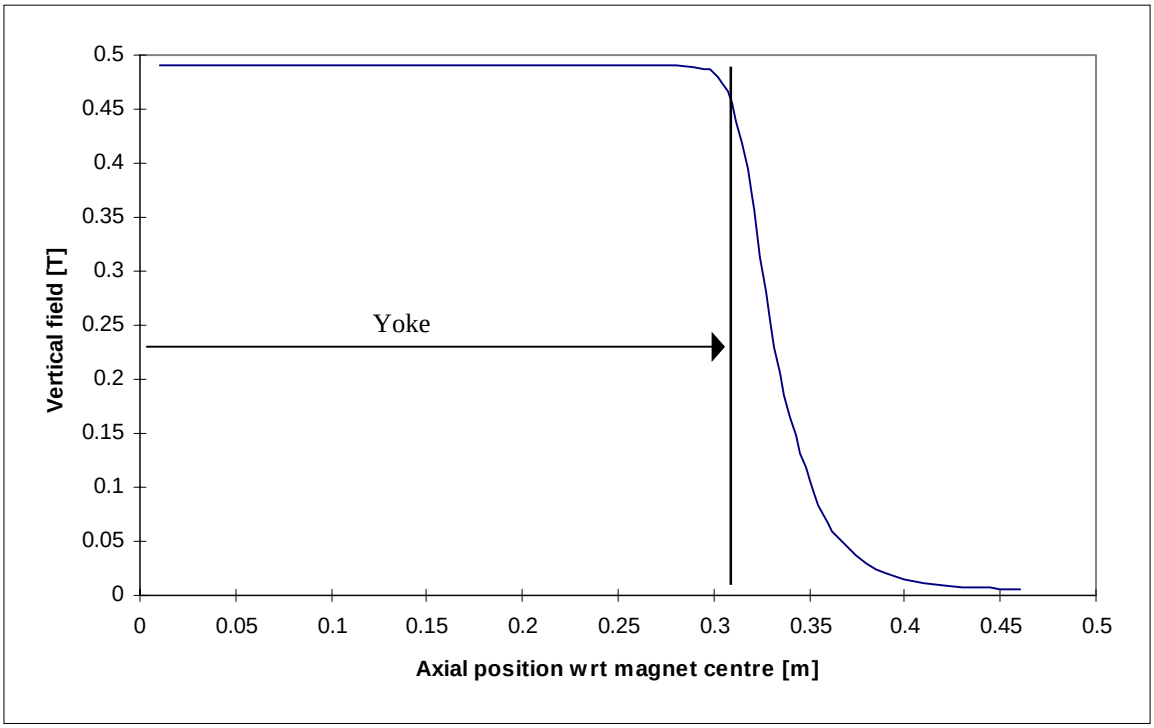

Figure R8 Longitudinal field distribution

References

[1] M. Thivent, Private Communication, *Prédétermination septum magnétique*.

* * *

APPENDIX II S

MAGNETIC AND MECHANICAL DESIGN OF THE 'THICK' EXTRACTION SEPTUM

The extraction from the main ring starts with an electrostatic septum that is followed by first a 'thin' and then a 'thick' magnetic septum. Figure S1 shows the 'thick' magnetic septum. This unit is designed to be run in series with the 'thin' septum that precedes it. Both septa are laminated with 1.5 mm laminations, but, since the field changes will be relatively slow, they are constructed using thick end plates (1.5 cm). The yokes are made in two equal halves. Each half is welded with tie bars between the thick end plates. The two halves are then assembled by bolts through the back yoke, so that the magnet can be easily opened.

Table S1 summarises the main parameters and the mechanical design is shown in Figures S1 to S4. For completeness Figure S4 includes the stray field comparison with and without a magnetic shield, although in the case of the 'thick' septum the vacuum chamber of the main ring is far enough away that the stray field is unimportant. Figure S5 shows the region of field uniformity ($\pm 5 \times 10^{-3}$) on the central transverse plane with a flat pole. Since this result is very good with respect to the other septa and since the beam passes more centrally in the aperture than for the 'thin' septum, it was decided to adopt the flat pole. Figure S6 shows in more detail the 2D field uniformity. Figure S7 shows the equivalent 3D-integerated field quality at the top field level. The axial truncation of the magnet and the saddle-ended coil degrade the quality of the magnet, but not by very much. Saturation has a negligible effect. In theory, it would be possible to shape the pole and improve the field quality, however, in the case of the 'thick' septum the field quality is more than adequate. Finally, Figure S7 shows the axial profile of the field to give a first indication of the field level at nearby equipment.

'Thick' magnetic injection septum: principal parameters	
Overall length [m]	1.0236
Yoke length [m]	0.9600
Overall width [m]	0.3360
Overall height [m]	0.3460
Packing factor	>0.975
Weight [t]	0.755
Nominal maximum field [T]	0..9775
Current for maximum field [A]	3897
Effective magnetic length at max. field [m]	1.0075
Aperture (width [m] × height [m])	0.1152 × 0.0400
Resistance (magnet) [Ω]	3.01×10^{-3}
Inductance (magnet) [H]	275.6×10^{-6}
Number of turns	8
Number of water circuits	8
Pressure reduction required from the nominal 7 bar (details to be decided)	-
Probable water flow [l/min]	~43.7

Table S1 'Thick' magnetic injection septum: principal parameters

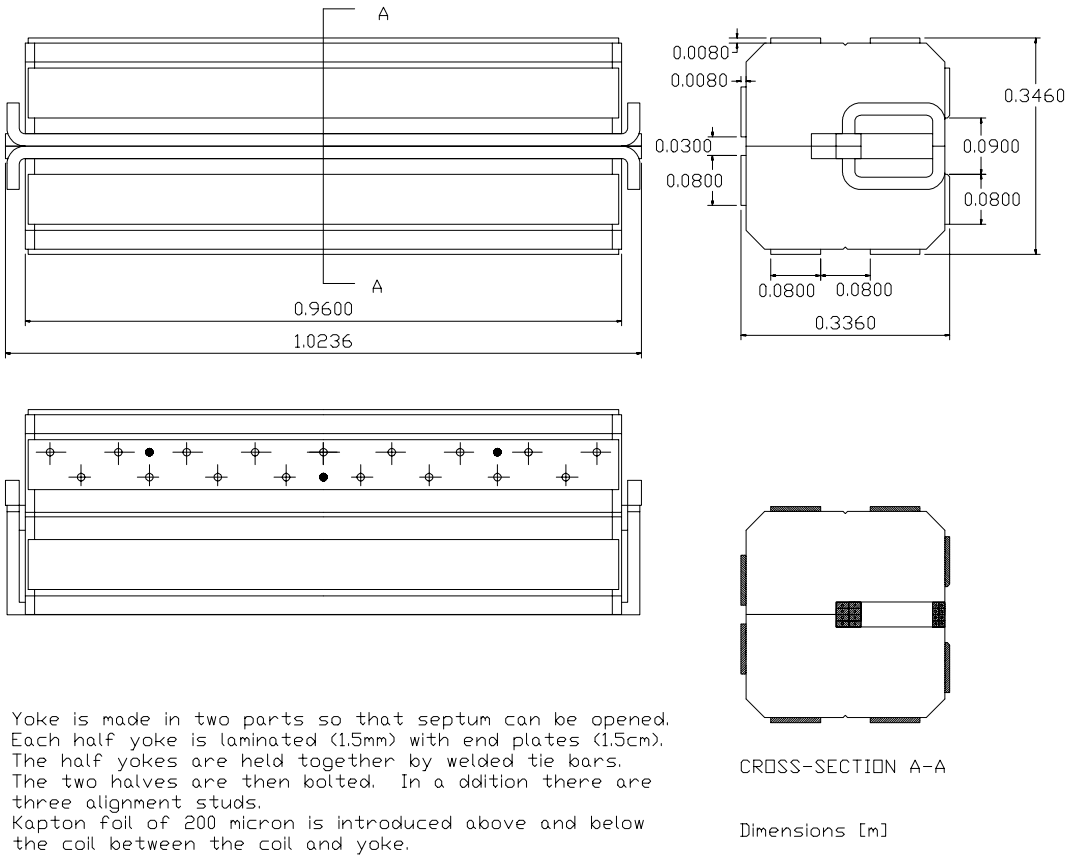

Figure S1 'Thick' extraction magnetic septum assembly

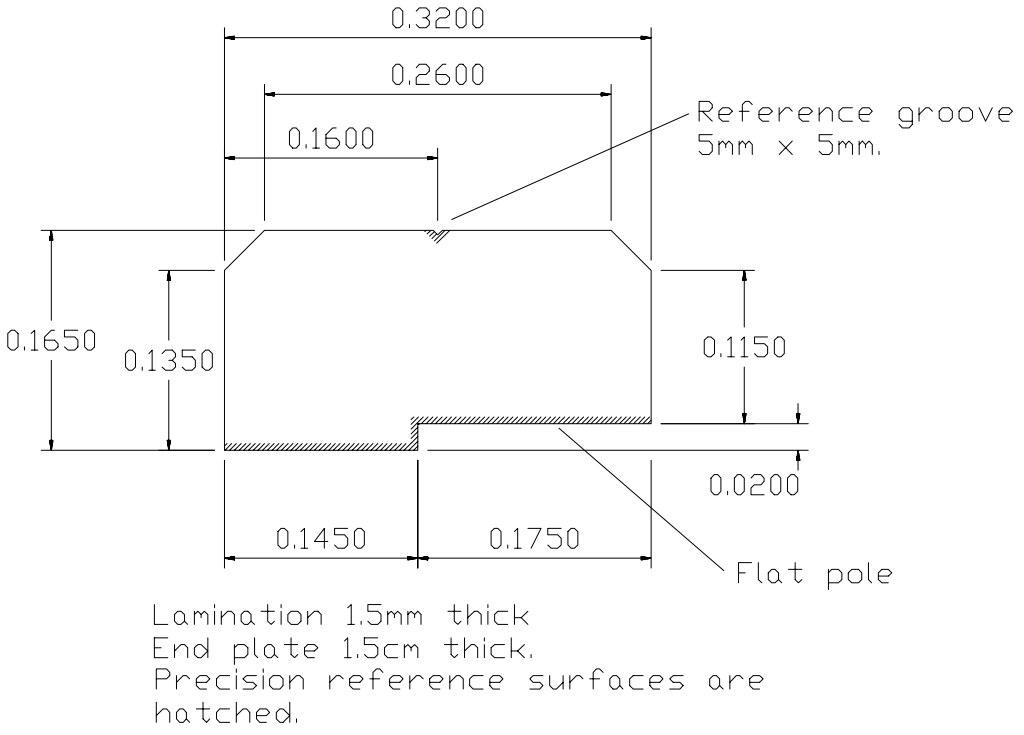

Figure S2 'Thick' extraction magnetic septum lamination and end plate

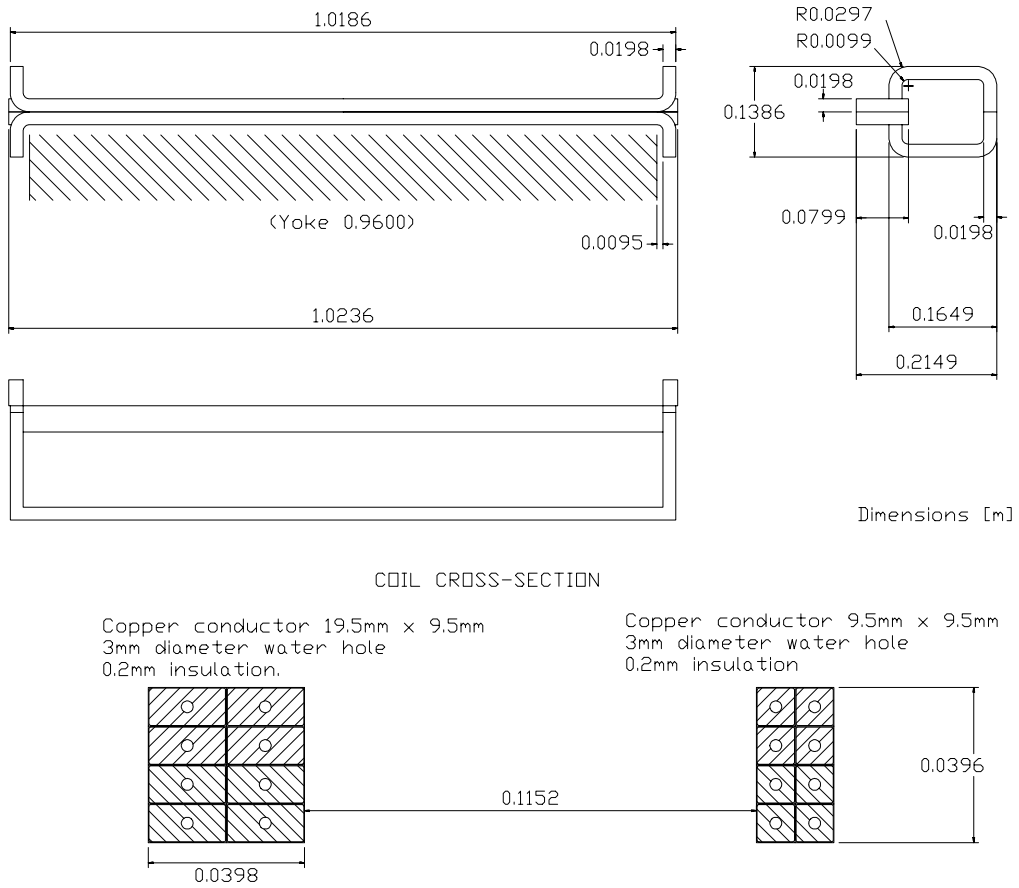

Figure S3 'Thick' extraction magnetic septum coil

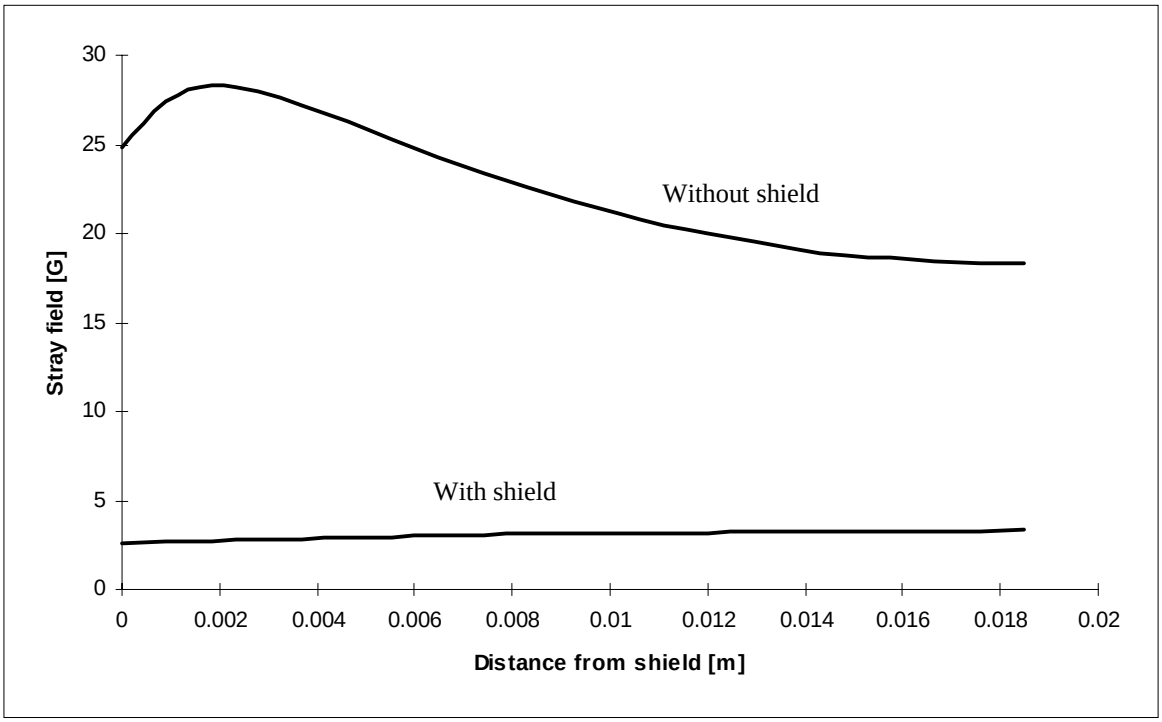

Figure S4 Comparison of stray field with and without magnetic shield 1 mm thick and mounted 0.5 mm from surface of coil and yoke

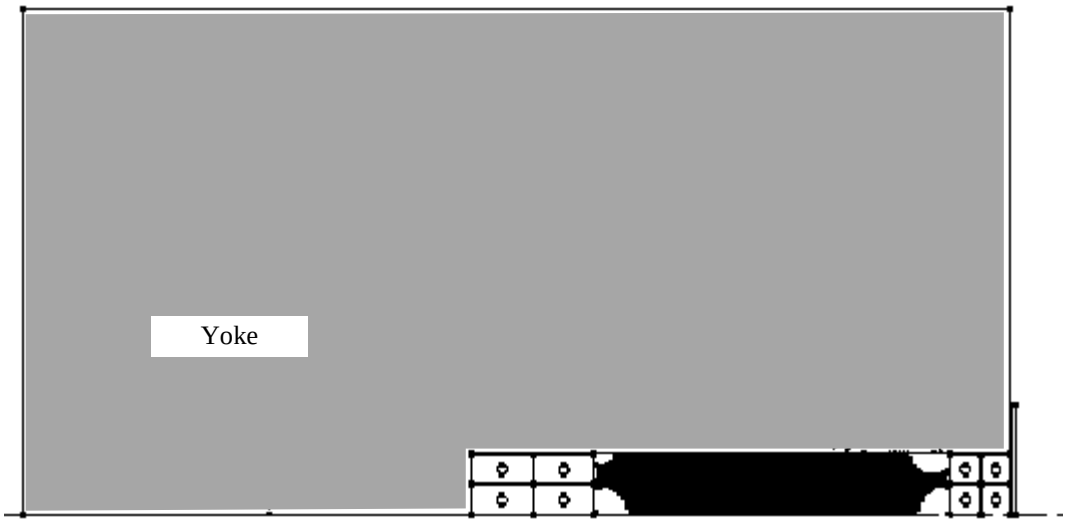

Figure S5 Region of field uniformity $\pm 5 \times 10^{-3}$ with a flat pole at top field 0.98 T

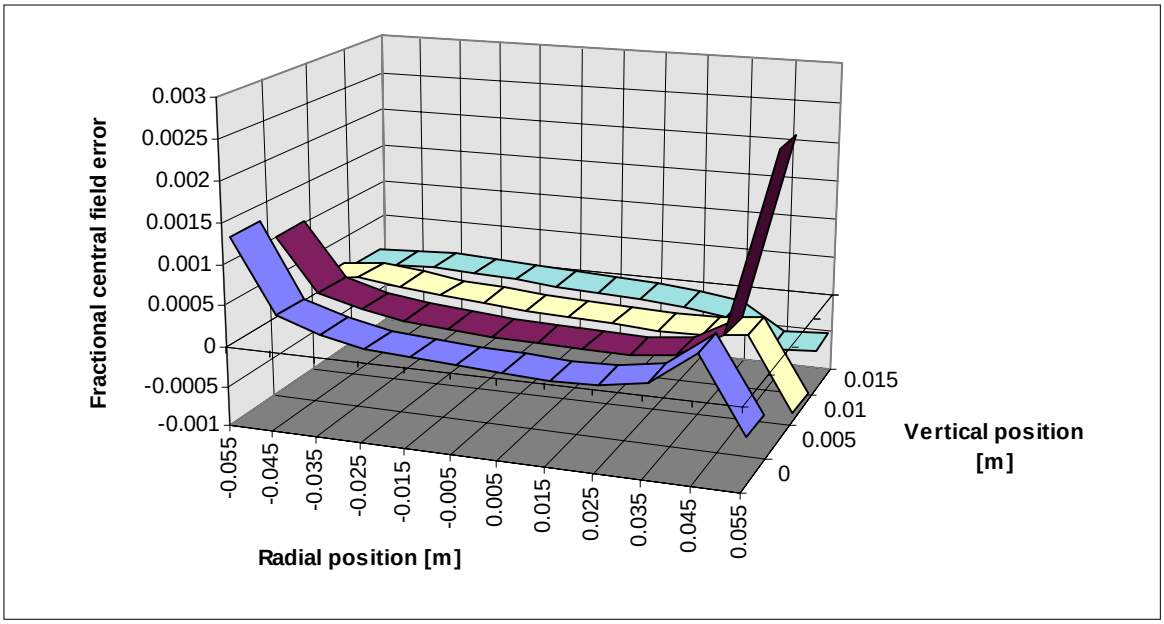

Figure S6 2D-field quality at top field of 0.98 T

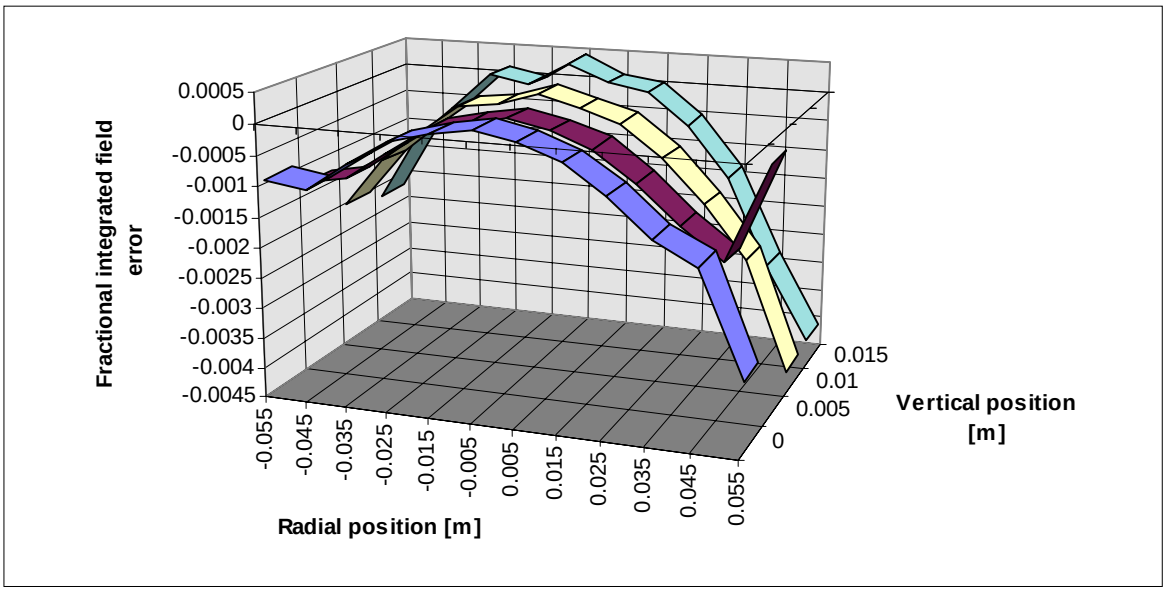

Figure S7 Integrated 3D-field quality at top field of 0.98 T

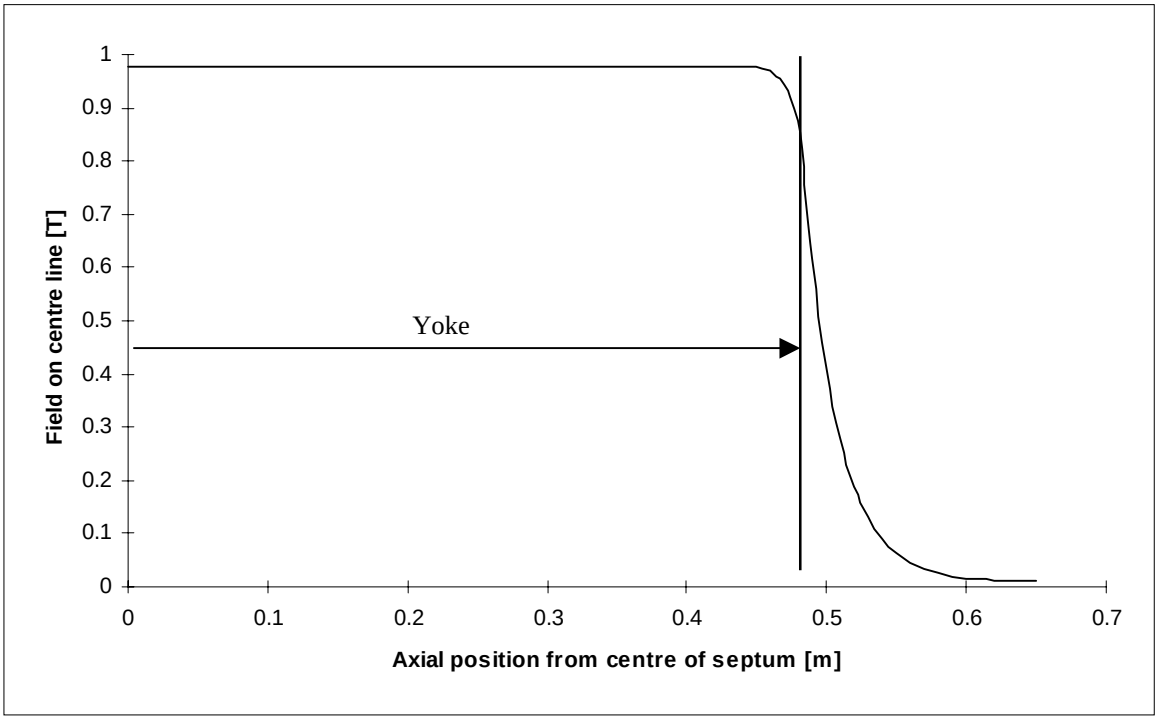

Figure S8 Longitudinal field distribution

References

[1] M. Thivent, Private Communication, *Prédétermination septum magnétique*.

* * *

APPENDIX II T

DESIGN OF THE ELECTROSTATIC INJECTION SEPTUM

Figure T1 shows a simplified drawing of the electrostatic injection septum. The main structure is made of stainless steel, but the septum foil is made from molybdenum. The thermal conductivity of stainless steel is too low for this application. This septum is slightly unusual in two ways. Firstly, all the feed throughs and adjustments are made from one side of the vacuum tank. This technique has been demonstrated in septa made in the CERN PS Division. Secondly, the electrodes are bent to follow the path of the deflected beam. The electrodes have two equal straight sections of 40 cm and the two section have a mutual angle of 60 mrad. The final section is aligned with the undeflected beam. The voltages are relatively low and no special surface finishes are required.

Electrostatic injection septum: principal parameters	
Overall length [m]	1.0375
Overall width [m]	0.856
Overall height [m]	0.520
Position of the centre line of the undeflected beam wrt the axis of the vacuum chamber [m]	0.100
Nominal position of septum foil wrt centre line of tank [m]	0.059
Adjustment in position of septum foil [m]	±0.005
Nominal position of the septum foil wrt to the centre line of the undeflected beam [m]	-0.041
Gap between foil and live electrode [m]	0.030
Length of ground electrode [m]	0.860
Length of live electrode [m]	0.800
Gradient for 7 MeV/u carbon ions [kV/cm]	20.8
Gradient for 20 MeV protons [kV/cm]	29.7
Voltage on electrode for 7 MeV/u carbon ions [kV]	62.5
Voltage on electrode for 207 MeV/u protons [kV]	89.0
Deflection of beam [rad]	0.060

Table T1 Electrostatic injection septum: principal parameters

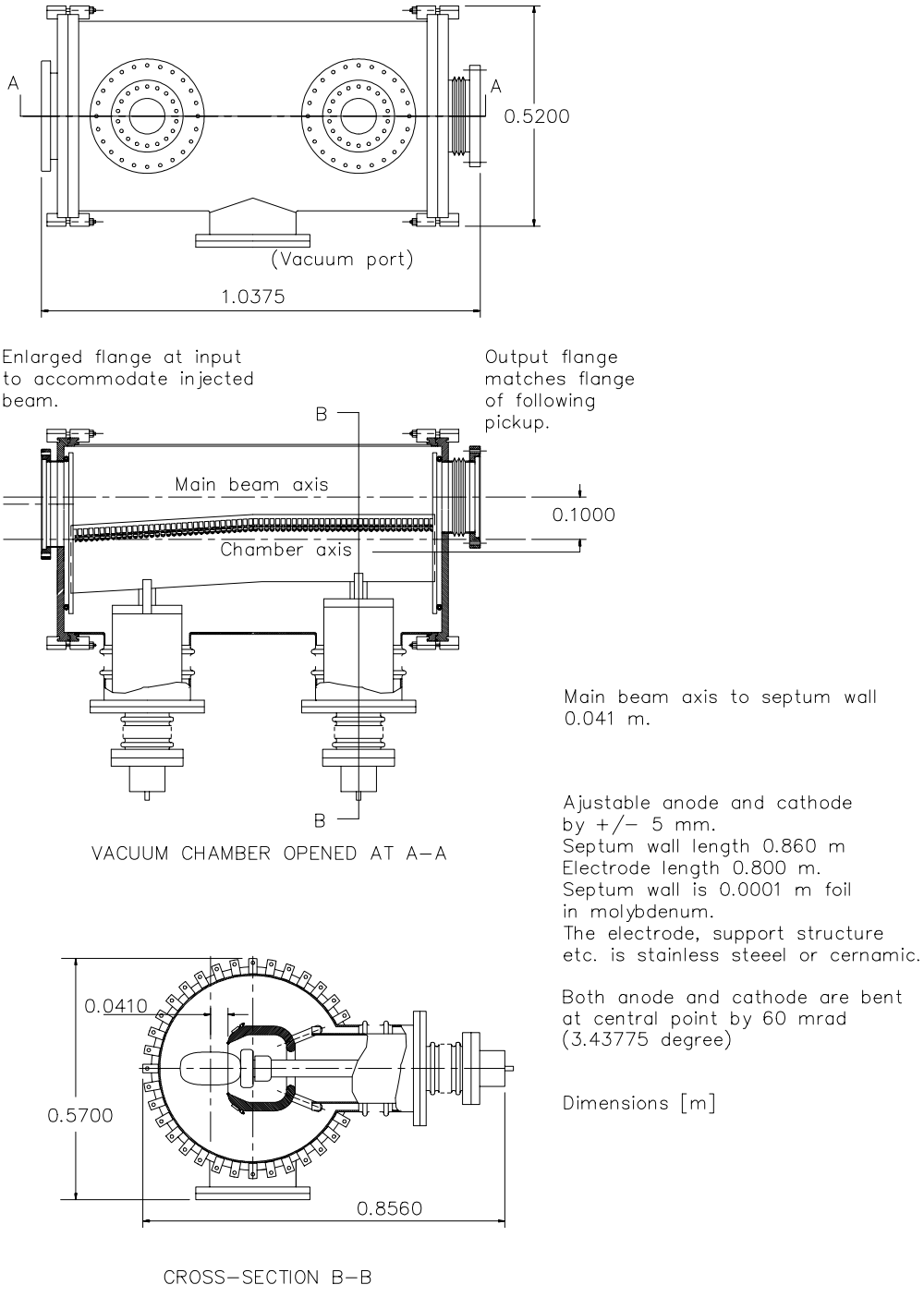

Figure T1 Basic design of the electrostatic injection septum
[beams pass from left to right]

* * *

APPENDIX II U

DESIGN OF THE ELECTROSTATIC EXTRACTION SEPTUM

Figure U1 shows a simplified drawing of the extraction septum. The main structure is made of stainless steel, but the septum wall is formed by tungsten wires spaced every 2.5 mm Tungsten is chosen for its high melting point. The voltages are relatively low and no special surface finishes are required.

The vacuum tank is somewhat larger in radius than it strictly needs to be. This arose because of an earlier idea to use the same design of vacuum tank for both the extraction and injection septa. The injection septum then had to be redesigned to solve a space problem, but there was insufficient time to redesign the extraction septum to take advantage of this change of plan.

Electrostatic extraction septum: principal parameters	
Overall length of tank[m]	1.000
Overall width [m]	0.892
Overall height [m]	0.520
Nominal position of backwall of ground electrode wrt centre line of tank [m]	-0.075
Nominal position of septum wires wrt centre line of tank [m]	0.035
Adjustment of septum wires [m]	±0.005
Nominal gap between wires and live electrode [m]	0.015
Adjustment of live electrode [m]	±0.005
Length of ground electrode [m]	0.860
Length of live electrode [m]	0.800
Gradient for 400 MeV/u carbon ions [kV/cm]	42.5
Voltage for 400 MeV/u carbon ions [kV]	63.7
Deflection of beam [rad]	0.0025

Table U1 Electrostatic extraction septum: principal parameters

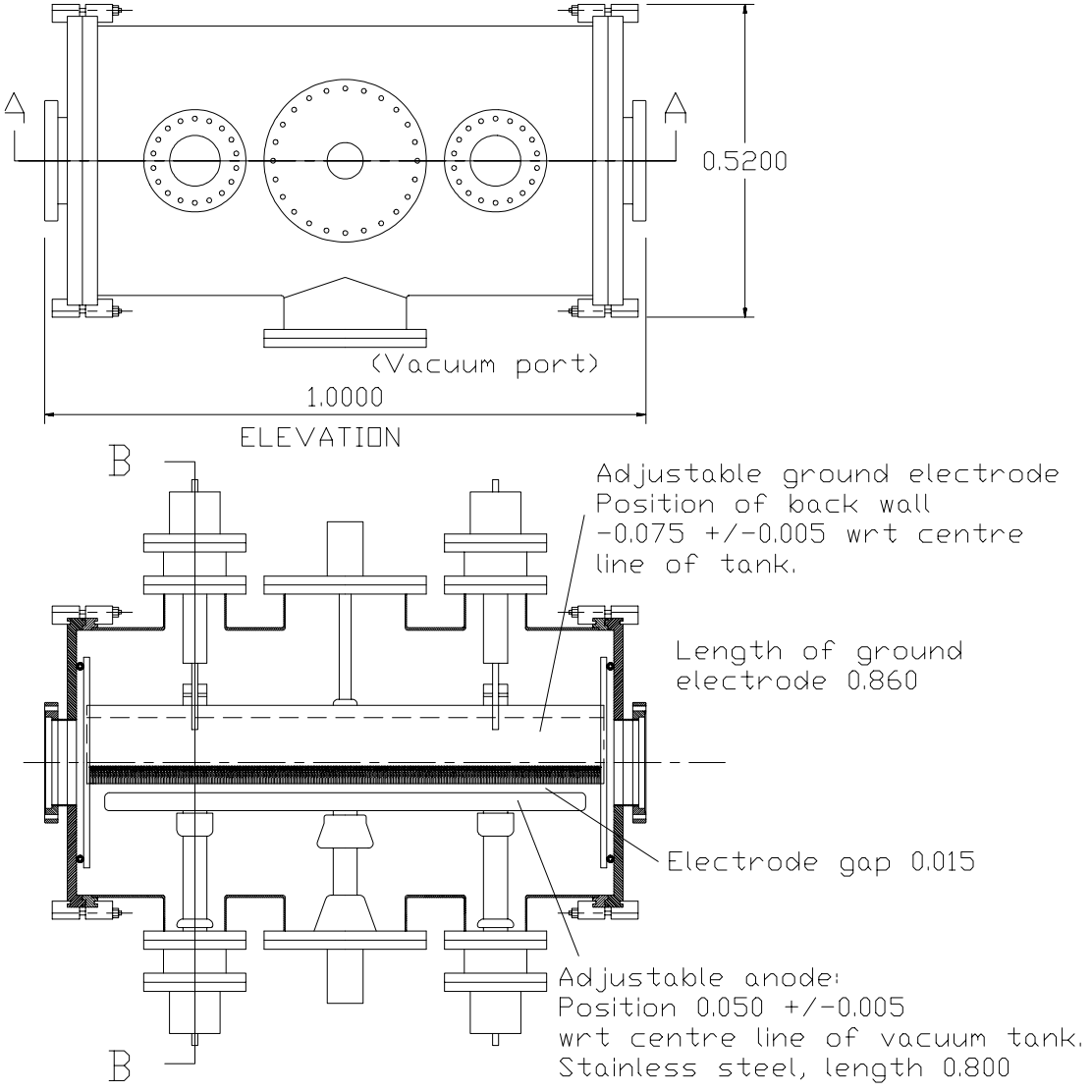

Figure U1 Basic design of the electrostatic extraction septum

* * *

APPENDIX II V

PRELIMINARY DESIGN OF THE EXTRACTION LINE QUADRUPOLES

The extraction line quadrupole has been designed with the idea of having a single design for all the extraction lines and gantries. This is not ideal and will need to be reviewed. One possibility is to use the injection line quadrupole from Appendix AA for the low-gradient units and then to use the present design, or a modified version, for the high-gradient cases.

The pole profile for this unit has not been designed. The construction is the usual four individual quadrants made from stacks of 1.5 mm thick laminations (packing factor >0.975) with end plates and welded tie bars. The quadrants are bolted together, so that the magnet can be easily opened. The main characteristics are summarised in Table V1 and in Figures V1 and V2.

Extraction line quadrupole: principal parameters	
Overall length [m]	0.5380
Yoke length [m]	0.3200
Overall width and height [m]	0.5040
Inscribed circle radius [m]	0.0400
Packing factor	>0.975
Weight [t]	0.17
Nominal maximum gradient (carbon ions) [T/m]	19.67
Current for maximum gradient[A]	250.5
Effective magnetic length at max. gradient [m]	0.350
'Good-field' region (all field levels)	At least ±27 mm horizontal; ±26 mm vertical
Integrated. gradient quality, (all field levels)*	At least $\pm 10^{-3}$
Resistance (magnet) [Ω]	0.0194
Inductance (magnet) [H]	-
Number of coils	4 (1 per pole)
Number of turns	200 (50 per pole)
Number of water circuits	4 (1 per coil)
Average turn length [m]	1.2
Length of a single water circuit [m]	60
Temperature rise in a single circuit [°C]	20.5
Water flow (magnet) [l/min]	3.4 (0.85 per circuit)
Pressure drop [bar]	7

* Requested value. Pole shape has not yet been designed in 2D or 3D.

Table V1 Extraction line quadrupole: principal parameters

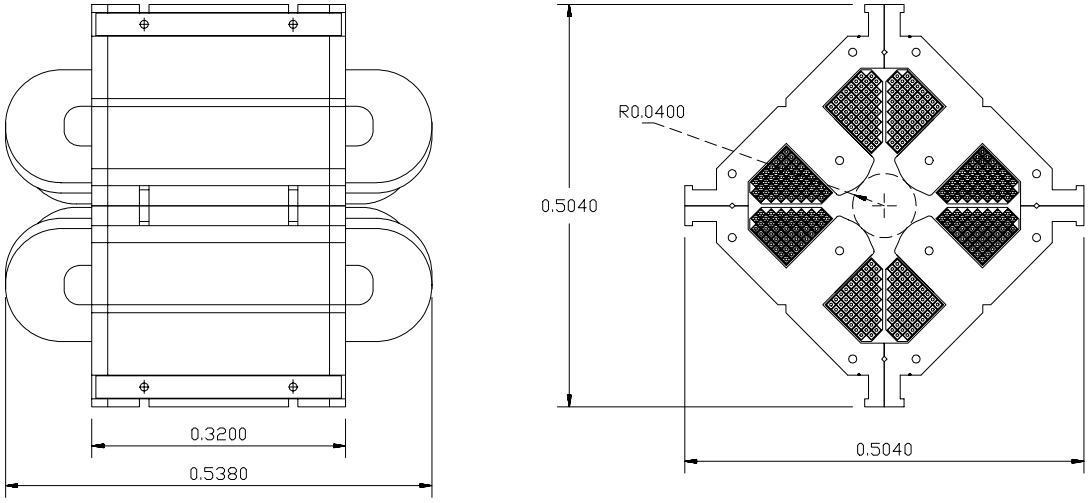

Figure V1 Extraction line quadrupole

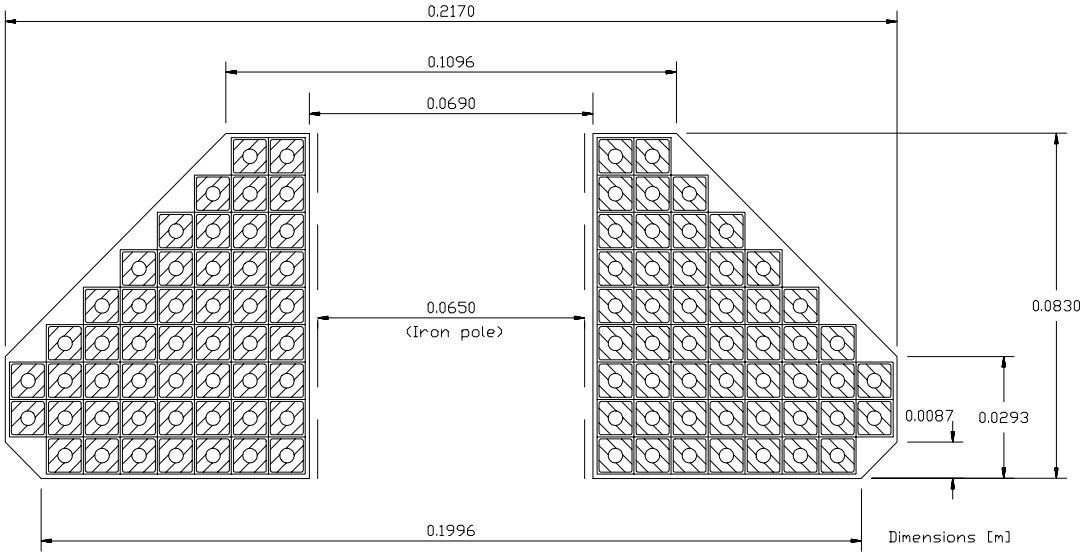

Conductor is copper 8mm x 8mm with a 3.5mm diameter water hole.
Conductor insulation wrap is 0.5mm. Ground insulation wrap is 1mm.

Figure V2 Coil for extraction line quadrupole

* * *

APPENDIX II W

MECHANICAL AND MAGNETIC DESIGN OF THE EXTRACTION LINE DIPOLES

The extraction line dipole is a C-type design. This makes it possible to use this dipole to switch the beam out of the main extraction line into the different treatment lines (T1 to T5). The design foresees a flat racetrack coil and a straight yoke. Since the magnet is relatively short, it is possible to accommodate the beam sagitta without making the dipole abnormally large. The construction is with 1.5 mm thick laminations held between thick endplates and welded with tie bars. The coil is made with two pancakes per pole in order that the pancakes are thin enough to be passed through the magnet gap for mounting on the poles. The pole profile is has been optimised in two dimensions and calculated in three dimensions without further modification. The main characteristics are summarised in Table W1. Figures W1 to W3 show the mechanical design. Figure W4 shows the boundaries of 2D-field qualities $\Delta B/B \leq 2 \times 10^{-4}$ and $\Delta B/B \leq 5 \times 10^{-4}$ at top field. The white boxes denote the limit of the required 'good-field' region. Thus, in two dimensions, the magnet is well inside the $\pm 5 \times 10^{-4}$ specification. Figure W5 shows the 3-D field quality, which is clearly out of tolerance. This leaves open the choice between shimming the magnets for the 3D end fields at the time of the magnetic measurements, or continuing with a 3-D magnetic design of the pole profile.

Extraction line dipole: principal parameters	
Overall length [m]	1.2420
Yoke length [m]	0.9600
Overall width [m]	0.7150
Overall height [m]	0.8000
Gap height on central orbit [m]	0.0620
Packing factor	>0.975
Weight [t]	3.25
Maximum field [T]	1.361
Current for maximum field[A]	576
Effective magnetic length at max. field [m]	1.033
'Good-field' region (all field levels)	At least ±41 mm horizontal.; ±26 mm vertical
2D-Field quality, $\Delta B/B$ (all field levels)	At least $\pm 5 \times 10^{-4}$
Sagitta [m]	0.0276
Resistance (magnet) [Ω]	0.0558
Inductance (magnet) [H]	0.0810
Number of coils	4 (2 per pole)
Number of turns	64 (16 per coil)
Number of water circuits	8 (2 per coil) All in parallel
Average turn length [m]	2.83
Length of a single water circuit [m]	45.28
Temperature rise in a single circuit [°C]	12.7
Water flow (magnet) [l/min]	18.1(2.26 per circuit)
Pressure drop [bar]	7

Table W1 Extraction line dipole: principal parameters

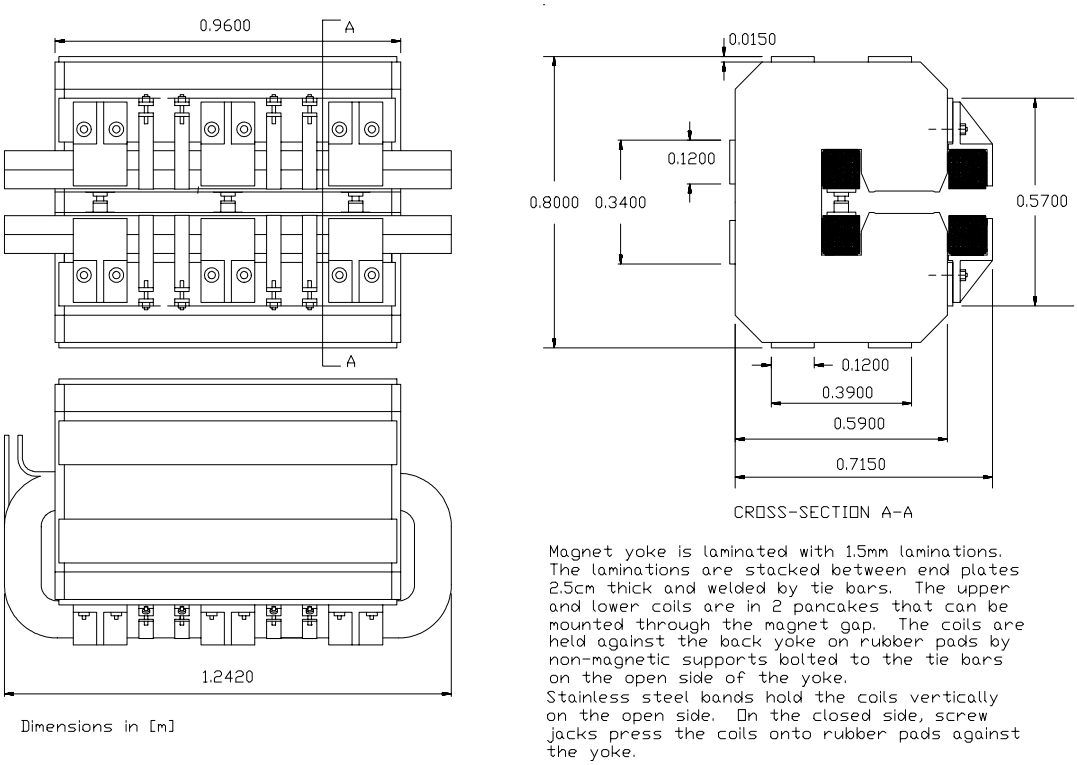

Figure W1 Extraction line dipole

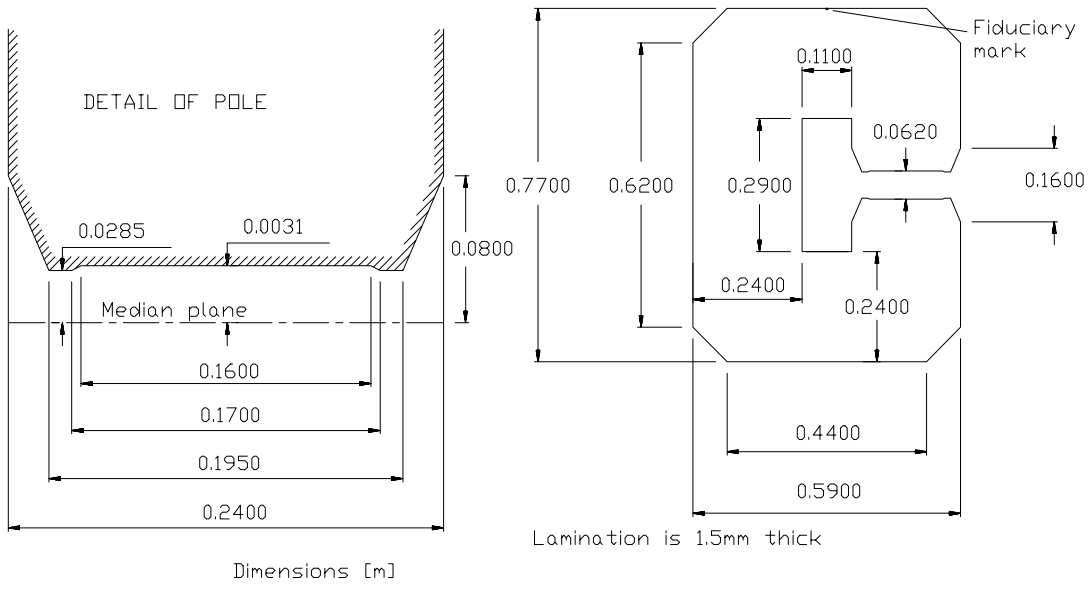

Figure W2 Extraction line dipole lamination

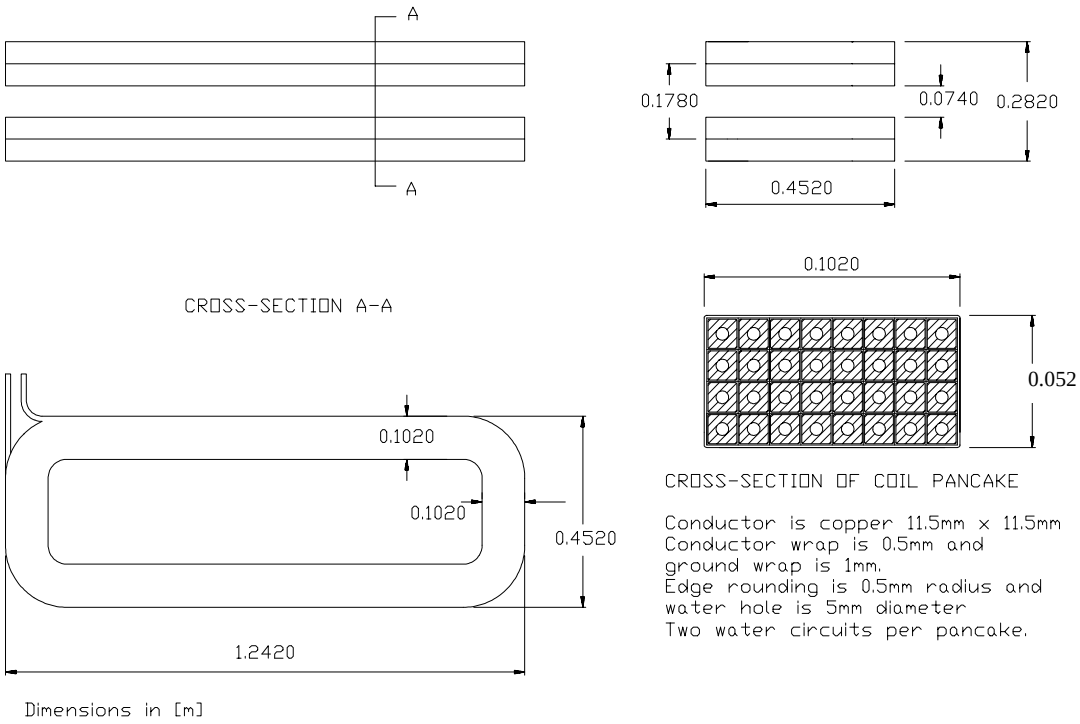

Figure W3 Extraction line dipole coil

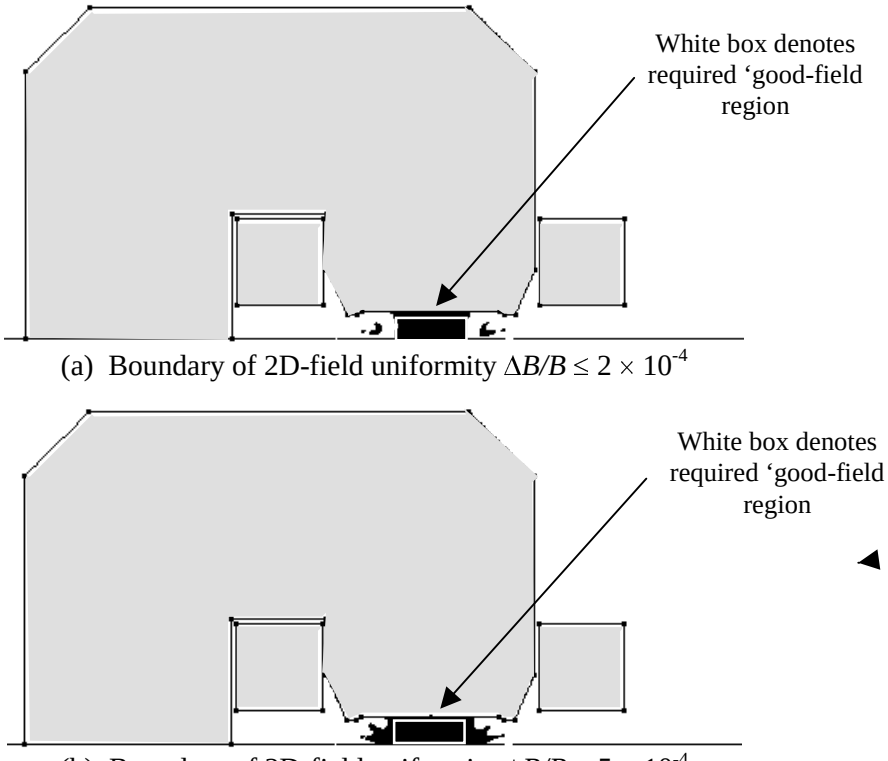

(a) Boundary of 2D-field uniformity $\Delta B/B \leq 2 \times 10^{-4}$

(b) Boundary of 2D-field uniformity $\Delta B/B \leq 5 \times 10^{-4}$

Figure W4 Extraction line dipole 2D-field uniformity

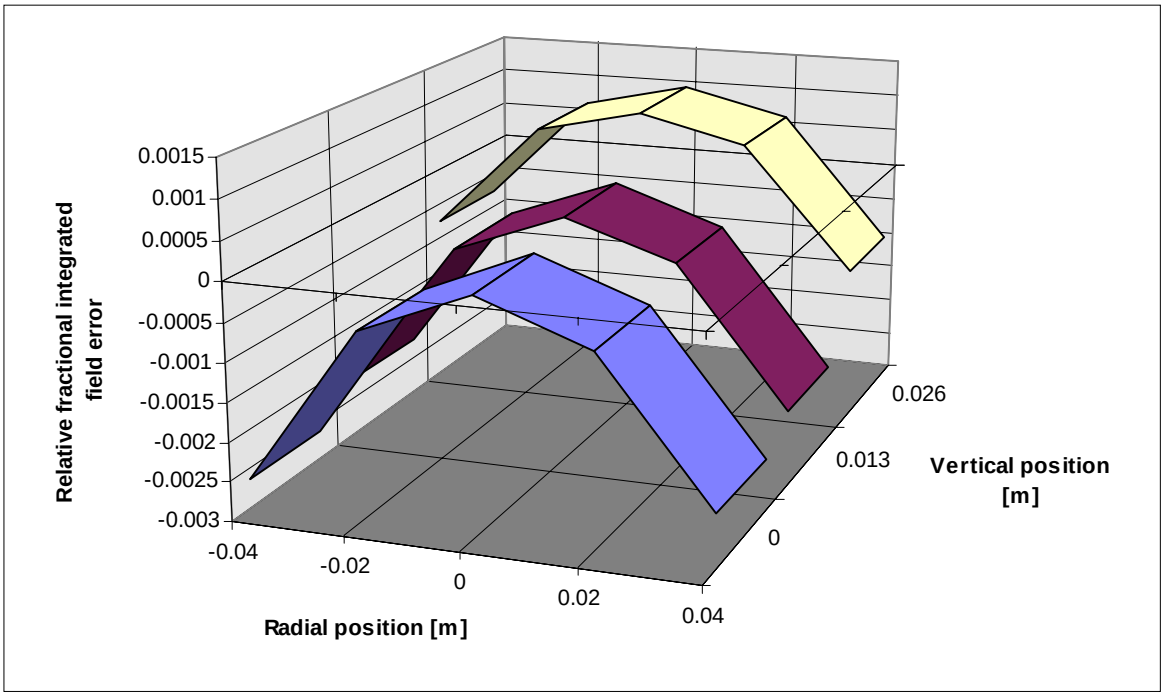

Figure W5 Extraction line dipole integrated 3D-field uniformity
[After 2D optimisation only]

* * *

APPENDIX II X

MECHANICAL AND MAGNETIC DESIGN OF THE 'RIESENRAD' DIPOLE

The 'Riesenrad' dipole is an H-type design with coils that extend into the pole gap giving the magnet the field quality of a window-frame design. The dipole curves by 90 degrees. The curvature is obtained by building the half yokes in segments. Each segment is a stack of 2 mm thick laminations that are glued and then machined to the correct angle. Twelve segments are needed to build a complete half yoke. The segments are held between thick end plates and welded with curved tie bars. In the present design, the two halves are welded together with thick cover plates to form the complete yoke. Cover plates are also welded on the top and bottom of the completed yoke. The cover plates endow the magnet with the necessary rigidity. The complete construction has been welded because of the limited space in the gantry. However, the design should be reviewed before manufacture, to see if it is possible to bolt the two magnet halves together to facilitate the changing of the vacuum chamber or coils in case of failure. The pole profile is calculated in two dimensions and the end fields will be compensated by shims added at the time of the measurements. This is preferred to a uniformly-distributed correction of the pole profile because the lattice functions change appreciably along the magnet. The strong curvature of the magnet has been modelled exactly in the magnetic calculations by computing the magnet in 2D cylindrical coordinates. The main characteristics are summarised in Table X1.

'Riesenrad' dipole: principal parameters	
Yoke length along central orbit [m]	5.5400
Bending radius on central orbit [m]	3.5269
Overall width of cross-section [m]	1.5300
Overall height of yoke [m]	1.0700
Overall height with coil at end [m]	1.4460
Gap height on central orbit [m]	0.2080
Packing factor	>0.975
Weight [t]	62
Nominal maximum field [T]	1.8
Current for maximum field[A]	4370
Effective magnetic length at max. field [m]	5.54
'Good-field' region (all field levels)	±100 mm horizontal; ±90 mm vertical.
Field quality, $\Delta B/B$ (all field levels)	At least $\pm 2 \times 10^{-4}$
Resistance (magnet) [Ω]	0.019
Maximum power dissipation [kW]	364
Inductance (magnet) [H]	0.039
Number of coils (inner coils and outer coils)	4 (2 per pole)
Number of turns (sum of inner and outer coils)	72 (36 per pole)
Number of turns in an outer coil	24
Number of turns in an inner coil	12
Number of water circuits in outer coils	6 (3 per coil) all in parallel
Number of water circuits in inner coils	4 (2 per coil) all in parallel
Average turn length in outer coils [m]	14.45
Average turn length in inner coils [m]	13.60
Length of single water circuit in outer coils [m]	115.6
Length of single water circuit in inner coils [m]	81.60
Temp. rise in a single circuit in an outer coil[°C]	24
Temp. rise in a single circuit in an inner coil [°C]	25
Water flow (magnet) [l/min]	214.2 (all circuits)
Pressure drop [bar]	7

Table X1 'Riesenrad' dipole: principal parameters

Figures X1 to X5 show the mechanical construction and the layout of the water circuits. Figure X6 shows the small asymmetry that exists in the magnetic flux. The yoke on the outer side of the curve has more iron and conducts more flux. The dividing line between the flux turning in the inner and outer halves of the yoke moves to a smaller radius and the magnet is almost perfectly self adjusting to give a uniform field in the gap despite the curvature effect in the yoke. Figures 7 to 9 show the 2D-field quality in the magnet.

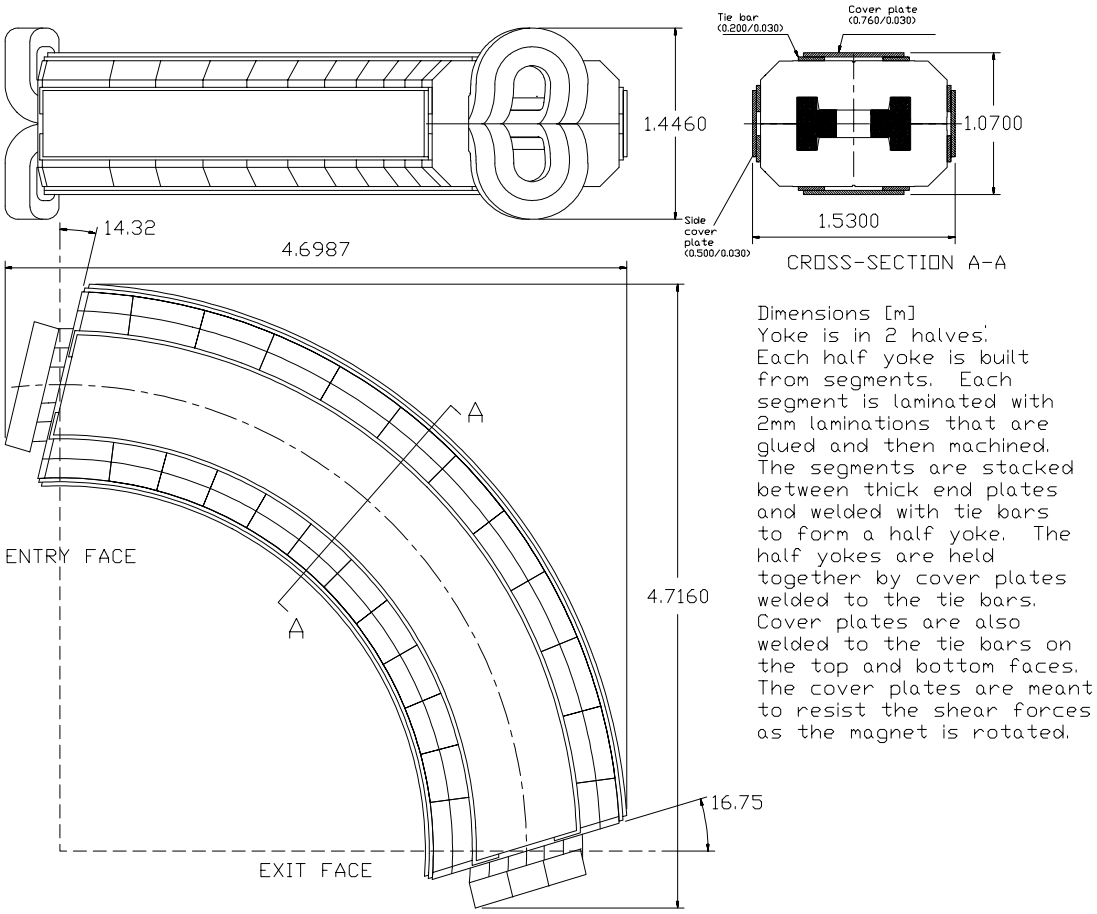

Figure X1 'Riesenrad' dipole

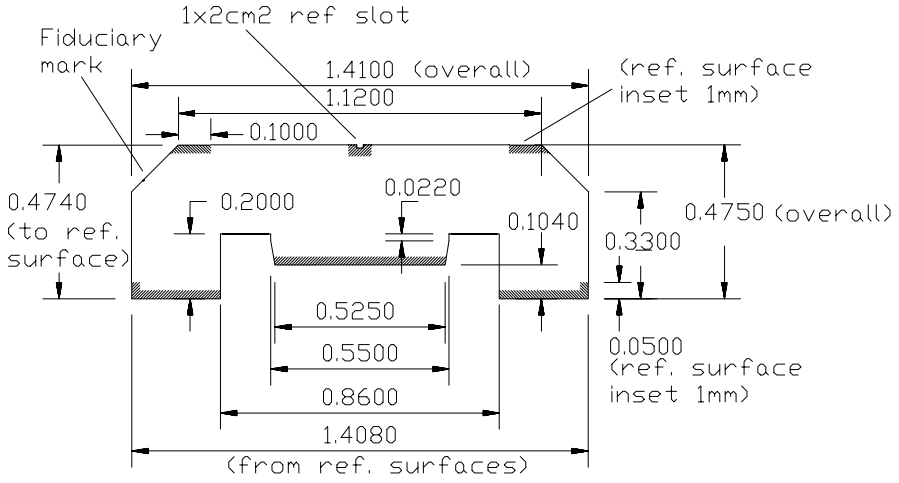

Dimensions [m]
Lamination 2mm thick soft carbon steel
Flat pole with small side taper
Precision surfaces (+/- 0.02mm) are hatched.

Figure X2 'Riesenrad' dipole lamination

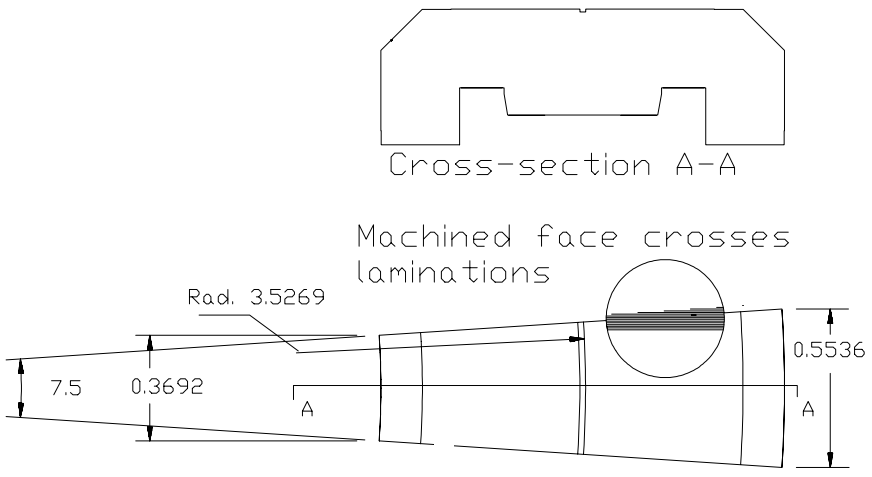

Basic yoke segment

Basic yoke segment is made by stacking and gluing laminations and then machining to a 7.5 degree sector.
Segment is curved by pressing laminations against a wall with a radius of curvature of 3.5269m.
End segements have to be specially machined for edge angles.

Figure X3 'Riesenrad' dipole yoke segment

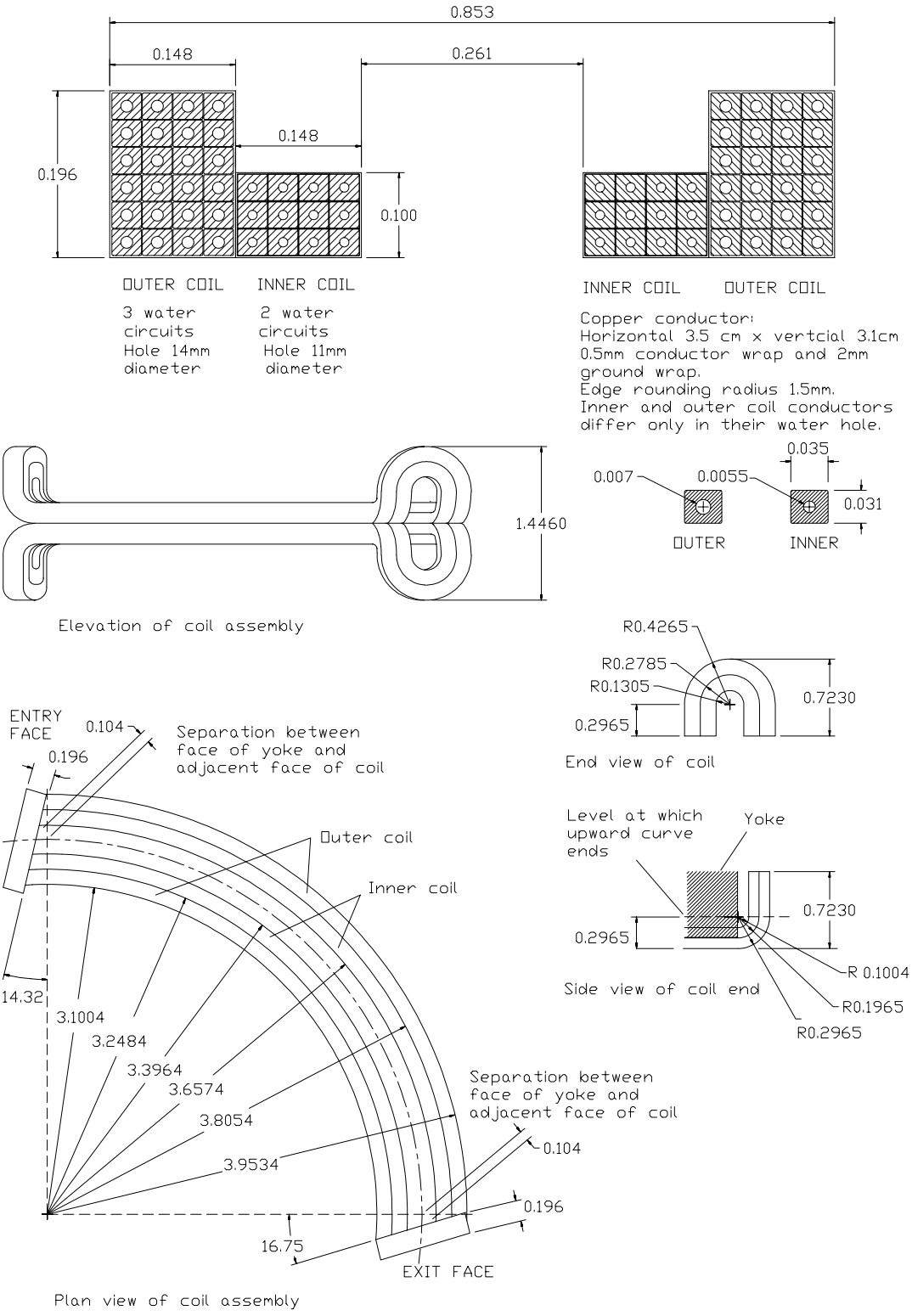

Figure X4 'Riesenrad' dipole coil

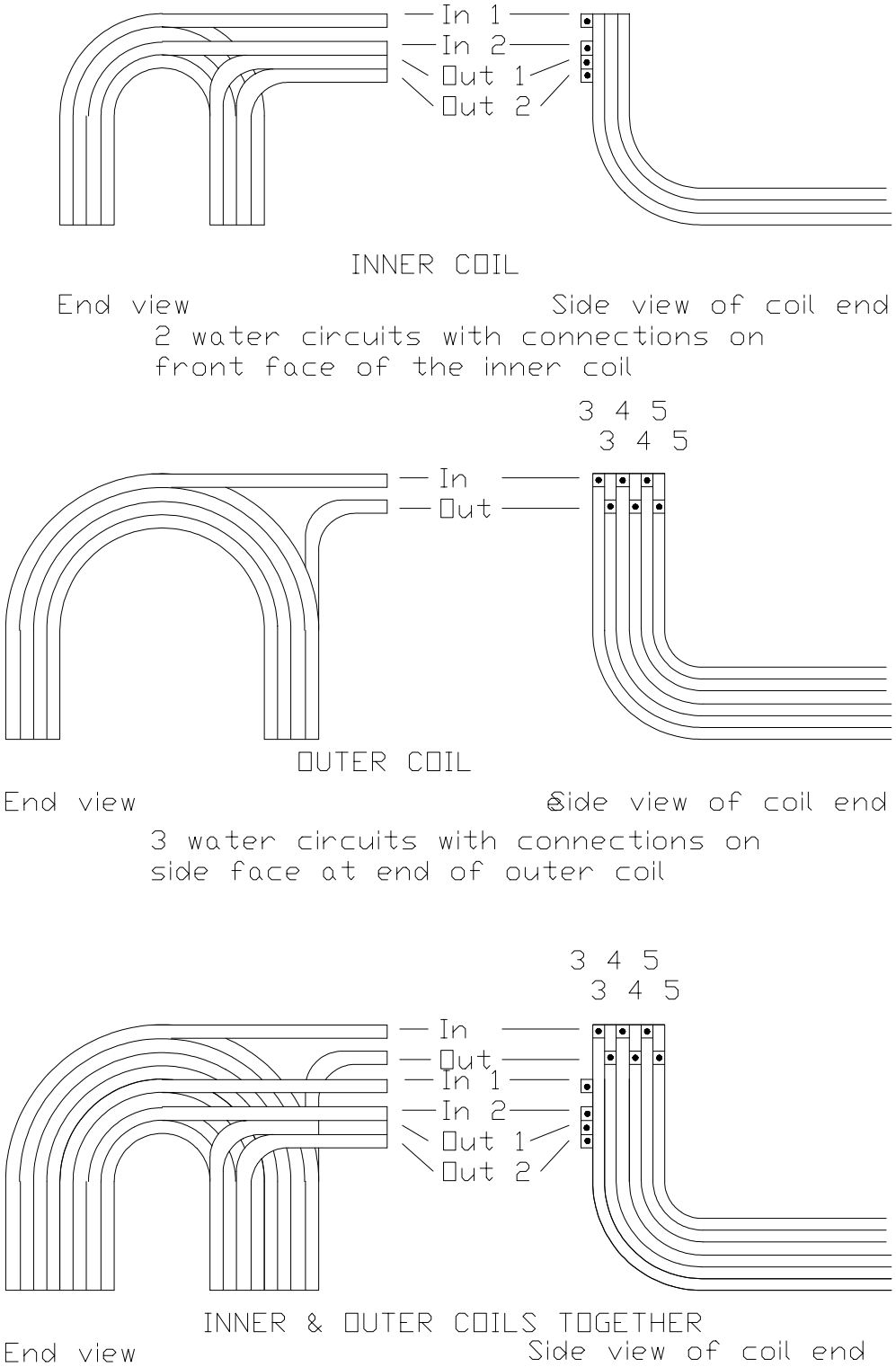

Figure X5 'Riesenrad' dipole water circuits

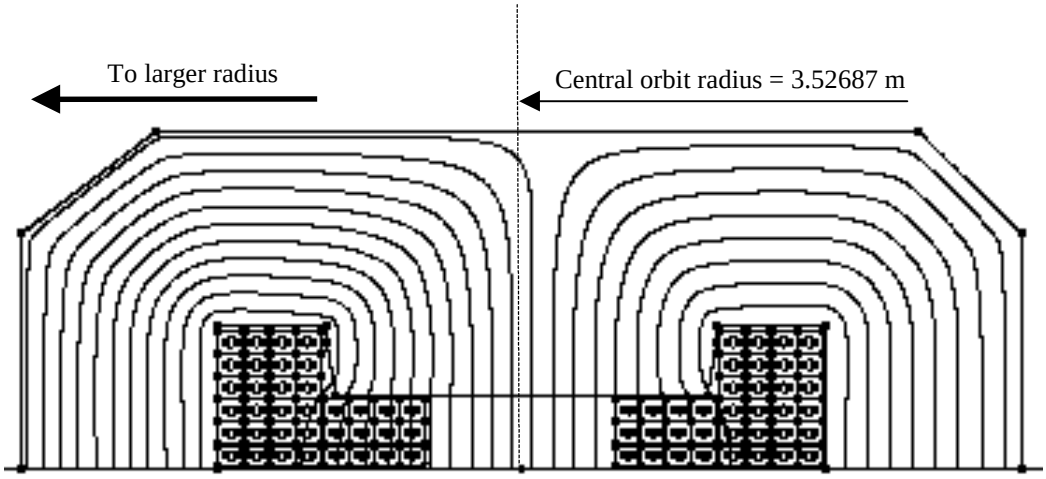

Figure X6 Asymmetric flux pattern in the 'Riesenrad' dipole
[Due to the curvature of the yoke, 5 flux lines go to the outer half of yoke and 3 to the inner half. The magnet is almost perfectly self-adjusting to give a uniform field in the gap.]

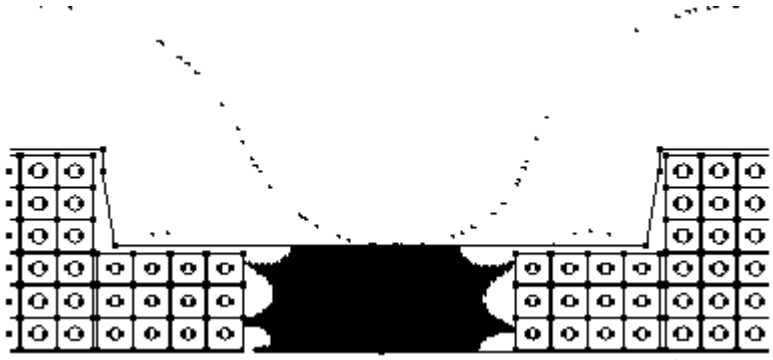

(a) Boundary of 2D-field quality region $\pm 2 \times 10^{-4}$

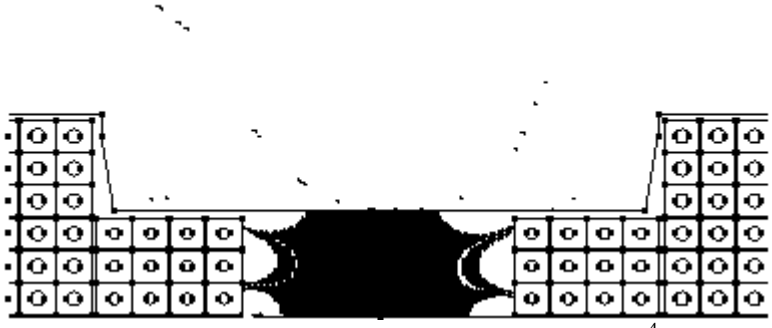

(b) Boundary of 2D-field quality region $\pm 10^{-4}$

Figure X7 'Riesenrad' dipole 2D-field uniformity at bottom field (0.3 T)

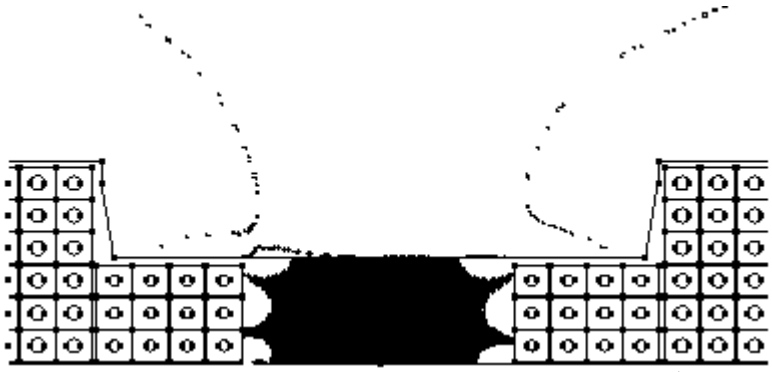

(a) Boundary of 2D-field quality region $\pm 2 \times 10^{-4}$

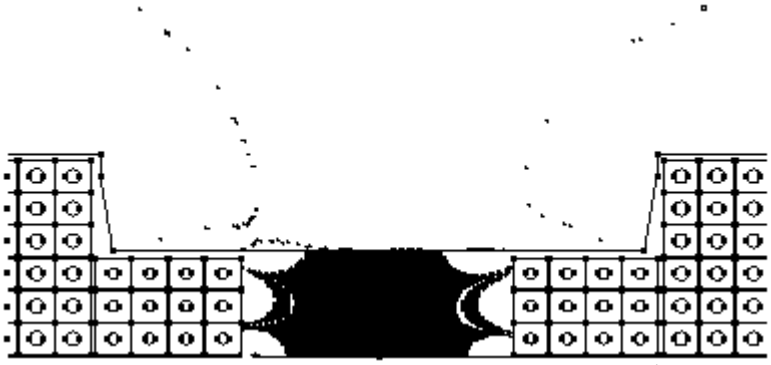

(b) Boundary of 2D-field quality region $\pm 10^{-4}$

Figure X8 'Riesenrad' dipole 2D-field uniformity at mid-field (1 T)

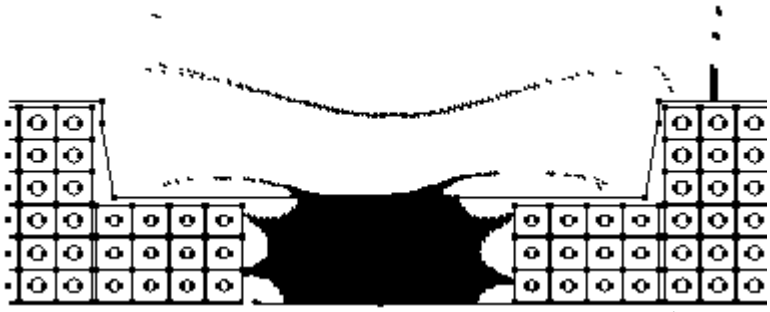

(a) Boundary of 2D-field quality region $\pm 2 \times 10^{-4}$

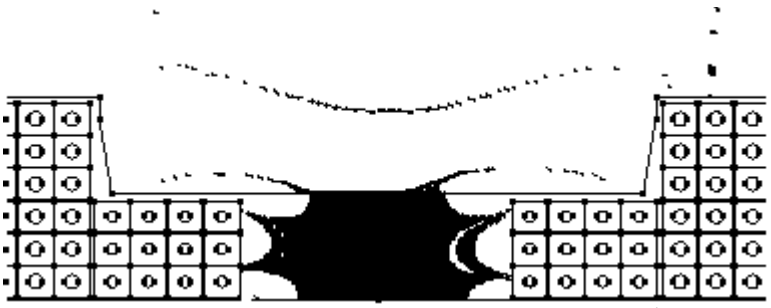

(b) Boundary of 2D-field quality region $\pm 10^{-4}$

Figure X9 'Riesenrad' dipole 2D-field uniformity at top field (1.8 T)

* * *

APPENDIX II Y

CONCEPT DESIGN OF THE RASTER SCANNING DIPOLES

The scanning dipoles have not been designed in any detail and the following parameters are meant only as a rough guide to what is need. The effective magnetic length has been set to 0.45 m. The overall dimensions with coil and covers will be longer. Table Y1 summarises the main parameters based on this assumption for the effective length and the maximum kick required of 12.5 mrad with the highest rigidity beam of 6.3464 Tm. The magnet may be required to run dc with maximum current.

Raster scanning dipole parameters	
Required kick [rad]	0.0125
Maximum rigidity [Tm]	6.3464
Effective magnetic lgth [m]	0.45
Maximum field [T]	0.1763
Pole gap [m]	0.080
Space between coils [m]	0.120
'Good' field region	At least ±25 mm horizontal; ±32 mm vertical
Field quality	$\leq \pm 10^{-3}$
Yoke	0.3 mm iron laminations, window-frame
Vacuum chamber	0.3 mm ribbed or 0.4 mm corrugated stainless steel
Maximum current [A]	281
No. of turns	40 (20 per coil)
No. of coil and type	2 [copper, water-cooled, 4 × 5 turns, saddle-shaped]
Average turn length [m]	1.66
Conductor size [mm]	8.2 × 8.2 with 3.5 mm diameter water hole
Current density [A/mm^2]	4.87
Water temperature rise (°C)	9.4 (coils in parallel)
Water flow [l/min]	2.38 (1.19 per coil)
Water pressure [bar]	7
DC magnet resistance [ohm]	2 × 0.01 (coils in series)
DC voltage [V]	5.62
Estimated stored energy [J]	54
Estimated inductance [H]	0.00137
Max. rise time [s]	0.01
Max. current ramp [As^{-1}]	28100
Max. ramp voltage [V]	38.5
Power converter	Current controlled, switch mode and programmable

Table Y1 Raster scanning dipole parameters

* * *

APPENDIX II Z

CONCEPT DESIGN OF THE CHOPPER DIPOLES

The chopper dipoles have not been designed in any detail and the following parameters are meant only as a rough guide to what is need. The effective magnetic length has been set to 0.3 m. The overall dimensions with coil and covers will be longer, but in the transfer line there is adequate space. Table Z1 summarises the main parameters of the bumpers based on this assumption for the effective length and the maximum kick required of 6.6 mrad with the highest rigidity beam. To ensure an efficient control of the beam at all times, the power converter must track the beam rigidity, so that the bump is always 14 ±1 mm with a rise time of 180 μs. The magnet will be required to run d.c. with maximum current.

Chopper dipole parameters	
	Bumper in SS MR 08
Required kick [rad]	0.0066
Maximum rigidity [Tm]	6.3464
Effective magnetic length [m]	0.3
Maximum field [T]	0.14
Pole gap [m]	0.086
Space between coils [m]	0.100
Field quality	$\pm 2 \times 10^{-3}$
Yoke	Ferrite, window-frame
Vacuum chamber	Ceramic, elliptical, 7 mm wall
Maximum current [A]	480
No. of turns	20 (10 per coil)
Coil	2 [copper conductor, water-cooled, double layer pancake 2 × 5 turn, saddle-shaped]
Average turn length [m]	1.25
Conductor size [mm^2]	9 × 11 with 2.5 mm dia water hole
Current density [A/mm^2]	5.1
Water temperature rise (°C)	9.1
Water pressure [bar]	7
Water flow [l/min]	1.67 (0.834 per coil)
DC power dissipation [W]	1052 (526 per coil)
DC magnet resistance [Ω]	0.0046 (0.0023 per coil)
Estimated stored energy [J]	20
Estimated inductance [μH]	174
Maximum rise time [μs]	180
Maximum ramp voltage [V]	464
Overshoot	< 7%
Power converter	Current controlled and programmable

Table Z1 Chopper dipole parameters

* * *

APPENDIX II AA

CONCEPT DESIGN OF THE INJECTION LINE QUADRUPOLES

The injection line quadrupole has been designed with the idea of having a single design throughout the injection lines. However, it requires exactly the same aperture (inscribed circle radius 0.040 m) and length (effective magnetic length 0.35 m) as the extraction line quadrupole in Appendix V. The difference is that the maximum gradient required (2.68 T/m) is much lower than for the extraction line (19.67 T/m). Thus the width, height and weight can be considerably reduced and the coil works with very realxed parameters. This opens the possibility that the injection line quadrupole may also be used for the low-gradient units in the extraction lines. The simple modification of having two water circuits of two coils rather than all four coils in series would considerably increase the operational range of the magnet. The main extraction line quadrupole can then be re-designed more specifically for high-gradient use.

The construction can be the usual four individual quadrants made from stacks of 1.5 mm thick laminations (packing factor >0.975) with end plates and welded tie bars. The quadrants should be bolted together, so that the magnet can be easily opened. The main design parameters are summarised in Table AA1.

Injection line quadrupole: principal parameters	
Yoke length [m]	0.32
Effective magnetic length [m]	0.35
Inscribed circle radius [m]	0.04
Nominal maximum gradient (carbon ions) [T/m]	2.68
Current for maximum gradient[A]	114
'Good-field' region (all field levels)*	$\geq \pm 28$ mm horizontal; ± 19.5 mm vertical
Integrated. gradient quality, (all field levels)*	$\leq \pm 10^{-3}$
Resistance (magnet) [Ω]	0.020
Inductance (magnet) [H]	-
Number of coils	4 (1 per pole)
Number of turns	60 (15 per pole)
Number of water circuits	1 (0.25 per coil)
Average turn length [m]	1.1
Length of the single water circuit [m]	66
Conductor cross-section [m^2]	0.008×0.008
Water channel radius [m]	0.0035
Temperature rise in a single circuit [°C]	5
Water flow (magnet) [l/min]	0.8
Pressure drop [bar]	7

* Requested values.

Table AA1 Injection line quadrupole: principal parameters

* * *

APPENDIX II BB

CONCEPT DESIGN OF THE INJECTION LINE DIPOLES

The extraction line dipole is a C-type design. This makes it possible to use this magnet to combine the carbon and proton transfer lines. The proposed construction is 1.5 mm thick laminations held between thick endplates and welded with tie bars. The beam sagitta are large and it would be advantageous to curve the dipole. Note that are two uses of the dipole with slightly different sagitta i.e. the 'dog-leg' 57.6 mm and the main bend 52.6 mm. However, the decision to curve and by how much can be made at the time of the detailed mechanical and magnetic designs. A flat racetrack coil is foreseen and it must be made so that it passes between the poles for mounting. The main design parameters are summarised in Table BB1.

Extraction line dipole: principal parameters	
Yoke length [m]	0.745
Effective magnetic length at max. field [m]	0.80
Maximum sagitta [m]	0.0576
Gap height on central orbit [m]	0.055
Packing factor	>0.975
Nominal maximum field [T]	0.55
Total number of ampere turn [A turn]	24070
Estimated water flow for 12°C temp. rise [l/min]	2.5
'Good-field' region (all field levels)*	At least ±28 mm horizontal; ±19.5 mm vertical assuming that yoke is curved
Field quality, $\Delta B/B$ (all field levels)*	$\leq \pm 5 \times 10^{-4}$
Coil parameters	Depends on how much yoke is curved

* Required values

Table BB1 Extraction line dipole: principal parameters

* * *

APPENDIX II CC

QUADRUPOLE SETTINGS FOR THE PHASE-SHIFTER-STEPPER MODULE

The following tables record settings for the phase-shifter-stepper. The intention is to demonstrate that the module can work over a range that is well beyond what will be needed in practice. The values have been obtained by matching with the vertical phase as a free-parameter. If certain results are in some way inconvenient, then the solutions can be modified by changing the vertical phase advance. The sub-tables for μ_x = 1.83 rad and 3.40 rad (i.e.~1.83 + π/2) correspond to the recommended settings for minimum and maximum horizontal spot sizes respectively. The highlighted settings are the values set in the demonstration lattice files on the accompanying CD-ROM. The sub-tables from μ_x = 1.83 to 3.40 rad constitute the useful range.

μ_x = 1.83 rad **(Values for minimum horizontal spot size)**

β_z =	1	2	5	10	15	20	27
QF EX12	0.4915	0.6232	**0.4233**	0.9169	0.9102	1.0109	1.1271
QD EX13	-0.4370	-0.7496	**-0.5882**	-1.2150	-1.3151	-1.4167	-1.5245
QF EX14	1.3515	1.6723	**2.0892**	2.5066	2.4271	2.5915	2.8194
QD EX15	-1.9118	-1.8740	**-2.0621**	-2.0114	-1.6895	-1.7145	-1.7731
QF EX16	1.4256	1.1099	**1.3037**	1.2153	0.2744	0.3172	0.4264
QD EX17	0.4952	0.5697	**0.7268**	0.4988	0.8797	0.8274	0.7495

μ_x = 2.09 rad

β_z =	1	2	5	10	15	20	27
QF EX12	-0.3120	-0.4505	-0.6140	-0.5817	-0.4278	-0.4837	-0.4319
QD EX13	1.2179	1.5169	1.0180	1.5587	1.3097	1.4221	1.2819
QF EX14	-0.3867	-0.3174	1.0962	-0.4542	-0.6555	-1.0680	-1.1031
QD EX15	-1.4282	-1.5147	-1.9344	-1.1144	-0.9362	-0.1005	0.0542
QF EX16	1.7801	1.7556	1.1896	0.4620	0.5403	-0.5000	-0.6020
QD EX17	-0.1729	-0.0482	0.6363	0.4706	0.2292	0.6594	0.6586

μ_x = 2.36 rad

β_z =	1	2	5	10	15	20	27
QF EX12	-0.6262	-0.7252	-0.8391	-0.9126	-0.7264	-0.9014	-0.7946
QD EX13	1.2545	1.3909	1.3291	1.3553	1.1568	1.4742	1.3519
QF EX14	-0.3358	-0.2391	0.0841	0.0198	-0.1982	-0.6512	-1.0960
QD EX15	-1.4353	-1.4779	-1.5009	-1.2257	-1.2969	-0.4147	0.4106
QF EX16	1.8019	1.6042	0.9784	0.1752	0.9126	-0.6135	-1.0223
QD EX17	-0.4739	-0.3335	0.0376	0.4599	-0.1171	0.6977	0.7092

μ_x = 2.62 rad

β_z =	1	2	5	10	15	20	27
QF EX12	-0.8743	-0.9214	-1.0385	-1.2192	-0.9242	-1.1652	-1.0681
QD EX13	1.2900	1.4599	1.3183	1.5497	1.1134	1.5213	1.4219
QF EX14	-0.2570	-0.3820	0.1045	-0.1367	-0.0806	-0.5744	-1.0437
QD EX15	-1.4847	-1.3995	-1.5335	-0.8462	-1.4113	-0.3439	0.4831
QF EX16	1.8226	1.6508	1.1155	-0.5279	1.1574	-0.8214	-1.1870
QD EX17	-0.6660	-0.6128	-0.2493	0.7650	-0.4116	0.7337	0.7252

μ_x = 2.88 rad

β_z =	1	2	5	10	15	20	27
QF EX12	-1.0517	-1.1124	-1.2217	-1.4314	-1.1088	-1.3913	-1.3076
QD EX13	1.3757	1.5049	1.3716	1.5824	1.1421	1.5684	1.5195
QF EX14	-0.3638	-0.3924	0.0509	-0.1223	-0.0608	-0.4937	-1.0179
QD EX15	-1.4544	-1.4211	-1.5551	-0.8490	-1.4760	-0.4324	0.4244
QF EX16	1.8584	1.6759	1.2210	-0.5956	1.2882	-0.8530	-1.2478
QD EX17	-0.8546	-0.7704	-0.4443	0.7491	-0.5973	0.7361	0.7435

μ_x = 3.14 rad

β_z =	1	2	5	10	15	20	27
QF EX12	-1.2319	-1.2934	-1.4171	-1.6440	-1.3056	-1.6062	-1.5076
QD EX13	1.4421	1.5613	1.4444	1.6490	1.2091	1.6812	1.6093
QF EX14	-0.3893	-0.4152	0.0058	-0.1597	-0.0591	-0.6399	-1.1604
QD EX15	-1.4929	-1.4598	-1.5903	-0.9405	-1.5427	-0.3875	0.5300
QF EX16	1.8811	1.6972	1.2580	-0.5198	1.3447	-0.9000	-1.3161
QD EX17	-0.9639	-0.8736	-0.5245	0.7073	-0.6828	0.7433	0.7384

μ_x = 3.40 rad **(Values for maximum horizontal spot size)**

β_z =	1	2	5	10	15	20	27
QF EX12	-1.3514	-1.5166	**-1.6936**	-1.8817	-1.5441	-1.8487	-1.7558
QD EX13	1.5501	1.6209	**1.5316**	1.7623	1.3387	1.8006	1.7573
QF EX14	-0.6178	-0.3792	**0.0421**	-0.3108	-0.1191	-0.7742	-1.2727
QD EX15	-1.4256	-1.5493	**-1.6475**	-1.0585	-1.5901	-0.4999	0.3929
QF EX16	1.9201	1.6842	**1.1134**	-0.3099	1.3289	-0.7772	-1.2520
QD EX17	-1.1231	-0.8626	**-0.3472**	0.6241	-0.6569	0.7156	0.7473

μ_x = 3.67 rad

β_z =	1	2	5	10	15	20	27
QF EX12	-1.6018	-1.7855	-2.0640	-2.1560	-1.8708	-2.1491	-2.0861
QD EX13	1.6448	1.7488	1.8001	1.8946	1.5874	1.9435	1.9251
QF EX14	-0.6264	-0.5077	-0.3143	-0.5860	-0.3859	-1.0280	-1.3714
QD EX15	-1.5136	-1.5599	-1.5311	-1.1854	-1.5336	-0.5819	0.0567
QF EX16	1.9118	1.6495	0.8919	0.1509	1.2062	-0.5340	-0.9835
QD EX17	-1.0798	-0.7824	-0.0493	0.3928	-0.4885	0.6378	-0.7207

μ_x = 3.93 rad

β_z =	1	2	5	10	15	20	27
QF EX12	-2.0762	-2.0861	-2.2858	-2.3796	-2.1855	-2.4788	-2.5136
QD EX13	1.8538	1.9473	2.0265	2.0158	1.8554	1.9879	2.0685
QF EX14	-0.8035	-0.9371	-1.0419	-1.0915	-0.9853	-1.1276	1.6922
QD EX15	-1.4941	-1.3753	-1.2164	-1.1142	-1.2538	-1.0138	0.0816
QF EX16	1.8029	1.6132	1.1271	0.8340	1.1815	0.5456	-0.6595
QD EX17	-0.7637	-0.7375	-0.3680	-0.1486	-0.4914	0.1026	0.5903

μ_x = 4.19 rad

β_z =	1	2	5	10	15	20	27
QF EX12	-2.1593	-2.2827	-2.2412	-2.3367	-2.3211	-2.8550	-2.9965
QD EX13	1.9795	2.0882	2.0686	2.0276	1.9554	2.1129	2.1142
QF EX14	-1.3465	-1.4859	-1.5513	-1.5753	-1.5285	-1.8135	-1.8915
QD EX15	-1.1493	-0.9706	-0.8537	-0.7999	-0.8591	-0.3496	-0.1586
QF EX16	1.8345	1.5898	1.3687	1.2651	1.3120	0.7300	0.5118
QD EX17	-1.0352	-0.8986	-0.8940	-0.7828	-0.7950	-0.2379	-0.0699

μ_x = 4.45 rad

β_z =	1	2	5	10	15	20	27
QF EX12	-2.3121	-2.3001	-2.1735	-2.2670	-2.2809	-2.6641	-2.7147
QD EX13	2.0637	2.1188	2.0604	2.0055	1.9380	1.9927	1.9408
QF EX14	-1.7512	-1.8185	-1.7781	-1.8242	-1.8002	-2.0444	-2.0428
QD EX15	-0.7623	-0.6415	-0.6916	-0.5962	-0.6298	-0.1039	-0.0957
QF EX16	1.7780	1.5936	1.4902	1.4169	1.4464	1.1314	1.1402
QD EX17	-1.1880	-1.1718	-1.2318	-1.1503	-1.1391	-0.8719	-0.8441

μ_x = 4.71 rad

β_z =	1	2	5	10	15	20	27
QF EX12	-2.2705	-2.2364	-2.1516	-2.2342	-2.3155	-2.3950	-2.5786
QD EX13	2.0600	2.1074	2.0561	1.9906	1.9379	1.8947	1.8523
QF EX14	-1.8867	-1.9166	-1.8695	-1.9321	-1.9822	-2.0299	-2.1534
QD EX15	-0.6883	-0.6322	-0.7071	-0.5772	-0.4642	-0.3485	-0.0156
QF EX16	1.8278	1.6837	1.5974	1.5331	1.4975	1.4574	1.3042
QD EX17	-1.4426	-1.4436	-1.4748	-1.4083	-1.3539	-1.3047	-1.1976

μ_x = 4.97 rad

β_z =	1	2	5	10	15	20	27
QF EX12	-2.2911	-2.2635	-2.2592	-2.3154	-2.3732	-2.4734	-2.4928
QD EX13	2.0680	2.1161	2.0862	2.0074	1.9421	1.8913	1.8153
QF EX14	-1.9514	-1.9734	-2.0048	-2.0503	-2.0892	-2.1706	-2.1627
QD EX15	-0.7118	-0.6731	-0.6044	-0.4961	-0.3958	-0.1770	-0.1827
QF EX16	1.8827	1.7526	1.6143	1.5734	1.5516	1.4706	1.4921
QD EX17	-1.6429	-1.6417	-1.6187	-1.5759	-1.5398	-1.4812	-1.4719

μ_x = 5.24 rad

β_z =	1	2	5	10	15	20	27
QF EX12	-2.4685	-2.3795	-2.3566	-2.4116	-2.4626	-2.5467	-2.5348
QD EX13	2.1083	2.1422	2.1057	2.0239	1.9535	1.8937	1.8131
QF EX14	-2.1190	-2.0548	-2.0546	-2.1077	-2.1474	-2.2225	-2.1862
QD EX15	-0.4769	-0.6263	-0.6240	-0.4966	-0.3907	-0.1790	-0.2646
QF EX16	1.8249	1.7704	1.6720	1.6326	1.6128	1.5408	1.5971
QD EX17	-1.7603	-1.7957	-1.7881	-1.7479	-1.7169	-1.6687	-1.6763

μ_x = 5.50 rad

β_z =	1	2	5	10	15	20	27
QF EX12	-2.6098	-2.5413	-2.5216	-2.5564	-2.5972	-2.6609	-2.6516
QD EX13	2.1323	2.1709	2.1339	2.0454	1.9712	1.9071	1.8254
QF EX14	-2.1640	-2.1202	-2.1188	-2.1453	-2.1759	-2.2332	-2.2011
QD EX15	-0.4470	-0.5592	-0.5616	-.4892	-0.4032	-0.2388	-0.3131
QF EX16	1.8410	1.7746	1.6903	1.6805	1.6717	-1.6236	1.6733
QD EX17	-1.9312	-1.9536	-1.9462	-1.9215	-1.8974	-1.8615	-1.8668

μ_x = 5.76 rad

β_z =	1	2	5	10	15	20	27
QF EX12	-2.7878	-2.7450	-2.7346	-2.7537	-2.7776	-2.8284	-2.8412
QD EX13	2.1577	2.1993	2.1624	2.0698	1.9925	1.9276	1.8455
QF EX14	-2.1592	-2.1473	-2.1540	-2.1558	-2.1647	-2.2086	-2.2025
QD EX15	-0.4829	-0.5208	-0.5040	-0.4877	-0.4552	-0.3319	-0.3344
QF EX16	1.8796	1.7877	1.7090	1.7286	1.7427	1.7141	1.7342
QD EX17	-2.1355	-2.1428	-2.1319	-2.1193	-2.1057	-2.0772	-2.0700

* * *

APPENDIX II DD

PIMMS PARAMETERS

PIMMS Group

CONTENTS

[Note that the Parameter List on the companion CD-ROM is an interactive EXCEL file. By editing the externally fixed data (shown in black in bold italic type), the file will re-compute and present the modified machine parameters. In the CD-ROM version, important calculated parameters appear in red in bold script. These parameters are not easily distinguished in the version present in this Appendix.]

1. Constants

Speed of light in vacuum [m/s]	***2.9979E+08***
Equivalent proton mass [GeV]	***0.938255***
Equivalent C4+ mass [GeV]	***11.175692***
Equivalent C6+ mass [GeV]	***11.174670***
Elementary charge [C]	***1.6022E-19***

2. Relativistic parameters and emittances for protons in synchrotron

Parameter	Injection before trapping	Critical point in rf cycle	First flat-top debunched	Last flat-top debunched
Kinetic energy/nucleon [MeV]	***20***	***23***	***60***	***250***
γ	1.021316	1.024514	1.063949	1.266452
β	0.203241	0.217443	0.341463	0.613612
$\beta\gamma$	0.207573	0.222774	0.363299	0.777111
Momentum [GeV/c]	0.194757	0.209018	0.340867	0.729128
Magnetic rigidity [Tm]	0.649639	0.697211	1.137011	2.432109
Revolution time [s]	1.2349E-06	1.1542E-06	.73499E-06	.40901E-06
Revolution frequency [MHz]	0.8098	0.8664	1.3606	2.4449
Norm. horiz. rms emit. [π mm mrad]]	***0.5190***	0.5190	0.5190	0.5190
Norm. vert. rms emit. [π mm mrad]]	***0.5190***	0.5190	0.5190	0.5190
Geom. horiz. rms emit. [π mm mrad]	2.5003	2.3297	**1.4286**	0.6679
Geom. vert. rms emit. [π mm mrad]	2.5003	2.3297	**1.4286**	0.6679
Total geom. horiz. emit. [π mm mrad]	12.5016	11.6486	7.1429	3.3393
Total geom. vert. emit. [π mm mrad]	12.5016	11.6486	7.1429	3.3393
Rms relative momentum spread	0.000537	0.001570	0.000894	0.000894
Full relative momentum spread	***0.002400***	***0.007020***	***0.004000***	0.004000

3. Relativistic parameters and emittances for carbon ions in synchrotron

Parameter	Injection before trapping	Critical point in rf cycle	First flat-top debunched	Last flat-top debunched
Kinetic energy/nucleon [MeV]	***7***	***8.5***	***120***	***400***
Charge state	***C6+***	C6+	C6+	C6+
γ	1.007517	1.009128	1.128863	1.429543
β	0.121927	0.134196	0.463977	0.714609
$\beta\gamma$	0.122843	0.135421	0.523767	1.021564
Average momentum/nucleon [GeV/c]	0.114395	0.126107	0.487743	0.951303
Magnetic rigidity [Tm]	0.763158	0.841297	3.253872	6.346413
Revolution time [s]	2.0584E-06	1.8702E-06	.54092E-06	.35120E-06
Revolution frequency [MHz]	0.4858	0.5347	1.8487	2.8473
Norm. horiz. rms emit [π mm mrad]]	0.7482	0.7482	0.7482	0.7482
Norm. vert. rms emit. [π mm mrad]]	0.7482	0.7482	0.7482	0.7482
Geom. horiz. rms emit. [π mm mrad]	6.0910	5.5253	**1.4286**	0.7324
Geom. vert. rms emit. [π mm mrad]	6.0910	5.5253	**1.4286**	0.7324
Total geom. horiz. emit. [π mm mrad]	30.4550	27.6264	7.1429	3.6622
Total geom. vert. emit. [π mm mrad]	30.4550	27.6264	7.1429	3.6622
Rms relative momentum spread	0.000537	0.00133	0.00089	0.00089
Full relative momentum spread)	***0.00240***	***0.00594***	***0.00400***	***0.00400***

4. Particle inventories (from patient back to source)

4.1 Proton active scanning with single-turn injection

Based on voxel scanning (raster scanning has less loss)

Point in acceleration chain	Efficiency	1/Efficiency	# of particles
At patient (for single spill)			***1.00E+10***
Scanning (5ms/voxel+1.5ms loss switching)	***77%***	1.30	1.30E+10
Transfer line	***100%***	1.00	1.30E+10
Extraction (ES 95%, MS 95%)	***90%***	1.11	1.44E+10
Stabilising start of spill	***90%***	1.11	1.60E+10
Acceleration	***100%***	1.00	1.60E+10
Trapping	***90%***	1.11	1.78E+10
Injection (single turn)	***95%***	1.05	1.87E+10
Linac	***85%***	1.18	2.20E+10
RFQ	***85%***	1.18	2.59E+10
LEBT	***90%***	1.11	2.88E+10
Contingency	***90%***	1.11	3.20E+10
No. of particles from source for fill			**3.20E+10**
Revolution time [s]			1.23E-06
Kicker rise time [s]			***250.E-09***
Source current [A]			**5.20E-03**
Nominal cycle time [s]	Ramp-up [s]	***0.72***	
	Spill [s]	***1***	
	Ramp-down [s]	***0.52***	2.24
Minimum duty cycle			4.40E-07
Current in transfer line for space-charge calculations			**3.58E-03**

4.2 Proton passive scanning with single-turn injection

Based on a high loss scatterer (60%)

Point in acceleration chain	Efficiency	1/Efficiency	# of particles
At patient (for single spill)			***2.00E+10***
Scanning (passive spreading)	***40%***	2.50	5.00E+10
Transfer line	***100%***	1.00	5.00E+10
Extraction (ES 95%, MS 95%)	***90%***	1.11	5.54E+10
Stabilising start of spill	***90%***	1.11	6.16E+10
Acceleration	***100%***	1.00	6.16E+10
Trapping	***90%***	1.11	6.84E+10
Injection (single turn)	***95%***	1.05	7.20E+10
Linac	***85%***	1.18	8.47E+10
RFQ	***85%***	1.18	9.96E+10
LEBT	***90%***	1.11	1.11E+11
Contingency	***90%***	1.11	1.23E+11
No. of particles from source for fill			**1.23E+11**
Revolution time [s]			1.23E-06
Kicker rise time [s]			***250E-09***
Source current [A]			**0.020**
Nominal cycle time [s]	Ramp-up [s]	***0.72***	
	Spill [s]	***0.25***	
	Ramp-down [s]	***0.52***	1.49
Minimum duty cycle			6.61E-07
Current in transfer line for space-charge calculations			**0.014**

4.3 Carbon ion active scanning with single-turn injection
Based on voxel scanning (raster scanning has less loss)

Point in acceleration chain	Efficiency	1/Efficiency	# of particles
At patient			***4.00E+08***
Scanning (voxel 5ms, switching 1.5 ms)	***77%***	1.30	5.19E+08
Transfer line	***100%***	1.00	5.19E+08
Extraction (ES 95%, MS 95%)	***90%***	1.11	5.76E+08
Stabilising start of spill	***90%***	1.11	6.40E+08
Rebunching to change harmonic	***90%***	1.11	7.11E+08
Acceleration	***100%***	1.00	7.11E+08
Trapping	***90%***	1.11	7.90E+08
Injection (single turn)	***95%***	1.05	8.31E+08
Stripping	***95%***	1.05	8.75E+08
Linac	***85%***	1.18	1.03E+09
RFQ	***85%***	1.18	1.21E+09
LEBT	***90%***	1.11	1.35E+09
Contingency	***90%***	1.11	1.49E+09
No. of particles from source for fill			**1.49E+09**
Revolution time [s]			2.06E-06
Kicker rise time [s]			***250E-09***
Source electrical current for C4+ ions [A]			**529.8E-06**
Nominal cycle time [s]	Ramp-up [s]	***0.87***	
	Spill [s]	***1***	
	Ramp-down [s]	***0.52***	2.39
Minimum duty cycle			7.57E-07
Current in transfer line for space-charge calculations			**465.1E-06**

4.4 Proton passive scanning with multi-turn injection
Particle inventory is identical to Section 4.2 after injection.

Point in acceleration chain	Efficiency	1/Efficiency	# of particles
Injected beam (multi-turn)			7.20E+10
Linac provides 3.1 effective turns over 28	***11%***	9.03	6.50E+11
RFQ	***85%***	1.18	7.65E+11
LEBT	***90%***	1.11	8.50E+11
Contingency	***90%***	1.11	9.45E+11
No. of particles from source for fill			**9.45E+11**
No. of turns to fill			2.80E+01
Filling time [s]			34.58E-06
Source current [A]			**4.4E-03**
Nominal cycle time [s]	Ramp-up [s]	***0.72***	
	Spill [s]	***0.25***	
	Ramp-down [s]	***0.52***	1.49
Minimum duty cycle			2.32E-05
Current in transfer line for space-charge calculations			**3.01E-03**

4.5 Carbon ion active scanning with multi-turn injection
Particle inventory is identical to Section 4.3 after injection.

Point in acceleration chain	**Efficiency**	**1/Efficiency**	**# of particles**
Injection (multi-turn)			8.31E+08
Linac provides 3.6 effective turns over 16	***23%***	4.44	3.69E+09
Stripping	***95%***	1.05	3.89E+09
RFQ	***85%***	1.18	4.57E+09
LEBT	***90%***	1.11	5.08E+09
Contingency	***90%***	1.11	5.65E+09
No. of particles from source for fill			**5.65E+09**
No. of turns to fill			1.60E+01
Filling time [s]			32.9E-06
Source electrical current for C4+ ions [A]			**110.E-06**
Nominal cycle time [s]	Ramp-up [s]	0.87	
	Spill [s]	1	
	Ramp-down [s]	0.52	2.39
Minimum duty cycle			1.38E-05
For space charge calculations electrical current for C6+ in transfer line			**108.E-06**

5. Particle fluxes and counting rates

	Protons		**Carbon ions**	
Active scanning	**Maximum**	**Minimum**	**Maximum**	**Minimum**
Particle count rate in 'nozzle', d*N*/d*t* [s^{-1}]	***1.00E+10***	1.60E+07	***4.00E+08***	6.40E+05
Spot size [mm^2]	***10 x 10***	***4 x 4 ****	10 x 10	4 x 4 *
Particle flux in 'nozzle', $d^2N/dS/dt$ [s^{-1} mm^{-2}]	1.00E+08	1.00E+06	4.00E+06	4.00E+04
Measurement bin [s]	50 or 100 E-06			
Clock frequency [Hz]	10 or 20 E+03			

* Note larger spots would have the same minimum flux density, but higher count rates.

Passive spreading				
Particle count rate in 'nozzle', d*N*/d*t* [s^{-1}]	***8.00E+10***	8.00E+08	-	-
Irradiation field [mm^2]	***200 x 200***	200 x 200		
Particle flux in 'nozzle', $d^2N/dS/dt$ [s^{-1} mm^{-2}]	2.00E+06	2.00E+04	-	-
Measurement bin [s]	0.01			
Clock frequency [Hz]	1000			

6. Geometry and lattice (see Fig. 1)

Total length of injection lines [m]	***81***
Circumference of main ring [m]	***75.24***
Total length extraction lines [m]	***352***

	Survey reference points for central orbits (see Fig. 1)			
	***X* [m]**	***Y* [m]**	***Z* [m]**	**Θ_H [rad]**
A - Origin for survey - Centre of SS-MR-01	***0.0000000***	***0.0000000***	***1.2000000***	***0.0000000***
B. - Exit electrostatic injection septum	1.3500000	0.0476000	1.2000000	0.0001000
C. - Geometric centre of ring	0.0000000	11.2774992	1.2000000	(not applicable)
D. - Entry electrostatic extraction septum	-9.1957403	3.5542853	1.2000000	5.4973616
E. - Entry 1st magnetic extraction septum	-1.7439963	-0.0514844	1.2000000	0.0008847
F. - Entry to 1st proton gantry line	31.5802750	6.9227145	1.2000000	0.4640930
G. - Entry to 1st proton fixed line	43.2052379	12.7416695	1.2000000	0.4640930
H. - Entry to 2nd proton gantry	54.8302008	18.5606244	1.2000000	0.4640930
I. - Entry to 1st fixed carbon line	66.4551637	24.3795794	1.2000000	0.4640930
J. - Entry to 1st carbon gantry	89.7050896	36.0174894	1.2000000	0.4640930
K. - End of dump line	113.4594959	47.9079205	1.2000000	0.4640930
L. - Matching point	3.2019592	16.6292738	1.2000000	3.6056857
M.- Exit to "dog leg"	12.7925536	21.4299117	1.2000000	3.6056857
N. - Exit of proton linac	24.0178725	27.0488224	1.2000000	3.6056857
O. - Entry to 'dog leg'	28.4156020	20.3176173	1.2000000	3.6056857
P. - Exit of carbon ion linac	42.8377857	27.5367404	1.2000000	3.6056857

[**Note:** Θ_H is angle from *X*-axis to the beam line viewed in the beam direction]

	Twiss parameters at survey reference points			
	β_x [m]	**α_x [m]**	**β_z [m]**	**α_z [rad]**
Ring values at point A on centre line				
Nominal injection optics (carbon)	8.308453	0.000000	2.880571	0.000000
Detuned space-charge injection (protons)				
Nominal acceleration (all particles)	8.308454	0.000000	2.880571	0.000000
Nominal extraction (all particles)	8.562042	0.000000	2.847754	0.000000
Injection values at point B				
Carbon ions	8.527808	-0.162485	5.700000	0.000000
Protons for passive spreading	7.031034	-0.199660	3.700000	0.000000
Injection lines				
L. - Matching point	5.697696	1.374086	5.697696	-1.374086
M. - Exit to 'dog leg'	5.697696	-1.374086	5.697696	1.374086
N. - Exit of proton linac (assumed)	***0.600000***	***0.000000***	***1.000000***	***0.000000***
O. - Entry to 'dog leg'	5.697696	1.374086	5.697696	-1.374086
P. - Exit of carbon ion linac (assumed)	***0.600000***	***0.000000***	***1.000000***	***0.000000***
Extraction lines				
D. - Entry electrostatic extraction septum	***5.000000***	***0.000000***	6.522903	-0.170839
E. - Entry magnetic extraction septum	19.694645	-0.941142	3.829498	0.609620
F. - Entry to 1st proton gantry line	3.000000	0.000000	3.000000	0.000000
G. - Entry to 1st proton fixed line	3.000000	0.000000	3.000000	0.000000
H. - Entry to 2nd proton gantry	3.000000	0.000000	3.000000	0.000000
I. - Entry to 1st fixed carbon line	3.000000	0.000000	3.000000	0.000000
J. - Entry to 1st carbon gantry	3.000000	0.000000	3.000000	0.000000
K. - End of dump line	3.000000	0.000000	3.000000	0.000000

NOTE: β_z values in the extraction lines are set by the phase-shifter-stepper in the range 1-27m.
The values in the above table have been chosen arbitrarily as the nominal 'hand-over' values.

	Dispersion parameters at survey reference points			
	D_x [m]	dD_x/ds [m]	D_z [m]	dD_z/ds [m]
Main ring values at point A				
All working conditions	0.000000	0.000000	0.000000	0.000000
Injection values at point B				
All working conditions	0.000000	0.000000	0.000000	0.000000
Injection lines				
Points L, M, N, O and P	0.000000	0.000000	0.000000	0.000000
Extraction lines				
D. - Entry electrostatic extraction septum	***1.942000***	***-0.025000***	0.000000	0.000000
E. - Entry magnetic extraction septum	4.208048	0.489268	0.000000	0.000000
F, **G**, **H**, **I**, **J** and **K**	0.000000	0.000000	0.000000	0.000000

7. Standard working lines

	Nominal injection	Unload line for sp. charge inj.	Nominal acceleration	Nominal extraction
Horizontal tune, Q_x	1.6800	1.7642	1.6800	1.6666
Vertical tune, Q_z	1.7200	1.8293	1.7200	1.7200
Horizontal chromaticity, dQ_x/(dp/p)	-3.5000	-3.5000	-3.6550	-3.6550
Vertical chromaticity, dQ_z/(dp/p)	-3.5000	-3.5000	-1.1580	-1.1580
Gamma transition	1.983	2.031	1.983	1.979

Note that the chromaticities are calcuated and set by tracking

8. The "waiting" beam at injection

Protons	**Injection**	**Extraction**			
Nominal full dp/p of beam	***0.00728***	***0.004***	(Total Ex=Ez=	12.50π mrad)	mm
Maximum allowable full dp/p of beam	***0.0085***	At least 0.0089			
Carbon ions	**Injection**	**Extraction**			
Nominal full dp/p of beam	***0.00586***	***0.004***	(Total Ex=Ez=	30.53π mrad)	mm
Maximum allowable full dp/p of beam	***0.0062***	At least 0.0089			

9. Betatron core

Length of core [m]	***1.5***	
Maximum flux change [Weber]	***2.386***	(I.e. +/- 1.193)
dp/p gain for carbon ions at 400MeV/u	0.0050	

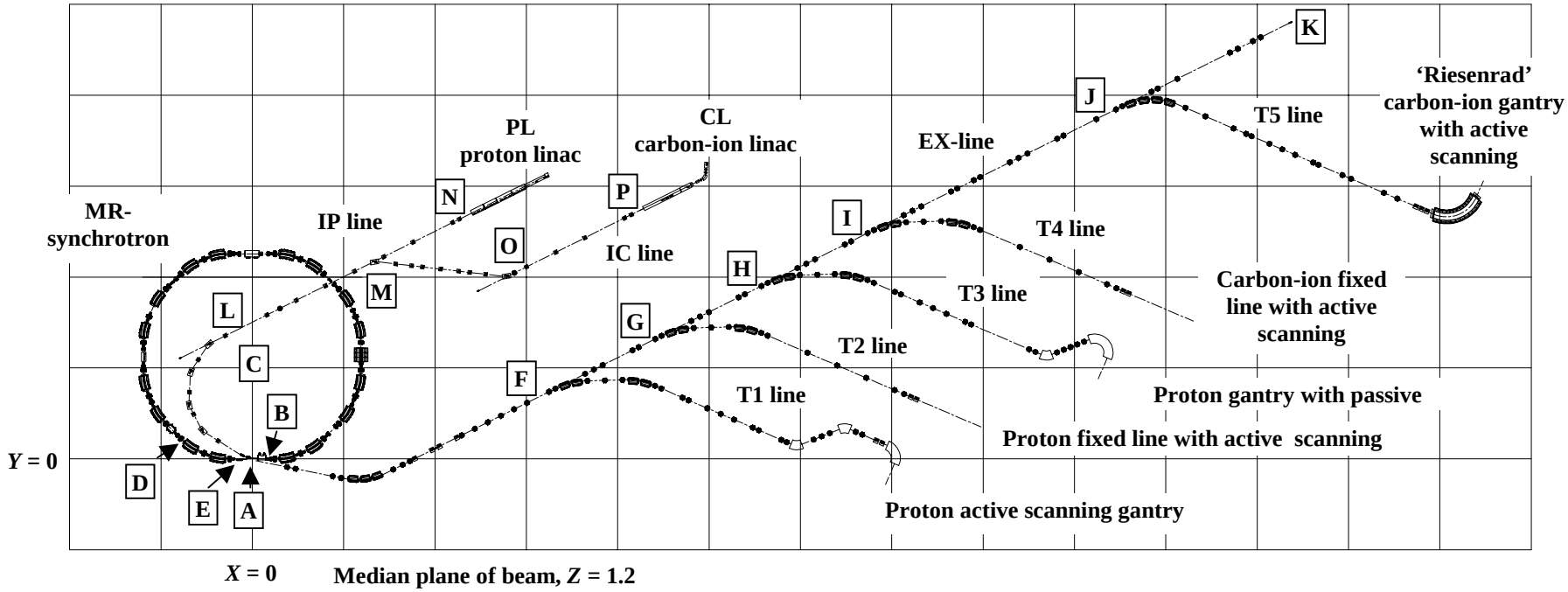

Grid size 10 m

Figure 1 Reference points in the PIMMS accelerator complex

10. At entry to electrostatic septum

Electrostatic septum kick [rad]	***0.0025***			
Effective length of electrostatic field [m]	***0.8000***			
Voltage at 1st extraction energy [kV/cm]	**For protons:**	3.6373	**For ions:**	27.5864
Voltage at top extraction energy [kV/cm]		13.9813		42.4881

10.1 Extraction separatrices for protons - at entry to electrostatic septum (see Fig. 2)

	Inner edge of beam		**Outer edge of beam**	
On-resonance protons	**60 MeV**	**250 MeV**	**60 MeV**	**250 MeV**
Radial position [m] (thickness of wire 0.1mm)	***0.035000***	0.035000	0.045028	0.045028
Angle [rad]	0.000449	0.000449	0.000338	0.000338
Spiral step [m]	**0.010028**	0.010028		
Off-resonance protons	**60 MeV**	**250 MeV**	**60 MeV**	**250 MeV**
Radial position [m] (thickness of wire 0.1mm)	0.035000	0.035000	0.040713	0.042249
Angle [rad]	0.000460	0.000481	0.000383	0.000387
Spiral step [m]	0.005713	0.007249		
Extracted momentum spread	**60 MeV**	**250 MeV**		
Momentum spread extracted from resonance	-0.001107	-0.000825		
Waiting' beam, Ex, tot, geom [π mm mrad]	7.143	3.339	(Theoretical values)	
Values given by extraction calculation	7.158	3.366	(Best matches obtained)	

10.2 Extraction separatrices for ions - at entry to electrostatic septum

	Inner edge of beam		**Outer edge of beam**	
On-resonance carbon ions	**120 MeV/u**	**400 MeV/u**	**120 MeV/u**	**400 MeV/u**
Radial position [m] (thickness of wire 0.1mm)	0.035000	0.035000	0.045028	0.045028
Angle [rad]	0.000449	0.000449	0.000338	0.000338
Spiral step [m]	0.010028	0.010028		
Off-resonance carbon ions	**120 MeV/u**	**400 MeV/u**	**120 MeV/u**	**400 MeV/u**
Radial position [m] (thickness of wire 0.1mm)	0.035000	0.035000	0.040713	0.042093
Angle [rad]	0.000460	0.000478	0.000383	0.000384
Spiral step [m]	0.005713	0.007093		
Extracted momentum spread	**120 MeV/u**	**400 MeV/u**		
Momentum spread extracted from resonance	-0.001107	-0.000860		
Waiting' beam, Ex, tot, geom [π mm mrad]	7.143	3.662		
Values given by extraction calculation	7.158	3.687		

11. At entry to magnetic septum (see Fig. 2)

11.1 Extraction separatrices for protons - at entry to magnetic septum

	Inner edge of beam		Outer edge of beam	
On-resonance protons	**60 MeV**	**250 MeV**	**60 MeV**	**250 MeV**
Radial position [m]	0.050365	0.050365	0.056025	0.056025
Angle [rad]	0.000291	0.000291	-0.000980	-0.000980
Off-resonance protons	**60 MeV**	**250 MeV**	**60 MeV**	**250 MeV**
Radial position [m] (thickness of wire 0.1mm)	0.046992	0.048072	0.050056	0.052014
Angle [rad]	-0.000982	-0.000791	-0.001380	-0.001296

11.2 Extraction separatrices for ions - at entry to magnetic septum

	Inner edge of beam		Outer edge of beam	
On-resonance carbon ions	**120 MeV/u**	**400 MeV/u**	**120 MeV/u**	**400 MeV/u**
Radial position [m]	0.050365	0.050365	0.056025	0.056025
Angle [rad]	0.000291	0.000291	-0.000980	-0.000980
Off-resonance carbon ions	**120 MeV/u**	**400 MeV/u**	**120 MeV/u**	**400 MeV/u**
Radial position [m] (thickness of wire 0.1mm)	0.046992	0.047935	0.050056	0.051771
Angle [rad]	-0.000982	-0.000815	-0.001380	-0.001310

11.3 Circulating separatrices at magnetic septum

On-resonance protons	**60 MeV**	**250 MeV**
Radial position [m]	0.027756	0.027756
Off-resonance protons		
Radial position [m]	0.024381	0.025462
On-resonance carbon ions	**120 MeV/u**	**400 MeV/u**
Radial position [m]	0.027756	0.027756
Off-resonance carbon ions		
Radial position [m]	0.024381	0.253243

11.4 Gap, radial position and space allocation for magnetic septum

Radial position of outermost circulating separartrix (on-resonance particles) [m]	0.027756
Radial position of innermost edge of extracted segments (off-resonance particles) [m]	0.046992
Determined by the innermost edge of the extracted segment and the circulating separatrices	**0.0192**
Clearance between circulating separatrix and vacuum pipe [m]	0.0020
Thickness of main ring vacuum pipe [m]	0.0015
Space for magnetic shield [m]	0.0010
Alignment tolerance and air gap [m]	0.0007
Insulation of septum coil [m]	0.0005
Septum coil [m]	0.0095
Insulation of septum coil [m]	0.0005
Alignment tolerance [m]	0.0005
Thickness of extraction vacuum pipe [m]	0.0010
Clearance between extraction vacuum pipe and extracted beam [m]	0.0020
Radial position of septum current wall [m]	**0.032956**

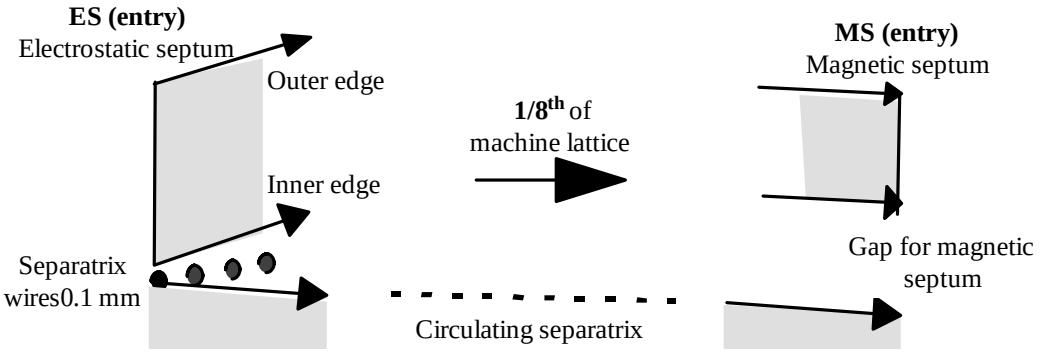

Figure 2 Schematic view of separatrices at the electrostatic and magnetic septa

12. Apertures and vacuum chambers

12.1 Nominal synchrotron vacuum chamber, physical aperture, "good-field" region

Some elements, e.g. kickers have special chambers and are treated individually in the main report.

Vacuum chamber	Stainless steel	2mm wall	Curved in dipoles	
Physical apertures	**Half-width**	**Half-height**	**Form**	
Outside main dipoles [m]	***0.070***	***0.037***	***'Super-ellipse'***	***(x/a)^3+(y/b)^3=1***
Inside main dipoles [m]	***0.07***	***0.032***	***'Super-ellipse'***	***(x/a)^3+(y/b)^3=1***
Good' field' region	**Injection**		**Top energy**	
	Half-width	**Half-height**	**Half-width**	**Half-height**
Outside main dipoles [m]	***0.0600***	***0.0300***	0.0600	***0.0150***
Inside main dipoles [m]	***0.0570***	***0.0280***	0.0570	***0.0145***

12.2 Nominal extraction-line vacuum chamber, physical aperture, "good-field" region

Some elements, e.g. bumpers have special chambers and are treated individually in the main report.

Vacuum chamber	Stainless steel	1.5mm wall	Curved in dipoles	
Physical apertures	**Half-width**	**Half-height**	**Form**	
Outside main dipoles [m]	***0.035***	***0.035***	***Circular***	
Inside main dipoles [m]	***0.350***	***0.026***	***'Super-ellipse'***	***(x/a)^3+(y/b)^3=1***
'Good' field region	**Half-width**	**Half-height**		
Outside main dipoles [m]	***0.0270***	***0.0260***		
Inside main dipoles [m]	***0.0410***	***0.0260***		

12.3 Nominal injection-line vacuum chamber, physical aperture, "good-field" region

Some elements, e.g. septa have special chambers and are treated individually in the main report.

Vacuum chamber	Stainless steel	1.5mm wall	Curved in dipoles	
Physical apertures	**Half-width**	**Half-height**	**Form**	
Outside main dipoles [m]	***0.035***	***0.035***	***Circular***	
Inside main dipoles [m]	***0.350***	***0.025***	***'Super-ellipse'***	***(x/a)^3+(y/b)^3=1***
Good' field' region	**Half-width**	**Half-height**		
Outside main dipoles [m]	***0.0280***	***0.0195***		
Inside main dipoles [m]	***0.0280***	***0.0195***		

13. Vacuum systems

	Synchrotron	Extraction line	Injection line
Target average pressure [Torr]	***1.00E-09***	***1.00E-08***	***1.00E-08***
Basic network of ion pumps	***16 x 100 l/s***	***17 x 30 l/s***	***4 x 30 l/s***
Additional pumps for crossings, rotatory joints etc.	***2 x 450 l/s***	***12 x 100 l/s***	***2 x 100 l/s***
TM mobile roughing mobile	***80-450 l/s***	***-***	***-***
No. of sector valves	***3***	***7***	***6***

14. Multi-turn injection

	Protons		Carbon ions	
Nominal injection energy [MeV/u]	***20.0***		***7.0***	
Precise d*p/p of beam* wrt C.O. of ring	***-0.0018***		***-0.0021***	
Horiz. functions β-x [m] and α-x of beam	**7.0310**	***-0.1997***	***8.5300***	***-0.1620***
(Matched to ring for carbon and detuned ring for protons)				
*D*x and d*D*x/ds of the incoming beam	**0.0000**	***0.0000***	***0.0000***	***0.0000***
Vert. functions β-z [m] and α-z of beam	**3.7000**	***0.0000***	***5.7000***	***0.0000***
(Mismatched wrt ring)				
*D*z and d*D*z/ds of incoming beam	**0.0000**	***0.0000***	***0.0000***	***0.0000***
Injected beam at exit to electrostatic septum in local ring coordinates				
Radial x [m] and dx/ds respectively	**-0.0456**	***-0.0004***	***-0.0476***	***-0.0001***
Vertical *z [m]* and dz/ds respectively	**0.0026**	***0.0000***	***0.0045***	***0.0000***
Injected beam emittances (total = 5 RMS)				
Horizontal [π mm mrad] (assumed)	**5.0000**		***8.0000***	
Vertical [π mm mrad] (assumed)	**5.0000**		***8.0000***	
Septum wall [m] (local ring coordinates)	**-0.0041**		***-0.0041***	
Initial kick in bumper magnets in ring [rad]	**0.0082**		***0.0074***	
No. of turns for linear collapse of inj. bump	***28.0000***		***16.0000***	
Effective turns inside wanted emittance	***3.1000***		***3.6000***	
Final diluted emittances (total = 5RMS)				
Horizontal [π mm mrad]	12.5016		30.4550	
Vertical [π mm mrad]	12.5016		30.4550	
Dilution factor	2.5		3.8	

15. Linac parameters (assumed)

	Proton	Carbon
Nominal energy [MeV/u]	***20***	***7***
Frequency [MHz]	***200.0***	***200.0***
Current [emA]	***0.110***	***4.400***
Pulse width [μs]	***200.0***	***200.0***
Repetition rate [Hz]	***1.0***	***1.0***
Norm. RMS emittance both planes [π mm mrad]	***1.0***	***1.0***
Unnorm. total emittances (5RMS) both planes [π mm mrad]	5	8
Twiss functions at entry to injection lines:		
$\alpha x = \alpha z$	***0.00***	**0.00**
βx	***0.60***	**0.60**
βz	***1.00***	**1.00**
d*p/p* RMS before debunching cavities	***0.0010***	**0.0015**
d*p/p* RMS after debunching cavities	***0.0005***	**0.0005**

16 Stripping foil C4+ to C6+ (approx. values)

Foil material	***Carbon***	
Foil thickness [micro-gm/cm2]	***200***	
Efficiency fpr stripping	***Eff= 95%***	
Energy loss per nucleus [MeV]	***0.034***	
Emittance blow-up	***7%***	($\beta x=\beta z$=2m assumed)
d*p/p* to be added quadratically	***0.00014***	
Temperature rise	***<40K***	

17. Tolerances (gantries not included)

Field tolerances	**Systematic across aperture**	**Random between units**	**Setting prec.**	**DAC**
Main dipole	***+/- 2E-4***	***+/- 8E-4***	***+/-8E-5***	***14 bit***
Main quadrupole	***+/- 5E-4***	***+/- 1.6E-3***	***+/- 3.5E-5***	***16 bit***
Sextupole	***+/- 4E-3***	***+/- 4E-3***	***+/- 4E-3***	***10 bit***
Dipole corrector	***< +/-1E-2***	***< +/- 1E-2***	***+/- 5E-3***	***12 bit + sign***
Betatron core	***-***	***-***		***18 bit + sign***
				(16 bit just acceptable)
Extraction line dipole	***+/- 5E-4***	***+/- 1E-3***	***+/-2.5E-4***	***12 bit***
Extraction line quadrupole	***+/- 1E-3***	***+/- 1E-3***	***+/-5E-4***	***12 bit + sign***
Injection line dipole	***+/- 5E-4***	***+/- 1E-3***	***+/-2.5E-4***	***12 bit***
Injection line quadrupole	***+/- 1E-3***	***+/- 1E-3***	***+/-5E-4***	***12 bit + sign***

Mechanical tolerances	**Profile**	**Length**	**Weight**	**Packing factor**
Main dipole	***+/- 0.01 mm***	***+/- 1.5 mm***	-	***96% +/-1.5%***
Main quadrupole	***+/- 0.01 mm***	***164 lamin.***	***+/- 1.6E-3***	***(70% nom.)***
Sextupole	***+/- 0.1 mm***	***143 lamin.***	***+/- 4E-3***	***(97.5% nom.)***
Dipole correctors	***+/- 0.1 mm***	***+/- 1 mm***	***-***	***96% +/-1.5%***

Extraction and injection line units not considered.

18. Current ripple tolerances for synchrotron

	Allowable current ripple $\Delta I/I_{max}$			
	10 Hz	**100 Hz**	**1000 Hz**	**10000 Hz**
Main dipole	1.2 E-04	1 E-05	8 E-07	1.5 E-06
Main quadrupoles (F!, F2, D)	1.2 E-04	1 E-05	8 E-07	1.5 E-06
Chromaticity sextupoles (SF, SD)	2.5 E-03	2 E-04	1 E-05	1 E-05
Resonance sextupole	2.5 E-03	2 E-04	1 E-05	1 E-05
Betatron core	2.5 E-03	2 E-04	1 E-05	1 E-05
Horizontal dipole correctors	5 E-03	1 E-03	1 E-04	1 E-04

19. Magnet and RF cavity inventory

	No. in operation	No. spares	Installed water [l/min]
Main dipole (1 family)	***16+1****	***1+ coils***	***751.4***
Main quadrupole (3 families)	***24+3****	***1+coils***	***148.5***
Main ring sextupole (3 families)	***5***	***1+coils***	***30.65***
Main ring horizontal corrector	***10***	***2***	***Air-cooled***
Main ring vertical corrector	***8***	***2***	***Air-cooled***
Betatron core	***1***	***0***	***Air-cooled***
Tune kicker	***2***	***1***	***Air-cooled***
Injection bumper	***2***	***1***	***Air-cooled***
Dump bumper	***2***	***1***	***Air-cooled***
Air-cored correction quadrupole	***1***	***0***	***Air-cooled***
Extraction line dipole	***23***	***coils***	***416.3***
Extraction line quadrupole	***130***	***2+coils***	***442***
Extraction line horizontal corrector	***20***	***1***	***Air-cooled***
Extraction line vertical corrector	***20***	***1***	***Aircooled***
Chopper bumpers	***4***	***1+coils***	***6.68***
Raster scanners	***9***	***2+coils***	***21.42***
Thin' magnetic extraction septum	***1***	***coils***	***12.5***
Thick' magnetic septum	***1***	***coils***	***43.7***
Electrostatic extraction septum	***1***	***selected comps***	***0***
Injection line dipole	***6***	***coils***	***15***
Injection line quadrupole	***25***	***1+coils***	***20***
Injection line horizontal corrector	***10***	***1***	***Air-cooled***
Injection line vertical corrector	***10***	***1***	***Air-cooled***
Magnetic injection septum	***2***	***coils***	***15***
Electrostatic injection septum	***1***	***selected comps***	***0***
RF cavity	***1***	***selected comps***	***105***
Riesenrad dipole	***1***	***0***	***214.2***
Proton gantry dipoles (not included)	***3***	***0***	***not incl.***
* Additional units are for the field display			
Total			2242.35

20. Magnet cycles (see Fig. 3)

Breakdown of synchrotron cycle	**Minimum**	**Maximum**	**Comments**
Parabola from bottom of cycle [ms]	70.00		
Flat bottom for injecting [ms]	50.00		Inject
Acceleration to extraction plateau [ms] *	110.78	693.98	Accelerate beam
Flat top extraction plateau [ms]	250	1000	Extract beam
Rapid start to up-ramp [ms]	8		No beam
Linear ramp [ms]	0	385.46	400 MeV/u carbon is top of cycle
Smooth end to ramp	50		No overshoot
Rapid start to down-ramp [ms]	8		
Linear down ramp	450.05		Always the same
Smooth end to ramp	50		No overshoot
End of cycle	8		

* Cosine form for RF programme and 'round-in' and 'round-out'.

Synchrotron cycle sets injection and extraction plateaux on the upwards hysteresis curve

Extraction line sets extraction settings on the downward hysteresis curve

Injection line sets injection settings on upward branch of hysteresis curve, but there are only 2 levels

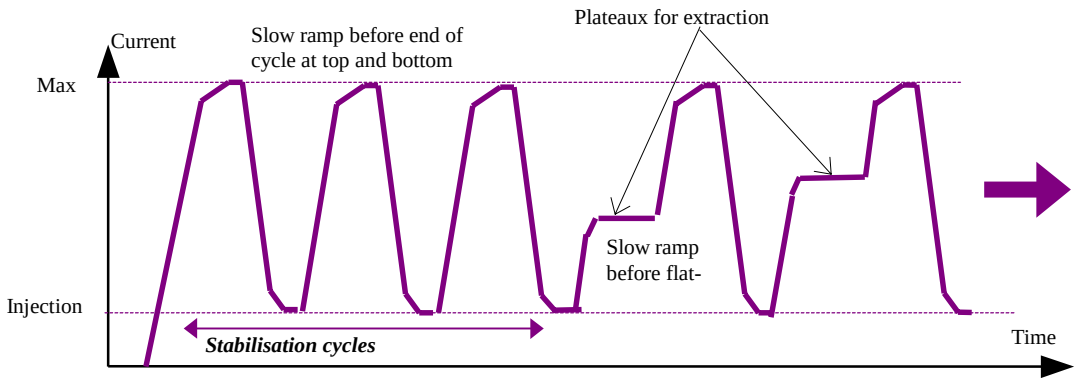

(a) Synchrotron current cycle

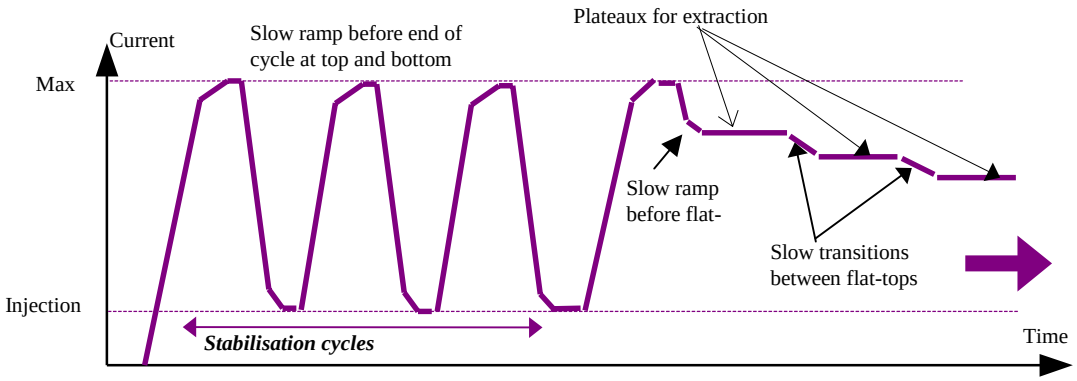

(b) Extraction line and gantry current cycle

Figure 3 Current cycle

21. Layout drawings

21.1 Mnemonics for sectors in the accelerator complex

Proton linac	PL	Main ring	MR
Carbon linac	CL	Main extraction line to dump	EX
Injection line from proton linac to main ring	IP	Secondary extraction lines from the main extraction line to treatment rooms	T1, T2, T3 etc,
Injection line from carbon linac to proton injection line	IC		

21.2 Mnemonics for accelerator elements

SS	Straight section (drift space)	BC	Betatron core	SH	Schottky monitor
QF	Focusing quadrupole	DK	Dump bumper	SC	Beam scraper
QD	Defocusing quadrupole	QK	Tune kicker	FO	Stripping foil
QR	Rotating quadrupole	ES	Electrostatic septum	ST	Beam stopper
QS	Skew quadrupole	MS	Magnetic septum	DP	Beam dump
QA	Air-cored, correction quad.	CA	RF cavity	CO	Collimator
XR	Resonance sextupole	CT	Fast current transformer	VP	Vacuum ion pump
XC	Chromaticity sextupole	DC	Slow current transformer	VG	Vacuum gauge
MB	Main dipole in synchrotron	WB	Wide-band pickup	SV	Sector valve
HB	Horiz. bending dipole in lines	LS	Scintillator screen	IC	Ionisation chamber
HC	Horiz. corrector dipole	PX	Horiz. beam position monitor	RF	Ridge filter
VC	Vert. corrector dipole	PY	Vert. beam position monitor	SC	Scatterer
SW	Switching dipole in lines	PM	Profile monitor	RA	Raster scanning dipole
BU	Bumper dipole				

The following layout drawings include all drift spaces in the synchrotron, the areas of principal interest in the extractions lines and the crossing point of the injection line and the synchrotron. For more detailed information, look on the CD-ROM at the element listings in the lattice files and look at the CAD layout drawings.

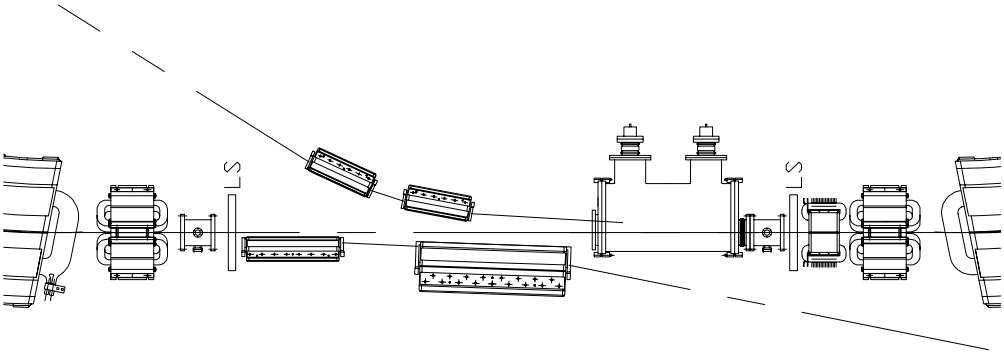

SS40-SS01-SS02

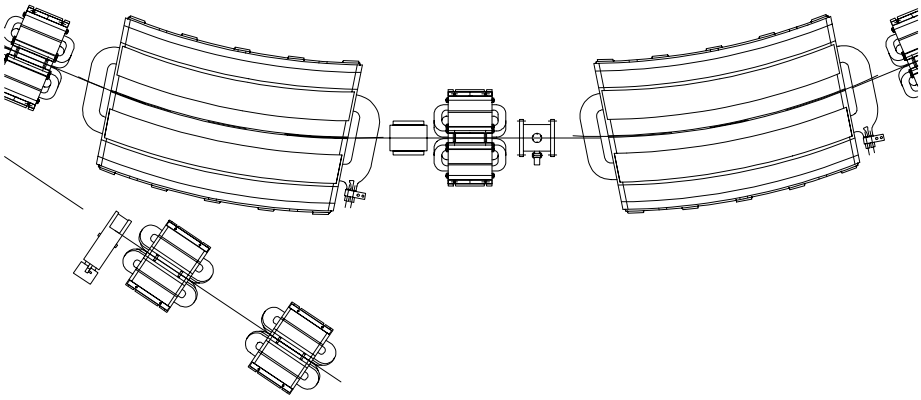

SS03 SS04

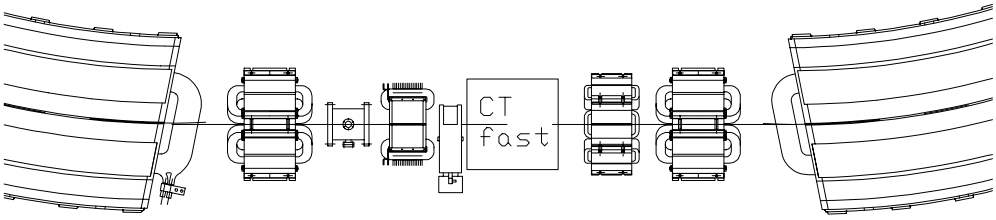

SS05-SS06-SS07

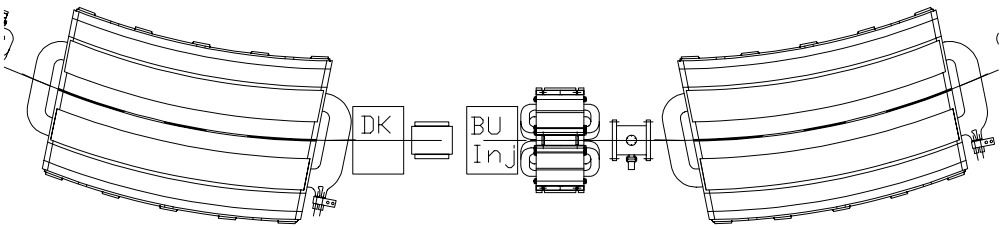

SS08-SS09

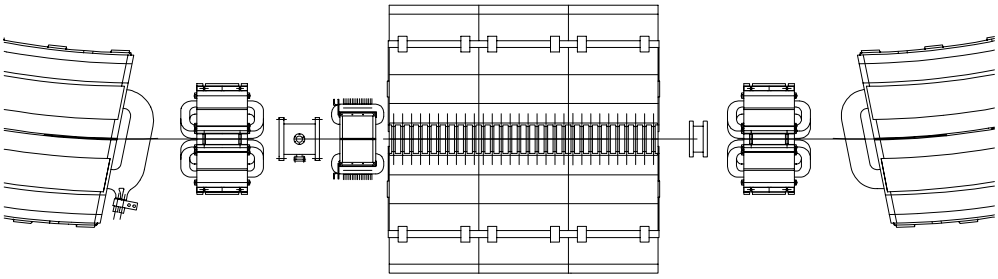

SS10-SS11-SS12

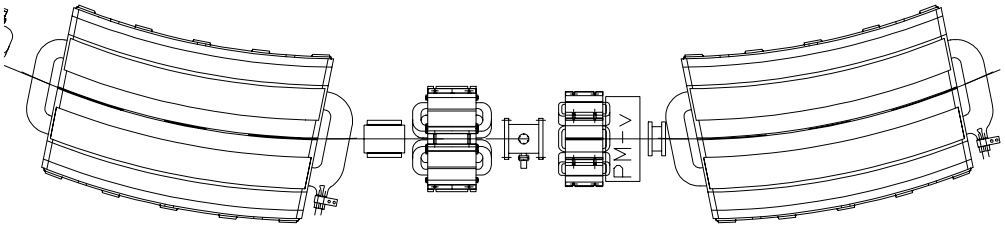

SS13-SS14

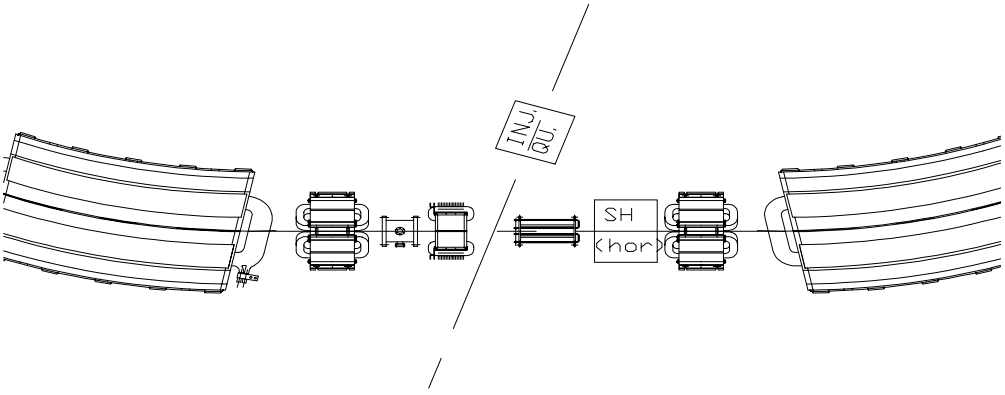

SS15-SS16-SS17

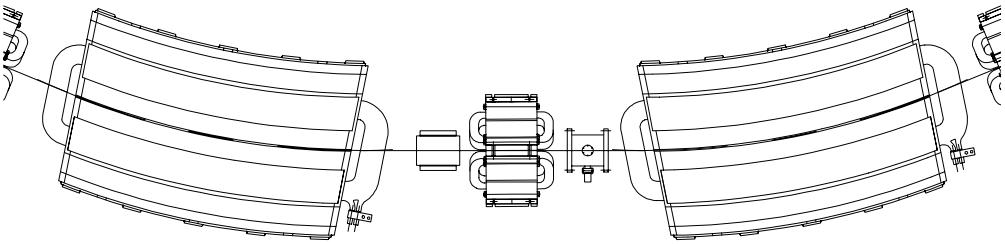

SS18-SS19

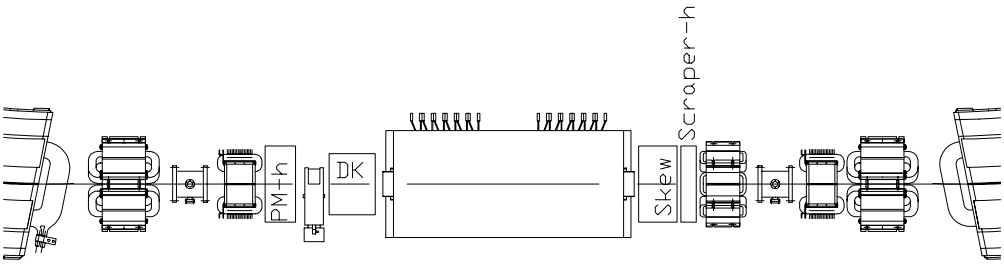

SS20-SS21-SS22

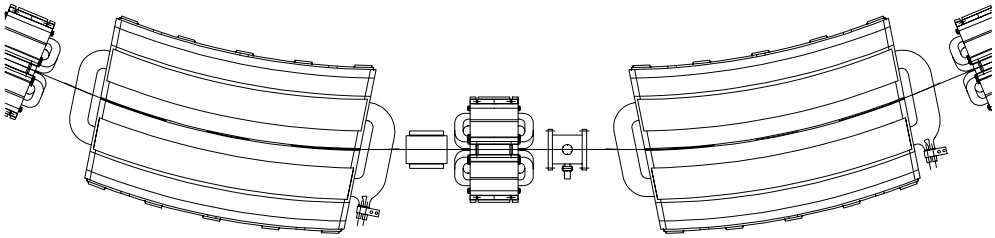

SS23-SS24

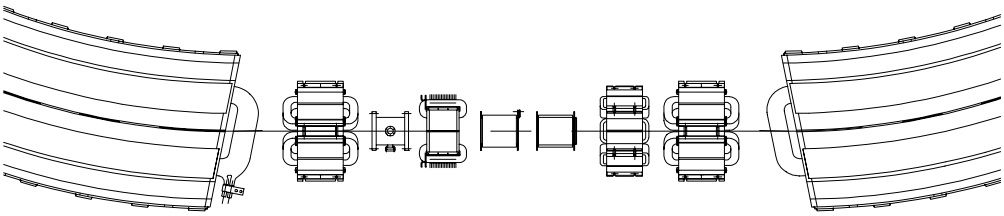

SS25-SS26-SS27

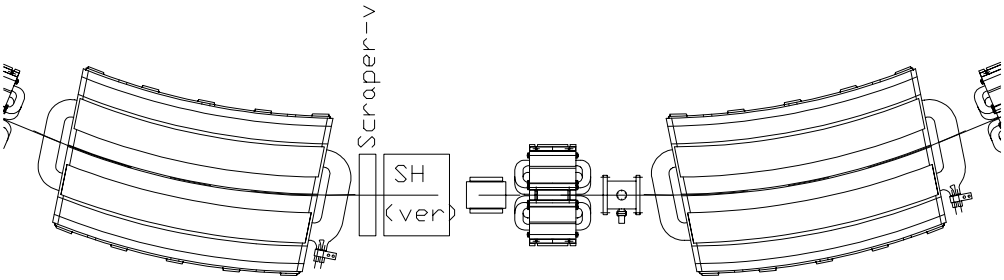

SS28-SS29

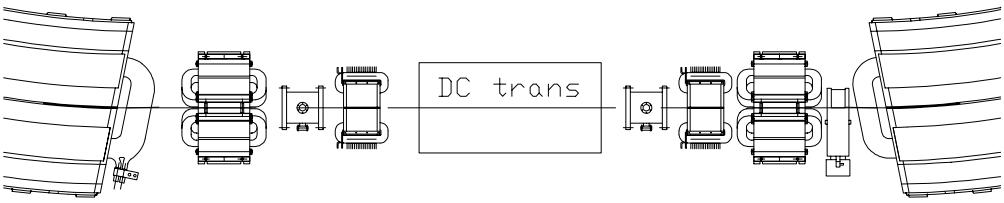

SS30-SS31-SS32

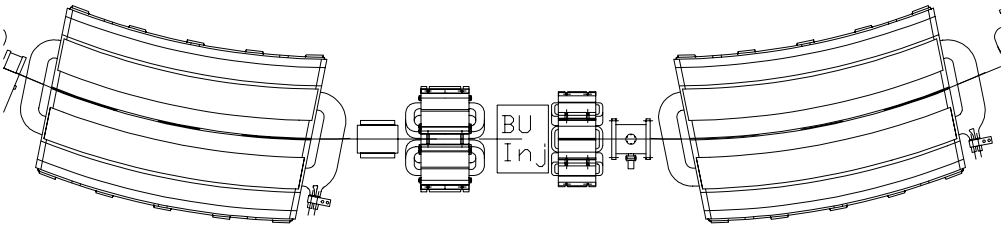

SS33-SS34

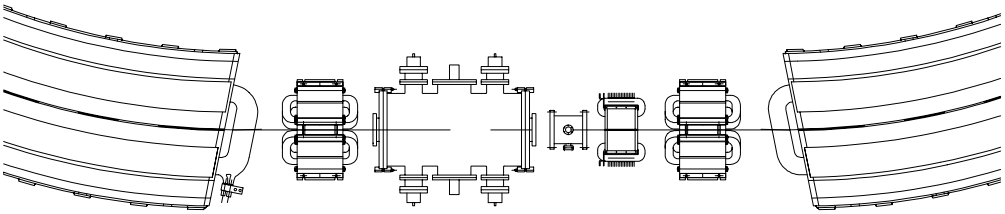

SS35-SS36-SS37

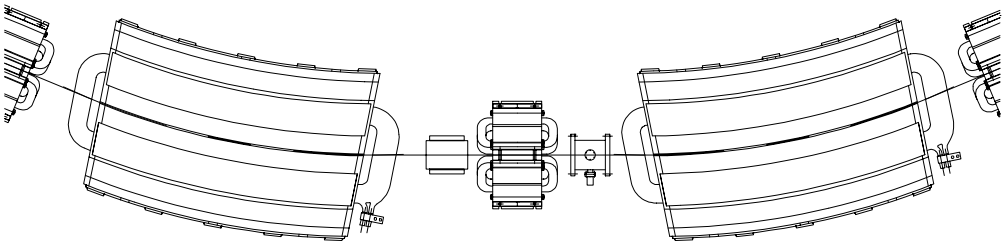

SS38-SS39

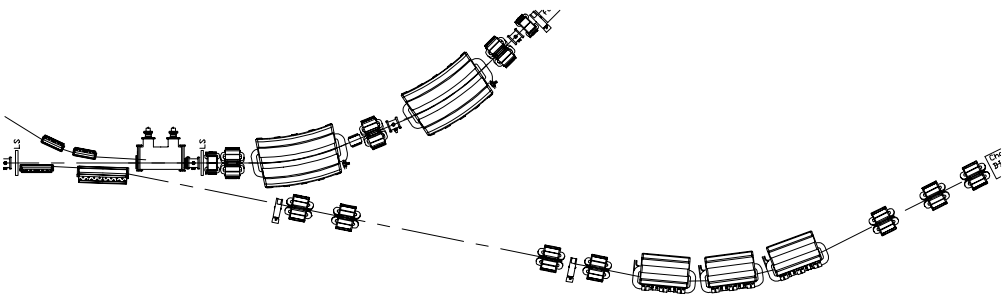

Region between the ring and the main extraction line with vehicle track

Chopper and phase-shifter-stepper in extraction line

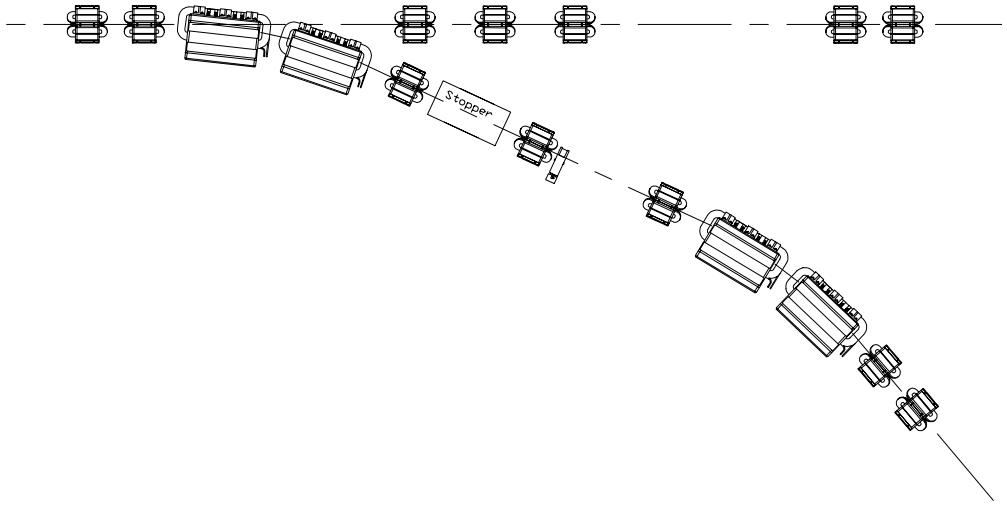

Standard proton extension/deflection module

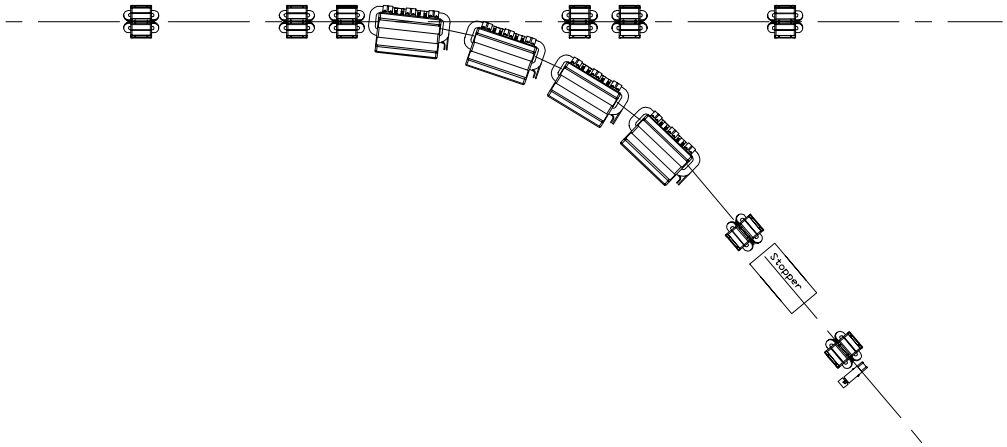

Riesenrad extension/deflection module

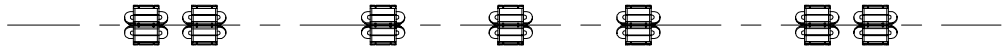

Standard proton rotator

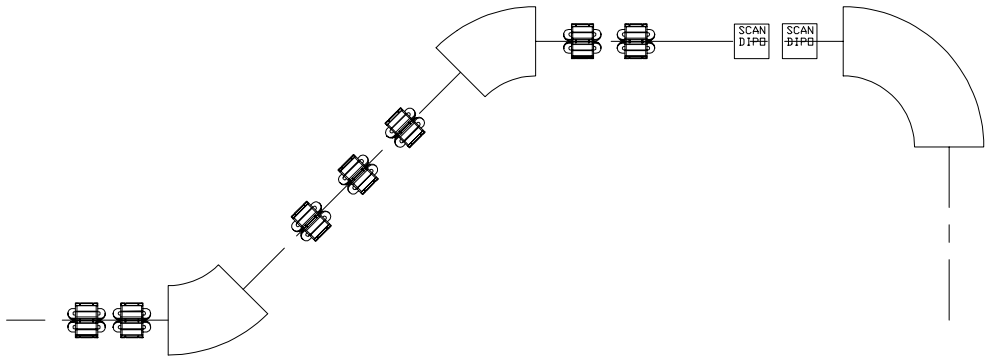

Proton gantry with active scanning

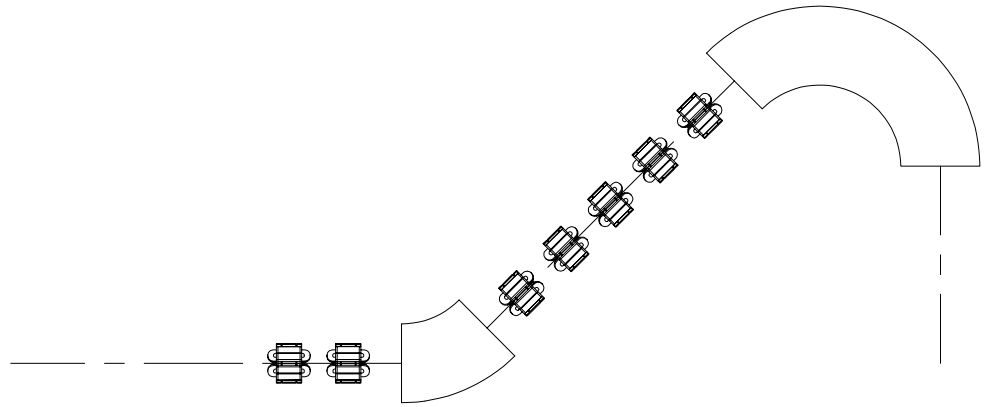

Proton gantry with passive spreading

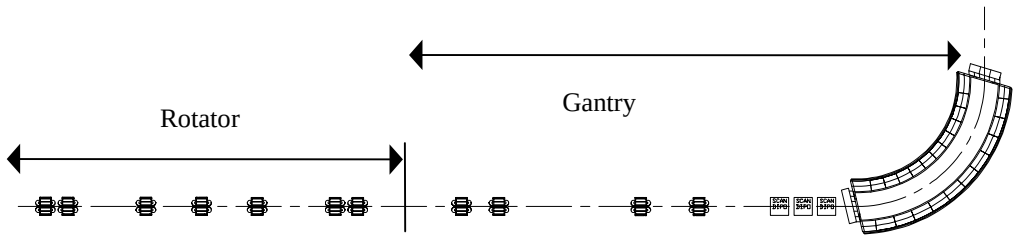

‘Riesenrad’ gantry with its rotator

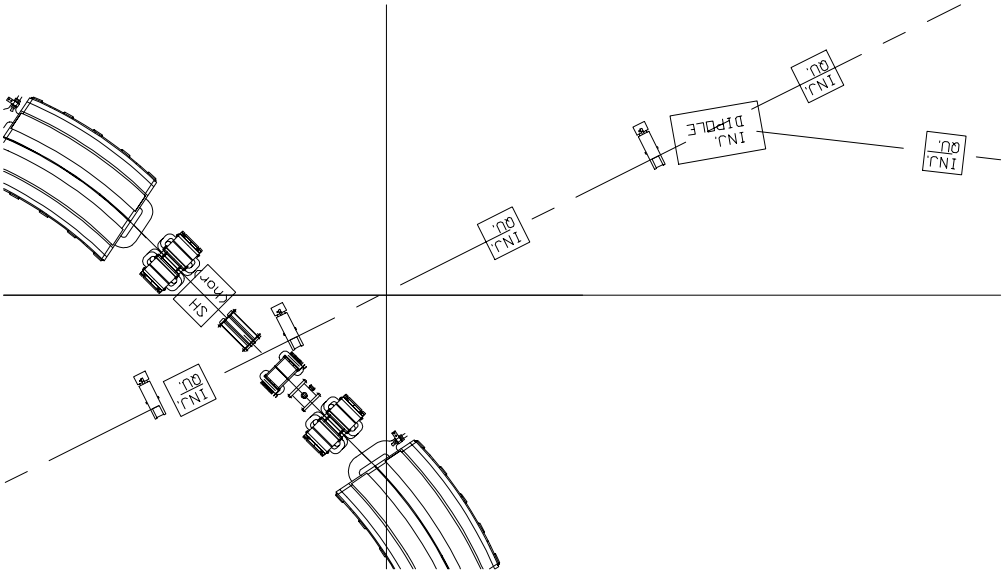

Region where injection line crossing ring

For design details of particular elements see Appendices E to BB.
For listings of the elements in the ring and lines see the lattice files on the CR-ROM
For magnet settings see the lattice files on the CD-ROM
To modifiy parameters use the interactive EXCEL file on the CD-ROM

* * *